# Deliverable 5.4 & 5.6: FUTuRE – Final technical report on radionuclide mobility in compacted clay systems and reversibility of sorption

Work Package 5

The project leading to this application has received funding from the European Union's Horizon 2020 research and innovation programme under grant agreement No 847593.

**Document information**

| | |
|---|---|
| Project Acronym | **EURAD** |
| Project Title | **European Joint Programme on Radioactive Waste Management** |
| Project Type | **European Joint Programme (EJP)** |
| EC grant agreement No. | **847593** |
| Project starting / end date | **1st June 2019 – 30 May 2024** |
| Work Package No. | **WP 5** |
| Work Package Title | **Fundamental Understanding of Radionuclide Retention** |
| Work Package Acronym | **FUTURE** |
| Deliverable No. | **D5.4 & D5.6** |
| Deliverable Title | **Final technical report on radionuclide mobility in compacted clay systems and reversibility of sorption** |
| Lead Beneficiary | **SCK CEN & PSI** |
| Contractual Delivery Date | **29.02.2024** |
| Actual Delivery Date | **25.01.2024** |
| Type | **Report** |
| Dissemination level | **Public** |
| Authors | **Norbert Maes (SCK CEN), Martin Glaus (PSI), Rainer Dähn (PSI), Sergey V. Churakov (PSI).** |

**To be cited as:**

Maes N., Glaus M., Rainer D., Churakov S.V. (eds). (2024): Final technical report on radionuclide mobility in compacted clay systems and reversibility of sorption. Final version as of 17.01.2024 of deliverable D5.4&D5.6 of the HORIZON 2020 project EURAD. EC Grant agreement no: 847593.

**Disclaimer**



**Acknowledgement**

This document is a deliverable of the European Joint Programme on Radioactive Waste Management (EURAD). EURAD has received funding from the European Union's Horizon 2020 research and innovation programme under grant agreement No 847593

| **Status of deliverable** | By | Date |
|---|---|---|
| Delivered (Lead Beneficiary) | Norbert Maes (SCK CEN), Martin Glaus (PSI), Rainer Dähn (PSI) | 28/11/2023 (first version)<br>17/01/2024 (final version) |
| Verified (WP Leader) | Sergey Churakov(PSI) | 15/12/2023 |
| Reviewed (Reviewers) | Sergey Churakov(PSI)<br>Norbert Maes(SCK CEN)<br>Martin Glaus(PSI)<br>Rainer Dähn (PSI)<br>Bernd Grambow (PMO) | 06/12/2023<br><br><br><br>26/12/2023 |
| Approved (PMO) | Bernd Grambow | 17/01/2024 |
| Submitted to EC (Coordinator) | ANDRA Coordinator | 25/01/2024 |

## Executive Summary

Within the EURAD WP5 FUTURE project, tasks 2.1 and 2.3 deal with the mobility of radionuclides in compacted clay and the reversibility of sorption, respectively.

The objectives of these tasks are to enhance the quantitative and mechanistic understanding of the impact on radionuclide mobility wrt. effects of solution composition and speciation, surface charge and microstructural properties of argillaceous porous media.

A “bottom-up” approach was followed using three pathways: i) *From dispersed to compacted solids* (Are sorption data measured in dispersed systems applicable for compacted systems?), ii) *From single minerals to clay rocks* (Can we describe the sorption and transport behaviour of radionuclides in mineral assemblages/clay host rocks by adding up effects described by model developed for the main mineral components?) and iii) *From single radionuclide to multi-component chemical systems* (How does the presence of competing elements influence the mobility of the radionuclide under study?).

These schemes were applied to three main groups of elements/radionuclides: weakly sorbing (anionic Se-species), moderately sorbing (Ra, Ba), and strongly sorbing (transition metals and lanthanides/actinides) and on a selection of clay phases (pure minerals: illite, smectites, kaolinite and their mixtures: clay rocks: Opalinus Clay (OPA), Callovo Oxfordian Clay (COx), Boda Claystone Formation (BCF).

Results obtained in the project provide convincing arguments that bottom-up schemes are applicable for the description of sorption processes albeit not always straightforward, as relevant underlying mechanisms and sorption competition aspects must be taken into account rigorously. The transferability of data and models has been established from dispersed to compacted systems and from single mineral to complex mineral assembly. New/missing data became available and have been successfully fed into sorption models.

Mechanistic understanding of anion exclusion and surface diffusion processes in saturated and partial saturated conditions has matured. More and more high-resolution techniques become used which enable the measurement of diffusion patterns for strongly sorbing radionuclides.

It is further demonstrated that mechanistic sorption models obtained from sorption studies can be applied in the interpretation of transport experiments if the pore water chemistry is properly taken into account.

An important breakthrough is the successful, in a number of systems, unification of sorption and diffusion concepts in which the same mechanistic models of sorption and chemical equilibrium are consistently used for the description of sorption and diffusion processes.

## Table of Contents

# Introduction

Within the EURAD WP5 FUTURE project, tasks 2.1 and 2.3 deal respectively with the mobility of radionuclides in compacted clay and the reversibility of sorption.

Because the task on mobility also comprises studies on sorption, these tasks are strongly connected and the outcome is reported in a combined report.

The objectives of these tasks are to enhance the quantitative and mechanistic understanding of the impact on radionuclide (RN) mobility wrt.:

- Charge effects (surface charge, anion exclusion, enhanced flux in the electric double layer)
- Solution chemistry and speciation (pH, Ionic Strength (IS), presence of competing elements)
- Microstructural effects (grain boundaries, water saturation, pore characteristics)

and to enable a better description of radionuclide mobility by identifying potential mobile surface species in relation to structural information.

The adopted approach is the so called “bottom-up” approach for which three schemes were considered:

- *From dispersed to compacted solids:* Are sorption data measured and models for dispersed systems applicable for compacted systems?
- *From single mineral to clay rock*: Can we describe the retention and transport behaviour of radionuclides (RN) in mineral assemblages/clay host rocks by adding up the effects described by the models developed for the main mineral components?
- *From single radionuclide to multi-element systems*: How does the presence of competing elements influence the mobility of the radionuclide under study?

The systems studied consisted of:

- Three main groups of elements/radionuclides: weakly, moderately and strongly sorbing radionuclides (further subdivided into transition metals (TM) and lanthanides/actinides (La/Ac)
- Single clay minerals (e.g. illite, smectites), clay mixtures and clay host rocks (OPA, COx, BCF), both in dispersed and compacted state.
- Fully saturated and partial saturated state

The methods used were ad(de)sorption experiments in dispersed and compacted systems, diffusion experiments (through-, in-, out-) and advanced spectroscopic characterisation techniques like EXAFS, µXAS, ATR-FTIR, LA-ICP-MS, TOF-SIMS/rL-SNMS, AMS,… used to get detailed information about metal speciation, redox state and/or high resolution spatial distribution of sorption complexes.

In order to streamline the R&D work of the different teams involved in the tasks (in view of the bottom-up schemes), and to achieve maximal complementarity between teams and already available data, a working matrix was set up at the start of the project. Two complementing matrices were set up, one for dispersed systems and one for compacted systems (see next page).

- Matrix for dispersed systems (in red - sorption reversibility)

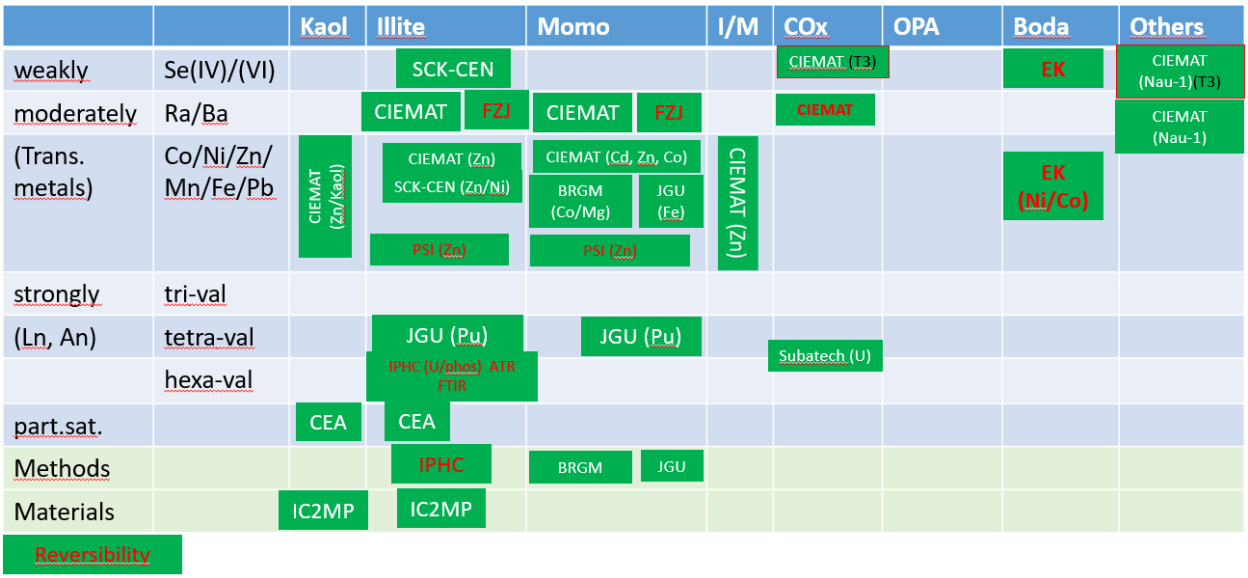


- Matrix for compacted systems

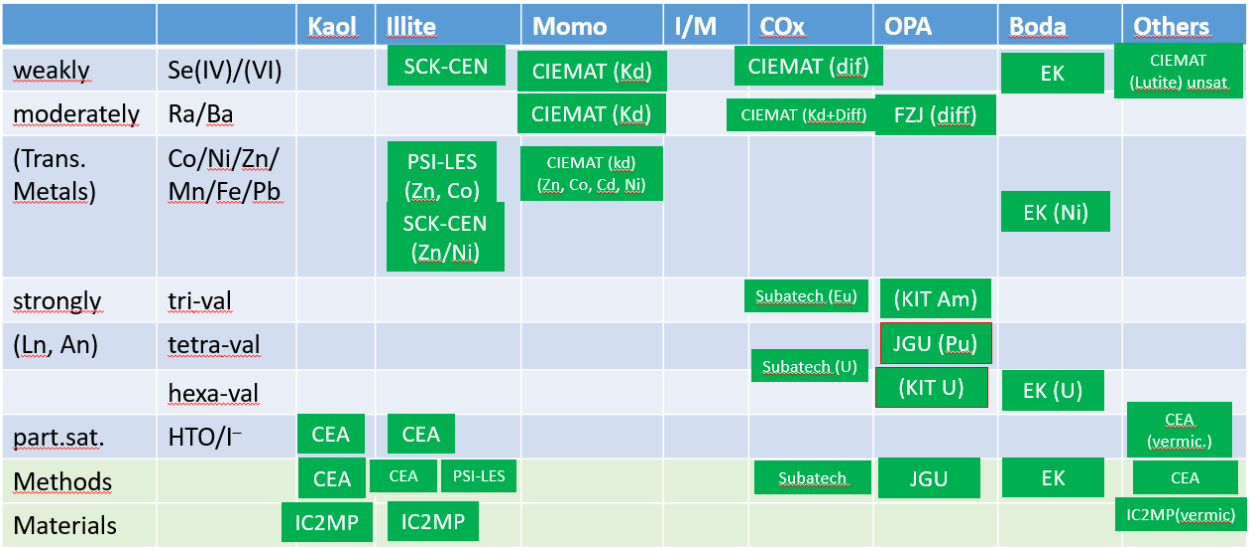


"Focus Groups" were established based on the main groups of elements studied + partial saturation to foster collaboration, data exchange, discussion of the results and to frame the outcome of the R&D work with respect to the project objectives.

The main chapters (1-5) of the report are in line with the subdivision of research activities into focus groups. The outcome/summary of achievements of the R&D related to the topic of the Focus Groups is summarised for each chapter based on a set of guiding questions that are related to the project objectives and which form the basis to update the SOTA report.

The guiding questions considered are:

- *Which new/missing data are made available that feed into sorption models (e.g. surface complexation constants)?*
- *Have you been able to show that batch sorption data are transferable to compact system?*
- *Are we able to transfer data from simple systems to complex systems? Could any differences between "pure" mineral phases and argillaceous rocks be observed?*
- *Can we adequately describe sorption competition?*
- *Have you been you able to show that sorption under certain conditions is irreversible, and if yes why?*
- *Has the knowledge on irreversible uptake processes improved currently used uptake/sorption models?*
- *Have the applied state-of-the-art spectroscopic, diffractometric and microscopic techniques been helpful to obtain a system understanding of irreversible uptake processes?*
- *Have you been able to describe your transport experiments based on mechanistic understanding (anion exclusion, surface diffusion, saturation degree, pore characteristics,…)?*
- *Did the advanced method(s) (e.g. spectroscopy) you used helped to come to better a understanding of the RN transport behaviour?*

# Chapter 1: Mobility of weakly/non-sorbing (anions) radionuclides in clay

Three research groups dealt with weakly sorbing anions within the Subtasks 2.1 and 2.3 of WP5 FUTURE. SCK CEN (Mol, Belgium) studied the mobility of selenate in pure illite. CIEMAT (Madrid, Spain) studied selenite adsorption in different clay materials including smectite (FEBEX clay) and nontronite (NAu-1 or NAu-2) and the Callovo-Oxfordian (COx) clay and selenite diffusion in COx and a Spanish sedimentary rock. EK (Budapest, Hungary) studied the adsorption and diffusion of selenite in samples representing Boda Claystone Formation (BCF), with co-operation of SCK CEN on diffusion modelling.

(note that the references for this chapter are combined at the end of the 3 contributions)

## 1. Mobility of monovalent and divalent anions in clays: comparison of through-diffusion of iodine ($I^-$) and selenate ($SeO_4^{2-}$) in illite

L. Van Laer, M. Aertsens, D. Verhaegen, N. Maes
*SCK CEN, Mol, Belgium*

### Abstract

The sorption and diffusion of the divalent selenate $SeO_4^{2-}$ has been investigated in Na-conditioned illite. The batch sorption experiments at pH 7 confirmed that selenate does not sorb under these experimental conditions. The diffusion of $SeO_4^{2-}$ was studied by means of through-diffusion experiments in flushed filter diffusion cells at a pH of 8.15 (pH representative for Boom Clay conditions). Diffusion studies of the neutral HTO (as benchmark) and iodine $I^-$ were performed as well in order to assess the difference in anion exclusion between monovalent and divalent non-sorbing anions. At a low ionic strength (0.01 M) the anion accessible porosity η of both anions (0.14 for $I^-$ and 0.06 for $SeO_4^{2-}$) was significantly lower than the accessible water porosity (average 0.41), which is due to the anion exclusion effect. This effect was more pronounced for the divalent $SeO_4^{2-}$ (±14% of total porosity) than the monovalent $I^-$ (±34% of total porosity). The obtained effective diffusion coefficients $D_e$ ($1.7 \times 10^{-11}$ m²/s for $I^-$ and $3.1 \times 10^{-12}$ m²/s) show that diffusion of anions is significantly lower than diffusion of water (average $D_e$ for HTO $1.7 \times 10^{-10}$ m²/s) at low ionic strength (0.01M). At higher ionic strength (0.1 M), this difference becomes smaller due to the decreasing anion exclusion effect (compression of the diffuse double layer). For $I^-$ the anion accessible porosity equalled even the water porosity (~no exclusion), but the effective diffusion coefficient $D_e$ ($5.5 \times 10^{-11}$ m²/s) was nevertheless still lower due to a lower apparent diffusion coefficient $D_a$. For $SeO_4^{2-}$ there are no results available for the higher ionic strength due to experimental problems.

### Introduction

One of the main objectives in the EURAD work package 5-FUTURe: 'Fundamental understanding of radionuclide retention and transport in clay and crystalline rocks' was to increase the fundamental insights of the impact of the diffusive double layer of the clay minerals on the mobility of radionuclides. While the diffusive double layer can lead to enhanced the flux of the cations in the system, the double layer reduces the mobility of anions by anion exclusion. This mechanism whereby anionic species become repelled by the negatively charged surface of the clay minerals, limits the accessibility of the anions to certain pores (smallest size and access restriction by constrictivity effects) and reduces their mobility to a more narrow domain ("free" water vs. "DL" water) in the bigger pores (anion accessible porosity < total water porosity). This exclusion effect is stronger at lower ionic strength due to the larger thickness of the electrical double layer. One of the questions is how strong the anion exclusion effect is for divalent ions. There are multiple studies available in the literature on monovalent ions (like chloride or iodide), but divalent ions are much less studied. Former studies performed by SCK CEN with divalent anions on Boom Clay (De Cannière et

al., 2010) lead to the hypothesis that this exclusion effect can be more pronounced for divalent anions, but this was not confirmed by dedicated studies.

The focus of this study is on the divalent $SeO_4^{2-}$ anion, since the mobility of this Se species is expected to be the highest among the different oxidation states of Se and hence of most interest for the safety case. While the more reduced $SeO_3^{2-}$ (selenite) species is known to sorb weakly/modestly on illite (log $K_d$ between 2 and 0.6 when pH varies from 3 to 8.5 at [Se] = 5 x $10^{-8}$ M) (Bruggeman, 2006), $SeO_4^{2-}$ seems not to sorb. Goldberg (2014) observed no significant sorption of $SeO_4^{2-}$ on montmorillonite, nor on illite, except below pH 3. Regarding diffusion studies, diffusion of selenate has been reported for $SeO_4^{2-}$ in montmorillonite (Glaus et al., 2017), in Boom Clay (De Cannière et al., 2010) and in Callovo-Oxfordian Clay (Savoye et al., 2021), but data for illite were not reported before.

In addition, the diffusion of the monovalent iodine ($I^-$) is studied as well, in order to compare diffusion of monovalent and divalent anions in the same clay matrix and experimental conditions. To explore the effect of ionic strength on the anion exclusion the diffusion was planned to be performed at two different ionic strengths (0.01 and 0.1 M). Unfortunately, the $SeO_4^{2-}$ diffusion experiments at higher ionic strength (0.1M) faced experimental difficulties, which could not get solved.

## Materials & methods

### Clay

The studied clay is the Na-conditioned Illite du Puy from the homogenised batch used before in the EC CatClay project (Altmann et al., 2015).

### Radiotracer

As $^{75}Se$ was only available on the market as selenite ($SeO_3^{2-}$, Se(IV)), the radiotracer solution needed first to be oxidised to the selenate form ($SeO_4^{2-}$, Se(IV)). First, different oxidation methods were tested with inactive selenite in order to check which approach was the most applicable. Oxidants as $MnO_4^-$ were not appropriate, since they could not be removed from the solution after oxidation. Hydrogen peroxide, $H_2O_2$, was chosen, since the remaining $H_2O_2$ can be removed by evaporating the solution. It is, however, the least efficient oxidising agent in the list of possible oxidants (Liu et al., 2019), but in combination with UV digestion (which can initiate the formation of hydroxyl radicals) it can be sufficiently effective. After a few tests, the oxidation of selenite with $H_2O_2$ proved to be the most efficient when performing the oxidation in a UV digestor during 1h. To verify the efficiency of the oxidation, the solutions were analysed with Triple Quadrupole ICP-MS (8900 ICP-QQQ; Agilent Technologies, Santa Clara, CA, USA). This technique allowed to measure the different species of Se. For the radiotracer, we relied on the identical behaviour of the active selenite, since it was not possible to analyse active solution.

For the $I^-$ tracer, $^{125}I$ was used in NaI form. To avoid that other I species will form, the spike was diluted in 1 mM $NaHSO_3$ acidified to pH<2 with $H_2SO_4$. For the benchmark test, the neutral HTO was used as radiotracer.

### Sorption

Batch sorption tests with inactive $SeO_4^{2-}$ and active $SeO_4^{2-}$ and $SeO_3^{2-}$ were performed in a NaCl background solution of 0.01 M (with 0.1 mM KCl in order to avoid K leaching out of the illite). The experiments were performed at the natural pH of the illite (~7.15) without adding buffer. Suspensions of 10 g/L were prepared by adding 15 mL background solution to 0.15 g of clay. For the inactive test, the background solution was spiked with cold $SeO_4^{2-}$ (5x$10^{-7}$ M) (5 replicates). For the test with radioactive $^{75}SeO_4^{2-}$/$^{75}SeO_3^{2-}$ an aliquot of the active tracer solution was added first tot the background solution (3 replicates). After taking a subsample to determine the initial activity ($C_{in}$), the clay was added. The sorption tests with $^{75}SeO_3^{2-}$ in parallel were run in order to check the difference in sorption between the two Se species. After minimum 3 days of equilibration (shaking), the suspensions were centrifuged at 21000 g for

2 hours. Subsamples were taken for analysis of the equilibrium concentration or activity ($C_{eq}$). The distribution coefficient $K_d$ was determined by

$$K_d = \frac{C_{in} - C_{eq}}{C_{eq}} \cdot \frac{L}{S} \quad (1)$$

With $C_{in}$ the initial concentration/acitivity, $C_{eq}$ the equilibrium concentration/activity, $L/S$ the liquid-solid ratio (L/kg). For the inactive samples the total Se was measured with ICP-MS (Agilent 7700x, Soil and Water Chemistry, KULeuven). The active $^{75}$Se was measured with gamma-analysis (Packard Cobra Quantum gamma counter, RDD SCK CEN).

## Diffusion

### *Experimental*

The through-diffusion of the monovalent $^{125}I^-$ and divalent $SeO_4^{2-}$ was studied together with the through-diffusion of the inert HTO tracer, which was used as benchmark in order to verify, if there were no anomalies in the compacted clay plugs. The experimental set-up used was the flushed filter diffusion cell set-up (design slightly adapted from Glaus et al. (2015) (*Figure 1*). Clay plugs with dimensions of 20 mm diameter and 15 mm thickness were compacted in the diffusion cell at a dry bulk density of 1.7 g/cm³. At both sides filters (inox 316L, average pore width 11 µm) were placed with a thickness of 1.67 mm, through which the upstream and downstream solutions are pumped (radially in and perpendicularly out). Prior to the diffusion experiment the clay was saturated by submerging the diffusion cell in the background solution in a desiccator connected to a vacuum pump for at least two weeks. Afterwards the diffusion cell was connected to the upstream and downstream reservoir and the clay was further equilibrated by pumping tracer-free background solution for a few more days before starting the diffusion experiment. Once the tracers were added, the upstream solution (100 mL) was sampled regularly (100 µL) to monitor the evolution of the upstream concentration. The target solution (15 mL) was replaced with a tracer-free solution on a regular base (daily at the start, going to 3-2-2 days regime) in order to keep the concentration at the target side as low as possible. A subsample of 5 mL was analysed each time.

As background solution NaCl was chosen instead of $NaClO_4$ to avoid any possible competition between the perchlorate and selenate anions. KCl was added in low concentration (0.1 mM) in order to avoid K leaching out of the illite. The pH (8.15) was kept stable by adding 2 mM TRIS (tris(hydroxymethyl)aminomethane) buffer to the solution. The objective was to perform experiments at two different ionic strengths, i.e. 0.01 and 0.1 M.

Analysis of the samples was done with Liquid Scintillation Counting (Liquid Scintillation Counter Packard TriCarb 2100TR, RDD SCK CEN) and gamma-analysis (Packard Cobra Quantum gamma counter, RDD SCK CEN). The $^{125}$I and $^{75}$Se activities were measured with gamma-analysis. LSC activities give the combined activity of HTO and the $^{125}$I or $^{75}$Se. The HTO activity could be determined by subtracting the activity of $^{125}$I or $^{75}$Se obtained by gamma-analysis from the LSC activity, taking into account the different measuring efficiencies of gamma and LSC.

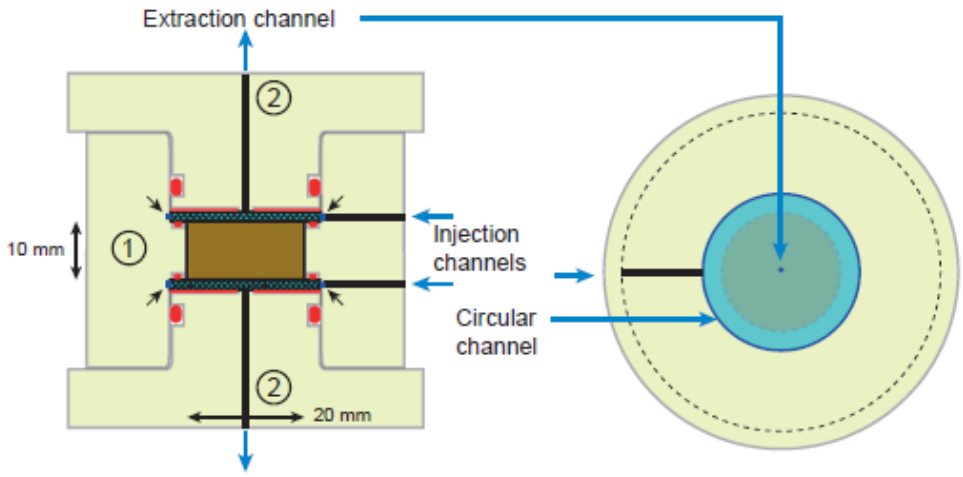


*Figure 1: Schematic presentation of the flushed filter diffusion cell (taken from Glaus et al., 2017).*

### *Parameter estimation*

Diffusion in a porous medium is determined by two parameters (i) the apparent diffusion coefficient $D_a$ ($m^2/s$) and (ii) the rock capacity factor $\eta R$ (-) being the product of the accessible porosity $\eta$ (-) and the retardation factor $R$ (-). The effective diffusion $D_e$ is defined as the product of the apparent diffusion coefficient and the capacity factor:

$$D_e = \eta R\, D_a \tag{2}$$

To take into account radioactive decay, the measured radionuclide concentrations are first recalculated to zero time. The diffusion parameters are determined by solving numerical solutions of the diffusion equation with the COMSOL® software coupled to Matlab for optimization. The optimal values are obtained by minimizing the $\chi^2$ function. Standard error theory is used to get the values of the errors (1σ) on the optimal values.

The boundary conditions of these experiments are that the tracer concentration in the upstream (resp. downstream) reservoir changes according to the flux into (resp. out from) the clay core. Besides, it is taken into account that after each measurement in the downstream reservoir, this reservoir is replaced by a tracer free volume. In case of flushed filters, the influence of the filters is neglected. The corresponding modelling code is *D2_diff_vol2_refresh*.

In order to compare the relative difference of the diffusion compared to the diffusion in water, the so-called 'normalised diffusion coefficient $D_{erw}$' or 'effective diffusion relative to water' is calculated as follows:

$$D_{erw} = \frac{D_e\,(anion) D_0\,(HTO)}{D_e\,(HTO) D_0 (anion)} \tag{3}$$

With $D_0$(HTO) = 2.20 × $10^{-9}$ m²/s, $D_0(I^-)$ = 2.06 × $10^{-9}$ m²/s and $D_0(SeO_4^{2-})$ = 1.07 × $10^{-9}$ m²/s (value of $SO_4^{2-}$, since no data are available for $SeO_4^{2-}$) (Li and Gregory, 1974).

## Results & discussion

### Sorption

The preliminary batch sorption test with $SeO_4^{2-}$ in NaCl 0.01 M at neutral pH (~7.15) confirmed that there was no significant sorption of selenate on the Na-conditioned Illite du Puy under these conditions. Therefore, it was decided not to perform a more extended sorption test. The sorption of $SeO_3^{2-}$ (selenite) was tested for comparison as well. Sorption appeared to be limited with $K_d$ values between 0.9 and 3.1 L/kg.

## Diffusion

For the experiments at 0.01 M with illite two replicates with HTO and $^{125}I$ and two with HTO and $^{75}SeO_4^{2-}$ were performed. The experimental data of the upstream concentration (Bq/mL), the downstream concentration (Bq/mL) and the downstream flux (Bq/cm²/day) are plotted together with the fitting results in *Figure 2* and *Figure 3*.

The experiments at the higher ionic strength of 0.1 M were unfortunately not successful. The experiments failed every time ±1 week after adding the radioactive spikes, except for one experiment with $^{125}I$. A leakage at the upstream side occurred every time due to blockage of the filter. Several tests were performed to find out what could cause this blockage of the filter (background solution, spikes, …), but no satisfactory explanation could be found for this recurring problem. For one experiment at 0.1 M with $^{125}I$ the blockage occurred only in a later phase of the experiments, hence we could obtain sufficient data points to model the data.

The obtained diffusion parameters are given in Table 1. Further, the $D_e$ and $\eta(R)$ for diffusion at 0.01 M are plotted in *Figure 4* to have a visual comparison. The $D_e$ values for HTO in illite packed at a bulk density of 1.7 g/cm³ (1.5-1.8 x $10^{-10}$ m²/s) correspond quite well to the $D_e$ obtained for HTO diffusion at 0.1 M in the CatClay project (average $D_e$ for SCK CEN diffusion experiments 1.85 (±0.29) x $10^{-10}$ m²/s). This confirms that the clay was properly compacted without any anomalies. The individual parameters that define $D_e$, i.e. the apparent diffusion coefficient $D_a$ and the capacity factor $\eta R$ show a larger variation, especially experiment 3 is deviating, but the overall $D_e$ values seem to be more robust. This is due to the mutual dependency of these parameters. In through-diffusion experiments $D_e$ is known to be the most reliable parameter.

The results of the diffusion parameters of the monovalent $I^-$ show clearly that the diffusion of the anion is significantly affected by the ionic strength, with $D_e$ at 0.01 M approximately 4 times smaller than at 0.1 M (keep in mind that only 1 result is available for $I^-$ at higher ionic strength). As retardation $R$ is assumed to be 1 (= no sorption) for HTO and $I^-$, the $\eta R$ can be reduced to accessible porosity $\eta$. This means that the accessible porosity for $I^-$ is approximately 3 times lower than for HTO for the ionic strength of 0.01 M. At the higher ionic strength of 0.1 M, the $\eta R$ showed a similar value as for HTO, hence the exclusion effect has diminished at this ionic strength. Since there is only one replicate and the knowledge that $\eta R$ and $D_a$ are correlated, it is of course difficult to make a strong conclusion on that, but the fact that the $D_a$ is similar at both ionic strengths (1.1-1.3 x $10^{-10}$ m²/s), which is in accordance to the expectations, gives more confidence in the $\eta R$ value. The $\eta R$ is, however, not the only factor that is affecting the effective diffusion. The $D_a$ of $I^-$ is approximately 3-4 times lower compared to HTO. When comparison is made relative to the diffusion in water ($D_{erw}$), it is shown that the $I^-$ diffusion is three times lower at 0.1 M and even ten times lower at 0.01 M ($D_{erw}$ 0.11).

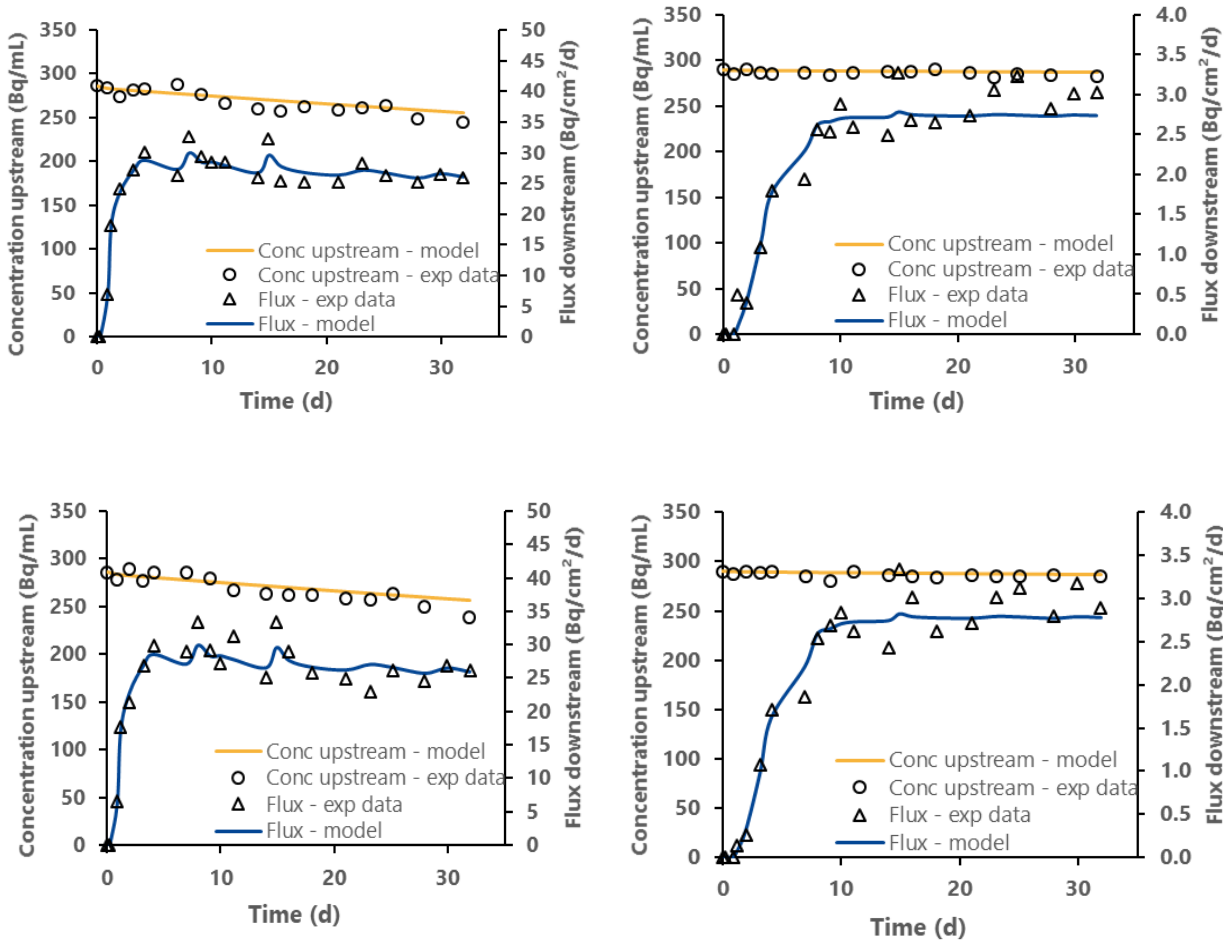


*Figure 2: Diffusion of HTO (left) and $^{125}I^-$ (right) of experiments E1 (top) and E2 (bottom) at ionic strength of 0.01 M (NaCl) and pH 8.15: experimental data (symbols) and fitted data (lines) of concentration inlet (Bq/mL) and flux outlet (Bq/cm²/d).*

The two replicate experiments with selenate at 0.01 M showed very reproducible parameters. Also for $SeO_4^{2-}$ no sorption has been observed, hence $\eta R$ can be reduced to the accessible porosity $\eta$ for this anion as well. It is expected that $\eta(R)$ would be higher at higher ionic strength as well, as observed for $I^-$, but the experiments failed unfortunately, so this could not be confirmed. The effect of the ionic strength on the anion exclusion could hence not be assessed for $SeO_4^{2-}$, but the comparison with the monovalent $I^-$ can still be made. The fit parameters show clearly that the diffusion of the divalent $SeO_4^{2-}$ is lower than for $I^-$. Both, $D_a$ and $\eta(R)$ parameters for $SeO_4^{2-}$ have values that are 2 times lower than for $I^-$. Hence, this results in a 4 times lower $D_e$. Compared relative to diffusion of water, selenate diffusion is 25 times lower ($D_{erw}$ 0.04).

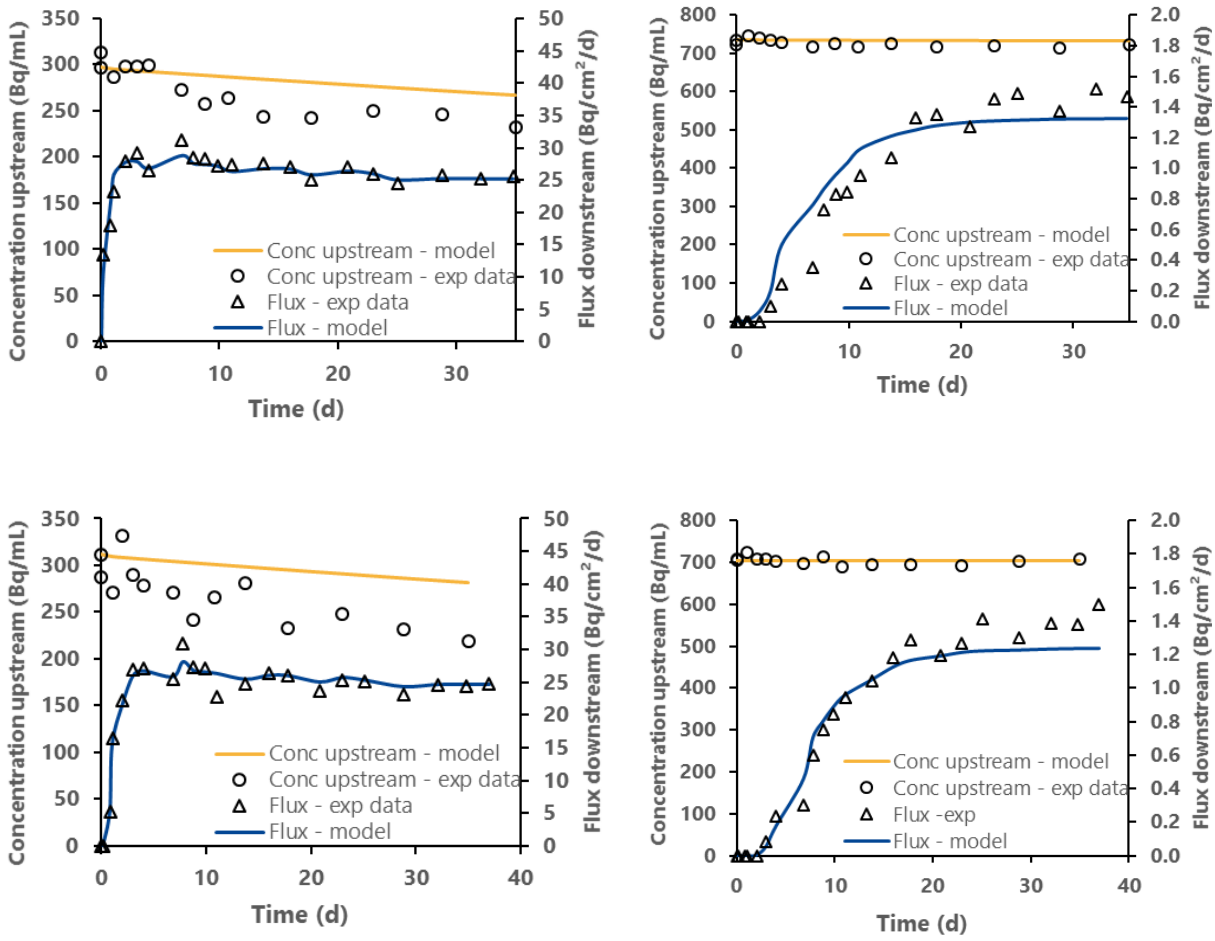


*Figure 3: Diffusion of HTO (left) and $^{75}SeO_4^{2-}$ (right) of experiments E3 (top) and E4 (bottom) at ionic strength of 0.01 M (NaCl) and pH 8.15: experimental data (symbols) and fitted data (lines) of concentration inlet (Bq/mL) and flux outlet (Bq/cm²/d).*

*Table 1: Fitted parameters ($D_a$ and ηR) and calculated ($D_e$) obtained from the through-diffusion experiments. The normalized diffusion coefficient ($D_{erw}$) expresses how the diffusion is related to the diffusion of HTO.*

**HTO**

| Exp | IS (M) | $D_a$ ($m^2/s$) | ηR (-) | $D_e$ ($m^2/s$) |
|---|---|---|---|---|
| 1 | 0.01 | **4.2E-10** ± 7.7E-12 | **0.42** ± 0.010 | **1.8E-10** ± 5.3E-12 |
| 2 | 0.01 | **4.0E-10** ± 1.1E-11 | **0.45** ± 0.016 | **1.8E-10** ± 7.9E-12 |
| 3 | 0.01 | **6.3E-10** ± 4.5E-11 | **0.27** ± 0.022 | **1.7E-10** ± 1.8E-11 |
| 4 | 0.01 | **4.3E-10** ± 2.2E-11 | **0.36** ± 0.025 | **1.5E-10** ± 2.2E-11 |

**$I^-$**

| Exp | IS (M) | $D_a$ ($m^2/s$) | ηR (-) | $D_e$ ($m^2/s$) | $D_{erw}$ |
|---|---|---|---|---|---|
| 1 | 0.01 | **1.3E-10** ± 5.6E-12 | **0.13** ± 0.010 | **1.7E-11** ± 1.4E-12 | **0.10** |
| 2 | 0.01 | **1.1E-10** ± 3.5E-12 | **0.15** ± 0.009 | **1.7E-11** ± 1.1E+12 | **0.10** |
| 10 | 0.1 | **1.3E-10** ± 1.1E-11 | **0.41** ± 0.049 | **5.5E-11** ± 8.0E-12 | **0.35** |

**$SeO_4^{2-}$**

| Exp | IS (M) | $D_a$ ($m^2/s$) | ηR (-) | $D_e$ ($m^2/s$) | $D_{erw}$ |
|---|---|---|---|---|---|
| 3 | 0.01 | **5.6E-11** ± 1.8E-12 | **0.06** ± 0.004 | **3.1E-12** ± 2.3E-13 | **0.04** |
| 4 | 0.01 | **5.5E-11** ± 2.2E-12 | **0.06** ± 0.004 | **3.1E-12** ± 2.6E-13 | **0.04** |

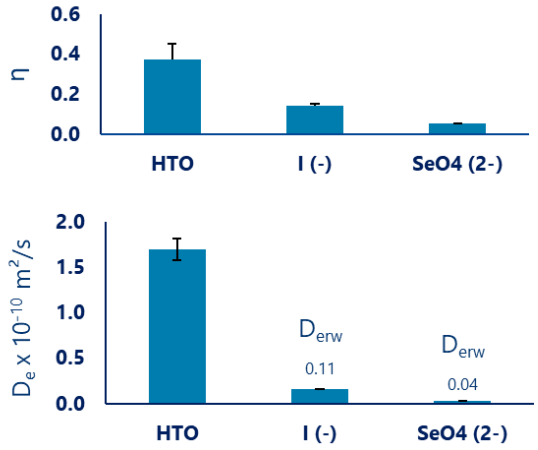


*Figure 4: Average ηR (reduced to η in the graph as R=1) and $D_e$ parameter values (n=2) for HTO, $I^-$, $SeO_4^{2-}$ in Na-illite du Puy at 0.01 M NaCl - pH 8.15.*

At last, the diffusion parameters of $SeO_4^{2-}$ in illite can be compared with earlier obtained diffusion parameters in other clays or clayrocks, just to see it in a wider context. The values cannot be compared directly with each other, as the experimental conditions (ionic strength, pH) and the clay properties are very different. The comparison shows that the diffusion parameters in illite are in the same order of magnitude than in Boom Clay ($D_e$ 7.3 x $10^{-12}$ $m^2/s$) (De Cannière et al., 2010) and Callovo-Oxfordian Clay ($D_e$ 1.9 x $10^{-12}$ $m^2/s$) (Savoye et al., 2021), while the $D_e$ in montmorillonite (packed at a density of 1.9 $g/cm^3$ and ionic strength of 0.1 M) is two (!) orders of magnitude lower (2.4 x $10^{-14}$ $m^2/s$) (Glaus et al., 2017).This is due to the interplay of the thickness of the diffuse double layer (DDL) with interparticle porosity/interlayer porosity, which leads at low IS to increased geometric factors (increased tortuosity) .

## Conclusions

The batch sorption experiments confirmed that the divalent $SeO_4^{2-}$ does not sorb on illite at the studied experimental conditions (pH 7.15). This means that the capacity factor $\eta R$ determined from the diffusion experiments can be simplified to the accessible porosity (when assuming that retardation is only caused by sorption). For $I^-$ and $SeO_4^{2-}$, the accessible porosity is smaller ($\eta$ 0.14 and 0.06 resp. at 0.01 M) than the total water porosity (±0.41 for HTO) due to the anion exclusion effect. The difference between the monovalent $I^-$ and the divalent $SeO_4^{2-}$ can be related to the valence state of both anions. The divalent anions are expected to be repelled stronger from the negatively charged clay surface.

One of the goals of this study was to assess the effect of the ionic strength on the anion exclusion as well. Unfortunately, the experiments performed at 0.1 M failed over and over and the experimental problems could not be solved in the projects time frame. Only for one experiment with $^{125}I^-$, a dataset could be obtained. Making conclusions on a single experiment is difficult, but the obtained diffusion parameters seem to confirm the expectations that at higher ionic strength the anion exclusion effect is smaller or even disappears ($\eta$ ($I^-$) 0.41 equal to the average $\eta$ (HTO)), since the thickness of the electrical double layer, where anions are repelled from the negatively charged clay surface, becomes thinner.

To conclude, the valence state (monovalent versus divalent anion) has a clear effect on the anion accessible porosity (factor 2.5) at low ionic strength and effective diffusion coefficient (factor 5) for the diffusion at 0.01 M in Na-conditioned illite (at pH ± 8.15). For higher ionic strength no conclusions could be drawn since the experiments failed, we could only observe an increase in accessible porosity (as expected) but could not establish the effect of the charge.

# 2. Adsorption and migration processes of selenium in clay minerals and clayrocks

M. García-Gutierrez, Fco. Javier León, A. M. Fernández, M. Mingarro, Tiziana Missana
*CIEMAT, Madrid, Spain*

## Abstract

Selenium (selenite) adsorption was analysed in different clay materials including smectite (FEBEX clay) and nontronite (NAu-1 or NAu-2) natural, oxidised and reduced and the Callovo-Oxfordian (COx) clay. Experiments were carried out with the materials in both dispersed and compacted state and included batch sorption tests and diffusion experiments. To analyse the effect of the water saturation degree on selenite diffusion a sample of Spanish sedimentary rock was used.

## Introduction

The activity planned by CIEMAT at the beginning of the FUTURE project in Task 2.1 (Radionuclide mobility in clays) with selenium were mainly thought as a support of the work to be carried out in Task 3, where redox processes are specifically studied. In Task 3, the main objectives of CIEMAT were: 1) to synthesize in laboratory clays with different $Fe^{2+}/Fe^{3+}$ content, and 2) to compare the retention of redox sensitive radionuclides on these materials, evaluating the possible role of iron (in the solid or aqueous phase) on selenite retention. To support the redox studies, we analysed the adsorption by nontronite (a Fe-rich clay) under different experimental conditions. First, the adsorption behaviour of selenite in the nontronite was compared to the sorption behaviour on a reference smectite material (FEBEX) thus, tests were carried out with the materials exchanged in sodium and under atmospheric conditions. Then, we performed studies with the nontronite previously oxidized (ferric nontronite) or reduced (ferrous nontronite) to analyse the possible differences, and experiments were carried out under anoxic atmosphere.

An additional objective of CIEMAT in Task 2.1 was to verify if distribution coefficients ($K_d$) measured under dispersed or compacted conditions are equivalent. This topic was investigated determining the $K_d$ in the compacted/consolidated state with special cells designed to the scope. These tests were carried out both with the FEBEX clay compacted at a density from 1 to 1.6 g/cm$^3$ and with the COx clay rock.

Finally, one of the interests of CIEMAT was to investigate radionuclide migration in clays under non saturated conditions, and diffusion tests were carried out in a Spanish sedimentary rock, taken at the site initially selected for the temporary high level waste repository in Spain.

## Materials & Methods

### Clays and contacting electrolytes

#### *Nontronite*

The clay minerals selected for the adsorption experiments were nontronites (NAu-1 and NAu-2) as-received and/or Na-exchanged. The main properties of the NAu clays are reported in Table 1. The NAu-1 clay has a 97% wt% of phyllosilicates (88 wt% nontronite and 9 wt% kaolinite), whereas NAu-2 has 95 wt% of phyllosilicates (100 % nontronite). Raw NAu clays have both a Ca-Mg character.

*Table 1: Cation exchange capacity, CEC and surface area, SA, of the nontronite samples*.

| Sample | CEC (meq/100 g) | BET/Total external SA ($m^2$/g) | TOTAL SA ($m^2$/g) |
|---|---|---|---|
| NAu-1 | 85 ± 1 | 58/63 | 729±4 |
| NAu-2 | 82 ± 3 | 44/47 | 541±2 |

NAu nontronites were duly characterized before the sorption tests (Fernández et al., 2023). An amount of the NAu-2 clays (fraction < 2mm) was oxidized (Jackson, 2005) or reduced (Stucki et al., 1984) . After this treatment, the Na in the exchange complex increases, but Ca and Mg still prevail.

For adsorption experiments, the clays previously crushed and sieved (< 64 µm). In some experiments, the clays were converted in their Na-form, using a standard method described elsewhere (Missana et al., 2021).

*Callovo Oxfordian clayrock*

The samples of Callovo-Oxfordian clay were sent to CIEMAT at the very beginning of the project (May 2019). Their reference number were: EST60797, OHZ 3008 K15 (COx-1) and EST60807 OHZ 3008 K18 (COx-2). These cores were preserved from the beginning in the anoxic glove box ($N_2$ + 1% $CO_2$). The cores were sliced for diffusion tests, part was crushed and sieved for sorption tests.

The aqueous solution used in the tests with the COx samples was a synthetic water representing COx clay porewater (Gailhanou et al., 2017).

A complete characterization of both core samples was performed. The semi quantitative quantification of the main mineral in the total fraction is: ~43-47 wt.% clay minerals, ~20 wt.% quartz, ~18-26 wt.% calcite, ~5-7 wt.% dolomite/ankerite, ~4-5 wt.% K-feldspars, ~2 wt.% plagioclases, ~1 wt.% titanium oxides (anatase) and traces of pyrite. The clay fraction consists of illite/smectite interstratifies (I/S ML) R0 type (4.5 wt.%), I/S ML R1 type (11.5 wt.%), illite/muscovite (75.6 wt.%), kaolinite (4.1 wt.%) and chlorite (3.6 wt.%).

The total CEC value for both core samples is 26.6 meq/100g, similar to that calculated as sum of the total cation exchange occupancies. At exchange sites on average, the Na occupancy is 3.8 meq/100g. The Ca occupancy is 9.8 meq/100g. The Mg occupancy is 9.3 meq/100 g, and the K occupancy is 1.8 meq/100g. Sr is also present at much lower contents.

The BET surface area is 41.8 ± 1.6 $m^2$/g and the total surface area of 145 ± 6 $m^2$/g. The chloride and sulphate inventories were determined from the aqueous leaching tests, the values being of 0.120 ± 0.007 mmol/kg for chloride and 0.961 ± 0.209 mmol/kg for sulphate, as average for both core samples.

*Spanish lutite*

The effects of the water saturation degree on selenite diffusion were analysed in a natural fine-grained sedimentary rock (lutite), and the samples selected were obtained from an intact core of a borehole (9.90–10.30 m depth) drilled at the Villar de Cañas site (Spain), that was considered as a possible location for a temporary surface disposal for high level radioactive waste. Before performing diffusion tests, the samples were characterized, to determine their properties (bulk density, average porosity, composition). The semiquantitative analysis gave the following mineralogical composition: 37 wt% gypsum, 25 wt% dolomite, 28 wt% phyllosilicates, 8 wt% quartz and 2 wt% accessory minerals. The presence of gypsum is potentially relevant in the selenite transport behaviour. An example of scanning electron microscope images of the sample is shown in Figure 1. Water in chemical equilibrium with the solid sample (pH = 8.13 and E.C.= 1988 mS/cm) was used in all the tests.

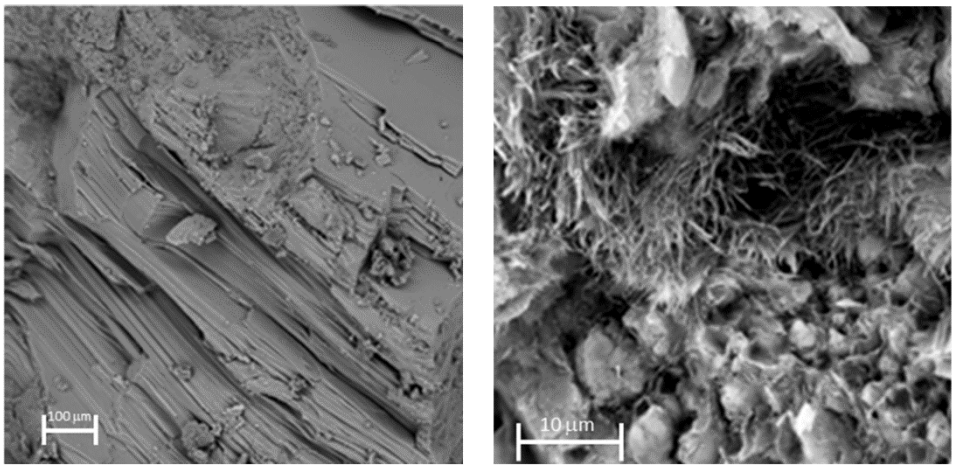


*Figure 1: SEM pictures of the lutite sample. a) gypsum crystals and b) dolomite crystals and palygorskite (fibrous clay mineral).*

## Radionuclides

The gamma emitter $^{75}$Se(IV) was supplied by Eckert & Ziegler (USA). It was measured using a Packard auto-gamma Cobra II 5003 counter with a 3" NaI (Tl activated) crystal.

## Types of experiments

Different types of experiments were carried out to fulfil the proposed objectives: batch sorption tests, sorption test in compacted/consolidated clays and diffusion experiments. Batch sorption tests in dispersed clays were carried out with the exchanged clays or raw clays in a wide range of experimental conditions (pH, ionic strength (I) and radionuclide concentration [RN]), to obtain a dataset wide enough for applying sorption modelling. Sorption kinetic tests (1-90 days); sorption edges (pH 3-11) and sorption isotherms were carried out suspending the exchanged clay in the corresponding electrolyte. In the case of the raw nontronites (NAu-1 or NAu-2), as they are naturally Ca-Mg clays, the tests were carried out with $Ca(ClO_4)_2$ as electrolyte. The chemistry of the contact water in equilibrium with the solid in the condition of the sorption experiments (1-3 g/L), was checked at the end of the experiments at least for 3 different pH (4, 7, 9) and ionic strengths. It is worth mentioning that significant leaching of Fe is observed under acidic conditions (or very low ionic strengths) from nontronite and the formation of secondary phases as aegirine or other Fe-(hydro)oxides cannot be ruled out. Adsorption tests were performed either under oxic or anoxic conditions, this will be indicated in each case.

Batch sorption test in compacted/consolidated clays, were carried out with consolidated COx samples and with the FEBEX clay compacted to a dry density between 1 and 1.6 g/cm$^3$. To carry out these tests, the samples (0.06 g) were confined between two sintered steel filter in a specially designed cell. These cells were immersed in the aqueous solution (approximately 7 mL) and left in contact during the selected time. In general, long-term kinetic test was carried out, trying to ensure that the adsorption equilibrium is reached. After the test, all the part of the cells were disassembled and the final activity in the water and in the clay, sample was measured, to determine the $K_d$. The activity in all the part of the cells was also measured.

Diffusion tests. In-diffusion tests were carried out to determine the apparent diffusion coefficients, $D_a$, of selenite in the selected materials. In the case of the COx clay, a standard in-diffusion test was carried out, whereas in the case of the Spanish lutite, the instantaneous planar source (IPS) method was used. Details of the experimental set-up for different types of diffusion experiments can be found elsewhere (García-Gutiérrez et al., 2006).

For studying the effects of water saturation in the lutite, the crushed and sieved rock was mixed with the equilibrium water necessary to obtain the five different saturation degrees (S): 60%, 70%, 80%, 90%, and

100%. Furthermore, the effect of the dry density (1.2, 1.4, or 1.65 g/cm$^3$) was additionally evaluated. More details on the used methodology can be found in (García-Gutiérrez et al., 2023a).

## Results & Discussion

### Selenite adsorption on nontronite

#### *Oxic conditions*

The tests carried out with Na-(NAu-1) clay under atmospheric conditions included: 1) adsorption edges at three different ionic strengths (0.01, 0.05 and 0.1 M) in $NaClO_4$ with a [Se]=$7.8\cdot10^{-9}$ M; 2) a sorption edge at I= 0.1 M and [Se]= $9.8\cdot10^{-5}$, and 3) sorption isotherms at pH=5 and pH=9 at the three different ionic strengths with a [Se] from $2\cdot10^{-9}$ to $1\cdot10^{-3}$ M.

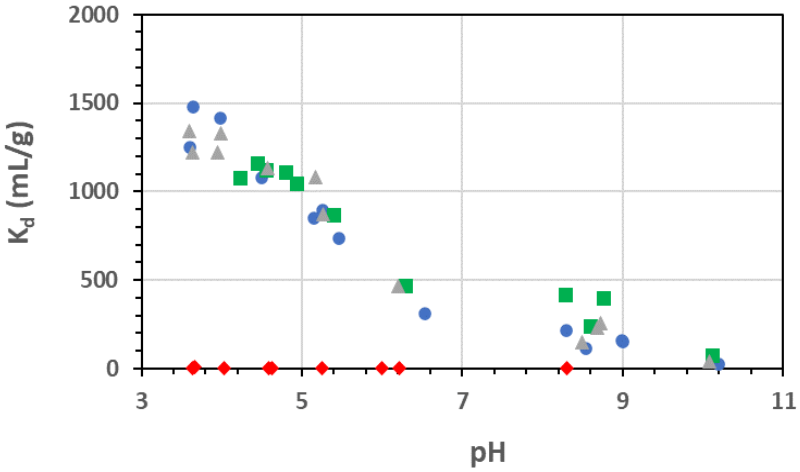


*Figure 2: Adsorption edges of selenite on Na-(NAu-1) at different ionic strengths in $NaClO_4$. (◆) 0.1 M; (▲) 0.05 M and (■) 0.01 M and [Se]=$7.8\cdot10^{-9}$ M. (◆) 0.1 M and [Se]=$9.8\cdot10^{-5}$ M.*

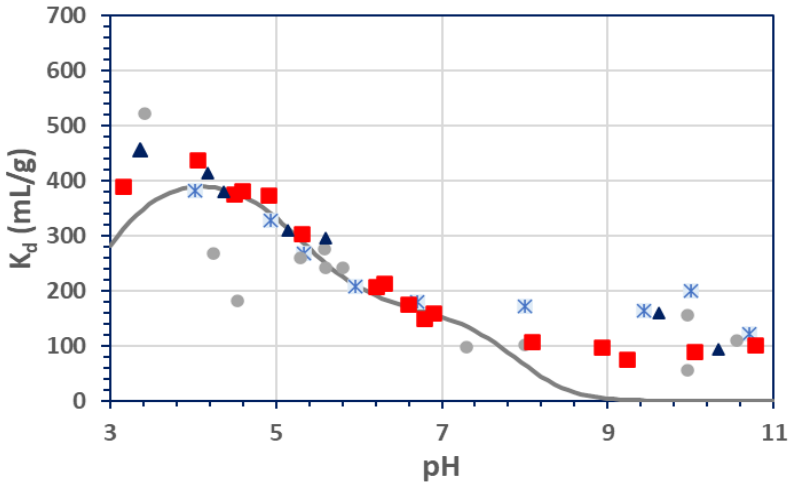


*Figure 3: Adsorption edges of selenite on Na-(FEBEX) at different ionic strengths in $NaClO_4$. (▲) 0.5 M; (■) 0.1 M, (■) 0.01 M and (*) 0.001 M and [Se]=$4\cdot10^{-10}$ M. Data taken from Missana et al. 2009.*

*Figure 2* shows the selenite distribution coefficient $K_d$ (mL/g) as a function of the pH (sorption edges) in the samples Na-(NAu-1) at the three different ionic strengths. Adsorption decreases with pH in agreement with the anionic character of selenite and there is not a clear dependence of sorption with the ionic strength, possibly indicating the formation of inner-sphere surface complexes with the edge sites of the nontronite. It is interesting noticing that at pH between 8 and 9, where sorption should tend to zero, a small but systematic (but scattered) adsorption is registered. At higher selenium concentrations ($9.8 \cdot 10^{-5}$ M) adsorption decreases significantly according to a non-linear behaviour of selenite sorption and the saturation of sorption sites. Selenite adsorption in nontronite shows features very similar to those previously observed in the Na-FEBEX smectite (*Figure 3*), but $K_d$ values are up to three times higher, especially in the acidic range of pH where selenite adsorption is maximum.

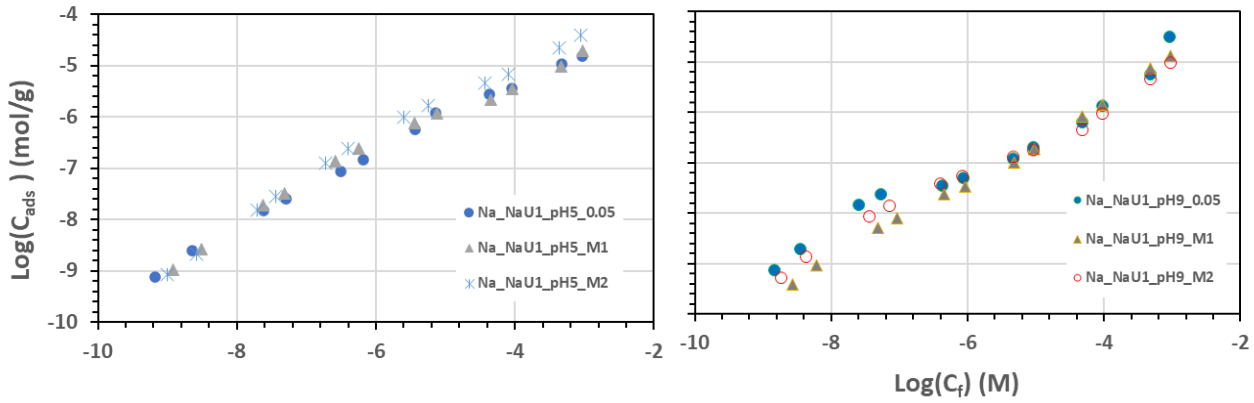


*Figure 4: Selenite sorption isotherms at three different ionic strengths and pH. Left: pH=5; Right: pH=9.*

*Figure 4* shows the adsorption isotherms of selenite by Na-(NAu-1) at pH 5 (left) and pH 9 (right) at three different ionic strengths. Results confirms that selenite adsorption by nontronite is not linear. An anomalous behaviour is observed at pH~9 and the lowest concentration, where a larger dispersion of data is observed (similar to what seen in the sorption edges). The mechanisms of retention for selenite at high pH can be the results of the formation of ternary surface complexes with $Ca^{2+}$ (or other divalent elements),(Missana et al., 2009a; Montavon et al., 2009), which can be present in trace concentrations even in the purified system, but it is difficult to predict. On the other hand, the effect of leached iron and the formation of secondary phases are most probably the responsible of the (enhanced) adsorption behavior under very acidic pH.

### *Anoxic conditions*

The tests were carried out under anaerobic conditions in a glove box under $N_2$ atmosphere with 1 % of $CO_2$.

Eh variation as a function of time was analysed in tests clay suspension at pH 5. Observed Eh did not decrease below 120 mV for any clay analysed in this report. Kinetic experiments were carried out with the Na-NAu-1 and Na-FEBEX and with the as-received and ferric NAu-2.

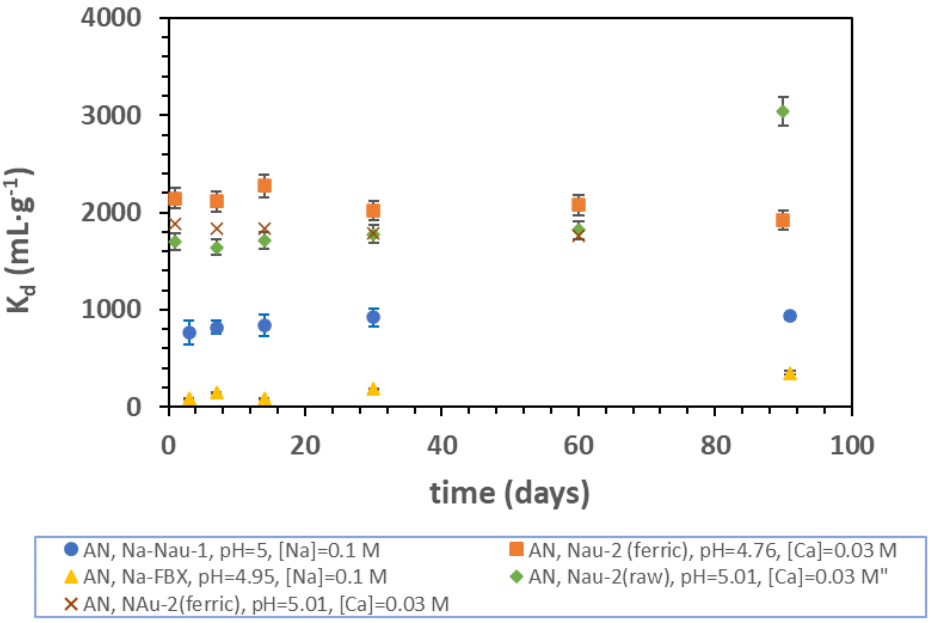


*Figure 5: Selenite sorption kinetics in different clays (pH 5). Anoxic conditions.*

Tests at pH 5 show very little or no kinetics for the long-term selenium retention under the analysed conditions. It is shown that nontronite adsorb selenite better than (FEBEX) smectite and that the Na-exchanged material adsorbs less than the as received nontronite material suspended in Ca electrolyte. At pH 8-9, in all the NAu-2 samples a significant sorption increase is observed within the first month, then the equilibrium is reached (data not shown). This is an indication that the presence of Ca might be relevant in the overall selenite retention under alkaline conditions. Considering the kinetic of the process, one can expect different mechanisms involved other than adsorption.

*Figure 6* shows the comparison of the selenite adsorption edges performed in the raw or ferric/ferrous NAu-2, which show that under very acidic conditions (pH<5), adsorption of selenite in the ferric clay is slightly higher than Se adsorption in the raw material, and that selenite adsorption in the ferrous clay is appreciably higher up to pH~7.

Higher Se sorption under acidic conditions can be explained by the formation of ternary complexes between Fe, Se and the surface of the clay, as suggested elsewhere (Missana et al., 2009b), but also the formation of secondary phases.

However, in the case of the ferrous clay, the observed sorption increase could be related to some redox effect triggered by the increase presence of Fe(II) in the clay structure.

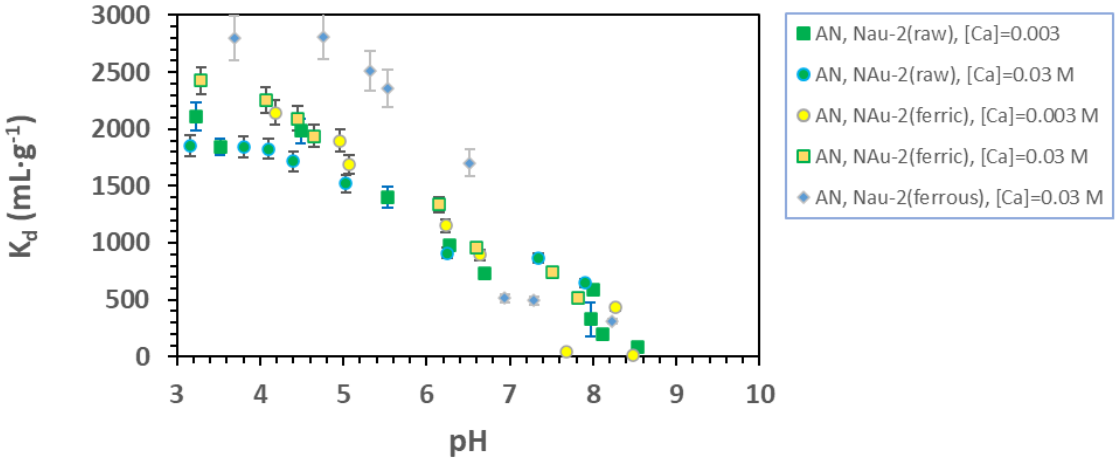


*Figure 6: Comparison of selenite adsorption edges in raw NAu-2 (green), ferric NAu-2 (yellow) and ferrous Nau-2 (grey).*

The modelling of the data on selenite adsorption in nontronite is ongoing. More data on the adsorption studies on nontronite will be available in a paper under preparation (León et al., 2023).

*Adsorption Tests with COx.*

Adsorption isotherms were carried out with the two COx clays samples are shown in *Figure 7*. As already shown in the literature, selenite adsorption in the COx (Savoye et al., 2021), as well as in other clayey samples (Frasca et al., 2014), strongly depends on the selenium concentration, being non-linear. Maximum $K_d$ (around 3000 mL·g$^{-1}$) are observed at low concentration (<1·10$^{-7}$ M), then the adsorption decreases abruptly as selenium concentration increases reaching values less than 10 mL·g$^{-1}$ for selenite concentration above 1·10$^{-4}$ M.

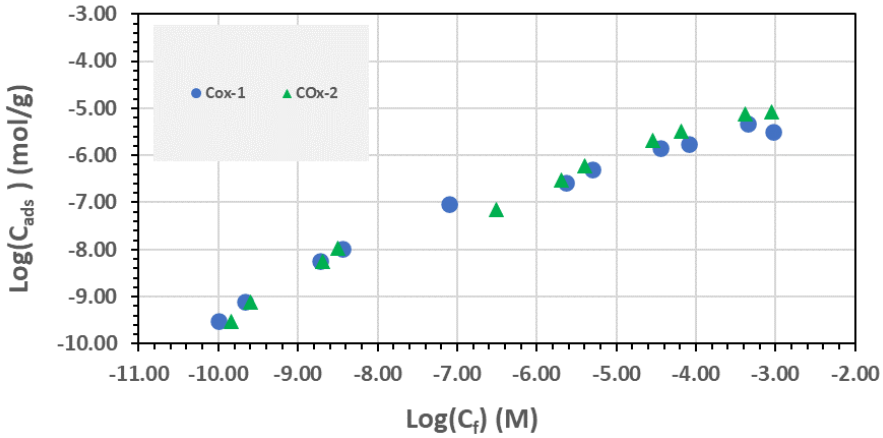


*Figure 7: Adsorption isotherms of selenite in COx clay samples.*

These adsorption isotherms provided us the reference values in the powdered material to compare with the $K_d$ values obtained in the consolidated clays.

## Batch sorption test in compacted/consolidated clays

Batch sorption tests in consolidated / compacted clays were carried out with the COx clay (consolidated) and with the FEBEX clay compacted at different compaction density. The initial [Se] for the tests with the COx clay was 1.56·10$^{-7}$ M. For this concentration, the $K_d$ obtained in the powdered material are in the linear zone (~ 2500-3000 mL·g$^{-1}$). The $K_d$ obtained in the consolidated material after a time of 15 or 30 days, are indeed much lower (<10 mL·g$^{-1}$); in a third test with a duration of 172 days, the obtained $K_d$ value was

126±63 mL·g$^{-1}$ considering the mean value of COx-1 and COx-2 (6 tests, eliminating higher and lower values), which is still lower than the value measured in batch. It must be mentioned that in this system the spread of the data is higher than in others, and methodology should be improved.

The $K_d$ values obtained upon 176 days in compacted FEBEX bentonite (pH=7±0.3) at different dry densities are shown in *Figure 8*. For these tests the initial [Se] was 1.6·10$^{-6}$ M. A dependence of the $K_d$ value on the compaction density cannot be appreciated, and the $K_d$ values determined in the compacted FEBEX are quite in line with those determined in the powdered clays at the same pH and solid to liquid ratio.

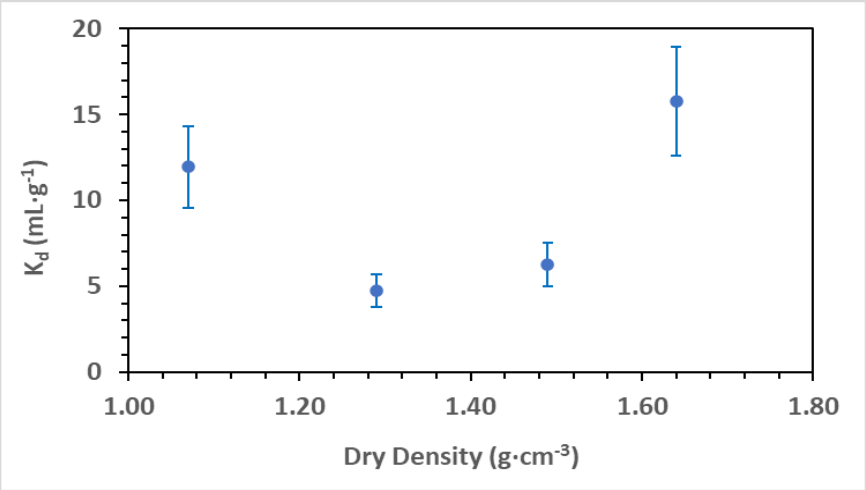


*Figure 8: $K_d$ values obtained in the FEBEX bentonite compacted to different dry densities.*

## Diffusion tests with selenite

### *Diffusion in COx clayrock*

Three independent in-diffusion tests for each sample were carried out with selenite in the COx clay, and an example of the diffusion profiles within the clay (left COx-1 and right COx-2) are shown in *Figure 9*.

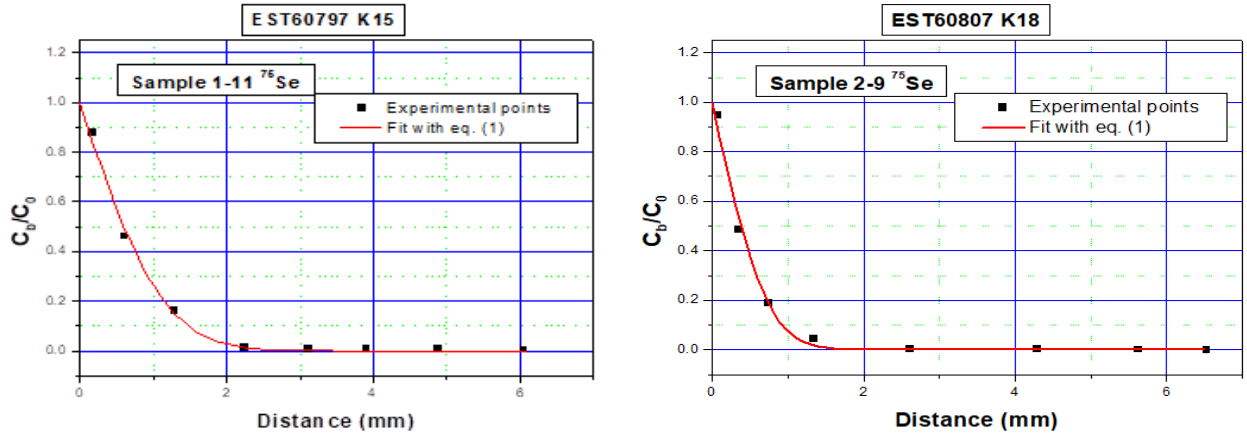


*Figure 9: Diffusion profiles for selenite in the in-diffusion tests: left COx-1 and right COx-2.*

To determine the apparent diffusion coefficients, $D_a$, the diffusion profiles could be nicely simulated using the approximation proposed by Crank (1975):

$$\frac{C}{C_0} = erfc\left(\frac{x}{2\sqrt{D_a \cdot t}}\right) \quad (4)$$

The mean apparent diffusion coefficients obtained with three different experiments are summarized in *Table 2*.

*Table 2: Apparent diffusion coefficients obtained from in-diffusion tests.*

| **Sample** | **$D_a$(Selenite) ($m^2/s$)** |
|---|---|
| **EST60797 K15** | $(1.1\pm0.3)\cdot10^{-13}$ |
| **EST60797 K18** | $(2.4\pm1.3)\cdot10^{-13}$ |

*Diffusion in a Spanish sedimentary rock: dependence on the water saturation degree and compaction density.*

The methodology used for studying selenite diffusion in this rock was the instantaneous planar source, IPS, method, (García-Gutiérrez et al., 2023b). Tests were done at different water saturation degree and dry density.

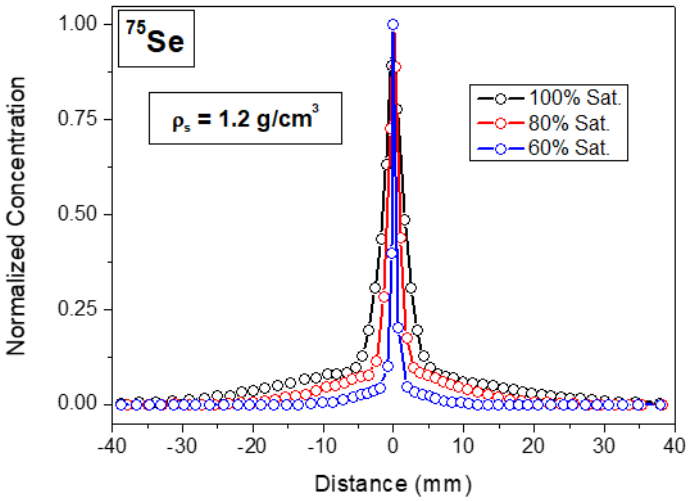


*Figure 10: Diffusion concentration profiles for the IPS tests at three different saturation degrees for $^{75}Se$ at 1.2 g/cm³ dry density.*

An example of the selenite diffusion profiles at different saturation degrees (*S*) obtained at the solid dry density of 1.2 g/cm³ is shown in *Figure 10*. Results clearly indicated that diffusion is faster for higher saturation degrees. However, the shape of the selenium diffusion profiles is significantly different than that observed for the conservative tracers HTO and $^{36}Cl$ (García-Gutiérrez et al., 2023b). Figure 10 shows that the central part of the diffusion profile presents a very narrow peak, even the extension of selenium diffusion is along 30 mm from the source.

This behaviour suggests that there must be (at least) two different species or processes controlling selenium diffusion in this material. Thus, the contribution of two diffusion profiles with "high" and "low" diffusion coefficients ($D_{a(high)}$ and $D_{a(low)}$), was used to simulate the results.

A small degree of oxidation to Se(VI) in the experiments, leading to the existence of selenate additionally to selenite cannot be ruled out. However, considering the proportion of the fast and slow diffusing species, and according to previous studies we consider that different retention mechanisms can be involved.

Lin et al. (2020) showed that gypsum can sequestrate selenite in its structure, for its similarity to sulphate. The incorporation / coprecipitation of selenite in gypsum may represent an additional retention process with different characteristics and kinetics than adsorption, and this could be the reason why two different diffusion profiles are observed. The apparent diffusion coefficient $D_{a(high)}$ and $D_{a(low)}$, determined under the different experimental conditions are summarized in *Table 3*.

*Table 3: Apparent diffusion coefficients obtained at different water saturation degrees (S) and clay dry density.*

| ***S* (%)** | **1.2 g/cm$^3$** | | **1.4 g/cm$^3$** | | **1.65 g/cm$^3$** | |
|---|---|---|---|---|---|---|
| | ***High*** | ***Low*** | ***High*** | ***Low*** | ***High*** | ***Low*** |
| **100** | $(2.0\pm0.4)\cdot10^{-10}$ | $(2.9\pm0.2)\cdot10^{-12}$ | $(1.0\pm0.3)\cdot10^{-10}$ | $(9.0\pm0.1)\cdot10^{-13}$ | $(3.6\pm1.2)\cdot10^{-11}$ | $(2.5\pm0.2)\cdot10^{-13}$ |
| **90** | $(1.7\pm0.2)\cdot10^{-10}$ | $(2.5\pm0.1)\cdot10^{-12}$ | $(7.2\pm0.3)\cdot10^{-11}$ | $(5.6\pm0.1)\cdot10^{-13}$ | $(1.5\pm0.2)\cdot10^{-11}$ | $(1.2\pm0.1)\cdot10^{-13}$ |
| **80** | $(8.2\pm1.1)\cdot10^{-11}$ | $(7.8\pm0.3)\cdot10^{-13}$ | $(4.4\pm0.8)\cdot10^{-11}$ | $(3.7\pm0.2)\cdot10^{-13}$ | $(4.3\pm1.2)\cdot10^{-12}$ | $(4.0\pm0.3)\cdot10^{-14}$ |
| **70** | $(5.2\pm1.4)\cdot10^{-11}$ | $(5.1\pm0.4)\cdot10^{-13}$ | $(1.6\pm0.2)\cdot10^{-11}$ | $(1.1\pm0.1)\cdot10^{-13}$ | $(1.9\pm0.4)\cdot10^{-12}$ | $(1.4\pm0.4)\cdot10^{-14}$ |
| **60** | $(1.5\pm0.4)\cdot10^{-11}$ | $(6.9\pm0.2)\cdot10^{-14}$ | $(5.3\pm1.1)\cdot10^{-12}$ | $(8.6\pm0.5)\cdot10^{-14}$ | $(8.3\pm0.5)\cdot10^{-13}$ | $(8.6\pm0.5)\cdot10^{-15}$ |

## Conclusions

The results obtained for selenite in the compacted FEBEX bentonite seems to indicate that, batch sorption data can be transferable to compact systems. Nevertheless, this could not be clearly shown in the case of the COx clay. Selenite adsorption isotherms indicated non-linear adsorption with maximum $K_d$ values of approximately 3000 mL/g at [Se]=$1\cdot10^{-7}$ M. Using a similar selenium concentration in batch sorption tests with consolidated samples, we could not reach this value even after 172 days of contact time. This may indicate a problem of kinetic, which might be different in the batch/consolidated systems, but also can be related to the fact that adsorption at the selected concentration is somewhat related to “strong” sites in the material. This is a point still under study.

In the case of Se(IV) adsorption in clays, different processes can influence se retention, as for example the presence of calcium or iron ions. Their effect is different if these ions are in the clay structure or aqueous phase. If the processes involved are adequately described, they can be accounted for evaluating the overall retention on nontronite. An accurate chemical characterization of the system is mandatory. Furthermore, the best probabilities to accurately model the “complex system” starting from simplest ones, when the additivity of sorption in different components can be demonstrated.

Batch sorption tests provided a lot of information on selenium retention in raw and treated nontronite. Complexation constants will be provided as far as the modelling is being completed.

The results obtained for selenium diffusion in the Spanish lutite as a function of compaction density and saturation degree are relevant. The possible coexistence of species with different diffusion coefficients has been analysed and successfully simulated.

Many spectroscopic techniques are limited to relatively high radionuclide concentrations and cannot be always used at the repository relevant concentrations. The formation of secondary phases from nontronite

with FTIR and Raman technique is under study and can provide useful data to be added in sorption modelling.

The theoretical way to describe sorption competition phenomenon is well defined and can be implemented in geochemical calculations. The main problem might be related to the lack of data or the poor description of the chemical system.

The irreversible sorption was not specifically considered for selenite. However, the results obtained in diffusion tests with the Spanish lutite, indicated that possibly the entrapment of selenite in gypsum is an additional process, which leads to a stronger retardation than surface adsorption. Indeed, these types of processes are expected to influence the kinetic of desorption. This is also valid for dissolution/coprecipitation process and the formation of secondary phases.

The presence of phases different from clay (even in small concentration) might be responsible for additional contribution in retention/transport processes.

An exhaustive description of the chemical system and kinetic processes is mandatory to transfer properly the information from one system to another.

# 3. Adsorption and diffusion of selenite on Boda Claystone Formation

O. Czömpöly, M. Fábián, J. Osán
*EK, Budapest, Hungary*

M. Aertsens
*SCK CEN, Mol, Belgium*

## Abstract

This study investigates adsorption and diffusion of selenite in Boda Claystone Formation (BCF) which is a potential host rock of a deep geological disposal of high-level radioactive waste. The experiments were performed on two diverse core samples: one albitic claystone sample characteristic for the entire BCF and one pyrite containing sample sparsely occurring in BCF. The experiments were carried out under atmospheric conditions. Batch experiments were carried out to study the kinetics of adsorption at a high initial concentration ($1.2 \times 10^{-3}$ M), the adsorption isotherms and reversibility were investigated in the $10^{-10}$ – $10^{-3}$ M concentration range. Adsorption onto petrographic thin sections was done to study the elemental distribution on the microscale and the oxidation state of selenium. The maximum of the distribution coefficient measured was $K_d \approx 200$ L/kg for $10^{-10}$ - $10^{-8}$ mol/l aqueous Se concentrations and a decrease down to 100 L/Kg was observed around $10^{-6}$ – $10^{-7}$ M equilibrium concentration, which showed similarities to other argillaceous rocks. Isotopic exchange experiments revealed reversibility of selenite adsorption. Diffusion was studied with through-diffusion and in-diffusion experiments. Using X-ray fluorescence, despite a low initial concentration of $2.3\times10^{-5}$ M in the in-diffusion experiment, a meaningful diffusion profile of selenium could be obtained, from which the selenite apparent diffusion coefficient $D_a^{selenite} = (1.5–4.3) \times 10^{-14}$ m$^2$/s and the selenite rock capacity factor $\alpha^{selenite} = 1.4–2.2$ were determined. As selenium species are redox sensitive the oxidation state of adsorbed species was studied with X-ray absorption near edge structure spectroscopy on Se-K edge. Adsorbed selenium remained in +IV oxidation state, however reduction was observed on the pyritic sample.

## Introduction

Boda Claystone Formation (BCF) (Fedor et al., 2019) is considered a potential host rock for high-level radioactive waste repository in Hungary. It has total clay mineral content similar to other widely studied clay formations e.g. COx and Opalinus clay (OPA). This oldest in Europe (265 Ma) clay has an over-consolidated, highly indurated character with low physical porosity ($\varepsilon_{tot} \approx 0.02$) (Sámson, 2015; Nuclear Energy Agency (NEA), 2022). As the early diagenesis of BCF occurred in oxidative environment, most of the previous studies regarding the migration of RNs in BCF were investigated under atmospheric conditions (Mell et al., 2006; Marques Fernandes et al., 2015; Gergely et al., 2016). To our knowledge studies regarding selenium retention and migration in BCF has not been published. The present study investigates the adsorption and diffusion properties of selenite in BCF under atmospheric conditions. In the pores of the buffer and backfill materials in radioactive waste repositories, $O_2$ is present after construction and decreases based on the consumption rate of $O_2$. Moreover, initially the moisture content could be insufficient to saturate the entire buffer/backfill. The conditions of the repository environment can be addressed with four possibilities: (i) in the early life aerobic and unsaturated which at some point becomes (ii) saturated, however during the evolution of repository conditions (iii) unsaturated/ (iv) saturated anaerobic conditions can coexist with aerobic phases. Adsorption and diffusion experiments at atmospheric conditions can provide valuable input for PA regarding an early failure of the repository.

The aim was to study the adsorption in wide concentration range, to determine the diffusion parameters and to verify the oxidation state of adsorbed selenium. Since many European countries consider argillaceous host rocks for deep geological repository, the obtained results were discussed in comparison to those reported for other clay rich rock systems.

The properties of BCF regarding selenite adsorption species were studied using an albitic claystone sample which is the most characteristic rock of the formation. Some experiments were carried out also with a pyrite containing sample originating from a specific layer formed under reductive environment. Radiotracer method was applied to measure the adsorption isotherm in the $10^{-10}$-$10^{-3}$ M range and to study the reversibility of adsorption on crushed rock samples. Adsorption experiments with inactive selenite involving petrographic thin sections aimed to find the minerals responsible for selenium uptake. In- and through-diffusion experiments on compact rocks were carried out using only inactive selenite. Microscale elemental distributions and selenium diffusion profiles along the diffusion axis were collected using microscopic X-ray fluorescence. Because of the moderate adsorption of selenite oxyanion onto clays, synchrotron radiation was applied. The oxidation state of the adsorbed selenium was studied applying X-ray absorption spectrometry.

## Materials & methods

### Boda Claystone

The BCF rocks investigated in this study belong to the BAF-2 borecore deepened in Boda Block including both albitic claystone and the reductive interbedding from depths of 324.52 – 324.71 m (Sample A) and 151.62-152.12 m (Sample P), respectively. The bulk dry density of BCF samples is between 2700-2800 kg/m$^3$, the cation exchange capacity varies between 100-150 cmol(+)/kg (Marques Fernandes et al., 2015). Main mineral and elemental composition, and total organic carbon content as provided with the samples by the Public Limited Company for Radioactive Waste Management (PURAM, Hungary) can be found in

*Table 1* (Sámson, 2015).

Diffusion values ($D_e$ and $\varepsilon$) for tritiated water (HTO) and $Cl^-$ have been already studied and published for BCF (Van Loon and Mibus, 2015). For HTO, the effective diffusion coefficient is $D_e^{HTO}=(1.17\pm0.02)\times10^{-11}$ $m^2/s$, for $Cl^-$ $D_e^{Cl-}=(3.95\pm0.24)\times10^{-13}$ $m^2/s$, anion accessible porosity was found to be 0.03±0.002, meanwhile the total porosity for HTO has been reported as $\varepsilon_{tot}$ = 0.076±0.005 (Van Loon and Mibus, 2015). One should note that these values were obtained for a different rock section of BCF, but they can be considered as a good estimate for BAF-2 albitic claystone. The BCF heterogeneity might also explain the much lower value $\varepsilon_{tot} \approx 0.02$ of Sámson (2015).

*Table 1: Mineral and oxide composition of studied BCF rocks in m/m% (Sámson, 2015). LOI (loss of ignition) means the mass loss in % experienced during heating the sample above 1050 °C for 2 hours, TOC stands for total organic carbon content*.

| Component | Sample A | Sample P |
|---|---|---|
| **Vermiculite** | 2 | 3 |
| **Illite** | 24 | 13 |
| **Chlorite** | 6 | 31 |
| **Quartz** | 7 | 18 |
| **Pyrite** | <1 | 2 |
| **Albite** | 43 | 26 |
| **K-feldspar** | <2 | <2 |
| **Calcite** | 5 | 3 |
| **Dolomite** | 8 | 4 |
| **Hematite** | 6 | <1 |
| **$SiO_2$** | 49.2 | 50.2 |
| **$Al_2O_3$** | 16.0 | 16.1 |
| **$Fe_2O_{3\ total}$** | 7.8 | 7.4 |
| **FeO** | | 3.9 |
| **$FeO_{\ total}$** | | 6.6 |
| **$Fe_2O_3$** | | 3.0 |
| **MgO** | 4.3 | 6.1 |
| **CaO** | 4.8 | 3.50 |
| **$Na_2O$** | 3.1 | 3.6 |
| **$K_2O$** | 4.5 | 2.8 |
| **MnO** | 0.14 | 0.14 |
| **$TiO_2$** | 0.84 | 0.81 |
| **$CO_2$** | 4.3 | 3.2 |
| **$P_2O_5$** | 0.31 | 0.17 |
| **LOI** | 8.3 | 8.5 |
| **TOC** | 0.11 | 0.24 |

## Sample preparation

For through-diffusion experiments a slice with a thickness of 5.6 mm was cut and polished from the full 62 mm diameter core of Sample A. Petrographic thin sections with an average thickness of 50 µm were prepared from sample A onto high purity silicon wafers for adsorption experiments. Cutting of full-core slices was not possible from Sample P, for this reason a 1.03×1.04×2 $cm^3$ cuboid was cut that could only be used for in-diffusion experiment. For performing batch adsorption experiments 50 g of each rock sample was crushed and sieved below 63 µm particle diameter. Prior to the launch of experiments both crushed and compact rocks were conditioned with synthetic porewater at pH 8.0±0.1 based on the method of Marques Fernandes et al. (2015). Because of the low porosity, only formation water was available for BCF, therefore the chemical composition of the pore water (Breitner et al., 2015) was calculated to be in equilibrium with atmospheric $p_{CO2}$, and under the constraint of calcite, dolomite and quartz saturation (Bradbury and Baeyens, 1998). TRIS (tris(hydroxymethyl)aminomethane) was applied as a pH buffer at 2 mM concentration.

## Adsorption experiments

Adsorption experiments were carried out in both dispersed (crushed rocks) and in compacted (thin sections) forms under atmospheric conditions. After addition of sodium selenite to the synthetic porewater the pH was readjusted to 8.0±0.1. Measurements of the initial speciation of selenium was performed with ion chromatography (Thermo Scientific Dionex Aquion equipped with AS 23 column and 4.5 mM $Na_2CO_3$/ 0.8

mM $NaHCO_3$ eluent). Selenium was present in selenite form in 96% meanwhile 4% of the selenium was found as selenate. The adsorption results were corrected for the selenate concentration. Savoye et al (2021) reported the presence of selenate around 6% in the radiotracer they applied, they explained the speciation change by radiolysis processes.

*Kinetic studies*

As a first step the kinetics of adsorption was studied with batch experiments to determine the required time to reach quasi-equilibrium of adsorption. The applied liquid-to-solid ratio (V/m) was 100 mL/g and 50 mL of the selenite containing synthetic porewater together with 0.50 g of crushed and conditioned rock were introduced into 100 mL shaker vessels, then put onto an orbital shaker for 28 days (Ohaus SHHD1619AL). The experiments were performed with Sample A and the initial selenite concentration was 1.2×10-3 M. The concentration of the solutions was monitored with ICP-OES (Perkin Elmer Avio 200).

*Adsorption isotherm*

To obtain the adsorption isotherm for sample A, solutions with $10^{-10}$ M to $10^{-3}$ M concentration of selenite (using sodium-selenite) were prepared. The initial concentrations were checked using ICP-OES until the limit of detection (approximately $10^{-7}$ M for selenium). $^{75}Se$ radioisotope ($Na_2{}^{75}SeO_3$ in aqueous solution, POLATOM) was used as a tracer and solutions were spiked with 20 kBq of $^{75}Se$ in the whole $10^{-3}$ M - $10^{-10}$ M range. For each concentration two replicas of 0.50 g conditioned, crushed rock were added to 100 ml vessels with 50 ml solution containing selenite and shaked for 28 days. After reaching equilibrium with batch experiments the suspensions were separated using 220 nm syringe filters. The activity of initial and final liquid phases was measured in the same batch by liquid scintillation counter (LSC) (Perkin Elmer Tri-Carb with Ultima Gold scintillation cocktail). Adsorption onto the wall of shaker vessels was studied and found negligible (below 1%).

In addition, the sorption of selenite at higher concentrations was also analysed by measuring the inactive Se concentration (with ICP-OES) after equilibration for 28 days. This was done for samples A and P (two replicas per concentration). The results are expressed in the form of distribution coefficient, $K_d$.

Experimental data of the adsorption isotherm of sample A was fitted with the two-site Langmuir isotherm model (Eqn. (5)). The fitting was carried out with OriginLab 2022b software.

$$C_s = S_{max,1}\frac{K_{L,1}\cdot C_{eq}}{1+K_{L,1}\cdot C_{eq}} + S_{max,2}\frac{K_{L,2}\cdot C_{eq}}{1+K_{L,2}\cdot C_{eq}} \quad (5)$$

where $C_s$ is the amount of selenite adsorption onto solid phase (mol/kg), $S_{max,i}$ ($i$ = 1, 2) is the adsorption capacity of site $i$ (mol/kg), $K_{L,i}$ is the adsorption potential of site $i$ (L/mol) and $C_{eq}$ is the equilibrium concentration (mol/L).

Inactive suspensions of $10^{-5}$, $10^{-4}$ and $10^{-3}$ M initial selenite concentration prepared from Sample A were filtered and washed, then pellets were pressed to study the oxidation state of adsorbed selenium on crushed claystone.

*Isotopic exchange experiments*

To study the reversibility of adsorption, suspension containing 0.50 g of crushed and conditioned rock of Sample A was added to 50 ml solution with varying selenite concentrations from $10^{-8}$-$10^{-3}$ M in duplicate. The suspensions were shaken for 28 days. Afterwards 5 ml of the suspensions were taken from the shaking bottles and filtered with 220 nm syringe filter. Its concentration was determined with ICP-OES. Radiotracer (20 kBq of $^{75}SeO_3^{2-}$) was added to the remaining suspensions in equilibrium with inactive sodium selenite. Right after radiolabeling, 5 ml initial sample was taken and filtered. After 28 days, LSC counting was performed on liquid phases of both the initial suspensions and those equilibrated with $^{75}Se$. The adsorbed fractions were calculated both for the inactive and active Se and compared for determining the reversibly adsorbed part of selenite, similarly to Rahman et al., (2019) used for assessment of arsenic sorption reversibility in soils.

*Elemental distribution of selenium on thin sections*

Two petrographic thin sections of sample A were immersed into selenite containing porewater ($10^{-4}$ and $10^{-3}$ M) for the same duration as batch experiments. After 28 days the thin sections were washed with ultrapure water and dried in vacuum. The lateral distribution of selenium and rock-forming elements was studied with µ-XRF mapping, while the oxidation state of selenium was investigated with (µ-)XANES.

*Analysis of adsorbed selenium and diffusion profiles using synchrotron-based techniques*

X-ray fluorescence (XRF) and X-ray absorption spectroscopy (XANES) measurements were performed at two beamlines. At Bessy-II synchrotron (Berlin, Germany) mySpot beamline µ-XRF and µ-XANES measurements were performed (Zizak, 2016). The beam was focused with polycapillary optics to 20 µm spot size. The measurements were performed on thin sections at 45°/45° geometry using a silicon drift detector (SDD) of 100 $mm^2$ active area. The measurements both on pressed pellets and thin sections were performed at the Elettra synchrotron XRF beamline (Trieste, Italy) (Karydas et al., 2018). In this case the focusing optics provide a quite large beam of roughly 500×300 $\mu m^2$ (H×V), whose size can be furtherly reduced by using exit slits. For the pressed pellets, the full beam was employed whereas for the thin sections a 450×50 $\mu m^2$ sized beam with shallow angle illumination was used to gain spatial resolution to study the diffusion profile in the rock. After obtaining the diffusion profile, XANES measurements were performed on selected points (for which the slits were fully opened). For XANES measurements Si(111) monochromators were applied at both beamlines. As selenite is present in the samples in very low amounts the excitation energy for XRF mapping was set to the peak of the white line (12664 eV) of its X-ray absorption spectrum.

## Diffusion experiments

For the through-diffusion experiment, a diffusion cell made of polycarbonate was applied (Mell et al., 2006). The claystone section divides the cell into upstream and downstream reservoirs with a volume of 165 mL each (Figure 1) and a clay surface of 19.64 $cm^2$. The claystone slice was glued in the cell then the two sides were screwed together. No filter was applied due to the very limited swelling of Boda claystone. After installing the diffusion cells both reservoirs were filled by synthetic porewater to saturate the BCF core disc. During the 6-week conditioning the solutions were changed every 2 days. The through-diffusion experiment was conducted at an initial concentration of $10^{-3}$ M of inactive sodium-selenite on a 62 mm diameter 5.6 mm thick slice of Sample A. The effective diameter available for diffusion was 50 mm. After finishing the experiment, the cell was disassembled, a piece of 5×10×5.6 $mm^3$ was cut from the centre of the claystone disc and a petrographic thin section was prepared for X-ray spectroscopy measurements.

Regarding the in-diffusion experiment a 3D printed sample holder was applied (Figure 1b). With a threaded rod the height of the cuboid from sample P could be manipulated in a way that only the bottom surface touched the liquid surface. The experiment was performed in a closed container with 100 ml porewater with an initial selenium concentration of $2.3\times10^{-5}$ M for 87 days. The clay surface was 1.07 $cm^2$. After finishing the experiment, a petrographic thin section was prepared for post-mortem analysis.

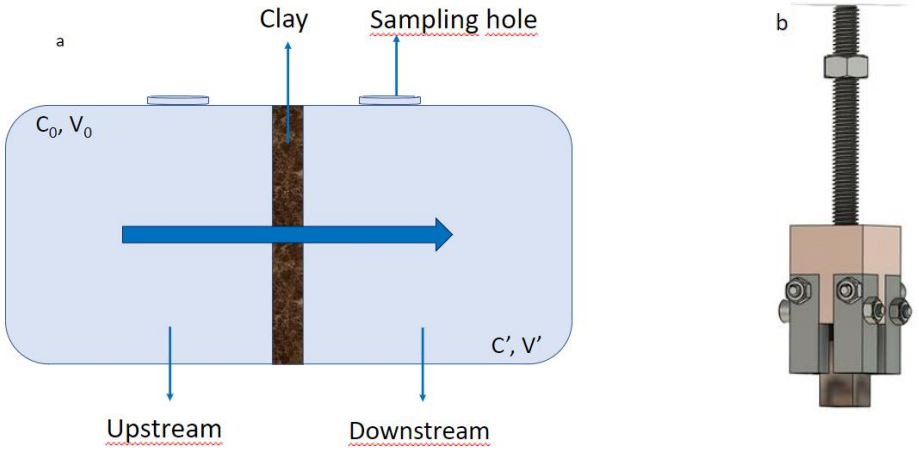


*Figure 1: Schematics of the through-diffusion cell (a) and the 3D printed sample holder for in-diffusion experiments (b).*

## Diffusion data modelling

Diffusive transport was described by one dimensional diffusion equation

$$\frac{\partial C}{\partial t} = D_a \frac{\partial^2 C}{\partial x^2} \tag{6}$$

where $C$ (x,t) is the concentration (mol/m$^3$ or counts/ m$^3$), $x$ is the position (m), $t$ is time (s) and $D_a$ stands for the apparent diffusion coefficient (m$^2$/s). In porous media, diffusion is characterized by two parameters: the apparent diffusion coefficient $D_a$ and the rock capacity $\alpha$ (-). For retarded species, the rock capacity $\alpha$ is related to the distribution coefficient $K_d$ (m$^3$/kg) by

$$\alpha = \varepsilon_{tot} + \rho K_d \tag{7}$$

where $\varepsilon_{tot}$ is the total porosity (-) and $\rho$ (kg/m$^3$) the dry bulk density. In that case, the retardation coefficient $R$ is the ratio $R = \alpha/\varepsilon_{tot}$ with $R > 1$. For nonsorbing species,

$$\alpha = \varepsilon \tag{8}$$

with $\varepsilon$ (-) the accessible porosity ($\varepsilon \leq \varepsilon_{tot}$). The effective diffusion coefficient $D_e$ (m$^2$/s) is the product $\alpha D_a$ ($D_e = \alpha D_a$).

For modelling, the diffusion equation is solved numerically by COMSOL coupled with MATLAB for optimization.

The background Se concentration in Boda Claystone (1.3± 0.3 mg/kg corresponding to (1.7± 0.4)×10$^{-5}$ mg/kg) is sufficiently low and could be neglected (see Fig. 3). Because in the through-diffusion experiment, neither the upstream nor the downstream reservoir are replaced, the VC-VC (Variable Concentration upstream and downstream) case (Takeda et al., 2008) should be solved in principle. In case the upstream and downstream compartments are sufficiently large, the VC-VC case can be approximated well by the CC-CC (Constant Concentration upstream and downstream with the upstream concentration $C_0$ much higher than the downstream concentration) case (Takeda et al., 2008). Here, after a sufficiently large time a quasi-stationary state is reached, and the concentration $C_{down}(t)$ in the downstream volume is given by (e.g. Aertsens, 2011)

$$C_{down}(t) = \alpha \frac{AL}{V_{down}} \; C_0 \left( \frac{D_a t}{L^2} - \frac{1}{6} \right) \quad (9)$$

where $L$ is the clay core length (m) ($L$ = 5.6 mm), $A$ is the surface available for diffusion (m$^2$) and $V_{down}$ is the volume of the downstream reservoir (m$^2$). This expression is valid only for not too large times (to remain consistent with the basic assumption $C_{down} << C_0$) and the breakthrough time $\tau$ (defined by $C_{down}(\tau) = 0$) is determined by the apparent diffusion coefficient:

$$\tau = \frac{L^2}{6\, D_a} \quad (10)$$

The through-diffusion experiment is modelled in two ways:

- assuming a single Se species: the evolution of the Se concentration in the downstream compartment is fitted as a function of time leading to $D_{a,Se}$ and $\alpha_{Se}$. Next these values are used to estimate the Se concentration (*i*) in the upstream compartment, and (*ii*) in the clay core, and compared to the experimental data.

- assuming two Se species: a fast-diffusing species $Se_{fast}$ (assumed selenate) and a slowly diffusing species $Se_{slow}$ (assumed selenite). The total Se concentration $C_{se}$ is the sum of the concentrations of both species:

$$C_{Se} = C_{Se,fast} + C_{Se,slow} \quad (11)$$

In agreement with the speciation calculations, the initial upstream concentrations $C_{0,fast}$ (resp. $C_{0,slow}$) of the fast (resp. slow) Se species are taken as

$$C_{0,fast} = 0.04\, C_0 \qquad C_{0,slow} = 0.96\, C_0 \quad (12)$$

with $C_0$ the initial total Se concentration in the upstream compartment.

Both Se species are assumed to diffuse independently from another in the clay according to their diffusion parameters: $D_{a,fast}$, $\alpha_{fast}$, $D_{a,slow}$ and $\alpha_{slow}$. The values of $D_{a,fast}$ and $\alpha_{fast}$, are fitted from the downstream evolution. Next, these values are used to estimate $C_{Se,fast}$ in the upstream volume and in the clay core. From the difference $C_{se,bulk} - (\alpha_{fast} C_{fast} / \rho)$ with $C_{se,bulk}$ the experimentally measured bulk concentrations and the wet and dry clay bulk densities assumed equal (justified by the very low total porosity of Boda clay), the values of $D_{a,slow}$ and $\alpha_{slow}$ are fitted, allowing to assess $C_{Se,slow}$. Finally, by expression *(11)* the concentration $C_{Se}$ can be evaluated in both upstream and downstream compartment as a function of time and compared to the experimental data.

For the in-diffusion experiment the Se evolution in the upstream compartment was not measured. Only a single Se species is assumed, and the diffusion parameters of this species are estimated from fitting the Se profile in the clay core. Clearly, this species corresponds to $Se_{slow}$.

# Results & discussion

## Adsorption experiments

### *Kinetics*

The kinetics of adsorption experiment was plotted in Figure 2, the saturation curve reached its maximum below 10 days. Missana et al. (2009) reported a similar kinetic behaviour of sodium-selenite adsorption onto Na-illite and Na-smectite under atmospheric conditions at a very low initial concentration ($10^{-10}$ M). Their results showed that 7 days of contact time was sufficient to reach equilibrium. Savoye et al. (2021) studied the adsorption of selenite onto Callovo-Oxfordian (COx) rock samples. They carried out the experiments in glovebox under a $N_2$/ 0.4% $CO_2$ atmosphere at different concentrations, where at the high concentration region ($10^{-4}$ – $10^{-3}$ M) $K_d$ reached equilibrium in 20 days, however at lower concentrations

slower kinetic took place, so they decided to obtain the adsorption isotherm after 110 days of contact time. There is no clear evidence for the differences in the time needed to reach saturation in the mentioned experimental set-ups. After all, suspensions and thin sections in the present study were shaken and immersed for 28 days.

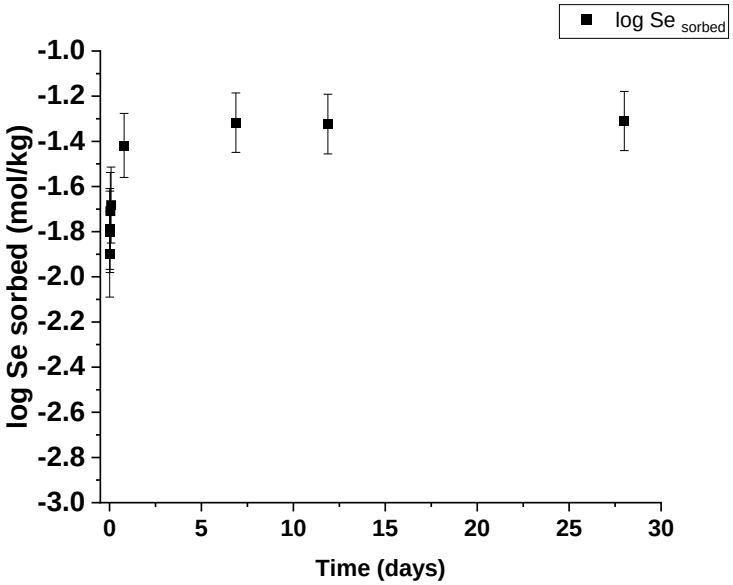


*Figure 2: Adsorption kinetics of sodium selenite on sample A at pH=8, initial selenite concentration was 1.2×10$^{-3}$ M and the liquid to solid ratio was 100 mL/g.*

### *Adsorption isotherm*

The obtained adsorption isotherm of Sample A (Figure 3) was compared to the ones measured with pure minerals. The maximum of $K_d$ (200 L/kg) was found in the low concentration experiments ($10^{-10}$ – $10^{-8}$ M). Around $10^{-6}$ M ($K_d \approx 100$ L/kg) the isotherms started to depart away and the amount of selenite adsorbed to BCF had one order of magnitude lower value. In the high concentration range ($10^{-6}$ – $10^{-3}$ M) adsorption experiments were carried out on both sample A and sample P. In this concentration range Sample P had higher selenite adsorption than the albitic sample. In the low concentration region, below $10^{-6}$ M, similar results were found to those obtained for Na-illite and Na-smectite (Missana et al., 2009a). Similarly to different argillaceous rocks (Frasca et al., 2014; Savoye et al., 2021), a decrease compared to pure minerals started around $10^{-7}$ – $10^{-6}$ M concentration, however the adsorption isotherm belonging to BCF appeared to have even lower $K_d$ value (Figure 3b). In previous studies the breakpoint in the isotherm was explained by the saturation of the adsorption sites. The lower $K_d$ value measured of BCF corresponds to the higher argillite content of the compared rocks. The studied OPA and Tournemire samples contained around 60% of clay minerals (Frasca et al., 2014), meanwhile the mineralogy of the COx sample characteristic of its depth of origin contains around 35-65% argillite (Savoye et al., 2021). In contrary, sample A has an illite and chlorite content altogether of 30-35% and sample P has around 40-45% of clay minerals. The lower selenite adsorption of Sample A compared to Sample P cannot be explained only by the difference in the clay mineral content. Despite the low TOC content (0.22 m/m%) in the Sample P, the $K_d$ values were more similar to other studied clays evolved under reductive conditions.

The results of the Langmuir isotherm fitting are presented in Table 2, the plot of the fit is shown in Figure 3c. The goodness of fit for the present study can be characterized with $R^2 = 0.99973$, reduced Chi-square = $8.21\times10^{-11}$. In the current study, two sorption sites were usedto reproduce the sorption isotherm sufficiently well, one site has high capacity but low affinity and another has a low capacity but high affinity. Frasca et al. (2014) also found that a two-site Langmuir model is in better agreement with their experimental data with $^{75}SeO_3^{2-}$ on OPA, Black Shales and Upper Toarcian Clays (Table 2). The site capacities of the

other clay-rich rocks seem to be lower than or similar to those of BCF Sample A, however the affinity values are at least one order of magnitude higher.

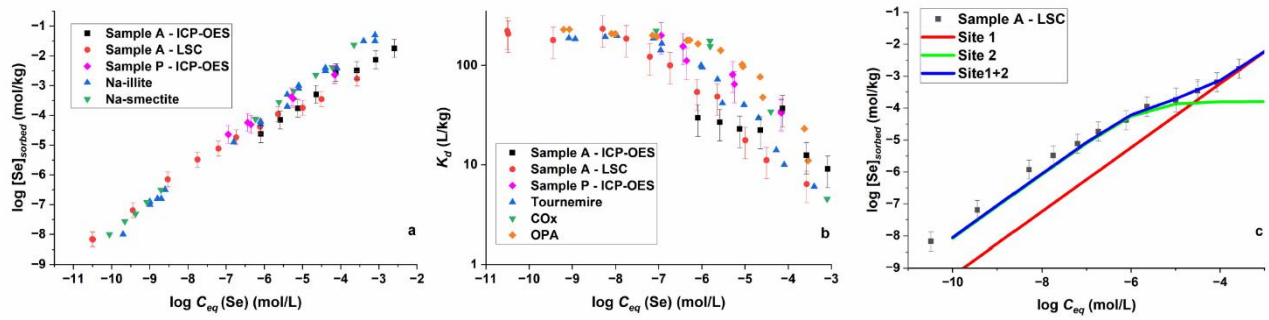


*Figure 3: Adsorption isotherm of selenite on BCF and pure clay minerals on panel (a) (Na-illite, Na-smectite) (Missana et al., 2009) and other argillaceous rocks on panel (b) (Tournemire, Callovo-Oxfordian and Opalinus clay) (Frasca et al., 2014). LSC and ICP-OES stand for the applied method to measure the initial and equilibrium activities and concentrations. On panel (c) the calculated contributions of the Langmuir sorption sites are plotted with the measured data for Sample A.*

*Table 2: Results of adsorption isotherm fitting with Langmuir parameters for BCF Sample A together with data published by Frasca et al. (2014) for Upper Toarcian, Black Shales and Opalinus Clay.*

| | $S_{max1}$ (mol/kg) | $K_{L1}$ (L/mol) | $S_{max2}$ (mol/kg) | $K_{L2}$ (L/mol) |
|---|---|---|---|---|
| **Sample A** | $1.9 \cdot 10^{-3}$ | $4.4 \cdot 10^{3}$ | $1.2 \cdot 10^{-4}$ | $8.37 \cdot 10^{5}$ |
| **Upper Toarc.** | $6.5 \cdot 10^{-4}$ | $1.6 \cdot 10^{5}$ | $2.9 \cdot 10^{-5}$ | $1.3 \cdot 10^{7}$ |
| **Black Shales** | $5.4 \cdot 10^{-4}$ | $7 \cdot 10^{5}$ | $2.6 \cdot 10^{-5}$ | $2.2 \cdot 10^{7}$ |
| **OPA** | $1.7 \cdot 10^{-3}$ | $2.1 \cdot 10^{5}$ | $1.4 \cdot 10^{-5}$ | $1.9 \cdot 10^{7}$ |

### *Lateral distribution of adsorbed selenium and rock-forming elements*

The results of the microscopic XRF measurements on petrographic thin section prepared from sample A with an initial concentration of $10^{-3}$ M of selenite show similar distribution of Fe, K and Se (Figure 4a,b,c). With scatter plots correlation was found among these elements which suggests that selenium is adsorbed on minerals containing both Fe and K, supposedly on illite as its structure is built up of $(K,H_3O)(Al,Mg,Fe)_2(Si,Al)_4O_{10}[(OH)_2,(H_2O)]$ blocks. (Figure 4d,e,f) (Osán et al., 2014). Illite and muscovite have the same main reflection (10 Å) in powder X-ray diffraction, but illite was confirmed to be the main clay mineral in BCF by complementary methods (Németh et al., 2016). Muscovite and biotite are scarce minerals in BCF (Németh et al., 2016), therefore the simultaneous presence of Fe and K could be linked to illite.

*Reversibility of adsorption*

Based on the results of the isotopic exchange experiments (presented in Figure 5), the adsorption of selenite onto BCF was obtained as reversible around 80-85% in the low concentration region meanwhile above $10^{-7}$ M equilibrium concentration the adsorption was found to be fully reversible. These findings are in-line with the Langmuir modelling of the adsorption isotherm, strong sites are dominant for the lower concentration range.

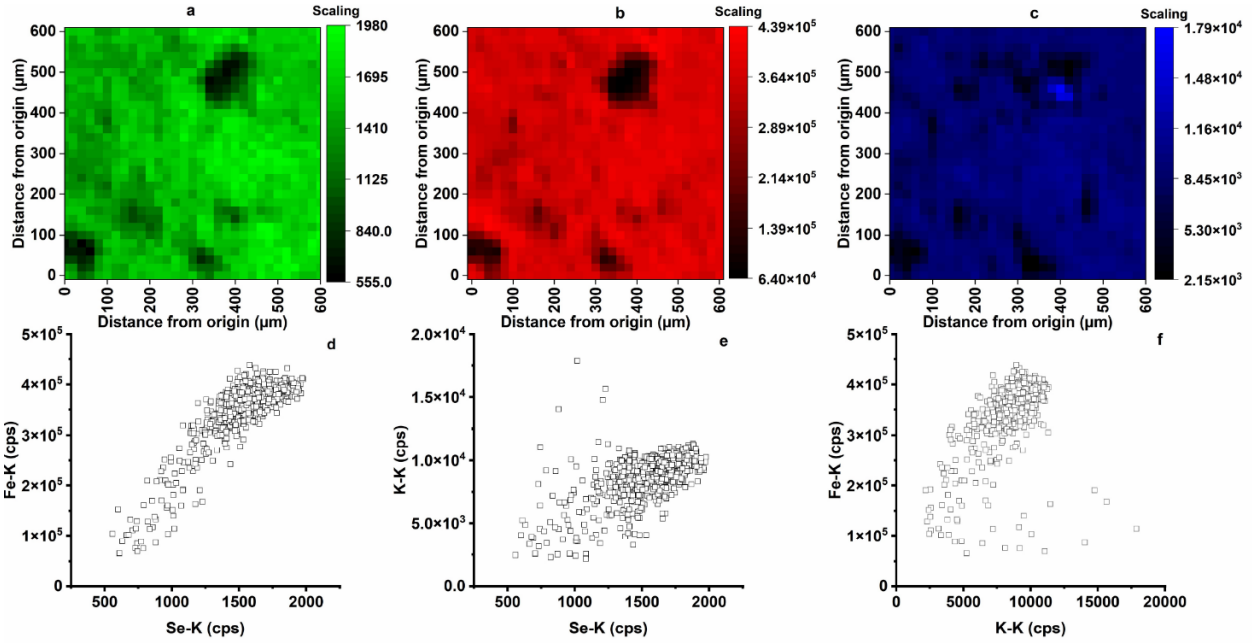


*Figure 4: Elemental distribution of Fe (panel (a)), K (panel (b)) and Se (panel (c)) on a petrographic thin section prepared from sample A obtained using µ-XRF. The initial concentration of Na-selenite was $10^{-3}$ M. On panel (d), (e), (f) scatter plots of Fe-K/Se-K, K-K/Se-K and K-K/Fe-K count rates, respectively.*

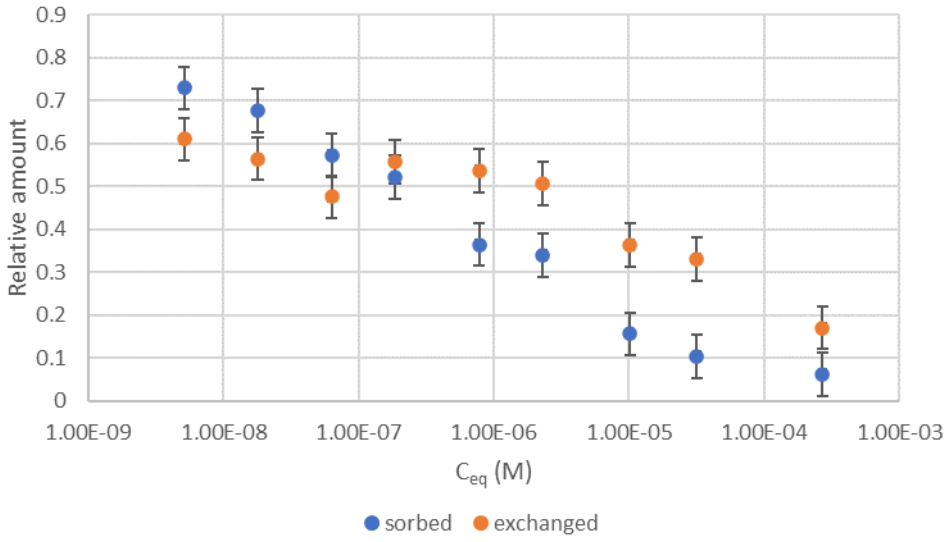


*Figure 5: Results (ratio of exchangeable sorbed selenium) of isotopic exchange experiment as a function of equilibrium concentration (mol/L). The adsorption was considered as fully reversible if the isotope exchangeable fraction was found higher than the adsorbed one.*

## Results of through-diffusion experiment

### *Assuming a single Se species*

The downstream concentration can be fitted well with the single species model(Figure 6). Because the downstream concentration (up to $2 \times 10^{-5}$ mol/L, Figure 6) is much lower than the approximately constant upstream concentration (around $1 \times 10^{-3}$ mol/L, Figure 6), the CC-CC model is a very good approximation for the VC-VC model. In line with expression *(*9), at sufficiently large times the downstream concentration is approximately a linear function of time (Figure 6). The predicted nearly constant upstream concentration agrees roughly with the experimental data (see Figure 6), but the predicted linear profile in the clay core does not agree at all with the experimental data suggesting that at least two types of diffusing Se species need to be included in the model. Although the fitted downstream concentrations agree reasonably well with the experimental data, the uncertainty on the values of $D_{app,Se}$ and $\alpha_{Se}$ is 60-70 % (Table 3).

### *Assuming two Se species*

The finally measured downstream concentration (see Figure 6) is about 50 % of $C_{0,\,fast}$ (Table 3), meaning that the entire time range cannot be fitted with the CC-CC model: unless possibly for very small times (where the quasi-stationary state is reached but also the downstream concentration is much lower than the initial concentration $C_{0,fast}$), only the VC-VC model is valid. In case the downstream concentration would have stayed all the time much lower than the upstream concentration, expression *(*9*)* shows how the shift $C_0 \rightarrow C_{0,fast}$ affects the optimal values: (i) the apparent diffusion coefficient does not change, and (ii) $\alpha\ C_0 = \alpha_{fast}\ ,\ C_{0,fast} = \alpha_{fast}\ 0.04\ C_0$ leading to $\alpha_{fast} = \alpha\ /\ 0.04 = 25\ \alpha$. This explains why (i) the ratio between $D_{app,fast}$ and $D_a$ is not too far from one ($D_{a,fast}\ /\ D_a \approx 2$, Table 3) and (ii) much smaller than the rock capacity factors ratio ($\alpha_{fast} \approx 21.6\ \alpha$, Table 3). The fit is poor resulting in very high uncertainties (> 100 %) on the values of $D_{app,fast}$ and $\alpha_{fast}$, making their values not very reliable.

From $D_{app,fast}$ and $\alpha_{fast}$, the bulk profile of $C_{fast}$ in the clay can be estimated and from the difference with the experimental data, a fair fit (Table 3) leads to $D_{a,slow}$ and $\alpha_{slow}$. It is verified that no $Se_{slow}$ diffuses to the downstream compartment during the entire duration of the experiment. The predicted evolution of the upstream concentration with two species is similar as for a single Se species (Figure 6).

The $D_a$ values of both Se species differ by nearly three orders of magnitude while the difference between their rock capacity factors is much smaller (Table 3). Assuming a total porosity $\varepsilon_{tot} = 0.02$, both species are retarded. In particular, the high (inaccurate) retardation factor for $Se_{fast}$, supposed to be the unretarded selenate is surprising and does not seem realistic. The corresponding $K_d$ value for $Se_{slow}$ is much lower than the value obtained from the batch sorption experiments.

Because in the present experiment no $Se_{slow}$ reaches the downstream compartment, an in-diffusion experiment with the same initial condition would lead to the same $Se_{slow}$ profile at the end of the experiment. In that case, no information about $Se_{fast}$ can be obtained: the in-diffusion experiment would have been fitted assuming a single Se species with initial concentration $C_0$ and the final peak would have been contributed totally to $Se_{slow}$. To allow a good comparison of the diffusion parameters with the in-diffusion experiment on sample P, also a fit with these same assumptions is performed on the present experiment (Table 3). Because the bulk concentration of $Se_{slow}$ is considerably higher than that of $Se_{fast}$ (Figure 6), the values of the $Se_{slow}$ diffusion parameters in both fits (considering $Se_{fast}$ vs. not taking it into account) are assumed to be similar, which is roughly confirmed by the fit results (Table 3). The $K_d$-values derived from the rock capacity factor are considerably lower than those derived in the adsorption isotherm (up to 200 L/kg).

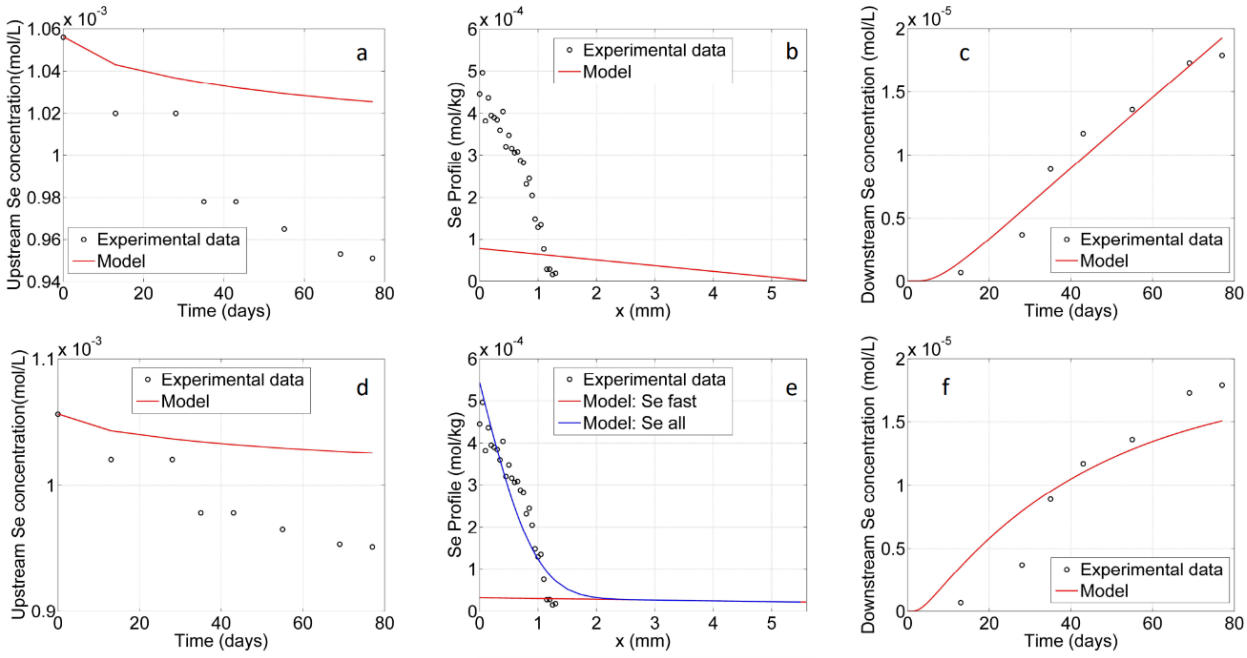


*Figure 6: Through-diffusion experiment (sample A): experimental data and model assuming a single diffusing Se species (top, panels a,b,c) and two diffusing Se species ($Se_{fast}$ and $Se_{slow}$, bottom, panels d,e,f). On panels a and d: Se concentration in the upstream compartment and model (data measured by ICP-OES). On panels b and e: Se profile in the clay core at the end of the experiment and model (data from shallow angle illumination XRF), On panels c and f: Se concentration in the downstream compartment and model (data measured by ICP-OES). For the single Se species (top, panels a,b,c), the diffusion parameters are fitted from the downstream evolution and used to predict the upstream evolution and the Se profile in the clay at the end of the experiment. For two diffusing Se species (bottom, panels d,e,f), the diffusion parameters of selenate are fitted from the downstream evolution. These values are used to predict the selenate profile in the clay and from the difference with the experimental data, the diffusion parameters of selenite are estimated. The upstream evolution is predicted with the diffusion parameter values of selenate and selenite. The predicted downstream concentration of selenite is zero.*

Savoye et al. (2021) found an effective diffusion coefficient around 1.9-5.3·$10^{-12}$ $m^2/s$ for $SeO_3^{2-}$ on COx clay. It is worth mentioning that they worked with $^{75}Se$ radiotracer which contained around 6% of $SeO_4^{2-}$ (selenate). They checked the speciation in the downstream reservoir and detected the presence of selenate only. The calculation of $D_e$ was performed from the concentration profile in the upstream/downstream reservoir. Idemitsu et al. (2016) studied the adsorption and diffusion properties of selenite on purified and compacted bentonite (Kunipia-F) which consisted of 99% montmorillonite. They reported a range for apparent diffusion coefficient as 2.5 × $10^{-11}$ to 1.9 × $10^{-13}$ $m^2/s$. As the rock capacity factor can be considered as $\rho K_d$ for montmorillonite (since the porosity is negligible), values measured on compacted BCF rock fall in the range measured on compacted bentonite. T. Wu et al. (2014) also studied the adsorption properties of Se(IV) species on compacted Gaomiaozi bentonite and found $D_e$ between 3.0×$10^{-12}$ $m^2/s$ and 5.3×$10^{-11}$ $m^2/s$ depending on the dry densities and the porosity of the sample (in their case the densities ranged from 1300 to 1800 $kg/m^3$).

## Results of in-diffusion experiments

Because no breakthrough can be obtained from this type of experiment, contrary to the through-diffusion experiment, the entire Se profile in the clay core is contributed to $Se_{slow}$. Apart from the region very close to the upstream compartment, a good fit is obtained (Figure 7). Fitting the $Se_{slow}$ peak of the through-diffusion experiment by totally neglecting $Se_{fast}$, the diffusion parameter values of both experiments differ less than a factor two (Table 3).

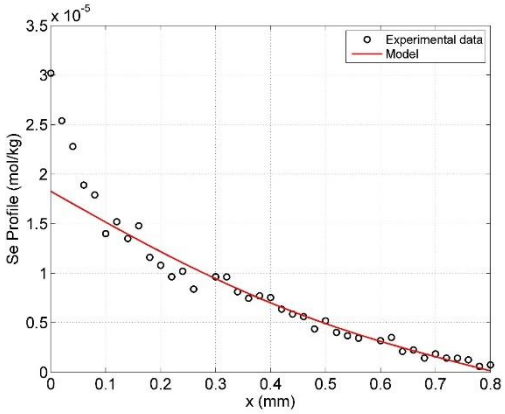


*Figure 7: In-diffusion experiment (sample P): Se profile in the clay core at the end of the experiment (data from shallow angle illumination XRF): experimental data and model assuming a single diffusing Se species (selenite).*

*Table 3: Summary of the Se diffusion parameters obtained from the experiments conducted in BCF. The distribution factor $K_d$ is calculated by assuming $\varepsilon_{tot}$ = 0.02 and $\rho$ = 2.7 kg/L.*

| | | $C_0$ (mol/L) | $D_a$ ($m^2/s$) | | | $\alpha$ (-) | | | $D_e$ ($m^2/s$) | | | $R$ (-) | $K_d$ (L/kg) |
|---|---|---|---|---|---|---|---|---|---|---|---|---|---|
| **Through-diffusion** | | | | | | | | | | | | | |
| **Se (all)** | $C_0$ | $1.06\cdot10^{-3}$ | $7.2\cdot10^{-12}$ | ± | $4.3\cdot10^{-12}$ | 0.21 | ± | 0.15 | $1.5\cdot10^{-12}$ | ± | $1.4\cdot10^{-12}$ | 10 | 0.07 |
| **$Se_{fast}$** | $C_{0,\ fast=0.04}C_0$ | $4.22\cdot10^{-5}$ | $1.5\cdot10^{-11}$ | ± | $4.7\cdot10^{-11}$ | 4.44 | ± | 20.60 | $6.7\cdot10^{-11}$ | ± | $3.7\cdot10^{-10}$ | 222 | 1.61 |
| **$Se_{slow}$** | $C_{0,slow=0.96}C_0$ | $1.01\cdot10^{-3}$ | $4.3\cdot10^{-14}$ | ± | $4.4\cdot10^{-15}$ | 1.44 | ± | 0.11 | $6.1\cdot10^{-14}$ | ± | $7.9\cdot10^{-15}$ | 72 | 0.52 |
| **$Se_{slow}$** | $C_{0,slow}=C_0$ | $1.06\cdot10^{-3}$ | $3.1\cdot10^{-14}$ | ± | $2.4\cdot10^{-15}$ | 1.95 | ± | 0.24 | $6.0\cdot10^{-14}$ | ± | $8.7\cdot10^{-15}$ | 98 | 0.70 |
| **In-diffusion** | | | | | | | | | | | | | |
| **$Se_{slow}$** | | $2.30\cdot10^{-5}$ | $1.5\cdot10^{-14}$ | ± | $2.0\cdot10^{-15}$ | 2.22 | ± | 0.16 | $3.3\cdot10^{-14}$ | ± | $5.0\cdot10^{-15}$ | 111 | 0.80 |

## Oxidation state of the adsorbed Se

The spectra of Se(0), $Na_2SeO_3$ are easily distinguishable. At selected points along the diffusion axis in the in-diffusion experiment on Sample P at one point visible alteration from the previously gathered spectrum occurred. With linear combination fitting evaluation involving the spectra of Se(0) and the sum spectra of the adsorbed $SeO_3$ species (Characteristic spectra), approximately 23±3% of selenium was found to be reduced to Se(0) (Figure 8). Overall, under the applied atmospheric conditions the Se oxidation state did not change significantly however, at points with high pyrite content local reduction could occur. The results are in good accordance with the presumption that $Na_2SeO_4$ is not sorbed onto BCF. Idemitsu et al. (2016) conducted their experiments with compacted montmorillonite under both atmospheric conditions and in Ar + 5% $H_2$ glovebox. They found with XANES measurements that Se remained in the oxidation state of +IV during the range of their experiment. As they worked with purified bentonite, pyrite was not present in the experimental conditions. Savoye et al. (2021) worked with Opalinus Clay containing around 1% pyrite under $CO_2/N_2$ glovebox. They studied a rock subjected to through-diffusion experiments with µ-XRF and µ-XANES. Close to the solid-liquid interface (in the vicinity of 1 mm) they experienced no change in the XANES spectra correlated to the spectra of selenite. Deeper in the solid state the characteristic peak of the white line of Se(0) appeared around 16660 eV. At local hot spots where Se was found to be concentrated the quantity of the reduced species emerged.

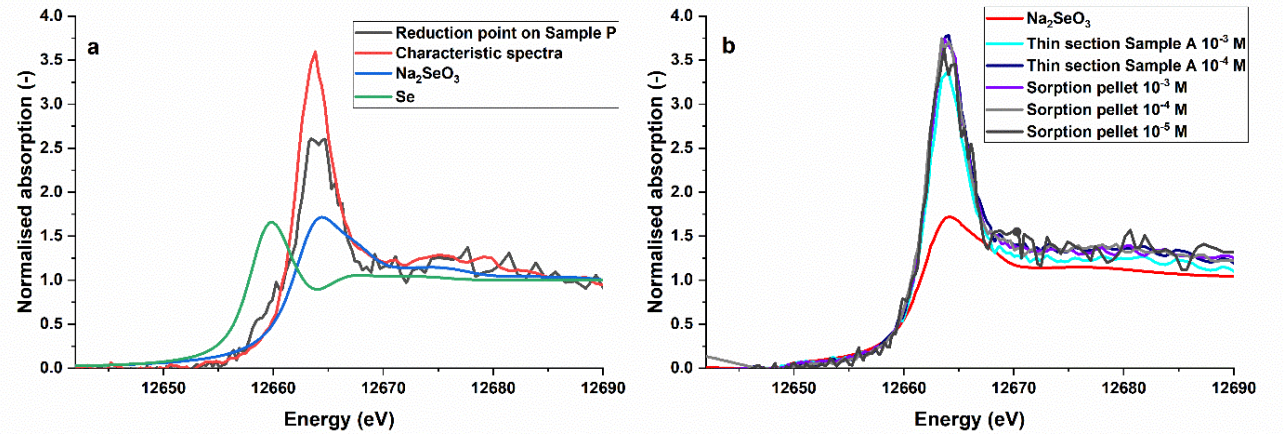


*Figure 8: XANES spectra of the sodium-selenite and the measured BCF Sample A in different forms at different concentrations (a) and the spectra showing reduction collected on in-diffusion Sample P (b).*

## Conclusions

Adsorption and diffusion properties of selenite on argillaceous core samples of the Boda Claystone Formation were investigated. Both compacted and crushed samples were studied under atmospheric conditions. Batch adsorption kinetics experiments showed that around 10 days of solid-liquid contact was already sufficient to reach equilibrium, however experiments were conducted for 28 days under atmospheric conditions. The adsorption isotherm at concentrations lower than $10^{-6}$ M has similar values obtained with pure clay minerals, Na-smectite and Na-illite. Above this concentration $K_d$ started to part away from the adsorption isotherm of pure minerals and the difference gets larger with increasing equilibrium concentration. Comparing to the adsorption isotherm collected on COx similarities were found, the $K_d$ started to decrease for concentrations higher than $10^{-6}$-$10^{-7}$ M. The adsorption isotherm on BCF although is even lower than the one on COx, the difference is caused by the lower clay mineral content of the BCF. Langmuir isotherm fitting suggests that two different sorption sites are present in BCF. In the low concentration region the strong sites (high affinity sites) on the studied BCF sample have similar capacity to the pure minerals, but above nd $10^{-7}$ M equilibrium concentration the strong sites start to saturate similarly to other (COx, OPA) clay-rich rock samples and $K_d$ starts to decrease. As selenate was identified in the initial solution used for diffusion experiments the through-diffusion data cannot be fitted with a single species model. The two species model roughly fits the experimental data resulting in diffusion parameters for both selenite and selenate. The obtained diffusion parameters are consistent with the values found from the in-diffusion experiment: a selenite apparent diffusion coefficient $D_a^{selenite}$ = (1.5-4.3) $\times 10^{-14}$ m$^2$/s and a rock capacity factor $\alpha^{selenite}$ =1.4-2.2. The selenate fit results are not reliable. Synchrotron radiation XRF with shallow angle illumination is a promising alternative to abrasive peeling and radiotracer method for diffusion profile measurements. The mass balance of selenium had sufficiently low error (around 7%) calculated from the concentration changes in the reservoirs and the calculated adsorbed selenium content of the rock. The oxidation state of adsorption selenium remained mostly +IV, however 23% reduction at one point on a sample with high pyrite content was experienced. The retention capabilities of BCF for selenite were found to be comparable to already studied argillaceous rocks (Opalinus Clay, Callovo-Oxfordian Clay), which is an important contribution for the safety assessment of a potential deep geological repository in BCF (Czömpöly et al., 2023).

## References

Aertsens, M., 2011. Migration in clay: experiments and models SCK CEN Report SCKCEN-ER-165 (SCK CEN, Mol, Belgium). Mol, Belgium.

Altmann, S., Aertsens, M., Appelo, T., Bruggeman, C., Gaboreau, S., Glaus, M., Jacquier, P., Kupcik, T., Maes, N., Montoya, V., n.d. Processes of cation migration in clayrocks: Final Scientific Report of the CatClay European Project.

Aurelio, G., Fernández-Martínez, A., Cuello, G.J., Román-Ross, G., Alliot, I., Charlet, L., 2010. Structural study of selenium(IV) substitutions in calcite. Chem Geol 270, 249–256. https://doi.org/10.1016/J.CHEMGEO.2009.12.004

Bailey, R.T., 2016. Review: Selenium contamination, fate, and reactive transport in groundwater in relation to human health. Hydrogeology Journal 2016 25:4 25, 1191–1217. https://doi.org/10.1007/S10040-016-1506-8

Bradbury, M.H., Baeyens, B., 1998. A Physicochemical Characterisation and Geochemical Modelling Approach for Determining Porewater Chemistries in Argillaceous Rocks. Geochim Cosmochim Acta 62, 783–795. https://doi.org/10.1016/S0016-7037(97)00387-6

Breitner, D., Osán, J., Fábián, M., Zagyvai, P., Szabó, C., Dähn, R., Marques Fernandes, M., Sajó, I.E., Máthé, Z., Török, S., 2015. Characteristics of uranium uptake of Boda Claystone Formation as the candidate host rock of high level radioactive waste repository in Hungary. Environ Earth Sci 73, 209–219. https://doi.org/10.1007/S12665-014-3413-4

Bruggeman, C., 2006. Assessment of the Geochemical Behaviour of Selenium Oxyanions under Boom Clay Geochemical Conditions . Katholieke Universiteit Leuven, Leuven.

Bruggeman, C., Maes, A., Vancluysen, J., Vandemussele, P., 2005. Selenite reduction in Boom clay: Effect of FeS2, clay minerals and dissolved organic matter. Environmental Pollution 137, 209–221. https://doi.org/10.1016/J.ENVPOL.2005.02.010

Crank, J., 1975. THE MATHEMATICS OF DIFFUSION CLARENDON PRESS OXFORD 1975.

Czömpöly, O., Fábián, M., Korányi, T.I., Nagy, G., Horváth, Z.E., Zizak, I., Pollastri, S., Aertsens, M., Osán, J., 2023. Adsorption and diffusion of selenite on Boda Claystone Formation. Appl Clay Sci 241, 106997. https://doi.org/10.1016/J.CLAY.2023.106997

Dähn, R., Scheidegger, A.M., Manceau, A., Curti, E., Baeyens, B., Bradbury, M.H., Chateigner, D., 2002. Th Uptake on Montmorillonite: A Powder and Polarized Extended X-Ray Absorption Fine Structure (EXAFS) Study. J Colloid Interface Sci 249, 8–21. https://doi.org/10.1006/JCIS.2002.8236

De Cannière, P., Maes, A., Williams, S., Bruggeman, C., Beauwens, T., Maes, N., Cowper, M., 2010. Behaviour of Selenium in Boom Clay, External report SCK•CEN-ER-120 10/PDC/P-9. Boeretang.

Descostes, M., Blin, V., Bazer-Bachi, F., Meier, P., Grenut, B., Radwan, J., Schlegel, M.L., Buschaert, S., Coelho, D., Tevissen, E., 2008. Diffusion of anionic species in Callovo-Oxfordian argillites and Oxfordian limestones (Meuse/Haute–Marne, France). Applied Geochemistry 23, 655–677. https://doi.org/10.1016/J.APGEOCHEM.2007.11.003

Fedor, F., Máthé, Z., Ács, P., Koroncz, P., 2019. New results of Boda Claystone research: Genesis, mineralogy, geochemistry, petrophysics. Geological Society, London, Special Publications 482, 75–92.

Fernández, A.M., León, F.J., Nieto, P., Alonso, U., Missana, T., 2023. Characterization of the NAu nontronites. Mineral Sheets of different Clays.

Frasca, B., Savoye, S., Wittebroodt, C., Leupin, O.X., Michelot, J.L., 2014. Comparative study of Se oxyanions retention on three argillaceous rocks: Upper Toarcian (Tournemire, France), Black Shales (Tournemire, France) and Opalinus Clay (Mont Terri, Switzerland). J Environ Radioact 127, 133–140. https://doi.org/10.1016/J.JENVRAD.2013.10.005

Gailhanou, H., Lerouge, C., Debure, M., Gaboreau, S., Gaucher, E.C., Grangeon, S., Grenèche, J.M., Kars, M., Madé, B., Marty, N.C.M., Warmont, F., Tournassat, C., 2017. Effects of a thermal perturbation on mineralogy and pore water composition in a clay-rock: An experimental and modeling study. Geochim Cosmochim Acta 197, 193–214. https://doi.org/10.1016/J.GCA.2016.10.004

García-Gutiérrez, M., Mingarro, M., Missana, T., 2023a. Determination of Kd values in batch/compacted systems experimental approach and data analysis. in preparation.

García-Gutiérrez, M., Mingarro, M., Morejón, J., Alonso, U., Missana, T., 2023b. Analysis of the Role of Water Saturation Degree in HTO, 36Cl, and 75Se Diffusion in Sedimentary Rock. Minerals 13, 593. https://doi.org/10.3390/MIN13050593/S1

García-Gutiérrez, M., Missana, T., Mingarro, M., Molinero, J., 2006. Overview of laboratory methods employed for obtaining diffusion coefficients in FEBEX compacted bentonite Descripción de los métodos de laboratorio empleados para obtener coeficientes de difusión en bentonita compactada FEBEX.

Gergely, F., Osán, J., Szabó, B.K., Török, S., 2016. Analytical performance of a versatile laboratory microscopic X-ray fluorescence system for metal uptake studies on argillaceous rocks. Spectrochim Acta Part B At Spectrosc 116, 75–84.

Glaus, M.A., Aertsens, M., Maes, N., Van Laer, L., Van Loon, L.R., 2015. Treatment of boundary conditions in through-diffusion: A case study of 85Sr2 + diffusion in compacted illite. J Contam Hydrol 177–178, 239–248. https://doi.org/10.1016/J.JCONHYD.2015.03.010

Glaus, M.A., Frick, S., Van Loon, L.R., 2017. Diffusion of selected cations and anions in compacted montmorillonite and bentonite, Technical report NTB 17-12, NAGRA. Villigen.

Goldberg, S., 2013. Modeling Selenite Adsorption Envelopes on Oxides, Clay Minerals, and Soils using the Triple Layer Model. Soil Science Society of America Journal 77, 64–71. https://doi.org/10.2136/SSSAJ2012.0205

He, H., Liu, J., Dong, Y., Li, H., Zhao, S., Wang, J., Jia, M., Zhang, H., Liao, J., Yang, J., Yang, Y., Liu, N., 2019. Sorption of selenite on Tamusu clay in simulated groundwater with high salinity under aerobic/anaerobic conditions. J Environ Radioact 203, 210–219. https://doi.org/10.1016/J.JENVRAD.2019.03.020

Idemitsu, K., Kozaki, H., Yuhara, M., Arima, T., Inagaki, Y., 2016. Diffusion behavior of selenite in purified bentonite. Progress in Nuclear Energy 92, 279–285. https://doi.org/10.1016/J.PNUCENE.2015.08.012

Jackson, M.L., 2005. Soil chemical analysis : advanced course : a manual of methods useful for instruction and research in soil chemistry, physical chemistry of soils, soil fertility, and soil genesis, second edition. ed. Parallel Press, Madison.

Karydas, A.G., Czyzycki, M., Leani, J.J., Migliori, A., Osan, J., Bogovac, M., Wrobel, P., Vakula, N., Padilla-Alvarez, R., Menk, R.H., Gol, M.G., Antonelli, M., Tiwari, M.K., Caliri, C., Vogel-Mikuš, K., Darby, I., Kaiser, R.B., IUCr, 2018. An IAEA multi-technique X-ray spectrometry endstation at Elettra Sincrotrone Trieste: benchmarking results and interdisciplinary applications. urn:issn:1600-5775 25, 189–203. https://doi.org/10.1107/S1600577517016332

Kläning, U.K., Sehested, K., 1986. Selenium(V). A pulse radiolysis study. Journal of Physical Chemistry 90, 5460–5464. https://doi.org/10.1021/J100412A112/ASSET/J100412A112.FP.PNG_V03

León, F.J., García-Gutiérrez, M., Fernández, A.M., Missana, T., 2023. Analysis of selenite adsorption processes in Fe-rich smectites. in preparation.

Li, Y.H., Gregory, S., 1974. Diffusion of ions in sea water and in deep-sea sediments. Geochim Cosmochim Acta 38, 703–714. https://doi.org/10.1016/0016-7037(74)90145-8

Lin, J., Chen, N., Feng, R., Nilges, M.J., Jia, Y., Wang, S., Pan, Y., 2020. Sequestration of Selenite and Selenate in Gypsum (CaSO4·2H2O): Insights from the Single-Crystal Electron Paramagnetic Resonance

Spectroscopy and Synchrotron X-ray Absorption Spectroscopy Study. Environ Sci Technol 54, 3169–3180. https://doi.org/10.1021/ACS.EST.9B05714

Liu, S., Salhi, E., Huang, W., Diao, K., von Gunten, U., 2019. Kinetic and mechanistic aspects of selenite oxidation by chlorine, bromine, monochloramine, ozone, permanganate, and hydrogen peroxide. Water Res 164, 114876. https://doi.org/10.1016/J.WATRES.2019.114876

Marques Fernandes, M., Vér, N., Baeyens, B., 2015. Predicting the uptake of Cs, Co, Ni, Eu, Th and U on argillaceous rocks using sorption models for illite. Applied Geochemistry 59, 189–199. https://doi.org/10.1016/J.APGEOCHEM.2015.05.006

Mell, P., Megyeri, J., Riess, L., Máthé, Z., Hámos, G., Lázár, K., 2006. Diffusion of Sr, Cs, Co and I in argillaceous rock as studied by radiotracers. J Radioanal Nucl Chem 268, 411–417. https://doi.org/10.1007/S10967-006-0178-6

Missana, T., Alonso, U., García-Gutiérrez, M., 2021. Evaluation of component additive modelling approach for europium adsorption on 2:1 clays: Experimental, thermodynamic databases, and models. Chemosphere 272, 129877. https://doi.org/10.1016/J.CHEMOSPHERE.2021.129877

Missana, T., Alonso, U., García-Gutiérrez, M., 2009a. Experimental study and modelling of selenite sorption onto illite and smectite clays. J Colloid Interface Sci 334, 132–138. https://doi.org/10.1016/J.JCIS.2009.02.059

Missana, T., Alonso, U., Scheinost, A.C., Granizo, N., García-Gutiérrez, M., 2009b. Selenite retention by nanocrystalline magnetite: Role of adsorption, reduction and dissolution/co-precipitation processes. Geochim Cosmochim Acta 73, 6205–6217. https://doi.org/10.1016/J.GCA.2009.07.005

Montavon, G., Guo, Z., Lützenkirchen, J., Alhajji, E., Kedziorek, M.A.M., Bourg, A.C.M., Grambow, B., 2009. Interaction of selenite with MX-80 bentonite: Effect of minor phases, pH, selenite loading, solution composition and compaction. Colloids Surf A Physicochem Eng Asp 332, 71–77. https://doi.org/10.1016/J.COLSURFA.2008.09.014

Németh, T., Máthé, Z., Pekker, P., Dódony, I., Kovács-Kis, V., Sipos, P., Cora, I., Kovács, I., 2016. Clay mineralogy of the Boda Claystone Formation (Mecsek Mts., SW Hungary). Open Geosciences 8, 259–274. https://doi.org/10.1515/GEO-2016-0024

Nuclear Energy Agency (NEA), 2022. Clay Club Catalogue of Characteristics of Argillaceous Rocks.

Osán, J., Kéri, A., Breitner, D., Fábián, M., Dähn, R., Simon, R., Török, S., 2014. Microscale analysis of metal uptake by argillaceous rocks using positive matrix factorization of microscopic X-ray fluorescence elemental maps. Spectrochim Acta Part B At Spectrosc 91, 12–23. https://doi.org/10.1016/J.SAB.2013.11.002

Puranen, A., Jonsson, M., Dähn, R., Cui, D., 2009. Immobilization of selenate by iron in aqueous solution under anoxic conditions and the influence of uranyl. Journal of Nuclear Materials 392, 519–524. https://doi.org/10.1016/J.JNUCMAT.2009.04.016

Rahman, M.S., Clark, M.W., Yee, L.H., Comarmond, M.J., Payne, T.E., Burton, E.D., 2019. Effects of pH, competing ions and aging on arsenic(V) sorption and isotopic exchange in contaminated soils. Applied Geochemistry 105, 114–124. https://doi.org/10.1016/J.APGEOCHEM.2019.04.016

Sámson, M. (ed), 2015. Final report of borehole BAF-2. (In Hungarian) Manuscript, PURAM, Paks, RHK-N-011/14.

Savoye, S., Schlegel, M.L., Frasca, B., 2021. Mobility of selenium oxyanions in clay-rich media: A combined batch and diffusion experiments and synchrotron-based spectroscopic investigation. Applied Geochemistry 128, 104932. https://doi.org/10.1016/J.APGEOCHEM.2021.104932

Séby, F., Potin-Gautier, M., Giffaut, E., Borge, G., Donard, O.F.X., 2001. A critical review of thermodynamic data for selenium species at 25°C. Chem Geol 171, 173–194. https://doi.org/10.1016/S0009-2541(00)00246-1

Stucki, J.W., Golden, D.C., Roth, C.B., 1984. Preparation and handling of dithionite-reduced smectite suspensions. Clays Clay Miner 32, 191–197.

Takeda, M., Nakajima, H., Zhang, M., Hiratsuka, T., 2008. Laboratory longitudinal diffusion tests: 1. Dimensionless formulations and validity of simplified solutions. J Contam Hydrol 97, 117–134. https://doi.org/10.1016/J.JCONHYD.2008.01.004

Tertre, E., Dazas, B., Asaad, A., Ferrage, E., Grégoire, B., Hubert, F., Delville, A., Delay, F., 2021. Connecting molecular simulations and laboratory experiments for the study of time-resolved cation-exchange process in the interlayer of swelling clay minerals. Appl Clay Sci 200, 105913. https://doi.org/10.1016/J.CLAY.2020.105913

Tian, Q., Guo, B., Chuaicham, C., Sasaki, K., 2020. Mechanism analysis of selenium (VI) immobilization using alkaline-earth metal oxides and ferrous salt. Chemosphere 248, 126123. https://doi.org/10.1016/J.CHEMOSPHERE.2020.126123

Van Loon, L.R., Mibus, J., 2015. A modified version of Archie's law to estimate effective diffusion coefficients of radionuclides in argillaceous rocks and its application in safety analysis studies. Applied Geochemistry 59, 85–94. https://doi.org/10.1016/J.APGEOCHEM.2015.04.002

Wu, H., Huang, W., Duan, Z., Luo, M., Wang, Z., Hua, R., 2020. Investigation of Se(IV) diffusion in compacted Tamusu clay by capillary method. Journal of Radioanalytical and Nuclear Chemistry 2020 324:2 324, 903–911. https://doi.org/10.1007/S10967-020-07089-6

Wu, T., Wang, H., Zheng, Q., Zhao, Y.L., van Loon, L.R., 2014. Diffusion behavior of Se(IV) and Re(VII) in GMZ bentonite. Appl Clay Sci 101, 136–140. https://doi.org/10.1016/J.CLAY.2014.07.028

Zizak, I., 2016. The mySpot beamline at BESSY II. Journal of large-scale research facilities JLSRF 2, A102–A102. https://doi.org/10.17815/JLSRF-2-113

# 4. Achievements with respect to project objectives – Conclusions

*New/missing data available for sorption models (e.g. surface complexation constants)*

Batch sorption tests provided new selenite sorption edge measurements for raw and treated nontronite, FEBEX and sorption isotherms on raw and treated nontronite, FEBEX, Callovo-Oxfordian Clay and Boda Claystone. Data interpretation including detailed sorption modelling for nontronite is on-going.

*Transferability of batch sorption data to compact system*

The results obtained for selenite in the compacted FEBEX bentonite suggest that batch sorption data can be transferred to compact systems. Nevertheless, this could not be clearly shown in the case of the COx clay. Using a similar selenium concentration in batch sorption tests with consolidated samples, a $K_d$ value measured in disperse for system could not be reached even after 172 days of contact time (García-Gutiérrez et al., 2023a). This may indicate importance of sorption kinetics, which might be different in the batch/consolidated systems, but also can be related to the fact that adsorption at the selected concentration is somewhat related to “strong” sites in the material. This point is still under study.

Modelling of Se(IV) through- and in-diffusion profiles on BCF rock samples provided consistent diffusion parameters, however, $K_d$ were found to be lower than expected from batch sorption experiments. In this context, it should also be noted that the derived values bear a high uncertainty and comparison should be done with care (Czömpöly et al., 2023).

*Transferability of data from model systems to complex systems*

In the case of Se(IV) adsorption in clays, different factors may influence the sorption properties, as for example the presence of calcium or iron ions. Their effect is different if they are in the clay structure or aqueous phase. If the processes involved are adequately described, they can be accounted for evaluating the overall retention on nontronite. An accurate chemical characterization of the system is mandatory. Furthermore, the best prospect to accurately model the “complex system” consists in starting from simplest ones, when the additivity of sorption in different components can be demonstrated.

The existence of materials different from clay (even in small concentration) in an argillaceous rock might be responsible of additional contribution in retention/transport processes.

*Adequate description of sorption competition*

The theoretical way to describe this phenomenon is well defined and can be implemented in geochemical calculations. The main problem might be related to the lack of data or the poor description of the chemical system.

*Irreversibility of sorption under certain conditions*

The irreversibility of selenite adsorption on BCF rocks was addressed by isotopic exchange experiments at EK. The adsorption of selenite onto BCF was obtained as reversible around 80-85% in the low concentration region meanwhile above $10^{-7}$ M equilibrium concentration the adsorption was found to be fully reversible. These findings are in-line with the Langmuir modelling of the adsorption isotherm, strong sites are dominant for the lower concentration range (Czömpöly et al., 2023).

However, the results obtained in diffusion tests in the Spanish lutite, indicated that possibly the entrapment of selenite in gypsum is a process different from adsorption, which produce a stronger retardation than

adsorption. Indeed, these types of processes are expected to influence the kinetic of desorption. This is also valid for dissolution/coprecipitation process and the formation of secondary phases (García-Gutiérrez et al., 2023b).

*State-of-the-art spectroscopic, diffractometric and microscopic techniques towards system understanding of irreversible uptake processes*

The oxidation state of adsorbed selenium could be successfully studied with XANES spectroscopy, even on the microscopic scale. Selenium was found to remain as +IV in the albitic claystone (formed under oxidative conditions) representative for the majority of BCF. However, 23% reduction was experienced at one point on a sample with high pyrite content (from a reductive region of the BCF core) (Czömpöly et al., 2023). Reduction of selenite can result in an increased and irreversible uptake.

*Description of transport experiments based on mechanistic understanding (anion exclusion, surface diffusion, saturation degree, pore characteristics,…)*

The valence state (monovalent versus divalent anion) has a clear effect on the anion accessible porosity (by factor of 2.5) and effective diffusion coefficient (by factor of 5) for the diffusion of Selenate, Se(VI), at 0.01 M in Na-conditioned illite (at pH ± 8.15).

All transport experiments conducted with Se oxyanions on the natural clay rocks have only been modelled using classical diffusion-retention transport models which does not account for possible changes in the speciation of this element.

*Advanced spectroscopy methods for better understanding of the transport behaviour*

FTIR and RAMAN techniques are under study by CIEMAT to provide info on secondary phase formation from nontronite. This should provide additional info for sorption modelling.

Ion chromatography (EK) was used to investigate Se(IV)/(VI) speciation ratio as input for the diffusion modelling.

Because of the sensitive nature of selenium oxyanions for redox reactions, its migration properties cannot be predicted without taking into consideration the possible speciation changes because of the different characteristics of each form. The oxidation state of adsorbed selenium could be successfully studied with XANES spectroscopy, even on the microscopic scale (EK).

Synchrotron radiation XRF (EK) with shallow angle illumination is a promising alternative to abrasive peeling and radiotracer method for diffusion profile measurements as was used on BCF (Czömpöly et al., 2023).

# Chapter 2: Mobility of moderately sorbing cationic radionuclides in clay

Two research teams conducted research on moderately sorbing cationic radionuclides (mainly Ra and Ba). FZJ (Julich, Germany) conducted adsorption experiments of Ra and Ba on model clay systems (illite and montmorillonite) and studied Ra diffusion behaviour in Opalinus Clay (in collaboration with PSI). This was further complemented with a study where they provided a process-based model describing transport induced co-precipitation and radionuclide retention ((Ba,Ra,Sr)$SO_4$ solid solution formation).

CIEMAT (Madrid, Spain) conducted research on the mobility of Ra, Ba (and Sr) in model clay systems (illite, nontronite, FEBEX) and Callovo-Oxfordian Clay.

## 1. Adsorption of $^{226}$Ra and Ba on clay minerals

M. Klinkenberg, F. Brandt, D. Bosbach
*FzJ, Julich, Germany*

B. Baeyens, M.M. Fernandes
*PSI, Villigen PSI, Switzerland*

The following report is a summary of the experiments and modelling results provided in Klinkenberg et al. (2021) and Marques Fernandes et al. (2023). For details, please refer to the respective publication.

Key questions/objectives:

- Is Ba a good chemical analogue for $^{226}$Ra and at which conditions?
- How can a thermodynamic model describe the effect of pH and ionic strength on the adsorption behaviour of Ba and Ra onto 2:1 clay minerals?

### Introduction

Argillaceous rocks are considered suitable for the construction of deep geological waste repositories for high-level radioactive waste in several waste management programs e.g. in Switzerland, Belgium, or France. To account for the retardation properties of clay minerals in these host rocks in safety studies, thermodynamic models capable of predicting the retention of radionuclides over a wide range of physico-chemical conditions are crucial. Illite, smectite and illite/smectite mixed layers are relevant constituents of various argillaceous host rocks. In addition, bentonites are envisaged as engineered barriers in underground waste disposal concepts. Montmorillonite, the major constituent of bentonite (up to 90 wt.-%) is an important barrier for potentially released radionuclides.

Adsorption data for $^{226}$Ra onto illite and montmorillonite are sparse in the literature. Because of this knowledge gap, the adsorption and diffusion of $^{226}$Ra in clay minerals are assumed to behave similar as Ba, based on chemical analogy. In order to verify this hypothesis and improve the quantitative understanding of the adsorption of $^{226}$Ra by 2:1 clay minerals, a combined adsorption and modelling study was carried out. Parallel adsorption experiments were carried out onto the homo-ionic Na forms of montmorillonite (SWy) and illite (IdP) in diluted systems and compared to the adsorption of Ba under the same conditions. $^{226}$Ra and Ba adsorption edges in the pH range 5 to 10 at different ionic strengths (0.01-0.3 M NaCl) and Ba isotherms (pH 5.1 – 9.0, $10^{-9}$ M < [Ba] > $10^{-2}$ M) were carried out on Na- SWy and Na-IdP. The 2-site Protolysis Non-Electrostatic Surface Complexation and Cation Exchange adsorption model (2SPNE SC/CE) developed for montmorillonite (Bradbury & Baeyens, 1997) and illite (Bradbury & Baeyens, 2009) reproduces the experimental data for both elements well.

## Materials & methods

The Na-SWy (SWy-2, Wyoming, USA) suspensions were prepared following the procedure as described in Baeyens & Bradbury (1995). The preparation and conditioning of the Na-IdP (IdP-2; Illite de Puy, Le Puy-en-Velay, France) suspensions was carried out in the same way as described in detail in the studies of Bradbury & Baeyens (2005) and Marques Fernandes & Baeyens (2019). The cation exchange capacity (CEC) of both clays was determined in earlier studies at neutral pH and yielded a value of 870 ± 35 meq·kg$^{-1}$ for SWy (Baeyens & Bradbury, 1997) and of 225±10 meq·kg$^{-1}$ for IdP (Marques Fernandes & Baeyens, 2019).

Three types of adsorption experiments were performed (a summary of all experiments is given in Table 1): (i) pH dependent adsorption of trace $^{226}$Ra and of trace Ba at different ionic strengths (edges); (ii) concentration dependent adsorption of Ba (isotherms) at constant pH and ionic strength; (iii) measurements of the adsorption of trace $^{226}$Ra as a function of increasing Ba concentrations (along the Ba isotherm). Adsorption edges were obtained by equilibrating trace concentrations of ($^{133}$Ba + $^{137}$Ba) or $^{226}$Ra with the respective clay from the acidic to the basic pH range at ionic strengths of 0.02 M to 0.3 M. Stable $^{137}$Ba was used as a carrier for $^{133}$Ba to adjust the total Ba concentrations. Different buffers (Sigma-Aldrich) at concentrations of 2·10$^{-3}$ M were used to prevent a pH drift in the adsorption experiments: $C_6H_{13}NO_4S$ (MES, for pH = 5.5, 6.2 and 6.8), $C_7H_{15}NO_4S$ (MOPS, for pH = 7.3), $H_2NC(CH_2OH)_3$ (TRIS, for pH = 7.9 and 8.5), or $C_8H_{17}NOS$ (CHES, for pH = 9.2 and 9.8). The pH was adjusted with 1 M NaOH and 1 M $HNO_3$, respectively. Ba adsorption isotherms were collected by labelling stable Ba solutions in the required concentrations with $^{133}$Ba with a fixed pH = 7.0 (MOPS buffer) and ionic strength of 0.02 M NaCl. Each standard solution containing $^{133}$Ba was equilibrated at least overnight before use to avoid interference by sorption of the tracer on the wall. An adsorption isotherm with only with $^{226}$Ra was not determined. However, if both trace $^{133}$Ba and trace $^{226}$Ra show similar adsorption with increasing Ba concentration, they can be considered as chemical analogues with respect to adsorption on the two clay minerals. The adsorption of trace $^{226}$Ra as a function of increasing Ba concentration was measured by labelling stable Ba solutions in the required concentrations with $^{226}$Ra, with a fixed pH = 7.0 (MOPS buffer) and ionic strength of 0.02 M NaCl.

All adsorption edges and isotherms were carried out at room temperature (21 ± 2 °C) under atmospheric air conditions (Table 1). The radioactive tracer solutions were prepared from well-characterized stock solutions. The $^{133}$Ba stock solution was purchased from Eckert and Ziegler, Isotope Products Laboratories (California, USA) and diluted in deionized water to produce an acidic stock solution (pH ~1), whereas the $^{226}$Ra stock solution (5 · 10$^{-5}$ mol L$^{-1}$) was prepared from $RaBr_2$ and measured against an independent standard. Samples were prepared in 50 mL polyethylene centrifuge tubes in duplicates. The centrifuge tubes were mounted into end-over-end shakers to react for 7 days. Phase separation was obtained by centrifugation and filtration (of some samples), and aliquots of the supernatants were analysed for their elemental concentrations. The pH of each sample was measured using a Metrohm combined electrode calibrated against commercially available buffers. The activity of $^{133}$Ba was determined from radio-assays of aliquots of the supernatants as well as of the labelled standard solutions prepared simultaneously at the start of the adsorption experiments using a Canberra Packard Cobra Quantum gamma counter. The concentration of $^{226}$Ra was determined by LSC-measurements using the ultra-low level liquid scintillation spectrometer Quantulus (Perkin Elmer, USA). For the analyses, 1 mL aliquots of the supernatants as well as of the labelled standard solutions were mixed with 19 mL of Ultima Gold LLT cocktail (Perkin Elmer, USA). The LSC-glass vials were glued gas tight with epoxy resin to avoid the release of Rn. The measurement of the samples was carried out after 38 days in equilibrium condition of $^{226}$Ra and Rn. The initial and equilibrium concentrations of $^{137}$Ba in the combined Ba/$^{226}$Ra experiment were analysed using an ICP-MS ELAN 6100 DRC (PerkinElmer SCIEX) instrument after dilution and acidification with $HNO_3$.

*Table 1: Summary of Ba and $^{226}$Ra adsorption experiments on Na-SWy and Na-IdP.*

| Clay | Element | Type of experiment | Ba or Ra initial concentration (M) | Ba equilibrium concentration range (M) | NaCl (M) | S/L (g $L^{-1}$) | pH |
|---|---|---|---|---|---|---|---|
| SWy | $^{133}$Ba | Edge | $3.3\cdot10^{-8}$ - $3.9\cdot10^{-8}$ | | 0.03 | 2.91 | 3.3 - 9.3 |
| SWy | $^{133}$Ba | Edge | $4.3\cdot10^{-8}$ - $3.7\cdot10^{-8}$ | | 0.3 | 2.96 | 2.6 - 10.6 |
| SWy | $^{226}$Ra | Edge | $2.0\cdot10^{-7}$ | | 0.02 | 2.21 | 5.5 - 10.2 |
| SWy | $^{226}$Ra | Edge | $1.9\cdot10^{-8}$ | | 0.14 | 8.33 | 5.6 - 10.2 |
| SWy | $^{226}$Ra | Edge | $1.8\cdot10^{-8}$ | | 0.3 | 13.95 | 5.7 - 9.9 |
| SWy | $^{137}$Ba/$^{133}$Ba | Isotherm | | $2.03\cdot10^{-9}$ - $1.8\cdot10^{-2}$ | 0.02 | 0.88 - 4.39 | 6.9 - 7.1 |
| SWy | $^{137}$Ba/$^{226}$Ra | Isotherm[a] | | [$^{137}$Ba] 0.0 - $1.7\cdot10^{-2}$ [$^{226}$Ra] $4.3\cdot10^{-9}$ - $5.9\cdot10^{-9}$ | 0.02 | 0.84 - 4.29 | 6.5 - 7.0 |
| IdP | $^{133}$Ba/$^{137}$Ba | Isotherm | - | $2.2\cdot10^{-10}$ – $7.2\cdot10^{-3}$ | 0.02 | 2.0 – 9.6 | 5.1 |
| IdP | $^{133}$Ba/$^{137}$Ba | Isotherm | - | $1.8\cdot10^{-9}$ – $1.9\cdot10^{-2}$ | 0.02 | 1.3 | 6.6 |
| IdP | $^{133}$Ba/$^{137}$Ba | Isotherm | - | $2.6\cdot10^{-10}$ – $1.0\cdot10^{-2}$ | 0.02 | 1.1 – 11.2 | 6.9 |
| IdP | $^{133}$Ba/$^{137}$Ba | Isotherm | - | $1.2\cdot10^{-10}$ – $6.9\cdot10^{-3}$ | 0.02 | 2.0 – 9.6 | 7.6 |
| IdP | $^{133}$Ba/$^{137}$Ba | Isotherm | - | $3.7\cdot10^{-11}$ – $7.2\cdot10^{-3}$ | 0.02 | 3.6 – 17.3 | 9.0 |
| IdP | $^{133}$Ba | Edge | $7.7\cdot10^{-8}$ | - | 0.02 | 1.3 | 5.1 – 10.9 |
| IdP | $^{133}$Ba | Edge | $3.6\cdot10^{-8}$ | - | 0.03 | 2.2 | 5.3 - 9.3 |
| IdP | $^{133}$Ba | Edge | $3.6\cdot10^{-8}$ | - | 0.3 | 1.9 | 5.5 - 10.6 |
| IdP | $^{226}$Ra | Edge | $8.0\cdot10^{-8}$ | - | 0.02 | 1.3 | 5.5 – 11.5 |
| IdP | $^{226}$Ra | Edge | $1.9\cdot10^{-8}$ | - | 0.14 | 15.1 | 5.5 – 9.3 |
| IdP | $^{226}$Ra | Edge | $1.9\cdot10^{-8}$ | - | 0.3 | 5.8 | 5.6 – 9.4 |
| IdP | $^{226}$Ra/$^{137}$Ba | Isotherm[a] | [$^{226}$Ra] $1.4\cdot10^{-7}$ | $3.5\cdot10^{-8}$ - $1.8\cdot10^{-2}$ | 0.02 | 1.3 | 7.0 |

[a]Ba isotherm in the presence of trace $^{226}$Ra

## Adsorption modelling

The adsorption of Ra and Ba on montmorillonite and illite is mainly controlled by $Ra^{2+}$-$Na^{+}$ and $Ba^{2+}$-$Na^{+}$ cation exchange reactions on the planar sites, which can be written as follows:

$$2\text{Na-clay} + Me^{2+} \leftrightarrow \text{Me-clay} + 2\ Na^{+} \quad (1)$$

$Me^{2+}$ are $Ra^{2+}$ or $Ba^{2+}$. To describe the reaction in terms of a so-called selectivity coefficient a mass action law is normally used. The selectivity coefficients in our studies ($K_c$) are defined according to the Gaines and Thomas convention (Gaines & Thomas, 1955), using the fractional scale for the adsorbed cations and the molarity scale for the cations in solution:

$$^{Me}_{Na}K_c = \frac{N_{Me}}{N_{Na}^2}\frac{[Na]^2}{[Me]}\frac{(\gamma_{Na})^2}{(\gamma_{Me})} \quad (2)$$

$N_{Me}$ and $N_{Na}$ are the equivalent fractional occupancies, defined as the equivalent of Na or Me adsorbed per kg of clay mineral divided by the cation exchange capacity (CEC) [eq/kg]; [Na] and [Me] are the aqueous molar concentrations (M) and $\gamma_{Na}$ and $\gamma_{Me}$ are aqueous phase activity coefficients. The selectivity coefficients for the cation exchange of $Ba^{2+}$ and $Ra^{2+}$ with respect to $Na^{+}$ on the planar sites (PS) of montmorillonite and illite were derived by fitting the experimental data with the cation exchange reactions. In contrary to montmorillonite where only PS are involved to model the experimental data, additional cation exchange sites were necessary to quantitatively describe the adsorption data for Ba and Ra.To model the experimental data at higher ionic strength and pH > 8, an additional adsorption mechanism had to be

considered. In this case the 2 site protolysis non-electrostatic surface complexation (2SPNE SC/CE) model for montmorillonite (Bradbury & Baeyens, 1997) and for illite (Bradbury & Baeyens, 2009) was applied. The uptake of Ra/Ba was described by surface complexation on the amphoteric edge sites of the respective clay mineral's platelets. The type of sites, the capacity and protolysis constants of these sites are defined in the 2SPNE SC/CE model. The surface complexation constants for $^{226}$Ra and Ba have been derived in this study from the experimental data. These thermodynamic calculations were performed with the code MINSORB (Bradbury & Baeyens, 1997), which is derived from geochemical code MINEQL (Westall et al., 1976), containing subroutines for calculating CE and SC reactions simultaneously. Aqueous activity coefficients were calculated using the Davies relation (Davies, 1962) with a value of 0.3 for the $C_D$ constant.

## Results & discussion

Fig. 1 shows the solid-liquid distribution ratios ($R_d$) of Ra and Ba as a function of pH and IS = 0.3 M NaCl on both clay minerals. The general adsorption behaviour of Ba as function of pH is similar for both clay minerals, with no pH dependency of $R_d$ up to pH ~ 8 and increasing adsorption at higher pH (Figure 1a, 1b). Differences in adsorption are observed between montmorillonite and illite, indicating a higher affinity of Ba for illite. The same trends as observed for Ba are also observed for $^{226}$Ra. Again, a higher affinity for Ra on illite is observed than for montmorillonite. However, consistently higher $R_d$ values for Ra as for Ba were measured.

The adsorption isotherm of $^{133}$Ba/$^{137}$Ba on montmorillonite (Figure 2a) at 0.02 mol/L NaCl and pH 7.0 exhibits a Langmuir-type behavior with a linear adsorption in the low concentration range [$Ba_{eql}$ < $10^{-5}$ M] becoming non-linear in the high concentration range of [$Ba_{eql}$] because of site saturation. The amount of Ba adsorbed at the highest [$Ba_{eql}$] concentration corresponds to 0.4 mol $kg^{-1}$, or 0.8 eq $kg^{-1}$ $Ba^{2+}$, i.e. ~90 % of the Na-CEC of SWy montmorillonite are used. This Ba isotherm was repeated in a separate experiment (open circles in Figure 2) under the same experimental conditions with $^{137}$Ba as a carrier for a $^{226}$Ra tracer. Both Ba and $^{226}$Ra follow exactly the same isotherm as $^{137}$Ba, i.e. $^{137}$Ba behaves as an ideal carrier for $^{226}$Ra.

The adsorption isotherms for Ba on montmorillonite and illite obtained via $^{133}$Ba/$^{137}$Ba adsorption experiments at I = 0.02 M NaCl and pH = 7 are shown in Figure 2 (blue symbols). The Ba isotherm on Na-SWy exhibits a Langmuir-type adsorption behaviour. On the other hand, the Ba isotherm on Na-IdP at low Ba equilibrium concentrations, [$Ba_{eql}$], is linear, whereas with increasing Ba concentration the adsorption becomes non-linear and exhibits a Freundlich-type behaviour. The non-linearity of the isotherms at $3\cdot10^{-8}$ M < [$Ba_{eql}$]<$3\cdot10^{-5}$ M suggests adsorption on at least two different exchange sites.

The combination of $^{137}$Ba as carrier and $^{226}$Ra as tracer reveals that for montmorillonite a similar behaviour is observed as for Ba (Figure 2a). In contrary, a different behaviour of Ra in comparison to Ba is seen on illite (Figure 2b). The adsorption of Ra decreases at [$Ba_{eql}$] > $10^{-7}$ M, which can be explained by competitive effects of Ba. If Ba and Ra would not compete at all, the log $R_d$ values of Ra should remain constant at 4.8 L/kg, which is experimentally not observed. However, if Ba and Ra were fully competing for the same cation exchange sites, the $R_d$ values for Ra should follow the adsorption of Ba, as shown for montmorillonite (Figure 2a), whereas this is clearly not the case for illite (Figure 2b).

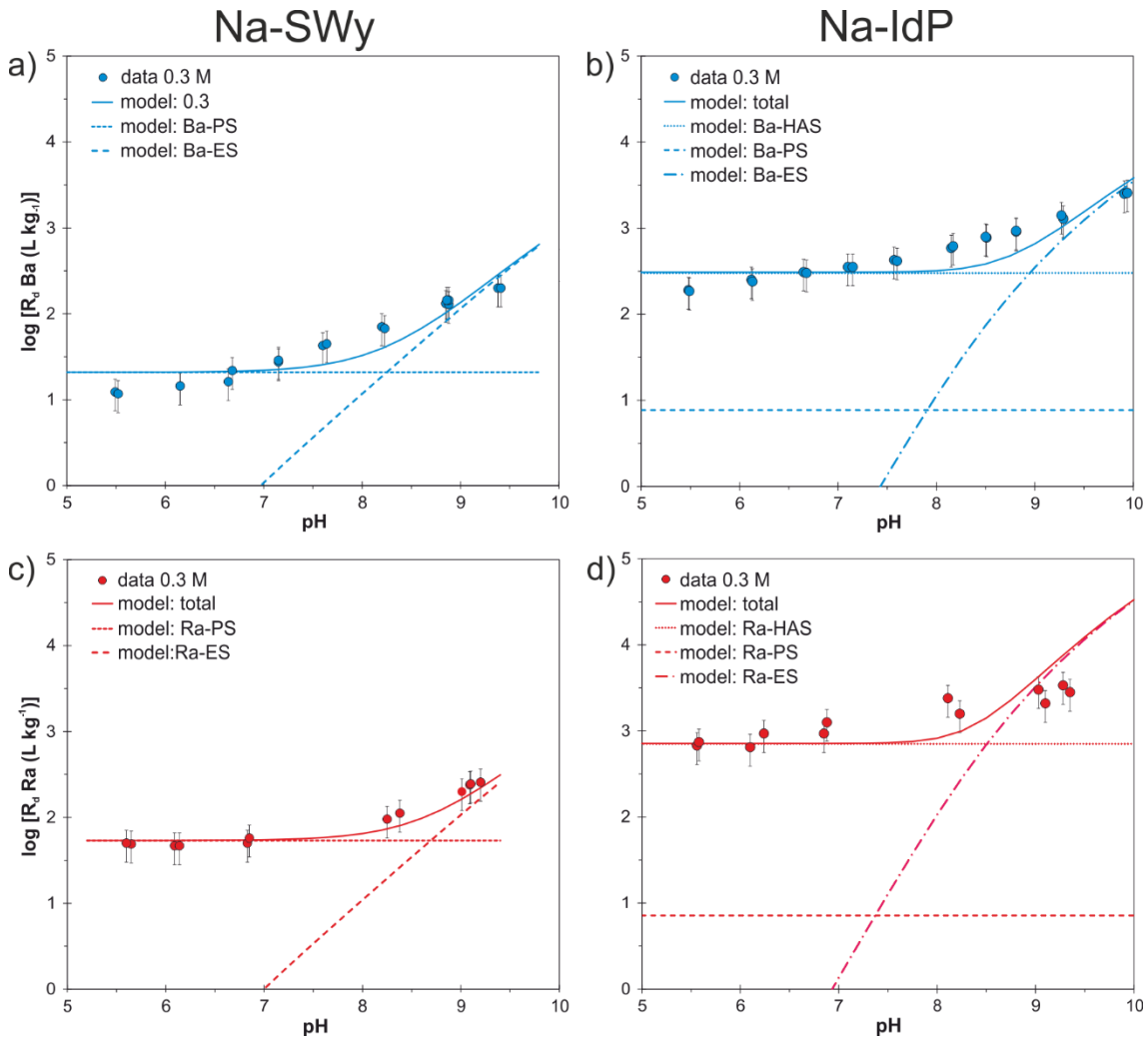


*Figure 1: Experimental and modelled results of pH-edges of Ba on a) Na-montmorillonite (Na-SWy) and b) Na-illite (Na-IdP) in 0.3 M NaCl. Adsorption edges of $^{226}$Ra on c) Na-SWy and d) Na-IdP in 0.3 M NaCl. PS = planar sites, ES = edge sites, HAS = high affinity sites.*

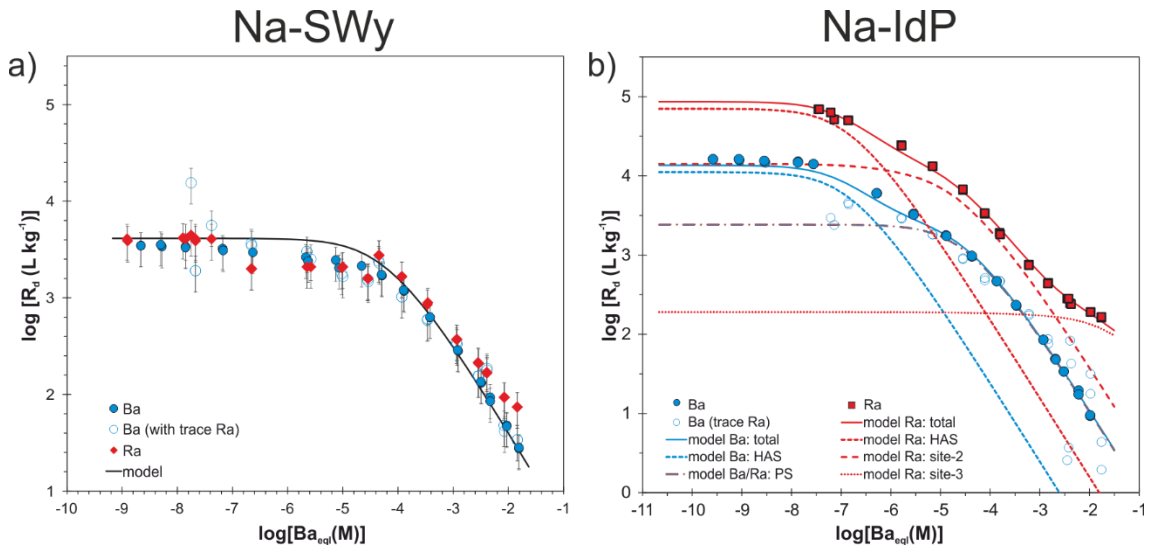


*Figure 2: a) Adsorption isotherms of $^{137}$Ba/$^{133}$Ba trace and $^{137}$Ba/$^{226}$Ra trace on Na-SWy. b) Adsorption isotherms of $^{133}$Ba/$^{137}$Ba and $^{137}$Ba/$^{226}$Ra trace on Na-IdP. Experimental and modelled results of experiments at I = 0.02 M NaCl and pH 7.*

The adsorption data for Ba and Ra on montmorillonite and illite have been modelled mainly by cation exchange as described in section 1.4. For montmorillonite only the planar sites were required to quantitatively describe the Ba and Ra uptake in the pH range 5 to ~ 8 at 0.02 M NaCl with a log $K_c$ (Ba-Na) = 0.7 (see Table 2). At high pH the increasing adsorption of Ba and Ra was modelled by a surface complexation mechanism using the 2SPNE SC/CE model (Table 3). Further, for most conditions, the montmorillonite adsorption model for Ba and $^{226}$Ra is identical, i.*e.,* Ba can be seen as a very good chemical analogue for Ra. Only at high pH and/or high ionic strength, the adsorption model for $^{226}$Ra on montmorillonite needed to be adapted slightly (see Table 3).

The modelling of Ba and Ra adsorption on illite appeared to be more complex compared to montmorillonite. As mentioned before, the Ba isotherm exhibits for $3 \cdot 10^{-8}$ M < [$Ba_{eql}$]< $3 \cdot 10^{-5}$ M a Freundlich type adsorption behaviour. This part of the isotherm could only be modelled by introducing a second high affinity cation exchange site (HAS). As shown in Figure 2b by the dotted blue line, the adsorption on this site illustrates the addition uptake of Ba on HAS and allows to completely fit the Ba isotherm on Na-IdP. The cation exchange reactions and corresponding selectivity coefficients are given in Table 2 and show that the selectivity of Ra is slightly higher than for Ba on the HAS. A further general trend in the selectivity behaviour observed for Ba and Ra on both clay minerals is that $K_c$ values for Ba/Ra-Na exchange increase at increasing ionic strengths (see results for pH-edges data in Table 2). The model for the adsorption of Ba on the edge sites of illite is similar to the one derived for montmorillonite, with identical site capacity and surface complexation constants for Ra and Ba (see Table 3).

Finally, to describe the complex behaviour of Ra adsorption as a function of increasing Ba-concentration, shown in Figure 2b, two additional sites (site-2 and site-3) are introduced into the model with capacities of 1 meq/kg). Introducing this additional site-2 for Ra and Ba improves the fit*, i.e.,* the Ra adsorption up to [$Ba_{eql}$] ~ $10^{-3}$ M is now well described (Figure 2b, solid red line). On site-2 a log $R_d$ value of 4.2 L/kg results from the calculated adsorption of Ra. Without competition of Ra and Ba for site-2, the $R_d$ values for Ra should stay constant at any Ba equilibrium concentration. However, the Ra $R_d$ values decrease as the Ba concentration ([$Ba_{eql}$] > $10^{-6}$ M) increases, which is most likely caused by competition of Ba with Ra on this site. Considering Ba exchange on site-2 with log $^{site\text{-}2}K_c$ (Ba-Na) of 1.3 results in a systematic decrease of the Ra adsorption. The contribution of Ra adsorption on site-2 is illustrated by the dashed red line in Figure 2b. For the complete description of Ra adsorption at [$Ba_{eql}$] > $10^{-3}$ M, a fourth site (site-3) with a fitted log $^{site\text{-}3}K_c$ (Ra-Na) = 2.3 was included in the model. Similar to the modelling on site-2 a competing log $^{site\text{-}3}K_c$ (Ba-Na) = -2.2 is necessary to fully reproduce the Ra adsorption data as shown in Figure 2b by the red solid line.

*Table 2: Summary of site types, capacities and selectivity coefficients required for the modelling of the Ra/Ba adsorption on planar sites (PS) on Na-SWy and on PS and high affinity sites (HAS) on Na-IdP.*

| **Cation exchange site type** | **Site capacity (meq/kg)** | | | | | |
|---|---|---|---|---|---|---|
| | **IdP** | | | **SWy** | | |
| Planar sites (PS) | 225 | | | 870 | | |
| High affinity sites (HAS) | 5 | | | - | | |
| Site-2 | 1 | | | - | | |
| Site-3 | 1 | | | - | | |
| **Experiment** | **pH-edges** | | | | | **Isotherms** |
| **NaCl concentration (M)** | 0.01* | 0.02 | 0.03 | 0.14 | 0.3 | 0.02 |
| **pH** | | 5 - 11 | | | | 7 |
| **Selectivity coefficient Ba/Ra – Na cation exchange reaction (log $K_c$)** | | | | | | |
| 2Na-SWy-PS+ $Ba^{2+}$ ↔ Ba-SWy + $2Na^+$ | - | 0.7 | - | - | 0.9 | 0.7 |
| 2Na-SWy-PS + $Ra^{2+}$ ↔ Ra-SWy + $2Na^+$ | 0.7* | 0.7 | - | 1.14 | 1.34 | 0.7 |
| 2Na-IdP-PS + $Ba^{2+}$ ↔ Ba-PS + $2Na^+$ | - | 1.05 | 1.05 | - | 1.05 | 1.05 |
| 2Na- IdP-HAS + $Ba^{2+}$ ↔ Ba-HAS + $2Na^+$ | - | 3.4 | 3.7 | - | 4.3 | 3.4 |
| 2Na-IdP-site-2 + $Ba^{2+}$ ↔ Ba-site-2+ $2Na^+$ | - | - | - | - | - | 1.3 |
| 2Na- IdP-site-3 + $Ba^{2+}$ ↔ Ba-site-3+ $2Na^+$ | - | - | - | - | - | -2.2 |
| 2Na- IdP-PS + $Ra^{2+}$ ↔ Ra-PS + $2Na^+$ | - | 1.05 | - | 1.05 | 1.05 | 1.05 |
| 2Na- IdP-HAS + $Ra^{2+}$ ↔ Ra-HAS + $2Na^+$ | - | 4.1 | - | 4.2 | 4.7 | 4.2 |
| 2Na-IdP-site2 + $Ra^{2+}$ ↔ Ra-site2+ $2Na^+$ | - | - | - | - | - | 4.2 |
| 2Na-IdP-site3 + $Ra^{2+}$ ↔ Ra-site3+ $2Na^+$ | - | - | - | - | - | 2.3 |
| **Selectivity coefficient Ra-Ba cation exchange reaction (log $K_c$)** | | | | | | |
| Ba-IdP -PS + $Ra^{2+}$ ↔ Ra-PS + $Ba^{2+}$ | - | - | - | - | - | 0.0 |
| Ba-IdP -HAS + $Ra^{2+}$ ↔ Ra-HAS + $Ba^{2+}$ | - | - | - | - | - | 0.8 |
| Ba-IdP -site2 + $Ra^{2+}$ ↔ Ra-site2 + $Ba^{2+}$ | - | - | - | - | - | 2.9 |
| Ba-IdP -site3 + $Ra^{2+}$ ↔ Ra-site3 + $Ba^{2+}$ | - | - | - | - | - | 4.5 |

*based on experimental data of Chen & Kocar, 2018.

*Table 3: Capacity of edge sites (weak type 2, $\equiv S^{W2}OH$), protolysis reactions and corresponding constants, as well as the surface complexation reactions and constants for Ba and $^{226}Ra$ on Na-IdP and Na-SWy.*

| | **Na-IdP** | **Na-SWy** |
|---|---|---|
| **Site type** | **Capacity** | |
| ES ($\equiv S^{W2}OH$) | $4.0 \cdot 10^{-2}$ mol·kg$^{-1}$ | |
| **Protolysis reactions** | **log K** | |
| $\equiv S^{W2}OH + H^+ \Rightarrow \equiv S^{W2}OH_2^+$ | log $K^+$ = 8.5 | log $K^+$ = 6.0 |
| $\equiv S^{W2}OH \Rightarrow \equiv S^{W2}O^- + H^+$ | log $K^-$ = -10.5 | log $K^-$ = -10.5 |
| **Surface complexation reactions** | **log $^{W2}$K** | |
| $\equiv S^{W2}OH + Ba^{2+} \Leftrightarrow \equiv^{W2}SOBa^+ + H^+$ | -4.2 | -5.0 |
| $\equiv S^{W2}OH + Ra^{2+} \Leftrightarrow \equiv^{W2}SORa^+ + H^+$ | -3.4 | -5.0 |

## Conclusions

The adsorption of $^{226}$Ra and Ba onto Na-montmorillonite and Na-illite, both safety relevant materials of future high-level radioactive waste repositories, was systematically investigated. The aim of the experimental work was to investigate and compare the general adsorption behaviour of $^{226}$Ra and Ba and to develop a model based on the 2SPNE SC/CE approach. The results indicate that for montmorillonite one 2SPNE SC/CE model can describe both, Ba and $^{226}$Ra with one edge site and one planar site. Ba can be seen as a good analogue for $^{226}$Ra in most conditions, except high pH and high ionic strength. $^{226}$Ra adsorption on montmorillonite is well described with slight modifications of the Ba model which considers a higher selectivity of $^{226}$Ra.

In comparison, Ba and $^{226}$Ra adsorption on illite is distinctively different from each other, with a significantly higher selectivity for $^{226}$Ra. A more complex model was derived describing the adsorption behavior as function of pH, ionic strength and $Ba^{2+}$ concentration, including one additional high affinity site for Ba adsorption and three types of high affinity sites for $^{226}$Ra. The additional $^{226}$Ra high affinity sites may be sub-sites of the Ba HAS sites. $^{226}$Ra adsorption on illite cannot be described adequately by just applying a Ba model, indicating that here Ba is not a good analogue for $^{226}$Ra.

## References

Baeyens, B., Bradbury, M.H., 1995. Technical report 95-05: A Quantitative Mechanistic Description of Ni, Zn and Ca Sorption on Na-Montmorillonite Part 11: Sorption Measurements. Villigen PSI, Switzerland.

Baeyens, B., Bradbury, M.H., 1997. A mechanistic description of Ni and Zn sorption on Na-montmorillonite Part I: Titration and sorption measurements. J. Contam. Hydrol. 27, 199–222. https://doi.org/10.1016/S0169-7722(97)00008-9

Bradbury, M.H., Baeyens, B. 1997. A mechanistic description of Ni and Zn sorption on Na-montmorillonite Part II: modelling. J. Contam. Hydrol. 27, 223-248. https://doi.org/10.1016/S0169-7722(97)00007-7

Bradbury, M.H., Baeyens, B., 2005. Modelling the sorption of Mn(II), Co(II), Ni(II), Zn(II), Cd(II), Eu(III), Am(III), Sn(IV), Th(IV), Np(V) and U(VI) on montmorillonite: Linear free energy relationships and estimates of surface binding constants for some selected heavy metals and actinide. Geochim. Cosmochim. Acta 69, 875–892. https://doi.org/10.1016/j.gca.2004.07.020

Bradbury, M.H., Baeyens, B., 2009a. Sorption modelling on illite Part I: Titration measurements and the sorption of Ni, Co, Eu and Sn. Geochim. Cosmochim. Acta 73, 990–1003. https://doi.org/10.1016/J.GCA.2008.11.017

Chen, M.A., Kocar, B.D., 2018. Radium Sorption to Iron (Hydr)oxides, Pyrite, and Montmorillonite: Implications for Mobility. Environ. Sci. Technol. 52, 4023–4030. https://doi.org/10.1021/acs.est.7b05443

Davies, C.W., 1962. Ion Association. Butterworths.

Gaines, G.L., Thomas, H.C., 1955. Adsorption studies on clay minerals. V. Montmorillonite-cesium-strontium at several temperatures. J. Chem. Phys. 23, 2322–2326. https://doi.org/10.1063/1.1741873

Klinkenberg, M., Brandt, F., Baeyens, B., Bosbach, D., Fernandes, M.M., 2021. Adsorption of barium and radium on montmorillonite: A comparative experimental and modelling study. Appl. Geochemistry 135, 105117. https://doi.org/10.1016/J.APGEOCHEM.2021.105117

Marques Fernandes, M., Baeyens, B., 2019. Cation exchange and surface complexation of lead on montmorillonite and illite including competitive adsorption effects. Applied Geochemistry 100, 190-202.

Marques Fernandes, M., Klinkenberg, M., Baeyens, B., Bosbach, D., Brandt, F., 2023. Adsorption of Ba and $^{226}$Ra on illite: a comparative experimental and modelling study. Appl. Geochemistry, submitted.

Westall, J.C., Zachary, J.L., Morel, F.M.M., 1976. MINEQL - General Algorithm for Computation of Chemical-Equilibirum in Aqueous Systems, in: Abstracts of Papers of the American Chemical Society. American Chemical Society, Washington, D.C., pp. 8–8.

# 2. Diffusion of $^{226}$Ra through Opalinus Clay

F. Brandt, M. Klinkenberg
*FZJ, Julich, Germany*

L.R. Van Loon, M.A. Glaus
*PSI, Villligen PSI, Switzerland*

## Introduction

The Swiss repository for nuclear waste is planned to be sited in the Opalinus Clay (OPA) formation (Nagra, 2002). OPA contains significant quantities of clay minerals which function as effective physical barriers and adsorb radionuclides. Diffusion is assumed to be the dominant transport mechanism for radionuclides in the case of water contact. Here, the retention properties play a very important role and therefore need to be included in the safety analyses of high-level nuclear waste repositories. Usually, the apparent diffusion coefficient $D_a$ is used to describe the diffusion of radionuclides. In the literature, different approaches are applied to obtain $D_a$: in-diffusion experiments, through-diffusion experiments, or the calculation of $D_a$ from the effective diffusion coefficient $D_e$ in combination with the independently obtained (sorption) distribution coefficient $R_D$ e.g., for Ra in OPA. Earlier publications (Van Loon et al. 2005, and references therein) have successfully tested that the use of sorption data values determined from dispersed systems for some cations relevant to the nuclear safety case could be justified for the prediction of diffusion in a consolidated clay rock. In this case experiments with dispersed clay were compared with diffusion experiments on the same, but consolidated material.

The adsorption and diffusion of radium in clay rocks is so far not quantitatively understood. Ba is often used as a chemical analogue for Ra. The solid-solution formation between Ra and sulfates which are present in host rocks like Opalinus clay (OPA) may add an additional retention potential. Here, we report new experimental data to improve the quantitative understanding of the retention of $^{226}$Ra in OPA. OPA samples originating from the Mont Terri Underground Rock Laboratory and synthetic OPA pore water (Van Loon et al. 2003) were used, both for diffusion and batch sorption experiments. Transport (diffusion) was measured both perpendicular and parallel to the bedding. Special cells that allowed the application of an axial confining pressure were used. Numerical simulations for single-species diffusion realised with the Comsol Multiphysics software® were used to obtain best-fit parameter values for the effective diffusion and sorption distribution coefficients.

## Materials & Methods

OPA samples originating from the Mont Terri Underground Rock Laboratory (bore hole BMA-A1) and synthetic OPA pore water (Van Loon et al. 2003) were used, both for diffusion and batch sorption experiments. The chemical composition of the OPA pore water is given in

*Table 1*.

*Table 1: Composition of synthetic OPA porewater (Van Loon et al. 2003) used in the batch sorption and diffusion experiments*.

| Element | Concentration |
|---|---|
| | **mol m$^{-3}$** |
| Na | $2.40 \cdot 10^{-1}$ |
| K | $1.61 \cdot 10^{-3}$ |
| Mg | $1.69 \cdot 10^{-2}$ |
| Ca | $2.58 \cdot 10^{-2}$ |
| Sr | $5.05 \cdot 10^{-4}$ |
| Cl | $3.00 \cdot 10^{-1}$ |
| $SO_4$ | $1.41 \cdot 10^{-2}$ |
| $CO_3/HCO_3$ | $4.76 \cdot 10^{-4}$ |
| pH | 7.6 |

Batch sorption experiments were carried out on crushed and sieved OPA with a particle size of ≤ 63 µm. The OPA powder was pre-equilibrated in synthetic OPA porewater. For the batch sorption experiments 20 mL of the OPA suspension with a S/L ratio of 117 g/L were put into 50 mL centrifuge tubes. These suspensions were spiked with 32 µL $^{226}$Ra tracer resulting in an initial Ra-concentration of $1.44 \cdot 10^{-8}$ mol/L. After 7 days of shaking and centrifugation, the aliquots of the clear supernatant were analysed by γ-spectrometry to determine the $^{226}$Ra content. The cation exchange capacity of the OPA was determined by the Cu-TRIEN method (Meier & Kahr 1999).

For the through-diffusion experiments, OPA core samples as presented in Figure 1 were prepared and put into diffusion cells as described in Van Loon et al. (2003, 2004).

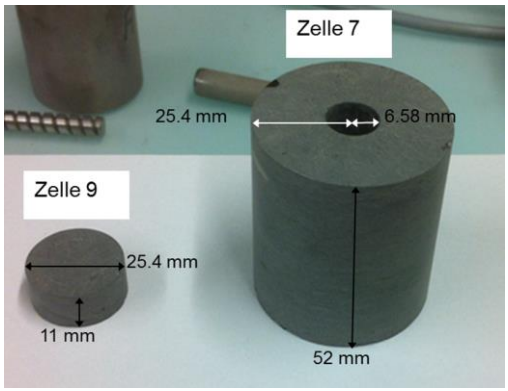


*Figure 1: Size and dimensions of OPA samples used in through diffusion experiments perpendicular (Zelle 9, planar) and parallel (Zelle 7, radial) to the bedding.*

To make the experiments comparable to earlier studies (Van Loon et al. 2003, 2004), before the diffusion experiments were started, the OPA core samples (Figure 1) were re-saturated with synthetic OPA pore water and loaded to a confining pressure of 7 MPa. Two repetitive through-diffusion experiments with a conservative tracer (HTO) were carried out perpendicular (planar) and parallel to the bedding (radial) (HTO experiments are performed to determine the basis transport parameters to which the others are compared, and they also serve as a quality check to compare to other data on comparable systems). The HTO starting activity was 643 Bq mL$^{-1}$ and 584 Bq mL$^{-1}$ respectively. The solutions at the down-stream boundary were

exchanged against tracer-free solutions at regular time intervals in order to maintain a comparably low concentration with respect to the upstream concentration. After completion of a through-diffusion experiment, the solutions in both containers were replaced by artificial pore water without tracer, and out-diffusion was started. At selected time intervals the activity in the solutions was measured, and then the solutions were replaced by fresh ones. This procedure was repeated until all the activity in the sample had diffused out. After out-diffusion, the solution in the large container was replaced by an OPA solution containing a new tracer, and through-diffusion was restarted on the same samples. After the second out-diffusion of HTO, the diffusion of $^{226}$Ra followed. The starting $^{226}$Ra concentration was $1.4 \cdot 10^{-9}$ mol/L. All HTO diffusion experiments are summarized in Table 2.

*Table 2: Summary of through-diffusion experiments: tracers, activity concentrations and volumes of the high- ($V_{high}$) and low-concentration ($V_{low}$) reservoirs for the HTO experiments.*

| Tracer | Direction | Samples | $V_{high}$ [$cm^3$] | $V_{low}$ [$cm^3$] | Activity concentration ($C_0$) [Bq $ml^{-1}$] |
|---|---|---|---|---|---|
| HTO-1 | parallel | BMA-A1-Z9 | 200 | 20 | 584 |
| HTO-2 | perpendicular | BMA-A1-Z7 | 500 | 50 | 643 |
| HTO-1 | parallel | BMA-A1-Z9 | 200 | 20 | 584 |
| HTO-2 | perpendicular | BMA-A1-Z7 | 500 | 50 | 643 |

The radiotracer concentrations of HTO and $^{226}$Ra were determined by LSC-measurements, using the ultra-low level liquid scintillation spectrometer Quantulus (Perkin Elmer, USA). For the analysis of the samples of the low activity reservoir, 7 mL of the aliquots were mixed with 13 mL of Ultima Gold LLT cocktail (Perkin Elmer, USA). For aliquots of the high activity reservoir 100 µL aliquot were mixed with 6.9 mL synthetic OPA pore water and 13 mL Ultima Gold LLT cocktail. For $^{226}$Ra measurements LSC-glass vials were glued gas tight with epoxy resin to avoid the release of Rn. The measurement of the samples was carried out after 38 days, when Rn was in secular equilibrium. A post-mortem analysis of the clay core of the planar diffusion experiment and the respective filters was carried out to look for secondary phases.

## Modelling

Numerical simulations of single-species diffusion of HTO and $^{226}$Ra, respectively, were carried out using Comsol Multiphysics® in a 1-D geometry representing the filter–clay–filter domains (linear or radial, for diffusion perpendicular and parallel, respectively, to the clay bedding). The time-dependent tracer concentrations in the solution reservoirs were calculated by flux integration using weak constraints and used as boundary conditions for the filter–clay–filter domains. The effective diffusion coefficients for the diffusion of HTO in the confining filters were chosen according to Appelo et al. (2010), those of $Ra^{2+}$ were scaled to those of HTO proportionally to the respective bulk diffusion coefficients. A zero-concentration boundary condition at the downstream side was assumed for HTO, while for $Ra^{2+}$ an averaged concentration was applied according to the accumulated $Ra^{2+}$ activity in the reservoir solution following the procedures described in Glaus et al. (2015). (Non-)linear sorption of $Ra^{2+}$ was taken into account via derivative expressions of a 1-site Langmuir isotherm. Best-fit parameter values and the respective parameter uncertainties (95% confidence level) were obtained from a parameter optimisation routine (using the lsqnonlin function in Matlab®), involving the Comsol Multiphysics® as a Matlab® script. The cumulated diffused mass at the target side and the source concentration of the diffusing species as a function of time were utilised as the source data. The effective diffusion coefficient and the total porosity were the fit parameters in the case of HTO, while in the case of $Ra^{2+}$, the Langmuir sorption parameters were treated as additional adjustable parameters, leaving the porosity identical to the value obtained from HTO.

## Results & discussion

From the sorption experiments, the distribution coefficient for $^{226}$Ra with OPA was determined to be $R_d$ = 36.6 L/kg. Sorption of the tracer on container walls was checked and is negligible. The cation exchange capacity was CEC (Cu-TRIEN) = 140 meq/kg.

The HTO through diffusion experiments resulted in a rock capacity factor $\alpha$ = 0.17 for the radial and $\alpha$= 0.20 for the planar core sample (*Table 3*). The values of the effective diffusion coefficient $D_e$ for HTO of $5.7 \cdot 10^{-11}$ $m^2 s^{-1}$ for the radial core sample and $1.5 \cdot 10^{-11}$ $m^2 s^{-1}$ (*Table 3*) for the planar core are in good agreement with previous studies on similar samples (Van Loon & Soler, 2004). Because HTO is considered as a non-sorbing tracer, i.e. $K_d$ = 0, the rock capacity factor, $\alpha$, equals the diffusion accessible porosity, $\varepsilon$. The value of the effective diffusion coefficient of HTO is in good agreement with the values measured by SCK CEN, AEA and CIEMAT earlier on similar samples, ranging between $(1.0 - 2.3) \cdot 10^{-11}$ $m^2 s^{-1}$, as well as the value for the diffusion accessible porosity, $\varepsilon$, which ranges between 0.12 and 0.26 in the literature (Van Loon et al., 2001).

*Table 3: Effective diffusion coefficient and rock capacity factors for the diffusion of HTO through OPA from two repetitive experiments.*

| | **$D_e$ [$10^{-11}$ $m^2$ $s^{-1}$]** | **α [-]** |
|---|---|---|
| parallel_1 | 5.8 | 0.18 |
| parallel _2 | 5.6 | 0.16 |
| perpendicular_1 | 1.4 | 0.19 |
| perpendicular_2 | 1.5 | 0.21 |

*Figure 2* shows the flux and total diffused activity for the diffusion of $^{226}$Ra parallel and perpendicular to the bedding. The curves show a transient phase in which the flux increases, and a steady-state phase in which the flux is constant and where the total diffused activity increases linearly with time. The breakthrough of $^{226}$Ra was monitored after 100 days (planar) and 120 days (radial), respectively, whereas the steady state occurred after about 400 days in both cases. A rapid early drop of the $^{226}$Ra-concentration in the source concentration reservoir was observed.

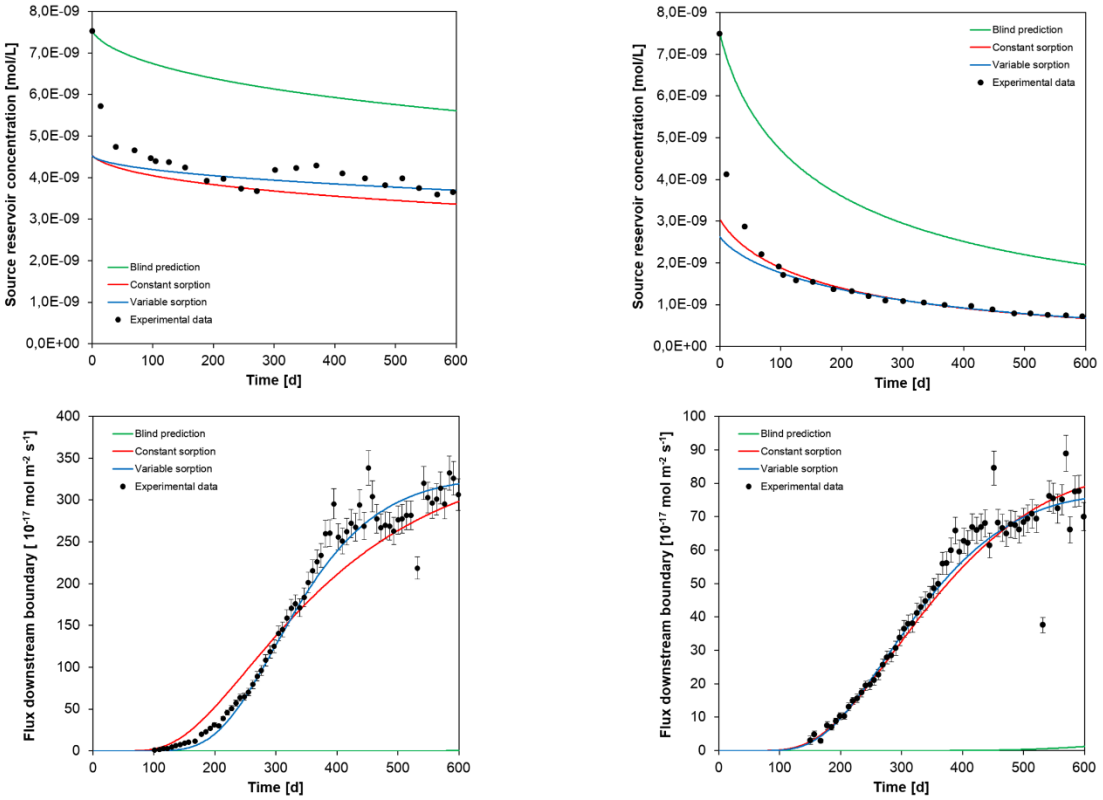


*Figure 2: $^{226}$Ra through diffusion in OPA clay a) parallel, b) perpendicular to the bedding. High concentration reservoir c) parallel, d) perpendicular to the bedding.*

Using the $R_d$ obtained by the batch adsorption experiments as input for the blind prediction of diffusion profiles (*Figure 2*, green line) is in complete disagreement with the experimental data. As a next scenario, best fit parameter values were tested by a diffusion model implying conservation of mass between source reservoir and downstream reservoir and the clay/filter domains. It was not possible to obtain adequate diffusion and sorption parameters with this approach, owing to the rapid decrease of the Ra concentration at the early stages of the diffusion experiments. The time-dependent concentration trends on the upstream and the downstream side are not compatible. This implies that additional mechanisms other than diffusion and adsorption occur in both experiments. Such a phenomenon has not been observed so far in diffusion experiments on Opalinus clay. As a workaround, the initial concentration is calculated to be lower than in the experiment, in order to simulate only the diffusive decrease of the tracer concentration in the upstream reservoir. This assumption is supported by the largely consistent concentration evolution after approx. 50 days running time of the experiments. The break-through of $Ra^{2+}$ was earlier than expected from blind predictions ($D_e$ from HTO and bulk diffusion ratio HTO/Ra, $R_d$ from batch sorption).

The $R_d$ derived from the diffusion experiments is consistently smaller than the $R_d$ obtained in the batch sorption experiments. $D_e$ is higher than expected from proportionality with diffusion coefficient of HTO and Ra in bulk water. This phenomenon was observed for other cations as well (Melkior et al., 2007) and is interpreted as surface diffusion. Refining the transport model to non-linear sorption conditions leads to a more realistic fit of the flux (colour lines in *Figure 2*) and best fit parameter values (*Table 4*).

*Table 4: Best fit parameter values determined from inverse modelling. Scenarios for the values comprising: constant sorption, variable sorption, C(dsb) = 0 or variable. * = range of sorption isotherms.*

| | $^{226}$Ra | |
|---|---|---|
| | $D_e$ [$m^2 s^{-1}$] | $R_d$ [L $kg^{-1}$] |
| Planar | (1.05 ± 0.2) $10^{-11}$ | 4 – 15* |
| Radial | (4 - 7) $10^{-11}$ | 4 – 15* |

The SEM analysis of the filters (*Figure 3*) confirmed the precipitation of a solid in the pores of the filter on the side of the high concentration reservoir. Based on EDX analyses this solid was identified as calcium ca carbonate. Due to the morphology, calcium carbonate appears to have formed rapidly and captured some of the $Ra^{2+}$ in solution which was then not available for diffusion anymore.

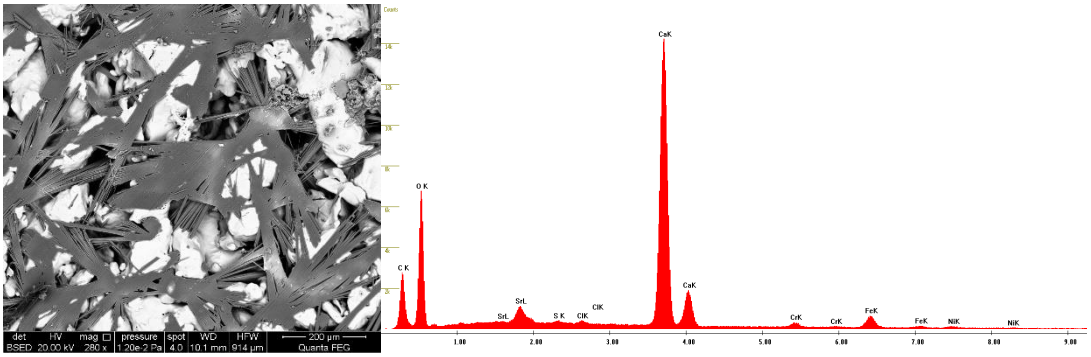


*Figure 3: a) calcium carbonate needle like crystals precipitated in the pores of the filter. b) EDX spectrum of calcite.*

## Conclusions

We report new experimental data to improve the quantitative understanding of the retention of $^{226}Ra$ in clay rocks relevant for nuclear waste management. OPA samples originating from the Mont Terri Underground Rock Laboratory and synthetic OPA pore water were used, both for diffusion and batch sorption experiments. Effective diffusion coefficients ($D_e$), rock capacity factors ($\alpha$) and diffusion-accessible porosities (ε) were determined using the through-diffusion technique. Transport (diffusion) was measured both perpendicular and parallel to the bedding. Special cells that allowed the application of an axial confining pressure were used. Experimental diffusion and sorption data for $^{226}Ra$ in OPA show an earlier tracer breakthrough in through diffusion than expected based on HTO diffusion and sorption experiments of $^{226}Ra$ in dispersed suspensions of OPA. The $R_d$ values obtained by simulation of diffusion data are smaller than the respective $R_d$ values from batch sorption experiments. This observation may be qualitatively explained by different concentrations of competing species in the in-situ pore water versus the dispersed system. The higher $D_e$ may be due to surface diffusion of $Ra^{2+}$, similar to diffusion of $Sr^{2+}$ and $Cs^+$ in OPA (Appelo et al., 2010). Our results showed a consistent ratio of anisotropic diffusion for between HTO and $Ra^{2+}$ for diffusion parallel and perpendicular to the clay bedding, as well as a consistent ratio of HTO and $Ra^{2+}$ geometry factors.

## References

Appelo, C.A.J., Van Loon, L.R., Wersin, P., 2010. Multicomponent diffusion of a suite of tracers (HTO, Cl, Br, I, Na, Sr, Cs) in a single sample of Opalinus Clay. Geochim. Cosmochim. Acta 74, 1201–1219. https://doi.org/10.1016/j.gca.2009.11.013

Glaus, M. a., Aertsens, M., Maes, N., Van Laer, L., Van Loon, L.R., 2015. Treatment of boundary conditions in through-diffusion: A case study of $^{85}Sr^{2+}$ diffusion in compacted illite. J. Contam. Hydrol. 177–178, 239–248. https://doi.org/10.1016/j.jconhyd.2015.03.010

Meier & Kahr, 1999. Determination of the cation exchange capacity (CEC) of clay minerals using the complexes of copper(II) ion with triethylenetetramine and tetraethylenepentamine. Clay and clay minerals 47, 386-388.

Melkior, T., Yahiaoui, S., Thoby, D., Motellier, S., Barthes, V., 2007: Diffusion coefficients of alkaline cations in Bure mudrock , Phys Chem Earth 32, 1-7, 453-462, https://doi.org/10.1016/j.pce.2006.04.035

Nagra, 2002. Project Opalinus Clay: Safety Report. Demonstration of Disposal Feasibility (Entsorgungsnachweis) for Spent Fuel, Vitrified High-Level Waste and Long-Lived Intermediate-Level Waste. Technical Report NTB 02-05. Wettingen, Switzerland.

Van Loon, L.R., Soler, J., Bradbury, M.H., 2001: DI Experiment: A Laboratory Comparison Exercise (SCK.CEN/AEA/CIEMAT). Unpublished Mont Terri Technical Note TN-2000-02, Mont Terri Project.

Van Loon, L.R., Soler, J.M., Bradbury, M.H., 2003. Diffusion of HTO, $^{36}Cl^-$ and $^{125}I^-$ in Opalinus Clay samples from Mont Terri: Effect of confining pressure. J. Contam. Hydrol. 61, 73–83. https://doi.org/10.1016/S0169-7722(02)00114-6

Van Loon, L.R.; Soler, J.M., 2004. Diffusion of HTO, $^{36}Cl^-$,$^{125}I^-$ and $^{22}Na^+$ in Opalinus Clay: Effect of Confining Pressure, Sample Orientation, Sample Depth and Temperature PSI-Bericht 04-03. Paul Scherrer Institut, Villigen PSI.

Van Loon, L.R., Wersin, P., Soler, J.M., Eikenberg, J., Gimmi, Th., Hernán, P., Dewonck, S., Savoye, S., 2004. In-situ diffusion of HTO, $^{22}Na^+$,$Cs^+$ and $I^-$ in Opalinus Clay at the Mont Terri underground rock laboratory. Radiochim. Acta 92, 757–763.

Van Loon, L.R., Baeyens, B., Bradbury, M.H., 2005. Diffusion and retention of sodium and strontium in Opalinus Clay: comparison of sorption data from diffusion and batch sorption measurement, and geochemical calculations. Appl. Geochem. 20, 2351–2363.

# 3. Adsorption and diffusion of Ra, Ba, Sr on clay minerals and clayrocks

M. García-Gutiérrez, M. Mingarro, A. M. Fernández and T. Missana
*CIEMAT, Madrid, Spain*

## Abstract

The objective of this report is to summarise CIEMAT activities in Task 2 (Radionuclide Mobility) of the EURAD WP FUTURE project, regarding adsorption and migration processes of alkaline earth metals in argillaceous rocks (Task 2.1). Part of the studies were also focused on the analysis of the irreversibility of adsorption processes (Task 2.3).

The mobility of barium, radium (and strontium) was analysed in different clay materials including smectite (FEBEX clay and NAu-1 nontronite), illite du Puy and the Callovo-Oxfordian (COx) clay. Clays were used as received or in homoionic form. Experiments were carried out with the materials in both dispersed and compacted state by means of batch sorption tests and diffusion experiments.

## Introduction

The principal aim of CIEMAT work in Task 2.1 is to provide information on radionuclide mobility in clays under different physical chemical conditions (e.g. type of material, porewater chemistry, presence of competing ions, compaction degree, temperature), to answer to the main questions posed at the beginning of the FUTURE project.

One of the main topics is to understand if distribution coefficients ($K_d$) measured under dispersed or compacted conditions are equivalent, and if the conclusions obtained for a certain radionuclide can be extrapolated to others. CIEMAT designed special cells to determine the distribution coefficients directly in compacted/consolidated materials trying to work under solid to liquid ratios and chemical conditions comparable to those applied in batch sorption experiments with powdered materials. It is worth highlighting that in the case of earth alkaline metals, the adsorption kinetic and the order of magnitude of $K_d$ values, for the dispersed and compacted system, were comparable, even if this conclusion could not be extrapolated to other radionuclides. The experience gained with these types of experiments will allow to improve the design of the cells and the methodology to minimise experimental problems with more sorbing radionuclides, that can still bias the final data interpretation.

A second important objective of the work performed by CIEMAT is related to the improvement of the understanding of sorption mechanisms in clays, and to the application of (simple) geochemical sorption modelling for data interpretation. Part of the sorption experiments were carried out with purified and homoionised clay materials (smectites and illite) to ease the identification of the main adsorption mechanisms and to focus on the evaluation of competitive effects of different ions on radionuclide retention, explaining the (apparent) variation of selectivity coefficients for ionic exchange, as a function of the ionic strength.

In Task 2.3 the principal aim is to analyse radionuclide adsorption with the emphasis on reversibility, trying to elucidate which mechanisms may control radionuclide retention at the long term, because irreversibility of sorption may be an additional safety function in the frame of radioactive waste disposals. Desorption tests were carried out in the purified clay minerals and in the natural rock (COx) and the main differences on radionuclide behaviour in the purified/natural systems were highlighted.

Finally, diffusion tests were carried out in the FEBEX bentonite with the aim of studying the coupled effects of dry density and temperature. Diffusion tests with different methodologies were also carried out with the COx clay.

# Materials and Methods

## Clays and contacting electrolytes.

The clay minerals selected for the adsorption experiments were smectite (FEBEX and NAu-1) and illite (du Puy). The Callovo Oxfordian (COx) was the selected clay rock. The FEBEX clay is a Ca-Mg clay, with high smectite content (94 ± 3%); a comprehensive characterisation of the clay can be found elsewhere (Huertas *et al.*, 2006). The NAu-1 clay is a nontronite (Fe-rich smectite) obtained from the Clay Mineral Society (Keeling et al., 2000). The illite du Puy comes from the region of Le Puy-en-Velay (France); it has a high illite content (93%), with kaolinite (7 %) (Gabis, 1958).

For adsorption experiments, the clays previously crushed and sieved (< 64 µm), were converted in their Na-form by washing them three times with 1 M $NaClO_4$ (Merck, purity 99.99%). No additional acid treatment of the clays, to eliminate carbonate minerals, was carried out. After the exchanging procedure, the clays were distributed in centrifuge tubes and mixed with ultrapure water (Milli-Q system, Millipore). The suspensions were centrifuged (600·g, 10 min) and the supernatant, containing the fine clay fraction was collected in polyethylene bottles. The clay remained in the centrifuge tubes was mixed with ultrapure water and centrifuged again. The cycle was repeated several times, until enough solid material was available. The ionic strength of the clay suspensions was changed by dialysis using $NaClO_4$ at different concentrations. The solid to liquid ratio of the different suspensions ranged from 1 to 3 $g \cdot L^{-1}$. Part of the obtained Na-clay was not subjected to particle fractionation; it was simply washed to eliminate the excess of salt, and was left drying in air or at a maximum temperature of 40 °C. The electrolyte used in adsorption tests with the Na-exchanged clays was $NaClO_4$. The same procedure was carried out to exchange the clays in Ca, when needed for comparison purposes. In the latter case the contacting electrolyte was $Ca(ClO_4)_2$.

The samples of Callovo-Oxfordian clay were sent to CIEMAT at the very beginning of the project (May 2019). They were two bore cores of 32 and 30 cm, drilled at 22.53-22.85 and 25.10-25.40 m in depth. Their reference number were: EST60797, OHZ 3008 K15 (COx-1) and EST60807 OHZ 3008 K18 (COx-2). These cores were preserved from the beginning in the glove box under anoxic conditions ($N_2$ + 1% $CO_2$). The cores were sliced for diffusion tests, part was crushed and sieved for sorption tests. The aqueous solution used in the tests with the COx samples was a synthetic water with the composition reported in Table 1.

*Table 1: Chemical composition of the water used for sorption/diffusion tests with the COx clay.*

| | **mg/L** |
|---|---|
| **pH** | 7.2 |
| **ALC.** | 3.34 |
| **$Cl^-$** | 1418 |
| **$SO_4^{2-}$** | 1499 |
| **$Ca^{2+}$** | 295 |
| **$K^+$** | 40 |
| **$Mg^{2+}$** | 162 |
| **$Na^+$** | 1036 |
| **$Sr^{2+}$** | 17.5 |

For diffusion experiments with the FEBEX clay, the clay was compacted at different dry densities and synthetic waters representative of the porewater at different compaction density were prepared (García-Gutiérrez et al. 2023b).

## Radionuclides

Radionuclides used for this study were: $^{226}Ra$ and $^{133}Ba$ supplied by Eckert and Ziegler Isotope Products. Radium is in the form of $Ra(NO_3)_2$ in $HNO_3$ 1 M and it is supplied with a carrier of Ba (10 µg/mL solution). Ba is in the form of $BaCl_2$ in HCl 0.1 M with a carrier of stable Ba (10 µg/mL solution). Some tests were also done with $^{85}Sr$, for comparison. The radionuclide is in the form of $SrCl_2$ in HCl 0.5 M, without carrier.

## Types of experiments

Different types of experiments were carried out to fulfil the proposed objectives: batch sorption tests, sorption irreversibility tests, sorption test in compacted/consolidated clays and diffusion experiments.

Batch sorption tests in dispersed clays were carried out with the exchanged clays in a wide range of experimental conditions (pH, ionic strength (I) and radionuclide concentration, [RN]) to obtain a dataset wide enough for applying sorption modelling. Sorption kinetic tests (1-90 days); sorption edges (pH 3-11) and sorption isotherms were carried out suspending the exchanged clay in the corresponding electrolyte.

Desorption tests to evaluate sorption irreversibility were carried out with all the exchanged clays and with the COx clay. These tests were designed to understand the kinetic behaviour of sorption and desorption processes. Several samples were prepared to determine the distribution coefficient for the sorption process ($K_{d,sor}$) at a certain contact time. Initially the sorption kinetics was followed from 1 day to 3 months approximately. Different samples were prepared for the studies of sorption kinetic and reversibility on $K_{d,sor}$ at 1 day, 1 week, 2 weeks, 1 month and 3 months. After sorption, the water/electrolyte solution was renewed, taking care of maintaining the equilibrium chemistry, and the solid was resuspended in the fresh solution. In each sample, desorption at different times was checked, to evaluate aging effects on contaminant release, calculating the distribution ratio upon desorption ($K_{d,\,des}$) at different times.

In all the experiments, natural clays were suspended in their equilibrium (synthetic) water, whereas the exchanged clays were suspended in the corresponding electrolyte solution ($NaClO_4$, $Ca(ClO_4)_2$, etc..). In the latter case, two pH were analysed (5 and 9) to account for the possible effects of different dominating retention processes (ion exchange or surface complexation at the edge sites).

Batch sorption test in compacted/consolidated clays, were carried out with consolidated COx samples and with the FEBEX clay (natural or exchanged) compacted to a dry density between 1.5 and 1.6 g/cm$^3$. To carry out these tests, the samples (0.06 g) were confined between two sintered steel filter in a cell specially designed. These cells were immersed in the aqueous solution (approximately 7 mL) and left in contact during the selected time. In general, long-term kinetic test was carried out, trying to ensure that the adsorption equilibrium is reached. After the test, all the part of the cells were disassembled and the final activity in the water and in the clay, sample was measured, to determine the $K_d$. The activity in all the part of the cells was also measured. A schematic of these tests and the cell used are shown in Figure 1.

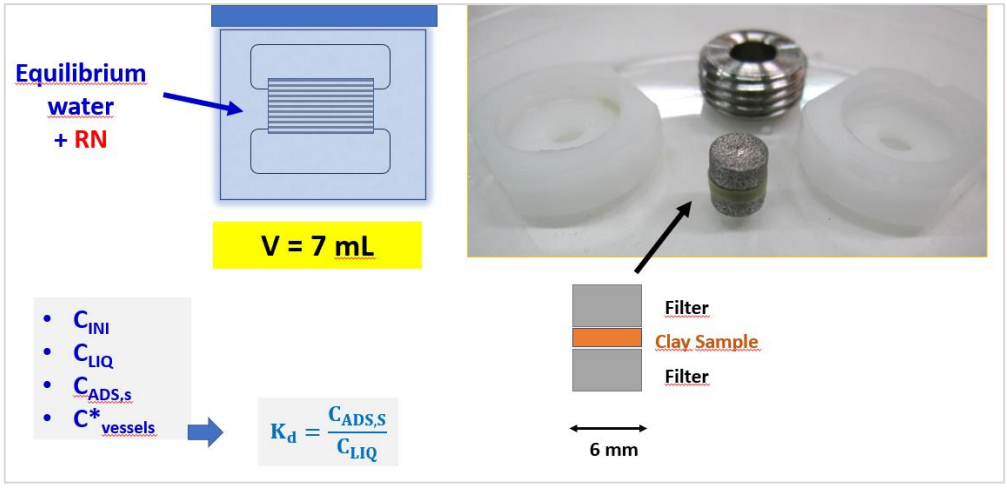


*Figure 1: Schematic of the batch sorption tests in compacted/consolidated clay samples.*

Diffusion tests were carried out in the consolidated COx clay and in the compacted FEBEX clay at different dry densities (1.40 - 1.65 g/cm$^3$). Both in diffusion (ID) and through diffusion (TD) experiments were carried out. In the case of the FEBEX clay, diffusion tests were carried out a different temperatures. Details of the experimental set-up for different types of diffusion experiments can be found elsewhere (García-Gutiérrez et al., 2006).

# Results & discussion

## Adsorption in dispersed clays

### Tests with the exchanged clays

Adsorption tests in all the Na-exchanged clays (illite and smectite) showed that adsorption dependent on pH is weak, whereas a significant dependence on the ionic strength is observed, indicating that the main contribution to Ba and Ra retention is cation exchange with a small contribution of surface complexation at high pH.

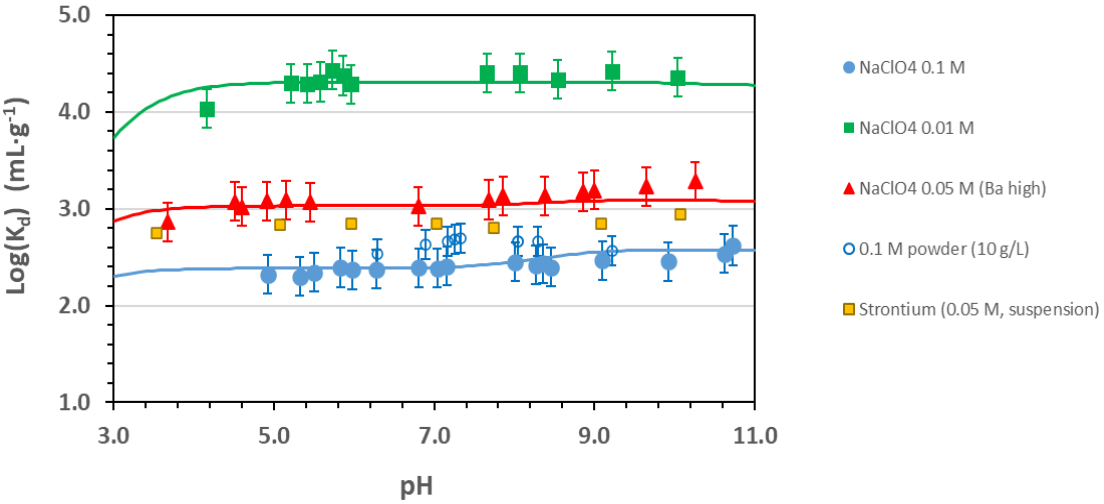


*Figure 2: Adsorption edges of Ba on Na-exchanged FEBEX clay at different ionic strengths in $NaClO_4$. Continuous lines represent the modelling of the adsorption curves, considering cation exchange and surface complexation.*

The study reveals the importance of trace aqueous ions as competitive elements (especially divalent), which must be accounted for the correct interpretation of experimental data and the determination of selectivity coefficients. Figure 2 shows the results obtained for Ba adsorption in the Na-FEBEX clay, and the corresponding modelling. In the first modelling steps, the selectivity coefficient seemed to vary with the ionic strength, indicating the possible competence with solute ions. However, it has been shown in previous works (Missana et al 2021), that even when exchanged and purified, clays leach traces of ions (divalent and trivalent), that even in very small concentrations may affect adsorption and the final interpretation of data, especially at low ionic strength.

Figure 3 shows an example of the differences in the modelling, when competing ions are considered or not. The selectivity coefficient measured for Ba-Na exchange in the FEBEX clay at the ionic strength of 0.1 M is 0.90, whereas to fit the data at 0.01 M we have to decrease it to 0.7. However, if the presence in solution of the measured Ca ($1 \cdot 10^{-5}$ M) and Al ($1 \cdot 10^{-4}$ M at pH 3) and the respective (Ca-Na) and (Al-Na) selectivity coefficients, determined experimentally in previous tests, we could simulate Ba adsorption data at all the ionic strengths with a one and the same selectivity coefficient.

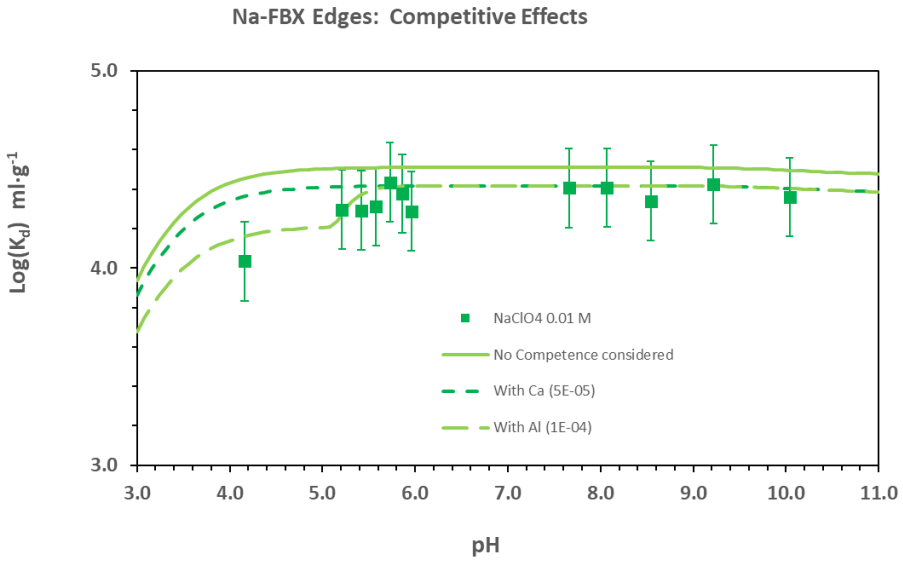


*Figure 3: Adsorption edges of Ba on Na-exchanged FEBEX clay at 0.01 M in $NaClO_4$. Continuous lines represent the modelling of the adsorption curves, considering the presence of competing ions (Ca and Al).*

Another point of interest is related to the behaviour of Ba adsorption as a function of the concentration (adsorption isotherms). Differently to what has been previously observed for Sr, in Ba adsorption, more than one site might be considered in Ca-exchanged FEBEX, but also illite. The isotherm at high [RN] concentration cannot be easily reproduced considering only one cation exchange site, as previously done for Sr in the same materials. This issue is still under investigation. More details on this work are made available in Missana et al. 2023a.

### Adsorption Tests with COx.

The adsorption isotherms and sorption kinetic tests performed with Ra and in the $CO_x$ clays samples are shown in Figure 4. Sorption isotherms (left) indicate linear adsorption up to the precipitation of barite, which is clearly observed at Ba equilibrium concentrations higher than $8 \cdot 10^{-7}$ M, due to the sulphate content of the water (Table 1). The kinetic of adsorption of Ba and Ra is shown in Figure 4 (right). The $K_d$ of both radionuclides keeps slowly increasing even after 90 days, indicating a slow kinetic process that can be interpreted by diffusion in minor mineral phases. In fact, in the case of the exchanged clays, no significant kinetic was observed during the uptake in all the different clays and experimental conditions.

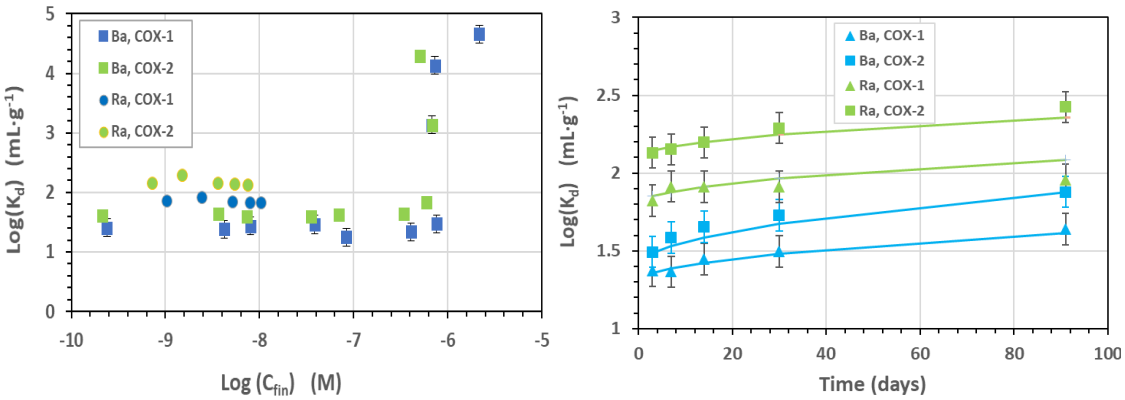


*Figure 4: Adsorption isotherms of Ba/Ra on COx clay samples (left). Adsorption kinetics of Ba/Ra in the COx clay samples.*

The adsorption in the $CO_x$-2 sample is slightly higher than in $CO_x$-1 and, in general, the adsorption of Ra is slightly higher than that of Ba.

## Desorption tests to evaluate adsorption irreversibility

Desorption tests were carried out both with the exchanged clays and with the COx clay. In the case of the exchanged clays, in desorption tests similar distribution coefficients as those measured in the sorption test were always obtained, in agreement with reversible adsorption, as can be seen in Figure 5, where an example with the data of Na-illite is shown.

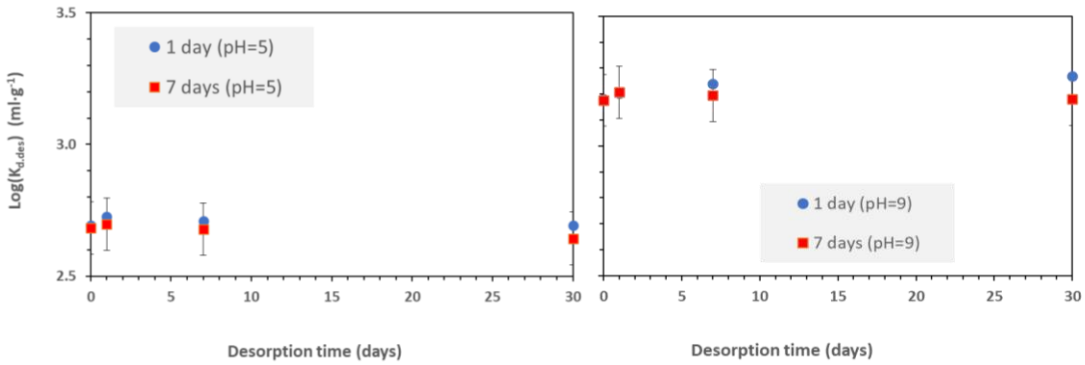


*Figure 5: Desorption tests of Ba in Na-illite (du Puy) at 0.05 M in NaClO4 at pH 5 (left) and pH 9 (right). Graphs shows the $K_{d,\ des}$ at different times, upon adsorption time of (■) 1 or (■) 7 days.*

However, the desorption behaviour in the COx is different. As can be seen in Figure 6, kinetic effects are observed both in adsorption and in desorption processes. At short desorption times, $K_{d,des}$ values were always higher than the $K_{d,sor}$ ones, indicating apparent irreversibility.

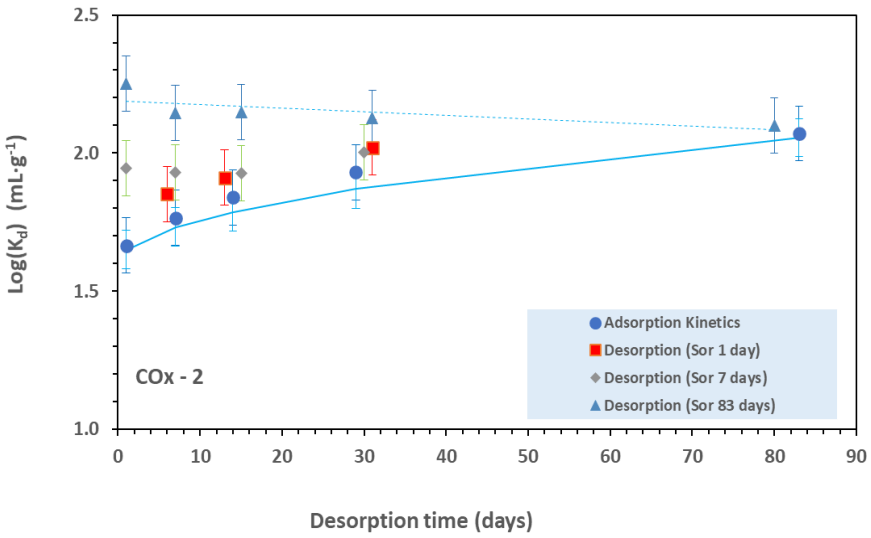


*Figure 6: Desorption tests of Ba in the COx-2 sample. Graphs shows the $K_{d,\ sor}$ and $K_{d,\ des}$ obtained upon adsorption time of (■) 1 day, (■) 7 days or (■)83 days.*

However, at larger desorption times, both values tend to match, indicating that the retention of Ra and Ba in these materials is likely reversible, even though kinetically controlled.

The precipitation of Ba or Ra in (radio)barite, which can occur due to presence of abundant sulphates, as could be observes in Figure 4 (left), will possibly produce an irreversible retention in the COx clay rock if

the metal concentration exceeds the solubility limit. More details on this work will be available in Missana et al. 2023b.

### Batch sorption test in compacted/consolidated clays

These tests were carried out both with the raw compacted FEBEX clay and with the COx clay with the experimental set-up shown in Figure 1. Figure 7 shows the comparison between the kinetic tests obtained in the powdered COx clay with the values obtained in the consolidated samples (Ba, left; Ra, right).

The distribution coefficients obtained in the compacted or powdered materials are in the same order of magnitude, and the adsorption kinetic observed in the process seems to be similar, within the time frame investigated (up to 240 days).

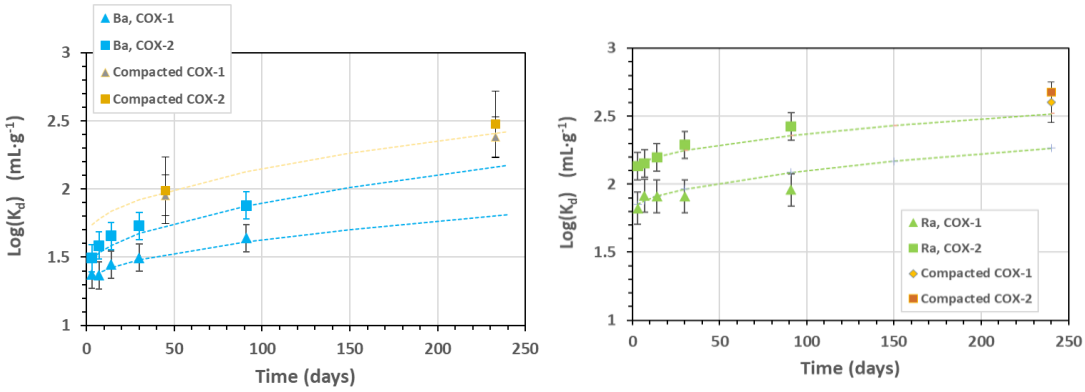


*Figure 7: Sorption kinetic tests in powdered COx clay compared with the data obtained in the consolidated material. Ba(left) and Ra(right).*

The tests with the FEBEX clay were carried out with the powdered clay and with the clay compacted at approximately 1.5 g/cm$^3$. To compare the distribution coefficients in both systems the pH was fixed to 7.0±0.5 and the ionic strength to 0.01 M with $NaClO_4$. The batch tests with the powdered material lasted 7 days, whereas larger contact times were used for the compacted samples. The main results obtained so far are summarised in Table 2.

*Table 2: $K_d$ values obtained in the powdered and compacted FEBEX clay. In both cases pH was fixed to 7 and the ionic strength to 0.01 M with $NaClO_4$.*

| Radionuclide | $K_d$ (powder) (mL/g) | Contact time (days) | $K_d$ (compacted) (mL/g) |
|---|---|---|---|
| $^{85}$Sr | **75.5 ± 3.3** | 7 | |
| | | 126 | 43.7± 11.1 |
| | | 188 | 49.8± 4.9 |
| | | 231 | 70.1± 7.0 |
| $^{133}$Ba | **221.2 ± 7.8** | 7 | |
| | | 222 | 158.4± 30.4 |
| | | 262 | 154.4± 56.0 |
| $^{226}$Ra | **882.2 ± 57.7** | 7 | |
| | | 226 | *309± 100* |
| | | 267 | 388.9± 84.0 |
| | | 420 | 569.9± 70.0 |

Results in Table 2 show that the distribution coefficients in the compacted FEBEX clay for Sr and Ba are very similar to that determined in the powdered system, even if the kinetic for reaching the equilibrium value is slower. This is especially true for Ra, for which upon 420 days, the determined distribution ratio might not be the value at the equilibrium. Further experiments addressing this topic are ongoing, larger contact times are possibly needed. More details on this work will be available in García-Gutiérrez et al. 2023a.

## Diffusion tests:

### COx clay rock

In-diffusion and through-diffusion experiments (with variable gradient concentration) were carried out to determine the diffusion coefficients of Ba and Ra in the $CO_x$ clay. An example of the results for in diffusion tests are shown in Figure 8. The simulations were carried out using two different approximations, from Put and Henrion (1992), and Crank (1975), to determine the apparent diffusion coefficients, $D_a$.

The mean apparent diffusion coefficients obtained with three experiments are summarised in Table 3.

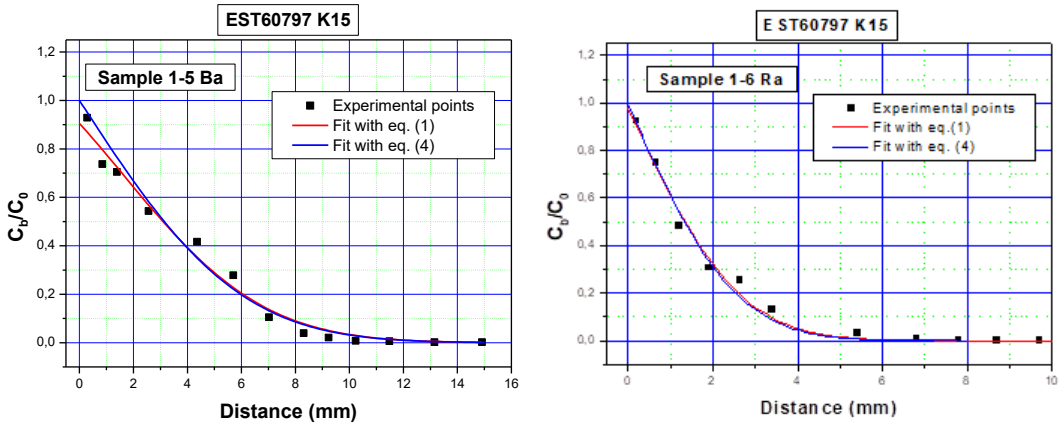


*Figure 8: Diffusion profiles in the in-diffusion tests for Ba(left) and Ra(right) in the COx clay.*

*Table 3: Apparent diffusion coefficients obtained from In-Diffusion simulating the diffusion profiles with two different analytical approximations.*

| **Sample** | **$D_a$(Ba) ($m^2/s$)** | | **$D_a$(Ra) ($m^2/s$)** | |
|---|---|---|---|---|
| | **Eq.1** | **Eq.2** | **Eq.1** | **Eq.2** |
| **EST60797 K15** | $(8.0 \pm 0.7)\cdot10^{-12}$ | $(8.1 \pm 1.6)\cdot10^{-12}$ | $(2.0 \pm 0.2)\cdot10^{-12}$ | $(2.1 \pm 0.4)\cdot10^{-12}$ |
| **EST60797 K18** | $(6.5 \pm 1.4)\cdot10^{-12}$ | $(6.7 \pm 1.6)\cdot10^{-12}$ | $(1.6 \pm 0.4)\cdot10^{-12}$ | $(1.7 \pm 0.3)\cdot10^{-12}$ |

Simulations shows that both the analytical approaches lead to very similar values for the apparent diffusion coefficients. The apparent diffusion coefficient is 3-4 times higher for Ba than Ra according to the observed lower Ba adsorption in the solid.

Through diffusion tests with a variable concentration gradient between the two reservoirs (for the radionuclide inlet and outlet) were also carried out, but satisfactory modelling of the data could not be reached yet. More details on this work will be available in García-Gutiérrez et al. 2023a.

### FEBEX clay

CIEMAT examined the combined effects of temperature (ranging from 25 to 80 ºC) and dry density of bentonite (from 1.2 to 1.65 g/cm$^3$) on the apparent diffusion coefficient, $D_a$, in the FEBEX clay, considering

the porewater chemistry at the different condition. Both conservative elements (HTO and Cl) and sorbing elements (Sr and Ba) were analysed. $K_d$ values for Sr and Ba were previously determined with the different porewaters, and at different temperature, as a support for diffusion experiments, showing the more relevant role of the competitive effects on sorption (due to the increase in the ionic strength of the porewater than temperature (Figure 9).

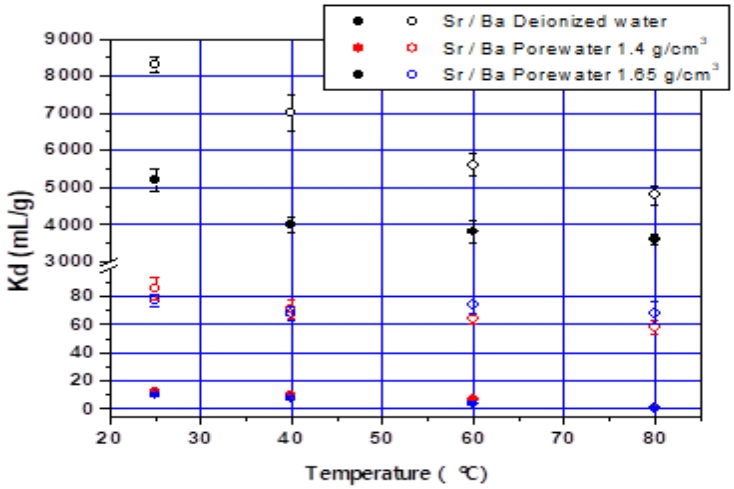


*Figure 9: $K_d$ values obtained as a function of the temperature for Sr (filled points) and Ba (open points) in deionized water and porewater calculated for 1.4 and 1.65 g/cm3.*

For all the radionuclides examined, $D_a$ decreased with increasing dry density and increased with increasing temperature. HTO diffusion in the clay at 1.2 g/cm$^3$ and 80 ºC had the highest $D_a$ ($1 \cdot 10^{-9}$ m$^2$/s), while Ba diffusion at 1.65 g/cm$^3$ and 25 ºC had the lowest $D_a$ ($3.6 \cdot 10^{-12}$ m$^2$/s). The experimental $D_a$ values were analysed using the Arrhenius law and the Stokes-Einstein equation revealing a reasonable agreement with Arrhenius behaviour, but deviation from the Stokes-Einstein equation for the clay with compaction densities greater than 1.4 g/cm$^3$. More details on this work will be available in García-Gutiérrez et al. 2023b.

## Oncoming publications related to research in FUTURE

- García-Gutiérrez M., Mingarro M., Missana T. (2023a, in preparation). Determination of $K_d$ values in batch/compacted systems experimental approach and data analysis.
- García-Gutiérrez M., Mingarro M., Missana T., (2023b, submitted). Temperature and dry density coupled effects on HTO, $^{36}$Cl, $^{85}$Sr and $^{133}$Ba diffusion through compacted bentonite.
- Missana T., García-Gutiérrez M., Mingarro M., (2023a, in preparation). Analysis of alkaline earth metals adsorption processes in Na- and Ca- exchanged clay minerals: role of radionuclide concentration, ionic strength, and the presence of competitive ions.
- Missana T., García-Gutiérrez M., Mingarro M., Fernández A.M., Alonso U. (2023b, submitted) Analysis of sorption ir/reversibility of Ba and Ra in different clays: a kinetic study.

## References

Crank J. (1975) The Mathemathic of diffusion, Clarendon Press, Oxford

Gabis V. (1958). Etude preliminaire des argiles oligocenes du Puyen-Velay (Haute Loire). Bull. Soc. Franc. Mineral Cristallog., 183-185.

García-Gutiérrez, M.; Cormenzana, J.L.; Missana, T.; Mingarro, M.; Molinero, J. (2006) Overview of laboratory methods employed for obtaining diffusion coefficients in FEBEX compacted bentonite. J. Iberian Geol. 32 (1) 37-53.

Huertas, F., Fariña, P., Farias, J., García-Siñeriz, J.L., Villar, A.M., Fernández, A.M., Martín, P.L., Elorza, F.J., Gens, A., Sánchez, M., Lloret, A., Samper, J., Martínez, M.A. (2006). FEBEX Project. Full-scale engineered barriers experiment for a deep geological repository for high level radioactive waste in crystalline host rock. Updated Final Report 1994-2004. Madrid: ENRESA.

Keeling J.L., Raven M.D., Gates W.P. (2000) Geology and characterisation of two hydrothermal nontronites from weathered metamorphic rock at the Uley graphite mine, south Australia Clay and Clay Minerals, 48(5) 537-548.

Missana T., Alonso U., García-Gutiérrez M. (2021) Evaluation of component additive modelling approach for europium adsorption on 2:1 clays: Experimental, thermodynamic databases, and models, Chemosphere. 272.

Put, M; Henrion, P. (1992) "Modelling of radionuclide migration and heat transport from a HLW-repository in Boom clay" EUR-14156.

# 4. A process-based model describing transport induced co-precipitation and radionuclide retention

J. Poonoosamy,
*FZJ, Jülich, Germany*

N. Prasianakis
*PSI, Villigen PSI, Switzerland*

## Abstract

In geological repositories for nuclear waste, co-precipitation with $BaSO_4$ solid solutions is expected to reduce the $^{226}Ra$ concentration in pore water, a radionuclide continuously produced by radioactive decay in uranium-bearing waste streams, thus limiting its migration towards the biosphere (Brandt et al., 2018, 2020; Heberling et al., 2018; Klinkenberg et al., 2018; Curti et al., 2010, 2019, Vinograd et al., 2018). The high relevance of $BaSO_4$ containing solid solutions as a sink of $^{226}Ra$ and $^{90}Sr$ has triggered the development of advanced thermodynamic models that allow to reliably assess the solubility of these radionuclides. However, thermodynamic models alone are not sufficient to describe the fate of such contaminants in subsurface systems. This is because co-precipitation processes in the porous matrices of the subsurface are typically influenced by the complex interplay of solute transport and dissolution/precipitation kinetics. The relatively slow advective velocities and thus diffusion-dominated transport of solutes encountered in various settings in the subsurface (e.g., in the engineered barrier system of nuclear waste repositories or in tight rock formations) will induce specific effects during the crystallization of solid solutions which are not or only rarely observed in bulk solution/batch experiments e.g. oscillatory zoning, i.e., the formation of successive layers of minerals with different composition or properties. Understanding the mechanisms that drive oscillatory zoning will enable to build realistic conceptual approaches that describe solid solution precipitation and therefore the fate of mobile radionuclides like $^{226}Ra$ in the subsurface. In this work (Poonoosamy et al., 2021), we revisit the oscillatory zoning of $(Ba,Sr)SO_4$ solid solutions by performing new experiments using a novel micronized lab-on-a-chip device. The device allows carrying out counter diffusion experiments with real-time monitoring of mineral growth by time lapse optical microscopy and in situ characterization by micro-Raman spectroscopy (Poonoosamy et al., 2019, 2020, 2022). The experiments were complemented by reactive transport models, which allow predicting the time-space evolution of transport pathways, aqueous solute concentrations, and relevant thermodynamic/kinetic parameters (e.g., saturation indices, precipitation rates). We used reactive transport modelling with newly implemented theoretical approaches such as the supersaturation function and classical nucleation theory (CNT) extended to solid solutions to predict the composition of the nucleating phases, and to determine the driving forces for the oscillatory zoning. Our investigations showed that the composition of the nucleating phases can be approximated by using CNT and that the oscillatory zoning results from a combination of limited diffusional transport of solutes and kinetically controlled precipitation reactions. The experimentally validated reactive transport models thus provides a rigorous description of solid solution formation precipitating under kinetic constraints and consequently a more accurate quantification of the mobile radionuclide in aqueous solution. The proposed conceptual modelling approach can be applied to describe more complex system e.g. $(Ba,Ra)SO_4$.

## Introduction

Co-precipitation of radionuclides in host phases is considered a relevant retention mechanism in some scenarios of safety cases for deep geological repositories for radioactive wastes. Ba and Ra released from the radioactive waste will react with porewater containing sulphate, triggering the formation of $(Ba,Ra)SO_4$ or even $(Ba,Sr,Ra)SO_4$ solid solutions. In the specific case of $^{226}Ra$, the solid solution with $BaSO_4$ irreversibly binds the contaminant in a stable phase, of which the mixing behaviour and thermodynamic properties are well described in the literature. However, for a rigorous assessment of the fate of $^{226}Ra$ with reactive transport modelling a conceptual approach describing transport-induced crystallization of solid

solutions in tightly confined porous media considering the effects of kinetics is needed. Indeed, the kinetics of crystallization of (Ba,Ra)$SO_4$ has to our knowledge not been determined so far.

With the main objective of providing an integrated experimental and theoretical approach to predict transport-induced precipitation of solid solutions in tightly confined porous media or fractured crystalline rocks, we investigated crystallization processes of solid solutions leading to oscillatory zoning and rationalize the crystallization kinetics of solid solutions. For this purpose, we considered the (Ba,Sr)$SO_4$ solid solution. The methodology used in this work combines Lab on a chip experiments and reactive transport modelling conducted within the framework of WP FUTURE and DONUT respectively.

## Materials & methods

The experimental setup consists of a microfluidic reactor that is connected to pumps and monitored by optical microscopy and Raman spectroscopy (Figure 1). The microfluidic reactor is composed of two adjacent supply channels and 50 growth chambers (Figure 1). The growth chambers have a length of 127 µm and 60 µm width. A narrow channel of 10 µm by 10 µm connects the supply channels to the growth chambers. The narrow connections between the supply channels and the growth chambers enable a diffusion dominated transport regime in the growth chamber. The barrier structures (Figure 1) consist of an array of rectangular pillars (of 7 µm length and 2.37µm width) and distanced by 0.6 µm placed in the middle of the chamber. They maintain mechanical stability of the chamber and serve as substrate to initiate the nucleation process. The microfluidic reactor was made out of PDMS (Polydimethylsiloxane) and closed with a glass cover.

The two inlets were each connected to a 1 mL syringe, dispensing a mixed solution of 9.9 mM of $SrCl_2$ and 1 mM $BaCl_2$ and a solution of 10.9 mM $Na_2SO_4$, respectively (Figure 1). The two outlets were linked to two effluent vessels. The microfluidic reactor was initially filled with deionized water, followed by the injection of the reacting solutions at a rate of 500 nL $min^{-1}$ using a syringe pump (Nemesys, Cetoni GmBH, Germany) for 20 hours. The diffusion of the reacting solutions fostered the precipitation of (Ba,Sr)$SO_4$ solid solutions in the chambers of the microfluidic device. The experiment was conducted at ambient temperature (21 ºC) and pressure. The microfluidic experiment was monitored using an automated inverted microscope (Witec alpha300 Ri Inverted Confocal Raman Microscope.

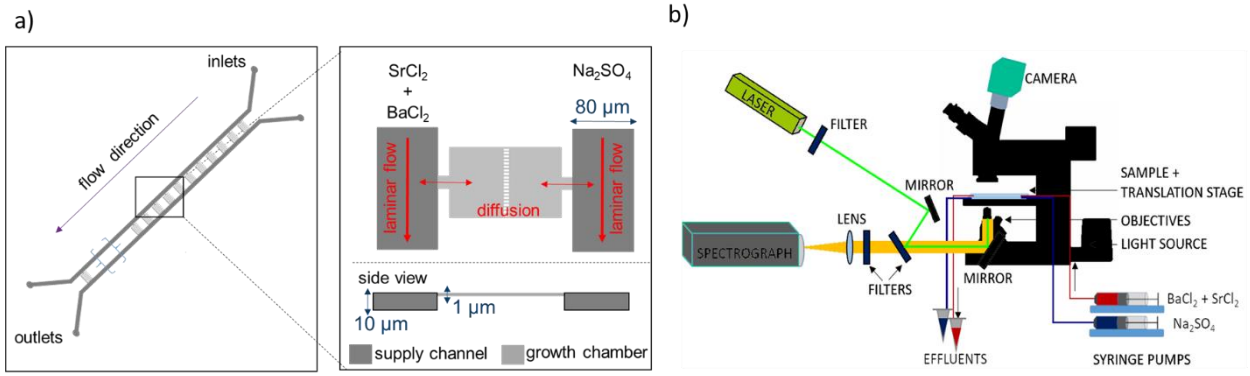


*Figure 1: a) Microfluidic reactor with an array of 50 growth chambers with an enlargement (right) of the growth chamber with an array of pillars constituting a barrier structure in the middle and b) schematic representation of the microfluidic setup.*

For the numerical modelling, several numerical algorithms are used at different steps to augment the information that can be extracted from the experiments. 1D Open-GeoSys-GEMs (OGS-GEMS) at the continuum level were conducted to decipher whether the zoning phenomena is a consequence of a diffusion-controlled precipitation or of a kinetically controlled reaction. We conducted two reactive transport studies at the continuum scale: (i) study 1, considering an instantaneous precipitation (thermodynamic equilibrium) of the two predominant solid solution compositions as extracted from the experiments, and (ii)

study 2 considering the kinetically controlled precipitation. The Advection-Diffusion Reaction Equation (ADRE) was solved using the OGS-GEMS code. For the case study 2, the precipitation rate of the stoichiometric composition was accounted for by crystal growth kinetics only.

## Results & discussion

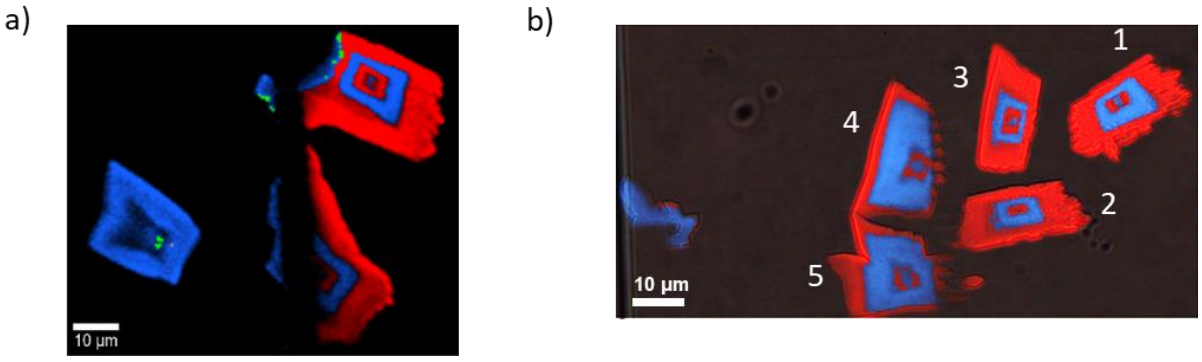


*Figure 2: Raman images collected from a) chamber 1 with alternating solid solution composition of $Ba_{0.5}Sr_{0.5}SO_4$ (blue) and $Ba_{0.05}Sr_{0.95}SO_4$ (red) b) chamber 4 with labelled crystals 1-5.*

The ingress of the mixed solutions of barium and strontium chloride solutions and sodium sulphate into the microfluidic reaction chambers triggered the formation of euhedral shaped crystals. The crystals were clearly distinguishable after 30 minutes reaction time in the monitored chambers. These crystals occurred at the pillars or at regions of irregularities on the wall of the chambers. The crystals appeared to grow by individual layers with alternating Sr-rich and Ba-rich composition, a zonation phenomenon. The respective composition was resolved by Raman imaging (Figure 2) showing the distribution of strontium (red) and barium (blue) enriched solid solutions within the single crystals.

### Kinetic versus thermodynamic control

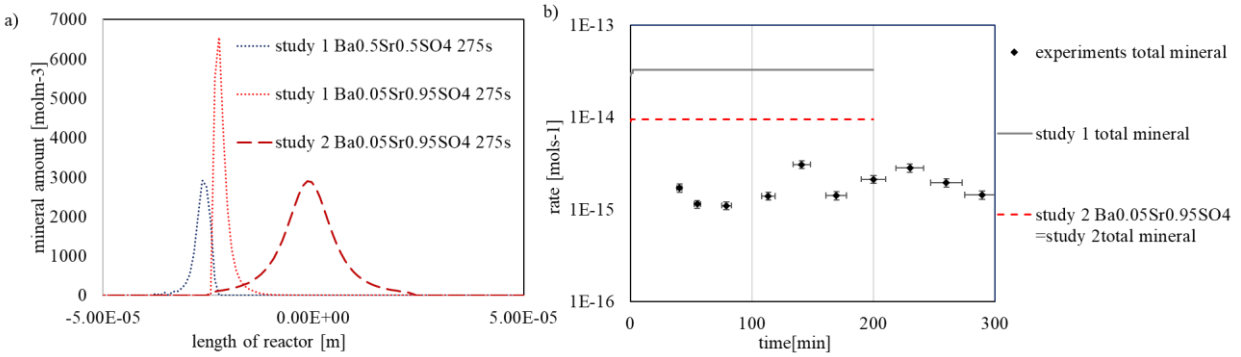


*Figure 3: a) Mineral distribution profiles of the two stoichiometric compositions $(Ba_{0.05}Sr_{0.95})SO_4$ and $(Ba_{0.5}Sr_{0.5})SO_4$ across a simulated 1D reactor for case study 1 at 275 s and case study 2 at 275 s. b) Comparison of simulated precipitation rates using OGS-GEM with instantaneous precipitation (case study 1) and with kinetic constraints (case study 2) against experimental results (total amount of minerals that precipitated per unit time).*

Figure 3a shows the predicted mineral precipitation across the 1D column for case study 1 and 2, respectively. In case study 1, both experimentally observed $Ba_{0.5}Sr_{0.5}SO_4$ and $Ba_{0.05}Sr_{0.95}SO_4$ precipitated. The precipitation starts in the left compartment, where the initial concentrations of $Ba^{2+}$ and the stoichiometric supersaturation ratio with respect to $Ba_{0.5}Sr_{0.5}SO_4$ are higher. In study 1, continuous re-

equilibration between the solid phases and aqueous solution is allowed, which explains the shift in the two maxima between the time 30 and 275 seconds in Figure 3. The re-equilibration is due to the dissolution of $Ba_{0.5}Sr_{0.5}SO_4$ in favour of the precipitation of $Ba_{0.05}Sr_{0.95}SO_4$. The sum of the associated rate of precipitation is one order of magnitude higher ($3.3\times10^{-14}$ mol $s^{-1}$) than the observed experimental rates ($1.8\pm0.1\times10^{-15}$ mol $s^{-1}$) (Figure 3). Two major outcomes are the results of this study. First, for the conditions of the experiment, diffusion coupled with thermodynamic equilibration results in large over prediction of the precipitation rates, verifying that the observed phenomena are not transport (diffusion) limited, and that the interplay of kinetics play a significant role. Second, such a modelling provides not only quantitative, but also qualitative very different results compared to the experimental observations. In contrast to experimental observations, there are no precipitates forming at the right compartment. When the kinetics of precipitation of the two stoichiometric compositions are considered (case study 2), only $Ba_{0.05}Sr_{0.95}SO_4$ precipitated in the simulation (Figure 3). The precipitation of $Ba_{0.5}Sr_{0.5}SO_4$ is kinetically hindered because of the lower kinetic constant of precipitation (~1 order of magnitude). A higher simulated precipitation rate of $Ba_{0.05}Sr_{0.95}SO_4$ ($9.0\pm0.1\times10^{-15}$ mol $s^{-1}$) in case study 2 compared to study 1 is observed and explained by the higher saturation ratios that can build up in the system since no other phase precipitates.

The presented continuum scale modelling scenarios cannot reproduce our experimental observations. Case study 1 with instantaneous precipitation overestimated the mineral precipitation rates, suggesting that the precipitation of oscillatory zoned crystals of $(Ba,Sr)SO_4$ is controlled by kinetics. In case study 2, which includes the crystal growth rates of minerals, the rate of precipitation was still higher than the experimental rates and the formation of $Ba_{0.5}Sr_{0.5}SO_4$ was kinetically suppressed. It can thus be inferred that the precipitation of $Ba_{0.5}Sr_{0.5}SO_4$ is controlled by processes that are kinetically slower and which are not included in the presented model, e.g., nucleation processes.

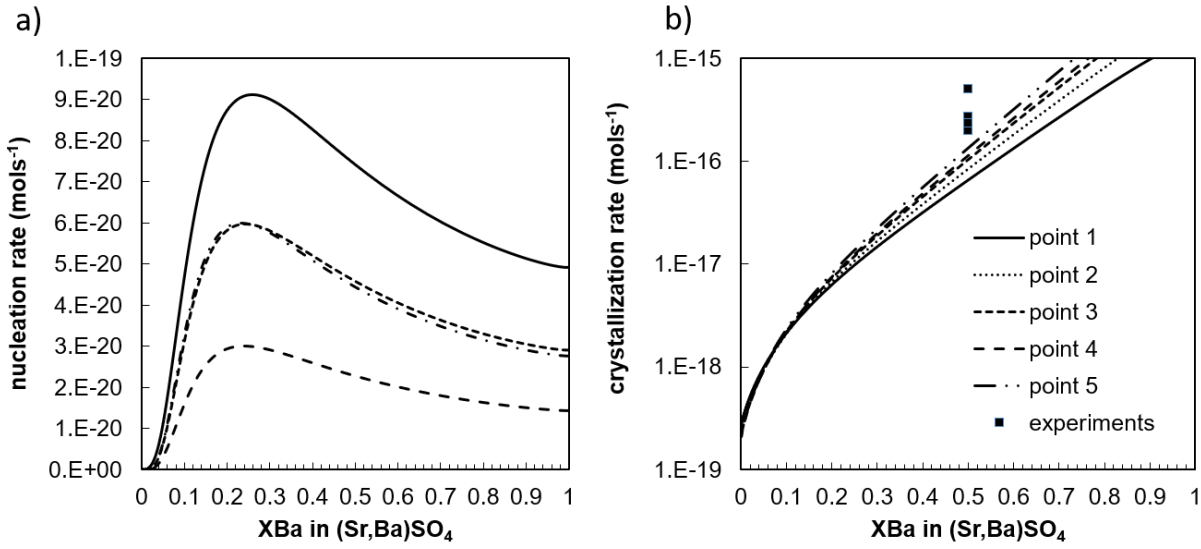


*Figure 4: a) Nucleation rates, and b) associated crystallization rates as function of the solid solution series calculated for several point (1-5) in the middle of the growth chambers.*

To verify this hypothesis, we sampled the simulated aqueous solution composition at different locations to compute the rate of nucleation and crystallization of $(Ba,Sr)SO_4$ solid solutions on the surface of $Ba_{0.05}Sr_{0.95}SO_4$ (Figure 4). The sampled points typically reflect the solution composition after the precipitation of $Ba_{0.05}Sr_{0.95}SO_4$. The solution chemistry with $\{Sr^{2+}\}/\{Ba^{2+}\}$ ~ 2, indicates that further nucleation of $Ba_{0.05}Sr_{0.95}SO_4$ is kinetically hindered but that other compositions with an increased Ba content can nucleate (shown by the maxima of the curves for points 1-5. The precipitation of barium enriched phases is kinetically favoured via nucleation mechanisms. After the precipitation of $Ba_{0.05}Sr_{0.95}SO_4$, the nucleation of barium enriched solid solutions becomes competitive enough to allow their precipitation. In fact, the switch to stoichiometric phases other than $Ba_{0.05}Sr_{0.95}SO_4$ could be explained by the fact that the nucleation rate of the other stoichiometric phases becomes higher than the rate of crystal growth of

$Ba_{0.05}Sr_{0.95}SO_4$. This successive nucleation and crystal growth operating at different rates (mol $s^{-1}$) can also explain the experimentally observed oscillating crystallization rates in Figure 4.

The solution chemistry after the precipitation of $Ba_{0.05}Sr_{0.95}SO_4$ favours crystallization of an almost pure barite (Figure 4), however, crystallization of solid solutions with compositions with $X_{Ba}$> 0.6 on the surface of $Ba_{0.95}Sr_{0.05}SO_4$ is unlikely and was observed only once at the pillars (crystal 3 in chamber 1), where the concentration of aqueous barium can build up in the system after clogging. Other factors related to the crystallography of the solid solutions could be decisive for the determination of the composition of the solid solutions that can precipitate. For instance, lattice mismatch that characterizes the differences between the lattice parameters of the growing solid solution and its substrate. Due to significant differences in lattice parameters between the growing phase and the substrate, only specific phases can precipitate. Such phenomena are common for the epitaxial growth of sulphate solid solutions[4]. Similarly, the surface tension and therefore the energetic barrier associated with the growth of solid solutions with $X_{Ba}$> 0.6 on the surface of $Ba_{0.95}Sr_{0.05}SO_4$ is relatively large, and is therefore unlikely to occur.

## Conclusions

We developed a lab on a chip experiment that enabled the systematic *in-situ* assessment of oscillatory zoned crystals of $(Ba,Sr)SO_4$ in a confined volume. Our investigations showed that the composition of the nucleating phase can be determined using classical nucleation theory extended to solid solutions. Our numerical and modelling studies were conducted at different levels, each providing significant information for the interpretation of the experiments. The continuum approach modelling, suggested that oscillatory zoning is not the result of the limited diffusion of solutes at least at the first stages. The switch between phases with different stoichiometry is likely caused by competition between nucleation and crystal growth of the two stoichiometric phases. Beside kinetics, other factors such as lattice mismatch or surface tension can also play an important role for the determination of the precipitating phases. In future work, we will integrate crystallization kinetics of solid solutions in our lattice Boltzmann model to create a digital twin of the system to resolve the geochemical processes at the mineral-solution interfaces.

## References

Brandt, F.; Klinkenberg, M.; Poonoosamy, J.; Weber, J.; Bosbach, D. The Effect of Ionic Strength and Sraq upon the Uptake of Ra during the Recrystallization of Barite. *Minerals* **2018**, *8*, doi:10.3390/min8110502.

Brandt, F.; Klinkenberg, M.; Poonoosamy, J.; Bosbach, D. Recrystallization and Uptake of 226Ra into Ba-Rich (Ba,Sr)SO4 Solid Solutions. *Minerals* **2020**, *10*, doi:10.3390/min10090812.

Curti, E.; Fujiwara, K.; Iijima, K.; Tits, J.; Cuesta, C.; Kitamura, A.; Glaus, M.A.; Müller, W. Radium uptake during barite recrystallization at 23±2°C as a function of solution composition: An experimental 133Ba and 226Ra tracer study. *Geochimica et Cosmochimica Acta* **2010**, *74*, 3553-3570, doi:https://doi.org/10.1016/j.gca.2010.03.018.

Curti, E.; Xto, J.; Borca, C.; Henzler, K.; Huthwelker, T.; Prasianakis, N. Modelling Ra-bearing baryte nucleation/precipitation kinetics at the pore scale: application to radioactive waste disposal. *European Journal of Mineralogy* **2019**, *31*, 247-262, doi:10.1127/ejm/2019/0031-2818.

Heberling, F.; Metz, V.; Böttle, M.; Curti, E.; Geckeis, H. Barite recrystallization in the presence of 226Ra and 133Ba. *Geochimica et Cosmochimica Acta* **2018**, *232*, 124-139, doi:https://doi.org/10.1016/j.gca.2018.04.007.

Klinkenberg, M.; Weber, J.; Barthel, J.; Vinograd, V.; Poonoosamy, J.; Kruth, M.; Bosbach, D.; Brandt, F. The solid solution–aqueous solution system (Sr,Ba,Ra)SO4 + H2O: A combined experimental and theoretical study of phase equilibria at Sr-rich compositions. *Chemical Geology* **2018**, *497*, 1-17, doi:https://doi.org/10.1016/j.chemgeo.2018.08.009.

Poonoosamy, J.; Westerwalbesloh, C.; Deissmann, G.; Mahrous, M.; Curti, E.; Churakov, S.V.; Klinkenberg, M.; Kohlheyer, D.; von Lieres, E.; Bosbach, D.; et al. A microfluidic experiment and pore scale modelling diagnostics for assessing mineral precipitation and dissolution in confined spaces. *Chemical Geology* **2019**, *528*, 119264, doi:https://doi.org/10.1016/j.chemgeo.2019.07.039.

Poonoosamy, J.; Soulaine, C.; Burmeister, A.; Deissmann, G.; Bosbach, D.; Roman, S. Microfluidic flow-through reactor and 3D Raman imaging for in situ assessment of mineral reactivity in porous and fractured porous media. *Lab on a Chip* **2020**, *20*, 2562-2571, doi:10.1039/D0LC00360C.

Poonoosamy, J.; Mahrous, M.; Curti, E.; Bosbach, D.; Deissmann, G.; Churakov, S.V.; Geisler, T.; Prasianakis, N. A lab-on-a-chip approach integrating in-situ characterization and reactive transport modelling diagnostics to unravel (Ba,Sr)SO4 oscillatory zoning. *Scientific Reports* **2021**, *11*, 23678, doi:10.1038/s41598-021-02840-9.

Poonoosamy, J.; Lu, R.; Lönartz, M.I.; Deissmann, G.; Bosbach, D.; Yang, Y. A Lab on a Chip Experiment for Upscaling Diffusivity of Evolving Porous Media. *Energies* **2022**, *15*, 2160.

Vinograd, V.L.; Kulik, D.A.; Brandt, F.; Klinkenberg, M.; Weber, J.; Winkler, B.; Bosbach, D. Thermodynamics of the solid solution - Aqueous solution system (Ba,Sr,Ra)SO4 + H2O: I. The effect of strontium content on radium uptake by barite. *Applied Geochemistry* **2018**, *89*, 59-74, doi:https://doi.org/10.1016/j.apgeochem.2017.11.009.

# 5. Achievements with respect to project objectives – Conclusions

*New/missing data available for sorption models (e.g. surface complexation constants)*

Data for both Ra and Ba sorption on Na-illite and Na-montmorillonite provided adequate information to develop sorption models in line with the 2SPNE SC/CE approach involving additional high-affinity cation exchange sites for both cations.

Batch sorption tests with Ba and Ra in homoionised clays (illite, FEBEX bentonite, Nontronite) allowed to determine the selectivity coefficients for the ion exchange with -Na and -Ca (as well as surface complexation constants) and to identify the importance of the competence of different ions (Ca, Al) on the ion exchange process.

*Transferability of batch sorption data to compacted system*

Results indicated that for Ba and Ra (and Sr), batch sorption data for FEBEX bentonite and COx are transferable to compacted systems. To evaluate properly the results, one must be sure that the water chemistry in the tests is always comparable. The kinetic of the adsorption processes might be different in the dispersed and compacted systems, therefore this is a very important parameter to be checked.

*Transferability of data from model systems to complex systems*

Presence of trace minerals in the COx might be the responsible for the different kinetic of sorption behaviour between the simple (purified) systems and the clay rock. Also, sulphate causes the precipitation of barite/radiobarite in the natural system, but it was not explicitly included in the analysis of the “simple system”. Again, an exhaustive description of the chemical system (and important processes) and kinetics is mandatory to transfer properly the information from one system to another.

The modelling of coupled effects may still represent an open issue. It is necessary to be able to identify all important processes and implement them correctly. To account for competition effects, an accurate chemical characterization of the system is mandatory. For what concerns adsorption data, we have the best probabilities to accurately model the “complex system” starting from simplest ones, when the additivity of sorption in different components can be demonstrated.

*Adequate description of sorption competition*

The theoretical way to describe this phenomenon is well defined and can be implemented in geochemical calculations. The main problem might be related to the lack of data or the poor description of the chemical system.

*Irreversibility of sorption under certain conditions*

Under the studied conditions in CIEMAT experiments, sorption of Ra and Ba on Na-illite and COx has been shown to be reversible. However, kinetic limitations were observed for sorption in natural systems. In the COx clay, Ba/Ra retention can be irreversible upon co-precipitation with sulphate.

*Improvement of currently used uptake/sorption models based on the knowledge on irreversible uptake processes*

An experimentally validated reactive transport model (implementing supersaturation function and classical nucleation theory) provided a rigorous description of solid solution formation precipitating under kinetic constraints and consequently a more accurate quantification of the mobile radionuclide in aqueous solution. The proposed conceptual modelling approach can be applied to describe more complex system e.g. $(Ba,Ra)SO_4$.

*Description of transport experiments based on mechanistic understanding (anion exclusion, surface diffusion, saturation degree, pore characteristics,…)*

Ra diffusion experiments on OPA were described with classical diffusion model. Using batch derived $K_d$ data as input to the transport model was not adequate to describe the diffusion data. Surface diffusion was observed.

The use of batch derived Ra sorption data ($K_d$) on OPA as input to model transport experiments in a classical way did not provide a good match with the diffusion data. Experimental diffusion and sorption data for $^{226}Ra$ in OPA show an earlier tracer breakthrough in through diffusion than expected based on HTO diffusion and sorption experiments of $^{226}Ra$ in dispersed suspensions of OPA. The $R_d$ values obtained by simulation of diffusion data are smaller than the respective $R_d$ values from batch sorption experiments. This observation may be qualitatively explained by different concentrations of competing species in the in-situ pore water versus the dispersed system. The higher $D_e$ may be due to surface diffusion of $Ra^{2+}$, similar to diffusion of $Sr^{2+}$ and $Cs^+$ in OPA (Appelo et al., 2010). No (reactive) transport modelling was performed in which surface diffusion formalisms are implemented.

In and Through Diffusion experiments on COx are modelled with the classical transport models. In-diffusion models provided relevant $D_a$ data but models describing the Through-Diffusion experiments in the COx clay were not yet fully satisfactory, this probably means that some relevant mechanism might still be overlooked. Modelling based on more enhanced mechanism was not performed.

# Chapter 3: Mobility of moderately sorbing transition metals in clay

Six research teams investigated the sorption and diffusion behaviour of transition metals.

CIEMAT (Madrid, Spain) compared the adsorption behaviour of Cd, Co and Zn on Na-FEBEX (dispersed and compacted) to develop a sorption model. They investigated Zn sorption on clay mixtures (smectite, illite and kaolinite) to test the applicability of a component additivity sorption approach.

SCK CEN (Mol, Belgium) studied the competition of Ni on sorption and diffusion of Zn in illite systems.

EK (Budapest, Hungary) focused on transferability of Ni(II) sorption from diluted to compacted systems on natural Boda claystone samples. Also reversibility and competition with Co(II) was investigated.

PSI (Viligen PSI, Switzerland) studies were three-fold. One study focused on the reversibility of Zn uptake by montmorillonite and illite by combining wet chemistry experiments with EXAFS to elucidate the retention mechanism at long term. The 2 other studies are focused on unravelling the surface diffusion phenomena by investigating the diffusion and retention of Co and Zn surface complexes in compacted illite pre-loaded with different cations and diffusion of Co in compacted vermiculite with varying grain size.

Based on an approach described by Soltermann et al. (2014), JGU (Mainz, Germany) and University of Heidelberg (Heidelberg, Germany) constructed an electrochemical cell for sorption experiments under controlled reducing conditions. It was tested for Fe(II) on Montmorillonite.

BRGM (Orléans, France) worked on the development of an electrostatic sorption model for montmorillonite based on a sound structural understanding allowing quantification and prediction of edge acid-base properties and other sorption properties including reversibility.

## 1. Sorption studies of transition metals (Cd, Co, Zn, Ni) on clay minerals (kaolinite, illite, FEBEX)

T. Missana, U. Alonso, M. García-Gutierrez
*CIEMAT, Madrid, Spain*

### Abstract

The objective of this report is to summarise CIEMAT activities in Task 2 (Subtask 2.1 Mobility of radionuclides in compacted clay) of the EURAD WP FUTURE, regarding adsorption and migration of transition metals in argillaceous rocks. The first aim of CIEMAT was to compare the adsorption behaviour of different transition metals (Cd, Co and Zn) in the Na-exchanged FEBEX smectite and to develop a sorption model considering their common behaviour. Secondly, the intention was to analyse the adsorption of Zn in clay mixtures (smectite, illite and kaolinite) and to verify if adsorption can be modelled as an additive component process. For this study, the FEBEX smectite, the Illite du Puy and a commercial kaolinite (Aldrich) were used. Sorption studies were separately carried out in each clay and then in mixtures of the three clays in different proportions.

The analysis of the difference between $K_d$ values determined in the dispersed or compacted system was done using the FEBEX clay.

### Introduction

The activity planned by CIEMAT at the beginning of the FUTURE project in Task 2.1 (Radionuclide mobility in clays) with transition metals was centred on two main issues. The first one was to analyse if transition metal adsorption in mixed clay is an additive process, considering the contribution of each clay present in the rock, and if the application of (simple) geochemical sorption modelling is enough for an adequate data interpretation of the processes involved in retention. The adsorption behaviour of divalent transition metals is quite different from that of other divalent elements as alkaline earth metals and its modelling entails additional difficulties.

To answer to this question, detailed sorption studies on the different clays (smectite, illite and kaolinite) were performed including as main variables the pH, the ionic strength, the concentration of radionuclide and the presence of carbonates.

For the modelling of the transition metal adsorption behaviour a previous selection of thermodynamic data was needed. The NEA/Thermo Chimie database, which was selected by Ciemat as the reference for thermodynamic constant selection, for example, does not contain data for Zn and other thermodynamic datasets must be considered.

Additionally, one of the interests of CIEMAT in FUTURE was to verify whether the distribution coefficients ($K_d$) measured under dispersed or compacted conditions are equivalent. CIEMAT designed special cells to determine the distribution coefficients directly in compacted/consolidated materials trying to work under solid to liquid ratios and chemical conditions comparable to those applied in batch sorption experiments with powdered materials. These tests were carried out both with the FEBEX clay compacted at a density of approximately 1.55±0.05 g/cm$^3$.

## Materials and methods

### Clays and contacting electrolytes

The clay minerals selected for the adsorption experiments were smectite (FEBEX), illite (du Puy) and kaolinite (Aldrich). For adsorption experiments, the clays previously crushed and sieved (< 64 µm), were converted in their Na-form by washing them three times with 1 M $NaClO_4$ (Merck, purity 99.99%). No additional acid treatment of the clays, to eliminate carbonate minerals, was carried out. After the exchanging procedure, the clays were distributed in centrifuge tubes and mixed with ultrapure water (Milli-Q system, Millipore). The suspensions were centrifuged (600·g, 10 min) and the supernatant, containing the fine clay fraction was collected in polyethylene bottles. The clay remained in the centrifuge tubes was mixed with ultrapure water and centrifuged again. The cycle was repeated several times, until enough solid material was available. The ionic strength of the clay suspensions was changed by dialysis using $NaClO_4$ at different concentrations. The solid to liquid ratio of the different suspensions ranged from 1 to 3 g·L$^{-1}$. Part of the obtained Na-clay was not subjected to particle fractionation; it was simply washed to eliminate the excess of salt, and was left drying in air or at a maximum temperature of 40 °C. For all the sorption experiments with the Na-clays $NaClO_4$ was used as electrolyte.

Raw FEBEX clay was used for the sorption experiments in compacted clay, and the compaction density for these tests was 1.5±0.05 g/cm$^3$.

### Radionuclides

The isotopes used for this study were $^{109}$Cd, $^{60}$Co, $^{65}$Zn and $^{63}$Ni. $^{109}$Cd (Eckert & Ziegler, Isotope Products) was in the form of $CdCl_2$ in 0.1 M HCl; $^{60}$Co (Areva) was in the form $CoCl_2$ in 0.1 M HCl, and $^{65}$Zn (Eckert & Ziegler, Isotope Products) was in the form $ZnCl_2$ in 0.5 M HCl. All the three isotopes are gamma emitters, therefore their activity was measured by gamma counting with a Cobra-II 5003 auto-gamma Packard counter with a 3" NaI (Tl) crystal. $^{63}$Ni is in the form of $NiCl_2$ in HCl 1 M, its activity has been measured by liquid scintillation counting.

### Types of experiments

Different types of experiments were carried out. Batch sorption tests in dispersed clays were carried out with the Na-exchanged clays (smectite, illite and kaolinite) analysing the variation with the most important parameters (pH, ionic strength (I) and radionuclide concentration, [RN]) to obtain a dataset wide enough for applying sorption modelling. Three different mixtures of the clays were prepared in different proportions (50%, 25%, 25%), and sorption tests were also carried out in these mixtures.

The chemistry of the contact water in equilibrium with the solid in the condition of the sorption experiments (1-3 g/L), was checked at the end of the experiments at least for 3 different pH (4, 7, 9) and ionic strengths.

Batch sorption test in compacted clays, were carried out with the natural FEBEX clay compacted to a dry density between 1.5 and 1.55 g/cm$^3$. To carry out these tests, the samples (0.06 g) were confined between two sintered steel filter in a cell specially designed. These cells were immersed in the aqueous solution (approximately 7 mL) and left in contact during different contact times to consider the possible sorption kinetic. After the tests, all the part of the cells were disassembled and the final activity in the water and in the clay was measured, to determine the $K_d$. The activity in the other parts of the cells was also measured.

## Results & discussion

### Adsorption experiments in single clays

#### Smectite

Adsorption experiments with FEBEX Na-clay were carried out with Zn, Co and Cd. Study included: Kinetic tests; adsorption edges at different ionic strengths (generally 0.01, 0.05 and 0.1 M) in $NaClO_4$ and two different radionuclide concentrations, and sorption isotherms at least at two different ionic strengths. Apart from the general need of improving our comprehension of the sorption processes involved in the retention of these elements in clays, depending on studied transition metal, specific objectives were also pursued.

In the case of Cd, for example, there was certain controversy in the literature, on the role played by chloride on $Cd^{2+}$ adsorption (Taylor et al., 1995; Saeki et al., 2012; El-Hefnawy et al., 2014). Additionally, a discussion on the early formation of Cd-carbonate precipitates was ongoing due to the very high uncertainty on the constant of formation of the otavite ($CdCO_3$).

In the case of $Zn^{2+}$ (but also for the other transition metals), several relevant thermodynamic constants are lacking in the reference database (NEA / Thermo Chimie) therefore, other literature source should have been used (e.g. IUPAC).

Experiments with Cd were carried out under atmospheric conditions. Figure 1 includes the results of Cd adsorption edges carried out at two different ionic strengths in $NaClO_4$ (0.1 and 0.01) at [Cd]=$9.18\cdot10^{-8}$ M; a third experiment was carried out in 0.1 M $NaClO_4$ and a higher Cd concentration ([Cd] = $1\cdot10^{-5}$ M) to better elucidate the contribution of strong and weak surface sites. Figure 1b compares the adsorption edges carried out in 0.1 M $NaClO_4$ ([Cd] = $1\cdot10^{-5}$ M) and carried out with different chloride concentrations. Results indicated that chloride can be neglected in the modelling because Cd adsorption is independent on its concentration.

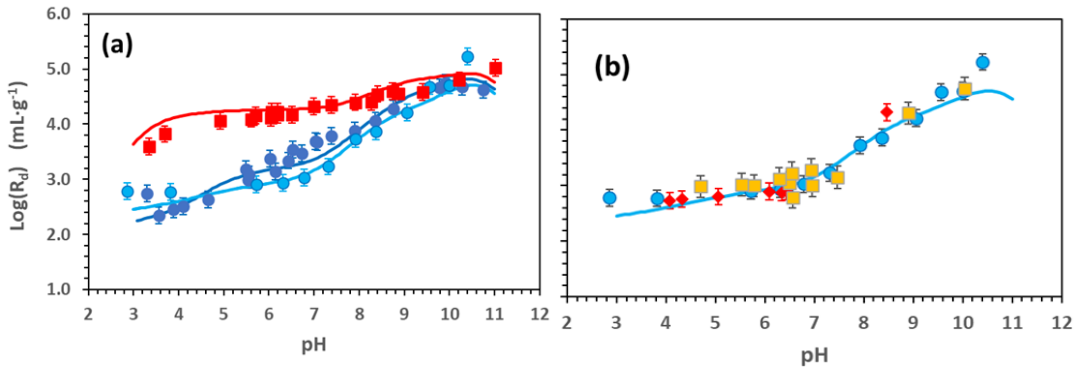


*Figure 1: Cd sorption edges: **(a)** (■) Comparison of sorption edges at two different Cd concentrations. [Cd]= $9.18\cdot0^{-8}$ M and 0.1M $NaClO_4$; (■)[Cd]= $1\cdot10^{-5}$ M and 0.1M $NaClO_4$; (■) [Cd] = $9.18\cdot10^{-8}$ M and 0.01M $NaClO_4$. (**b**) Comparison of sorption edges with different contents of chloride. (■) Reference standard test (Cd]=$1\cdot10^{-5}$ M with HCl and $CdCl_2$); (◆) [Cd]=$1\cdot10^{-5}$ M with $Cd(ClO_4)_2$ and traces of $^{109}CdCl_2$ ($1\cdot10^{-8}$ M); (■) [Cd]=$1\cdot10^{-5}$ M without Cl (only $HClO_4$ and $Cd(ClO_4)_2$. The line represents the model calculations.*

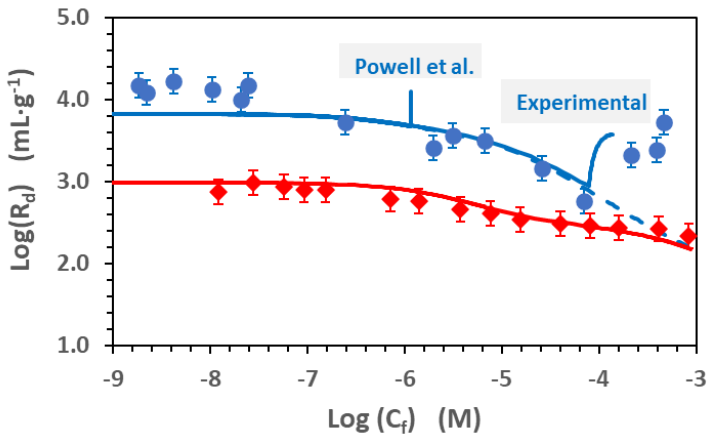


*Figure 2: Cd adsorption isotherms in Na-smectite in 0.1 M $NaClO_4$. (■) pH=7.8 and (◆) pH 5.1. The lines represent the model calculation The concentrations where precipitation is predicted by IUPAC database.*

Figure 2 shows the Cd sorption isotherms obtained at two different pH values (7.8 and 5.1) in 0.1 M $NaClO_4$. The isotherms show a non-linear Cd adsorption, which decreases as Cd concentration increases. In the adsorption isotherm at pH 7.8, a sudden increase in the distribution coefficient is observed, when the Cd aqueous concentration exceeds approximately $8 \cdot 10^{-5}$ M. This behaviour is usually related to precipitation processes. At pH 5.1, no signs of precipitation could be appreciated at any Cd concentration.

Figure 3 shows the comparison of ATR-FTIR spectra of the clay before and after the adsorption of Cd at high concentration, which indicate the appearance of peaks related to the possible presence of Cd precipitation. The spectra of otavite is included in the graph and the "new" peaks are consistent with the presence of otavite traces.

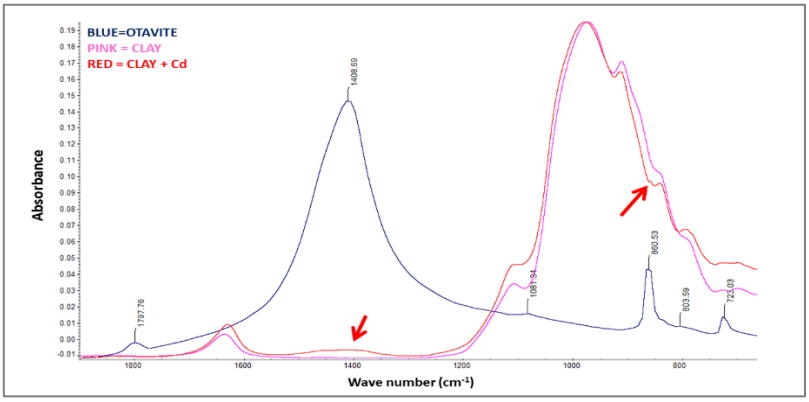


*Figure 3: Comparison of the ATR-FTIR spectra of the clay before and after the adsorption of Cd [$3 \cdot 10^{-3}$ M] at pH=8 in NaClO4 0.01 M. The reference spectra of otavite is also included for comparison.*

Thus, it can be supposed that otavite is the main solid controlling the solubility under the conditions of our experiments, however the precipitation observed in the adsorption isotherms occurs at a concentration of almost two orders of magnitude higher than that calculated by the solubility constant for otavite provided by Powell et al. (2011) and our data would be more in agreement with the value provided by Stipp et al. (1995). As a general consideration, it is important to remark that for a reliable modelling, updated and reliable thermodynamic data bases are fundamental.

Considering the dependence on Cd adsorption with both the ionic strength and pH, the modelling of Cd adsorption data was carried out considering the contribution of cation exchange (Cd-Na) and surface complexation in strong and weak surface functional sites at the edges of the clay particles, SOH, as reported in different previous works of our group (Missana et al., 2021). Specifically for Cd, all the

information about the model details, parameters and applied procedures can be found in Missana et al. (2023a).

In general, similar adsorption in smectite than that observed for Cd was seen for Co and Zn, as can be seen for example in Figure 4, which shows the comparison of the adsorption edges performed at the ionic strength of 0.1 M $NaClO_4$, for the three metals. This similarity justified, at least in a first instance, the use of the same modelling approach for all the transition metals.

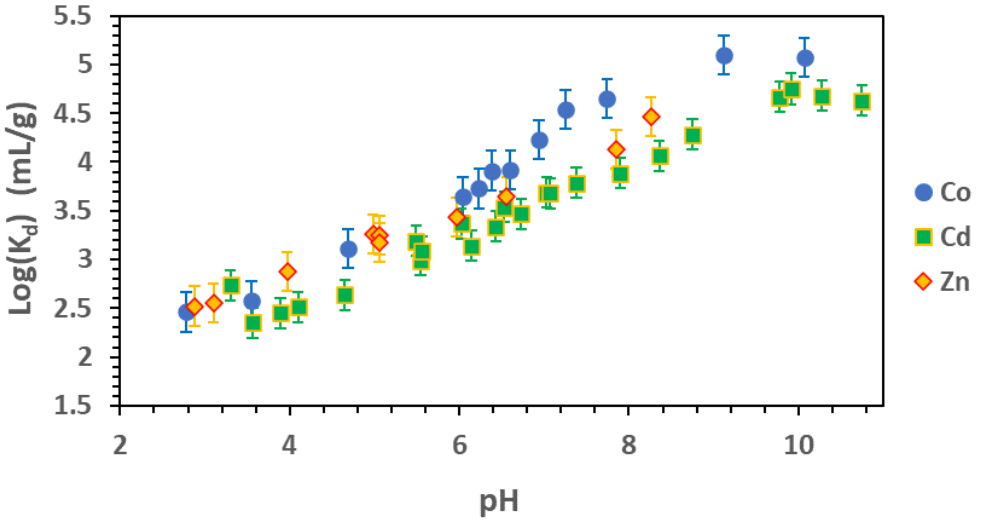


*Figure 4: Comparison of the adsorption edges in Na-FEBEX clay for Cd, Zn and Co in $NaClO_4$ 0.1 M.*

### Illite and Kaolinite

As a previous step of the adsorption study of Zn in clay mixtures, adsorption tests were carried out also on Na-illite and Na-kaolinite. Figure 5 shows an example of the Zn adsorption edges (left) and adsorption isotherms (right) obtained in the illite in $NaClO_4$ 0.1 M. The adsorption isotherms at pH~8.5 indicate that for aqueous [Zn] >1% $10^{-5}$ M, precipitation is possible. As already seen in the case of smectite, Zn adsorption behaviour in illite is mainly the result of cation exchange (Zn-Na) under acidic conditions and surface complexation in the SOH sites at the edge of the clay particles under neutral and alkaline conditions. As also observed in the isotherm, adsorption on illite is not linear so the existence of strong and weak SOH sites should be considered.

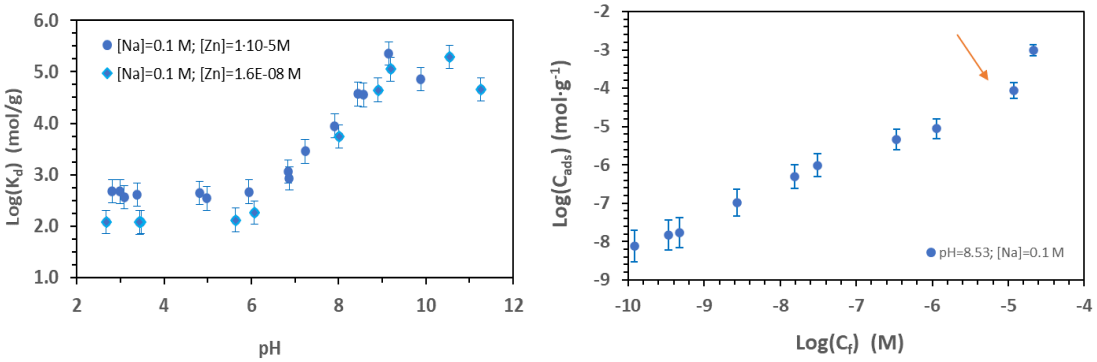


*Figure 5: Examples of sorption tests of Zn in Na-illite in 0.1 M $NaClO_4$. Left: sorption edges; Right: Sorption isotherms.*

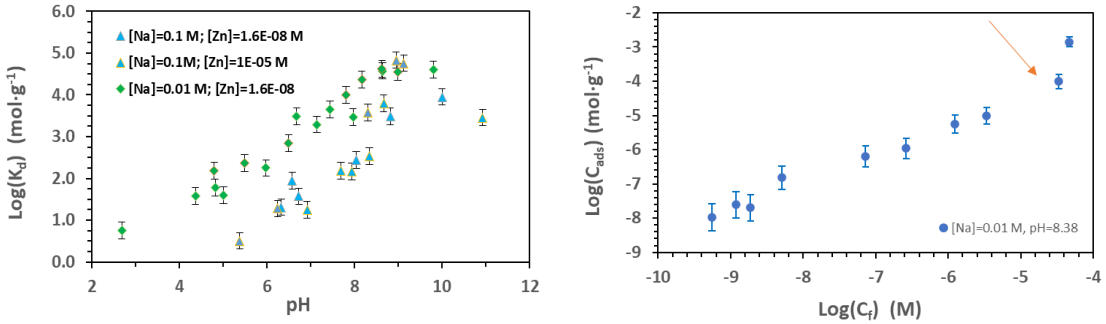


*Figure 6: Examples of sorption tests of Zn in Na-kaolinite in 0.1 M $NaClO_4$. Left: sorption edges; Right: Sorption isotherms, orange arrow indicates the onset of precipitation.*

Figure 6 shows an example of the Zn adsorption experiments with kaolinite. The adsorption edges (Figure 6, left) were obtained at the ionic strengths of 0.1 and 0.01 M in $NaClO_4$; the adsorption isotherm at pH 8.4 and 0.01 M is shown in the right part of Figure 6. The adsorption in kaolinite (especially at 0.1 M) is much lower than that observed in smectite or illite. This is partially due to the almost complete suppression of the cation exchange in this material. As previously observed in the case of illite, the adsorption isotherms at pH~8.4 indicates that Zn precipitation occurs for aqueous [Zn] >1% $10^{-5}$ M, also for kaolinite. Furthermore, the Zn adsorption isotherm is not linear so that, also in this case, the existence of strong and weak SOH sites should be considered.

### Clay Mixtures

Different clay mixtures (MIX 1, MIX 2 and MIX 3) were prepared, each with different proportion of Na-exchanged smectite, illite and kaolinite. MIX 1 contained approximately 50 % smectite, 25 % illite and 25 % kaolinite; MIX 2 contained approximately 50 % illite, 25 % smectite and 25 % kaolinite and MIX 3 contained approximately 50 % kaolinite, 25 % smectite and 25 % illite. Figure 7 shows the adsorption edges obtained with these mixtures in $NaClO_4$ 0.01 M. The graphs are compared with the data of pure smectite (where the highest adsorption is observed) and those of kaolinite (where the lowest adsorption is observed).

Within the experimental error, the adsorption in the three mixtures is similar (MIX 1>MIX 2 ~ MIX 3), with a mayor contribution provided by the presence of smectite, which favours Zn retention.

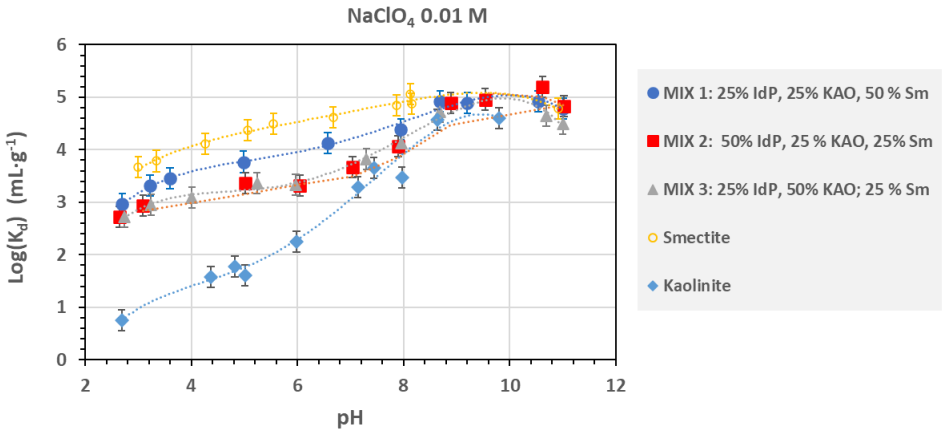


*Figure 7: Adsorption edges of Zn in different mixtures of smectite, illite and kaolinite in 0.01 M $NaClO_4$. Lines are drawn to guide the eye (IdP: illite du Puy, KAO: kaolinite, Sm: smectite).*

Preliminary calculations seem indicating that Zn adsorption in the mixtures is additive, however, modelling of Zn adsorption in mixtures data is not yet complete. More details on Zn adsorption in the single clay minerals and clay mixes will be available in Missana et al (2023b) (oncoming FUTURE article).

### Batch sorption test in compacted/consolidated clays

Batch sorption tests in compacted clays were carried out with the natural FEBEX clay (~1.5 g/cm$^3$) and with four different radionuclides: Cd, Zn, Co and Ni. The cells with the compacted clay (0.06 g) were immersed in 7 mL of $NaClO_4$ 0.01 M at pH 7-8. Batch sorption tests with the powdered clay under similar conditions (solid to liquid ratio, pH and electrolyte) were carried out before. In preliminary studies, we observed very low $K_d$ values after measurements for contact times lower than 1 month, compared to the values obtained in the powdered clay. Therefore, we decided to analyse only experiments that lasted more than 100 days, and to determine the $K_d$ at least at three different times (up to 419 days). If within this period, a clear kinetic was not observed, the considered $K_d$ value was the mean of all the tests performed (without the lower and higher value). If kinetic was observed, the considered value was the one obtained from tests at the longer time. In this case, this cannot be considered as an equilibrium value, therefore is not the "final" $K_d$. Table 1 shows the summary of the results obtained for the natural FEBEX clay in the $NaClO_4$ electrolyte (0.01 M).

*Table 1: Summary of the results of $K_d$ obtained in the compacted FEBEX (0.01 M in $NaClO_4$).*

| Element | [RN] | Kinetic factors observed | Contact times (days) | pH | $K_d$ (measured) (mL·g$^{-1}$) |
|---|---|---|---|---|---|
| **$^{65}$Zn** | 8.0·10$^{-6}$ M | NO | 142-263 | 7.13±0.18 | 91±8 |
| **$^{60}$Co** | 5.0·10$^{-8}$ M | YES | 219-419 | 8.30±0.22 | *1445 ± 200* |
| **$^{109}$Cd** | 9.0·10$^{-6}$ M | NO | 225-266 | 7.30±0.60 | 136±38 |
| **$^{63}$Ni** | 2.0·10$^{-7}$ M | YES | 224-418 | 7.30±0.30 | *312±50* |

In the case of transition metals, the uptake behaviour the compacted material was much slower than observed in the powdered clay, and in many case the sorption equilibrium has not been reached even after 400 days of the contact time. Due to these incontestable kinetic effects, it is difficult to draw clear conclusions about the differences between the adsorption in powdered/compacted state, in the case of transition metals. However, the experience gained with these types of experiments will allow improving the design of the cells and the methodology to minimise experimental problems that can bias the interpretation of data.

## Conclusions with respect to the task objectives

Batch sorption tests provided valuable information on Cd, Co and Zn adsorption behaviour of three different clays (smectite, illite and kaolinite and their mixtures). Complexation constants will be provided as far as the modelling is being completed.

The results obtained for transition metals indicate that the uptake process in the compacted clay has a much slower kinetic that the uptake in the powdered material, so, it is not clear if the equilibrium is reached. In the cases where equilibrium is (apparently) reached, as for $^{65}$Zn or $^{109}$Cd, the $K_d$ values measured in the compacted clay are much lower than those obtained in the powdered clay. An exhaustive description of the chemical system, relevant selection of experimental variables and the knowledge of kinetic are mandatory to properly transfer the information from one system to another.

Our studies aimed to verify whether adsorption of Zn in the clay mixtures can be described using an additive component model. As far as the present results indicate, Zn adsorption in the clay mixtures is additive.

.

## Oncoming documents related to research in future

- García-Gutiérrez M., Mingarro M., Missana T. (2023, in preparation). Determination of $K_d$ values in batch/compacted systems experimental approach and data analysis.
- T. Missana, U. Alonso, García-Gutiérrez M. (2023b, in preparation): Modelling of Zn adsorption in clay minerals and clay mixtures.

## References

El-Hefnawy, M.E.; Selim, E.M.; Assaad, F.F.; Ismail, A.I. The effect of chloride and sulfate ions on the adsorption of Cd2+ on clay and sandy loam Egyptian soils. Sci. World J. 2014, , 806252.

Missana T., Alonso U., García-Gutiérrez M. (2021) Evaluation of the component additive modelling approach for europium adsorption on 2:1 clays: experimental, thermodynamic databases and models. Chemosphere, 272:129877.

Missana T., Alonso U., Mayordomo N., García-Gutiérrez M. (2023a) Analysis of Cadmium Retention Mechanisms by a Smectite Clay in the Presence of Carbonates, Toxics, 11(2), 130.

Powell, K.J.; Brown, P.L.; Byrne, R.H.; Gajda, T.; Hefter, G.; Sjöberg, S.; Wanner, H. (2011) Chemical speciation of environmentally significant metals with inorganic ligands Part 4: The Cd2++ OH−, Cl−, CO32−, SO42−and PO43−systems. Int. Union Pure Appl. Chem, 83, 1163–1214.

Saeki, K.; Kunito, T. Influence of chloride ions on cadmium adsorptions by oxides, hydroxides, oxyhydroxides, and phyllosilicates. Appl. Clay Sci. 2012, 62, 58–62.

Stipp, S.L.; Parks, G.A.; Nordstrom, D.K.; Leckie, J.O. (1995) Solubility-product constant and thermodynamic properties for synthetic otavite, CdCO3(s), and aqueous association constants for the Cd(II)-CO2-H2O system. Geochim. Cosmochim. Acta, 57, 2699–2113.

Taylor, P.; Lumsdon, D.G.; Evans, L.J.; Bolton, K.A. The influence of pH and chloride on the retention of cadmium, lead, mercury, and zinc by soils. Soil Sediment Contam. 1995, 4,137–150.

# 2. Competition effect of Ni on Zn diffusion in compacted illite

L. Van Laer, J. Govaerts, M. Aertsens, D. Verhaegen, N. Maes
*SCK CEN, Mol, Belgium*

## Abstract

As radionuclide (RN) sorption behaviour is affected by competition with other elements in dispersed clay systems, it is of interest to verify how competition affects RN transport behaviour in compacted clay systems. The sorption and diffusion of zinc (Zn) in competition with nickel (Ni) as blocking metal was assessed with Na-conditioned illite in order to determine if knowledge gained from disperse systems can be transferred to compacted systems. For the experimental conditions studied here, competition was only observed at Ni concentrations that were higher than the background Zn concentration of $5x10^{-7}$ M (combination of concentration released from the illite or present in the background solution and the RN concentration of the spike). The sorption of Zn at pH 7 and ionic strength of 0.1 M was decreased with a factor 3 when Ni was added in a concentration of $1 \times 10^{-4}$ M (log $K_d$ from 3.9 to 3.45). The diffusion of Zn was studied with a Membrane Confined Diffusion Cell (MCDC) for which a 2D model with rotational geometry was successfully implemented. Diffusion was studied in the same Ni concentration range as the sorption studies ($3 \times 10^{-9}$ M – $1 \times 10^{-4}$ M), but even at the highest concentration there was no competition effect observed on the diffusion behaviour. The $D_e$ of Zn in compacted illite at pH 7 (0.1 M) ranged between 2.07 and 2.72 x $10^{-10}$ m²/s (omitting one experiment with less good fits).

## Introduction

Studying diffusion of moderately and strongly sorbing radionuclides in clay is not straightforward since these type of radionuclides tend also to adsorb to the materials used in the experimental set-up (filters, tubing,…). To overcome this problem, PSI-LES developed the Membrane Confined Diffusion Cell (MCDC) (Glaus et al., 2015), where sorption on the experimental set-up is minimized by using a non-sorbing membrane as interface between the clay and the solution and by avoiding the use of tubing. With this cell, the in-diffusion of sorbing radionuclides can be studied by fitting the concentration evolution in the solution and the RN profile in the clay at the end of the experiment.

Until now, the diffusion of single RN's were mainly studied, but in real systems there will be a mix of radionuclides and chemical elements originating from different sources (metal corrosion of canister, elements released in the clay pore water due to changing geochemical conditions,…). As these elements also sorb to the clay sorption sites, they can potentially compete (block sorption sites) with the radionuclides released from the waste. With regard to safety assessment this competition effect needs to be quantified. Earlier studies performed on various binary metal systems (one trace metal in the presence of an increasing concentration of blocking metal) by Marques Fernandes & Baeyens (2019, 2020) and by Orucoglu et al. (2022) showed that competition for the sorption binding sites can indeed play a role for some combinations of elements. Competition is, in general, observed for the elements with the same valence, but a similar valence is not a guarantee for competition. For instance, $Pb^{II}$ appeared to be only partially competitive with $Ni^{II}$ or $Co^{II}$, while $Ni^{II}$ was even not competitive with $Pb^{II}$ (Marques Fernandes & Baeyens, 2019, 2020). This means that the competition effects depend on the sorption mechanism and sorption reversibility, and the direction of the exchange reactions. A next step is to assess the extent of the competition effects observed in batch sorption experiments with dispersed clay under relevant transport conditions in compacted clay systems.

Therefore, the focus of this study was on assessing the competition effect of Ni as blocking metal on the diffusion (and sorption) of $^{65}Zn$. Marques Fernandes and Baeyens (2020) studied the competition effect on the sorption in the other way around (Zn as blocking element for trace Ni sorption) and observed that the sorption of Ni was slightly affected at increasing Zn concentration, especially in the range of $10^{-5}$- $10^{-4}$ M. According to the model calculations using the 2SPNE SC/CE model a decrease of 1.5 log unit between $10^{-9}$ M and $10^{-4}$ M is predicted, but the experimental data show some scatter, so it is difficult to judge if this effect is as large as predicted. In this study, the main objective was to determine the competition effect of

Ni on the diffusion of $^{65}Zn$ over a similar range of Ni concentrations. In preparation to diffusion experiments in compacted systems, the sorption of Zn at various Ni concentrations was assessed in order to determine the competition effect in a dispersed system. According to former studies on single element systems with illite, Ni is expected to sorb slightly less strong than Zn at trace concentrations (log $K_d$ ±5.1 vs. ±3.8), but for concentrations above $10^{-6}$ M the sorption strength is expected to be similar (Bradbury and Baeyens, 2005; Montoya et al., 2017; Marques Fernandes and Baeyens, 2020).

## Materials & Methods

### Clay

The studied clay is Na-conditioned Illite du Puy from the batch used before in the EC CatClay project (Altmann et al., 2015) (sorption and diffusion) and the Na-conditioned montmorillonite STx-1 (The Clay Minerals Society) (only sorption).

### Sorption

Batch sorption experiments were performed with illite and montmorillonite. The background solution used was $NaClO_4$ 0.1 M with 0.1 mM KCl in order to avoid K leaching out of the illite and buffered with 2 mM MOPS (3-morpholinopropane-1-sulfonic acid) buffer to stabilise the pH at ±7.0. Stock solutions of $NiCl_2.6H_2O$ were prepared in ultrapure water. Aliquots of these stock solutions were added to the background solution in order to obtain final Ni concentrations of 3 x $10^{-9}$, 1 x $10^{-7}$, 3 x $10^{-6}$ and 1 x $10^{-4}$ M. Suspensions of 1 g/L were prepared by adding 1 mL of a stock suspension solution (20 g/l) to 20 mL background solution. In a final step, $^{65}Zn$ was added in trace amount to all suspensions. After shaking the suspensions for 1 week to reach sorption equilibrium, a subsample of the suspension (1 mL) was taken to determine the initial activity ($C_{in}$). Subsequently, the suspensions were centrifuged at 21000 g for 2 hours. Subsamples were taken for analysis of the equilibrium concentration or activity ($C_{eq}$). The distribution coefficient $K_d$ was determined by

$$K_d = \frac{C_{in} - C_{eq}}{C_{eq}} \cdot \frac{L}{S}$$

With $C_{in}$ the initial acitivity, $C_{eq}$ the equilibrium activity, L/S the liquid-solid ratio (L/kg). The $^{65}Zn$ was measured with gamma-analysis (Packard Cobra Quantum gamma counter, RDD SCK CEN).

In addition, blank suspensions (without added Ni and Zn) were shaken and centrifuged as well. The supernatant was then analysed by ICP-MS (Agilent 7700x, Soil and Water Chemistry, KULeuven) in order to determine the background Ni and Zn concentration which is in equilibrium with the illite and montmorillonite.

### Diffusion

#### Experimental

The in-diffusion of $^{65}Zn$ was studied in a 0.1 M $NaClO_4$ background solution (+ 0.1 mM KCl, to prevent K-leaching from the illite) at pH ±7.0 buffered by 2 mM MOPS.

The in-diffusion experiments were performed with Membrane Confined Diffusion Cells (design by PSI, described in Glaus et al., 2015) Figure 1 (left). Pre-moisturised illite powder (equivalent of 0.347 g dry clay) was packed as a clay plug of ±10 mm at a target bulk density of 1.7 g/cm³. Since the length of the clay plug could vary slightly, the final bulk density varied between 1.65 and 1.9 g/cm³. After compaction of the clay, there was first a filter placed at the bottom for the saturation phase. The cells were submerged in the background solution in a desiccator which was held under vacuum or a period at least of 3-4 weeks in order to obtain full saturation of the clay plug. Afterwards, the flange was replaced with a flange with membrane. For the membrane a PVDF hydrophylic membrane (Durapore, 0.22 µm pore size, 70% porosity, 125 µm thickness) was chosen. Two layers of membrane with a total thickness of 250 µm were placed at the clay surface. During the experiment the clay could get slightly deformed due the swelling pressure of the clay

(Figure 1, right), as the membrane is not rigid enough to avoid that. The $^{65}Zn$ activity in the solution was followed on a regular basis by measuring each time a subsample of 1 mL with gamma-analysis (Packard Cobra Quantum gamma counter). After analysis, the sample was transferred back to the solution in order to keep the volume constant. The experiments lasted between 84 and 133 days. When stopping the experiments, a picture was taken from the clay deformation after removing the top flange. When cutting the clay, first the deformation bulb was cut in 3 slices. Then, the clay plug was further sliced at a resolution of 100-200 µm. The clay slices were weighed in order to calculate the exact thickness of the slices. These slices were analysed with gamma measurement as well.

Two experiments were run with $^{65}Zn$ only and stopped after 84 (I7B) and 133 (I7C) days. Afterwards, diffusion experiments (in duplicate) were started with four different Ni concentrations in the background solution (which was added simultaneously with the $^{65}Zn$). In total 10 diffusion experiments were performed. These experiments lasted 92 (1A), 105 (1B, 4A, 4B) and 106 (2A, 2B, 3A, 3B) days.

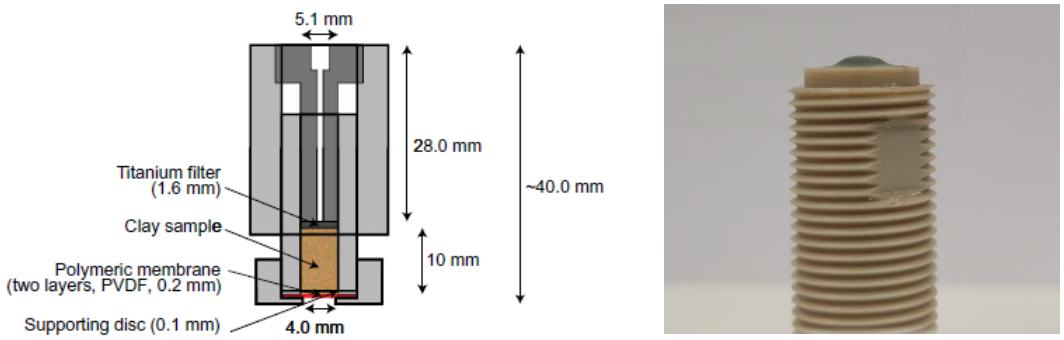


*Figure 1: Schematic presentation of the Membrane Confined Diffusion Cell (from Glaus et al., 2015) (left) and picture of the sample cylinder with on top the clay deformation (right).*

### Modelling

All experiments were evaluated using an in-diffusion model implemented in the finite-element analysis Comsol Multiphysics code. A rotational 2D geometry was applied in order to take into account the difference between the diameter of the clay plug (5.1 mm) and the cell aperture (4 mm). This difference implies that the solution is only in contact with the membrane over the surface of the aperture (12.4 mm²). Further, the deformation of the clay through the aperture due to swelling is also taken up in the geometry (Figure 2). The shape of the deformation can be described with a quadratic curve. The coordinates of the clay deformation were determined by plotting the clay surface points on a picture with WebPlotDigitizer (https://apps.automeris.io/wpd/). The geometry parameters (membrane and clay plug), bulk density and porosity of the clay were used as input parameters. Porosity was calculated from the bulk density, assuming a particle density of 2.65 g/cm³. For the membrane a pore diffusion coefficient of ~9 x $10^{-10}$ m²/s was derived (based on the equation of Millington and Quirk (1961) using the reported effective porosity of 0.70. The fit parameters were the pore diffusion coefficient $D_p$ of the clay and the distribution coefficient $K_d$. The effective diffusion coefficient $D_e$, the apparent diffusion coefficient $D_a$ and the retardation factor $R$ could then be calculated from these fit parameters according to the following equations:

$$D_a = \frac{D_p}{R} \qquad \textit{(eq 1)}$$

$$D_e = \eta R D_a = \eta D_p \qquad \textit{(eq 2)}$$

$$R = 1 + \frac{\rho_b K_d}{\eta} \qquad \textit{(eq 3)}$$

with $\eta$, the effective porosity of the clay plug and $\rho_b$ the dry bulk density.

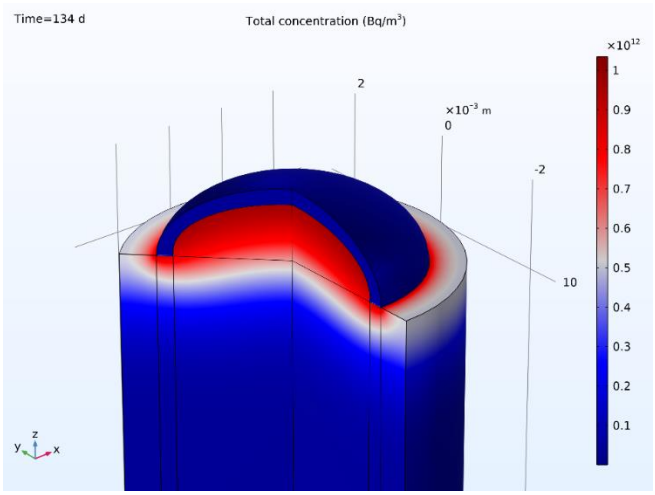


*Figure 2: 2D in-diffusion model with rotational symmetry. Depicted is the upper part of the clay, the membrane and the deformation through the aperture of the diffusion cell. The surface plot of the total concentration shows that most of the activity is still retained in this deformation after 134 days (experiment I7C).*

## Results & discussion

### Sorption

The sorption of Zn on illite and montmorillonite at pH 7 and 0.1 M ionic strength was investigated with Ni concentrations added between $3x10^{-9}$ and $1x10^{-4}$ M. The concentration of Ni originating from illite/montmorillonite or the background solution was around $1.5 \times 10^{-8}$ M. This concentration cannot be neglected and is hence summed to the artificially added concentration. The background concentration of Zn appeared, however, to be significantly higher with a concentration around $5x10^{-7}$ M and in addition, the RN concentration of the $^{65}Zn$ spike was in the same order of magnitude (due to the low specific activity of the spike solution).

Figure 3 shows the distribution coefficient of Zn for the initial Ni concentrations (background + added concentration). The duplicate samples without artificially added Ni are plotted as well (log $[Ni^{2+}]$ -7.8). The sorption of Zn on illite at these experimental conditions proved to be strong with a log $K_d$ value of 3.9, which is in line with the results reported by Montoya et al. (2017). Sorption on montmorillonite is one order of magnitude lower with a log $K_d$ of ± 3.0, which agree very well with the results obtained by Baeyens and Bradbury (1997) on SWy-1 montmorillonite.

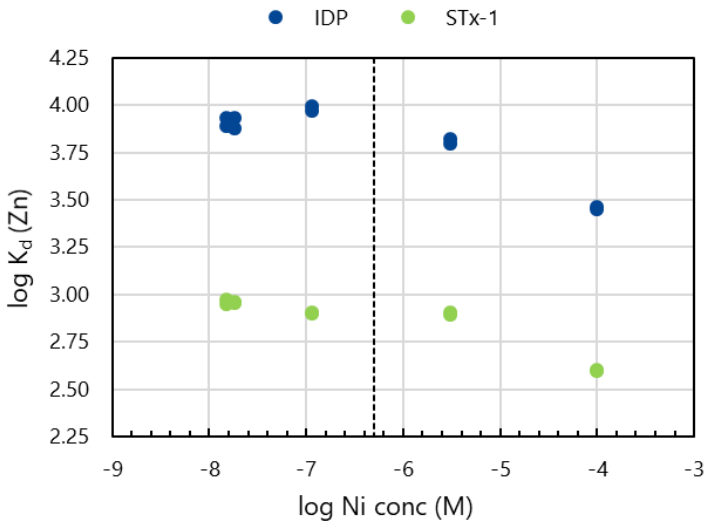


*Figure 3: Distribution coefficient of Zn as a function of initial Ni concentration for Na-conditioned Illite du Puy (IDP) (blue dots) and Na-conditioned montmorillonite (STx-1) (green dots, analytical uncertainty on the log $K_d$ value ranges between 0.03 and 0.13). The background concentration of Zn measured in the solution equilibrated with illite is presented with the dashed line.*

When investigating the effect of competition, it is important to bear in mind the background concentration of Zn (presented with the dashed line), as this concentration is significantly high. As expected, Ni appeared not to be competitive for the sorption of Zn at Ni concentrations below this concentration level. For Ni concentrations above this level, there is a very small decrease in $K_d$ observed for the Ni concentration of 3 x $10^{-6}$ M for the sorption experiments on illite, but it is difficult to judge if this difference is significant. For the highest Ni concentration of 1 x $10^{-4}$ M sorption ($K_d$) is reduced by a factor of 3. Marques Fernandes and Baeyens (2020) observed a similar decrease in $K_d$ in the concentration range between $10^{-6}$ and $10^{-4}$ M for $Zn^{II}$ as blocking element for Ni sorption (which has a slightly lower $K_d$ than for Zn at trace concentrations). For montmorillonite, there was only an effect observed at this highest concentration, i.e. a reduction of $K_d$ by a factor of 2.3.

## Diffusion

The experimental data (inlet activity and cumulative activity in the clay) are presented together with the fitted model in Figure 4 for experiments I7B and I7C without added Ni and in Figure 5 for the experiments with different concentrations of Ni. The top of the deformation was determined by plotting the surface points of the deformation on the picture. For I7C the deformation was 0.9 mm high. The resolution of the pictures of the other clay plugs was unfortunately too low to determine the lengths accurately, but sufficient to verify that the deformation lengths were similar with maximum of 0.2 mm difference. The clay profiles with activity of $^{65}Zn$ per weight of clay are presented in Figure 6.

I7B

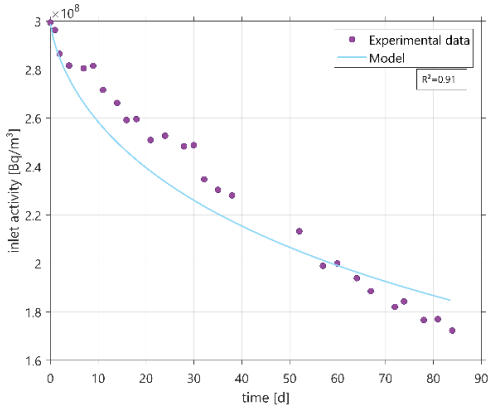


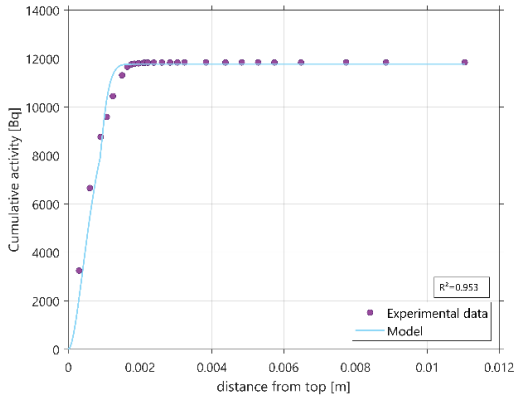


I7C

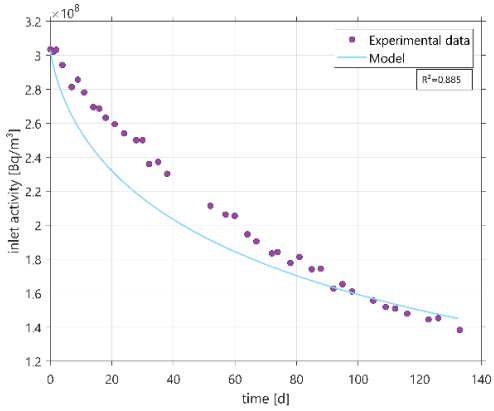


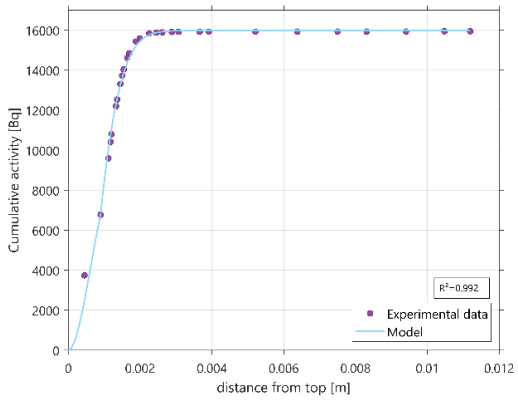


*Figure 4: Experimental (points) and fitted (line) data for the diffusion experiments **without added Ni**: a) activity in solution (Bq/mL) as function of time; b) cumulative activity of $^{65}Zn$ in the clay plug. The distance in the clay is calculated from the top of the deformation bulb of the clay. (Top – sample 17b; bottom – sample 17c).*

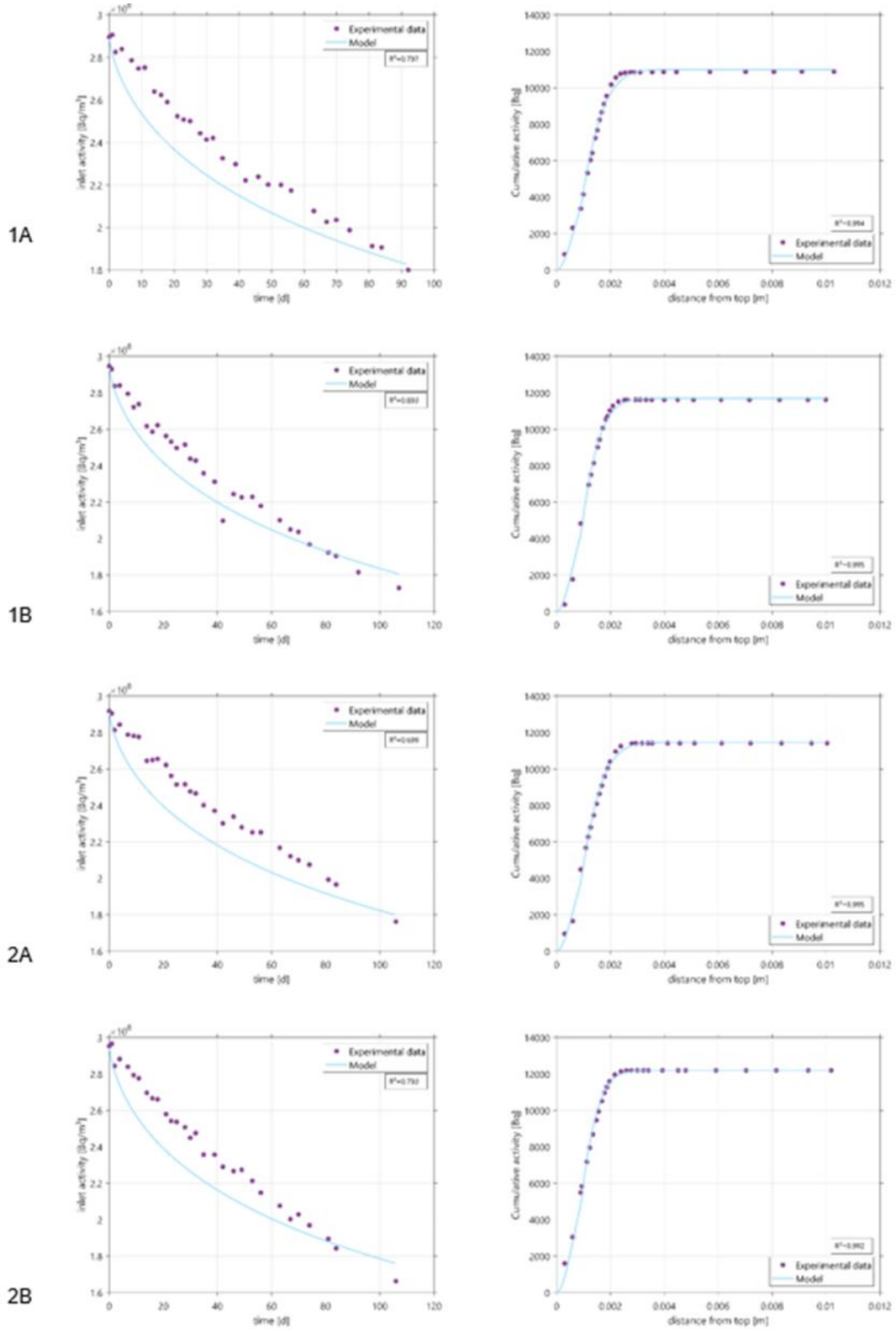


*Figure 5: Experimental (points) and fitted (line) data of Zn diffusion experiments* ***at varying Ni concentrations****: a) activity in solution (Bq/mL) in function of time; b) cumulative activity of* $^{65}Zn$ *in the clay plug. The distance in the clay is calculated from the top of the deformation bulb of the clay. (From top to bottom sample 1a & 1b –* $[Ni]=3\ 10^{-9}$ *mol/l , 2a & 2b –* $[Ni]=1\ 10^{-7}$ *mol/l)*

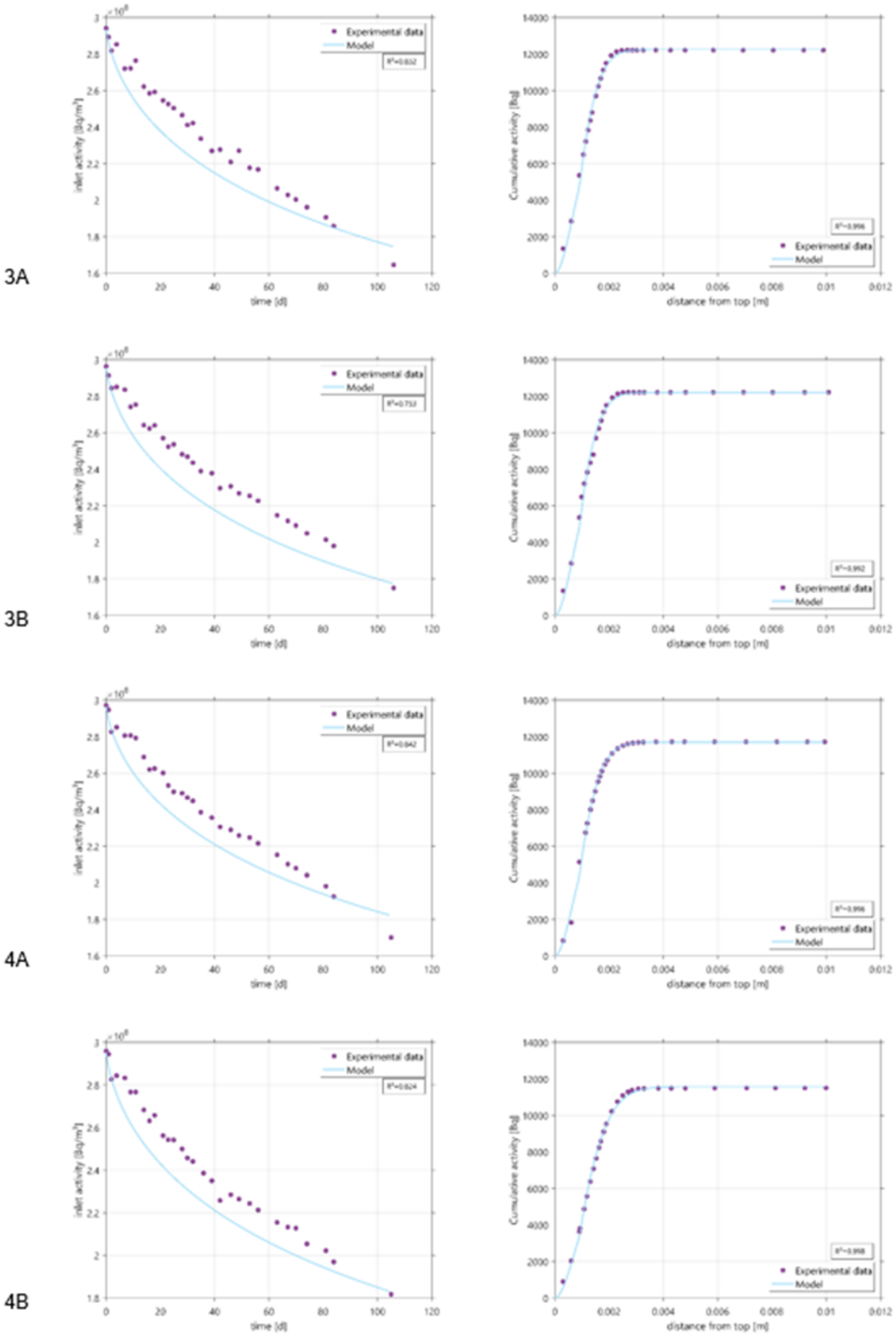


*Figure 5 (continued): Experimental (points) and fitted (line) data of Zn diffusion experiments* ***at varying Ni concentration****s: a) activity in solution (Bq/mL) in function of time; b) cumulative activity of* $^{65}Zn$ *in the clay plug. The distance in the clay is calculated from the top of the deformation bulb of the clay. (From top to bottom sample 3a & 3b –* $[Ni]=3\ 10^{-6}$ *mol/l, 4a & 4b -* $[Ni]=1\ 10^{-4}$ *mol/l)*

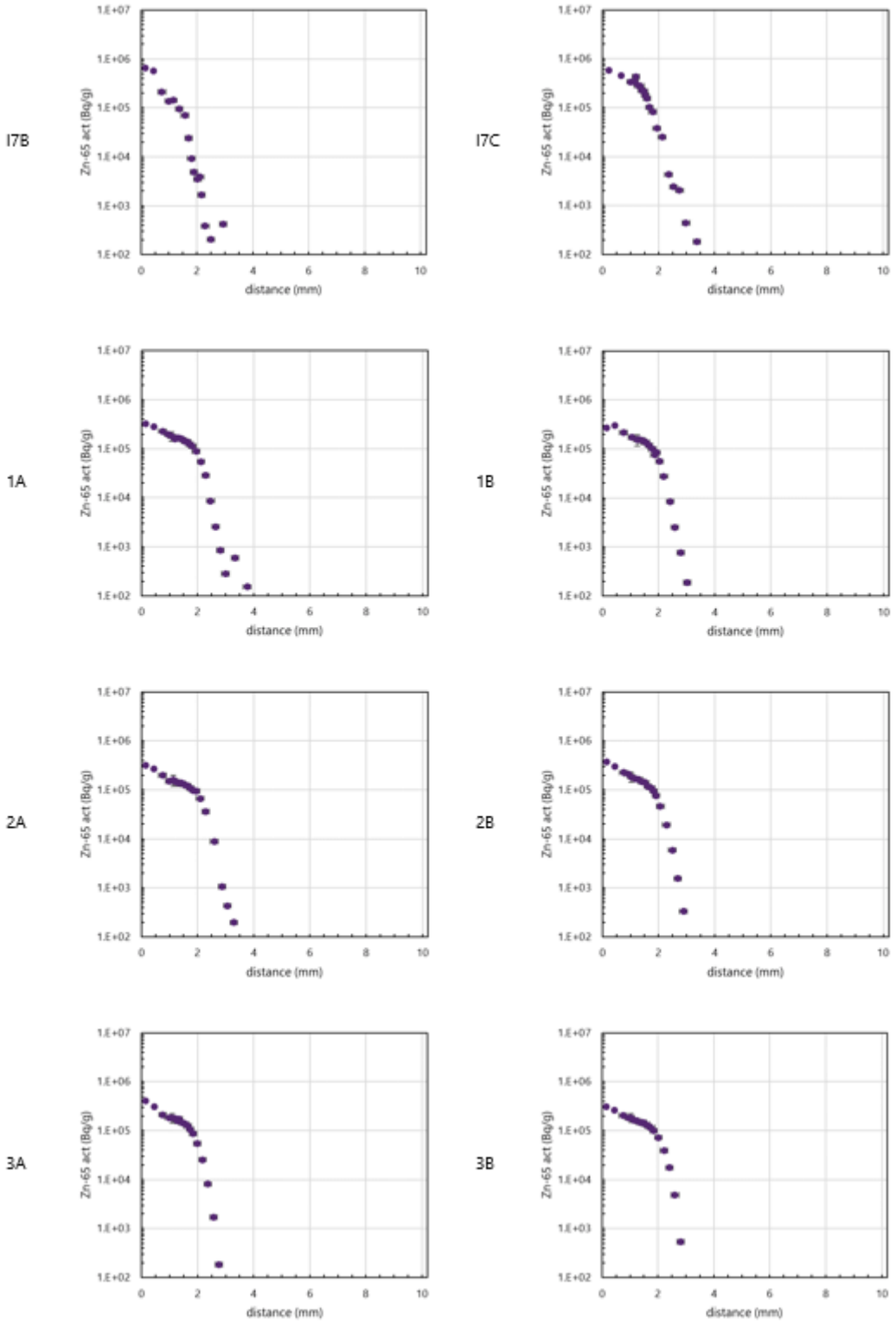


*Figure 6: Profiles of $^{65}Zn$ activity (Bq/g wet clay) in the clay. Note that the y-axis is in log scale.*

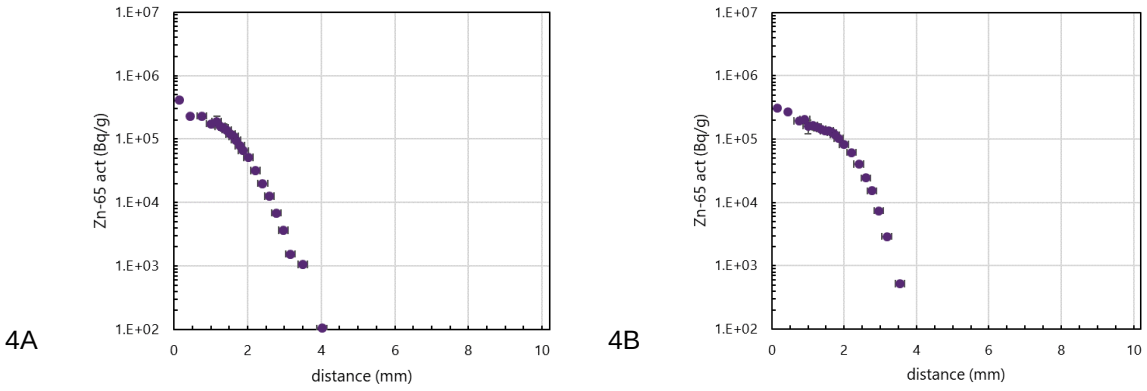


*Figure 6 (Continued): Profile of $^{65}Zn$ activity (Bq/g wet clay) in the clay. Note that the y-axis is in log scale.*

In Table 1 an overview of the fitted and calculated parameters for all experiments is given. The numerical mass balance errors, calculated from the activity lost in the solution and the activity found back in the clay, were very low with a maximum value of 0.4%. This is a confirmation for the successful implementation of the 2D geometry in the model. Further, an important attention point for 2D modelling is that the strongly contrasting diffusion parameters (diffusion in solution and filter (membrane) much higher than in clay) can lead more easily to numerical instability compared to 1D modelling, but a good quality of the mesh will avoid this problem. As a sanity check simplified 1D simulations were also performed, which yielded values in the same order of magnitude. This again is a confirmation of the correct implementation of the 2D model. Since a significant part of the activity is found back in the deformation (32 to 45% of total for experiments 1B to 4B which had the same duration), it is important to take the deformation into account. The slight decrease in bulk density caused by this deformation has not been taken into account yet.

*Table1: Diffusion parameters determined with 2D transport modelling.*

| | added | | | Fitted | | | | Calculated | | |
|---|---|---|---|---|---|---|---|---|---|---|
| Exp | Ni conc | $\rho_b$ | $\eta$ | $K_d$ | | $D_p$ | | $D_a$ | $D_e$ | log R |
| | M | g/cm³ | - | x10³ L/kg | | x10$^{-10}$ m²/s | | x10$^{-14}$ m²/s | x10$^{-10}$ m²/s | - |
| I7B | 0 | 1.68 | 0.37 | 9.84 | (8.42-11.48) | 2.43 | (2.08-2.84) | 0.54 | 0.89 | 4.65 |
| I7C | | 1.65 | 0.38 | 5.91 | (5.79-6.04) | 5.97 | (5.78-6.16) | 2.30 | 2.25 | 4.41 |
| 1A | 3x10$^{-9}$ | 1.81 | 0.32 | 2.03 | (1.98-2.08) | 8.71 | (8.4-9.04) | 7.51 | 2.76 | 4.06 |
| 1B | | 1.87 | 0.29 | 2.49 | (2.43-2.56) | 7.23 | (6.99-7.47) | 4.56 | 2.13 | 4.20 |
| 2A | 1x10$^{-7}$ | 1.86 | 0.30 | 2.19 | (2.14-2.24) | 7.92 | (7.68-8.18) | 5.80 | 2.36 | 4.14 |
| 2B | | 1.83 | 0.31 | 3.06 | (2.97-3.15) | 6.71 | (6.45-6.99) | 3.71 | 2.08 | 4.26 |
| 3A | 3x10$^{-6}$ | 1.89 | 0.29 | 2.91 | (2.85-2.97) | 7.55 | (7.34-7.76) | 3.93 | 2.16 | 4.28 |
| 3B | | 1.85 | 0.30 | 3.00 | (2.92-3.09) | 6.86 | (6.59-7.13) | 3.72 | 2.07 | 4.27 |
| 4A | 1x10$^{-4}$ | 1.88 | 0.29 | 2.54 | (2.49-2.6) | 7.26 | (7.04-7.48) | 4.41 | 2.11 | 4.22 |
| 4B | | 1.87 | 0.29 | 1.86 | (1.83-1.89) | 9.23 | (9.02-9.46) | 7.82 | 2.72 | 4.07 |

Experiments I7B and I7C were two replicates, with the only difference that the first was stopped after 84 days and the latter after 134 days. The fitted parameters differed significantly. This might be explained by the slightly less good fits obtained for I7B. It is not clear that this is due to the shorter duration of the experiment, which corresponds to less data points of inlet activity and a more narrow clay profile (less points to fit) or due to another yet undefined reason. When comparing the results with the other diffusion

experiments (with varying Ni concentrations), it can be seen that the values of I7C, especially the effective diffusion coefficient $D_e$, which is the most robust parameter, are closer to the values of these Ni series experiments than to I7B.

For the series of the diffusion experiments with different Ni concentrations the derived parameters are in a quite narrow range with $D_p$ varying between 6.7 and 9.2 x $10^{-10}$ m²/s and $K_d$ between 1860 and 3060 L/kg. The $D_e$ calculated from these parameters varies only between 2.08 and 2.76 x $10^{-10}$ m²/s. There was no significant effect of the Ni concentration on diffusion observed. Further, the obtained $K_d$ values are in the same order of magnitude as the experimentally defined $K_d$ values in the batch sorption experiments with average log $K_d$ (omitting I7B) of 3.44 compared to log $K_d$ of ±3.9 for the Zn sorption at low Ni concentration. The most plausible explanation for the absence of a competition effect for diffusion in the compacted clay is the higher S/L in the compacted clay, which provides more binding capacity than in the dispersed systems, where saturation of the sites is likely the explanation for the observed competition effect. Although the weight of the slice of the first mm of the clay plug (0.034 g), where most of the Zn is traced back, compared to the total volume of the solution (100 mL) is in the same order of magnitude as in the disperse systems, the amount of solution volume in direct contact with the clay is of course much lower and hence there is more binding capacity (clay) per unit of Ni that can readily be sorbed.

The experimental data of 3A were used to verify in how far the uncertainty on the deformation length could affect the diffusion parameters. The data were re-fitted with the assumption that the deformation length was only 0.7 mm instead of 0.9 mm. The obtained parameter values showed that this is only slightly affecting the diffusion parameters. $D_p$ decreased only 4% (7.2 x $10^{-10}$ m²/s) and the $K_d$ value was only 16% higher (3370).

The results obtained at pH 7 could be compared with the results published by Glaus et al. (2015) for similar diffusion experiments with Na-illite packed at 1.7 g/cm³ and performed at pH 5 and 9 in a background solution with 0.1 M ionic strength. They obtained in general slightly lower $D_a$ values (2.3 x $10^{-14}$ m²/s for pH 5 and 4.5 x $10^{-15}$-5.3 x $10^{-16}$ m²/s for pH 9) and slightly higher $K_d$ (4.4x$10^4$ L/kg at pH 5 and 1.6-2x$10^5$ L/kg at pH 9), but the combined (and more robust) $D_e$ values range in between the $D_e$ values obtained by them ($D_e$ (pH 5) ~7 x $10^{-10}$ m²/s - $D_e$ (pH 9) ~ 1.5 x $10^{-10}$ m²/s), which is according to the expectations since sorption of Zn at pH 7 is expected to be higher than at pH 5, but lower than pH 9.

## Conclusions

For Zn sorption on illite and montmorillonite, competition with Ni only starts to become important when the Ni concentration exceeds the Zn total background concentration. At $10^{-4}$ M Ni the Zn sorption decreased from log $K_d$ ±3.9 to ±3.45. The diffusion experiments were performed at the same background concentration of Ni. From the sorption study one could already expect that the lower concentrations would not affect the Zn diffusion behaviour. For the highest concentration, at which $K_d$ decreased by a factor of 3 (0.5 log unit) in the disperse system (batch experiment), there was, however, no clear effect of competition observed. Hence, to conclude, the competition effect of Ni on Zn sorption was observed for disperse systems, but not when studying Zn diffusion in compacted clay systems, at least for Ni concentrations up to $10^{-4}$ M. Higher concentrations of Ni are not likely to be expected in the deep geological disposal concept.

## References

Altmann, S. M. Aertsens, T. Appelo, C. Bruggeman, S. Gaboreau, et al. (2015) Processes of cation migration in clayrocks: Final Scientific Report of the CatClay European Project. <cea-01223753> https://hal.science/

Baeyens, B., Bradbury, M.H. (1997) A mechanistic description of Ni and Zn sorption on Na-montmorillonite. Part I: Titration and sorption measurements. Journal of Contaminant Hydrology 27, 199-222.

Bradbury, M.H., Baeyens, B. (2005) Experimental and Modelling Investigations on Na-Illite: Acid-Base Behaviour and the Sorption of Strontium, Nickel, Europium and Uranyl. PSI- bericht 05-02, Paul Scherrer Institute, Villigen and NAGRA technical report 04-02, NAGRA, Wettingen, Switzerland.

Glaus, M., Aertsens, M., Appelo, C.A.J., Kupcik, T., Maes, N., Van Laer, L. (2015) Cation diffusion in the electrical double layer enhances the mass transfer rates for $Sr^{2+}$, $Co^{2+}$ and $Zn^{2+}$ in compacted illite. Geochimica et Cosmochimica Acta 165, 376-388.

Marques Fernandes, M., Baeyens, B. (2019) Cation exchange and surface complexation of lead on montmorillonite and illite including competitive adsorption effects. Applied Geochemistry 100, 190-202.

Marques Fernandes, M., Baeyens, B. (2020) Competitive adsorption on illite and montmorillonite: experimental and modelling investigations. Technical report 19-05, NAGRA, Wettingen, Switzerland.

Millington, R.J. and Quirk, J.P. (1961) Permeability of porous solids. Transactions of the Faraday Society 57, 1200.

Montoya, V., Baeyens, B., Glaus, M.A., Kupcik, T., Marques Fernandes, M., Van Laer, L., Bruggeman, C., Maes, N., Schäfer, T. (2017) Sorption of Sr, Co and Zn on illite: Batch experiments and modelling including Co in-diffusion measurements on compacted samples. Geochimica et Cosmochimica Acta 223, 1-20. (https://doi.org/10.1016/j.gca.2017.11.027)

Orucoglu, E., Grangeon, S., Gloter, A., Robinet, J.C., Madé, B., Tournassat, C. (2021) Competitive Adsorption Processes at Clay Mineral Surfaces: A Coupled Experimental and Modeling Approach. Earth and Space Chemistry 6, 144-159. (DOI: 10.1021/acsearthspacechem.1c00323)

# 3. Sorption studies of Ni(II) on Boda Claystone Formation: transferability, reversibility and competition with Co(II)

O. Czömpöly, Z. Fogarassy, T. Kolonits, J. Osán, F. Szabó
*EK, Budapest, Hungary*

## Abstract

Experiments of EK were focused on a natural argillaceous rock system, Boda Claystone Formation (BCF), which is a candidate host rock for high-level radioactive waste in Hungary. Transferability of sorption phenomena from diluted systems to compacted systems was tested on BCF petrographic thin sections on Si holders involving inactive $Ni^{2+}$. Irreversibly formed Ni-containing phases in the natural BCF rock sample were investigated on the nanoscale using transmission electron microscopy coupled with energy-dispersive X-ray spectrometry. Suspension samples prepared at $10^{-3}$ M initial ($10^{-5}$ M equilibrium) concentration of $Ni^{2+}$ were used for identification of individual mineral phases and their composition. The sorption reversibility was also studied in equilibrium conditions using isotope exchange involving inactive $Ni^{2+}$ ions and radiotracer ($^{63}Ni$). Competitive sorption of $Ni^{2+}$ and $Co^{2+}$ ions on crushed BCF rock samples (and petrographic thin sections) studies aimed on the distribution of competing ions at sorption sites. A concentration range of $10^{-8}$ – $10^{-2}$ M was investigated with stable ions of interest.

## Introduction

Deep geological repositories for high-level radioactive waste will have several engineering and natural barriers. As the disposal is designed for thousands of years, release of radionuclides might occur during this time period. Migration across the natural barrier and in consequence our safety is determined by retardation of the released radionuclides. As natural barrier, clay rich rocks are considered as adequate host rocks due to their excellent retention capability of radionuclide (RN) components (as they have high adsorption capacity) (Dähn et al., 2002, 2021; Osán et al., 2014). Clay minerals have negative charges which are compensated by adsorption of cations (Tertre et al., 2021). Due to this phenomenon, clay minerals have high cation exchange capacity. The safety of repositories is evaluated with performance assessment (PA) analysis which evaluates the consequences of a RN escape from the waste packages. Retention characteristic of the host rock is a crucial parameter for the models used in PA analysis.

The main source of nickel in the radioactive waste packages is the neutron activation of structural components of nuclear reactor vessels. Nickel has five stable isotopes ($^{58}Ni$, $^{60}Ni$, $^{61}Ni$, $^{62}Ni$, $^{64}Ni$) found also in natural environments. The others are radioactive and related to anthropogenic activities, the most important is $^{63}Ni$ with a half-life of 100 years. The most frequent oxidation state of nickel is +II however it can be oxidized to +III and +IV states and reduced to +I under certain conditions with complexing agents. In geochemical environment the most important oxidation state of Ni is the +II.

The adsorption mechanism of nickel onto clay minerals was widely studied, adsorption isotherms and constants, potentiometric titration data are available for main clay minerals. Clay minerals and argillaceous rocks have high sorption capacity of nickel due to surface complexation as dominant phenomenon, however the reversibility of the adsorption of nickel on clay minerals was not investigated yet. At high nickel concentrations ($10^{-4}$- $10^{-3}$ M) formation of Ni-Al layered double hydroxide around clay particles were reported on pure minerals systems of illite and montmorillonite (Dähn et al., 2006; Marques Fernandes et al., 2015). Nevertheless, on natural clay rich rock media the formation of neo-formed nickel rich pyhillosilicates were not shown yet.

In general, adsorption is studied on crushed samples with batch experiments, however during a potential leakage of the waste packages through the engineering barriers the radionuclides contact compacted natural barrier. Therefore, the result on crushed systems needs to be transferable to intact rocks. In radioactive waste packages whole variety of RNs are present and competition for the adsorption sites can occur. RNs with similar structures and properties (for instance caesium and rubidium) can interact with each other and impact the adsorption capacity of each species.

In Hungary Boda Claystone Formation (BCF) is considered as a potential host rock for high-level radioactive waste repository (Fedor et al., 2019). BCF has total clay mineral content similar to other widely studied clay formations (COx, OPA), meanwhile it has unique features since it is the oldest in Europe (265 Ma) and it has an over-consolidated, highly indurated character with low physical porosity (≈0.02). As the early diagenesis of BCF occurred in oxidative environment, most of the studies regarding the migration of RNs in BCF were investigated under atmospheric conditions previously (Gergely et al., 2016; Marques Fernandes et al., 2015; Mell et al., 2006).

The aim was to study the adsorption, at the high concentration ($10^{-3}$ M) to study the potential formation newly formed nickel rich phases and to study the reversibility of adsorbed nickel with isotopic exchange experiments in the $10^{-8}$-$10^{-3}$ M range. The effect of competition for sorption sites were investigated in a two components system between nickel and cobalt in the range of $10^{-7}$ – $10^{-3}$ M. The transferability of adsorption was studied with petrographic thin sections with initial concentration of $10^{-3}$ and $10^{-4}$ M.

## Materials and methods

### BCF core samples

Representative core sections of the BAF-2 drilling carried out in the Boda Block (April-August 2014) (Sámson, 2015) were provided by the Public Limited Company for Radioactive Waste Management (PURAM, Hungary) and accompanied with characterization results. Core sections from 340–760 m depths representing the major albitic claystone formed under oxidative conditions were selected for the present study. The background concentrations of Ni and Co in the selected core sections are 42.2–46.6 mg/kg Ni and 16.3–17.8 mg/kg Co (Sámson, 2015).

### Synthetic porewater

The composition of the formation water was determined in the BAF-2 drilling report (Sámson, 2015), however it is not representative for the porewater itself. For this reason a modelled porewater composition is used for the experiments (Breitner et al., 2015; Marques Fernandes et al., 2015). The major porewater composition is very close to that extracted directly from a BCF core by a modified cryodesiccation (LN2 freezing) method (Fedor et al., 2019).

### Sample preparation

Petrographic thin sections with an average thickness of 50 µm were prepared onto high purity silicon wafers. Small pieces of selected core samples from BCF were mounted by bee wax onto quartz glass holders and cut to ca. 1 mm by Buehler IsoMet Low Speed Saw and subsequently ground down to ca. 50 µm. The 20×20 $mm^2$, 380 µm thick Si wafer was mounted by epoxy resin onto the grinded sample surface and after fixation the section was reheated in order to melt the bee wax and the Si holder by the sample mounted onto it was removed. Finally, the surface of the samples was polished by 0.25 µm diamond paste. Examples of the prepared thin sections are shown in Figure 1.

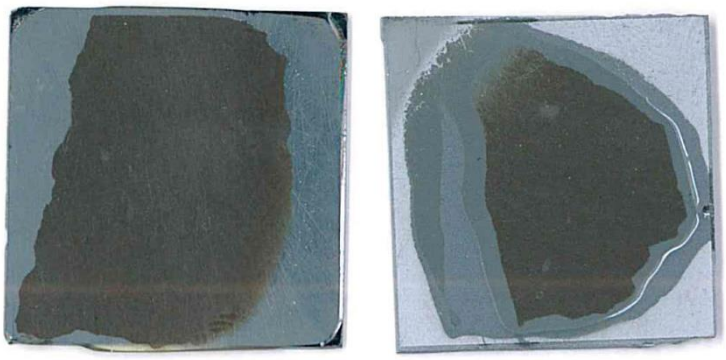

*Figure 1: Petrographic thin sections prepared from BCF core onto 20×20 $mm^2$ Si wafers.*

For batch adsorption experiments, 50 g of the rock sample was crushed and sieved to below 63 µm particle diameter. Both the crushed and compact rocks were conditioned with synthetic porewater at pH 8.0±0.1 prior to the experiments, using the method of Marques Fernandes et al. (2015). Due to low porosity, only formation water was available for BCF, so the chemical composition of the porewater (Table 2) was calculated to be in equilibrium with atmospheric $pCO_2$ and under the constraint of calcite, dolomite, and quartz saturation, as outlined in (Bradbury & Baeyens, 1998). To buffer the pH, TRIS (tris(hydroxymethyl)aminomethane) was used at a concentration of 2 mM.

### Adsorption experiments

Adsorption experiments were conducted on both crushed rocks and thin sections under atmospheric conditions. After addition of nickel(II) nitrate to the synthetic porewater the pH was readjusted to 8.0±0.1. To investigate the effect of competition between $Ni^{2+}$ and $Co^{2+}$ ions, nickel(II) nitrate and cobalt(II) chloride were added separately and also together at different concentrations. Adsorption onto the wall of shaker vessels was studied and found negligible (below 1%). The results are shown in the form of distribution coefficient ($K_d$), and adsorbed radionuclide concentration $C_{sorb}$ which can be calculated as:

$$K_d = \frac{C_{in} - C_{eq}}{C_{eq}} \cdot \frac{V}{m} \quad (1)$$

$$C_{\text{sorb}} = \left(C_{\text{in}} - C_{\text{eq}}\right) \cdot \frac{V}{m} \quad (2)$$

where $C_{in}$ and $C_{eq}$ are the initial and equilibrium concentrations (in case of ICP-OES mol/L, in case of LSC counts/50 µL), $V$ is the volume of the liquid phase (mL) and $m$ is the mass of clay (g).

### Kinetic studies

The initial step involved studying the kinetics of adsorption through batch experiments to determine the time required to achieve quasi-equilibrium for adsorption. The liquid-to-solid ratio (V/m) used was 100 mL/g, and 50 mL of synthetic porewater containing nickel along with 0.5+/-0.02 g of crushed and conditioned rock, was introduced into 100 mL shaker vessels. The vessels were then placed on an orbital shaker (Ohaus SHHD1619AL) for 28 days. The experiments were conducted on Sample A, and the initial concentration of nickel was $1.38\times10^{-3}$ M. The concentration of the solutions was monitored using ICP-OES (Perkin Elmer Avio 200). The pH of the equilibrium solutions was not monitored. However generally we experienced that Boda Claystone has a very strong buffer effect and even with TRIS the pH of the equilibrium solutions increases to 8.3±0.1 (from initial 8.0±0.1).

### Isotopic exchange experiments

To investigate the reversibility of adsorption, a suspension containing 0.21 g of crushed and conditioned rock was added to a 50 ml solution with varying nickel concentrations ranging from $10^{-10}$-$10^{-3}$ M in duplicate. The suspensions were shaken for 31 days, and then 5 ml of the suspensions were taken from the shaking bottles and filtered using a 220 nm syringe filter. The concentration was determined using ICP-OES until its detection limit. Next, radiotracer (50 kBq of $^{63}NiCl_2$) was added to the remaining suspensions, which were in equilibrium with inactive nickel nitrate. Immediately after radiolabelling 5 ml as initial sample was taken and filtered. After 30 days, LSC counting was performed on the liquid phases of both the initial suspensions and those equilibrated with $^{75}Se$. The adsorbed fractions were calculated for both the inactive and active Ni and compared to determine the reversibly adsorbed part of nickel, similar to the approach used by Rahman et al. (2019) for assessing As sorption reversibility in soils.

### Adsorption experiments on petrographic thin sections

Each 20×20 $mm^2$ Si wafers with BCF thin sections on top was placed to a 100-ml PP beaker filled with 50 ml synthetic porewater by a special holder prepared from PTFE. The solutions were identical to those used for batch experiments with crushed rock samples, but only the high concentration range of $10^{-5}$ – $10^{-2}$ M ($Ni^{2+}$) was investigated. For the initial experiments the liquid phase was kept without circulation, but later it was decided to use a magnetic stirrer and an incubator to keep the solution circulating at a constant temperature of 20°C.


*Figure 2: Experimental setup for adsorption studies on thin sections.*

### Sample preparation and measurement to identify newly formed nickel-rich phases

Two replicates of 0.21 g of crushed and conditioned rock were added to 100 ml vessels containing 50 ml of the nickel solution and the suspensions were shaken for 28 days to reach equilibrium. Afterward, the suspensions were centrifuged for 5 minutes at 1100 rcf. The supernatant were not spilled until the preparation of the TEM grids. Right before the measurement the supernatant was decanted and 20 ml of Type-I water was introduced to the centrifuge tubes. The settled particles were resuspended and drops (approximately 3 times 10 µL) were transferred onto a copper mesh grid coated with lacey carbon support film. The copper grid was then dried under infrared light for 3 hours. Cross-sectional transmission electron microscopy (XTEM) technique was used to study the particles in BCF. This measurement was carried out using a FEI-Themis (scanning) transmission electron microscope (STEM) equipped with a Cs corrected objective lens in High Resolution Transmission Electron Microscope (HRTEM) mode, which provides a point resolution of approximately 0.07 nm. The microscope was operated at 200 kV. Elemental mapping was carried out using energy-dispersive X-ray spectrometry (EDS) operating the instrument in STEM mode.

### Microscopic X-ray fluorescence

Measurements of the petrographic thin sections were performed on an in-house developed laboratory µXRF setup (Gergely et al., 2016), allowing point analysis and recording of 2D elemental maps. Since the X-ray source cannot be moved, scanning is performed through the movement of the sample across a stationary X-ray microbeam. A low-power rhodium-anode X-ray source (iMOXS, IfG, Berlin, Germany) coupled with a polycapillary minilens (IfG, Berlin, Germany) was used to form a 20 µm microbeam. In order to detect the emitted characteristic X-rays, a Peltier-cooled Si drift detector (SDD) with an active area of 30 $mm^2$ (KETEK, Munich, Germany) was used. The measurement process is computer-controlled by an in-house developed LabView-based software specifically designed for the system (Gergely et al., 2016). It controls the sample stage, the spectrum acquisition process, and displays the optical image of the sample. In addition, synchrotron-radiation µ-XRF measurements were performed at Bessy-II (Berlin, Germany) mySpot beamline (Zizak, 2016). The beam was focused with polycapillary optics to 20 µm spot size. The measurements were performed on thin sections at 45°/45° geometry using a silicon drift detector (SDD) of

100 mm$^2$ active area. 2D elemental maps were recorded using a 20 µm step-size, and 30 s dwell time per pixel on selected representative areas of a few mm$^2$ on each thin section. Concentrations of the elements of interest (Ni, Co) and major elements were calculated based on the sum spectra of the measured areas evaluated using the PyMCA software.

## Results and discussion

### Transferability of sorption phenomena from diluted systems to compacted systems

It is in general important to know if sorption phenomena are transferable from diluted systems involving crushed rocks to compacted systems keeping the argillaceous rocks intact. For microspectrometry studies petrographic thin sections are usually applied allowing to study the distribution of mineral phases in an intact form. For this reason, the transferability was studied on petrographic thin sections of Boda Claystone through comparison to batch experiments, both of them involving Ni(II) cations.

Figure 3 summarises the results of the distribution coefficient $K_d$ (panel a) and the amount of Ni sorbed (panel b). Regarding batch experiments on disperse systems, the present results applying only inactive Ni and ICP-OES analysis of the liquid phase are well in line with former results involving $^{63}$Ni radiotracer and LSC (Marques Fernandes et al., 2015). The concentration range was extended to $10^{-2}$ M, $K_d$ decreases gradually for concentrations above $10^{-5}$ M, from ≈ $10^4$ L/kg to ≈ 30 L/kg.

Due to the high L/S ratio (≈ 1500 L/kg) for thin sections, the differences between initial and equilibrium concentrations were small, therefore the Ni content of the solid phase determined by laboratory or synchrotron micro-XRF was considered to calculate the corresponding equilibrium concentration.

Initially the liquid phase was kept without circulation (green triangles in Figure 3), resulting in an order of magnitude lower sorbed amount of Ni than expected from batch experiments. Since the suspensions are shaken during the batch experiment, it was decided to force circulation of the liquid phase using magnetic stirrer for the sorption experiments involving thin sections. Using circulation of the liquid phase (blue squares in Figure 3), the agreement of thin sections with batch experiments is better. $K_d$ values and the sorbed amounts of Ni and well in line for moderate concentrations $8\times10^{-5}$ M, but lower than expected for concentrations as high as $10^{-3}$ M.

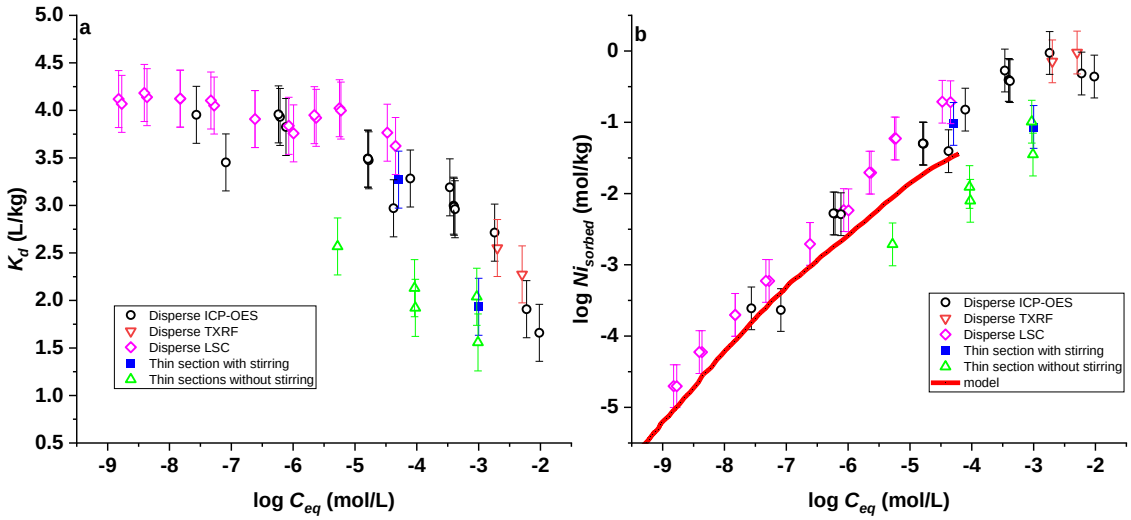


*Figure 3: Obtained distribution coefficient ($K_d$) and the adsorbed amount versus the equilibrium concentration ($C_{eq}$) obtained with different experimental setups. Disperse ICP-OES, TXRF and LSC means batch experiments with crushed samples, liquid phase analysed with the respective method. Disperse LSC points and model curve were redrawn from Marques Fernandes et al. (2015).*

## Identification of irreversibly formed phases on micro/nanoscale in natural rock sample

Batch sorption data of Ni(II) on Boda Claystone were underpredicted with the 2 site protolysis non electrostatic surface complexation and cation exchange (2SPNE SC/CE) sorption model for illite (Bradbury & Baeyens, 2009) at the high-concentration range above $10^{-6}$ M (Marques Fernandes et al., 2015) (see Figure 3 Panel b). It was confirmed by EXAFS studies that a surface induced precipitation of Ni solids occurs in addition to sorption via surface complexation and ion exchange phenomena (Marques Fernandes et al., 2015). Dähn et al., (2006) observed neoformed Ni phyllosilicate particles on montmorillonite treated with high Ni concentrations by TEM suggesting that the irreversibly formed Ni phases can be identified on the nanoscale in natural argillaceous rocks as well.

TEM and EDS investigations were performed on unique particles. In accordance with the expectations no adsorbed Ni on rutile, albite and hematite was identified. Ni was found to be connected to crystallites of clay minerals characteristic for BCF (illite and chlorite), which were identified based on the layer distances of R=10 Å (illite) and R=14 Å for chlorite Figure 4. Ni was enriched on the edges of particulates with a double concentration of Fe (Figure 5, Table 6). The formation of new Ni-containing phase was confirmed at the nanoscale but its unambiguous identification needs further investigation.

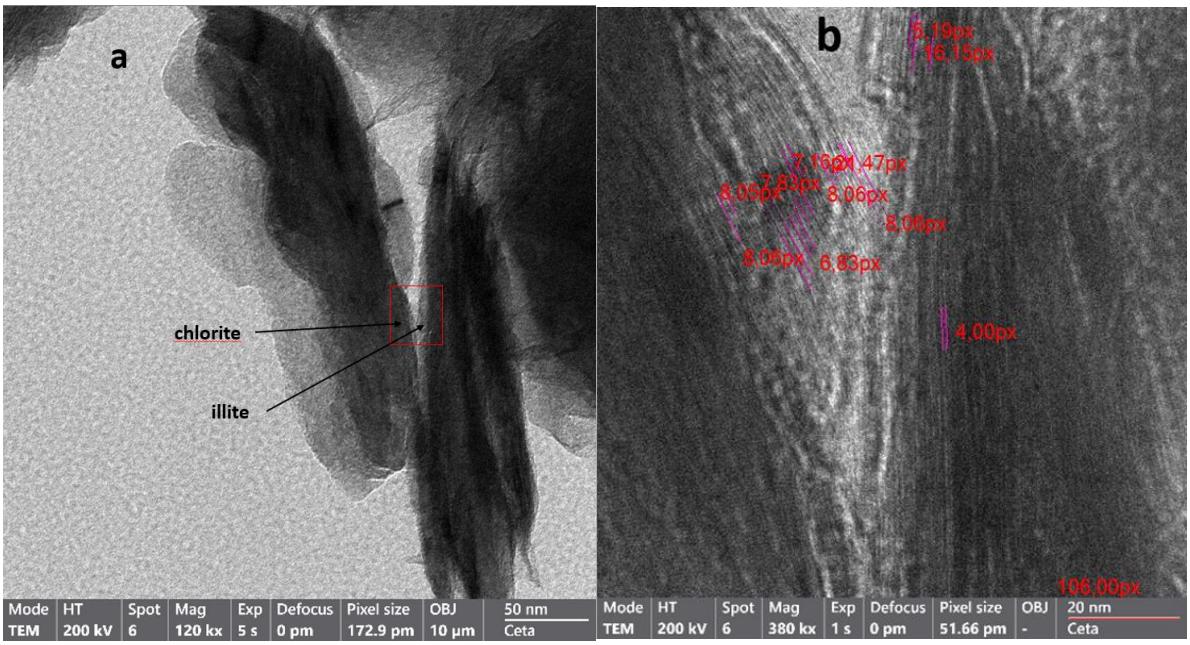


*Figure 4: TEM image of the overlapping particles on panel (a) and high-resolution image of the overlay with visible lattice spacings on panel (b). The particles could be classified based on the lateral distances: chlorite (lattice spacings of 8.06 px ≈ 14 Å ) and illite (lattice spacings of 5.2 px ≈ 10 Å).*

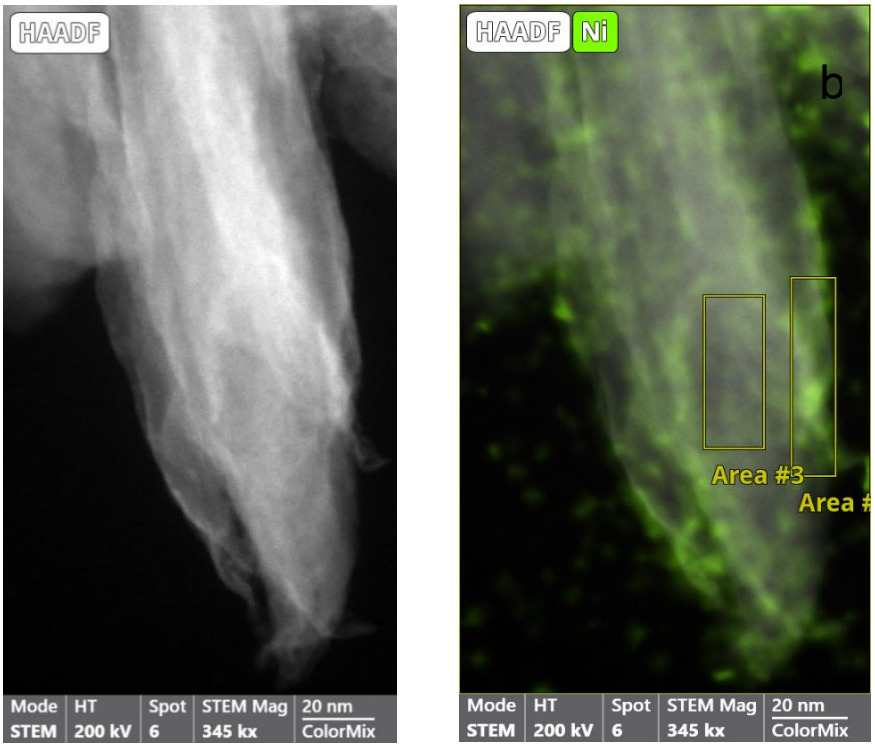


*Figure 5: Annular dark-field image (panel a) and nickel elemental map (panel b) of the investigated area around the illite particle. Enrichment of nickel was identified and the composition of main elements (Si, Mg, Al) of the nickel-rich phase altered from illite Table 5.*

*Table 5: Elemental composition of the studied area presented in Figure 5. Area1 (full) gives the composition of the whole map, Area 2 corresponds for the nickel rich phase around the illite particle and Area 3 gives the average composition of the illite particles treated with Ni ($C_{in}$ = $10^{-3}$ M).*

| Z | El. | at% | +/- | at% | +/- | at% | +/- |
|---|---|---|---|---|---|---|---|
| | | **Area1 (full)** | | **Area2** | | **Area3** | |
| 8 | O | 57.92 | 2.07 | 56.4 | 1.96 | 55.69 | 2.11 |
| 11 | Na | | | 1.35 | 0.36 | 1.17 | 0.27 |
| 12 | Mg | 6.57 | 1.25 | 4.36 | 0.88 | 9.31 | 1.72 |
| 13 | Al | 9.19 | 1.68 | 7.87 | 1.47 | 9.7 | 1.77 |
| 14 | Si | 13.07 | 2.21 | 11.18 | 1.95 | 12.16 | 2.09 |
| 17 | Cl | 0.36 | 0.07 | 0.62 | 0.19 | 0.21 | 0.09 |
| 19 | K | 1.04 | 0.18 | 1.1 | 0.26 | 0.69 | 0.15 |
| 20 | Ca | 0.24 | 0.03 | 0.41 | 0.12 | 0.23 | 0.06 |
| 26 | Fe | 5.52 | 0.72 | 5.16 | 0.7 | 6.93 | 0.9 |
| 28 | Ni | 6.09 | 0.87 | 11.55 | 1.56 | 3.92 | 0.58 |

## Study of sorption reversibility in equilibrium conditions

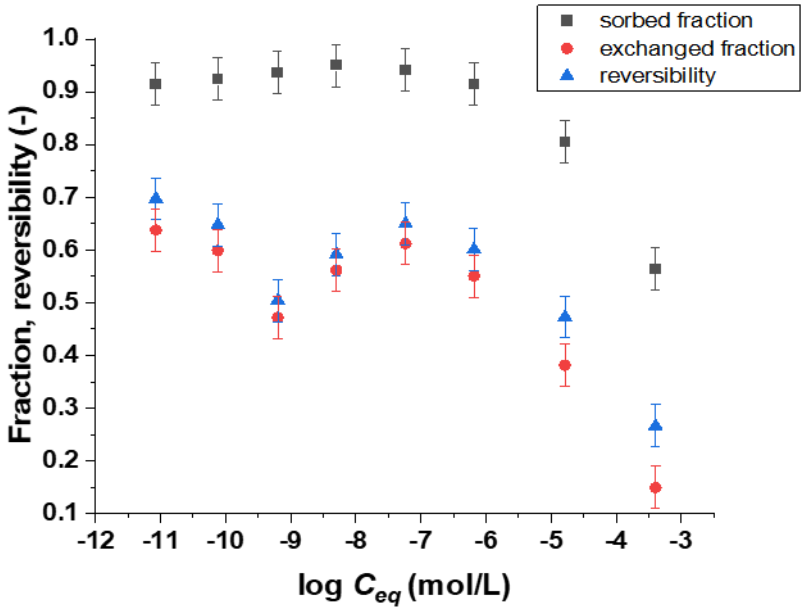


*Figure 6: Sorbed, exchanged fraction and reversibility as a result of isotope exchange experiments involving inactive Ni and $^{63}$Ni radiotracer. Sorbed fraction: $(C_{in}-C_{eq})/C_{in}$; Exchanged fraction: $(A_{in}-A_{eq})/A_{in}$ where A is the $^{63}$Ni activity; Reversibility: ratio of exchanged and sorbed fractions.*

Sorption reversibility was also studied by adding $^{63}$Ni radiotracer while keeping the equilibrium conditions. The isotope exchangeable fraction is determined by both the availability of strong sorption sites and formation of new phases. The maximum reversibility was found as 0.7 that can be explained by the contribution of strong sorption sites Figure 6. As the strong sites reach saturation at around $10^{-7}$ M equivalent concentration for illite (Marques Fernandes et al., 2015), the sorption reversibility is expected to increase with increasing concentrations. However, due to the formation of new phase causes a decrease of reversibility reaching as low as 0.3 for the highest concentration studied $C_{eq} = 5\times10^{-4}$ M Figure 6.

## Competition of metals in clay systems

### Adsorption kinetics

Figure 7 illustrates the results of kinetics study of adsorption experiment, where constant $K_d$ was reached after approximately 30 days for both Ni and Co.

Previously the kinetics of Ni adsorption was examined on former borecores (namely 'Ib-4 540 m' and 'D-11') from BCF with different initial concentrations of Ni ($8.57 \times 10^{-5}$ M, $8.57 \times 10^{-6}$ M, and $8.57 \times 10^{-8}$ M). The study was terminated after 17 days as it was deemed sufficient time to achieve quasi-equilibrium. No significant differences were observed in the results obtained for the various initial concentrations. The study was conducted under a liquid-to-solid ratio of 238 L/kg and at pH values between 8.0-8.2. The kinetics of Co uptake was not investigated, as it was assumed that it shares similar characteristics with Ni (Marques Fernandes et al., 2015). On conditioned Na-illite with an initial Ni(II) concentration of $2.8 \times 10^{-9}$ M in 0.1 M $NaClO_4$, equilibrium was reached in just 3 days. The liquid-to-solid ratio in that experiment was 3333 L/kg (Poinssot & Bradbury, 1999).

The longer equilibration time observed in the present study can be explained by the formation of new Ni/Co-rich phases which is dominant in the studied concentration range and it a slower process than surface complexation and ion exchange.

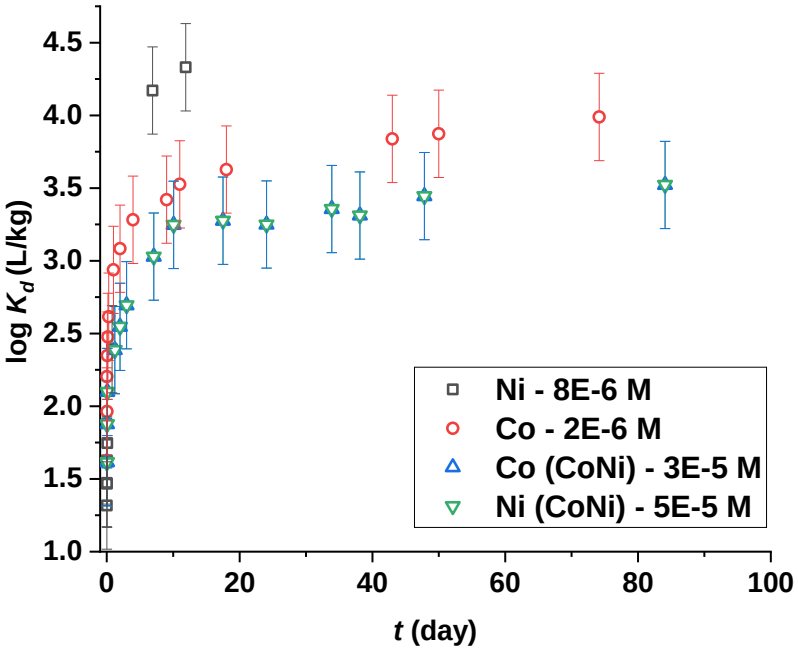


*Figure 7: Adsorption kinetics of nickel and cobalt on BCF at pH=8 in synthetic Boda porewater. The study was conducted with Ni and Co independently and in competitive conditions. In the legend part the final (quasi-equilibrium) concentration is presented. The liquid-to-solid ratio (L/kg) was 100, 250 and 1000 for the kinetics study of Ni, Co and Co-Ni competition, respectively.*

### Adsorption isoterms

The sorption isotherms of Ni(II) and Co(II) were found to be similar if only Ni(II) or Co(II) ions were added to the synthetic porewater in batch experiments Figure 8. In the high concentration region ($10^{-2}$ –$10^{-4}$ M) where adsorption mainly occurs via ion-exchange and formation of new phase is dominant, Ni has higher $K_d$ values, meanwhile in the $10^{-6}$ –$10^{-4}$ M region (where adsorption takes place at the weak sites) the $K_d$ values of cobalt are higher and get closer (half order of magnitude lower) to the ones collected without competitive conditions.

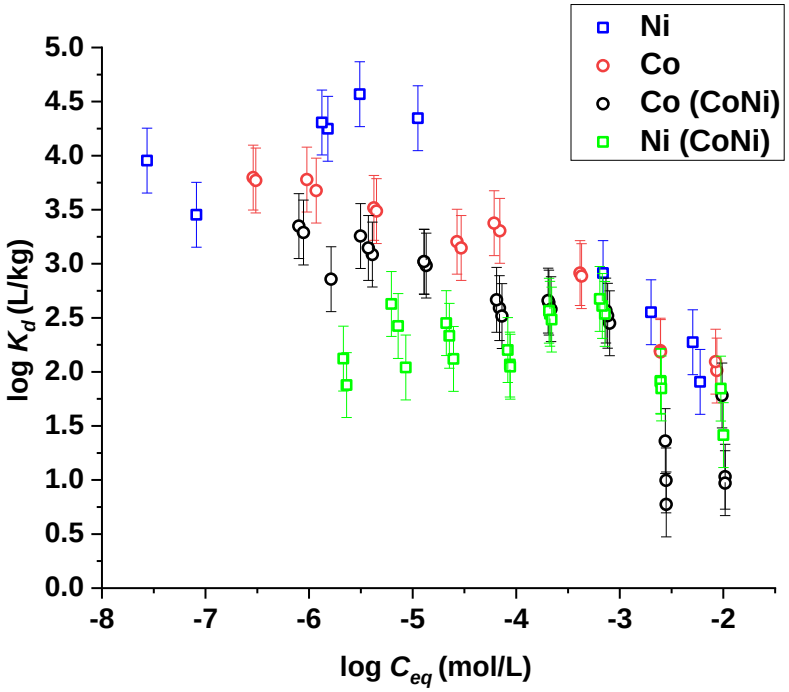


*Figure 8:* Distribution coefficient ($K_d$) versus equilibrium concentration ($C_{eq}$) obtained at pH=8. Co and Ni means the radionuclides were separately present, while Co (CoNi) and Ni (CoNi) shows the data obtained for Co and Ni in competitive conditions, respectively.

## Conclusions

Sorption experiments using petrographic thin sections were found to be appropriate for studying transferability of sorption parameters from disperse (crushed rock) to compact (intact rock) systems. However, the appropriate circulation of the liquid phase is important to have similar circumstances for the two kinds of experiments. Without circulation of the liquid phase, the sorbed Ni amount can be an order of magnitude lower for thin sections than expected from batch experiments on crushed rock.

Microscopy (TEM) and spectroscopy (EDS) confirmed the formation of new Ni-containing phase at the nanoscale even for natural argillaceous rock (BCF) (for high Ni concentrations) but its unambiguous identification needs further investigation. Isotope exchange method revealed a gradual decrease of sorption reversibility in the $10^{-7}$ – $10^{-3}$ M concentration range that is in line with surface induced precipitation of Ni solids.

Competition of Ni(II) and Co(II) resulted in suppressing the sorption of Ni(II) on the weak sites in favour of Co(II) for BCF albitic claystone.

## References

Bradbury, M. H., & Baeyens, B. (1998). A Physicochemical Characterisation and Geochemical Modelling Approach for Determining Porewater Chemistries in Argillaceous Rocks. *Geochimica et Cosmochimica Acta*, *62*(5), 783–795. https://doi.org/10.1016/S0016-7037(97)00387-6

Bradbury, M. H., & Baeyens, B. (2009). Sorption modelling on illite Part I: Titration measurements and the sorption of Ni, Co, Eu and Sn. *Geochimica et Cosmochimica Acta*, *73*(4), 990–1003. https://doi.org/10.1016/J.GCA.2008.11.017

Breitner, D., Osán, J., Fábián, M., Zagyvai, P., Szabó, C., Dähn, R., Marques Fernandes, M., Sajó, I. E., Máthé, Z., & Török, S. (2015). Characteristics of uranium uptake of Boda Claystone Formation as the candidate host rock of high level radioactive waste repository in Hungary. *Environmental Earth Sciences*, *73*(1), 209–219. https://doi.org/10.1007/S12665-014-3413-4

Dähn, R., Baeyens, B., & Fernandes, M. M. (2021). Zn uptake by illite and argillaceous rocks. *Geochimica et Cosmochimica Acta*, *312*, 180–193. https://doi.org/10.1016/J.GCA.2021.07.001

Dähn, R., Jullien, M., Scheidegger, A. M., Poinssot, C., Baeyens, B., & Bradbury, M. H. (2006). Identification of neoformed Ni-phyllosilicated upon Ni uptake in montmorillonite: A transmission electron microscopy and extended x-ray absorption fine structure study. *Clays and Clay Minerals*, *54*(2), 209–219. https://doi.org/10.1346/CCMN.2006.0540206/METRICS

Dähn, R., Scheidegger, A. M., Manceau, A., Curti, E., Baeyens, B., Bradbury, M. H., & Chateigner, D. (2002). Th Uptake on Montmorillonite: A Powder and Polarized Extended X-Ray Absorption Fine Structure (EXAFS) Study. *Journal of Colloid and Interface Science*, *249*(1), 8–21. https://doi.org/10.1006/JCIS.2002.8236

Fedor, F., Máthé, Z., Ács, P., & Koroncz, P. (2019). New results of Boda Claystone research: Genesis, mineralogy, geochemistry, petrophysics. *Geological Society, London, Special Publications*, *482*(1), 75–92.

Gergely, F., Osán, J., Szabó, B. K., & Török, S. (2016). Analytical performance of a versatile laboratory microscopic X-ray fluorescence system for metal uptake studies on argillaceous rocks. *Spectrochimica Acta Part B: Atomic Spectroscopy*, *116*, 75–84.

Marques Fernandes, M., Vér, N., & Baeyens, B. (2015). Predicting the uptake of Cs, Co, Ni, Eu, Th and U on argillaceous rocks using sorption models for illite. *Applied Geochemistry*, *59*, 189–199. https://doi.org/10.1016/J.APGEOCHEM.2015.05.006

Mell, P., Megyeri, J., Riess, L., Máthé, Z., Hámos, G., & Lázár, K. (2006). Diffusion of Sr, Cs, Co and I in argillaceous rock as studied by radiotracers. *Journal of Radioanalytical and Nuclear Chemistry*, *268*(2), 411–417. https://doi.org/10.1007/S10967-006-0178-6

Osán, J., Kéri, A., Breitner, D., Fábián, M., Dähn, R., Simon, R., & Török, S. (2014). Microscale analysis of metal uptake by argillaceous rocks using positive matrix factorization of microscopic X-ray fluorescence elemental maps. *Spectrochimica Acta Part B: Atomic Spectroscopy*, *91*, 12–23. https://doi.org/10.1016/J.SAB.2013.11.002

Poinssot, C., & Bradbury, M. H. (1999). *Experimental studies of Cs, Sr, Ni, and Eu sorption on Na-illite and the modelling of Cs sorption*.

Rahman, M. S., Clark, M. W., Yee, L. H., Comarmond, M. J., Payne, T. E., & Burton, E. D. (2019). Effects of pH, competing ions and aging on arsenic(V) sorption and isotopic exchange in contaminated soils. *Applied Geochemistry*, *105*, 114–124. https://doi.org/10.1016/J.APGEOCHEM.2019.04.016

Sámson, M. (ed). (2015). *Final report of borehole BAF-2. (In Hungarian) Manuscript, PURAM, Paks, RHK-N-011/14*.

Tertre, E., Dazas, B., Asaad, A., Ferrage, E., Grégoire, B., Hubert, F., Delville, A., & Delay, F. (2021). Connecting molecular simulations and laboratory experiments for the study of time-resolved cation-exchange process in the interlayer of swelling clay minerals. *Applied Clay Science*, *200*, 105913. https://doi.org/10.1016/J.CLAY.2020.105913

Zizak, I. (2016). The mySpot beamline at BESSY II. *Journal of Large-Scale Research Facilities JLSRF*, *2*, A102–A102. https://doi.org/10.17815/JLSRF-2-113

# 4. Reversibility of Zn uptake by montmorillonite and illite

R. Dähn, B. Baeyens, P. Cruz Hernandez, M.M. Fernandes
*PSI, Villigen PSI, Switzerland*

## Abstract

The adsorption of radionuclides on clay minerals in engineered and geological barrier systems is a main pillar in the safety case for deep geological disposal of radioactive waste. One of the open questions is related to the adsorption reversibility and the nature of mechanism that controlling the retention in the long-term.

Zn adsorption on homo-ionic Na-SWy and Na-IdP was studied at loadings of 2 mmol/g up to 60 mmol/kg in 0.1 M NaCl at pH 7 at a S/L ratio of 1.4 g/l. These Zn adsorption samples were allowed to equilibrate for a reaction time of up 2 years. In a second series of experiments, Zn adsorption samples were prepared with similar loadings as in the first series in 0.1 M NaCl at pH 7, but at a high S/L ratio of 14.2 g/l. After a reaction time of 1 day the samples were diluted by a factor of 10 in 0.1 M NaCl, containing no Zn, to reach a S:L ratio of 1.4 g/L at pH 7. These samples, denoted as Zn desorption samples, were prepared to investigate the desorption behaviour of Zn on both clay minerals.

The EXAFS data after two years of reaction time at low loadings for both clay minerals show remarkable similarities with a spectrum of Zn intrinsically present in IdP and SWy. This indicates that Zn has a similar structural environment, *i.e.,* Zn is located in the continuity of octahedral sheets. The EXAFS results for the adsorption and desorption data for the low loaded samples are identical indicating that the Zn surface complexes remain unchanged during the time period of 2 years. At higher Zn loadings changes in the EXAFS spectra indicate that desorption processes affect these samples.

## Introduction

Clay minerals contribute substantially to the surface chemical reactivity of soils or sedimentary argillaceous rocks. Because of their small particle size (< 2 μm), high surface area, and high surface charge (permanent & variable), clay minerals control the fate of heavy metals in the geosphere via different uptake mechanisms. The main processes for the retention of trace concentrations of heavy metals are adsorption to clay edge or “broken bond” sites, and incorporation into clay mineral structures.

Zn is a divalent transition metal similar to Ni and Co in its chemical behaviour and can thus also be considered as a natural analogue for radioactive $^{59}$Ni and $^{60}$Co arising from nuclear spent fuel and radioactive waste. The release of radionuclides from a radioactive waste repository can be considerably retarded due to interactions with clay minerals. For example, bentonite containing >75 wt.% dioctahedral smectites (montmorillonite) is foreseen as a backfill material in the Swiss and Swedish concept for a high level radioactive waste repository (Nagra, 2002; SKB, 2001).

Over the past decades surface complexation models (SCMs) such as the 2SPNE SC/CE model (Bradbury and Baeyens, 1997) have been developed to quantitatively describe the adsorption of metals with valences from II to VI on montmorillonite (*e.g.,* (Bradbury and Baeyens, 2005)). However, none of the existing SCMs take into account the irreversibility of uptake processes. This irreversibility can be caused by the neoformation of new phases or the incorporation of transition and heavy metals in the montmorillonite/illite structure. The incorporation can occur due to clay dissolution and re-crystallisation processes or via solid-state diffusion. A comprehensive overview of metal sorption reversibility was written by Tournassat et al. (2013).

Dähn et al. (2021) investigated recently with EXAFS the uptake of Zn by IdP and two argillaceous rocks, Opalinus Clay and Boda Claystone. The uptake of Zn by illite was studied in 0.1 M NaCl at near-neutral pH and Zn loadings varying from 2.1 to 42 mmol/kg. The Zn uptake by the two argillaceous rocks was carried out in 0.1 M NaCl at pH 7.2 and in their respective porewaters at pH 8.0 to evaluate the influence of porewater composition. The Zn loadings varied from 1.8 to 86 mmol/kg and 1.7 to 60 mmol/kg for Opalinus Clay and Boda Claystone, respectively. On IdP with prolonged reaction times of up to two years, the

formation of Zn precipitates was not observed. Dähn et al. (2021) concluded that this behaviour could indicate that the Zn surface complexes are stable over a time period of two years, and dissolution and recrystallization processes might not play a significant role in the Zn-IdP uptake process. The aim of this study is therefore to reduce the gap of the current knowledge between short-time sorption and long-time incorporation processes by applying EXAFS spectroscopy on 2:1 clay minerals which have been in contact with Zn at room temperature for 2 years, and samples where after a adsorption time of 1 day the clay mineral suspension was subject to a desorption experiment for 2 years.

The information gained from the proposed study is of great importance for safety assessments related to future radioactive waste repositories worldwide. It will enable us to improve SCMs used in waste management to assess the mobility and fate of radionuclides in the geosphere. Furthermore, information obtained on the long term behaviour of transition and heavy metals in clay minerals is crucial when adsorption processes need to be extrapolated to times scales relevant for the environment.

## Materials and methods

### Illite and montmorillonite

#### Illite

The source material used in the present study was Illite du Puy (IdP) (Gabis, 1958) collected from an 80 m thick Oligocene geological formation in the region of Le Puy-en-Velay (Haute-Loire), France. IdP samples were crushed, then powdered in a mortar and sieved until the clay passed the size of 240 mesh (≤63 µm). The cation exchange capacity (CEC) of the purified IdP was measured by isotope dilution technique (Baeyens and Bradbury, 2004). CEC measurements on different IdP clay batches at neutral pH in $5{\cdot}10^{-3}$ M $CsNO_3$ yielded an average Cs-CEC value of 225 ± 10 $meq{\cdot}kg^{-1}$ (Fernandes and Baeyens, 2019). The external surface area of the conditioned IdP is ~129 $m^2g^{-1}$ (Poinssot et al., 1999).

#### Montmorillonite

The montmorillonite SWy-2 (SWy) used in this study was purchased from the Source Clay Minerals Repository of the Clay Minerals Society. The < 0.5 µm montmorillonite fraction used in this study was obtained in purification and conditioning processes. The cation exchange capacity (CEC) of the conditioned SWy measured by the $^{22}Na$ isotopic dilution method is 870 ± 35 meq $kg^{-1}$ (Baeyens and Bradbury, 1995). The external surface area of the SWy is ~84 $m^2g^{-1}$ (Van Olphen and Fripiat, 1979).

### Adsorption and desorption experiments

In a first series of experiments, Zn adsorption on homo-ionic Na-SWy and Na-IdP was studied at low, intermediate and high loadings in 0.1 M NaCl at pH 7 at a S/L ratio of 1.4 g/l. In a second series of experiments, Zn adsorption samples were prepared with similar loadings as in the first series in 0.1 M NaCl at pH 7, but at a high S/L ratio of 14.2 g/l. After a reaction time of 1 day the samples were diluted by a factor of 10 in 0.1 M NaCl, containing no Zn, to reach a S:L ratio of 1.4 g/L at pH 7. These samples, denoted as Zn desorption samples, were prepared to investigate the desorption behaviour of Zn on both clay minerals. $^{65}Zn$ labelled samples were employed to perform the adsorption and desorption behaviour over time, whereas for the EXAFS measurements sample free of the radioisotope $^{65}Zn$ after a reaction time of 2 years were prepared. All experiments were performed in glove boxes under $N_2$ atmosphere ($O_2$ < 0.1 ppm).

#### Zn adsorption on IdP and SWy at low S/L ratio

Zn adsorption was carried out on IdP and SWy at pH 7.0 in 0.1 M NaCl background electrolyte. A series of Zn solutions covering the concentration range for the low, medium and high loaded samples were prepared at pH 7.0 in 0.1 M NaCl. The IdP and SWy suspensions and Zn solutions were set to pH 7.0 using MOPS buffer. The solutions were labelled with $^{65}Zn$ radiotracer (Eckert & Ziegler Isotope Products, Valencia, California, USA). The maximum Zn concentrations used in the adsorption isotherm measurements was $5.6 \times 10^{-4}$ M, more than two orders of magnitude below the predicted solubility limits for $ZnO/Zn(OH)_2$ (Baes and Mesmer, 1976).

Aliquots of conditioned Na-IdP and Na-SWy suspensions were pipetted into 500 ml PE bottles followed by additions of the labelled $ZnCl_2$ solutions. The samples were shaken end-over-end up to 520 days and 280 days for IdP and SWy, respectively. To quantify the evolution of adsorption over time, the experiment (500 ml) was regularly sampled. Radioassay of aliquots of the supernatants as well as of the labelled standard solutions (prepared simultaneously at the start of the adsorption experiments) were performed using a Canberra Packard Cobra Quantum counter together with standard labelled solutions.

#### Zn adsorption at high S/L ratio and desorption at low S/L ratio on IdP and SWy

For the desorption experiments first Zn adsorption samples at a high S/L ratio of 14 g/L were prepared. Standard solutions with a Zn initial concentration of 5 x $10^{-3}$ M were labelled with $^{65}Zn$. Aliquots of clay suspensions were pipetted into 200 ml PE bottles followed by additions of the labelled $ZnCl_2$ solutions to achieve the desired Zn loadings. To quantify the adsorption of the high S/L ratio samples after 1 day, 40 ml of the homogenous sample were centrifuged and the supernatants were radio assayed for $^{65}Zn$ in a gamma counter and the pH was measured.

For the quantification of the reversibility, the 50 ml of the samples were then diluted with 0.1 M NaCl to reach the same S/L as in the adsorption system *i.e.,* 1.4 g/L. To quantify the evolution of adsorption over time, the experiment was regularly sampled (up to 520 days and 280 days for IdP and SWy, respectively). The samples were removed from the glove box and centrifuged at 1 h at 108'000*g* max., before returning them to the glove box for pH measurement. Aliquots of the supernatant were taken for radio assay of $^{65}Zn$ together with standard labelled solutions.

### EXAFS sample preparation

For the EXAFS measurements, Zn loaded IdP and SWy samples were prepared for batch adsorption and desorption experiments in 500 ml polypropylene vessels in a similar way as described the previous sections, but in the absence of $^{65}Zn$ tracer, *i.e.,* only with stable Zn. After the given equilibration time, phase separation of the suspensions was carried out by centrifugation, the supernatants were separated from the wet pastes which were filled into polyethylene sample holders and sealed with Kapton tape. The pH of the supernatants was measured and the solutions were analysed for major cations by ICP-OES.

Three IdP/SWy adsorption and three desorption samples with increasing Zn loadings (2 mmol/kg, 20 mmol/kg and 60 mmol/kg) were prepared in 0.1 M NaCl at pH 7.2 ± 0.1. The samples were investigated spectroscopically after 2 years equilibration time. EXAFS measurements were also performed on IdP and SWy without addition of external Zn (IdP/SWy-$Zn_{incor}$) to determine the structure of intrinsic Zn in IdP and SWy.

### EXAFS data collection and reduction

The Zn K-edge spectra were collected at the Diamond Light Source (Harwell, UK) at beamline ID-20 scanning. All spectra were recorded at room temperature using Si(111) crystals and a Canberra 64-pixel Ge solid-state monolith detector. Energy calibration was performed simultaneously by measuring in transmission mode a Zn foil (9659 eV). Higher order harmonics were rejected by the use of mirrors. Several spectra were averaged to improve the signal to noise ratio.

EXAFS data were reduced using the Athena-Artemis-IFEFFIT package (Newville, 2001; Ravel and Newville, 2005). The Fourier transforms (FT) were obtained from the $k^3\chi$ ($k$) functions between $k$ = 2.4 – 11 $Å^1$, using a Kaiser-Bessel window function (apodization parameter of 1).

FT peaks of interest were selected and fitted in reciprocal space with the Artemis interface of the IFFEFIT software. Amplitude and phase shifts functions were calculated with FEFF 8.40 (Ankudinov et al., 1998; Rehr et al., 1991), using the montmorillonite structure given by Tsipursky and Drits (1984), in which one Al was replaced by Zn (Dähn et al., 2011). The amplitude reduction factor $S_0^2$ was set to 0.85 (Dähn et al., 2011; Dähn et al., 2021; Manceau et al., 1998; O'Day et al., 1994; Schlegel and Manceau, 2006).

Throughout the data analysis, which was performed on the inverse Fourier transforms ($FT^{-1}$) of the first and second shells, the number of degrees of freedom in the least-squares refinements was reduced by fixing

the Debye Waller factor ($\sigma_j$) and $\Delta E_0$ (the shift between theoretical and experimental threshold energy) to the value obtained for the lowest concentrated sorption samples. EXAFS distances ($R_{Zn\text{-}j}$) and coordination numbers ($CN_{Zn\text{-}j}$) were allowed to float. It was not possible to fit any of the experimental data of IdP and SWy using a Zn-Zn pair and/or a combination of Zn-Zn and Zn-Si/Al pairs. This finding suggests that the formation of a Zn nucleation phase (e.g. $ZnOH_2$, Zn phyllosilicates) can be ruled out under the employed reaction conditions in the IdP and SWy uptake system.

## Results: Zn-illite/montmorillonite

### Zn adsorption on IdP and SWy

The Zn uptake on IdP increased from log $R_d$ = 4.9 L/kg (1 day) to 5.9 L/kg (523 days) for the low loaded samples. Similar, the log $R_d$ of Zn in the SWy system increased at low loadings also from 3.4 L/kg (1 day) to 4.4 L/kg (280 days). On IdP a similar trend was observed for the Zn adsorption at medium loading with an increase of log $R_d$ from 3.2 (1 day) to 4.6 (523 days). The adsorption of Zn on IdP at high loading and on SWy at medium and high loading exhibited a significantly lower $R_d$ increase with reaction time.

### Zn desorption on IdP and SWy

In the desorption experiments at low Zn loading there is nearly no change in the $R_d$ values with reaction time for IdP and SWy. The log $R_d$ values for long reaction times match within one log unit with the ones from the adsorption experiments (IdP-ads-low = 5.9 L/kg *vs*. IdP-des-low = 5.0 L/kg; SWy-ads-low = 4.4 L/kg *vs*. SWy-des-low = 4.2 L/kg). For the samples at medium and high Zn loadings a change of log $R_d$ was observed (0 day: IdP-des-high = 2 L/kg *vs.* 523 days: IdP-des-high = 3.5 L/kg; 0 day: SWy-des-high = 2.2 L/kg vs. 270 days: SWy-des-high = 2.6 L/kg).

### EXAFS results on IdP

The $k^3\chi(k)$ EXAFS spectra obtained for intrinsic Zn in “as received” IdP and Zn in the adsorption and desorption samples at low Zn loadings (IdP-ads-low and IdP-des-low) samples are nearly identical (Fig. 1 left). This indicates that Zn taken up is adsorbed to edge positions which have a very similar coordination environment as Zn atoms incorporated in the structure. The spectra of the samples with a medium Zn loading of 20 mmol/kg for adsorption and desorption are also almost identical, indicating the desorption experiment has not changed the structural environment of Zn at the clay mineral surface. In the ICP-OES measurements of the samples with high Zn concentration there was a difference in the loadings observed between adsorption (60 mmol/kg) and desorption (30 mmol/kg) samples, indicating that it was possible to remove 30 mmol/kg of the adsorbed Zn. In none of the samples Zn-Zn backscattering pairs could be observed

Data analysis showed that in the “as received” IdP sample Zn is surrounded by one O shell at 2.07 Å, one Al Shell at 3.02 Å and one Si shell at 3.25 Å. The Zn treated IdP is surrounded by 2.5(9) Al at 3.02(3) Å and 4.4(9) Si at 3.25(1) Å. Data analysis for the Zn samples after 2 years reaction time indicates that variations in the $CN_{Zn\text{-}Al}$ are within the experimental error and vary between 2.4 - 3.2. The $R_{Zn\text{-}Al}$ are identical to the values of the “as received” IdP sample (3.02(2) Å). The $R_{Zn\text{-}Si}$ of all Zn treated samples except for the IdP-ads-high sample are identical (3.22(2) Å). Only the IdP-ads-high sample exhibit a longer $R_{Zn\text{-}Si}$ of 3.25(2) Å. The $CN_{Zn\text{-}Si}$ were ~4.

### EXAFS results on SWy

The $k^3\chi(k)$ EXAFS spectra obtained for intrinsic Zn in “as received” SWy and Zn in the adsorption and desorption samples at low Zn loadings (SWy-ads-low and SWy-des-low) are very reminiscent of IdP (Fig. 1 right). Data analysis showed that the local environment of the “as received” SWy sample consists of $CN_{Zn\text{-}O}$ = 5.0(5), $R_{Zn\text{-}O}$ = 2.07(1) Å, $CN_{Zn\text{-}Al}$ = 1.6(9) $R_{Zn\text{-}Al}$ = 3.04(1) Å, $CN_{Zn\text{-}Si}$ = 2.7(9), $R_{Zn\text{-}Si}$ = 3.26(2) Å. The Zn treated SWy sample is surrounded by one O shell at 2.06 – 2.09 Å, one Al Shell at 2.99- 3.03 Å and one Si shell at 3.24 – 3.31 Å which is consistent with octahedral Zn in a 2:1 phyllosilicate environment (Schlegel et al., 2001). With increasing loading increasing differences in the $k^3\chi(k)$ EXAFS spectra between adsorption and desorption samples are observed.

Data analysis for the Zn samples after 2 years reaction time indicates that the $CN_{Zn\text{-}Al}$ are decreasing with increasing loading, both for the adsorption and desorption samples (from 2.1(9) to 1.0(7)). Similarly $CN_{Zn\text{-}Si}$ are decreasing with increasing loading, from 2.9(9) to 1.3(8) for the adsorption and from 2.7(9) to 1.3(8) for the desorption samples. Within the error the $R_{Zn\text{-}Al}$ and $R_{Zn\text{-}Si}$ are very similar in all six samples, ~3.00(2) Å and 3.30(2) respectively.

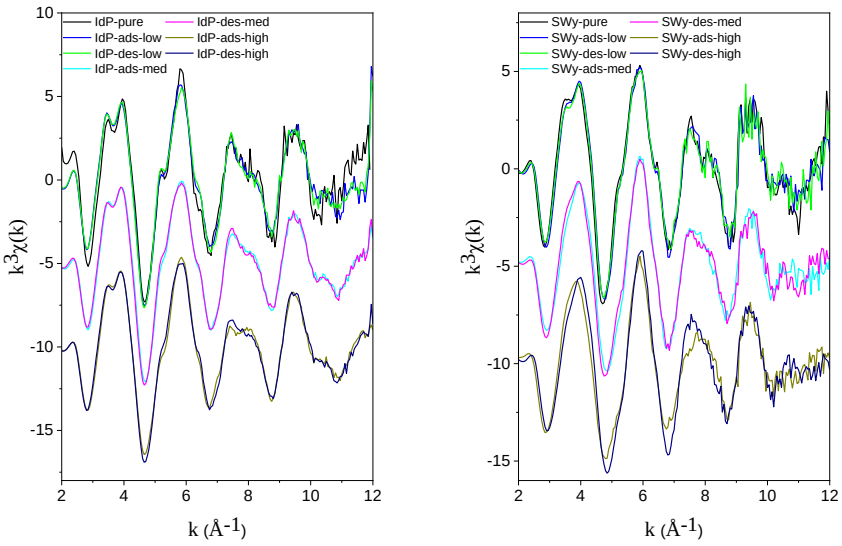


*Figure 1: (left) Comparison of $k^3$-weighted Zn K-edge EXAFS spectra of IdP-pure with IdP adsorption and desorption samples, (right) Comparison of $k^3$-weighted Zn K-edge EXAFS spectra of SWy-pure with SWy adsorption and desorption samples.*

## Discussion

In this study the adsorption and desorption behaviour of Zn on illite and montmorillonite in 0.1 M NaCl at neutral pH was investigated, by combining wet chemistry experiments with EXAFS measurements. EXAFS data obtained for both 2:1 clay minerals indicate that surface complexation is the dominant retention mechanisms rather than the formation of new phases (Marques Fernandes et al., 2015) at Zn loadings up to 60 mmol/kg for illite and montmorillonite, respectively.

The uptake of Zn on both IdP and SWy with prolonged reaction times of up to two years, showed that the formation of Zn precipitates were not observed. The differences between the EXAFS spectra of IdP obtained from adsorption and desorption samples at various loadings are modest after 2 years of reaction time indicating that under the employed reaction conditions the Zn surface complexes are very stable over time. Changes in the structural parameters for adsorption and desorption samples at similar loadings were within experimental errors. Data analysis indicates that at the lowest Zn loading of 2 mmol/kg the Zn surface complexes are similar for IdP and SWy and are very stable with time. At higher Zn loadings up to 50% of the adsorbed Zn could be removed from the clay mineral surface. The remaining Zn continued to be attached as an inner sphere surface complex.

## Acknowledgement

The help of the staff of the beamline ID-20-scanning at the DLS is gratefully acknowledged.

## References

Ankudinov A. L., Ravel B., Rehr J. J. and Conradson S. D. (1998) Real-space multiple-scattering calculation and interpretation of x-ray-absorption near-edge structure. *Physical Review B* **58**, 7565-7576.

Baes C. F. and Mesmer R. E. (1976) *The Hydrolysis of Cations*. John Wiley and Sons, New York.

Baeyens B. and Bradbury M. H. (1995) A quantitative mechanistic description of Ni, Zn and Ca sorption on Na-montmorillonite. Part I: Physico-chemical characterisation and titration measurements. *PSI Bericht Nr. 95-10. Paul Scherrer Institut, Villigen, Switzerland and Nagra Technical Report NTB 95-04, Nagra, Wettingen, Switzerland*.

Baeyens B. and Bradbury M. H. (1997) A mechanistic description of Ni and Zn sorption on Na-montmorillonite. Part I: Titration and sorption measurements. *Journal of Contaminant Hydrology* **27**, 199-222.

Baeyens B. and Bradbury M. H. (2004) Cation exchange capacity measurements on illite using the sodium and cesium isotope dilution technique: effects of the index cation, electrolyte concentration and competition: modeling. *Clays and Clay Minerals* **52**, 421-431.

Bradbury M. H. and Baeyens B. (1997) A mechanistic description of Ni and Zn sorption on Na-montmorillonite. Part II: Modelling. *Journal of Contaminant Hydrology* **27**, 223-248.

Bradbury M. H. and Baeyens B. (2005) Modelling the sorption of Mn(II), Co(II), Ni(II), Zn(II), Cd(II), Eu(III), Am(III), Sn(IV), Th(IV), Np(V) and U(VI) on montmorillonite: Linear free energy relationships and estimates of surface binding constants for some selected heavy metals and actinides. *Geochimica et Cosmochimica Acta* **69**, 875-892.

Bradbury M. H. and Baeyens B. (2009) Sorption modelling on illite Part I: Titration measurements and the sorption of Ni, Co, Eu and Sn. *Geochimica Et Cosmochimica Acta* **73**, 990-1003.

Bradbury M. H. and Baeyens B. (2011) Predictive sorption modelling of Ni(II), Co(II), Eu(III), Th(IV) and U(VI) on MX-80 bentonite and Opalinus Clay: A "bottom-up" approach. *Applied Cay Science* **52**, 27-33.

Dähn R., Baeyens B. and Bradbury M. H. (2011) Investigation of the different binding edge sites for Zn on montmorillonite using P-EXAFS – the strong/weak site concept in the 2SPNE SC/CE sorption model. *Geochimica et Cosmochimica Acta* **75**, 5154-5168.

Dähn R., Baeyens B. and Fernandes M. M. (2021) Zn uptake by illite and argillaceous rocks. *Geochimica Et Cosmochimica Acta* **312**, 180-193.

Fernandes M. M. and Baeyens B. (2019) Cation exchange and surface complexation of lead on montmorillonite and illite including competitive adsorption effects. *Applied Geochemistry* **100**, 190-202.

Manceau A., Chateigner D. and Gates W. P. (1998) Polarized EXAFS, distance-valence least-squares modeling (DVLS) and quantitive texture analysis approaches to the structural refinement of Garfield nontronite. *Physics and Chemistry of Minerals* **25**, 347-365.

Nagra (2002) Project Opalinus Clay: Safety Report. Demonstration of disposal feasibility for spent fuel, vitrified high-level waste and long-lived intermediate-level waste (Entsorgungsnachweis). *Nagra Technical Report* **02-05**.

Newville M. (2001) IFFEFFIT: interactive XAFS analysis and FEFF fitting. *Journal of Synchrotron Radiation* **8**, 322-324.

O'Day P. A., Brown Jr. G. E. and Parks G. A. (1994) X-ray absorption spectroscopy of cobalt (II) multinuclear surface complexes and surface precipitates on kaolinite. *Journal of Colloid and Interface Science* **165**, 269-289.

Poinssot C., Baeyens B. and Bradbury M. H. (1999) Experimental and modelling studies of caesium sorption on illite. *Geochim. Cosmochim. Acta* **63**, 3217-3227.

Ravel B. and Newville M. (2005) ATHENA, ARTEMIS, HEPHAESTUS: Data analysis for X-ray absorption spectroscopy using IFEFFIT. *Journal of Synchrotron Radiation* **12**, 537-541.

Rehr J. J., Mustre de Leon J., Zabinsky S. and Albers R. C. (1991) Theoretical x-ray absorption fine structure standards. *Journal of the American Chemical Society* **113**, 5135-5140.

Schlegel M. L. and Manceau A. (2006) Evidence for the nucleation and epitaxial growth of Zn phyllosilicate on montmorillonite. *Geochimica et Cosmochimica Acta* **70**, 901-917.

Schlegel M. L., Manceau A., Charlet L. and Hazemann J. L. (2001) Adsorption mechanisms of Zn on hectorite as a function of time, pH, and ionic strength. *American Journal of Science* **301**, 798-830.

SKB (2001) Programme for research, development and demonstration of methods for the management and disposal of nuclear waste. *Swedish Nuclear Fuel and Waste Management Co (SKB), Stockholm, Technical Report, TR-01-30*.

Tournassat C., Grangeon S., Leroy P. and Giffaut E. (2013) Modeling specific pH dependent sorption of divalent metals on montmorillonite surfaces. A review of pitfalls, recent achievements and current challenges. *American Journal of Science* **313**, 395-451.

Tsipursky S. I. and Drits V. A. (1984) The distribution of octahedral cations in the 2:1 layers of dioctahedral smectites studied by oblique-texture electron diffraction. *Clay Minerals* **19**, 177-193.

Van Olphen H. and Fripiat J. J. (1979) *Data Handbook for clay materials and other non-metallic minerals.* Pergamon Press, New York.

# 5. Diffusion and retention of Co and Zn surface complexes in compacted illite preloaded with different cations

D. Zerva[1,2], M. Glaus[1], S. V. Churakov[1,2]
[1]*PSI, Villigen PSI, Switzerland*
[2]*University of Bern, Bern, Switzerland*

## Introduction

Surface diffusion phenomena in clay minerals have been reported in numerus studies, describing the enhanced mass fluxes of cationic species and consequently a higher than expected effective diffusion coefficient ($D_e$) of cations in compacted systems during the diffusion experiments. Therefore, a good understanding of the transport behaviour through clays and clay rocks is crucial to the long-term safety assessment of clay barrier systems, which have been selected by many countries as a host rocks for the disposal of radioactive waste.

The electrical double layer (EDL) model has been used to explain the enhanced fluxes and the large effective diffusion coefficients ($D_e$) of $Sr^{2+}$, $Co^{2+}$ and $Zn^{2+}$ as well as their dependence of the electrolyte solution ionic strength (Glaus et al., 2015b).

The EDL diffusion/sorption model is extensively described in Glaus et al., 2020. In brief, the 2SPNE-SC/EDL (two site protolysis non-electrostatic surface complexation and electrical double layer) can be considered as a variant of the two-site protolysis non-electrostatic surface complexation and cation exchange (2SPNE-SC/CE) model (Bradbury and Baeyens, 1997; Glaus et al., 2015b). This extended model describes: 1) the surface complexes within the EDL, bound to the planar sites of the clay system and uses the Donnan potential approach ($\Psi_D$). The surface charge neutralization occurs within a) the Stern layer (inner sphere complexes) which are considered immobile and within b) the diffuse layer (outer sphere complexes) which are considered mobile. 2) The immobile surface complexes bound to the edged sites (weak and strong sites) (fig. 1). The effective diffusion coefficient $D_e$ of a given species diffused in a clay system can be calculated from equation 1 and can be influenced by a) the geometrical factor "*G*" and the distribution ratio of the mobile species in the clay system (Appelo et al., 2010; Glaus et al., 2015b).

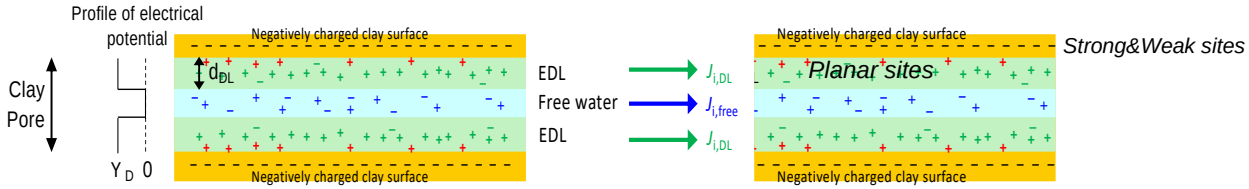


*Figure 1: Left: Schematic representation of the Donnan approach for an EDL at the planar clay surfaces. Species in blue (ions in free pore water) and green color (surface complexations in the Donnan volume) are assumed mobile, while red surface complexes are considered as immobile in the Stern layer. The Donnan potential ($\Psi_D$), the negative charge of the clay, is zero at the diffuse layer-pore water interface (neutralization of the negatively charged clay surface). Right: conceptual representation of sites locations.*

The geometrical factor "*G*" is a measure of the tortuosity of the porous media. The distributed cations within the EDL (Stern and diffuse layer) are influenced by several solution characteristics. Additionally, the thickness of the Donnan layer ($d_{DL}$) or diffuse layer, which establishes the formal volumetric division between the bulk water and the diffuse layer domain and consequently the distribution ratio between the mobile species ($\frac{C_{DL}}{C_{free}}$) is also affected.

$$D_e = \varepsilon \frac{D_w}{G}\left(C_{free} + \frac{C_{DL}}{C_{free}} q_n\right) \quad (1)$$

Where $G$ is the geometrical factor (-), $D_w$ the diffusion coefficient of an ion in bulk water, $C_{free}$ the concentration of the RN in the free space (pore water), $C_{DL}$ the concentration of the species in the diffuse layer and $\varepsilon$ the porosity of the porous medium. The $q_n$ (-) is a factor (fit value) that is introduced to account for different molecular mobilities of the diffusing species in these different types of water. Therefore, we can assume that if the cationic loading of the clay can affect the extent of the diffuse layer, then it will also affect the concentration ratio between the mobile species and consequently the $D_e$ values.

So far, in clay minerals like illite the phenomenon has been intensively studied from pore water chemistry point of view: The variation in pH and in background electrolyte concentrations (Glaus et al., 2020; Glaus et al., 2015b) revealed the dependency of $D_e$ and $R_d$ on both of these two parameters. The variation in background $Ca^{2+}$ concentration (competition effect) demonstrated that increase in the $Ca^{2+}$ concentration leads to decrease of the $D_e$ even for the strongly sorbing radionuclides like $^{57}Co^{2+}$ (Glaus et al., 2021).

From a structural point of view, the specific surface area (SSA) of Na_illite and Cs_illite was measured in the past (Aylmore et al., 1970) and the nitrogen absorption method gave values 195 and 184 $m^2/g$, respectively.

On the other hand, evidence of different microstructure and $D_e$ values for the same cationic tracer has been reported for swelling clays conditioned to homoionic forms: Ca_bentontite and Na_bentonite (Choi and Oscarson, 1996) have different turtousities. The same has been observed for montmorillonites. The bentonite loaded with $Ca^{2+}$ has a less tortuous porous path and larger quasicrystals leading to a higher $D_e$ for HTO, $I^-$ and $Sr^{2+}$(Sanchez et al., 2008). The presence of a gel phase in Na_bentonite and the absence of it in the aggregated Cs_bentonite has been observed (Melkior et al., 2009). The absence of this gelly phase in Cs_bentonite results in a less tortuous diffusion path leading to a higher $D_e$ value for the HTO and a lower $D_e$ for the $^{22}Na^+$ in comparison to Na_ bentonite. The authors introduced the surface diffusion ratio $\varphi$, which is a normalization of the $D_e$ of a given cation to the $D_e$ of an uncharged species (HTO), to quantify the extent of this phenomenon. The results revealed the presence of surface diffusion because $\varphi>1$ for Na and Ca_bentonite and almost $\varphi \cong 1$ for Cs_bentonite.

According to equation 2, the ratio of the diffusion coefficients in bulk water ($\frac{D_{w(HTO)}}{D_{w(cation)}}$) under given conditions is higher than one then the ratio between the $D_e$(cation) and $D_e$*(HTO)* will define the presence (for $\varphi > 1$) or not of the surface diffusion phenomenon.

$$\varphi = \frac{D_e(cation)}{D_e(HTO)} * \frac{D_w(HTO)}{D_w(cation)} \quad (2)$$

Which is in agreement with the definition of surface diffusion of Glaus et al (2015):

$$\frac{\mathrm{D_e(cation)}}{\mathrm{D_e(HTO)}} > \frac{\mathrm{D_w(cation)}}{\mathrm{D_w(HTO)}} \quad (3)$$

Additionally, in the work of Melkior et al, 2009 the numbers of the water layers within the interlayer space of Ca, Cs, K, and Na bentonite/montmorillonite are well summarized suggesting that the $\Delta_H$ values affects the number of water layers (higher $\Delta_H$, more water layers), increasing the interlayer porosity and resulting in higher $D_e$ of HTO.

Still it is not clear if this structural differentiation is due to accessibility to hydrated cations interlayer or it also affects the microstructure of the planar surface.

So far, to the authors' knowledge, only two studies exist in the literature regarding the cationic loading viz. the cations that neutralize the negative surface charge of illite. Little data exist for the clarification between different interparticle structures and the cationic interactions. Sanchez et al (2008) using a dry bulk density of 1.9 g/ml calculated $D_e$ values for Na-illite higher than one of Ca_ illite and attributed this behaviour to the difference in index cation solvation. In this case despite the lack of the explanation the results can't be evaluated in terms of electrical double layer theory due to the high degree of compaction (Marry and Turq, 2003).

A better understanding of cationic distribution into the EDL and especially in the Stern layer has been obtained from X-Ray Reflective data and molecular dynamics simulation (Bourg et al., 2017) studying

muscovite, a dioctahedral phyllosilicate-non swelling clay mineral. According to this study $Cs^+$, $Rb^+$ and $K^+$ form complexes in a closer proximity with the charged surface clay than the $Na^+$ and $Li^+$. This is in agreement with previous work findings (Kosakowski et al., 2008) where $Na^+$ prefers to form outer sphere complexes out of the Stern layer.

The aim of this paper is to provide answers to the mechanisms inducing surface diffusion. Therefore in the present work, the influence of the hydration energy ($\Delta_H$) of different cations on the clay's surface charge neutralization is studied and its impact on the electrical double layer structure and on the sorption properties.

Different cationic species have different hydration energy ($\Delta_H$) and in the alkali metals, increasing the ionic radii and the coordination number (CN)(Mahler and Persson, 2012), we can observe a decrease in hydration energy (table 1). As a result, one notable implication is that the Columbic forces (Dor et al., 2020) stemming from the negative lattice charge of the clay can more readily disrupt the bonds, for instance, between $Cs^+$ and its surrounding water molecules. Consequently, this leads to an increased formation of complexes between $Cs^+$ and the clay surface within the Stern layer (SL), and a lower concentration of mobile species in the diffuse layer ($d_{DL}$). Additionally, it is expected that the sorption distribution coefficient ($R_d$) of a given radionuclide will be influenced since the cations under study exhibit different selectivity (Teppen and Miller, 2006).

*Table 1: Coordination numbers, ionic radii and hydration energies of the alkali metals under study.*

| Alkali metal | CN | Ionic radii Å | $\Delta_H$ (KJ/mol) |
|---|---|---|---|
| **Li** | 4-6 | 0.6-0.79 | -519 |
| **Na** | 5-6 | 1.02-1.07 | -406 |
| **K** | 6-7 | 1.38-1.46 | -320 |
| **Cs** | 8 | 1.73 | -264 |

## Materials and methods

### Materials

Illite from de Puy France (from now on called IdP) was used and converted to different homoionic forms using 2 different approaches: for the through diffusion of HTO and for the in diffusion-profile analysis of $^{57}Co^{2+}$ , the IdP was conditioned to Na_IdP following the procedure as it is described elsewhere (Glaus et al., 2015a). After the compaction in the diffusion cells, in situ conversion to the different homoionic forms took place by passive saturation of the compacted clays using the corresponding electrolyte solutions.

For the in diffusion-profile analysis, IdP was pre-conditioned directly to different homoionic forms following the procedure of (Glaus et al., 2015a). In this procedure Li_IdP, Na_IdP, K_IdP and Cs_IdP were produced using the corresponding electrolyte solutions. After freeze-drying, the clay material was sieved to a grain size <250 μm. Both the stock tracers' solutions were diluted in HCl and $^{57}Co^{2+}$ was free of stable isotope carrier while $^{65}Zn^{2+}$ had the stable isotope carrier at much higher concentration.

### In diffusion – Profile analysis

Approximately 0.3 g of homoionic form of illite were used and compacted to a dry bulk density of 1.5 g/ml into 24 MCDCs (Membrane Confined Diffusion Cells). A detailed schematic view of the diffusion cells can be found in Glaus at el 2015b. Before the start of in diffusion of $^{57}Co^{2+}$ and $^{65}Zn^{2+}$ every homoionic form of illite was immersed into corresponding electrolyte solutions of 3 different concentrations (0.03M, 0.1M and 0.5M) for the fully saturation of them. No pH buffer was used to avoid the introduction of ions that are not already present in the system. Instead, the pH is adjusted by equilibration of clay and solution; pH monitoring took place. No changes on the pH were observed during the entire duration of the experiment.

The pH values were ranging from 5.5 to 4.2 with the lower values involving electrolyte solution of 0.5 M. The experiments were carried out under atmospheric conditions at a temperature of 21-23 $^{o}$C and each cell was immersed in 30 ml of the corresponding electrolyte solution with a tracer concertation of 100 Bq/ml. In figure 2 the reader can see a schematic representation of the steps of in diffusion and profile analysis.

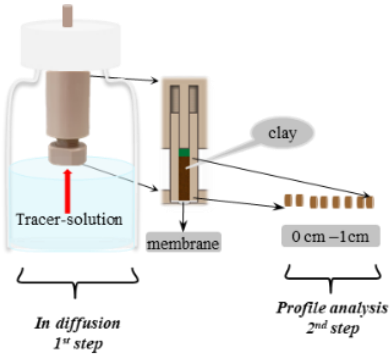


*Figure 2: During the in diffusion step the tracer depletion in the reservoir is measured during regular time intervals. A hydrophilic membrane is placed between the sample and the solution to prevent loss of material. The experiment is completed with the segmentation of the sample and the measurement of the activity in each segment.*

## Through diffusion

Through diffusion experiments were conducted for the calculation of effective diffusion coefficient ($D_e$) of HTO for these forms of illite. For this, the experimental set up described in Van Loon et al. (2003) was used. The electrolyte concentration does not affect the $D_e$ of the HTO as mentioned before and that for was used the concentration of 0.1 M for each one of the electrolyte solution. The initial concentration of HTO in the upstream reservoir was 2.3 $10^{-7}$ mol/m$^3$.

## Simulations

For all in diffusion experiments the effective diffusion coefficient $D_e$ and sorption distribution coefficient $R_d$ values were obtained from Matlab® parameter optimization routine minimizing error function. This inverse modelling procedure uses Comsol Multiphysics ® model extracted as a Matlab script. Chemical equilibrium speciation in solution and at the clay interface are calculated using the geochemical simulation code Phreeqc. Detailed information about the numerical procedures can be found in Glaus et al 2020.

## Supplementary measurements

Supplementary measurements was necessary to be done both for the acquisition of parametric values used as inputs for the speciation calculations and for testing the sensitivity.

*Specific surface measurements (BET)*

The specific surface area was determined by nitrogen adsorption. The different subsamples were weighed to an accuracy of 0.001 grams and thoroughly desorbed of primary adsorbed gases by heating under vacuum at 105ºC for 60h with the BELPREP – vac III pretreatment device. Approximately 0.2 grams of sample were analysed in a sample cell with a volume of 0.5 cm$^3$. Adsorption isotherms were measured in equilibrium with liquid nitrogen using a BELSORP-miniX surface analyser. The $N_2$-surface area was calculated using the Brunauer, Emmet and Teller method (BET) for a pressure range of $P/P_0$ from 0.05 to 0.3. The specific surface area (expressed as m$^2$/g) was obtained from the $N_2$- BET results and the sample weight. Pore size distribution was obtained from adsorption/desorption isotherm by Barrett, Joyner and Halenda method (BJH).

### Grain density

Similarly, the grain density $\rho_s$ (g/ml) for all these clays obtained by pycnometer measurements. For each type of illite three pycnometer with an approximately 25 ml volume were used. Two grams of clay were used for each probe, and the air trapped within the pores was removed using a vacuum desiccator. A constant temperature of 20 $^{o}$C (± 0.1) was ensured by placing the pycnometers in water bath.

## Results

### Specific surface area and grain density

The following table (table 2) presents the results for specific surface area, grain density, and pore diameter of the homoionic forms of illite. The grain density results do not follow like the gradual alteration of macroscopic picture. Instead, increasing ionic radii of the index cation leads to a corresponding increase in specific surface area and a decrease in pore diameter**.**

*Table 2: Results for the grain density, specific surface area and pore diameter of the homoionic forms of illite.*

| **Illite form** | **Grain density ($\rho_s$)** (g/ml) | **SSA** ($m^2/g$) | **Pore diameter** (nm) |
|---|---|---|---|
| Li_IdP | 2.75 | 116 | 12.10 |
| Na_IdP | 2.87 | 118 | 11.23 |
| K_IdP | 2.84 | 121 | 10.32 |
| Cs_IdP | 2.84 | 123 | 10.36 |

### Diffusion of HTO

The $D_e$ values of HTO tracer is an essential parameter for the interpretation of data for cations. Its used to normalize the $D_e$ values for each tracer according to their $D_w$ and to reveal not only the existence or not of the surface enhanced diffusion, but above all its extent and its variation for different species according to the equation (2) & (3). Moreover as an indirect observation, we could have a first impression if the micro-geometry and consequently the diffusion path of these forms varies. The $D_e$ for the steel filters was set to 1 $10^{-10}$ (± 0.25) $m^2/s$ and it is the value for unused filters (Glaus et al., 2008). The average calculated rock capacity ($\alpha$) of 0.40 is in a good agreement with the total average grain porosity of 0.45. The results are summarized in table 3.

*Table 3: Summary of the $D_e$ and α values of the HTO for each homoionic form of illite. The $D_e$ values are normalized to the average total porosity 0.46. In the parenthesis are the absolute uncertainty values (average of the minimum and maximum values).*

| Homoionic form of illite | Electrolyte solution | Electrolyte concentration (M) | $D_e$ (x$10^{-10}$) ($m^2$/s) | α (-) |
|---|---|---|---|---|
| **Li_IdP** | LiCl | 0.1 | 1.6±0.45 | 0.39±0.13 |
| **Na_IdP** | NaCl | 0.1 | 1.5±0.45 | 0.38±0.13 |
| **K_IdP** | KCl | 0.1 | 1.4±0.4 | 0.39±0.12 |
| **Cs_IdP** | CsCl | 0.1 | 1.5±0.55 | 0.41±0.13 |

## Diffusion of $^{57}Co^{2+}$

After the in situ conversion of Na_illite to the corresponding homoionic forms, the in diffusion started with initial tracer concentration of $2.5 \cdot 10^{-7}$ mol/$m^3$ (or $2.5 \cdot 10^{-10}$ M). According to previous studies (Bradbury and Baeyens, 2009; Marques Fernandes et al., 2015), for the Na_IdP the sorption mechanism at electrolyte concentration 0.1 M and at pH > 4 is dominated by the surface complexes at the edge sites with a small contribution of cation exchange species. Additionally cobalt at concentrations Co < $10 \cdot 10^{-7}$ M is preferentially bound to the strong sites (Montoya et al., 2018).

The results obtained from the experiment involving a 0.03 M electrolyte concentration demonstrate that Co exhibits comparable behaviour in both Li_IdP and Na_IdP systems. Specifically, Co depletion in the reservoir solution was observed in both systems, and the corresponding profiles were found to be similar. Similar consistent results were obtained for the K_IdP and Cs_IdP systems, where the depletion of Co was found to be smaller in the CsCl reservoir and the corresponding diffusion profile of the clay was the shortest (Fig 3). The profile analysis for K_IdP in 0.1 and 0.5 M are currently unavailable, but based on the so far results, the diffusion depth of $^{57}Co^{2+}$ in Na_IdP is the mostly affected by the variation of the electrolyte concentration (Fig 3-5). The fused order of diffusion profiles in 0.5 M could suggest a combined effect of electrolyte concentration and $\Delta_H$.

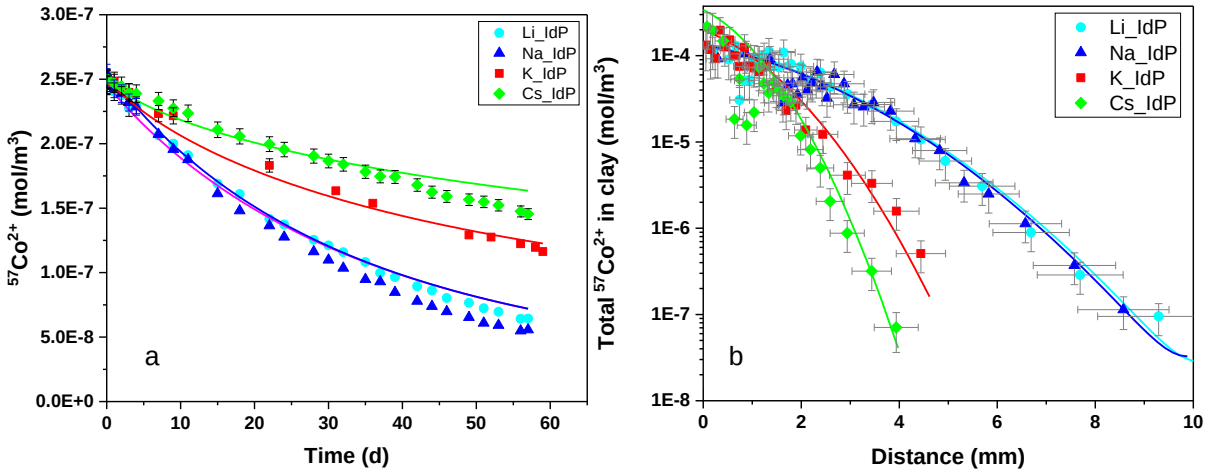


*Figure 3: In-diffusion experiments with $^{57}Co^{2+}$ at pH ~5.5 showing the tracer concentration depletion in the reservoir solution with electrolyte concentrations of 0.03 M (a) and the profile of tracer concentration in the clay (b) as a function of the homoionic form of illite (IdP) (cf. the legend). Markers represent the experimental data and fit curves were obtained from the best-fit parameter values given in Table 4.*

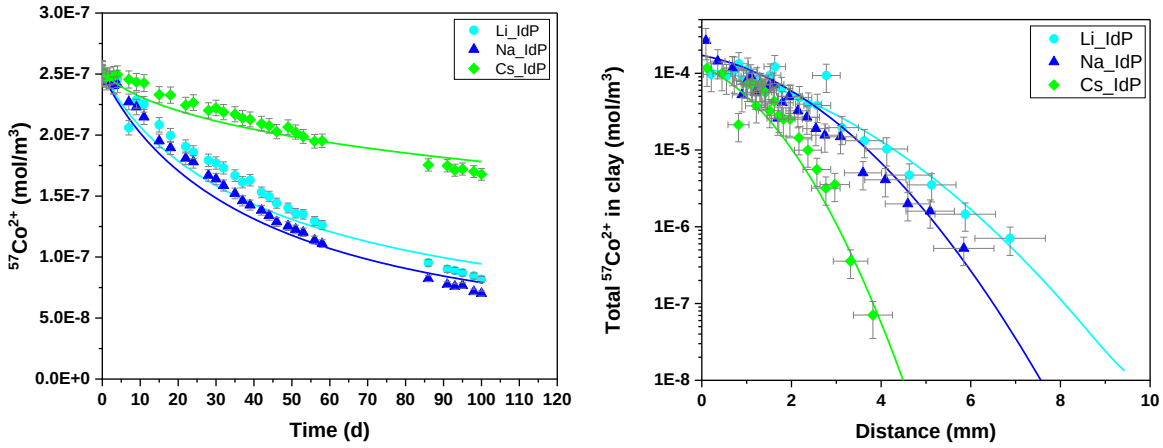


*Figure 4: In-diffusion experiments with $^{57}Co^{2+}$ at pH ~5.5 showing the tracer concentration depletion in the reservoir solution with electrolyte concentrations of 0.1 M (a) and the profile of tracer concentration in the clay (b) as a function of the homoionic form of illite (IdP) (cf. the legend). Markers represent the experimental data and fit curves were obtained from the best-fit parameter values given in Table 4. The results of K_IdP are still not available.*

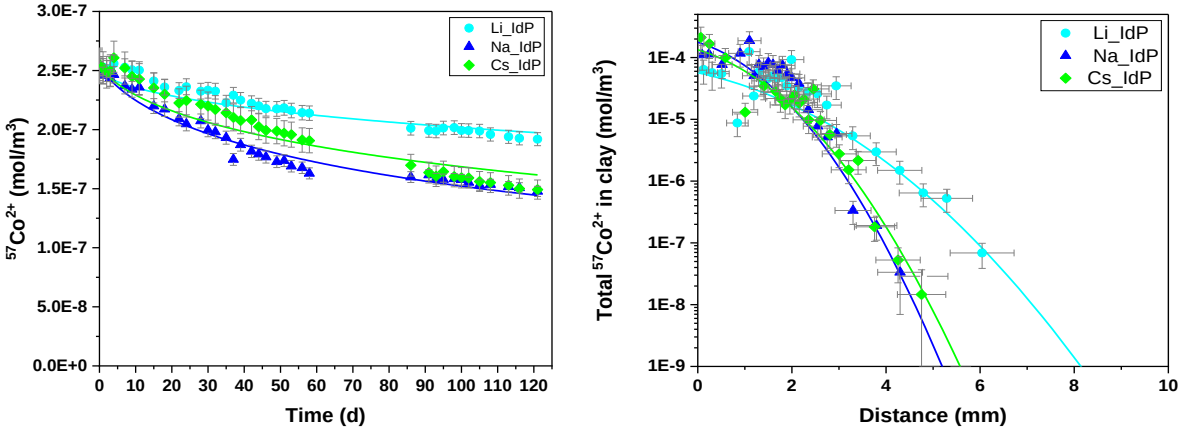


*Figure 5: In-diffusion experiments with $^{57}Co^{2+}$ at pH ~5.5 showing the tracer concentration depletion in the reservoir solution with electrolyte concentrations of 0.5 M (a) and the profile of tracer concentration in the clay (b) as a function of the homoionic form of illite (IdP) (cf. the legend). Markers represent the experimental data and fit curves were obtained from the best-fit parameter values given in Table 4. The results of K_IdP are not yet available.*

## Diffusion of $^{65}Zn^{2+}$

The conversion of illite to the different homoionic forms was done during their conditioning as it described in Glaus et al 2015a for the case of Na_IdP. The total concentration (included the amount of the stable isotope) was 6 $10^{-4}$ mol/m$^3$ (or 5.5 $10^{-7}$ M). The pH of the experiment ranges from 4.2 to 5.5 and according to Montoya et al 2017, strong sorption occurs from the pH 3 in Na_IdP, therefore a small contribution of cation exchange will be expected at the 0.03 M for Na_illite while surface complexation will dominate especially to higher electrolyte concentrations.

The results obtained from the profile analysis indicate significant differences. Specifically, in the case of 0.03 M and 0.1 M electrolyte solutions, the diffusion depth observed in the Na_IdP system was found to be greater compared to that of K_IdP and Cs_IdP systems, which are observed to have the same diffusion depth (Fig 6 & 7). However, for the 0.5 M solution, the profiles displayed unexpected behaviour and with

rather high calculated uncertainties of the diffusion depths (Fig 8). Table 5 provides a summary of the $D_e$ and $R_d$ best-fit values obtained from the parameter optimization and the experimental data.

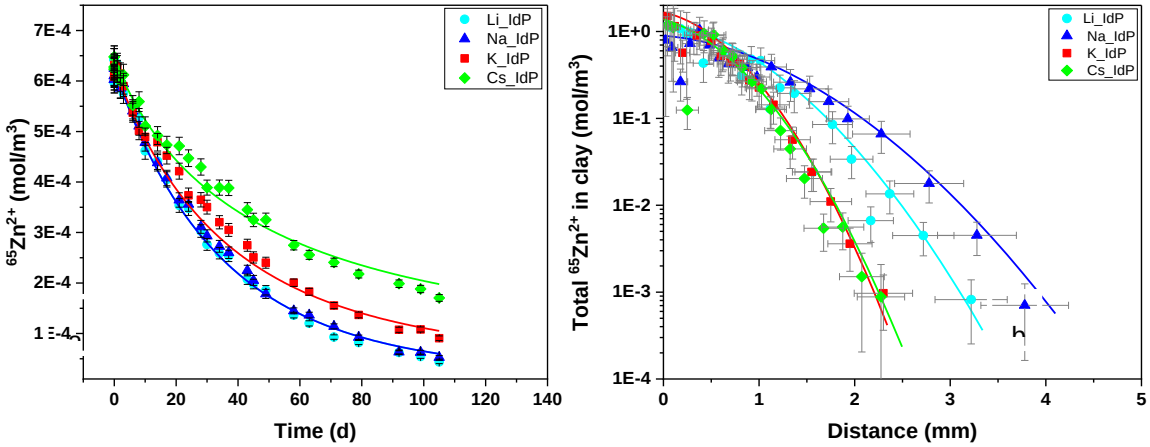


*Figure 6: In-diffusion experiments with $^{65}Zn^{2+}$ at pH~5 showing the tracer concentration depletion in the reservoir solution with electrolyte concentrations of 0.03 M (a) and the profile of tracer concentration in the clay (b) as a function of the homoionic form of illite (IdP) (cf. the legend). Markers represent the experimental data and fit curves were obtained from the best-fit parameter values given in Table 5.*

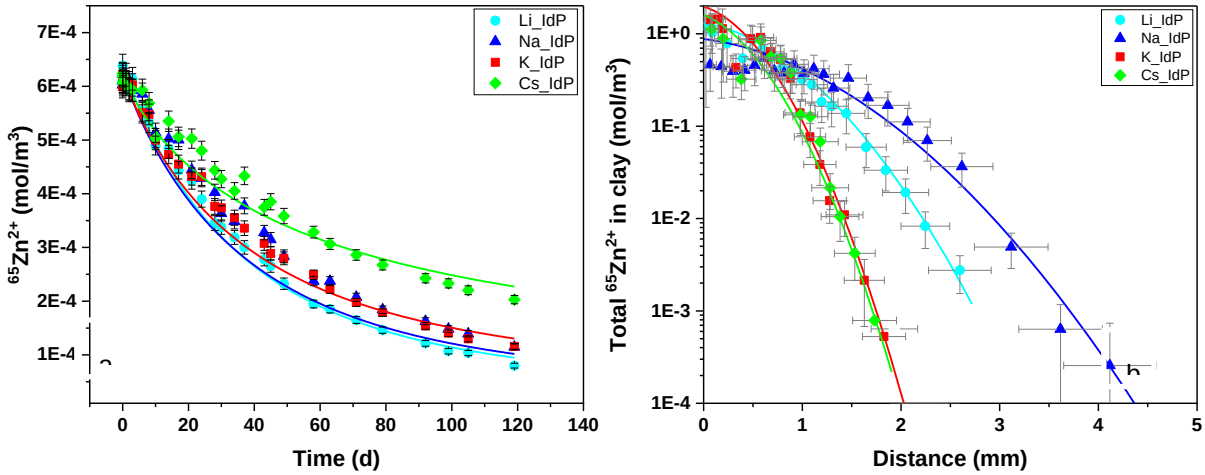


*Figure 7: In-diffusion experiments with $^{65}Zn^{2+}$ at pH 4.5-5 showing the tracer concentration depletion in the reservoir solution with electrolyte concentrations of 0.1 M (a) and the profile of tracer concentration in the clay (b) as a function of the homoionic form of illite (IdP) (cf. the legend). Markers represent the experimental data and fit curves were obtained from the best-fit parameter values given in Table 5.*

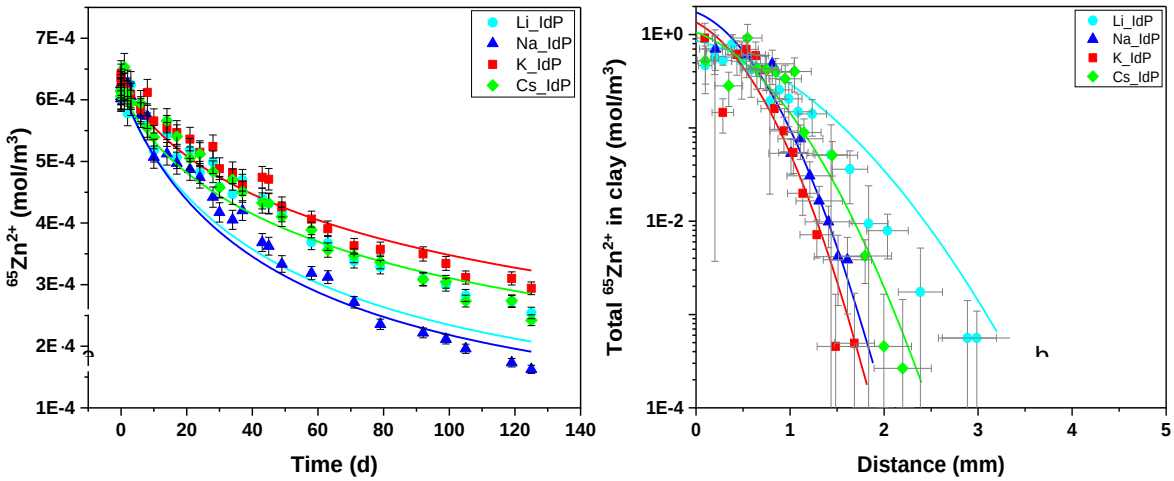


*Figure 8: In-diffusion experiments with $^{65}Zn^{2+}$ at pH~4.5 showing the tracer concentration depletion in the reservoir solution with electrolyte concentrations of 0.5 M (a) and the profile of tracer concentration in the clay (b) as a function of the homoionic form of illite (IdP) (cf. the legend). Markers represent the experimental data and fit curves were obtained from the best-fit parameter values given in Table* 5.

*Table 4: Experimental condition and best-fit parameter values from the diffusion experiments with $^{57}Co^{2+}$ with a dry bulk density of 1500 (+/-50) Kg/m$^3$ and $D_e$ for the filters 2 $10^{-10}$ m$^2$/s. In the parenthesis are the minimum and maximum values of each parameter.*

| Experiment | pH | Electrolyte solution | Background electrolyte (M) | $D_e$ $\text{mean}\ ^{\text{max}}_{\text{min}}$ m$^2$/s | $R_d$ $\text{mean}\ ^{\text{max}}_{\text{min}}$ m$^3$/Kg |
|---|---|---|---|---|---|
| 1.Li_IdP | 5.8 | LiCl | 0.03 | $3.17^{5.8}_{1.7} \times 10^{-9}$ | $3^{5.7}_{1.6}$ |
| 1.Na_IdP | 5.8 | NaCl | 0.03 | $2.65^{4.6}_{1.5} \times 10^{-9}$ | $2.8^{5.1}_{1.6}$ |
| 1.K_IdP | | KCl | 0.03 | $4.32^{9.9}_{1.9} \times 10^{-10}$ | $1.5^{3.8}_{0.6}$ |
| 1.Cs_IdP | 5.3 | CsCl | 0.03 | $1.54^{2.8}_{0.87} \times 10^{-10}$ | $0.83^{1.5}_{0.4}$ |
| 2.Li_IdP | 5.8 | LiCl | 0.1 | $5.08^{8}_{3.2} \times 10^{-10}$ | $1^{1.7}_{0.6}$ |
| 2.Na_IdP | 5.8 | NaCl | 0.1 | $4.94^{8.7}_{2.8} \times 10^{-10}$ | $2.1^{4.3}_{1.13}$ |
| 2.K_IdP | n.a. | KCl | 0.1 | n.a. | |
| 2.Cs_IdP | 5.3 | CsCl | 0.1 | $5.62^{9.8}_{3.2} \times 10^{-11}$ | $0.5^{0.9}_{0.3}$ |
| 3.Li_IdP | 5.8 | LiCl | 0.5 | $3.3^{0.15}_{0.74} \times 10^{-11}$ | $1^{4.4}_{0.2}$ |
| 3.Na_IdP | 5.2 | NaCl | 0.5 | $8.29^{0.13}_{5.5} \times 10^{-11}$ | $0.9^{1.5}_{0.6}$ |
| 3.K_IdP | n.a. | KCl | 0.5 | n.a. | |
| 3.Cs_IdP | 4.9 | CsCl | 0.5 | $6.52^{0.1}_{4.2} \times 10^{-11}$ | $0.6^{1}_{0.4}$ |

*Table 5: Experimental condition and best-fit parameter values from the diffusion experiments with $^{65}Zn^{2+}$ with a dry bulk density of 1500 (+/-50) Kg/m³ and $D_e$ for the filters 2 $10^{-10}$ m²/s.*

| Experiment | pH | Electrolyte solution | Background electrolyte (M) | $D_e$ mean $^{max}_{min}$ m²/s | $R_d$ mean $^{max}_{min}$ m³/Kg |
|---|---|---|---|---|---|
| 1.Li_IdP | 5.3 | LiCl | 0.03 | $2.34^{7.1}_{0.8} \times 10^{-9}$ | $64^{204}_{21}$ |
| 1.Na_IdP | 5.4 | NaCl | 0.03 | $2.44^{5.4}_{1.1} \times 10^{-9}$ | $21.5^{50}_{9.3}$ |
| 1.K_IdP | 5.5 | KCl | 0.03 | $5.38^{9.7}_{3} \times 10^{-10}$ | $16.4^{31}_{8.7}$ |
| 1.Cs_IdP | 4.7 | CsCl | 0.03 | $2.15^{3.4}_{1.4} \times 10^{-10}$ | $6^{9.6}_{3.7}$ |
| 2.Li_IdP | 5.1 | LiCl | 0.1 | $6.24^{11}_{3.7} \times 10^{-10}$ | $13.2^{23.7}_{7.3}$ |
| 2.Na_IdP | 5.1 | NaCl | 0.1 | $7.3^{13}_{4} \times 10^{-10}$ | $8^{15.4}_{4.16}$ |
| 2.K_IdP | 5.2 | KCl | 0.1 | $2.37^{4}_{1.4} \times 10^{-10}$ | $13.4^{23.3}_{7.66}$ |
| 2.Cs_IdP | 4.6 | CsCl | 0.1 | $1.06^{1.8}_{0.61} \times 10^{-10}$ | $5.6^{10}_{3.1}$ |
| 3.Li_IdP | 4.7 | LiCl | 0.5 | $2.0^{3.2}_{1.3} \times 10^{-10}$ | $3.3^{5.5}_{2}$ |
| 3.Na_IdP | 4.9 | NaCl | 0.5 | $1.25^{2.1}_{0.7} \times 10^{-10}$ | $7.8^{13.5}_{4.5}$ |
| 3.K_IdP | 4.9 | KCl | 0.5 | $4.82^{8.5}_{2.7} \times 10^{-11}$ | $3.13^{5.8}_{1.7}$ |
| 3.Cs_IdP | 4.2 | CsCl | 0.5 | $7.85^{0.15}_{4} \times 10^{-11}$ | $2.84^{5.8}_{1.4}$ |

# Discussion

## Diffusion

The effect of electrolyte concentration on the $D_e$ values for Co shows a noticeable distinction between the Li_IdP/Na_IdP and Cs_IdP systems.

From previous studies (Glaus et al 2015) it has been well established that Co and Zn in Na illite have a similar diffusive behaviour. The same can be observed in the present study for all types of illite (Fig 9). The results for both tracers are in a very good agreement with the already described observation that the diffusivity decreases as a function of the cation loading following the decrease of the $\Delta_H$ of the given cation (Fig 10). Except for the Cs Illite, the negative surface charge is only partially screened at the lower electrolyte concentrations (0.03 M and 0.1 M), and significant amount of tracer is present in the diffuse double layer. The screening increases in the Li, Na and K sequence, as affinity of the ions to the Stern layer increases with $\Delta_H$ decreasing in this sequence. Accumulation of ions in the Stern layer (either due to the lower hydration energy ions or increasing background electrolyte concentration), reduces the enrichment of mobile species in the diffuse layer. Cs_IdP does not show dependence on electrolyte concentration because of the low $\Delta_H$ of the Cs ion. Even at lower electrolyte concentrations, Cs accumulation in the Stern layer screens the surface charge and suppresses the formation of diffuse layer.

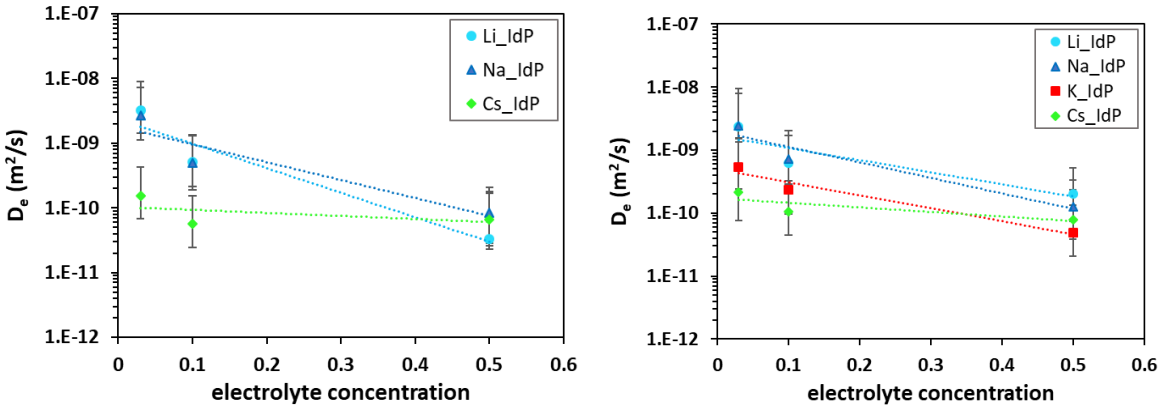


*Figure 9: $D_e$ values of $^{57}Co^{2+}$ (left) and $^{65}Zn^{2+}$ (right) as a function of electrolyte concentration (mol/l).*

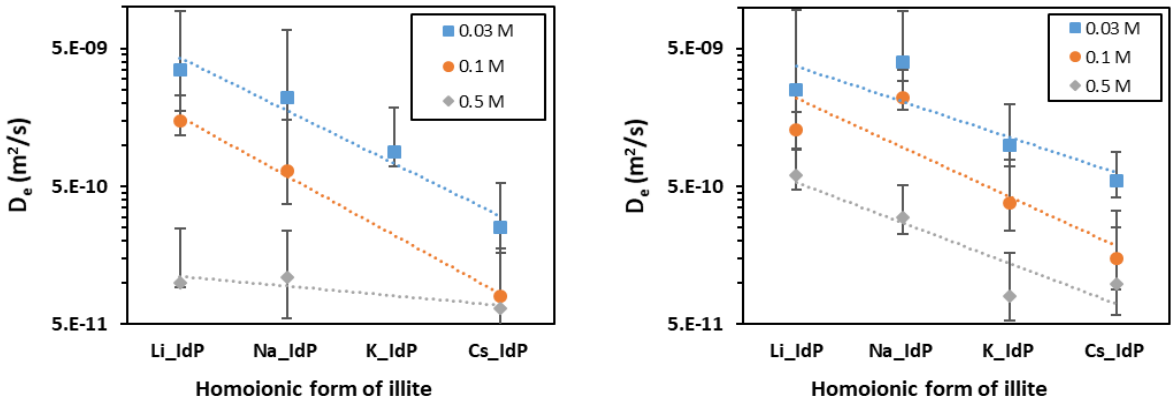


*Figure 10: $D_e$ values of $^{57}Co^{2+}$ (left) and $^{67}Zn^{2+}$ (right) as a function of homoionic form of illite.*

## Sorption

Our current knowledge on the sorption of cobalt and zinc is restricted to experiments with Na_IdP and we can only indirectly conclude about the sorption mechanisms in the other homoionic forms of illite. In Fig. 11 (left), we can see the strong dependency of $R_d$ values on electrolyte concentration indicating that the dominant sorption mechanism is the cation exchange reactions for Li and Na illite. However, this is not the case for Cs illite where we do not observe variation of the $R_d$ as a function of the electrolyte concentration and probably the dominant mechanism is the surface complexation in the Stern layer. The same has been observed for the Cs_IdP in the case of Zn along with the Na_IdP (Fig 11-right).

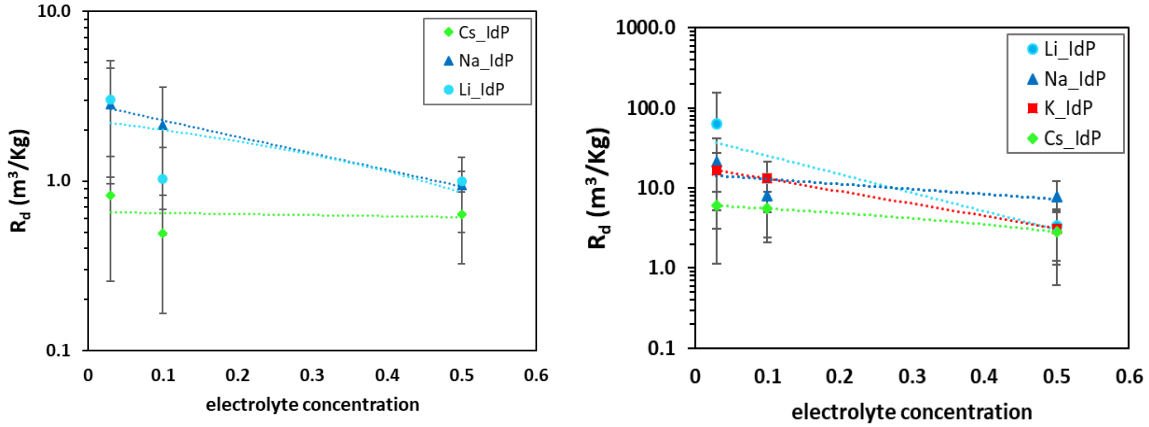


*Figure 11: $R_d$ values of $^{57}Co^{2+}$ (left) and $^{65}Zn^{2+}$ (right) as a function of electrolyte concentration (mol/l).*

### Surface diffusion

In terms of structure, we would expect the formation of complexes to follow a specific order based on ionic radii and hydration energies. Specifically, this order would be $Cs^+$, $K^+$, $Na^+$, $Li^+$ starting from the surface of illite and extending to the diffuse layer. Accordingly, we would expect a gradual diminishing concentration of the mobile species in the diffuse layer from Li to Cs illite leading to a decrease of their contribution to the measured flux. However, the findings so far (Fig 12) have divided the homoionic forms of illite into two groups: one comprising Li and Na_IdP and the other comprising K and Cs_IdP. This aligns with the observation made by Bourg et al. in 2017, where $K^+$ and $Cs^+$ were found to prefer the ditrigonal cavities of the siloxane surface (2.5-3.5 Å from z=0) of clay (muscovite), while $Li^+$ and $Na^+$ prefer the triad of surface oxygen of the tetrahedral sheet (2-2.5 Å from z=0). This suggests that the effect of ionic radii and coordination number may, to some extent, screen out the impact of hydration energy. The results obtained in the present study and the calculation of the surface diffusion index $\varphi$ (Fig 12) indicate the effect of the cationic loading in illite on the surface diffusion ratio with the following order for both Zn and Co tracers $\varphi_{Li\_IdP} \approx \varphi_{Na\_IdP} > \varphi_{K\_IdP} > \varphi_{Cs\_IdP}$.

To ensure a more comprehensive understanding of the diffusion mechanism and to avoid drawing incorrect conclusions, it is essential to interpret the combined sorption and diffusion parameters in terms a speciation model. This will enable us to gain insight into the distribution of mobile surface complexes within the electrical double layer. Additionally, further investigation of the anion exclusion phenomena can shed light on the impact of the EDL on the structure.

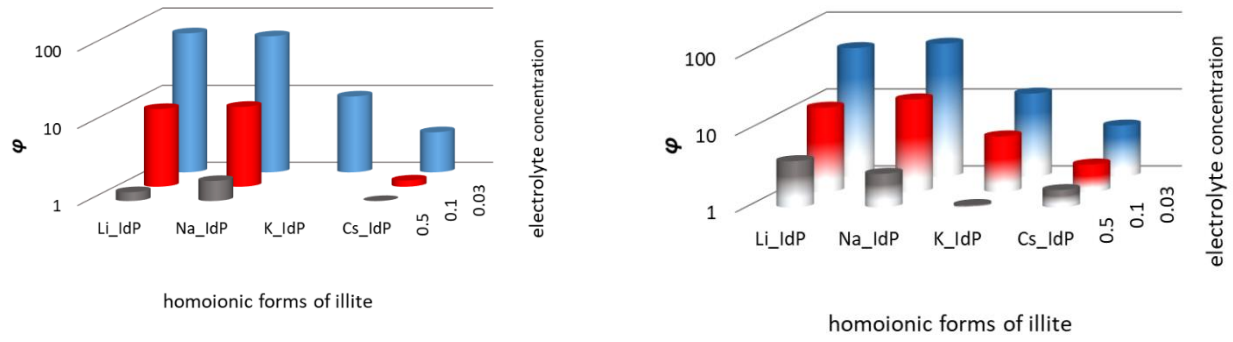


*Figure 12: φ values for $^{57}Co^{2+}$ (left) and for $^{65}Zn^{2+}$ (right).*

## Conclusions

The present investigation focuses on understanding the mechanisms behind surface diffusion, particularly in relation to the hydration behaviour of various cations and their impact on equilibrium distribution within the stern and diffuse layers of clay minerals.

Key finding from the experimental results is the effect of the cation loading on the $D_e$ values for both transition metals. A possible explanation for this observation could be that this selectively binding of cations has a clear influence on the surface negative charge shielding. More specifically, the extent of surface charge neutralization could depend on the enthalpy of hydration of the cation. Cations characterized by lower hydration enthalpies tend to compensate a higher degree of the clay's negative charge closer to the surface (inner-sphere complexation in the Stern layer). This results in a reduced degree of surface charge neutralization taking place within the diffuse layer, thus leading to reduced mobile species and lower Donnan volume. Contrary, a cation possessing a higher enthalpy of hydration can bring about the opposite effect.

Moreover, from the HTO experiments can be observed that the preferential bonding sites (Li and Na on triad oxygen and K and Cs on hexagonal cavities) on the clay surface, have no effect on the microstructure.

Any possible differences on the calculated G factor will be within the range of the experimental uncertainties among the 4 homoionic forms of illite.

The outcomes derived from the sorption distribution values are noteworthy showing the effect of cation loading: In the case of $^{57}$Co we can again distinguish the 2 groups (1 trend of Li and Na and the other of Cs). Conversely, the discrimination between such groupings is less evident in the case of $^{65}$Zn.

For a more in-depth interpretation of the results more information may be needed, such as detailed sorption studies in which the individual contribution of the planar and edge type binding sites would be investigated – using Li, K and Cs homoionic forms of illite.

Conclusively as for surface diffusion, the structure of cations suggests an expected order of complex formation affected by the binding site and the corresponding hydration enthalpies of the index cation, leading to a predicted gradual diminishment of mobile species enrichment in the diffuse layer from Li to Cs illite. However, the study divides the homoionic forms of illite into two groups (Li and Na_IdP versus K and Cs_IdP), which suggests that factors like ionic radii and coordination number might moderate the impact of hydration energy.

## References

Appelo C. A. J., Van Loon L. R. and Wersin P. (2010) Multicomponent diffusion of a suite of tracers (HTO, Cl, Br, I, Na, Sr, Cs) in a single sample of Opalinus Clay. *Geochimica et Cosmochimica Acta* **74**, 1201-1219.

Aylmore L. A. G., Sills I. D. and Quirk J. P. (1970) Surface Area of Homoionic Illite and Montmorillonite Clay Minerals as Measured by the Sorption of Nitrogen and Carbon Dioxide. *Clays and Clay Minerals* **18**, 91-96.

Bourg I. C., Lee S. S., Fenter P. and Tournassat C. (2017) Stern Layer Structure and Energetics at Mica-Water Interfaces. *J Phys Chem C* **121**, 9402-9412.

Bradbury M. H. and Baeyens B. (1997) A mechanistic description of Ni and Zn sorption on Na-montmorillonite .2. Modelling. *Journal of Contaminant Hydrology* **27**, 223-248.

Bradbury M. H. and Baeyens B. (2009) Sorption modelling on illite Part I: Titration measurements and the sorption of Ni, Co, Eu and Sn. *Geochimica Et Cosmochimica Acta* **73**, 990-1003.

Choi J. W. and Oscarson D. W. (1996) Diffusive transport through compacted Na- and Ca-bentonite. *Journal of Contaminant Hydrology* **22**, 189-202.

Glaus M. A., Frick S. and Van Loon L. R. (2020) A coherent approach for cation surface diffusion in clay minerals and cation sorption models: Diffusion of Cs+ and Eu3+ in compacted illite as case examples. *Geochimica et Cosmochimica Acta* **274**, 79-96.

Glaus M. A., Frick S. and Van Loon L. R. (2021) Competitive Effects of Cations on the Diffusion Properties of Strongly Sorbing Trace Cations in Compacted Illite and Opalinus Clay. *Acs Earth Space Chem* **5**, 2621-2625.

Glaus M. A., Rossé R., Van Loon L. R. and Yaroshchuk A. E. (2008) Tracer diffusion in sintered stainless steel filters: measurement of effective diffusion coefficients and implications for diffusion studies with compacted clays. *Clays and Clay Minerals* **56**, 677-685.

Glaus M. A., Aertsens M., Maes N., Van Laer L. and Van Loon L. R. (2015a) Treatment of boundary conditions in through-diffusion: A case study of (85)Sr(2+) diffusion in compacted illite. *J Contam Hydrol* **177-178**, 239-248.

Glaus M. A., Aertsens M., Appelo C. A. J., Kupcik T., Maes N., Van Laer L. and Van Loon L. R. (2015b) Cation diffusion in the electrical double layer enhances the mass transfer rates for Sr2+, Co2+ and Zn2+ in compacted illite. *Geochimica et Cosmochimica Acta* **165**, 376-388.

Kosakowski G., Churakov S. V. and Thoenen T. (2008) Diffusion of Na and Cs in montmorillonite. *Clays and Clay Minerals* **56**, 190-206.

Mahler J. and Persson I. (2012) A Study of the Hydration of the Alkali Metal Ions in Aqueous Solution. *Inorg Chem* **51**, 425-438.

Marques Fernandes M., Ver N. and Baeyens B. (2015) Predicting the uptake of Cs, Co, Ni, Eu, Th and U on argillaceous rocks using sorption models for illite. *Applied Geochemistry* **59**, 189-199.

Marry V. and Turq P. (2003) Microscopic simulations of interlayer structure and dynamics in bihydrated heteroionic montmorillonites. *J Phys Chem B* **107**, 1832-1839.

Melkior T., Gaucher E. C., Brouard C., Yahiaoui S., Thoby D., Clinard C., Ferrage E., Guyonnet D., Tournassat C. and Coelho D. (2009) Na+ and HTO diffusion in compacted bentonite: Effect of surface chemistry and related texture. *J Hydrol* **370**, 9-20.

Sanchez F. G., Van Loon L. R., Gimmi T., Jakob A., Glaus M. A. and Diamond L. W. (2008) Self-diffusion of water and its dependence on temperature and ionic strength in highly compacted montmorillonite, illite and kaolinite. *Applied Geochemistry* **23**, 3840-3851.

Teppen B. J. and Miller D. M. (2006) Hydration energy determines isovalent cation exchange selectivity by clay minerals. *Soil Science Society of America Journal* **70**, 31-40.

# 6. Diffusion of $^{57}$Co tracer in compacted vermiculite, variation of grain size

D. Zerva[1,2], S. Churakov[1,2], M. Glaus[1]
*[1]PSI, Villigen PSI, Switzerland*
*[2]University of Bern, Bern, Switzerland*

E. Ferrage, F. Hubert, E. Tertre
*IC2MP, Poitiers, France.*

## Introduction

Surface diffusion phenomena in clay minerals have been extensively investigated in numerous studies. These studies have documented the diffusive transport of surface-associated cationic species at the basal surfaces of negatively charged clay minerals, leading to a higher effective diffusion coefficient ($D_e$) for cations in compacted systems. This behaviour has significant implications for the long-term safety assessment of clay barrier systems, which have been chosen as host rocks for the disposal of radioactive waste by several countries. As a result, gaining a comprehensive understanding of the transport mechanisms within clays and clay rocks is of great importance for ensuring the efficiency and safety of these waste disposal systems.

For the explanation of surface diffusion, the 2SPNE-SC/EDL (two site protolysis non-electrostatic surface complexation and electrical double layer) model has been used (Glaus et al., 2020). According to this model, immobile surface complexes are formed at the edge surfaces and within the EDL (planar surface), immobile surface complexes are bound in the Stern layer, while mobile species are located in the diffuse layer (Fig.1).

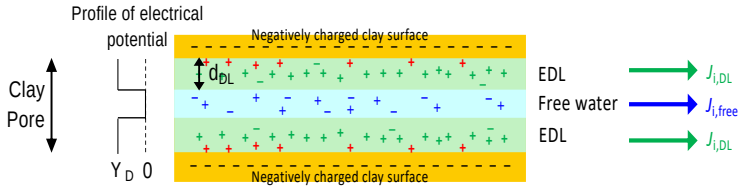


*Figure 1: Left: Schematic representation of the Donnan approach for an EDL at the planar clay surfaces. Species in blue (ions in free pore water) and green color (surface complexations in the Donnan volume) are assumed mobile, while red surface complexes are considered as immobile in the Stern layer. The Donnan potential ($\Psi_D$), the negative charge of the clay, is zero at the diffuse layer-pore water interface (neutralization of the negatively charged clay surface). Scheme adopted from Eurad D5_1_SOTA Future)*

According to equation 1 the distribution of cations within the EDL (Stern and diffuse layer) is influenced by several parameters describing the solution chemistry and clay surface properties. Additionally, the thickness of the Donnan layer ($d_{DL}$) or diffuse layer, establishes the formal volumetric division between the bulk water and the diffuse layer domain and consequently affects the distribution ratio between the mobile species ($\frac{C_{DL}}{C_{free}}$)

$$D_e = \varepsilon \frac{D_w}{G} \left(C_{free} + \frac{C_{DL}}{C_{free}} q_n\right) \quad (1)$$

where $G$ is the geometrical factor related to the microstructure (tortuosity) of the clay (-), $D_w$ the diffusion coefficient of in bulk water, $C_{free}$ the concentration of a species in the pore water, $C_{DL}$ the concentration of the species in the diffuse layer and $\varepsilon$ the porosity of the porous medium. The $q_n$ (-) is a molecular mobility factor (fit value) of the species.

Surface diffusion has been observed and studied from chemical point of view i) in illite (non swelling) clay mineral, by varying the solution parameters (Glaus et al., 2020, 2021; Glaus et al., 2015) or the cationic loading (Zerva et al., ongoing study – see other contribution this volume) and ii) in Na_bentonite by studying

the diffusion of $Na^+$ as a function of the external solution ionic strength (Bourg et al., 2008) and Na_montmorillonite in a high compaction and by studying the $Na^+$ and $Sr^{2+}$ diffusion as a function of ionic strength (Glaus et al., 2007).

On the other hand, bentonite has been studied also from geometrical point of view (Melkior et al., 2009). The presence of a gel phase in Na_bentonite and its absence in the aggregated Cs_bentonite has been observed. The absence of this gelly phase in Cs_bentonite results in a less tortuous diffusion path leading to a higher $D_e$ value for the HTO and a lower $D_e$ for the $^{22}Na^+$ in comparison to Na_ bentonite. The authors introduced the surface diffusion ratio $\varphi$, which is a normalization of the $D_e$ of a given cation to the $D_e$ of an uncharged species (HTO), to quantify the extent of the phenomenon. The results revealed the presence of surface diffusion because $\varphi$>1 for Na and Ca_bentonite and almost $\varphi \cong 1$ for Cs_bentonite.

According to equation 2, if the ratio of the diffusion coefficients in bulk water ($\frac{D_{w(HTO)}}{D_{w(cation)}}$) under given conditions is higher than one then the ratio between the $D_e$*(cation)* and $D_e$*(HTO)* will define the presence (for $\varphi > 1$) or not of the surface diffusion phenomenon.

$$\varphi = \frac{D_e(cation)}{D_e(HTO)} * \frac{D_w(HTO)}{D_w(cation)} \quad (2)$$

Which is in agreement with the description of surface diffusion of Glaus et al (2015):

$$\frac{\mathrm{D_e(cation)}}{\mathrm{D_e(HTO)}} > \frac{\mathrm{D_w(cation)}}{\mathrm{D_w(HTO)}} \quad (3)$$

Moreover, the effect of different grain sizes on the microstructure has been studied on Na_vermiculite (Tertre et al., 2018), a swelling clay mineral with a structure similar to smectite. According to these results in the smallest grain fractions (0.1-0.2 and 1-2 µm) the diffusion of HDO does not present any significant difference. However, this is not the case for the higher grain size of 10-20 µm where the $D_e$ of HDO is approximately 2 times smaller than those obtained for the finest size fraction. Another significant finding is the difference of (theoretical) CEC values (Table 1) among the different particles (Reinholdt et al., 2013) as well as the increasing amount of desorbed $Cs^+$ with the decrease of the grain size (Dzene et al., 2015).

So far, the effect of the grain size of a clay particle on the surface diffusion has been demonstrated on Na_vermiculite using $^{22}Na^{2+}$ (S. Savoye, S. Lefevre. EURAD D5_4&6 – see contribution further in this volume) but it is still an open question if the strongly sorbing radionuclides can also be affected.

In this study diffusion experiments were performed with vermiculite a 2:1 layer structure clay mineral of smectite group containing hydrated exchangeable cations, primarily Ca and Mg, in the interlayer (figure 2). The in diffusion – profile analysis technique was applied using 3 grain fractions of conditioned (Na_vermiculite) forms (Tertre et al., 2018) and $^{57}Co^{2+}$ tracer. The obtained experimental results allow the evaluation of the particle size effect on $D_e$ values of $Co^{2+}$ and their influence on the surface diffusion phenomena.

*Table 6: Theoretical CEC values for different grain size of vermiculite (Reinholdt et al., 2013).*

| Grain size (µm) | Total CEC (meq/100 g) | External CEC (edge+basal) (meq/100g) |
|---|---|---|
| 10-20 | 214 | < 1 |
| 1-2 | 221 | 11 |
| 0.1-0.2 | 258 | 70 |

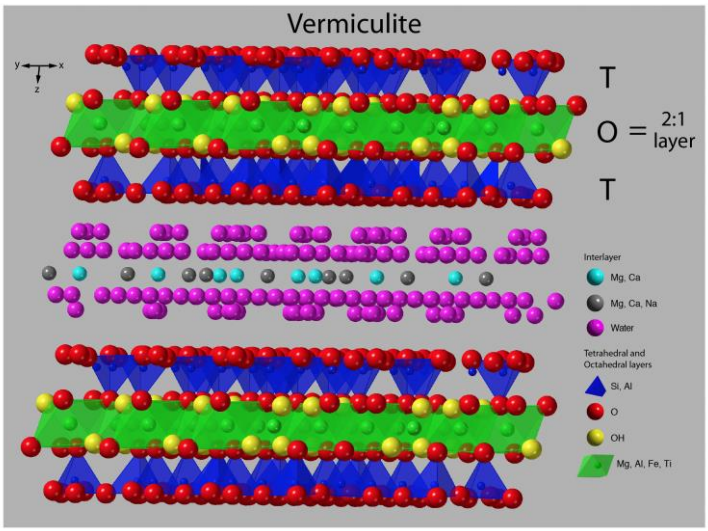


Figure 2: Atomic structure model of vermiculite (taken from usgs.gov).

## Materials and methods

### Materials

Vermiculite samples from Santa Olalla (Huelva, Spain) were received from University of Poitiers in France in three different size fractions of particles, i.e., 0.1−0.2, 1−2, and 10−20 µm. These particles were obtained using a previously established protocol based on the sonication of vermiculite macrocrystals (1−4 mm) immersed in water (Tertre et al., 2018). The conversion procedure to Na_vermiculite is described elsewhere (Tertre et al., 2018).

### In diffusion – Profile analysis

Approximately 0.2 g of Na_vermiculite was used and compacted to cylindrical samples (diameter 0.5 mm, length 4-5 mm) at a dry bulk density of 1.5 g/ml into 6 Membrane Confined Diffusion Cells. From each grain size, two compacted samples were prepared and labeled A1 and A2 for the 0.1-0.2 µm grain size, B1 and B2 for the 1-2 µm and C1 and C2 for the 10-20 µm. Before the start of in diffusion of $^{57}Co^{2+}$ each compacted sample was immersed into 0.1 M NaCl for the fully saturation of them. The pH is passively adjusted by equilibration of clay and solution; pH monitoring took place. Slight changes of the pH were observed during the whole duration of the experiment. The pH values at the end of the saturation (0.1 M NaCl) were ~ 6.5, at the beginning of the in diffusion of $^{57}Co^{2+}$ ~ 7.2 and at the end of in diffusion again at ~ 6.7. The experiments were carried out under atmospheric conditions at a temperature of 21-23 $^{o}$C and each cell was

immersed in the NaCl solution with an initial tracer concentration of 100 Bq/ml of carrier-free $^{57}Co^{2+}$ tracer and an added background concentration of stable-isotope $Co^{2+}$ of 1 nM.

### Simulations

All of the diffusion experiments with illite were evaluated and the calculations of the effective diffusion coefficient $D_e$ and sorption distribution coefficient $R_d$ values were obtained with Matlab® parameter optimization routine. This inverse model uses Comsol Multiphysics ® model extracted as a Matlab script. Detailed information about the numerical procedures can be found in Glaus et al. (2020).

## Results and Discussion

### Diffusion of $^{57}Co^{2+}$

Fig. 3 shows the results for each sample belonging to the different size fractions (A1, B1, C1). The results between tracer reservoir depletion and the profile analysis are fully consistent. The strongest depletion in the reservoir and the higher $R_d$ values are observed at the A1 sample with the smallest grain size (0.1-0.2 µm). The difference in diffusion depth between the 2 smallest grain sizes is rather unclear but between these 2 and the largest grain size is evident (Fig. 3). The best-fit parameter values for $D_e$ and $R_d$ values obtained with Matlab parameter optimization are listed in Table 2.

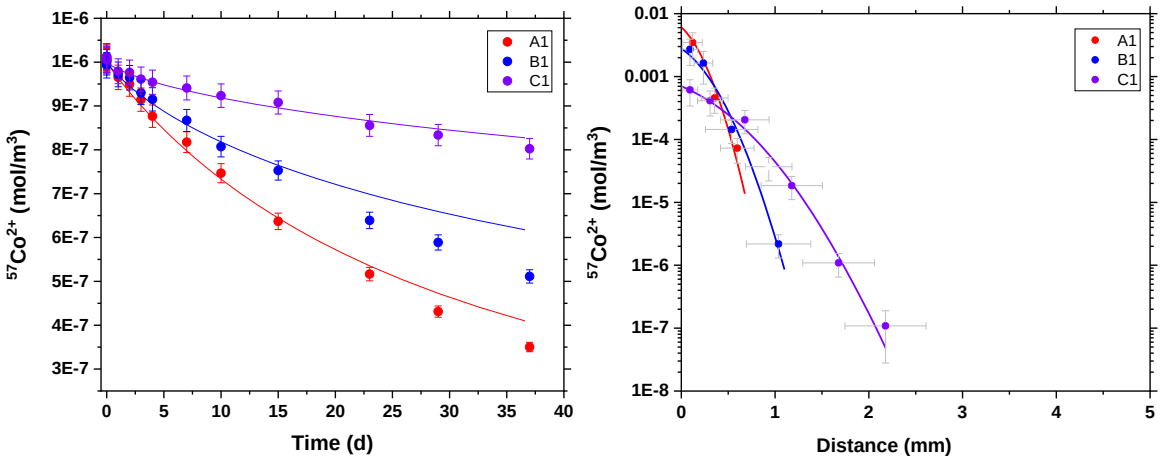


*Figure 3: left image: the tracer depletion follows the reverse order of the grain size: decreasing the grain size, the tracer depletion increase. Right image: The diffusion depth of different grain size. A1= 0.1-0.2 µm, B1= 1-2 µm, C1=10-20 µm.*

*Table 2: Experimental condition and best-fit parameter values for vermiculite from the diffusion experiments with $^{57}Co^{2+}$ with a dry bulk density of 1500 (+/-50) kg/m$^3$ and $D_e$ for the filters 2x10$^{-10}$ m$^2$/s.*

| Experiment | Grain size | Electrolyte solution | Background concentration | $D_e$ | $R_d$ |
|---|---|---|---|---|---|
| | µm | | M | m$^2$/s | m$^3$/Kg |
| A_1 | 0.1-0.2 | NaCl | 0.1 | $2.0^{3.4}_{1.1} \times 10^{-10}$ | $17.3^{31.8}_{9.4}$ |
| B_1 | 1-2 | NaCl | 0.1 | $8.5^{16.0}_{4.6} \times 10^{-11}$ | $4.0^{8.1}_{2}$ |
| C_1 | 10-20 | NaCl | 0.1 | $4.5^{5.9}_{3.5} \times 10^{-11}$ | $0.7^{0.9}_{0.5}$ |

The superscripts and subscripts of the $D_e$ and $R_d$ values are respectively the higher and the lower boundary values.

The results of $^{57}Co^{2+}$ in vermiculite reveal that although the $D_e$ value of A is distinct from the $D_e$ values of B and C in absolute terms, they are nevertheless within the range of uncertainty. (Fig. 4 left). The same applies to the normalized values of $D_e$ of HDO, (Tertre et al., 2018) to the present sample porosities, according to the Archie's Law under the given experimental conditions (Fig. 4 right).

The difference that can be observed is that the $D_e$ for HDO for the 2 smallest grain sizes exhibit similarity to each other and differ from the larger one. Conversely, for the case of $^{57}Co^{2+}$ the $D_e$ value of 0.1-0.2 µm is distinguished from the $D_e$ values of 1-2 and 10-20 µm. It is important to note that the observed differences in $D_e$ values of $^{57}Co^{2+}$ are partially obscured by the associated uncertainties.

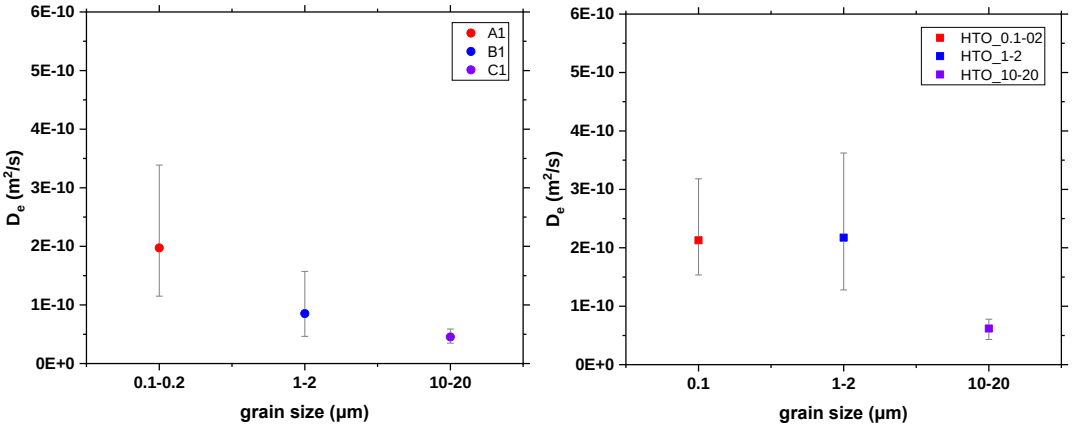


*Figure 4: On the left the $D_e$ values of $^{57}Co^{2+}$ and on the right the $D_e$ normalized values for HDO. A1= 0.1-0.2 µm, B1= 1-2 µm, C1=10-20 µm.*

The $R_d$ best fit values are negatively correlated to the grain size (fig 5), increasing the grain size, the sorption distribution coefficient ($R_d$) decreases.

The diffusion profile follows the order A1≈B1<C1 and a corresponding trend of the $D_e$ values would be expected. However, the order of the $D_e$ values is $D_e$_A1>$D_e$_B1>$D_e$_C1. Based on our results, we cannot decide whether sorption of $Co^{2+}$ is governed by planar or edge surface.

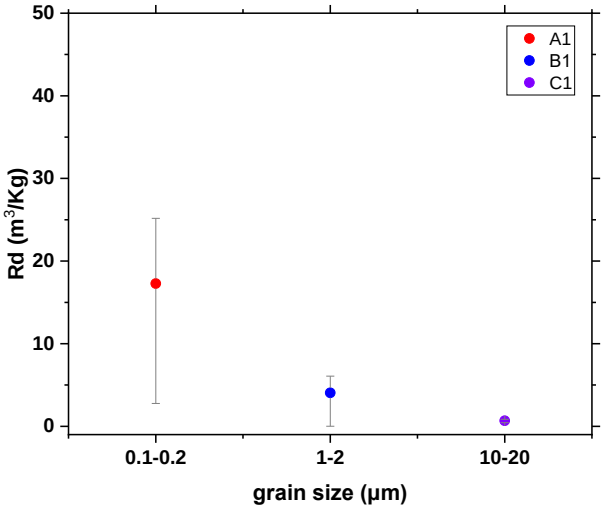


*Figure 5: Sorption distribution values of $^{57}Co^{2+}$ in vermiculite.*

## Surface diffusion

A prerequisite for the calculation of surface diffusion (eq. 2) is that the $D_e$ of HTO and a cation are derived from experimental data obtained from compacted clay samples having the same (or similar) porosity. For that the $D_e$ values of HTO (Tertre et al 2018) were normalized to the porosity of the present samples. These

normalized values were calculated using Archie's Law and with the assumption that the material-specific constant *m* (1.81) is the same for all grain sizes.

According to the calculated *φ* values (surface diffusion index) no significant difference can be noticed among the 3 grain sizes. The *φ* values are 3, 1, 2 for the A, B1 and C1 samples respectively (Fig. 6). The presence of the surface diffusion has been qualitatively demonstrated as in the case of $^{22}Na^{2+}$ (S. Savoye, S. Lefevre. EURAD D5_4&6 – see contribution further in this volume). In order to have a proper estimation of surface diffusion effects, it is suggested that selectivity studies for both of $Na^{+}$ and $Co^{2+}$ to be done and in continuation speciation calculations for the determination of the $(\frac{C_{DL}}{C_{free}})$ ratio.

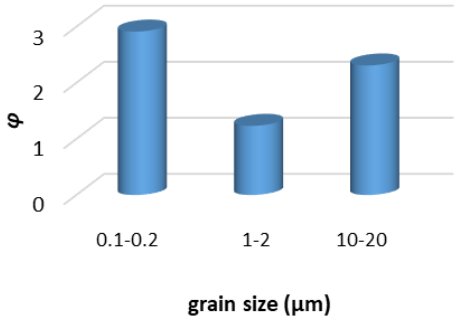


*Figure 6: φ values for $^{57}Co^{2+}$ in vermiculite.*

## Conclusions

The present investigation demonstrate, for the first time in the scientific literature, the importance and extend of surface diffusion of strongly sorbing radionuclides in compacted vermiculite. The $D_e$ values of $Co^{2+}$ exhibit a nearly identical pattern in both 0.1-0.2 and 1-2 µm grain size, aligning closely with the normalized $D_e$ values of the uncharged HDO. The observed phenomenon is limited compared to that observed in illite, as reported by Zerva et al (EURAD Deliverable 5.4 & 5.6: FUTuRE, chapter 3).

The surface diffusion can be influenced by the geometrical properties of the clay (G factor) or by the distribution ratio of the mobile species $(\frac{C_{DL}}{C_{free}})$. Although the surface diffusion is present across all grain sizes and based on the available evidence geometry is the most influencing factor, the extent to which grain size or the mobile distribution ratio affects this phenomenon remains unclear.

For a more in-depth interpretation of the results more information may be needed, such as detailed sorption studies in which the individual contribution of the planar and edge type binding sites would be investigated – using again different size fractions of vermiculite. The different size fractions exhibit different ratios of basal and edge surfaces (as demonstrated in the literature (Reinholdt et al., 2013)). Consequently, their incremental contribution to the overall sorption behaviour is also expected to vary. All these details are presently not known.

## References

Bourg I. C., Sposito G. and Bourg A. C. M. (2008) Modeling the diffusion of Na in compacted water-saturated Na-bentonite as a function of pore water ionic strength. *Applied Geochemistry* **23**, 3635-3641.

Dzene L., Tertre E., Hubert F. and Ferrage E. (2015) Nature of the sites involved in the process of cesium desorption from vermiculite. *J Colloid Interf Sci* **455**, 254-260.

Glaus M. A., Frick S. and Van Loon L. R. (2020) A coherent approach for cation surface diffusion in clay minerals and cation sorption models: Diffusion of Cs+ and Eu3+ in compacted illite as case examples. *Geochimica et Cosmochimica Acta* **274**, 79-96.

Glaus M. A., Frick S. and Van Loon L. R. (2021) Competitive Effects of Cations on the Diffusion Properties of Strongly Sorbing Trace Cations in Compacted Illite and Opalinus Clay. *Acs Earth Space Chem* **5**, 2621-2625.

Glaus M. A., Baeyens B., Bradbury M. H., Jakob A., Van Loon L. R. and Yaroshchuk A. (2007) Diffusion of Na-22 and Sr-85 in montmorillonite: Evidence of interlayer diffusion being the dominant pathway at high compaction. *Environmental Science & Technology* **41**, 478-485.

Glaus M. A., Aertsens M., Appelo C. A. J., Kupcik T., Maes N., Van Laer L. and Van Loon L. R. (2015) Cation diffusion in the electrical double layer enhances the mass transfer rates for Sr2+, Co2+ and Zn2+ in compacted illite. *Geochimica et Cosmochimica Acta* **165**, 376-388.

Melkior T., Gaucher E. C., Brouard C., Yahiaoui S., Thoby D., Clinard C., Ferrage E., Guyonnet D., Tournassat C. and Coelho D. (2009) Na+ and HTO diffusion in compacted bentonite: Effect of surface chemistry and related texture. *J Hydrol* **370**, 9-20.

Reinholdt M. X., Hubert F., Faurel M., Tertre E., Razafitianamaharavo A., Francius G., Prêt D., Petit S., Béré E., Pelletier M. and Ferrage E. (2013) Morphological properties of vermiculite particles in size-selected fractions obtained by sonication. *Applied Clay Science* **77-78**, 18-32.

Tertre E., Savoye S., Hubert F., Prêt D., Dabat T. and Ferraget E. (2018) Diffusion of Water through the Dual-Porosity Swelling Clay Mineral Vermiculite. *Environmental Science & Technology* **52**, 1899-1907.

EURAD (2021) Deliverable D5_1 State of the Art report on the understanding of radionuclide retention and transport in clay and crystalline rocks - Chapter 3.1: Transport processes in host rocks.

EURAD (2023) Deliverable D5.4 & 5.6: FUTuRE – Final technical report on radionuclide mobility in compacted clay systems and reversibility of sorption. Chapter 3. Zerva et al: Diffusion and retention of Co and Zn surface complexes in compacted illite preloaded with different cations.

EURAD (2023) Deliverable D5.4 & 5.6: FUTuRE – Final technical report on radionuclide mobility in compacted clay systems and reversibility of sorption. Chapter 5. S. Savoye, S. Lefevre: Influence of geometry and saturation degree on radionuclide mobility in clay.

# 7. Electrochemically controlled sorption experiments of Fe(II) with Montmorillonite

M. Breckheimer, S. Amayri, J. Lohmann, M. Matejcek, M. Maxeiner, E. Schaffner, T. Reich
*Johannes Gutenberg University, Mainz, Germany*

A. Rudolph
*Heidelberg University, Heidelberg, Germany*

## Abstract

This study describes an approach in enhancing the geochemical control in sorption experiments by an electrochemical stabilization of reduced metal species relevant for the disposal of nuclear waste in deep geological repositories. Based on the experimental setup and approach described by Soltermann et al. (2014) an electrochemical cell was constructed, manufactured, commissioned and characterized, adapted to sorption experiments with an in situ sampling for determining the equilibrium concentration of the metal species.

In initial studies the experimental setup was further characterized and optimized with a first application in sorption experiments of Fe(II) with the clay mineral montmorillonite at pH 6.2 in 0.1 M $NaClO_4$. Analytical access was established in a tracer approach ($^{55}Fe$) with liquid scintillation counting (LSC) and complementary inductively coupled plasma mass spectrometry with an octopole reaction system (ORS-ICP-MS), giving access to the total Fe content.

Competing sorption effects, significantly influencing the performance of the experimental setup, were identified and are discussed in the following. Their resolution or mitigation are a prerequisite for applying this experimental approach in sorption studies of relevant, reduced actinide species.

## Introduction

The mobility of radionuclides in a geological repository, eventually released of their waste forms, is controlled by retention and migration processes with the different components in a multi-barrier repository concept. These processes are dependent on the individual aqueous speciation of the radionuclides, controlled by the geochemical conditions developing or prevailing in the post-closure phase in the respective barrier material resp. its pore or ground water. Geochemical conditions are defined and partly interconnected by pH, $pCO_2$, oxidation-reduction potential (ORP resp. Eh), ionic strength, pore water composition, mineral surfaces in contact with the aqueous phase (Churakov et al., 2020; Pearson et al., 2003) and microbial activity, governing the fate of mobilized radionuclide species through speciation and solubility, sorption and precipitation.

Clay rock, considered as a potential host rock for a deep geological repository, exhibits structural and compositional features controlling its geochemical conditions and contributing to its suitability as a host rock retaining the radionuclide inventory from the biosphere. Besides transport related properties as low hydraulic conductivity and high retention capacity, effectively limiting transport to molecular diffusion, clay rocks and their anoxic pore waters exhibit in situ reducing conditions mainly controlled by the redox couple $FeS_2/SO_4^{2-}$ (Pearson et al., 2003). An expected anoxic corrosion of steel canisters, initially containing the high-level radioactive waste, will further release ferrous iron contributing to the reducing conditions (Churakov et al., 2020). These conditions will lead to the formation of reduced species of the eventually released radionuclides, exhibiting a high retention due to sorption on mineral phases or precipitation due to low solubilities of the respective solid phases.

In studying the mobility of these reduced radionuclides, e.g., the relevant tri- and tetravalent actinide species, it is desirable to reproduce and control the corresponding geochemical conditions as accurate and comprehensive as possible in the experiment. In laboratory experiments, with a potentially necessary

reduced complexity concerning the geochemical conditions, the reducing conditions are accessible by stabilizing the relevant reduced actinide species through an addition of reducing agents like dithionite or hydroquinone (Neck et al., 2007). Another approach and without adding an additional chemical component to the system is based on an electrochemical technique, motivated and described by Aeschbacher et al. (2010) in probing the redox-activity of humic substances or of Fe-bearing clay minerals by nonmediated or mediated electrochemical approaches (Sander et al., 2015).

Soltermann et al. (2014) extended this analytical approach by inducing strongly reducing conditions through an active electrolysis in a dedicated electrochemical cell, stabilizing a ferrous iron species in a simultaneous sorption experiment with clay minerals. Mancini et al. (2021) subsequently applied this approach in a modified setup studying sorption of Fe(II) in cementitious systems. The approach of Soltermann et al. (2014) motivated the here reported study with transferring this experimental approach eventually to the investigation of reduced actinide species in sorption experiments with relevant clay rock constituting mineral phases. Ferrous iron is also of interest due to its occurrence via anoxic steel corrosion, its contribution to the reducing conditions and potential sorption competition with relevant radionuclide species.

The emphasis of this study was on the construction, commissioning and initial characterization of an electrochemical cell (Aeschbacher et al., 2010; Soltermann et al., 2014), leading to first sorption experiments of Fe(II) with clay mineral phases, trying to reproduce the results of Soltermann et al. (2014) validating the operation of the electrochemical cell.

Several issues concerning the operation of the electrochemical cell in this setup and sample system were identified, some remaining open, with the need to be resolved or mitigated before advancing this experimental setup to the investigation of reduced actinides in experiments studying their mobility with relevant barrier materials.

## Materials & methods

### Electrochemical cell

For an enhanced control of the geochemical conditions and electrochemical stabilization of reduced elemental species in sorption experiments, an electrochemical cell, motivated and based on the cell described by Soltermann et al. (2014), was constructed, manufactured, commissioned (Maxeiner, 2020; Matejcek, 2020) and subsequently characterized and optimized (Schaffner, 2021; Rudolph, 2022).

The electrochemical cell Figure 1 consists of two compartments (PEEK), separated by a membrane filter. The bulk compartment, hosting the electrochemical setup and accepting about 77 mL of in total 100 mL of electrolyte solution resp. suspension, contained the individual clay mineral suspension in the sorption experiments, whereas the attached sampling compartment (with approx. 23 mL) should allow the sampling of the equilibrium concentration of the analyte. The bulk compartment is stirred by a magnetic stirrer. Both compartments exhibit an opening for sampling and probing the pH value. pH measurements (BlueLine 16 pH micro combination electrode, SI Analytics, Mainz, Germany; inoLab pH/Cond 720, WTW, Weilheim, Germany) were conducted with interrupting the electrolysis. The electrolyte of the pH electrode was changed to 3 M NaCl to prevent a precipitation of poorly soluble $KClO_4$ in contact with the intended background electrolyte $NaClO_4$. Necessary pH modifications were conducted with diluted $HClO_4$ (AnalaR NORMAPUR, VWR International, Leuven, Belgium) and NaOH (carbonate-free, VWR International).

Different membrane materials were applied and studied during the characterization of the electrochemical cell: cellulose nitrate filters (pore size 0.45 µm, Ø 47 mm, Sartorius Stedim Biotech GmbH, Göttingen, Germany) and track-etched polycarbonate membrane filters (Isopore membrane filters, pore sizes 0.2 µm and 0.4 µm, Ø 47 mm, Merck Millipore, Merck KGaA, Darmstadt, Germany), ultimately leading to the application of polycarbonate membrane filters (pore size 0.2 µm) in sorption experiments, guaranteeing a retention of the suspended clay particles in the bulk compartment.

The electrochemical setup (cf. Figure 1) consisted of a three-electrode setup of working (WE), reference (RE) and counter electrodes (CE). Following Soltermann et al. (2014), the working electrode material was chosen as glassy carbon (Sigradur G, HTW Hochtemperatur-Werkstoffe GmbH, Thierhaupten, Germany)

with a suitable working voltage window with its overpotential for hydrogen evolution (Mabbott, 2020). Reference and counter electrode were prepared in-house with a Ag wire, electrolytically coated with AgCl, resp. a coiled Pt wire (Goodfellow Cambridge Ltd., Huntingdon, England), both enclosed in glass tubes, closed by an upper cap (flange stoppers, Saint-Gobain Performance Plastics Verneret, Charny, France) and a mounted porous frit (Corning Vycor resp. Schott Coralpor, BASi Research Products, West Lafayette, IN, USA), attached to the lower glass tube opening with a heat shrink tube (PTFE). The inner electrolyte was chosen as 3 M NaCl preventing a potential precipitation of poorly soluble $KClO_4$. The performance of the Ag/AgCl reference electrode used in experiments was regularly verified by measuring the differential potential against commercial Ag/AgCl reference electrodes (MF-2052, BASi Research Products, West Lafayette, IN, USA; Dri-Ref 2, World Precision Instruments, Sarasota, FL, USA), not employed in electrolytical operations. Electrochemical control was achieved using a potentiostat (Wenking HP96 resp. POS2, Bank Elektronik - Intelligent controls GmbH, Pohlheim, Germany).

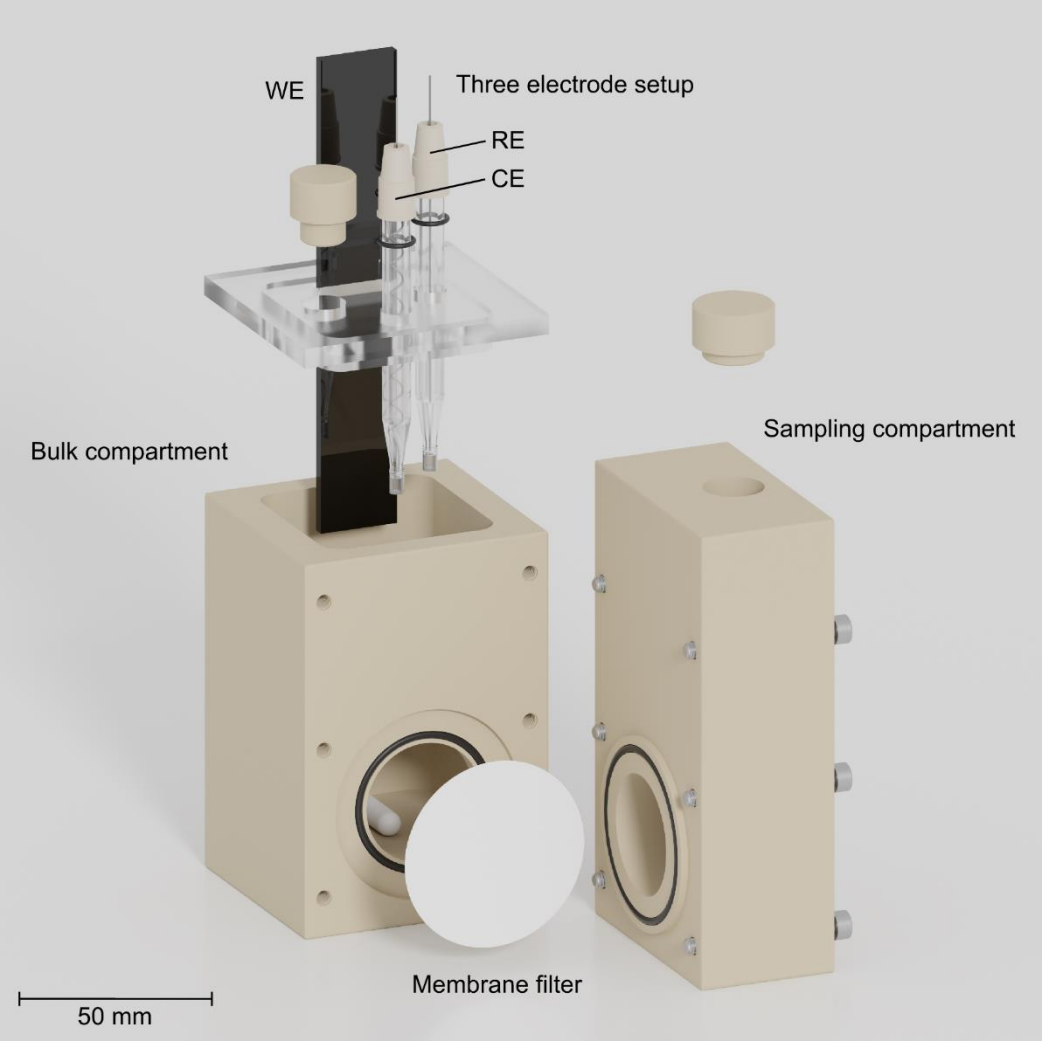


*Figure 1*: *Schematic representation of the electrochemical cell and its components in this study. Construction motivated and based on the cell described in Soltermann et al. (2014). View on detached bulk and sampling compartment, separated by a membrane filter. Bulk compartment with elevated three electrode setup with working (WE), reference (RE) and counter electrodes (CE). A more detailed description can be found in the text. Visualization generated with Blender (2023).*

To allow for a continuous monitoring of applied potential and current and optional control of the potentiostatic operation, a data acquisition and control device (USB-6211, National Instruments, Austin, TX, USA) was adapted to the potentiostats with a custom interface (DAQExpress 5.1, National

Instruments), also including the monitoring of environmental parameters of the inert gas atmosphere ($pO_2$, $pH_2O$). This setup allowed for a flexible development and adaptability of corresponding measurement and control modules for potentiostatic operation including chronocoulometry as well as, optionally, cyclovoltammetry.

A minimal $O_2$ concentration proved essential for the electrochemical operation, necessitating the transfer of the experiment from the initially used benchtop containment unit (soloLAB, Solo Containment, Stockport, UK), operated by manual inert gas purging ($N_2$, subsequently Ar) to a glovebox workstation with a gas purification unit (Ar operated, nominal $O_2$ < 0.1 ppm, ~25°C, UNIlab, M. Braun Intergas-Systeme GmbH, Garching, Germany).

### Clay minerals

Clay minerals were obtained from the Source Clays Repository (The Clay Minerals Society, Purdue University, West Lafayette, IN, USA). Na-montmorillonite (SWy-2, Wyoming, USA), as a potential mineral phase of an engineered clay barrier, was used as sorbent in sorption experiments with Fe(II). To simplify the complexity of interactions expected with Na-montmorillonite, a purification of electrolytes and conditioning of the clay mineral were preceding the sorption experiments (Baeyens and Bradbury, 1995; Baeyens and Bradbury, 1997). $NaClO_4$ ($NaClO_4$ x $H_2O$, for analysis, Merck KGaA, Darmstadt, Germany) electrolyte solutions (Millipore water, 18.2 MΩ cm, Millipore GmbH, Schwalbach, Germany) were purified of potential sorption-competing contaminants by surface complexation with $Al_2O_3$ (Sigma Aldrich, 99.99%), whereas the montmorillonite was conditioned to a homo-ionic Na form, size-fractionated to <0.5 µm and conditioned to the ionic strength of the chosen background 0.1 M $NaClO_4$ electrolyte.

Aliquots (40 mL) of the SWy-2 montmorillonite suspensions were transferred to anoxic conditions by purging the stirred suspensions with Ar for at least 3 h. An evaporative loss was compensated in the following regaining the chosen ionic strength. A determination of the solid-to-liquid ratio ensued.

### Liquid scintillation counting

$^{55}Fe$, employed as a tracer in this study, decays via electron capture with detectable secondary decay radiation of its daughter $^{55}Mn$ emitting X-ray fluorescence radiation and Auger electrons. Liquid scintillation counting (LSC) represents a suitable radioanalytical technique for quantification of this tracer. Due to the monoenergetic nature of Auger electrons and the accompanying X-ray radiation, a modified approach determining the TDCR-based counting efficiency has to be chosen (Hidex, 2021).

The corresponding radioanalytical method was established in our laboratory (Rudolph, 2022) utilizing the liquid scintillation counter Hidex 300 SL (Hidex Oy, Turku, Finland) and the scintillation cocktail Ultima Gold XR (PerkinElmer, Boston, MA, USA). The treatment of efficiency for $^{55}Fe$ with a documented correction factor (Hidex, 2021) was confirmed with the reference scintillation cocktail (Hidex AquaLight+) and the specified activity concentration of the $^{55}Fe$ tracer solution.

### ORS-ICP-MS

A second, complementary analytical technique for the determination of the Fe carrier ($^{nat}Fe$) resp. total Fe concentration was established with inductively coupled plasma mass spectrometry (ICP-MS, Agilent 7500ce resp. 7900, Agilent Technologies, Santa Clara, CA, USA), coupled with an integrated octopole collision/reaction system (ORS). The He collision mode allowed suppressing isobaric polyatomic interferences of $^{56}Fe^+$, e.g., $^{40}Ar^{16}O^+$, crucial for the application of this method in Fe analytics [Maxeiner, 2020; Matejcek 2020].

Measurements were normalized to an added internal Ir-193 calibration standard. Each series of measurements was preceded by determining an external calibration with a series of dilutions of a Fe calibration standard (PlasmaCAL, SCP Science, Quebec, Canada).

### $^{55}$Fe-tracer & carrier

Initial studies made use of an existing $^{55}$Fe tracer solution that was characterized by Maxeiner (2020) and Matejcek (2020) via LSC, UV-Vis spectroscopy and ORS-ICP-MS. The molar ratio of $^{55}$Fe to total Fe was determined to approximately $10^{-6}$, not allowing an access to lower Fe concentrations in sorption experiments. Therefore, an $^{55}$Fe tracer solution with an appropriate molar tracer-to-total ratio of 2.1 x $10^{-2}$ was acquired (NEZ043, PerkinElmer, Boston, MA, USA; initial activity concentration of 1.1 x $10^{6}$ Bq µL$^{-1}$). The tracer was provided as ferric iron dissolved in 0.5 M HCl, but subsequently diluted by a factor of $10^{-3}$ in anoxic 0.5 M $HClO_4$ (Suprapur, Merck KGaA, Darmstadt, Germany) as the stock solution used in this study.

### Membrane diffusion kinetics of Fe(III)

Initial studies, characterizing the electrochemical cell, were done determining the time necessary to reach a distributional equilibrium of the ferrous iron analyte between the bulk and sampling compartment, separated by membrane filters with sub-micron pore sizes. In a first approximation, and without anoxic conditions and not deploying the electrochemical setup, the studied analyte was chosen as ferric iron due to its similar ionic radius, higher charge and potentially associated larger hydration sphere, gaining an upper limit for the necessary equilibration time.

The experiments were conducted under aerobic conditions with preparing a background electrolyte solution of 100 mL of 0.1 M $NaClO_4$ with 0.1% $HNO_3$ (pH~1.7) in the electrochemical cell. Several track-etched polycarbonate membrane filters with pore sizes 0.1 µm, 0.2 µm and 0.4 µm were studied (Isopore membrane filters, Ø 47 mm, Merck Millipore, Merck KGaA, Darmstadt, Germany). Upon adding a $^{55}$Fe(III) tracer solution to the bulk compartment, resulting in an activity concentration [$^{55}$Fe(III)] = 44 kBq L$^{-1}$ and total concentration [Fe(III)] = 5.4 x $10^{-6}$ M, both compartments were sampled time-dependently with small aliquots of 250 µL for up to three days. The samples were radio-assayed by LSC.

The time-dependent evolution of the tracer concentration in the sampling compartment could be modelled with first-order distributional kinetics, deriving a half-life and minimum equilibration time.

### Transport of clay particles through the membrane

Initial sorption experiments of Fe(II) with clay mineral phases and the determination of the equilibrium concentration via ORS-ICP-MS provided an indication of the presence of clay particles in the analyte solution due to non-systematic fluctuations during the measurements (Schaffner, 2021). Since the purification and conditioning of the clay mineral phases results in a particle size fraction <0.5 µm (Baeyens and Bradbury, 1995; Baeyens and Bradbury, 1997; Tan et al., 2017) and the initially chosen polycarbonate membrane filter pore size (0.4 µm) falls only slightly short of this upper particle size limit, a potential clay particle transport through the membrane can not to be excluded.

To investigate this observation, sorption experiments of Fe(II) with montmorillonite (SWy-2) employing different polycarbonate membrane pore sizes (0.2 µm, 0.4 µm) were conducted in an approach simulating the eventually planned sorption experiments under controlled reducing conditions with a duration of approximately two weeks. Contrary to planned isotherm experiments, the analyte concentration is not subsequently increased beginning with a trace concentration, but already initially with an increased concentration [Fe(II)] = 1 x $10^{-4}$ M (activity concentration of [$^{55}$Fe(II)] = 0.8 MBq L$^{-1}$). From both compartments aliquots are eventually sampled and subjected to ultracentrifugation, separating potentially present clay particles. Determining their potential existence in the solution of the sampling compartment is carried out by radio-assaying the respective aliquots by LSC, utilizing the sorbed $^{55}$Fe tracer as an indicator.

The sorption experiments were conducted under controlled environmental (glovebox, Ar atmosphere, nominal $O_2$ < 0.1 ppm, ~25°C) and electrochemically controlled reducing conditions. The background electrolyte consisted of 0.1 M $NaClO_4$ stabilized at pH 6.2 with 2 x $10^{-3}$ M of a pH buffer (2-morpholinoethanesulfonic acid monohydrate (MES), Merck Millipore, Merck KGaA, Darmstadt, Germany).

After an initial electrolysis of the background electrolyte solution at -847 mV (vs. Ag/AgCl, -640 mV vs. SHE) and reaching a minimal reductive background current, the $^{55}$Fe(III) tracer was added under an active electrolysis. 24 h later the clay mineral phase was added to the bulk compartment as an anoxic clay suspension with identical background electrolyte, resulting in a solid-to-liquid ratio of approx. 1 g $L^{-1}$ in a total electrolyte volume of 100 mL. Over the course of the experiment, a systematic positive pH drift between pH 6.1 and pH 6.7 in both compartments was observed and correspondingly adjusted to the target pH value. A potential contamination of the sampling compartment with clay particles during pH measurements was considered and the probing order correspondingly adapted.

After an experiment duration of two weeks, aliquots (8 mL) of both compartments were drawn and one aliquot of each compartment centrifuged (PC centrifuge bottle, Beckman Coulter, Brea, CA, USA), first at 5000 rpm (4025 g, 5 min, 3K30, SIGMA Laborzentrifugen GmbH, Osteroden, Deutschland) and finally at 30000 rpm (108800 g, 1 h, Avanti J-30I Centrifuge, Beckman Coulter). Both uncentrifuged aliquots and supernatants of the centrifuged aliquots were radio-assayed via LSC. In preparatory experiments no significant influence of suspended clay particles, acting as sorbent, on the determination of the $^{55}$Fe tracer concentration via LSC could be observed.

Additional qualitative and semi-quantitative (relative) information of the spatial activity distribution of the employed membrane filters was accessible via a radiographic imager (FLA-7000, FUJIFILM Europe GmbH, Düsseldorf, Germany).

### Sorption isotherm experiments of Fe(II) with clay minerals

The experimental conditions described in the previous paragraph were in general also applied to the sorption isotherm experiments of Fe(II) with Na-montmorillonite (SWy-2). Some adaptions were introduced after initial experiments extending the characteristics of the electrochemical cell.

After an initial sorption isotherm experiment with SWy-2, utilizing a polycarbonate membrane filter with a pore size of 0.4 µm (Schaffner, 2021), later experiments were conducted using a smaller pore size of 0.2 µm (Rudolph, 2022). Whereas Schaffner (2021) applied solely ORS-ICP-MS as analytical method in a tracer-less approach, Rudolph (2022) conducted the experiments with a tracer, utilizing both LSC and ORS-ICP-MS, with the latter giving access to an independent and complementary determination of the equilibrium and total Fe concentration. This combined approach is described in the following.

With observing a systematic increase of the pH during the continuous electrolysis in the membrane transport study described above, the dependence of the background current on the applied potential in the background electrolyte solution (0.1 M $NaClO_4$, 2 x $10^{-3}$ M MES, pH 6.2) was investigated (Rudolph, 2022) by gradually decreasing the applied potential from the ORP of the background solution (ca. +250 mV vs. Ag/AgCl) to -1000 mV (vs. Ag/AgCl) and determining the reductive background current. It was concluded that the originally applied potential of -640 mV (vs. SHE) caused an increased reductive background current due to the electrolysis of water and could be significantly reduced by increasing the potential to -540 mV (vs. SHE, -747 mV vs. Ag/AgCl), still outside the stability field of water at pH 6.2, providing reducing conditions, but not observing significant pH drifts in later experiments.

After an initial pre-equilibration of the electrochemical cell with the background electrolyte, the applied potential was gradually reduced to -747 mV (vs. Ag/AgCl) until a constant and minimal background current was reached. Subsequently, the $^{55}$Fe(III) tracer was added to the bulk compartment, resulting in an initial concentration of [Fe(II)] = 7.4 x $10^{-8}$ M corresponding to an activity concentration of [$^{55}$Fe(II)] = 5.5 MBq $L^{-1}$. After 24 h (membrane pore size 0.4 µm) resp. 48 h (0.2 µm) of pre-equilibration, aliquots of the sampling compartment were drawn and the anoxic clay mineral suspension was added to the bulk compartment, resulting in a solid-to-liquid ratio of approx. 1 g $L^{-1}$ with a total volume of 100 mL.

The sorption isotherm was determined by successively increasing the total Fe(II) concentration by one order of magnitude with the addition of freshly prepared solutions of $FeCl_2$ x 4 $H_2O$ (AnalaR NORMAPUR, VWR International, Leuven, Belgium) with the background electrolyte. After a compartment equilibration time of 24 h (pore size 0.4 µm) resp. 48 h (0.2 µm) aliquots of the sampling compartment were drawn for LSC (1000 µL) and ORS-ICP-MS (1000 µL), both acidified with the same volume of 0.02% $HNO_3$,

preventing a precipitation of potentially reoxidized ferric iron solid phases. After probing the pH during an interrupted electrolysis, the total Fe concentration was subsequently increased by an order of magnitude in five steps to 5 x $10^{-3}$ M, preserving the total volume of 100 mL. With adjusting the pH after a short initial electrolysis, the equilibration interval started again.

The equilibrium concentration of Fe(II) was eventually determined via radio-assaying (LSC) the $^{55}$Fe tracer with a variable but known Fe tracer-to-total ratio and complementary measured via ORS-ICP-MS. For a validation of the calculated total iron concentration, the added ferrous chloride solutions were also sampled, acidified and measured via ORS-ICP-MS.

After initial sorption isotherm experiments had shown significant sorption competing effects as sorption on different components of the electrochemical cell, an additional sampling of the bulk compartment with the contained clay suspension was introduced with drawing 50 µL of the stirred suspension, probing the net amount of sorbed $^{55}$Fe(II) on the clay particles via LSC with considering the simultaneously probed equilibrium concentration. The feasibility of determining the tracer content in the presence of (sorbent) clay particles was shown before. The sampled aliquots were again acidified with the same volume of 0.02% $HNO_3$.

## Results & discussion

### Commissioning of the electrochemical cell setup

A controlled anoxic environment could be identified as a decisive condition for operating the electrochemical cell. This could be achieved in a glovebox workstation with gas purification unit, providing a nominal $O_2$ concentration of <0.1 ppm.

The previous observation of an increase of the reductive background current and an associated significant pH drift during electrolysis could be minimized to the extent that the geochemical conditions in the proposed experiments could be stabilized with only minor pH adjustments necessary.

### Optimized retention of clay particles

As described above, non-systematic fluctuations in ORS-ICP-MS measurements, probing the equilibrium concentration of the sampling compartment in sorption experiments, gave an indication on the presence of clay particles. Since the purification and conditioning procedure of the montmorillonite mineral phases limits the particle size distribution (PSD) to <0.5 µm (Baeyens and Bradbury, 1995; Baeyens and Bradbury, 1997) and the PSD of the studied clay minerals also features a size fraction less than the initially employed pore size of 0.4 µm (Tan et al., 2017), a potential transport of clay particles through the membrane filter could not be excluded.

First, track-etched polycarbonate membrane filters with different pore sizes (0.1 µm, 0.2 µm, 0.4 µm) were studied regarding the diffusion kinetics of Fe(III) in the cell setup (cf. **Erreur ! Source du renvoi introuvable.** 2) at approx. pH 1.7. Applying first-order kinetics, a set of half-lives and minimum durations, necessary for reaching an equilibrium (>99%) between bulk and sampling compartments, were obtained (cf. Table 1). The described minimum sampling interval in Soltermann et al. (2014) of 24 h with an employed pore size of 0.4 µm could be confirmed.

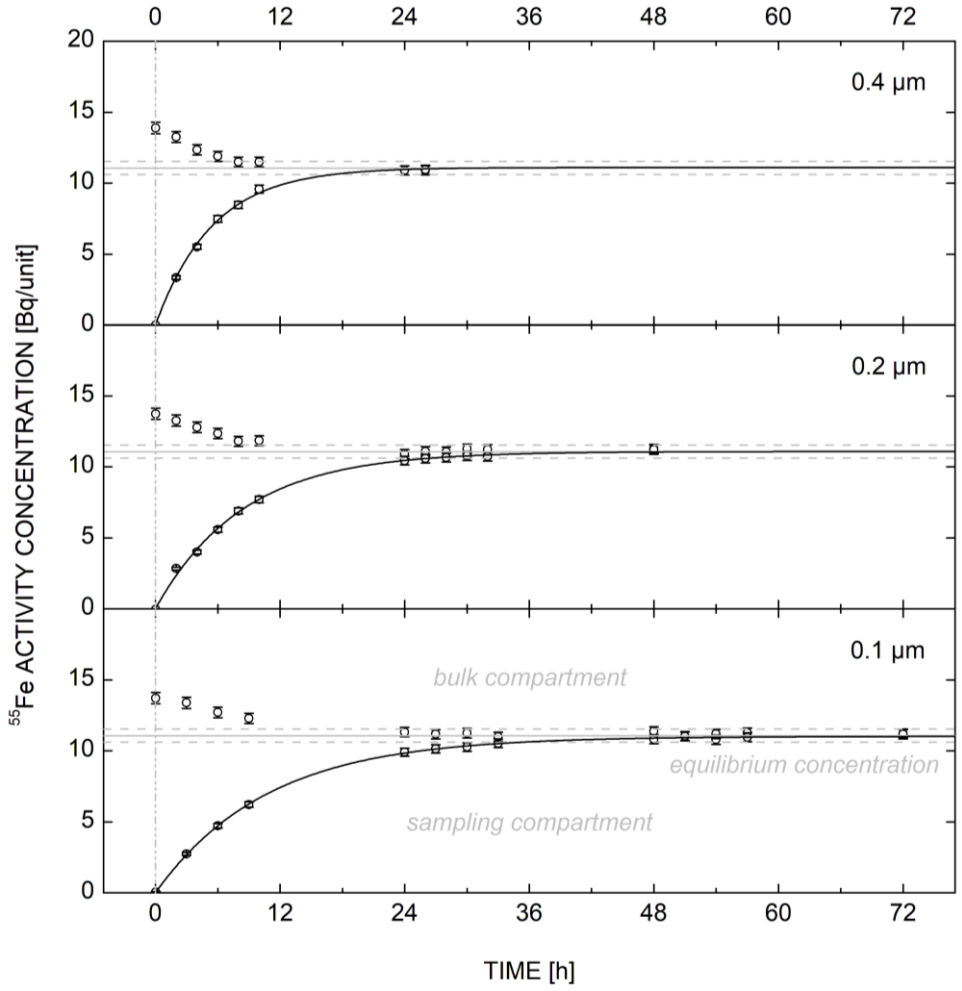


*Figure 2*: *Membrane filter diffusion kinetics of Fe(III) with different polycarbonate membrane pore sizes in the electrochemical cell setup. Activity concentrations of bulk and sampling compartments, both converging to the equilibrium concentration, shown as grey line with error range. The activity concentrations of the sampling compartment are fitted with first-order distributional kinetics (parameters cf. Table 1).*

*Table 1*: *Diffusion kinetics of Fe(III) through polycarbonate membrane filters. Determined half-lives $t_{1/2}$ in first-order distributional kinetics and derived equilibration times $t_{eq}$ (>99%).*

| Pore size [µm] | $t_{1/2}$ [h] | $t_{eq}$ [h] (>99%) |
|---|---|---|
| | | |
| 0.4 | 3.8±0.1 | 25 |
| 0.2 | 5.8±0.2 | 39 |
| 0.1 | 7.5±0.1 | 50 |

Subsequently, a potential particle transport through the membrane filters (0.2 µm, 0.4 µm) was studied in sorption experiments of Fe(II) with montmorillonite (SWy-2), following the sorption isotherm experiments of Soltermann et al. (2014) at one chosen analyte concentration.

Figure 3 shows a comparison of determined $^{55}$Fe activity concentrations of respectively sampled aliquots of the bulk and sampling compartments, ending the experiment after two weeks. $^{55}$Fe is applied in this

sorption experiment as an indicator of clay particles through the formation of a sorbate. The separation of potential particles through ultracentrifugation shows a significant effect for the sampling compartment with a pore size of 0.4 µm. Whereas aliquots of both bulk and sampling compartments show similar equilibrium concentrations after ultracentrifugation, only the non-centrifuged aliquot of the sampling compartment with an employed pore size of 0.4 µm shows a significantly increased activity concentration in comparison to the centrifuged aliquot, indicating the presence of sorbate particles, not retained by the membrane filter under the applied experimental conditions.

Reducing the pore size to 0.2 µm indicated a sufficient retention of clay particles and the suitability of this membrane filter. This conclusion has to be considered with the limitation of only one respectively performed experiment, though. But it yielded a sufficient indication to adapt the experiment to this pore size in the ensuing sorption isotherm experiments, guaranteeing a retention of clay particles and a distributional equilibrium between the two compartments.

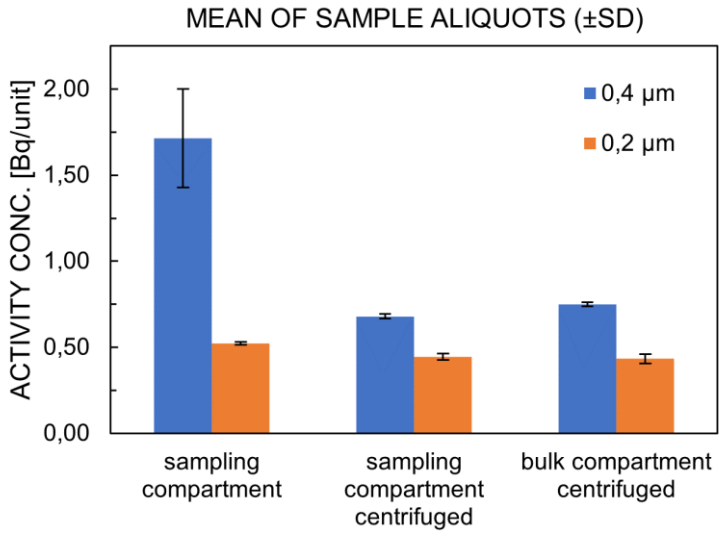


*Figure 3*: *Retention of clay particles in sorption experiments of Fe(II) with montmorillonite (SWy-2) at pH 6.2 with two membrane filter pore sizes of 0.4 µm and 0.2 µm. Comparison of drawn aliquots of the bulk and sampling compartments and determination of the equilibrium concentration by separating potential clay particles by ultracentrifugation. An increased apparent equilibrium concentration in a non-centrifuged aliquot (0.4 µm) can be observed, indicating the presence of clay particles in the respective sampling compartment when employing a pore size of 0.4 µm.*

Contributing to this conclusion are the different visual and radiographic appearances of the membrane filters after the respective experiments (cf. Figure 4). The visual appearance indicates an increased immobilization of clay particles at or in the membrane with a pore size of 0.4 µm, coinciding with an increased relative activity, as observed in radiographic imaging.

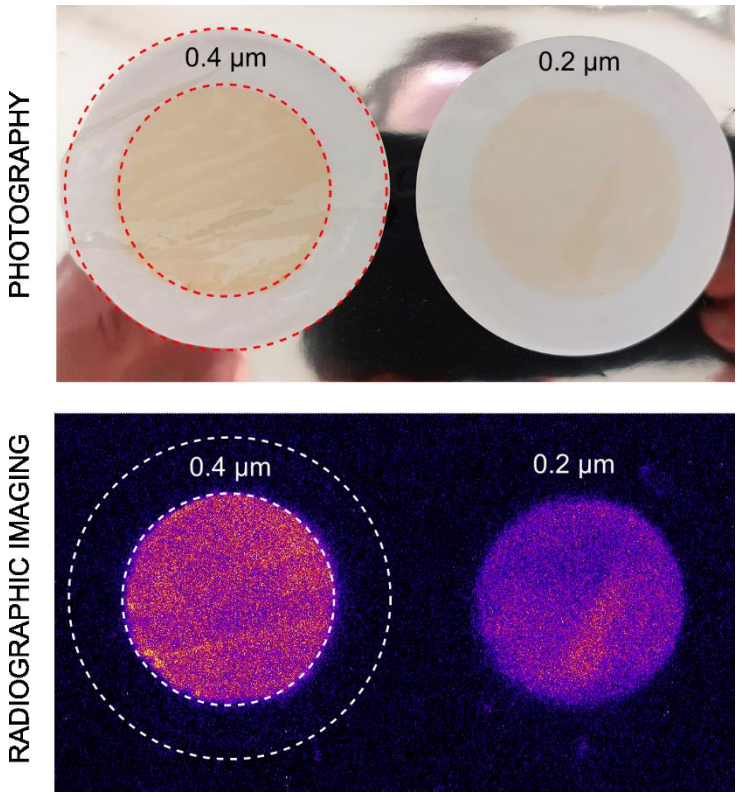


*Figure 4*: *Comparison of the membrane filters with pore sizes of 0.4 µm and 0.2 µm, studying a potential clay particle transport through the membranes in identical sorption experiments of Fe(II) with montmorillonite (SWy-2) under electrochemical control. Combined are an optical photograph and a radiographic image, showing the spatial distribution of immobilized clay at or in the membranes resp. the distribution of the $^{55}$Fe tracer after the experiment. Both representations show the surface of the membrane that was oriented to the bulk compartment, containing the clay suspension.*

## Sorption isotherm experiments - challenges identified and remaining

Sorption isotherms of Fe(II) with montmorillonite (SWy-2), determined in this study (Schaffner, 2021; Rudolph, 2022), are shown in Figure 5 in comparison to reproduced sorption isotherm data from Soltermann et al. (2014) (cf. Figure 4 therein). Whereas Soltermann et al. (2014) compared anoxic, non-reducing conditions ("Anoxic: batch" and "Anoxic: EC") with strongly reducing conditions ("-0.64 V: EC"), either conducted in batch experiments or in an electrochemical cell (EC), the isotherms reported in this study were solely generated under anoxic, reducing conditions with electrochemical control.

Three isotherms of this study are shown in Figure 5: Schaffner (2021), employing a membrane filter pore size of 0.4 µm and applying ORS-ICP-MS as the only analytical method, and Rudolph I (2022) as well as Rudolph II (2022) with a reduced pore size of 0.2 µm, suppressing a potential particle transport through the membrane, and applying LSC and ORS-ICP-MS in a combined analytical approach, probing the equilibrium and total Fe concentrations, with additionally probing the clay suspension in the latter experiment.

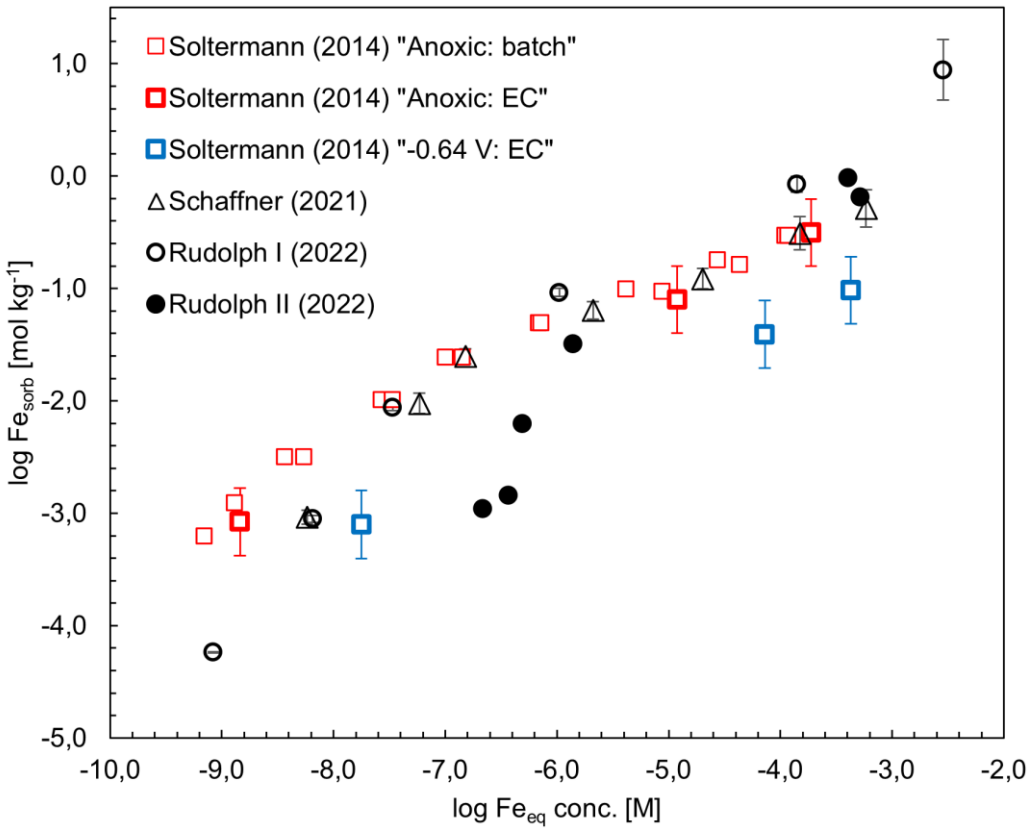


*Figure 5*: *Sorption isotherms of Fe(II) with montmorillonite (SWy-2) at pH 6.2 in 0.1 M $NaClO_4$ in a comparison between the reported experiments and the sorption isotherms described by Soltermann et al. (2014). Isotherm data reproduced from Figure 4 in Soltermann et al. (2014). Reported sorption isotherms potentially affected by adverse effects, influencing their validity.*

The sorption isotherms Schaffner (2021) and Rudolph I (2022) show in general a similar trend. Both isotherms show a general resemblance to the isotherms described in Soltermann et al. (2014), but the latter determined under anoxic, non-reducing conditions.

Rudolph II (2022), considering a potential sorption competition of cell components, shows besides a general resemblance a deviation at lower (trace) concentrations with a decreased sorption. This might be attributable to a potentially isolated determination of the sorption of Fe(II) on the clay mineral phase. At higher concentrations, the isotherm again follows the trend of the other determined isotherms.

Different adverse effects, influencing the validity of the experiment, were identified this study.

With probing the individually prepared Fe(II) solutions, applied for gradually increasing the total Fe concentration in the sorption isotherm experiment, a significant deviation of the calculated and measured Fe concentrations was identified via ORS-ICP-MS. This may be attributable to unknown deviations in the preparation process of the Fe(II) stock solutions. ORS-ICP-MS therefore allowed an independent analytical determination of the total Fe content over the course of the experiment.

Also to be considered is a potential Fe background concentration contributing to the total Fe content, especially at lower (trace) concentrations, limiting the accessible concentration range, as, e.g., experienced and recognizable in the sorption isotherm Rudolph II (2022). A background is either caused by a relevant Fe content of employed chemicals and/or components of the electrochemical cell, potentially still contaminated after a previous sorption experiment despite a thorough decontamination. ORS-ICP-MS also allows for determining the total Fe content, independent of the tracer technique.

Significant sorption competing effects could be identified at the lower (trace) total Fe concentrations. In a systematic decontamination of the cell compartments and electrodes of the electrochemical cell after the respective sorption experiments, around 40% of the initially deployed $^{55}Fe$ activity of 0.5 MBq could be recovered. As a consequence of this significant effect, it can be assumed that the sorption isotherms Schaffner (2021) and Rudolph I (2022) describe the sorption not only on the clay mineral but also on the electrochemical cell and its components.

After this observation, a modified approach was chosen, additionally probing the clay suspension, yielding the superimposed equilibrium concentration and sorbed Fe content, resulting in the sorption isotherm Rudolph II (2022) (cf. Figure 5). The accessible concentration range is limited by a potentially incomplete decontamination of the cell setup resulting in an increased Fe background. In comparison to the previous sorption isotherms of this study, a lower sorption of Fe(II) can be observed at lower (trace) concentrations, indicating the elimination or mitigation of sorption competing effects.

The unexpected increase in sorption at log $Fe_{eq} \sim 6.3$ indicates a potentially insufficient equilibration between all involved components in this experiment (Rudolph, 2022). The sampling interval in this study was derived of an isolated investigation of the membrane diffusion of ferric iron in acidic medium, without integrating further experimental components like the electrochemical setup. Possibly, this approach does not sufficiently consider the interactions between analyte, sorbent and the experimental components and their respective and potentially differing time constants. At least an upper limit can be derived of the reported transport studies of clay particles through the membrane filter. Under relevant geochemical conditions and electrochemical control in sorption experiments, an equilibrium between the two cell compartments could be determined after a duration of two weeks. In specific and corresponding experiments with montmorillonite (SWy-2), Soltermann et al. (2014) conducted their experiments for 30 days. A repeated investigation of equilibrium kinetics under a preferably entire consideration of experimental components and conditions should contribute to a clarification of the observed inconsistencies.

Besides a competing sorption on cell components, precipitation of poorly soluble ferric iron solid phases could also contribute to the loss of iron (tracer) over the course of the experiment due to a potential non-quantitative reduction or reoxidation of the reduced species at the anode. Since the speciation is only deduced indirectly of a systematic response of the electrochemical system during potentiostatic chronocoulometry, a direct in situ speciation technique would be beneficial for the electrochemical stabilization of reduced species. The ferrozine assay, e.g., gives an access quantifying ferrous iron besides ferric iron but is limited by a necessary minimum analyte concentration and non-continuous, ex situ probing.

At the end of the batch experiments the remaining suspension resp. solution volume in the electrochemical cell was determined and resulted in a total volume reduction of 5-10% over the duration of the experiments, despite a constant volume balancing and compensation for drawn sample aliquots. Since the electrochemical cell was not closed with gas-tight seals, this effect could most probably be caused by evaporative losses due to the glovebox, absorbing water from the inert gas atmosphere, combined with the thermal discharge of the magnetic stirrer. Previous observations of a positive pH drift with simultaneously increasing $O_2$ levels and increasing reductive background currents while applying strongly reducing conditions, also gave an indication of an accompanying electrolytic decomposition of water during electrochemical operation outside the stability field of water. The described increase of the applied potential to a less negative value (-540 mV vs. SHE) stabilized the geochemical conditions regarding a potential pH drift.

In general, an enhanced control of the applied geochemical conditions would be preferable as, e.g., in an in situ pH monitoring and control as demonstrated, e.g., by Aeschbacher et al. (2010). But since this would introduce additional components into the experiment, further sorption competing effects should be considered.

In conclusion, the sorption isotherms reported in this study have to be critically considered with regard to the identified adverse effects.

## Conclusions

Based on an approach described by Soltermann et al. (2014), an electrochemical cell for sorption experiments under controlled reducing conditions was constructed, commissioned and characterized. The electrochemical setup was expanded by an online monitoring of the applied electrochemical potential and current under potentiostatic control.

This study focused on sorption experiments of Fe(II) with Na-montmorillonite (SWy-2). Two independent and complementary analytical methods were established in LSC and ORS-ICP-MS, probing the Fe analyte concentration in a tracer approach and the total Fe content, respectively.

Initial studies investigated the kinetics of the diffusion of Fe(III) through the membrane filter, separating a clay suspension and an attached sampling compartment in sorption experiments. In addition, a potential transport of clay particles through the membrane filters was investigated, resulting in the application of a reduced pore size of 0.2 µm. First sorption isotherms of Fe(II) with montmorillonite (SWy-2) at pH 6.2 in 0.1 M $NaClO_4$ were determined. Several adverse effects, especially a significant sorption competition on cell components, prevented a direct differentiation of Fe sorption on the clay and the experimental setup, and therefore limited the validity of the obtained sorption isotherms. Some adverse effects have been mitigated, e.g., by additionally probing not only the equilibrium concentration of Fe in the sampling compartment but also in the clay suspension itself, deriving a potentially isolated sorption on clay. But some effects remain unresolved, like the significant sorption competition on cell components.

Before applying this electrochemical approach to sorption studies of redox-sensitive actinides, the observed adverse effects have to be understood and resolved.

## Acknowledgments

The contributions of students to this study within the framework of their bachelor (M. Mat.) and master thesis (M. Max., E. S., A. R.) are acknowledged. The mechanical and electronics workshops of the research reactor TRIGA Mainz (Johannes Gutenberg University Mainz, Germany) are acknowledged for the construction and fabrication of the electrochemical cell respectively for maintenance and support in commissioning of the electrochemical setup. The radiation protection group of TRIGA Mainz is acknowledged for handling the purchase of the $^{55}Fe$ tracer. Ch.E. Düllmann and D. Renisch are acknowledged for access to the radiographic imager. Merck Millipore (Merck KGaA, Darmstadt, Germany) is acknowledged for providing samples of polycarbonate membrane filters for initial membrane diffusion experiments.

## References

Aeschbacher, M., Sander, M., Schwarzenbach, R.P., 2010. Novel Electrochemical Approach to Assess the Redox Properties of Humic Substances. Environmental Science and Technology 44, 87-93. https://doi.org/10.1021/es902627p.

Baeyens, B., Bradbury, M.H., 1995. NAGRA Technical Report 95-04. A Quantitative Mechanistic Description of Ni, Zn and Ca Sorption on Na-Montmorillonite. Part I: Physico-Chemical Characterisation and Titration Measurements. Paul Scherrer Institut (Würenlingen and Villigen, Switzerland).

Baeyens, B., Bradbury, M.H., 1997. A mechanistic description of Ni and Zn sorption on Na-montmorillonite Part I. Titration and sorption measurements. Journal of Contaminant Hydrology 27, 199–222. https://doi.org/10.1016/S0169-7722(97)00008-9.

Blender, 2023. Blender, a free and open-source 3D creation suite. Version 3.5.1. Licensed under the GNU General Public License (GPL). http://www.gnu.org/copyleft/gpl.html.

Churakov, S.V., Hummel, W., Marques Fernandes, M., 2020. Fundamental Research on Radiochemistry of Geological Nuclear Waste Disposal. Chimia 71, 1000-1009. https://doi.org/10.2533/chimia.2020.1000.

Hidex, 2021. Liquid Scintillation Measuring Procedures: New Developments, Radionuclides from Nuclear Fission Activities, Fe-55 and Ca-41 in Decommissioning Activities by TDCR-LSC. Hidex Oy, Turku, Finland. https://hidex.com/ebooks/liquid-scintillation-measuring-procedures/measuring-procedures/radionuclides-from-nuclear-fission-activities/2-3-11-fe-55-and-ca-41-in-decommissioning-activities-by-tdcr-lsc.

Mabbott, G.A., 2020. Electroanalytical Chemistry – Principles, Best Practices, and Case Studies. In: Chemical Analysis – A Series of Monographs on Analytical Chemistry and Its Applications. Series Editor: M. F. Vitha. Vol. 187. John Wiley & Sons, Inc. https://doi.org/10.1002/9781119538721.

Mancini, A., Wieland, E., Geng, G., Lothenbach, B., Wehrli, B., Dähn, R., 2021. Fe(II) interaction with cement phases: Method development, wet chemical studies and X-ray absorption spectroscopy. Journal of Colloid and Interface Science 588, 692-704. https://doi.org/10.1016/j.jcis.2020.11.085.

Matejcek, M., 2020. Elektrochemische Präparation von Fe(II)-Lösungen und Analyse mittels ICP-MS. Bachelor thesis. Department of Chemistry, Johannes Gutenberg University Mainz, Mainz, Germany.

Maxeiner, M., 2020. Development and Characterization of an Electrochemical Cell for Sorption Experiments. Master thesis. Department of Chemistry, Johannes Gutenberg University Mainz, Mainz, Germany.

Neck, V., Altmaier, M., Fanghänel, T., 2007. Solubility of plutonium hydroxides/hydrous oxides under reducing conditions and in the presence of oxygen. Comptes Rendus Chimie 10, 959-977. https://doi.org/10.1016/j.crci.2007.02.011.

Pearson, F.J., Arcos, D., Bath, A., Boisson, J.-Y., Fernández, A.M., Gäbler, H.-E., Gaucher, E., Gautschi, A., Griffault, L., Hernán, P., Waber, H.N., 2003. Mont Terri Project - Geochemistry of Water in the Opalinus Clay Formation at the Mont Terri Rock Laboratory. Reports of the Federal Office for Water and Geology (FOWG), Geology Series, No. 5, Federal Department of Environment, Transport, Energy and Communications, Switzerland.

Rudolph, A., 2022. Bestimmung der Sorption von Eisen(II) an Montmorillonit unter definierten Redoxbedingungen in einer elektrochemischen Zelle. Institute of Environmental Physics, Heidelberg University, Heidelberg, Germany, and Department of Chemistry, Johannes Gutenberg University Mainz, Mainz, Germany.

Sander, M., Hofstetter, T.B., Gorski, C.A., 2015. Electrochemical Analyses of Redox-Active Iron Minerals: A Review of Nonmediated and Mediated Approaches. Environmental Science and Technology 49, 5862-5878. http://dx.doi.org/10.1021/acs.est.5b00006.

Schaffner, E., 2021. Sorption von Eisen(II) an Tonmineralien unter definierten Redoxbedingungen in einer elektrochemischen Zelle. Master thesis. Department of Chemistry, Johannes Gutenberg University Mainz, Mainz, Germany.

Soltermann, D., Baeyens, B., Bradbury, M.H., Marques Fernandes, M., 2014. Fe(II) Uptake on Natural Montmorillonites. II. Surface Complexation Modeling. Environmental Science and Technology 48, 8698-8705. https://dx.doi.org/10.1021/es501902f.

Tan, X., Liu, F., Hu, L., Reed. A.H., Furukawa, Y., Zhang, G., 2017. Evaluation of the particle sizes of four clay minerals. Applied Clay Science 135, 313-324. http://dx.doi.org/10.1016/j.clay.2016.10.012.

# 8. Towards a mechanistic understanding of cation sorption by montmorillonite edges: experimental and modelling approaches

E. Orucoglu, S. Grangeon
*BRGM, Orléans, France*

C. Tournassat
*Université d'Orléans, Orléans, France*

## Introduction

Clay, and in particular montmorillonite, a dioctahedral smectite, is one of the most reactive phases in the environment towards cations such as metals. This reactivity is due to its crystal structure, which consists in the parallel stacking of layers, themselves composed of an octahedral sheet sandwiched between two tetrahedral sheets. The octahedral sheet is made of edge-sharing octahedra, with Mg and Al forming the centre of the octahedron and being coordinated to six oxygen atoms. The tetrahedral sheet is essentially made of $SiO_2$ tetrahedra. The presence of isomorphic substitutions in the octahedral and tetrahedral sheets is at the origin of a permanent layer charge which is essentially compensated for by hydrated interlayer cation. The presence of broken bonds at the layer edges is another source of electric charge, compensated for by $H^+$, which can be exchanged with cations.

The electric fields generated by the permanent layer charge is mainly located on the basal surface, but may extend and hence influence the edge surface potential, depending on the physico-chemical composition of the solution and on the montmorillonite structure. This is termed the "spill-over effect".

The relative importance of edge (surface complexation) and interlayer (cation exchange) sorption in overall montmorillonite reactivity depends on the physico-chemical conditions prevailing in the equilibrium solution, and in particular on pH, ionic strength, and nature of the background electrolyte. At low pH, adsorption is dominated by cation exchange processes on basal surfaces. In contrast, at pH values close to neutrality or higher, adsorption is dominated by surface complexation reactions on edge surfaces. Correspondingly, the value of ionic strength has a large influence on the adsorption extent at low pH, while it has a limited influence at high pH. This work focuses on sorption by montmorillonite edges, that is surface complexation, which is currently less constrained than exchange in clay interlayer, at basal surfaces.

An additional source of difficulty in quantifying montmorillonite reactivity is related to the fact that various ions from the solution can compete for sorption on both edge and basal surfaces, with the ratio of ions on the solid, at equilibrium, depending for example on the concentration of the various ions in the solution and on their relative affinity for montmorillonite surface.

Understanding, and hence being able to model and ultimately predict the sorption of ions such as metals by montmorillonite requires a sound understanding of montmorillonite structure. In the frame of the development of an "electrostatic model", which takes into account the spill-over effect, for example, several pieces of information must be gained from experimental or modelling approaches, including: (i) the layer structure (e.g., cis-vacant or trans-vacant) must be known to calculate a sound electrostatic potential, (ii) it must be ensured that the crystal edges are crystalline, in order to be able to calculate the acid-base properties of the various edge sites, (iii) it must be checked if cation exchange at clay edges is reversible.

This report is a summary of some of the main results and conclusions that were detailed in three publications and which deal with (i) a detailed review of the mechanisms of ion sorption by montmorillonite (Liu et al. (2022) , (ii) the determination of the layer and edge structure of the Kunipia montmorillonite clay, the study of sorption reversibility at edge sites, in the Pb/Co and Pb/Mg/Zn systems, and the application of an electrostatic model (see Orucoglu et al., 2022), and (iii) the use of first-principles molecular dynamics

and surface complexation modelling for the determination of the acid-base properties of montmorillonite with a crystal structure representative of that of the Kunipia clay (Gao et al., 2023).

Since the report is aimed at providing a concise overview of the work conducted in the frame of the present Eurad project, only the most significant results were arbitrarily selected and not all the materials and methods information are reported. The reader is referred to the publications for an exhaustive view.

## Materials and methods

### Scanning-transmission electron microscopy

Structural characterization was performed using a Nion Ultra-STEM 200 operated at 100 kV in scanning transmission electron microscopy (STEM) mode. Data were collected both in bright-field, in medium-angle annular dark-field (MAADF), and high-angle annular dark-field (HAADF) conditions. To determine the cis-vacant or trans-vacant nature of the clay, data were compared to images that were calculated using the QSTEM software (Koch, 2002) and structure models from Tsipursky and Drits (Tsipursky and Drits, 1984). A “supercell” approach modelling method was used in which a single layer was extracted along **c**. Samples were prepared following a method from the literature (Nadeau, 1985) that was adapted for the present needs. Briefly sample were redispersed in an aqueous solution to satisfy a 0.05 $g \cdot L^{-1}$ solid concentration. The dispersion was sonicated for 15 min to promote delamination of clay mineral layers and put onto a mica disc and dried one night under room conditions to obtain oriented clay particles. Then, the sample was put into an oven at 50 °C for one night and placed in a desiccator for cooling and then prevacuumed for 20 min by vacuum pump. The sample was coated with carbon at 5 nm thickness. Carbon-coated mica samples were put into milli-Q water to separate carbon-coated clay particles from the mica disc. Carbon-coated clay particles were taken from the surface of the water and placed onto lacey carbon copper grid.

### First Principles Molecular Dynamics

Structure models are detailed in the corresponding publication (Gao et al., 2023). CP2K/Quickstep package based on mixed Gaussian plane wave scheme was used to carry out all simulations (Lippert et al., 1997). Perdew–Burke–Ernzerhof functional was applied for exchange correlation effects (Pewdew et al., 1996), and Goedecker–Teter–Hutter pseudopotentials were used to represent the core electron state (Goedecker et al., 1996). The dispersion correction was applied in all calculations with the Grimme-D3 method (Grimme et al., 2011; Grimme et al., 2010). A double-ζ valence augmented with polarization basis set (VandeVondele and Hutter, 2007) was employed for H, O, Mg, Al, and Si, and the plane wave cutoff was set to be 400 Ry.

Born–Oppenheimer molecular dynamics simulations were carried out with a wave function optimization tolerance of $10^{-6}$. Canonical ensemble (NVT) conditions were imposed using a Nóse–Hoover chain thermostat with a target temperature of 300 K. (47) The MD time step was set to be 0.5 fs. For each system, we conducted an initial equilibration simulation of 3.0 ps, followed by a production period of 5.0–10.0 ps.

### Acidity Constant Calculations

The pKa values of the edge surface sites were computed using the half-reaction scheme of the FPMD-based vertical energy gap method (Cheng et al., 2014; Costanzo et al., 2011). In this method, the proton of an acid (denoted as AH) is gradually transformed into a ghost atom, and the free energy of the transformation is calculated according to the thermodynamic integration approach. Full details are given in the Supporting Information of the corresponding publication (Gao et al., 2023).

The investigated edge surface sites were ≡Al/Mg$(OH_2)_2$, ≡Al/Mg$(OH_2)$OH, ≡Si(OH), ≡Al$(OH_2)$, ≡Si$(OH)_2$Al/Mg, ≡SiO(OH)Al/Mg, and ≡Al/Si/Mg(OH)Al for the surfaces perpendicular to [010], [0$\bar{1}$0], [110], and [$\bar{1}\bar{1}$0] of a trans-vacant structure. The slashes represent the different octahedral or tetrahedral connection sites. Details, including the sites considered or not, is available in the corresponding publication (Gao et al., 2023).

### Surface Complexation Modelling

A modified version of PHREEQC that considers the spillover of electrostatic potential from basal surfaces was used to construct SCMs for clay layer edge surfaces. It is available in the corresponding publication (Gao et al., 2023). A key feature is that the electrostatic potential of edge surfaces is negative when the edge surface charge is zero.

### Sorption and competition experiment

The sorption of Co was tested with purified Kunipia clay. For the experiment presented in the present report, the experimental conditions were as follows. In a first step, the clay suspension was equilibrated at a solid-to-liquid ratio of 10.1 g $L^{-1}$, pH 6.9, and in 0.3 M NaCl. Then, $Co^{2+}$ was added, with a solution concentration of 12 mmol $L^{-1}$. In a third step, $Mg^{2+}$ was added, with a solution concentration of 11.1 mmol $L^{-1}$. Details are available in the corresponding publication (Orucoglu et al., 2022).

## Results and discussion

### Structure of the Kunipia clay

Seen perpendicular to the *ab* plane (i.e., to the layer plane), and at low magnification, the different isolated clay particles and their possible overlap were determined from the analysis of the image grey level Figure 1a and 1b). Isolated particles were selected for further high-resolution imaging (Figure 1c), on which the study of the grey level perpendicular to the particle edge allowed observing a periodic signal, which is a fingerprint of the atomic periodicity (lattice repetition in the *ab* plane) within the clay layer and hence of the crystalline nature of the clay (Figure 1d). This periodicity extended up to the very end of the particle, which is evidence for the crystalline nature of the edges. An amorphous edge structure would have manifested itself by a constant grey level having a value equal to the mean of the crystalline part. It would have extended over at least one lattice length, and would have been easily observed given the spatial resolution that was achieved for this experiment.

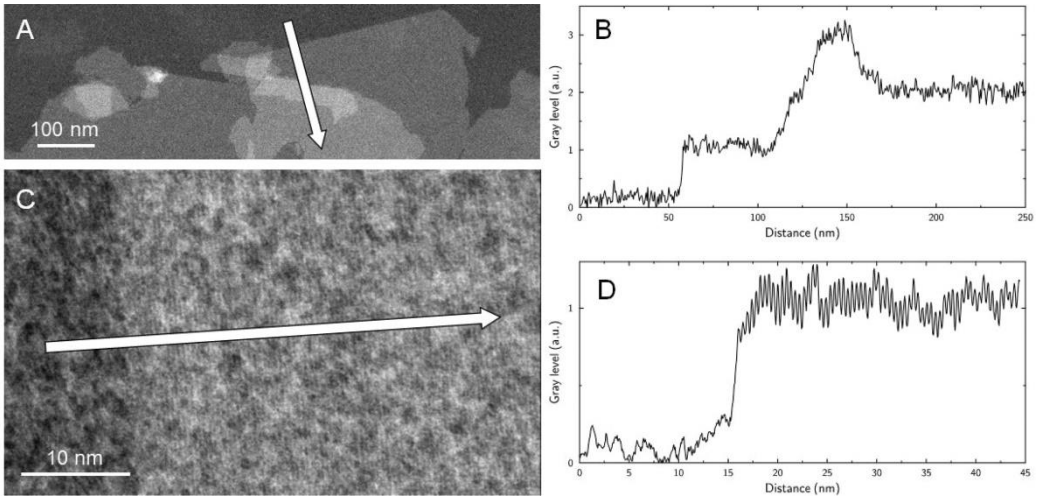


*Figure 1: STEM imaging of clay particles. (A) STEM-HAADF image at low magnification showing the layers, seen perpendicular to the layer plane. (B) STEM-HAADF profile along the direction indicated by the arrow in panel A. The intensity offset have been roughly set to zero for the carbon film and the profile shows steps as a function of the numbers of layers. (C) STEM-HAADF image at the edge of a layer, seen perpendicular to the layer plane. (D) STEM-HAADF profile along the direction indicated by the arrow in panel C. The ~0.45 nm periodicity is visible up to the surface plane. The small intensity decay at the last layers is due to the edge roughness and the integration width. The integration width for both profiles is 40 nm. Modified after Orucoglu et al. (2022).*

To further study the structure of the Kunipa clay, the structure models of a trans-vacant Figure 2a) and a cis-vacant (Figure 2b) clay were calculated. Then, isolated clay particles were analysed. It was first ensured that their orientation relative to the beam was adequate to collect high-resolution images (Figure 2c). The criteria for deciding if the crystal was correctly oriented was (i) an overall grey level typical for an isolated layer (Figure 2b) and (ii) a diffraction pattern typical for a layer perpendicular to the beam (hexagonal symmetry, symmetrical diffraction spots). Then, atomic-scale images were collected and compared to the calculated ones. It could be concluded from this analysis that the Kunipia clay has cis-vacant structure (Figure 2d).

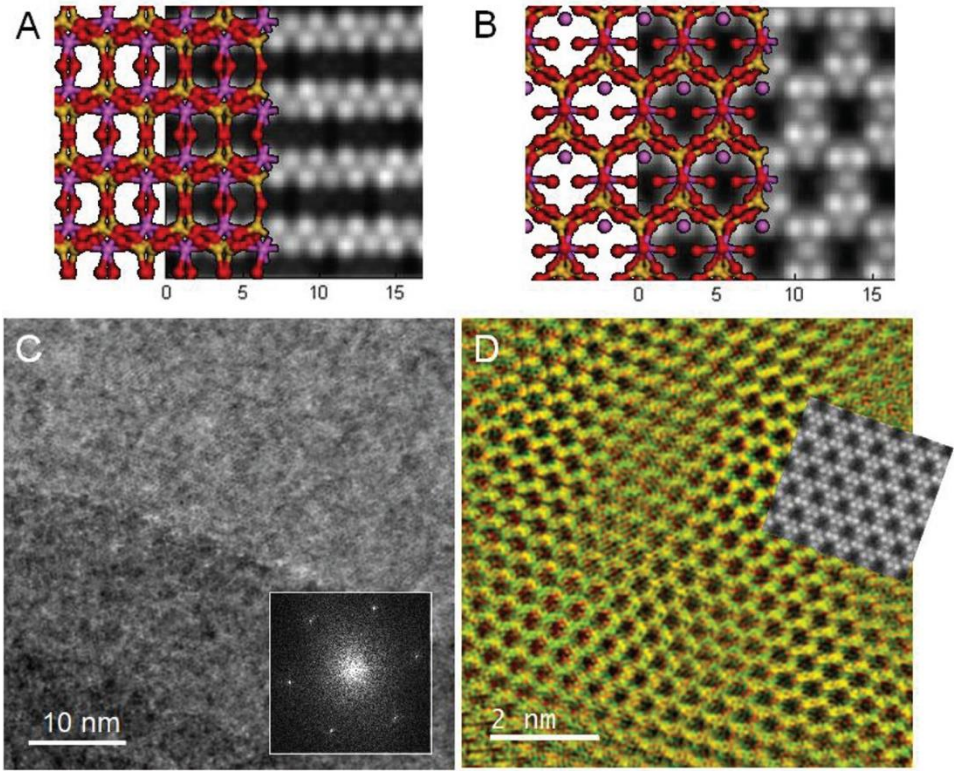


*Figure 2: Top: atomic model and corresponding STEM-HAADF calculated images for trans-vacant (A) and cis-vacant (B) layer structures. Yellow, purple, and red balls are for, respectively, silicon, aluminum, and oxygen. The images are about 1.5 × 1.5 nm. Crystallographic planes are indicated on the cis-vacant structure. Bottom: (C) STEM-HAADF image containing a clay layer (top, light gray) and the amorphous carbon from the sample holder (bottom, dark gray). The fast Fourier transform of the clay is shown as an inset and is indexed for a [001] zone axis. Edge surface is of (110) type. (D) STEM-HAADF image of the clay shown in panel C after Fourier filtering. Calculated image for cis-vacant structure is overlapped. Modified after Orucoglu et al. (2022).*

It can be concluded from the present STEM analysis that the Kunipia clay has cis-vacant structure with crystalline edges. Determining the reactivity of the various montmorillonite edge sites requires that the acidity constants are known. This was done previously by modelling the acid-base titration curves, but using a trans-vacant structure (Tournassat et al., 2016). However, trans-vacant and cis-vacant structures have very different edge structure. Cis-vacant structures are not centrosymmetric Figure 3, which indicates that the edges perpendicular to [010], [0$\bar{1}$0], [110], and [$\bar{1}\bar{1}$0] crystallographic directions are different. In addition, different positions of structural OH groups and isomorphic substitutions lead to more complex edge surface groups (Kéri et al., 2017; Tournassat et al., 2004). It thus appeared necessary to investigate the acidity constants of the cis-vacant structures.

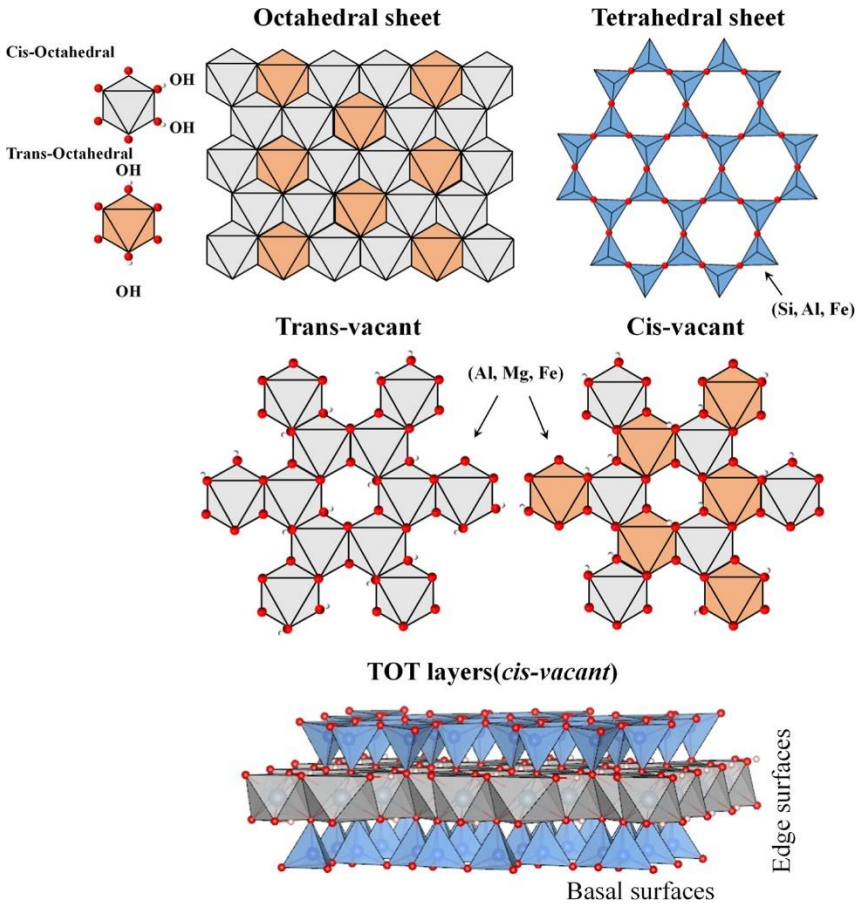


*Figure 3: From top to bottom: octahedral and tetrahedral sheets, octahedral sheet with trans-vacant and cis-vacant configurations, TOT layers. Modified after Gao et al. (2023).*

Compared with the trans-vacant model, the surface perpendicular to [010] of cis-vacant model has a special structure with symmetrical vacancy surrounded by ≡Si(OH)$_2$Al/Mg and ≡Si(OH). Similar to the trans-vacant edge perpendicular to [010] direction, the cis-vacant model also has ≡Al(OH$_2$)$_2$ and ≡Si(OH) sites on [0$\bar{1}$0] direction. Both surfaces perpendicular to [110] and [$\bar{1}$10] on the cis-vacant model are inclined edges which are similar to the trans-vacant edge perpendicular to [110]. Such bevelled surfaces have different silanol groups, that is, ≡Si(OH)U (silanol on upper T-sheet) and ≡Si(OH)L (silanol on lower T-sheet). For edge perpendicular to [$\bar{1}$10], there are ≡Al(OH$_2$)$_2$ and ≡Al(OH)Al sites. In addition, the edge perpendicular to [110] has the same type of surface sites (i.e., ≡Al(OH$_2$) and ≡Si(OH)Al) as the trans-vacant edge perpendicular to [110]. In the case of $Mg^{2+}$ substitution, ≡Si(OH)2Mg and ≡Mg(OH$_2$)$_2$ appeared on surfaces perpendicular to [010] and [$\bar{1}$10], while the surface sites on surfaces perpendicular to [0$\bar{1}$0] and [110] are the same to the No-sub model because the cis-octahedron substituted by $Mg^{2+}$ is inside the bulk phase.

Using First-Principle molecular dynamics, the acidity constants (pKa) from edge sites of a cis-vacant structure could be evaluated with a accuracity of 1.6 pKa units and compared to those previously obtained for trans-vacant structure Table 1.

*Table 1: Summary of pKa Values of Edge Sites on Individual Surfaces of Trans/Cis-Vacant Models (tv and cv, Respectively). Tv values after (Liu et al., 2014). Modified after Gao et al. (2023).*

| | sites | tv ⊥ [010] | tv ⊥ [110] | cv ⊥ [010] | cv ⊥ [0$\bar{1}$0] | cv ⊥ [110] | cv ⊥ [1$\bar{1}$0] |
|---|---|---|---|---|---|---|---|
| No-sub | ≡Si(OH) | 7 | 8.0U/8.3L | 6.8 | 8.1 | 6.3U/6.8L | 7.4U/8.1L |
| | ≡Al(OH2)2 | 3.1 | | | 5.7 | | 7 |
| | ≡Al(OH)(OH2) | 8.3 | | | 9.8 | | |
| | ≡Al(OH2) | | 5.5 | | | 5.6 | |
| | ≡Si(OH)Al | | 1.7 | | | –11.7 | |
| | ≡Si(OH)2Al | | | –0.8 | | | |
| | ≡Si(O)(OH)Al | | | 5.9 | | | |
| | ≡Al(OH)Al | | | | 13.2 | | 17.6 |
| Mg-sub | ≡Si(OH) | 10.8 | 11 | 9 | 11 | 9.1U/10.4L | 8.9U/9.2L |
| | ≡Mg(OH2)2 | 13.2 | | | | | 15.1 |
| | ≡Si(OH)Mg | | 4.2 | | | | |
| | ≡Al(OH2)2 | | | | 5.9 | | |
| | ≡Al(OH)(OH2) | | | | 10.1 | | |
| | ≡Al(OH2) | | | | | 8.5 | |
| | ≡Si(OH)Al | | | | | –7.1 | |
| | ≡Si(OH)2Mg or ≡Si(O)(OH)Mg | | | 5.3/8.8 | | | |
| | ≡Mg(OH)Al | | | | 16.6 | | 18.7 |

The newly obtained cis-vacant model was tested for its capacity to reproduce published potentiometric titration data (Figure 5) (Duc et al., 2005; Tournassat et al., 2016). Proportions of edge surface directions were set at 0.3/0.7 for surfaces perpendicular to [010] and [110] in the trans-vacant model and 0.15/0.15/0.35/0.35 for the surfaces perpendicular to [010], [0$\bar{1}$0], [110], and [1$\bar{1}$0] in the cis-vacant model, in agreement with atomic force microscopy (AFM) results, showing a predominance of edge surfaces perpendicular to [110] and [1$\bar{1}$0] compared to those perpendicular to [010] (Kraevsky et al., 2020). Additional calculation hypotheses are available in (Gao et al., 2023). The consideration of a cis-vacant instead of a trans-vacant structure had a significant influence on the edge surface charge (Gao et al., 2023), but it had little effect on the prediction of potentiometric titration results Figure 4. An almost perfect agreement with the experimental data can be achieved by adjusting the pKa values of edge surface sites in the limit of the ±1.6pKa unit uncertainty, but such a refinement was not deemed justified in light of the uncertainties in the experimental data (Tournassat et al., 2016). This comparison highlights the lack of modelling constraint provided by potentiometric titration data. Potentiometric titration curves of montmorillonite measured as a function of ionic strength do not exhibit a crossover point because of the spillover effect of basal surface potential on edge surfaces. In addition, because of the predominance of the basal surfaces over the edge surfaces, electrophoretic measurements of Na-montmorillonite particles always result in negative ζ potential values (Leroy et al., 2015). Consequently, no point of zero charge of edge surfaces and iso-electric point can be determined accurately. At last, the smooth decrease of proton charge with pH does not allow the identification of individual pKa values from the presence of inflexions in the titration curves. Nevertheless, it is considered that this cis-vacant model is improved compared to the previously published trans-vacant model because a good agreement between predicted and measured proton charge was found ( Figure 4) and because this cis-vacant model takes into account the most recent insights on clay edge surface structure and reactivity.

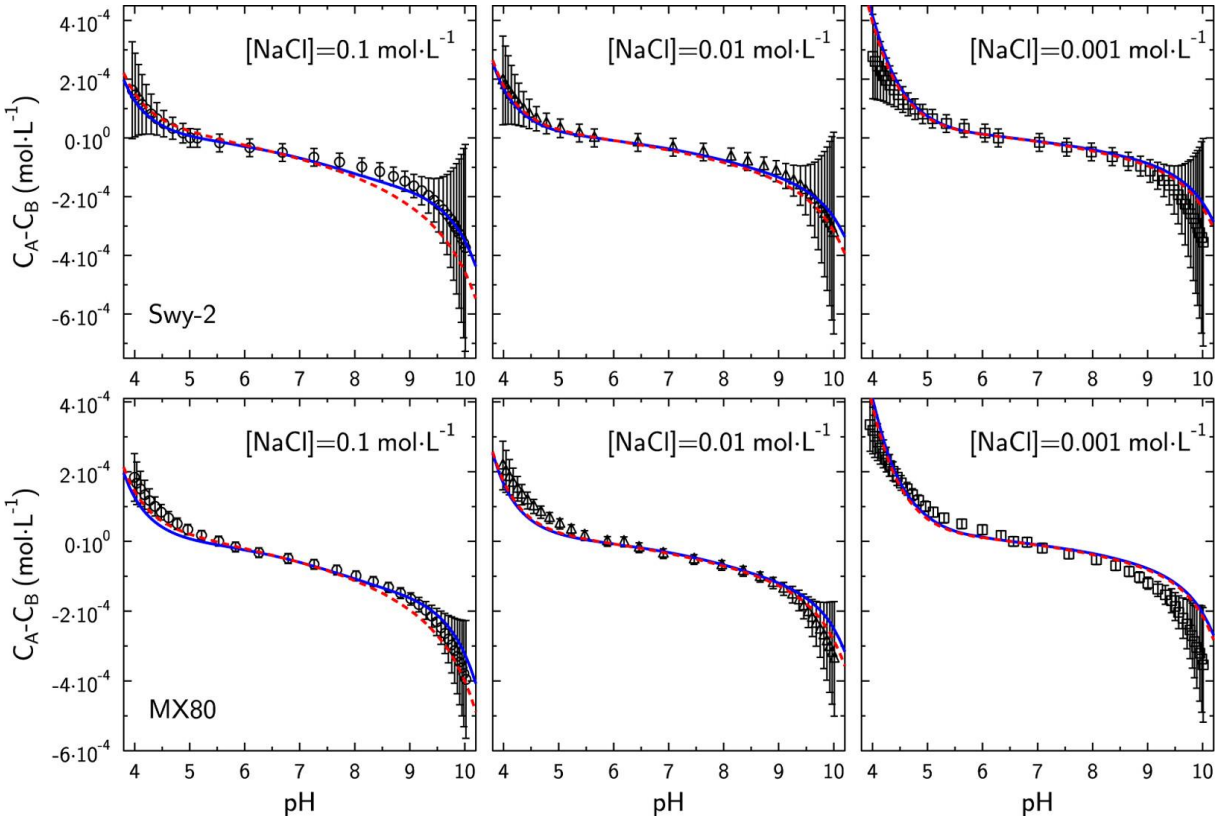


*Figure 4: Comparison of model predictions (lines) and potentiometric titration data (symbols) for MX80 montmorillonite (bottom) and SWy-2 montmorillonite (top) as reported by Tournassat et al. 2016. The specific edge surface area was set to 12 and 14 $m^2 \cdot g^{-1}$ for, respectively, MX80 and Swy-2 montmorillonite as by Tournassat et al. 2016 The relative abundance of edges perpendicular to [010] and [110] was set at 0.3/0.7 for the trans-vacant model (plain blue lines) and that of edges perpendicular to [010], [0$\bar{1}$0], [110], and [$\bar{1}\bar{1}$0] was set at 0.15/0.15/0.35/0.35 for the cis-vacant model (dashed red lines) in agreement with AFM results . Modified after Gao et al. (2023).*

With a sound understanding and capacity to model the structure and acidity constant of the montmorillonite edges, the sorption of Co at montmorillonite edges was tested and quantified, and both the kinetics of sorption and the reversibility upon competition with Mg was also quantified. Mg was selected because it is a major element from many pore waters from geological formations envisioned for nuclear waste storage (for example the Callovian-Oxfordian formation and the Boom clay formation – see Gaucher et al., 2009; Honty et al., 2022).

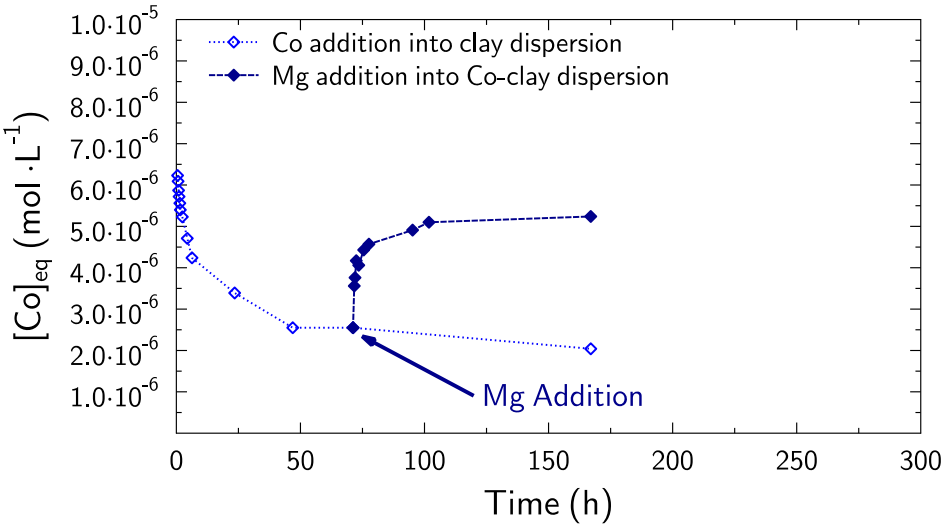


*Figure 5: Time-dependent $Co^{2+}$ adsorption/desorption on/from Kunipia-F clay mineral surfaces at pH ~6.9. The order of reagents additions is indicated in the inner caption. Closed symbols indicate that a competitor ($Mg^{2+}$) was added at time ~70 h. Modified after Orucoglu et al. (2022).*

In Figure 5, it can be observed that the initial Co concentration in solution was 6 $10^{-6}$ mol $L^{-1}$. The kinetics of Co sorption lasted ~50 h, after which equilibrium was reached. Then, after addition of Mg, Co was released in solution, which shows that Co/Mg sorption competition for montmorillonite edges exists, and that Co sorption is reversible.

The role of $Mg^{2+}$ on overall metal or radionuclide adsorption is usually related to competition processes for cation exchange sites on basal surfaces only. However, these experimental results could not be explained without a specific adsorption mechanism for $Mg^{2+}$ on the clay mineral edge surfaces. Additionally, Mg substitutions in the octahedral sheet of the montmorillonite layer are observed and adsorption processes on clay mineral edges may be described as a possible initiation of an epitaxial growth of clay mineral layers. Finally, The $Mg^{2+}$ concentration value investigated in the present study (10 mmol·$L^{-1}$) is matching with the range of concentration commonly observed in clay sedimentary rocks or in marine sediment pore waters (Grangeon et al., 2015) and the $Mg^{2+}$ competition effect observed in this experiment can also be observed in most of clayey natural environments. Usage of the adsorption data obtained on pure clay mineral phases, and the models that have been built using these data may overestimate the retention properties of these clay mineral phases when applied to natural environments.

Data acquired in the frame of EURAD WP FUTURE were combined with those obtained in other projects (see Orucoglu et al., 2022) to produce an electrostatic model for sorption by montmorillonite edges that could reproduce new and literature data.

## Summary, conclusions, and future work

From the selected extracts from publications that benefited from funding by EURAD WP FUTURE provided above, it can be concluded that the work conducted allowed obtaining a multi-scale understanding of the structure, reactivity, and sorption capacity of montmorillonite edges. It could be demonstrated that the Kunipia clay has crystalline edges and a cis-vacant layer structure. This atomic-scale study allowed building an electrostatic model grounded on a sound structural understanding. This model allowed quantifying and predicting the edge acid-base properties, and the sorption properties, including sorption reversibility.

## References

Cheng J., Liu X., VandeVondele J., Sulpizi M. and Sprik M. (2014) Redox potentials and acidity constants from density functional theory based molecular dynamics. *Accounts of Chemical Research* **47**, 3522-3529.

Costanzo F., Sulpizi M., Valle R. G. D. and Sprik M. (2011) The oxidation of tyrosine and tryptophan studied by a molecular dynamics normal hydrogen electrode. *The Journal of chemical physics* **134**, 06B615.

Duc M., Gaboriaud F. and Thomas F. (2005) Sensitivity of the acid–base properties of clays to the methods of preparation and measurement: 2. Evidence from continuous potentiometric titrations. *Journal of Colloid and Interface Science* **289**, 148-156.

Gao P., Liu X., Guo Z. and Tournassat C. (2023) Acid–Base Properties of Cis-Vacant Montmorillonite Edge Surfaces: A Combined First-Principles Molecular Dynamics and Surface Complexation Modeling Approach. *Environmental Science & Technology* **57**, 1342-1352.

Gaucher E. C., Tournassat C., Pearson F. J., Blanc P., Crouzet C., Lerouge C. and Altmann S. (2009) A robust model for pore-water chemistry of clayrock. *Geochimica et Cosmochimica Acta* **73**, 6470-6487.

Goedecker S., Teter M. and Hutter J. (1996) Separable dual-space Gaussian pseudopotentials. *Physical Review B* **54**, 1703.

Grangeon S., Vinsot A., Tournassat C., Lerouge C., Giffaut E., Heck S., Groschopf N., Denecke M. A., Wechner S. and Schäfer T. (2015) The influence of natural trace element distribution on the mobility of radionuclides. The exemple of nickel in a clay-rock. *Applied Geochemistry* **52**, 155-173.

Grimme S., Ehrlich S. and Goerigk L. (2011) Effect of the damping function in dispersion corrected density functional theory. *Journal of computational chemistry* **32**, 1456-1465.

Grimme S., Antony J., Ehrlich S. and Krieg H. (2010) A consistent and accurate ab initio parametrization of density functional dispersion correction (DFT-D) for the 94 elements H-Pu. *The Journal of chemical physics* **132**, 154104.

Honty M., Frederickx L., Wang L., De Craen M., Thomas P., Moors H. and Jacops E. (2022) Boom Clay pore water geochemistry at the Mol site: Experimental data as determined by in situ sampling of the piezometers. *Applied Geochemistry* **136**, 105156.

Kéri A., Dähn R., Krack M. and Churakov S. V. (2017) Combined XAFS spectroscopy and ab initio study on the characterization of iron incorporation by montmorillonite. *Environmental science & technology* **51**, 10585-10594.

Koch C. T. (2002) *Determination of core structure periodicity and point defect density along dislocations*. Arizona State University.

Kraevsky S. V., Tournassat C., Vayer M., Warmont F., Grangeon S., Wakou B. F. N. and Kalinichev A. G. (2020) Identification of montmorillonite particle edge orientations by atomic-force microscopy. *Applied Clay Science* **186**, 105442.

Leroy P., Tournassat C., Bernard O., Devau N. and Azaroual M. (2015) The electrophoretic mobility of montmorillonite. Zeta potential and surface conductivity effects. *Journal of Colloid and Interface science* **451**, 21-39.

Lippert B. G., Parrinello M. (1997) A hybrid Gaussian and plane wave density functional scheme. *Molecular Physics* **92**, 477-488.

Liu X., Cheng J., Sprik M., Lu X. and Wang R. (2014) Surface acidity of 2: 1-type dioctahedral clay minerals from first principles molecular dynamics simulations. *Geochimica et Cosmochimica Acta* **140**, 410-417.

Liu X., Tournassat C., Grangeon S., Kalinichev A. G., Takahashi Y. and Marques Fernandes M. (2022) Molecular-level understanding of metal ion retention in clay-rich materials. *Nature Reviews Earth & Environment* **3**, 461-476.

Nadeau P. (1985) The physical dimensions of fundamental clay particles. *Clay Minerals* **20**, 499-514.

Orucoglu E., Grangeon S., Gloter A., Robinet J.-C., Madé B. and Tournassat C. (2022) Competitive Adsorption Processes at Clay Mineral Surfaces: A Coupled Experimental and Modeling Approach. *ACS Earth and Space Chemistry* **6**, 144-159.

Pewdew J., Burke K. and Ernzerhof M. (1996) Generalized gradient approximation made simple. *Phys. Rev. Lett* **77**, 3865.

Tournassat C., Ferrage E., Poinsignon C. and Charlet L. (2004) The titration of clay minerals: II. Structure-based model and implications for clay reactivity. *Journal of Colloid and Interface Science* **273**, 234-246.

Tournassat C., Davis J. A., Chiaberge C., Grangeon S. and Bourg I. C. (2016) Modeling the acid–base properties of montmorillonite edge surfaces. *Environmental Science & Technology* **50**, 13436-13445.

Tsipursky S. I. and Drits V. (1984) The distribution of octahedral cations in the 2: 1 layers of dioctahedral smectites studied by oblique-texture electron diffraction. *Clay minerals* **19**, 177-193.

VandeVondele J. and Hutter J. (2007) Gaussian basis sets for accurate calculations on molecular systems in gas and condensed phases. *The Journal of chemical physics* **127**, 114105.

# 9. Achievements with respect to project objectives - Conclusions

*New/missing data available for sorption models (e.g. surface complexation constants)*

Valuable new sorption data for Cd, Co and Zn on smectite, illite, kaolinite (and mixtures) became available. Interpretative modelling to extract surface complexation constants is on-going.

Based on a study of Soltermann et al. (2014) JGU and the University of Heidelberg constructed an electrochemical cell with the aim to control redox conditions in sorption experiments with redox sensitive tracers. The emphasis was on the construction of the electrochemical cell validating its operation by reproducing original data from Soltermann et al. (2014) for Fe(II) sorption on montmorillonite. Several adverse effects, especially a significant sorption competition on cell components, prevented a direct differentiation of Fe sorption on the clay and the experimental setup, and therefore limited the validity of the obtained sorption isotherms.

BRGM worked on the development of an electrostatic sorption model for montmorillonite which considers the layer structure (e.g., cis-vacant or trans-vacant) and the structure of crystal edges to properly calculate the acid-base properties of the various edge sites. In particular, they studied and modelled the sorption reversibility at edge sites of Kunipia clay, in the Pb/Co and Pb/Mg/Zn systems.

*Transferability of batch sorption data to compact system*

The results obtained for sorption of transition metals on dispersed and compacted Na-FEBEX bentonite indicate that the uptake process in the compacted clay has a much slower kinetic that the uptake in the powdered material, so, not clear if the equilibrium is reached. In the cases where equilibrium is (apparently) reached, as for $^{65}$Zn or $^{109}$Cd, the $K_d$ values measured in the compacted clay are much lower than those obtained in the powdered clay. An exhaustive description of the chemical system, relevant selection of experimental variables and a rigorous differentiation between diffusion and sorption kinetics are mandatory to properly transfer the information from one system to another.

Ni competes with Zn for sorption on illite in disperse systems. Diffusion of Zn in compacted illite does not seem to be affected by the presence of Ni at the concentration levels investigated ($10^{-9}$ to $10^{-4}$ mol/l). The $K_d$ calculated from the diffusion experiments were an order of magnitude lower than in dispersed systems.

Sorption experiments using petrographic thin sections were found to be appropriate for studying transferability of Ni sorption parameters from disperse (crushed rock) to compact (intact rock) BCF systems. However, the appropriate circulation of the liquid phase is important to have similar circumstances for the two kinds of experiments. Without circulation of the liquid phase, the sorbed Ni amount can be an order of magnitude lower for thin sections than expected from batch experiments on crushed rock.

*Transferability of data from model systems to complex systems*

The sorption of Zn on clay mixtures (Illite/smectite/kaolinite) can be described in an additive way.

It is desirable to understand the effects of ions in solution, not only to evaluate ion competition but also to understand the formation of secondary phases of precipitates that can change completely the mobility behaviour.

*Adequate description of sorption competition*

Competition of Ni(II) and Co(II) resulted in suppressing the sorption of Ni(II) on the weak sites in favour of Co(II) for BCF albitic claystone. Data are not yet interpreted quantitatively in terms of sorption models.

In principle sorption competition can be adequately described even if its relevance depends on 1) the number of sorption site available; 2) the type of sorption mechanism; 3) the abundance of the “competitive ion”.

*Irreversibility of sorption under certain conditions*

Microscopy (TEM) and spectroscopy (EDS) confirmed the formation of new Ni-containing phase (at high Ni concentrations $10^{-3}$ M) at the nanoscale even for natural argillaceous rock (BCF) but its unambiguous identification needs further investigations. Isotope exchange method revealed a gradual decrease of sorption reversibility in the $10^{-7}$ – $10^{-3}$ M concentration range that is in line with surface induced precipitation of Ni solids.

Adsorbed Zn species on IdP and SWy systems up to a loading of ~20 mmol/kg are very stable over 2 years reaction time. The structural properties of the Zn surface complexes remain unchanged.

*State-of-the-art spectroscopic, diffractometric and microscopic techniques towards system understanding of irreversible uptake processes*

Microscopy (TEM) and spectroscopy (EDS) were used to investigate the formation of new Ni-containing phase at the nanoscale in natural argillaceous rock of Boda Clay Formation.

Combination of wet chemistry experiments and EXAFS were used to elucidate the long term retention mechanism of Zn by montmorillinite and illite. They indicated that Zn-surface complexes (for loadings up to 20 mmol/kg) on illite and montmorillonite remained unchanged for a reaction period up to 2 years.

Structural characterization using STEM-HAADF was used to elucidate the layer and edge structures of Kunipia-F montmorillonite. Combined with first principles molecular dynamics and surface complexation modelling acid-base properties were determined.

*Description of transport experiments based on mechanistic understanding (anion exclusion, surface diffusion, saturation degree, pore characteristics,…)*

Despite known competition of Ni on sorption of Zn onto illite, Zn transport was not influenced by the presence of Ni at the concentration levels investigated ($10^{-9}$ to $10^{-4}$ mol/l).

The diffusion and retention of Zn and Co in compacted illite pre-loaded with different cations provided insights on the mechanisms inducing surface diffusion. The type of hydrated cation determines the electric double layer properties. The surface diffusion index $\varphi$ indicate the role of the cationic loading of illite with the following order for both of the tracers $\varphi_{Li\_IdP} \approx \varphi_{Na\_IdP} > \varphi_{K\_IdP} > \varphi_{Cs\_IdP}$.

Co diffusion in compacted vermiculite with different grain sizes showed the presence of surface diffusion to occur, but the impact of the grain size on this phenomena remained unclear. The effective diffusivity can be influenced by the geometrical properties of the clay (G factor) or by the distribution ratio of the mobile species between the diffuse layer and the bulk aqueous phase ($\frac{C_{DL}}{C_{free}}$). Although the surface diffusion is evident for all grain sizes, geometric effects appear to be the strongest influencing factor. The extent to which grain size or the mobile distribution ratio affects this phenomenon remains unclear.

# Chapter 4: Mobility of strongly sorbing (La/Ac) radionuclides in clay

Chapter 4 comprises studied on the mobility of strongly sorbing lanthanides/actinides in clay systems conducted by four research teams.

IPHC (Strasbourg, France) addressed the mechanisms of (co)sorption of uranyl ions and phosphate ligands in presence of carbonate on the surface of Na-illite by combining batch sorption, electrophoretic mobility analysis and in-situ ATR-FTIR spectroscopy to monitor the clay-solution interface throughout the (co)sorption process.

SUBATECH (Nantes, France), in collaboration with BRGM and ANDRA, investigated i) the retention of Eu on compacted COx and ii) the retention of U(IV/VI) on the COx formation where they go from lab based models to *in natura* conditions.

Pu(IV) diffusion in Opalinus Clay rocks was studied by JGU (Mainz, Germany) using TOF-SIMS to analyse the geochemical interactions with the host rock.

EK (Budapest, Hungary) investigated the diffusion behaviour of uranyl ions in natural Boda clay samples.

The diffusion behaviour of U(VI) and Am(III) in Opalinus Clay was investigated by KIT (Karlsruhe, Germany) in the framework of a PhD project co-funded under the iCross project and the data were shared within the FUTURE project.

## 1. Uranyl speciation studies at the Illite - solution interface

M. Del Nero, S. Yao Guo, O. Courson, S. Meyer-Georg, R. Barillon
*CNRS - IPHC, Strasbourg, France*

## Abstract

Although is well known that phosphate ions (noted P) and / or carbonate ions (noted C) may concur and effect the long term uptake of uranyl ions in a variety of geochemical systems, including in clayey formations envisaged as long term barriers to radionuclide migration in far field of high level nuclear waste repository, experimental and spectroscopic work is still needed to document the surface speciation of U and P on relevant clay minerals such as illite.

We addressed the mechanisms of (co)sorption of trace levels of uranyl ions (1-10µM) and/or phosphate ligands (50µM-250µM), under atmospheric $CO_2$ or at high concentration of carbonate ligands, on the surface of a homoionic Na-illite by combining batch sorption experiments, electrophoretic mobility (EM) analyses, and in situ ATR FTIR spectroscopy monitoring of clay-solution interface throughout the (co)sorption process. Regarding phosphate ions, macroscopic data indicated that the percentage of P sorption is dependent on pH (for pH > 6), aqueous phosphate concentration, and clay-to-solution ratio of the experiment, i.e., the surface coverage of the clay by phosphate. The macroscopic and EM data further suggested a predominant mechanism of strong sorption of phosphate ions onto Illite, which confers negative charges on the mineral surface and involves several sorption species and/or surface sites on clay edges (limited amounts of high-affinity and low-affinity aluminol sites, respectively). In situ IR data showed that, at acidic pH, three types of phosphate surface species form at the Illite-solution interface: an outer-sphere surface complex (OSSC) of phosphate ($\equiv \mathrm{SOH_2^+ \cdots H_2PO_4^-}$), an inner-sphere surface complex (ISSC) of phosphate, probably a monodentate binuclear surface complex ($\equiv \mathrm{(SO)_2PO_2}$), and, in very limited amounts, a monoprotonated monodentate binuclear surface complex ($\equiv \mathrm{(SO)_2(OH)PO}$) or an Al-phosphate surface precipitate. Sorption of phosphate ions proceeds by initial formation of the OSSC of phosphate, which dominates surface speciation only at short reaction times (< 1 day) and low aqueous P concentrations and transforms with time into the ISSC of phosphate.

Regarding uranyl ions, macroscopic data indicated that the percentage of uranyl sorption is dependent on pH, on aqueous U concentration and clay-to-solution ratio of the experiment, i.e., the clay surface coverage by U, as well as on the concentration of phosphate ligands (at acidic pH) while carbonate ligands have only

slight signature on U percent sorption. However, ATR FTIR experiments suggested that uranyl carbonato surface species were formed at illite surface. In the presence of phosphate ligands, the macroscopic and EM data suggested mostly reversible mechanisms of P and U co-sorption that is controlled by negative charges on the mineral surface and involve several types of uranyl phosphate surface species, depending on key parameters and/or surface sites present on the clay edges (limited amounts of high-affinity and low-affinity sites, respectively). In situ IR data provided strong evidence that, at acidic pH, three types of inner sphere uranyl phosphate surface complex form at the illite-solution interface, under the conditions studied. Two surface complexes formed rapidly at high and low affinity surface sites, respectively, with formation of the latter increasing with U surface coverage, and competed successfully against formation of outer-sphere and inner sphere surface complexes of phosphate. At high U concentration (10 µM) and reaction time (>1day), a third U-P surface complex having an autunite-like structure (likely as U-P polynuclear surface species) appears to additionally form on the NaIdP surface. Strikingly, in the presence of $Fe^{3+}$ ions, only the latter species was identified to form together with Fe-phosphate surface precipitates.

## Introduction

Storage of high-level radioactive wastes (HLW) in deep geological repositories in clay rock formations (such as Boom clay, Callovo-Oxfordian clay, Cox, and Opalinus clay, OPA) are considered by several countries as an important strategy [1]. Clay minerals as illite are major constituents of these argillaceous formations, e.g., [2,3], and have remarkable properties such as a high capacity of radionuclides (RN) retention, which make these formations prospective geological barriers for HLW [1,3–6]. It has long been known that sorption at surfaces of clays may strongly retard the environmental migration of U(VI), which is potentially mobile [7,8]. Gaining a comprehensive and mechanistic understanding of uranium(VI) sorption processes onto clays, under a variety of physicochemical conditions, is thus essential to increase the robustness of models used to predict the environmental fate of U(VI).

During last decades, numerous experiments and/or surface complexation modelling studies have suggested that a strong chemical sorption of uranyl ions prevails onto clay minerals or rocks [3,5,9–13]. Experiments have also shown that the presence of phosphate ligands, which are ubiquitous in clay-solution systems, promotes the U sorption at mineral surfaces [14–18], and may trigger nucleation and precipitation of U(VI) phosphates. Further molecular scale work has provided evidence that uranyl ions are sorbed onto montmorillonite as exchangeable $UO_2^{2+}$ in clay interlayers at acidic pH and, with increasing pH, as additional inner sphere U(VI) surface complex (ISSC) of uranyl and / or U(VI) polynuclear surface species [5,19–21] and / or uranyl carbonato ISSC [22]. Multiple U(VI) surface species were also identified by Attenuated Total Reflectance Fourier Transform Infrared (ATR FTIR) spectroscopy to co-exist at the surface of montmorillonite in contact with a solution at near-neutral pH and at a low concentration of U (20 µM) [23]. Two spectroscopic studies have so far been devoted to co-sorption of uranyl and phosphate ions (noted P, hereafter) onto surfaces of clays [24,25], with the latter highlighting a transition between formation of U(VI)-phosphate ISSC and U(VI)-phosphate surface precipitates with U surface coverage. Hence, U(VI) is sorbed at surfaces of clays in a variety of chemical forms, depending on key parameters, such as pH, presence of ligands, and U surface coverage governed by mineral surface properties. Further spectroscopic work is thus needed to identify the mechanisms of (co)sorption of U(VI) and phosphate / carbonate ions onto Illite, which is of interest for better understanding the uptake of U(VI) on illite-rich clays such as those envisioned as far-field HLW repository host rocks. To this end, providing data from *in situ* spectroscopic monitoring of the Illite – ligand - solution interface during the U sorption process as a function of key parameters, e.g. pH, reaction time and surface coverages, is mandatory.

Moreover, some spectroscopic studies have reported either a low binding of phosphate ions on the clay surface in the absence of U(VI) [25] or a strong sorption of P onto clay rocks driven by presence of minor phases like metal-(oxihydr)oxides and / or cations like Fe [26–28]. In contrast, other studies have reported the formation of ISSC of phosphate at the edge sites of kaolinite [29,30]. There appears thus that further work is needed to identify the (multiple) sorption species of phosphate formed onto clays having a more complex structure than kaolinite, e.g., such as Illite, in the absence and presence of Fe ions. This would

provide useful information on the affinity of clayey fractions of rocks towards RN, as P sorption is expected to influence clay surface reactivity [31].

The aim of this study was to identify the mechanisms *(i)* of sorption of phosphate / carbonate ligands and *(ii)* of co-sorption between low level concentrations of U(VI) and the ligands onto a homo-ionic Na-Illite, in the absence or presence of $Fe^{3+}$ ions. First, batch sorption experiments were carried out to quantify macroscopic sorption of U and/or P in a wide range of pH (3-8), at various clay-to-solution ratio (1-3 $g.L^{-1}$), concentrations of U (1-10µM) and/or phosphate ions (20-200 µM) and / or $Fe^{3+}$ ions (0-10 µM) under atmospheric conditions, and/or under an atmosphere at high $pCO_2$ (2,5%). Measurements of electrophoretic mobility (EM) of suspended clay particles, and its variation with key parameters studied, were performed to determine the charges imparted by sorption reactions to the clay surface and to gain information on surface species formed. Second, experiments of *in situ* monitoring of clay - U(VI) – phosphate / carbonate – solution interface by ATR FTIR spectroscopy were conducted in order to identify the surface speciation of U, as a function of time and total concentration of uranyl (2-10 µM) or phosphate (50-200 µM) ions, i.e., surface coverage, or at high carbonate concentration ($[C]_{I,aq}$: 100mM). Sorption species were characterized by (changes in) coordination environments of sorbed phosphate / carbonate units that were deduced from changes in FTIR spectra of Illite-aqueous solution interface. Spectroscopic data and macroscopic data presented here provide useful information on the surface speciation of uranyl ions and / or phosphate/carbonate ligands (co)sorbed onto Illite, which could serve modelling of migration behaviour U(VI) in argillaceous formations.

## Materials and methods

### Source materials

All the solutions used in experiments were prepared by using ultrapure Milli-Q water (purity > 18 MΩ·cm) and reagent grade chemicals. Source material was an argillaceous clay (called “Illite du Puy”) collected in the Massif Central Mountains in France and provided by the company “Argile Verte du Velay”. Two clay stock samples were used. The first one, noted here as “IdP”, corresponds to the particle size fraction < 77 µm of the source material. The second one, noted here as “NaIdP”, was obtained by purification of a sample of IdP in order to convert initial Illite into a Na-homoionic Illite. The subsample was conditioned by acid washing and subsequent exchange of the exchangeable cations against $Na^+$ by using the method detailed by Glaus et al. [32]. The treatment was expected to remove hydrolysed products -such as hydroxy-aluminum compounds-, phosphate impurities and soluble minerals like calcite [6,32]. Final sample was dried at 40°C, powdered in an agate mortar and sieved. The size fraction < 75 µm was taken as the final NaIdP stock sample, which was stored in a desiccator until its use in experiment.

### Characterization of Illite du Puy

#### Mineralogical and chemical analyses

Mineralogical compositions of IdP and NaIdP were obtained from X-ray diffraction (XRD) analyses conducted with a Bruker diffractometer. Measurements were performed on the whole-rock samples and the clay size (< 2 µm) fractions after various sample treatments [33]. Minerals of the clay fraction were identified by values of their (inter)layer spacing [34]. A semi-quantitative estimation of the percentage of each clay mineral was made by using the software DIFFRAC.EVA (error in measurements reproducibility of < 5 %). Major element and trace element analysis of the (Na)IdP samples and their clay size fraction were made by using inductively coupled plasma optical emission spectrometer (ICP-OES) and inductively coupled plasma mass spectrometer (ICP-MS), respectively. Analytical precision was lower than 0.1 % (wt% oxides) and 5-20 %, respectively (< 10 % for U concentrations > 10 $\mu g \cdot g^{-1}$).

#### Specific surface area

Specific surface areas were determined by $N_2$-BET measurements using an ASAP2420 surface area and porosity analyser. Values of 92 and 107 $m^2 \cdot g^{-1}$ were found for IdP and NaIdP, respectively, in agreement with that reported by Bradbury and Baeyens [13,35].

### Preliminary experiments of (Na)IdP-solution interactions

Experiments were conducted in order to determine chemical composition of solutions in contact with IdP or NaIdP, respectively. Batch experiments were performed under atmosphe and at a given ionic strength value of 0.005M (NaCl), at different solid-to-solution ratios ($R_{S/L}$: 0.5 to 6g.L$^{-1}$), reaction time (24 hours – 7 days), and pH (3-7). Suspensions of (Na)IdP were prepared in individual (50mL) polypropylene tubes at desired values of $R_{S/L}$ and initial pH and were then equilibrated by gently shaking end-over-end during a desired reaction time. After equilibration step, final pH was measured (uncertainty: 0.05 pH unit) and the suspensions were centrifuged at 9000 rpm for 3 hours for a solid–solution separation (cut-off: 16 nm for Illite). A defined volume of supernatant was taken from each individual tube and was acidified at pH < 1 (with 67% $HNO_3$) for analysis of major and trace elements by ICP-OES and ICP-MS, respectively.

## Macroscopic sorption

### Phosphate ions sorption

Batch sorption experiments were carried out at 298K under atmosphere to evaluate the effect of pH, total concentration of phosphate ions (noted $[P]_{I,aq}$), and solid-to-solution ratio ($R_{S/L}$) on the retention of P at the NaIdP–solution interface. Batch experiments were carried out to obtain: (i) phosphate sorption edges ($pH_F$: 3-8) at various $R_{S/L}$ and phosphate concentrations ($[P]_{I,aq}$: 20 µM and $R_{S/L}$: 1, 2 or 3 g.L$^{-1}$, respectively; $[P]_{I,aq}$: 100 µM and $R_{S/L}$: 3 g.L$^{-1}$) and (ii) phosphate sorption isotherms at pH = 4 ($[P]_{I,aq}$: 20-200µM, $R_{S/L}$: 3 g.L$^{-1}$). The experiments were conducted as follows. Suspensions of NaIdP in 0.005 M NaCl electrolyte solutions were pre-equilibrated for 3 days in 15mL polypropylene centrifuge tubes, at desired values of $R_{S/L}$ and pH. After 3 days of pre-equilibration, an aliquot of a stock phosphate solution of 0.05 M was added in the tubes to achieve the desired $[P]_{I,aq}$ value and the tubes were gently shaken end-over-end for 4 days. Final pH were measured after a 4-days contact time. Separation between solid and solution was carried out by centrifugation of suspensions for 3 hours at 9000 rpm. The supernatants were then removed from the tubes. An aliquot was taken for electrophoretic mobility (EM) measurements. Another aliquot was taken for chemical analyses after acidification at pH < 1 by addition of 2% $HNO_3$. Each experiment was performed in duplicate. Blank experiments without solid were also conducted.

### (Co)sorption of uranyl ions

First, batch experiments were carried out at 298K, without addition of any ligand (other than dissolved carbonate in equilibrium with air), to evaluate the effect of pH, total concentration of uranyl ions ($[U]_{I,aq}$) and clay-to-solution ratio on the macroscopic uptake by NaIdP. Sorption edges were obtained in the pH range 3-8, at different values of $[U]_{I,aq}$ (1 and 12 µM) and $R_{S/L}$ (1, 2 and 3 g.L$^{-1}$). Sorption isotherms ($[U]_{I,aq}$: 1-25 µM, $R_{S/L}$: 3 g.L$^{-1}$) were also obtained at pH 3, 3.5 and 4, respectively. Experiments were conducted (in duplicates) as described above except that a known volume of a U(VI) stock solution ([U]=4.61×10$^{-3}$ M, acidified at pH 1 by HCl) was introduced in the tubes to achieve defined $[U]_{I,aq}$ values.

Second, batch experiments of U(VI) sorption onto NaIdP were performed at a partial pressure of $CO_2$ of 2.5% in order to evaluate the effect of carbonate ligands on the pH-dependency of uranyl ion sorption ($[U]_{I,aq}$: 12 µM, $R_{S/L}$: 3 g.L$^{-1}$). Experiments were conducted as described previously except that all solutions / samples were prepared in a glove box in a $pCO_2$ of 2.5% was maintained during experiment.

Third, co-sorption experiments were conducted to investigate the effect of the presence of phosphate ligands on the uptake of uranyl ions by NaIdP, at different values of pH and $[U]_{I,aq}$, and for a given clay-to-solution ratio ($R_{S/L}$ = 3 g.L$^{-1}$). Sorption edges of U/P were obtained in the pH range 3-8, at two different U concentrations ($[U]_{I,aq}$ = 1 and 12 µM, respectively) and a moderate concentration of P ($[P]_{I,aq}$= 100 µM). Sorption isotherms of uranyl ions (for $[U]_{I,aq}$: 1-12 µM) were also obtained at pH 4 and at two concentrations of phosphate ions ($[P]_{I,aq}$: 20 and 100 µM, respectively). Experiments were conducted as described above except that known volumes of the stock solutions of phosphate ions and uranyl ions, respectively, were added simultaneously to the individual tubes in order to achieve desired $[P]_{I,aq}$ and $[U]_{I,aq}$ values in experiments. Complementary sorption experiments were carried out to investigate the (competitive) effect of the presence of $Fe^{3+}$ on the U-P co-sorption. In such cases, desired volumes of stock solutions of U(VI),

Fe(III) and phosphate ions were adding simultaneously to the centrifuge tubes to achieve the desired aqueous sorbate concentrations ($[U]_{I,aq}$=12 µM, $[Fe]_{I,aq}$=10 µM and $[P]_{I,aq}$=100 µM). Moreover, two of the U-P co-sorption experiments (at $pH_F$ equal to 5.2 and 4.1, respectively) were used for studying the kinetics of desorption of U(VI) and the reversibility of the (co)sorption processes. After the step of equilibration of the two above-mentioned sorption experiments, the pH of the suspensions was brought to a value of 3.2 in the individual tubes. The tubes were gently rotated end-over-end and shaken during ca. 15 days. Aliquots of the suspensions were regularly taken for solid-solution separation. Supernatants were prepared and used for chemical analysis of final aqueous U concentration.

For all investigated cases, blank experiments without solid were also performed.

#### Analysis of experimental solutions of sorption experiments

Measurements of EM of suspended particles present in supernatant aliquots collected at the end of the sorption experiments were made by using a Zetasizer Nano equipment (Malvern). Each sample was measured three times and standard error was then calculated. Final aqueous phosphate concentrations ($[P]_{F,aq}$) in experiments were analysed by ion chromatography (Eco IC, Metrohm, uncertainties of 1 – 10%) and / or by ICP-OES. Final aqueous concentration of uranium ($[U]_{F,aq}$)were obtained by ICP-MS analyses. Percentage (%) and amount (µmol. $g^{-1}$) of sorbates sorbed were calculated as follows:

$$\%\ sorbed = \frac{C_i - C_{eq}}{C_i} \times 100 \qquad Amount\ sorbed = (C_i - C_{eq}) \times \frac{V}{M}$$

$C_i$ and $C_{eq}$ are aqueous concentrations of sorbate (µmol.$L^{-1}$) in initial and final experimental solution, respectively, $V$ the volume of solution (in L) and $M$ the mass of solid (in g). Uncertainties on percentage of sorption and surface coverage were estimated to be lower than 10% for both U and P.

### In-situ ATR FTIR experiments

#### Procedures of clay deposition on the ATR crystal

Acquisition of IR spectra at the mineral-solution interface was carried out by using a Bruker Equinox IFS 55 infrared spectrometer equipped with an ATR cell containing a ZnSe horizontal crystal (with an angle of incidence of 45°, a crystal size of 7.2×1.0×0.7 $cm^3$ and 5 internal reflections) and a MCT detector (system cutoff: ca. 900 $cm^{-1}$) that was cooled down by liquid nitrogen during FTIR spectra acquisition. Prior to experiment, the ZnSe crystal was either coated with a thin film of IdP or NaIdP brought subsequently in contact with a 0.005M NaCl electrolyte, or it was directly brought in contact with a pre-equilibrated NaIdP suspension (from which clay particles are left to settle and cover the crystal). Both methods have the advantage of allowing an in-situ monitoring of solid–solution interface along sorption.

The former method was shown to be powerful to monitor sorbate sorption, with a good reproducibility of the experiments and an increased sensitivity for surface species, and is given in details elsewhere [15,36]. It was used here to monitor the dissolution of (Na)IdP and to gain insights into IR vibrations due to mineral's structure and or to structural reorganization of the interface with time. The latter method, i.e., covering of the crystal with an equilibrated two-layers NaIdP–electrolyte solution system, was used to monitor sorption of uranyl / iron ions and/or phosphate / carbonate ligands at the clay-solution interface, for near-equilibrated systems (in order to avoid IR signals due to solid dissolution). It was conducted as follows: *(i)* a NaIdP suspension was prepared (contact time of 3 days, $R_{S/L}$= 3 g.$L^{-1}$, pH 4), *(ii)* 10 mL of suspension were pipetted and added into the ATR cell, *(iii)* the suspension was left to settle for 3 days and (iv) an ATR FTIR spectrum was taken as a reference baseline prior to sorbate addition.

#### Monitoring of the clay-solution interface

In-situ ATR FTIR spectroscopy experiments were performed to monitor the clay–solution interface during interaction of (Na)IdP with a 0.005 M NaCl electrolyte solution ($R_{S/L}$=3 g·$L^{-1}$). After coating of the ATR crystal with a dried thin film of IdP or NaIdP, 10 mL of the electrolyte solution were added in the ATR cell, in order to perform FTIR measurements of clay–solution interface (pH 6.2 for IdP, pH 4 for NaIdP) under atmospheric $CO_2$. A similar experiment was conducted to investigate sorption of carbonate ligands on

NaIdP surface (at pH 7.6). Covering of the ATR crystal with a two layers NaIdP–electrolyte solution system was made in a glove box under $N_2$ atmosphere. The system was left to re-equilibrate in a glove box under a controlled atmosphere ($pCO_2$: 2.5%) For all experiments, an FTIR spectrum was recorded as a reference baseline and (Na)IdP-solution interactions were monitored during 3 hours. Each IR spectrum was recorded during 20 min with an average of 2000 scans/spectrum (resolution of 4 $cm^{-1}$).

### Monitoring of the clay–solution interface along sorption processes

First, ATR FTIR experiments were performed to monitor *in-situ* the sorption of phosphate ligands at the interface between NaIdP and a near-equilibrated electrolyte solution, and to gain insights into IR vibration bands of sorption species ($R_{S/L}$=3 $g.L^{-1}$). Two experiments were performed. The first one was devoted to monitor the NaIdP-phosphate-solution interface as a function of reaction time ($[P]_{I,aq}$: 100 µM, pH 4). After covering of the ATR crystal with the two-layers NaIdP-electrolyte solution system and recording of a reference baseline, a defined amount of a stock phosphate solution was added in the cell in order to achieve a $[P]_{I,aq}$ value of 50 µM. IR spectra of the interface were recorded during 1 hour (one spectrum per 20min.). Total concentration of aqueous P added was then increased to 100 µM and IR spectra were collected as a function of time ($t_R$ up to 3 days). The second one aimed at investigating the NaIdP-solution interface during a continuous increase of $[P]_{I,aq}$ from 100 µM to 300 µM. The experiment was performed as described above up to the collection of IR spectra at $[P]_{I,aq}$ of 100 µM, for a $t_R$ value of 17h (which was shown to allow appearance of IR signals of sorbed ISSC of phosphate). $[P]_{I,aq}$ was then raised from 100 to 300 µM by successive additions every hour of 50 µM of phosphate ions. IR spectra were collected after each addition and then every twenty minutes.

Second, experiments were performed to monitor by ATR FTIR spectroscopy the *in situ* evolution of the (Na)IdP - solution interface during (co)sorption of uranyl ions and phosphate/carbonate ions, for trace levels of U ($[U]_{I,aq}$ : 2-10 µM). Two experiments were performed to gain insights into the effects of uranyl concentration and reaction time, respectively, on the mechanisms and species involved in co-sorption process of U and P. The first one was carried out to monitor changes in coordination environments of sorbed P along an increasing of $[U]_{I,aq}$ (2-10 µM). It started by addition (100 µM) of aqueous P to a two-layers NaIdP–solution system prepared in the ATR cell (two successive additions of a small volume of a stock phosphate solution to reach a $[P]_{I,aq}$ value of 50 µM) before recording of the FTIR interface spectra during 2 hours. Then, the concentration of U was progressively increased by stepwise additions of small volumes of a stock solution of U to increase $[U]_{I,aq}$ by 2 µM per hour. After each addition, FTIR interface spectra were recorded. The second experiment aimed at monitoring the NaIdP-solution interface as a function of reaction time ($t_R$ = 3 days) along the process of (co)sorption of phosphate ions and uranyl ions (simultaneous additions in the ATR cell of small volumes of the P stock solution and U stock solution to reach values of $[U]_{I,aq}$ of 8 µM and $[P]_{I,aq}$ of 100 µM, and recording of FTIR interface spectra during 3 days). A complementary experiment was also performed to study the effect of $Fe^{3+}$ ions on the co-sorption of P and U. The experiment was conducted as described before except that U(VI) (10µM), Fe(III) (10µM) and phosphate (100µM) ions were introduced simultaneously in the ATR cell, before recording of the interface spectra for ~3 days. In a similar manner, ATR FTIR were performed to investigate the effect of carbonate ligands. The NaIdP-carbonated solution interface and the changes in coordination environments of sorbed carbonate ligands were monitored along uranyl sorption process, (simultaneous additions in the ATR cell of small volumes of a $NaHCO_3$ solution and a U stock solution to reach values of $[U]_{I,aq}$ of 10 µM and $[C]_{I,aq}$ of 100mM, and recording of FTIR spectra during 3 days).

For all systems investigated, blank experiments (without clay) were also performed by using electrolyte solutions at various total concentrations of sorbates, in order to: *(i)* get values of detection limits of the technique for solution species, *(ii)* record IR spectra of aqueous species taken as “references” for sorption species, and *(iii)* identify a possible formation of precipitates, depending on conditions.

### Analysis of FTIR spectra

Analysis of the FTIR spectra was focused on the region 900–1200 $cm^{-1}$ characterized by the presence of the $\upsilon_3$ P-O(M) antisymmetric stretching and / or $\upsilon_1$ P-O(M) symmetric stretching (M: hydrogen or metal

atom) vibration bands [37–41] or 1300-1400 $cm^{-1}$ characteristics of C-O stretching vibrations [42]. The software *OriginPro*© version 9.1 was used for baseline correction and decomposition of the FTIR interface spectra, in order to resolve IR bands with Gaussian lines and least-square fitting. No constraints were applied on adjustable parameters (band's position, intensity and width). Previously published studies of uranyl coordination environments by using vibrational spectroscopy were mainly focused on the infrared-active U-O antisymmetric stretching band ($\upsilon_3$) at 900–980 $cm^{-1}$ and on the Raman-active U-O symmetric stretching band ($\upsilon_1$) at 800–880 $cm^{-1}$ [43,44]. For complexes of uranyl ions formed in solution or at mineral surface, the $\upsilon_3$ of the uranyl unit was found to be in the range 890–954 $cm^{-1}$ [15,44,45]. The $\upsilon_3$ band of uranyl unit was not easily observable in IR spectra of NaIdP–solution systems, due to a high IR absorption of clays at ~950 $cm^{-1}$ (e.g.,[26]) and system cutoff at ~900 $cm^{-1}$.

## Results and discussion

### Composition of Illite du Puy and interactions with solution

Mineralogical compositions of IdP and NaIdP are given in *Table A1* (*appendix A*). Calcite is the major mineral in IdP, followed by feldspars (mainly potassic) and clays, i.e., Illite and kaolinite. Quartz and siderite are minor minerals and hematite an accessory mineral. The clay fraction has a composition dominated by Illite, then kaolinite. NaIdP is composed by Illite, feldspars and small amounts of kaolinite and quartz, while no carbonates (calcite, siderite) nor hematite were detected by XRD analysis.

Major element compositions of clays (*Table A2- appendix A*) are consistent with those of silicate rocks dominated by K-feldspars, carbonates and clays. $Fe_2O_3$ represents a significant percentage (> 5%). Thus, iron minerals may represent less than 5% and / or Fe is incorporated in the clay's structure, as proposed by Poinssot et al. [46]. Removal of carbonate minerals upon conditioning is marked by a sharp decrease of percentage of CaO from IdP to NaIdP. Treatment also led to removal of phosphates. Chemical composition of NaIdP is consistent with that given for Na-Illite by Bradbury and Baeyens [13,35]. Trace metal compositions are given in *Table A3* (*appendix A*). The order of concentrations ($\mu g \cdot g^{-1}$) is as follows: Rb, Ba, Zn (> 150) > Cr, Cs (80-100) > Pb, As, La, Cu, Ga, Ni (50-20) > others (U: 3$\mu g \cdot g^{-1}$). Concentrations are lower in NaIdP than in IdP for Sr, As and Ln, due to clay conditioning.

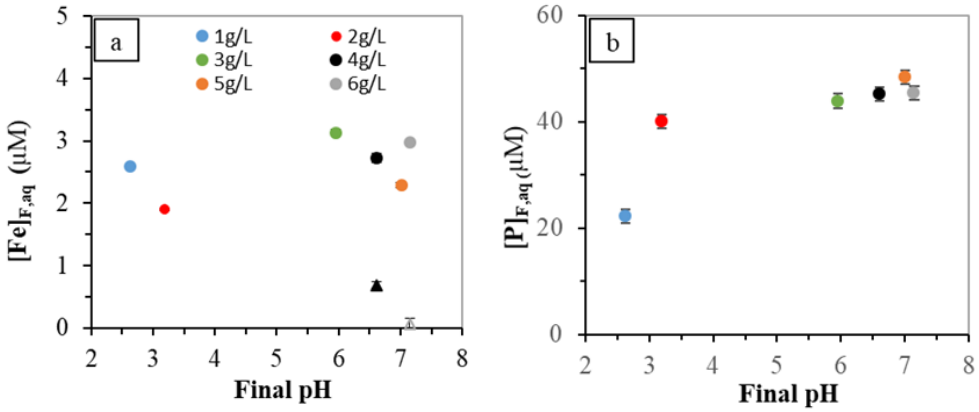


*Figure 1: Final concentrations of (a) Fe ions and (b) phosphate ions vs. final pH of solutions contacted with IdP at various clay - solution ratios ($R_{S/L}$: 1-6 $g.L^{-1}$). Experimental conditions: initial pH 2-3, 0.005M NaCl electrolyte, 5 days contact time. Cercle and triangle symbols are for solutions centrifuged and filtered at 3 kDa, respectively.*

Compositions of solutions equilibrated with (Na)IdP at different clay-to-solution ratio ($R_{S/L}$) are given in *Tables A4-5 and Figures A1-2 (appendix A)*. For IdP, final aqueous concentrations of cations (noted $[]_{F,aq}$) are in the order: $[Ca]_{F,aq} > [K]_{F,aq} > [Mg]_{F,aq}$. Major anions are phosphate ions that reach an almost constant concentration for a range of $R_{S/L}$ (*Figure 1*) and fluoride ions. Concentrations of U remain in the ppb level. Results of speciation calculations performed by using the Visual MINTEQ code and the database used are reported in *Tables A6-8 (appendix A)*. Phosphate ions and carbonate ions are major ligands influencing

speciation of trace metals for solutions at pH 4–7 and at pH >6.8, respectively, under atmospheric $CO_2$. Values of $[Ca]_{F,aq}$ and $[anions]_{F,a}$ are much lower for NaIdP than IdP, while $[Fe]_{F,aq}$ displays a constant value (ca. 3µM) whatever sample, pH and $R_{S/L}$ (*Figure 1*). At near-neutral pH, its value decreases with filtration threshold, which suggests formation of colloidal phases containing Fe, regardless of the clay sample. These data support a need for spectroscopic work to elucidate surface speciation of phosphate ions, which are expected to strongly affect the sorption of U onto Illite du Puy.

## Macroscopic sorption behaviour

### Uranyl sorption edges and isotherms

*Figure 2* shows the effects of pH on the (co)sorption of U(VI) and on particle EM, in NaIdP - solution systems containing or not phosphate ions. There were observed S-shaped uranyl sorption edges whose values of $pH_{50}$ (where percentage of U sorption is equal to 50%) are in the acidic pH domain. In the absence of P, a ten-fold increase in $[U]_{I,aq}$ induces a small shift in $pH_{50}$ and U(VI) uptake is almost complete in the pH range 6-8. This suggests that multiple sorption species and/or clay surface sites are involved in uptake of U at pH < 5, for the U surface coverage studied (< 3.8 µmol·g$^{-1}$, *Figure 2*a). A limited change in the contributions of high and low affinity surface sites at clay edge platelets are likely. If considering that each uranyl ion sorbed is bound to a single edge sorption site, the calculated value of surface site occupancy by U is very low (ca. 0.02 sites.nm$^{-2}$). This value is lower than those reported in literature for density of total sites at edges of illite (e.g., 2.31 sites.nm$^{-2}$ [47], 0.4 sites.nm$^{-2}$ [13,35]) or low-affinity sites on clay basal planes (e.g., 13-16 sites. nm$^{-2}$ [48]). However, Bradbury and Baeyens [13,35] considered in their modelling studies of the sorption of uranyl ions onto Illite du Puy that a small amount (ca. 0.01 sites·nm$^{-2}$ or 2 µmol·g$^{-1}$) of very high affinity sites are present at the clay edges. Based on their work, it is expected that high affinity surface sites present at NaIdP particle edges are involved in strong interactions with sorbates and control the sorption of U(VI) at the lowest concentration studied, while a limited fraction of lower-affinity edge surface sites may contribute to U sorption at higher concentration. Complementary sorption isotherms acquired at pH 3, 3.5 and 4.1 in an extended U concentration range ($[U]_{I,aq}$: 1-25µM) are given in *appendix A* (*Figures A3-A4*). A slight increase in U percent sorption, and a non-linear increase in amount sorbed, suggest formation of additional uranyl sorption species at highest U concentrations studied, including possibly (surface) precipitates. Decrease of $R_{S/L}$ (*Figures A5-A6, appendix A*) induced a shift of U sorption edges, which further confirm that a small amount of very high affinity sites exists at NaIdP edges [13,35]. Such sites may be responsible for sorption of trace level of U at the clay edge platelets, while at high U concentration and low $R_{S/L}$, multiple sites and/or uranyl sorption species may be involved. Under a high $pCO_2$, the macroscopic sorption of uranyl ions is slightly decreased (by ca. 10%) in pH range 6-8 (data not shown).

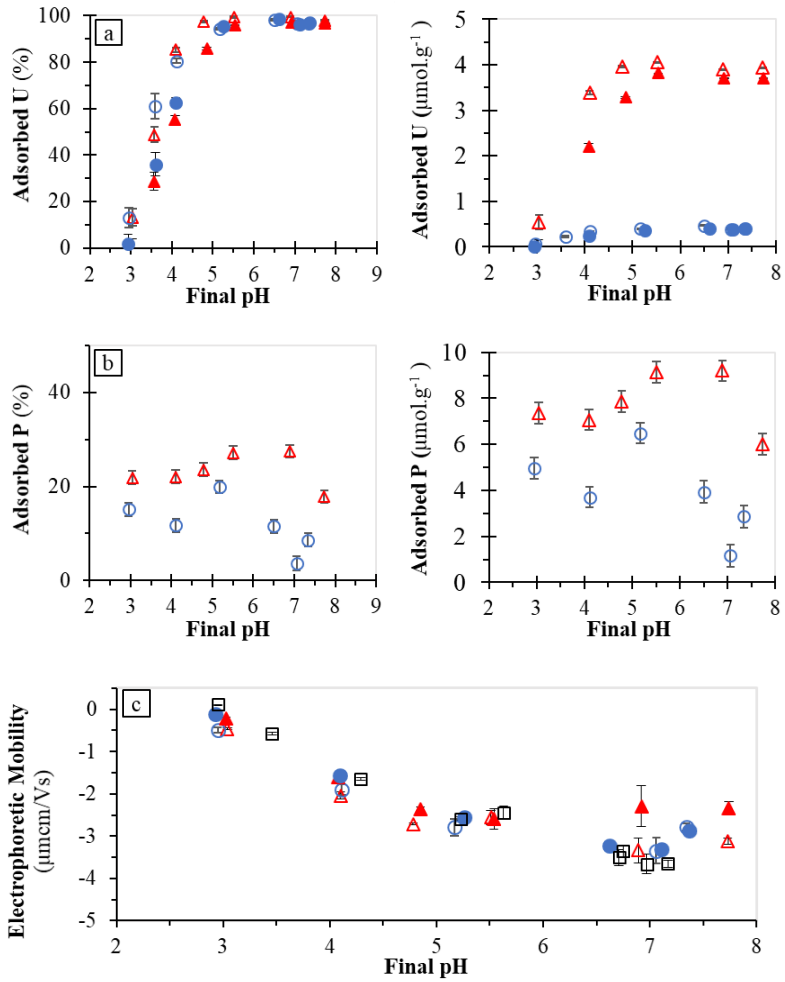


*Figure 2:* Sorption of uranyl ions (a) and phosphate ions (b), and particle electrophoretic mobility (c), as a function of final pH for 3 g·L$^{-1}$ NaIdP contacted ($t_R$= 4 days) with 0.005 M NaCl electrolyte solutions at different total concentrations of U(VI) ($[U]_{I,aq}$ = 0, 1 or 12 µM) and phosphate ions ($[P]_{I,aq}$ = 0 or 100 µM). NaIdP-electrolyte systems were pre-equilibrated ($t_{pre-eq}$ = 3 days) prior to sorbate addition. EM data of blank experiments (without U and P - × plot). (○: $[U]_{I,aq}$ = 1µM and $[P]_{I,aq}$ = 100 µM - Δ: $[U]_{I,aq}$ = 12 µM and $[P]_{I,aq}$ = 100 µM - ▲,● without P - □: Blank).

### Sorption edges and isotherms of phosphate ions

*Figure 3* shows sorption edges of phosphate ions at different concentration ($[P]_{I,aq}$ : 20 µM and 100 µM) and NaIdP-to-solution ratio ($R_{S/L}$ = 1, 2 and 3 g·L$^{-1}$). The percentage of P sorbed is quite constant in the pH range 3-6, and decreases for pH values higher than 6. Several hypothesis may account for this pH dependence. First, a progressive deprotonation of the amphoteric silanol sites present at clay surfaces is expected when increasing pH to values higher than 6. Second, a pH value of 6 coincides with appearance of the $HPO_4^{2-}$ aqueous species. These features contribute to an increasing of electrostatic repulsion between clay surface and aqueous phosphate at (near) neutral pH, which is unfavourable to phosphate adsorption [49]. *Figure 3* shows that the pH-dependence of surface coverage of NaIdP by phosphate ions (in µmol·g$^{-1}$) does not depend on clay-to-solution ratio, at low $[P]_{I,aq}$, suggesting similar sorption sites and/or sorption species. An increasing of $[P]_{I,aq}$ results in a decrease of percentage of P sorbed and concomitant (non-linear) increase of surface coverage. This illustrates the existence and involvement in P sorption of multiple phosphate surface species / sites, at high P surface coverage.

*Figure 4* shows the sorption isotherm of phosphate ions at acidic pH ($pH_F$: 4±0.05; $[P]_{I,aq}$). There was observed a decrease in the percentage of P sorption with $[P]_{I,aq}$. Surface coverage by phosphate increases

when increasing $[P]_{I,aq}$ up to ca. 50-60µM. Such a behaviour is typical of successive formation of surface complexes of distinct stability and / or implications of high-affinity and low-affinity surface sites. A plateau in amount of phosphate ions sorbed (at 5-6 µmol.g$^{-1}$) is observable in *Figure 4*, for $[P]_{I, aq}$ > ~60 µM. This suggests a saturation of total sites available for P retention and no significant involvement of processes like (surface) precipitation of phosphate phases, in the conditions investigated.

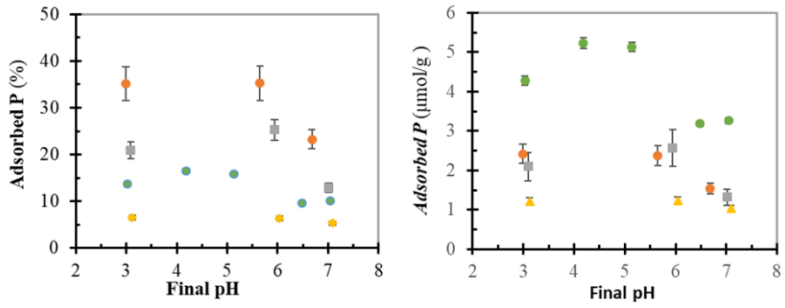


*Figure 3:* Sorption edges of phosphate ions onto NaIdP at different clay-to-solution ratios - $R_{S/L}$ (♦: 1g·L$^{-1}$, ■: 2g·L$^{-1}$ or ●●: 3g·L$^{-1}$) and total P concentrations - $[P]_{I,aq}$ (♦■●: 20µM or ●: 100µM). Experimental conditions: 0.005 M NaCl electrolyte, reaction time ($t_R$) of 4 days, NaIdP-electrolyte solution system pre-equilibrated 3 days ($t_{pre-eq}$).

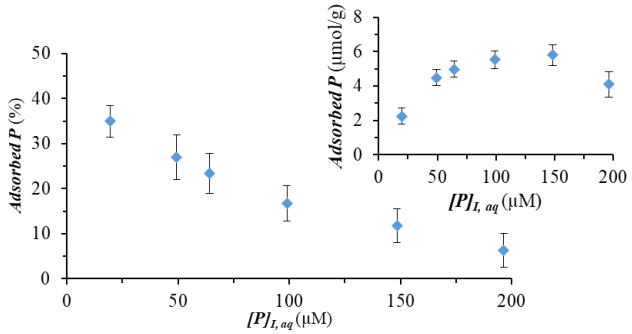


*Figure 4: Sorption isotherms of phosphate ions (results in % of adsorbed P; insert: P surface coverage in µmol.g$^{-1}$) onto NaIdP, at pH 4 and at $[P]_{I,aq}$ in the range 20-200 µM. Experimental conditions: 0.005 M NaCl electrolyte solutions, $R_{S/L}$ = 3 g·L$^{-1}$, $t_R$ = 4 days, $t_{pre-eq}$ = 3 days.*

### Effect of phosphate ligand on the macroscopic sorption of U

*Figure 2*a shows that the presence of phosphate ions ($[P]_{I,aq}$ = 100 µM) led to a significant shift of the U(VI) sorption edges towards lower pH values, for the U concentrations studied ($[U]_{I,aq}$=1 and 12 µM). At acidic pH, significant increases in surface coverages of the clay by U were observed, too (1-2 and 3-4 µmol U.g$^{-1}$ at pH 3-4 and 4-5, respectively, at $[U]_{I,aq}$ = 12 µM). Hence, at acidic pH, the presence of P promotes the sorption of U(VI) onto NaIdP. There was also observed an increase of the percentage of phosphate sorbed with an increase of U concentration in experiment, in the pH range investigated (*Figure 2*b and Figure A7 in appendix A). Clay surface coverage by P was increased, too (of ca. 2 and 6 µmol P.g$^{-1}$ at acidic and near-neutral pH, respectively). Thus, the increase in U sorption observed upon addition of phosphate ligands in the NaIdP-solution systems was likely due to the formation of (multiple) ternary uranyl phosphate surface complexes and/or U(VI) phosphate surface precipitates. Furthermore, based on the values published by Bradbury and Baeyens [13,35] for the surface sites of the conditioned Illite du Puy (about 2 µmol.g$^{-1}$ or 0.01 sites.nm$^{-2}$), we can hypothesize that formation of uranyl phosphate surface complexes on NaIdP involved high- and low-affinity hydroxyl sites present on the clay edges, for experiments performed

at high $[U]_{I,aq}$ and $[P]_{I,aq}$. Complementary U sorption isotherms acquired for a wide range of U concentrations (*Figures A3-4 in appendix A*) show, that at acidic pH, the promotion of uranyl ion sorption upon addition of P is higher at high $[U]_{I,aq}$ (≥12µM) than at low $[U]_{I,aq}$, suggesting that multiple uranyl phosphate species are successively formed in NaIdP-phosphate-solution systems when $[U]_{I,aq}$ increases. Since limited formation of uranyl phosphate colloidal phases was observed in the absence of NaIdP (5-10% of total U, for $[U]_{I,aq}$=1-10 µM and $[P]_{I,aq}$=100 µM, see *Figure A8* in appendix A), the contribution of a U(VI) phosphate precipitation mechanism from supersaturated solutions cannot be excluded to explain the increased retention of U observed in systems at the highest value of $[U]_{I,aq}$ studied (25 µM). Experimental results of competitive sorption of U(VI) and Fe(III) on NaIdP in the presence of phosphate ligands, as function of pH (3-8), indicated that no significant effect of the presence of Fe ions on the $pH_{50}$ value of uranyl ions (*Figure A9, appendix A*). A very slight decrease in the percentage of Fe sorption at pH 4 is observable when comparing data obtained in the presence and in the absence of U (data not shown). For a given pH, the percent sorption of P is slightly higher –and or equal within our analytical uncertainty-, than that recorded under similar conditions without U and Fe.

### Effect of sorption on electrophoretic mobility

Figure 2c shows pH dependency of EM values for NaIdP-0.005 M NaCl solution suspensions at different $[P]_{I,aq}$ values. In the absence of any potential-determining ion other than $OH^-/H^+$, NaIdP particles display a low value of isoelectric point (IEP ≈ 3), *i.e.*, of pH at which EM and surface potential are equal to zero. This is consistent with previous studies reporting a low value of isoelectric point (IEP) for illitic minerals [50,51]. A sharp decrease of EM with pH is observable, which may reflect both a structural negative charge of Illite and successive (de)protonations with pH of amphoteric surface functional groups (like silanol then aluminol/ferrinol sites) present at clay surface edges in NaIdP. Figure 2c also reveals that, in the acidic pH range, EM of suspended NaIdP is diminished and the point-of-zero charge (PZC) shifts towards a lower pH (< 3) at high aqueous phosphate concentration ($[P]_{I,aq}$ = 100 µM). This feature evidences a mechanism of strong sorption of phosphate ions that adds negative charges to the clay surface, such like a mechanism of formation of inner sphere surface complexes (ISSC) of phosphate by exchange of surface ligands. Regarding U sorption, there was observed that sorption of 1-12 µM of uranyl ions at acidic pH values has no significant effect on EM values, within our experimental uncertainties. An effect is visible at near-neutral pH (~7) where the quantitative sorption of U induces an increase of EM (for $[U]_{I,aq}$ = 12 µM), which suggests the formation of U sorption species imparting positive charges to the clay surface. However, in the presence of phosphate ligands, sorption of U slightly decreased the EM values of the clay particles in the pH range studied, *i.e.*, it conferred negative charges on the mineral surfaces, suggesting the involvement of phosphate anions in the uranyl surface species formed.

### Reversibility of the sorption of U in the presence of phosphate ligands

The results of the desorption experiments of uranyl ions ($[U]_{I,aq}$ = 12 µM) previously sorbed at pH values of ~4 and ~5, respectively, and in the presence of phosphate ligands ($[P]_{I,aq}$ = 100 µM), are presented in *Figure 5*. There was observed a sharp decrease of the percentage of U sorption when bringing the experimental pH from its initial value to a value of 3.2. There was found that the U(VI) desorption is fast and almost complete within a few hours. Actually, the percentage of total U retained at pH 3 onto clay surface after a few-hours desorption was found to be around 20% (which is slightly higher than the percentage of U sorption at pH 3 under similar conditions of U and P concentrations, see *Figure 2*a). These features provide evidence that the U-P co-sorption process is mostly reversible under the conditions investigated, and that the uranyl phosphate surface species formed onto NaIdP at acidic pH are most likely U-P surface complexes, at low concentrations of U (≤ 10 µM).

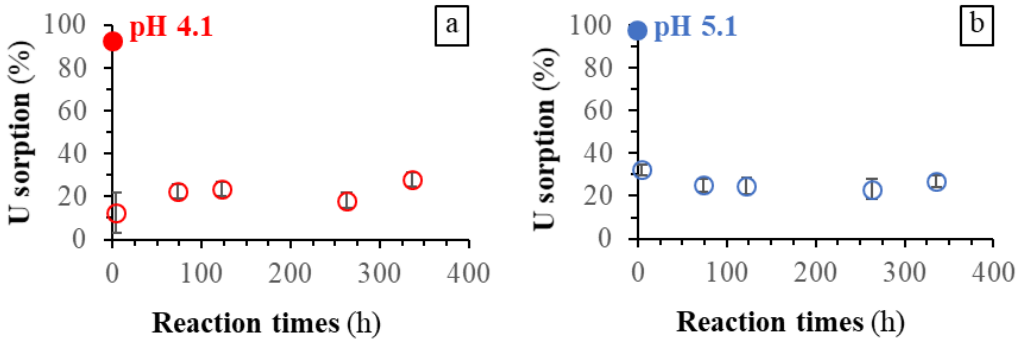


*Figure 5: Results on the kinetics of desorption of U(VI) previously sorbed in the presence of phosphate ions onto NaIdP at (a) a pH of 5.1 and (b) a pH of 4.1 (full circles), after a decrease of experimental pH to a value of 3.2 (empty circles). Conditions: $[P]_{I,aq}$ = 100µM, $[U]_{I,aq}$=12.5µM, $R_{S/L}$ = 3g·L$^{-1}$, 0.005M NaCl electrolyte solution.*

### Discussion on the macroscopic (co)sorption data

The sorption edges of phosphate ion presented here show that the percentage of phosphate sorption onto NaIdP is maximal at acidic pH (3-6) and decreases with increasing pH, consistently with previous studies of P sorption onto aluminum-oxide, Illite, and kaolinite [27,30,36]. Our data moreover suggest the successive formation of different phosphate surface species with increasing $[P]_{I,aq}$ (< 200 µM) or with decreasing $R_{S/L}$. Alternately, high-affinity and low-affinity surface sites may be successively involved in formation of phosphate surface species, up to a surface coverage of ca. 5-6 µmol.g$^{-1}$ (for which no clay surface sites are available anymore for P sorption). Such a limiting surface coverage is consistent with values of surface concentrations of low affinity and high affinity aluminol sites expected for NaIdP clay platelets [13,35]. That P surface coverage reaches a plateau also indicate no formation of surface precipitates of Al-phosphate. The EM data indicate charge reversal and a shift in IEP to a lower pH as a consequence of P sorption, which clearly supports that a strong sorption [36,37,41,52–54] of phosphate ions occurs onto Illite, i.e., ISSC of phosphate are formed at aluminol sites and impart negative charges to the surface. This may be favoured at acidic pH by a first step of electrostatic attraction between positively charged sites (protonated aluminol sites as $\equiv SOH_2^+$) and $HPO_4^{2-}$ and $H_2PO_4^-$ ions near surface (formation of phosphate outer sphere surface complex, OSSC).

Our U(VI) macroscopic sorption data indicate that several sorption mechanisms / species contribute to the uptake of uranyl ions by NaIdP, too, depending on key parameters such as pH, U concentration and clay-to-solution ratio. A decrease in the percent sorption of U, at a given acidic pH, was observed when increasing U concentration in a certain range (1-10 µM) or when decreasing clay-to-solution ratio. These trends support that a very low amount of high affinity sorption sites (< 0.02 sites. nm$^{-2}$) at NaIdP edges become progressively saturated while low affinity surface sites are increasingly involved in U sorption, in the above-mentioned conditions. This is consistent with the work by Bradbury and Baeyens [13,35] of the sorption of trace metals and actinides onto Na-Illite. These authors could fit successfully the macroscopic data on the sorption of uranyl ions (at a concentration of ~0.1µM) by considering a mechanism of cation exchange implying $UO_2^{2+}$ in clay interlayer space (and dominating in the pH range 2.5-3.5) and the strong sorption of U by formation of uranyl surface complexes of the types $\equiv SO^sUO_2^+$, $\equiv SO^sUO_2OH$ and $\equiv SO^sUO_2OH_2^-$ that involve high affinity sites (noted $\equiv SO^s$) present in low amounts (ca. 0.01 sites·nm$^{-2}$) at clay edges. Several EXAFS analyses have moreover provided evidence that uranyl ions are sorbed, at low pH, as exchangeable $UO_2^{2+}$ in the interlayer space of smectitic clays, and at moderately acidic pH, as additional inner-sphere uranyl surface complex and / or U(VI) polynuclear surface species, depending on surface coverage [5,19–21]. Based on spectroscopic results, Troyer et al. [25] could fit their sorption isotherms of uranyl ions (1-10 µM) on montmorillonite by using in surface complexation modelling three types of species, namely, cation-exchanged $UO_2^{2+}$ (noted $UO_2X_2$), a cationic surface complex ($\equiv SOUO_2^+$) and a ternary uranyl carbonate surface complex ($\equiv SOUO_2CO_3^-$), which dominated at pH 4, 6 and 8, respectively. Our macroscopic data are consistent with those reported in the above-mentioned studies.

They suggest sorption of uranyl ions via formation of inner sphere surface complexes of U(VI) onto high affinity and low affinity surface sites NaIdP edges, at acidic pH, in most of the conditions investigated. As no significant effect of U(VI) sorption on EM is observable at pH < 5, it is possible that the sorption of U(VI) onto NaIdP included the deprotonation of protonated hydroxyl sites (ferrinol / aluminol) followed by formation of $\Xi SO^sUO_2^+$ and / or the formation of $\Xi SO^sUO_2OH$ surface complexes. Our data also show only a slight decrease of U(VI) uptake by clay at basic pH (7-8) in presence of a high concentration of carbonate ligands, which suggest that aqueous carbonates do not compete successfully against hydroxyl surface sites for coordination of U and / or sorbed uranyl species are formed, which is to be further studied for illite.

In contrast, uranyl sorption edges and isotherms presented here show that the presence of phosphate ligands promotes sorption of U(VI) at acidic pH onto NaIdP, particularly at a high U concentration (10 µM). Sorption of phosphate ions is enhanced by an increase of U concentration in experiment, too. This suggests that (part of) uranyl ions were sorbed at NaIdP – phosphate – solution interface via formation of ternary uranyl phosphato surface complex(es) and/or U(VI) phosphate surface precipitates. Experimental results, such as non-linear increase of U and P surface coverages with increasing U concentration (from 1 to 10 µM), highlighted moreover the formation of multiple U-P sorption species and/or implication of several types of surface sites. Desorption experiments provided strong evidence that the sorption of U in the presence of phosphate ions is a reversible process, i.e., it occurs via uranyl (phosphate) surface complex formation. Formation of such surface complexes were shown to impart negative charges to the clay surface throughout the pH range investigated, which is an indication of participation of phosphate anions to the surface complexes formed. Based on values of high-affinity sites given by Bradbury and Baeyens [13,35] for the conditioned Illite du Puy (ca. 2 µmol·g$^{-1}$ or 0.01 sites.nm$^{-2}$), it is likely that formation of uranyl phosphato surface complexes formed in experiments at high U and concentrations (12 µM and 100 µM, respectively) would involve both high- and low-affinity (amphoteric) sites at the clay edge platelets. Batch sorption results also suggest no macroscopic signature of a potential competition between sorption onto NaIdP of uranyl ions and Fe ions, in the presence of phosphate ligands, which has to be confirmed by spectroscopic studies.

## ATR FTIR studies

ATR FTIR data on phosphate / uranyl-phosphato / uranyl-carbonato / Fe(III) solution species are *in appendix B*. Related calculated aqueous speciation are given in *figures A11-A12 in appendix A*.

### Clay – solution interactions

ATR FTIR based monitoring of the interface between clay (IdP or NaIdP) and a solution (at pH 6 and 4, respectively), allowed to identify positions of vibration bands of IdP structure / surface and their evolution with the time. Figure 6a shows the time evolution of *in-situ* IR spectra collected at IdP–solution interface. There was observed a strong “negative” absorbance in the region 800-1200 cm$^{-1}$, whose growing rate decreased with time. Spectra decomposition provided values of six band maxima (at 835, 873, 912, 979, 1040 and 1110 cm$^{-1}$). The three first bands can be attributed to OH bending vibrational mode of Al-Mg-OH, Al-Fe-OH and Al-Al-OH, respectively, in structure of clay minerals [55,56]. The bands at 979 [56], 1040 and 1110 cm$^{-1}$ correspond to SiO stretching vibrational mode [56–58]. Main band at 980 cm$^{-1}$ is characteristics for Si-O stretching vibration of Si-O-H groups and it may reflect the presence of OH groups at surface of polymerized silica [58]. Hence, the “negative” absorbance provides evidence for processes of dissolution and surface reorganization of clay with time. Figure 6b shows the time evolution of *in-situ* IR spectra of NaIdP–solution interface. “Negative” absorbance at 800-1200 cm$^{-1}$ (stabilized after ca 3 hours) show three band maxima (917, 966, and 1008 cm$^{-1}$). The band at 1008 cm$^{-1}$ is characteristics of Si-O stretching band in micas group [59]. Under a high $pCO_2$ atmosphere, interface between NaIdP and solution at pH 7.6 (*Figure A10, appendix A*) shows complex reorganizations, which may include precipitation of secondary phases with hydroxyl surface groups (e.g., bands at ca. 920 cm$^{-1}$ due to OH bending of Al-Al-OH and at 980 cm$^{-1}$ due to Si-O stretching of Si-O-H) and their further disappearance due to dissolution and/or surface ligand exchange involving carbonate ions.

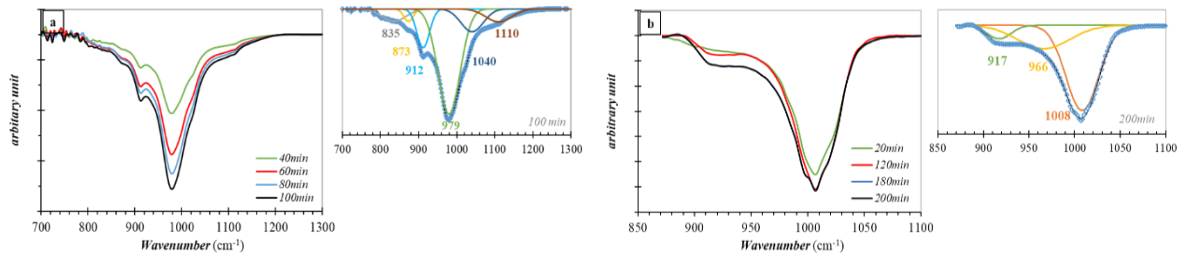


*Figure 6: Evolution of in situ ATR FTIR spectra recorded at: (a) IdP–solution and (b) NaIdP–solution interface, as a function of time, and results of spectra decomposition (insert). Experimental conditions: 0.005 M NaCl electrolyte solution at pH (a) 6.2 and (b) 4.0 added to a thin clay coating on ATR crystal.*

### ATR FTIR monitoring of phosphate sorption at clay – solution interface

***Effect of reaction time*.** Figure 7a shows the FTIR spectra recorded by *in situ* monitoring of NaIdP–solution interface along sorption of phosphate ions at pH 4. A weak absorbance appeared in the region 1050-1250 $cm^{-1}$ after addition of 50 µM of P and increased slightly with $[P]_{I,aq}$ (up to 100 µM). From short to intermediate $t_R$ (up to ca. 19h), there was observed the progressive shift of the IR absorption signals towards the region 1000-1100 $cm^{-1}$ and absorbance increase, which becomes dramatic at $t_R$ of 3 days. It could be inferred from spectra decomposition (Figure 7b) that short-term spectra ($t_R$ < 1h20min) were dominated by two broad bands centred (at 1075 and 1160 $cm^{-1}$). Peak maxima position of these broad bands were similar to those recorded for the phosphate–water system under similar conditions but their intensity is higher. This suggests that at least a fraction of aqueous phosphate ions was involved in the formation of a phosphate surface species onto NaIdP (noted 'P-species A'). The intensity of the two bands of P-species A shows a decrease with time (for $t_R$ > 2 hours), until disappearance. In contrast, intensity of a band centred at 1035$cm^{-1}$ increases slightly during first hours ($t_R$ < 8h) and shows then a dramatic increase (at $t_R$ = 3 days). A poorly-defined band at ca. 1132 $cm^{-1}$ could be also identified and was found to be independent of $[P]_{I,aq}$ and $t_R$. A shoulder at a lower wavenumber (at 1003 $cm^{-1}$) and a band positioned at 1095$cm^{-1}$ are also present in IR interface spectra collected at intermediate and long reaction times. We assign these bands (1003, 1035, 1095 and 1132 $cm^{-1}$) to $\upsilon_3$ (P-O), as IR active $\upsilon_1$ (P-OM, M: metal or hydrogen atom) bands are located at wavenumbers lower than 900 $cm^{-1}$ [38]. The maxima positions of $\upsilon_3$ (P-O) bands are different from those of aqueous $H_2PO_4^-$ species and P-species A, which evidences that at least another phosphate surface species, whose contribution grows with time, is formed at the interface (P-species B). Further addition of phosphate ions (100 µM) to the 3-days aged system induced no significant change in band's intensity, which rather suggests that no additional surface complex / precipitate of phosphate was forming onto NaIdP under the investigated conditions. Increase of absorbance of the band at 1035 $cm^{-1}$ and decrease of that at 1075 $cm^{-1}$ with time might reflect the kinetics of a conversion from outer sphere to inner sphere surface complex of phosphate.

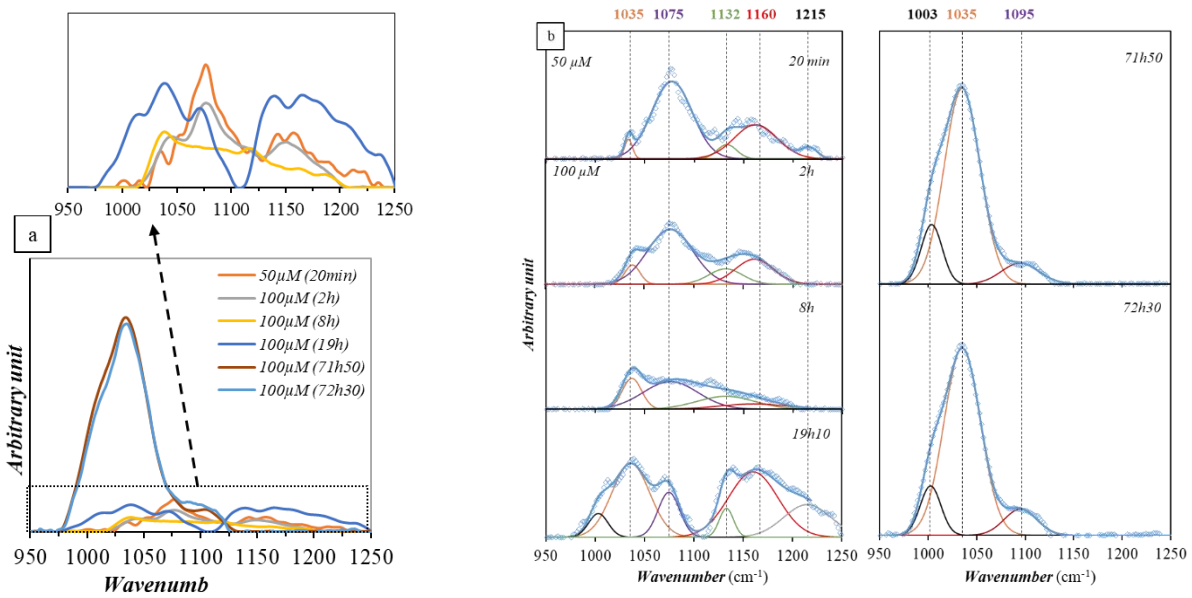


*Figure 7: (a) Evolution of in situ ATR FTIR spectra recorded at NaIdP–phosphate-solution interface, as a function of time, and (b) results of spectra decomposition. Experimental conditions: 0.005 M NaCl electrolyte solution at pH 4, $[P]_{I,aq}$ of 50 µM (20min), 100 µM ($t_R$: 2 hours up to 3 days). Aqueous P was added to a two-layers solution-clay deposited on the ATR crystal.*

***Effect of phosphate ion concentration.*** Figure 8 shows the FTIR spectra recorded by *in-situ* monitoring of P sorption at NaIdP–solution interface as a function of $[P]_{I,aq}$ (50-300 µM), at pH 4 and moderate reaction time ($t_R$ < 24 hours). IR absorbance was increased with increasing phosphate concentration (Figure 8a). At low concentration, a well-defined band at 1075 $cm^{-1}$ and a broad band with a maximum at 1160 $cm^{-1}$ and a shoulder at 1215$cm^{-1}$ (attributable to P-species A) as well as a band at 1132 $cm^{-1}$, is observable (Figure 8b). The bands of P-species A are visible in the range of phosphate concentration 50-250 µM. An increasing of absorbance was also observable with increasing $[P]_{I,aq}$, which appeared to be due to the growing of a well-defined P-O stretching band with a maxima at 1035 $cm^{-1}$. At $[P]_{I,aq}$ > 150 µM, small bands centred at 1005 and 1095 $cm^{-1}$ increased with increasing phosphate concentration. These bands (1003, 1035, 1095 and 1132 $cm^{-1}$) are similar to those identified for P-species B.

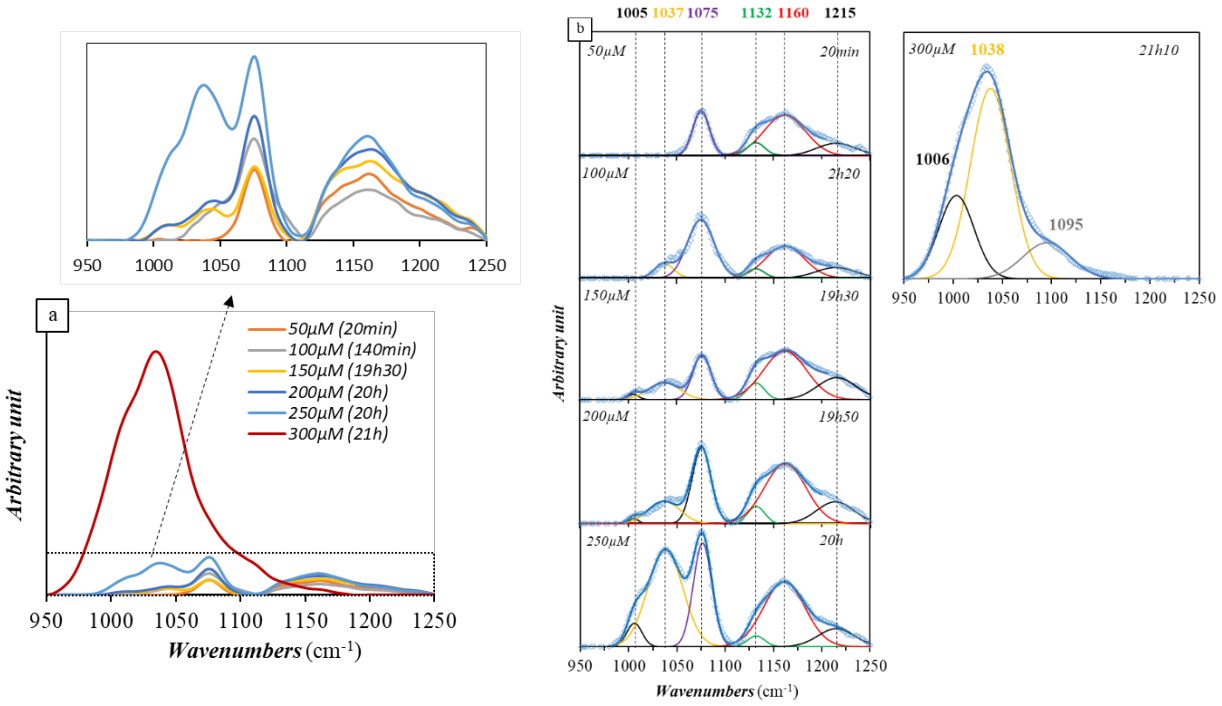


*Figure 8: (a) In situ ATR FTIR spectra results of the sorption of phosphate at NaIdP–solution interface as a function of phosphate concentration ($[P]_{l,aq}$ : 50-300 µM) and (b) results of spectra decomposition. Experimental conditions: 0.005 M NaCl electrolyte solution at pH4, $t_R$ up to 19 hours. Aqueous P was added to a two-layers solution-clay deposited on the ATR crystal.*

***Surface speciation of sorbed phosphate ions*.** ATR FTIR data of P sorption at Illite–solution interface has revealed the existence of two types of phosphate surface species forming at pH 4. One of them, the P-species A, has two $\upsilon_3$ bands at 1075, 1160 $cm^{-1}$ and a broad band centred at 1215 $cm^{-1}$. These band positions are very similar to those of the dissolved phosphate species ($H_2PO_4^-$, $C_{2v}$), as reported by [41], with the band at 1215 $cm^{-1}$ being assigned to the δ(P-OH) bending mode [37,38,40,41]. That the band at 1215 $cm^{-1}$ of the δ(P-OH) bending mode was observed during P sorption process (while it was not observed in IR analyses of phosphate – electrolyte solution system) suggested formation of OSSC species of phosphate. Accumulation of negatively charged phosphate ions by electrostatic attraction as counter-ions to balance positively charged edge sites created at interface, i.e., $\equiv SOH_2^+$ sites, and/or by weak hydrogen bonding to surface water/surface hydroxyls, increased their absorbance. Number and peak positions of P-OH bands of the weakly sorbed phosphate should be the same as for corresponding aqueous P species [37]. We thus conclude that P-species A is an OSSC of diprotonated phosphate ions ($\equiv SOH_2^+ \cdots H_2PO_4^-$) formed at NaIdP–solution interface, which predominates phosphate surface speciation at short reaction times and / or at low phosphate concentrations, only. In contrast, the second phosphate surface species identified as P-species B has four $\upsilon_3$ bands (1005, 1037, 1095 and 1132 $cm^{-1}$) whose intensity increases with reaction time -except the poorly-defined band at 1132 $cm^{-1}$- and predominates at a long $t_R$ (> 24 hours). Borgnino et al. [26] have shown in an ATR FTIR study of phosphate sorption at the Fe-modified montmorillonite–solution interface that, at low pH value, two ISSC of phosphate were formed at the surface of iron(III) (hydr)oxides present as minor phases in the clay rock. The first one was shown to be an unprotonated bidentate surface complex, $\equiv (FeO)_2PO_2$, (with $\upsilon_3$ bands at 1088, 1049 and 941 $cm^{-1}$). The authors suggested a $C_{2v}$ or lower molecular symmetry for this ISSC, whose band maxima positions resulted from shifts of $\upsilon_3$ bands of $H_2PO_4^-$. The second one was proposed to be a monoprotonated bidentate surface complex, e.g., $\equiv (FeO)_2(OH)PO$ with a $C_1$ molecular symmetry (bands' positions at 1128, 1011 and 978 $cm^{-1}$). Dolui et al. [29] investigated by *in situ* ATR FTIR the mechanisms of phosphate sorption ($[P]_{l,aq}$ = 100 µM) at acidic pH onto kaolinite and identified five $\upsilon_3$ bands (1138, 1108, 1086, 1074 and 1061 $cm^{-1}$). They reported the formation of multiple surface species of phosphate ions onto kaolinite with a predominant

surface species (ISSC or surface precipitate) formed at edge aluminol sites, whose band position was at 1138 $cm^{-1}$. Li et al. [39] studied surface speciation of phosphate ions at α-$Al_2O_3$–electrolyte solution interface from pH 5 to 9 and found five IR bands for P surface species (at 1130-1131, 1092-1096, 1053-1060, 1020-1025 and 1005-1010 $cm^{-1}$). The authors concluded on co-existence of two surface complexes species of phosphate ions as predominating surface species at pH 5: a monoprotonated bidentate binuclear surface complex, as ≡ $(AlO)_2(OH)PO$, and an unprotonated bidentate binuclear surface complex, as ≡ $(AlO)_2PO_2$. Del Nero et al. [36] investigated the sorption mechanisms of phosphate at acidic pH onto α-$Al_2O_3$ by *in situ* ATR FTIR and reported formation at low surface coverage of an ISSC of phosphate (possibly IR bands at 1084 and 1033 $cm^{-1}$) and, when increasing P surface coverage, of a surface precipitate of Al-phosphate incorporating $Al^{3+}$ ions released by mineral dissolution (band at 1137 $cm^{-1}$). Based on bands' positions and above-mentioned literature data, we assign the three $\upsilon_3$ bands (at 1005, 1037 and 1095 $cm^{-1}$) identified in our study for P-species B to a monodentate binuclear surface complex species formed at edge surface sites of clay, i.e., ≡ $(SO)_2PO_2$ (S: Al and / or Fe). The small $\upsilon_3$ bands at 1132 $cm^{-1}$ can be tentatively assigned to limited formation of a monoprotonated monodentate binuclear surface complex ≡ $(SO)_2(OH)PO$ (S: Al and / or Fe), as similar band position were reported for ISSC of phosphate of the type ≡ $(AlO)_2(OH)PO$ ([39]) and ≡ $(FeO)_2(OH)PO$) [26] formed onto Al- and Fe-oxides, respectively, and / or to low amounts of Al-phosphate surface precipitates [36].

### In situ ATR FTIR experiments of (co)sorption of uranyl ions

***Co-sorption of uranyl and carbonate ions.*** Results of ATR FTIR monitoring of sorption of U(VI) at pH 8 at the NaIdP-solution interface (*Figure 9*), performed in the presence of carbonate ligands, shows a decrease in absorbance and a slight shift towards higher frequencies of C-O stretching bands (range: 1300-1400$cm^{-1}$) when compared to those of $HCO_3^-$ ions. The shift in band positions is similar than that observed for formation of aqueous uranyl carbonate complexes (*Figure B4, Appendix B*). However, formation of such complexes was observed at much lower C concentration in the NaIdP-solution system than in solution, which suggests formation of uranyl carbonate surface species on the clay surface. Note that there was observed a change in configuration of surface hydroxyls at wavenumbers < 1150$cm^{-1}$.

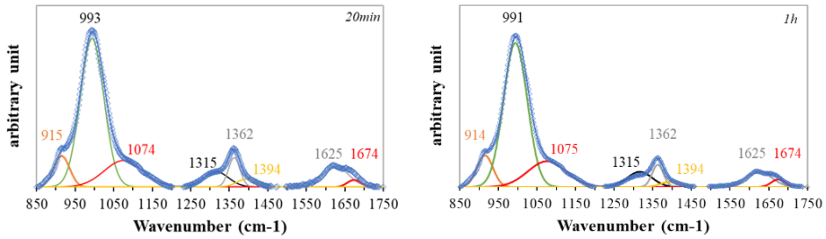


*Figure 9: Decomposition spectra of in situ ATR-FTIR experiments of the (co)sorption of carbonate and uranyl ions at NaIdP–solution interface at 20min/1h reaction time (conditions: pH8, [U]=10µM, [$CO_3^{2-}$] =100mM, $R_{S/L}$ =3g·$L^{-1}$, 0.005M NaCl electrolyte).*

***U-P (co)sorption: effect of uranyl ion concentration.*** Figure 10a gives NaIdP-phosphate-solution interface spectra recorded along an increase of total U(VI) concentration. Decomposition of spectra obtained before addition of U (at $[P]_{I,aq}$ of 100µM, spectra 1 and 2, cf. Figure 10b) is consistent with our previous ATR FTIR data of sorption of phosphate ions (cf. §0: bands related to P-species A and P-species B). First addition of U ($t_R$ = 2 h) induced disappearance of the bands of ISSC P-species B (1037 and 1132 $cm^{-1}$) and the rapid appearance of a band at ca. 1050 $cm^{-1}$. This provides strong evidence of a change in the coordination environment of sorbed $PO_4$ units. The latter band increased with an increase of U(VI) concentration. In contrast, the bands at 1075 and 1157 $cm^{-1}$ of P-species A showed a decrease in intensity with increasing $[U]_{I,aq}$, concomitantly to the increase of the band at 1050 $cm^{-1}$. Spectra decomposition data (Figure 10b) show a small band centred at ~1126 $cm^{-1}$, too, which can be assigned to $\upsilon_3$ P-O vibration mode and whose weak absorbance was independent of uranyl concentration. Possibly, this band corresponds to a uranyl phosphate surface species (noted "U-P species A") formed in limited amount and at low U concentration. As the band at 1050 $cm^{-1}$ cannot be attributed to a change in configuration of surface hydroxyl groups during sorption of uranyl ions, because it was not detected on IR interface spectra recorded

during “blank” experiments of U(VI) sorption (at pH<5 and at $[P]_{l,aq}$ = 0, data not shown), its existence and growth with $[U]_{l,aq}$ provides strong evidence of formation of another uranyl-phosphate surface species (referred to as “U-P species B”) onto Illite. In summary, IR data recorded during (co)sorption of U and P, as a function of $[U]_{l,aq}$ and for a short reaction time ($t_R$ <7h), show : *(1)* the fast formation of a uranyl phosphato surface species formed in limited amounts (U-P species A with a band at 1125 $cm^{-1}$) and of another uranyl phosphato surface species (U-P species B with a band at 1050 $cm^{-1}$), which induced disappearance of P-species B (at $t_R$ < 3h), and *(2)* the growth of U-P species B with an increasing of U concentration.

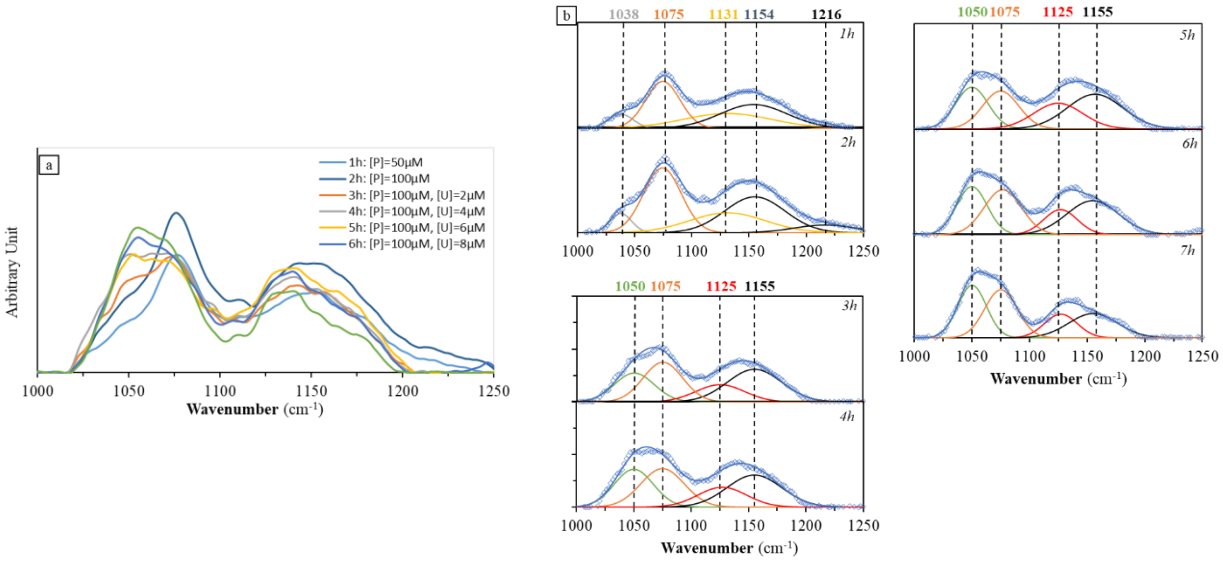


*Figure 10: Results of in situ ATR-FTIR experiments of the (co)sorption of phosphate and uranyl ions at NaIdP–solution interface with increasing U(VI) concentration (conditions: pH 4, $[U]_{l,aq}$ in the range 0–10µM, $[P]_{l,aq}$=50-100 µM, , $R_{S/L}$ =3g.$L^{-1}$, $t_R$=1-7h, 0.005M NaCl electrolyte): (a) FTIR interface spectra and (b) spectra decomposition. See main text and § 2.4.3 for experimental procedure.*

***U-P (co)sorption: effect of reaction time ($t_R$).*** *In situ* ATR FTIR monitoring as a function of time ($t_R$ = 3 days) of the (co)sorption of uranyl and phosphate ions in NaIdP–solution system is illustrated in Figure 11. A broad band with a low absorbance was observable in the range 1025 – 1125 $cm^{-1}$ for spectra recorded within a reaction time of 20 hours. The small band at 1123 $cm^{-1}$ of U-P species A was observable only in the very short term. For $t_R$ < 20 hours, spectra were decomposed in five bands of weak absorbance (Figure 11b). A set of bands is assigned to P-species A (maxima positions at 1075 and 1160 $cm^{-1}$) and displayed a decrease in intensity with $t_R$. In contrast, the other bands (at 1053, 1081 $cm^{-1}$, and 1114 $cm^{-1}$) showed an increase in intensity with $t_R$. The band at ~1055 $cm^{-1}$ was assigned to the U-P species B and remained constant after 7 h. After a $t_R$ of 20 hours, there was observed a broad band exhibiting two maxima and extending in the region 950-1125$cm^{-1}$, with its absorbance increasing with time until stabilization at $t_R$ = 3 days (Figure 11a). A well-defined band at 992 $cm^{-1}$ was observable at $t_R$ > 20 hours and its intensity increased concomitantly with that of the band at 1081 $cm^{-1}$ along the sorption process. These two bands, and the small band at 1114 $cm^{-1}$, are tentatively gathered and are attributed to P-O vibrations of a single uranyl phosphate surface species formed at a long reaction time (referred to as “U-P species C”), due to their similar evolution during sorption. In summary, IR data recorded during (co)sorption of uranyl and phosphate ions at the NaIdP–solution interface as a function of time (3 days) show: *(1)* the presence at a short reaction time of P-species A that disappears rapidly ($t_R$ < 5h), *(2)* the formation at low $t_R$ and in limited amounts of the U-P species A (band at 1125 $cm^{-1}$), *(3)* the formation of U-P species B (main band at 1052 $cm^{-1}$) whose growth stabilizes after $t_R$ = 1 day, *(4)* the late appearance (at $t_R$ = 1 day) and growth with time of an uranyl phosphate surface species that becomes dominant at $t_R$ = 3 days (U-P species C with bands at 992, 1081 and 1114 $cm^{-1}$).

***U-P (co)sorption: Effect of $Fe^{3+}$ ions.*** Unlike macroscopic results, the IR spectroscopy study shows some evidence of competitive sorption between U(VI) and Fe(III) in the presence of phosphate ligands at acidic

pH (pH 4). In-situ ATR-FTIR spectra collected after simultaneous addition of uranyl ions, $Fe^{3+}$ ions and phosphate ligands ($[U]_{I,aq}$=10µM, $[Fe]_{I,aq}$=10µM and $[P]_{I,aq}$=100µM) in a NaIdP-solution system at pH 4 show spectra with low signal-to-noise ratios and low IR absorption, making spectra decomposition and interpretation difficult (*Figure A13, appendix A*). Nevertheless, based on comparison with IR spectra recorded during the U-P (co)sorption, and Fe-P co-sorption (data not shown), it seems that various surface species were formed, whose contributions varied with time. Decomposition of spectra shows six bands (at 1039, 1076, 1084, 1119, 1155 and 1175 $cm^{-1}$) attributed to P-O stretching bands ($\upsilon_3$). The bands at 1076 and 1155 $cm^{-1}$ are ascribed to the P-species A. No uranyl phosphate species of types U-P species A nor U-P species B were found. Only the bands corresponding to U-P species C (formed at long reaction time in the absence of Fe) are visible. Formation of Fe(III) phosphate surface precipitates is also possible (as these species have a main band peaking at ca. 1080 $cm^{-1}$, data not shown). The band observable at 1039 $cm^{-1}$ accounts probably to formation of P-species B.

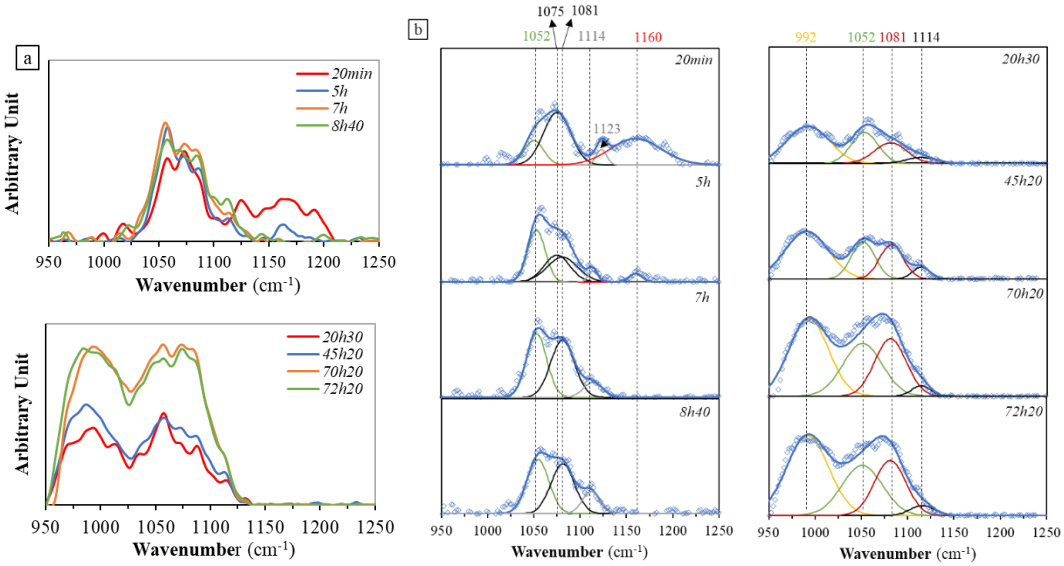


*Figure 11: Results of in situ ATR FTIR experiments of the (co)sorption of phosphate and uranyl ions at NaIdP–solution interface with increasing reaction time (conditions: pH 4, $[U]_{I,aq}$ = 8 µM, $[P]_{I,aq}$ = 100 µM, , $R_{S/L}$ = 3 g.L$^{-1}$, 0.005 M NaCl electrolyte): (a) FTIR interface spectra (8 points- Savistzky-Golay algoritm smoothed) and (b) spectra decomposition. See main text and § 0 for experimental procedure.*

***Discussion on surface speciation of U(VI) at the NaIdP – phosphate/carbonate - solution interface.*** *In situ* ATR FTIR data of the sorption of uranyl ions at surface of NaIdP in the presence of carbonate ligands provides evidence of a significant reorganization of the clay-solution interface at high pH, and suggest the formation of uranyl carbonate surface complexes *(one needs to mind that the used CO2 concentrations are much higher than those prevailing under typical disposal conditions)*. Although spectroscopic evidences using complementary techniques are necessary to confirm these results, this interpretation is consistent with previously published spectroscopic studies reporting formation of uranyl carbonato ISSC onto metal oxides and at edge sites of smectite [22,60].

ATR FTIR experiments of the U – P (co)sorption conducted at varying U concentration or as a function of reaction time provided valuable information about speciation of surface complexs. It was found that several species contribute to the phosphate surface speciation during U-P co-sorption, with three types of uranyl phosphate surface species being identified. At short reaction times (< 7 h), two uranyl phosphate species were identified onto NaIdP, with the first one (U-P species A) being formed at low U concentration and the second one (U-P species B) growing with an increase in U concentration. It is to note that, when phosphate ions were added before U in experiment, the formation of these two U-P species affected the IR signals of previously-formed phosphate surface species (with no U), i.e., it led to disappearance of IR bands of pre-existing ISSC of phosphate and in a decrease in bands' intensity of OSSC of phosphate. Thus, pre-existing phosphate surface species formed onto NaIdP were desorbed and / or converted rapidly upon addition of uranyl ions into U-P surface species. The latter are interpreted as being inner sphere uranyl phosphate

surface species formed at edge sites of the clay platelets. The U-P species A has a (weak) IR band at ~1125 $cm^{-1}$, which is independent of concentration of uranyl ions, which suggests that its formation took place at high-affinity sites existing in limited amounts on clay edges. It can be rulled out that, these species represent a surface precipitate (e.g., $(UO_2)_3(PO_4)_2{\cdot}4H_2O_{(s)}$) and / or an outer sphere surface complex (i.e., $UO_2HPO_4$ $(H_2O)_4$) having a band at 1122 $cm^{-1}$. In such cases, its absorbance would increase with U concentration [36]. Conversely, U-P species B displays an IR band at ~1050 $cm^{-1}$ whose intensity increases with U concentration and it dominates phosphate speciation at intermediate reaction times (7 hours). This species is likely a uranyl phosphato ISSC forming at low affinity sites onto clay edges. Actually, the band at 1050$cm^{-1}$ can hardly be attributed to an OSSC of uranyl phosphate (having IR bands at positions close to those of aqueous $UO_2H_2PO_4^+{}_{(aq)}$ species), because an OSSC complex would display two bands at 1052 and 1170$cm^{-1}$ of similar intensities. It is to note that formation, at a short reaction time during our ATR FTIR (co)sorption experiments, of two types of U-P inner sphere surface complexes has prevented the formation of (VI)-phosphate colloids, which were observed in the absence of clay and under similar solution conditions. Formation of uranyl-phosphate ISSC surface complexes onto NaIdP is in good agreement with previously published spectroscopic studies of the (co)sorption of uranyl and phosphate ions at surfaces of aluminum / iron (hydr)oxide, $SiO_2$ and clays [14,25,61,62].

At a long reaction time (3 days) and high U concentration, two uranyl phosphate species were identified to exist onto NaIdP, namely, U-P species B remaining stable in the long term and another species (U-P species C) whose intensity was increasing with reaction time. The latter uranyl-phosphate surface species has three $\upsilon_3$ P-O antisymmetric stretching band at 1114, 1080 and 992 $cm^{-1}$, which indicates a $C_{2V}$ or lower molecular symmetry (likely $C_1$) of $PO_4$ unit. The bands' positions of U-P species C are quite different than those observed on IR spectra of uranyl phosphate solutions, ruling out formation of uranyl phosphate OSSC and / or U(VI) phosphate colloids formed directly from solution. These positions are shifted significantly with respect to those reported in the literature for the group of autunite minerals but they compare well with them (1118, 1074 and 985$cm^{-1}$ for autunite, and 1118, 1048 and 985$cm^{-1}$ for meta-autunite [63]). Hence, we hypothesize that U-P species C is an autunite-like surface species. Troyer et al. [25] have investigated by EXAFS and TRLFS the effect of increasing concentrations of phosphate and uranyl ions (0.025-100 µM) on the uptake of U(VI) by montmorillonite at pH 4-6. These authors have evidenced a transition between formation of uranyl phosphate surface complexes at low coverage of the clay, and surface precipitates of U(VI)-phosphates at high surface coverage. If the U-P species C represented a U(VI) phosphate precipitate formed on NaIdP, this would imply that its formation occurred in very limited amounts under our experimental conditions (despite the dominance of its signal on the IR spectra), because our desorption data indicate reversible co-sorption mechanisms. Therefore, we believe that the U-P species C is rather an autunite-like uranyl phosphate surface complex (e.g., as a polynuclear complex) that forms on NaIdP at a high reaction time. Strikingly, in the presence of $Fe^{3+}$ competing ions, only such a uranyl phosphate species is formed at the interface together with a surface precipitate of iron(III) phosphate.

## Conclusions

This study provides valuable information on the mechanisms of phosphate ion sorption at the Illite – solution interface, for a range of aqueous phosphate concentrations (20-200 µM) and clay-to-solution ratios investigated that led to low to moderate coverage of the clay surface by P (2-6 $\mu mol{\cdot}g^{-1}$). It was found that the percentage of P sorption is dependent on pH and phosphate concentration. Macroscopic and EM data suggested moreover mechanisms of strong phosphate ion sorption, which added negative charges to the clay surface and could involve multiple sorption species and/or surface sites present on the clay edges (high affinity sites and low amounts of low affinity sites, respectively). Data acquired by *in situ* monitoring of the Illite-solution interface by ATR FTIR spectroscopy provided evidence that at acidic pH inner-sphere phosphate surface complexes are the primary surface species and their concentration increase with contact time time and aqueous phosphate concentration. The dominant species are probably monodentate binuclear surface complexes, i.e., $\equiv (SO)_2PO_2$ (S: Al and / or Fe), involving hydroxyl surface sites on the clay edges. These surface species were characterized by $\upsilon_{as}$(P-O) bands positioned at 1003, 1035 and 1095 $cm^{-1}$, and were formed by transformation over time of an outer-sphere phosphate surface complex that dominates phosphate surface speciation at low reaction times and low P concentration. The information

on phosphate surface speciation provided by this study is useful for better understanding the surface reactivity of clays in natural systems. The obtained knowledge of U speciation in binary system provide basis for further studies of complex ternary systems of radionuclide-phosphate-clay-solution, which are of major interest, for example, in assessing the safety of high-level radioactive waste disposal in clay rocks.

Moreover, to our best knowledge, the present study is among the first ones combining macroscopic experiments and in situ ATR FTIR study to investigate the (co)sorption mechanisms of phosphate ions and trace levels of uranyl ions at illite–solution interface. All the macroscopic data reported here pointed at several sorption mechanisms / surface sites contributing to the uptake of uranyl ions by NaIdP and depending on key parameters such as pH, U concentration, clay-to-solution ratio and carbonate or phosphate ligand concentration. In peculiar, data indicated that a low amount of high affinity sorption sites (<0.02 sites·nm$^{-2}$) existing at NaIdP edge platelets can strongly interact with U and become progressively saturated, while low affinity surface sites are increasingly involved in U sorption, when increasing U concentration (1-10 µM) or decreasing clay-to-solution ratio (1-3 g·L$^{-1}$) in experiment. It was also shown that presence of carbonate ligands at high pH has no significant effect on macroscopic sorption of U, while formation of uranyl carbonate surface complexes is suggested by ATR-FTIR studies.

In contrast, phosphate ligands enhance the sorption of U(VI) at acidic pH onto NaIdP and, conversely, the uptake of phosphate ions by the clay surface is promoted by an increase of the U concentration in sorption experiment. Macroscopic and EM data highlighted formation of several types of uranyl phosphate species imparting negative charges to the clay surface and / or several types of sorption sites, with the mechanisms of U-P co-sorption remaining highly reversible. Data acquired by *in situ* monitoring of the illite-solution interface by ATR FTIR spectroscopy provided evidence that uranyl ions and phosphate ions were (co)sorbed at acidic pH mainly via the formation of three types of inner-sphere uranyl phosphate surface complexes: a surface complex forming rapidly at high affinity surface sites and displaying a (weak) $\upsilon_3$(P-O) band at ~1125 cm$^{-1}$, an additional complex forming at low affinity sites in increasing amounts with U concentration and displaying a band at ~1050 cm$^{-1}$, -with these two complexes competing successfully against formation of inner sphere phosphate surface complexes-, and, finally, an “autunite-like” uranyl phosphate surface complex (e.g., such as a polynuclear complex) having $\upsilon_3$(P-O) bands at 1114, 1080 and 992 cm$^{-1}$ and appearing at a long reaction time (>1 day) and at high U concentration (10 µM). Because Illite is an important constituent of argillaceous formations envisaged for deep HLW repositories and phosphate ligands are omnipresent in argillaceous rocks and ground/ surface waters, the macroscopic and IR spectroscopic data acquired in the present study may serve in safety assessment of the repositories and may be useful for better understanding U(VI) migration / retention in the environment.

## Acknowledgments

We thank for analyses of clay samples: ITES (Institut Terre et Environnement de Strasbourg, Strasbourg University, France) for mineralogical analyses, SARM-CRPG (Service d’Analyse des Roches et Minéraux, Centre de Recherches Pétrographiques et Géochimiques, Nancy, France) for major element and trace element analysis, and ECPM (École de Chimie des Polymères et Matériaux, Strasbourg, France) for BET measurements. We are grateful to the A. Boos for giving us access to the ICP-OES and ICP-MS equipments of the “Plateforme des Inorganiques” of IPHC for our solution analyses.

## References

[1] B. Grambow, Geological Disposal of Radioactive Waste in Clay, ELEMENTS. 12 (2016) 239–245. https://doi.org/10.2113/gselements.12.4.239.

[2] P. Krejci, T. Gimmi, L.R. Van Loon, On the concentration-dependent diffusion of sorbed cesium in Opalinus Clay, Geochimica et Cosmochimica Acta. 298 (2021) 149–166. https://doi.org/10.1016/j.gca.2021.01.012.

[3] G. Montavon, S. Ribet, Y.H. Loni, F. Maia, C. Bailly, K. David, C. Lerouge, B. Madé, J.C. Robinet, B. Grambow, Uranium retention in a Callovo-Oxfordian clay rock formation: From laboratory-based models

to in natura conditions, Chemosphere. 299 (2022) 134307. https://doi.org/10.1016/j.chemosphere.2022.134307.

[4] G. Sposito, N.T. Skipper, R. Sutton, S. -h. Park, A.K. Soper, J.A. Greathouse, Surface geochemistry of the clay minerals, Proceedings of the National Academy of Sciences. 96 (1999) 3358–3364. https://doi.org/10.1073/pnas.96.7.3358.

[5] M. Marques Fernandes, B. Baeyens, R. Dähn, A.C. Scheinost, M.H. Bradbury, U(VI) sorption on montmorillonite in the absence and presence of carbonate: A macroscopic and microscopic study, Geochimica et Cosmochimica Acta. 93 (2012) 262–277. https://doi.org/10.1016/j.gca.2012.04.017.

[6] V. Montoya, B. Baeyens, M.A. Glaus, T. Kupcik, M. Marques Fernandes, L. Van Laer, C. Bruggeman, N. Maes, T. Schäfer, Sorption of Sr, Co and Zn on illite: Batch experiments and modelling including Co in-diffusion measurements on compacted samples, Geochimica et Cosmochimica Acta. 223 (2018) 1–20. https://doi.org/10.1016/j.gca.2017.11.027.

[7] K. Maher, J.R. Bargar, G.E. Brown, Environmental Speciation of Actinides, Inorg. Chem. 52 (2013) 3510–3532. https://doi.org/10.1021/ic301686d.

[8] S.A. Cumberland, G. Douglas, K. Grice, J.W. Moreau, Uranium mobility in organic matter-rich sediments: A review of geological and geochemical processes, Earth-Science Reviews. 159 (2016) 160–185. https://doi.org/10.1016/j.earscirev.2016.05.010.

[9] G.D. Turner, J.M. Zachara, J.P. Mckinley, S.C. Smith, Surface-charge properties and UO z' adsorption of a subsurface smectite, (1996). https://doi.org/10.1016/0016-7037(96)00169-X.

[10] M. Marques Fernandes, A.C. Scheinost, B. Baeyens, Sorption of trivalent lanthanides and actinides onto montmorillonite: Macroscopic, thermodynamic and structural evidence for ternary hydroxo and carbonato surface complexes on multiple sorption sites, Water Research. 99 (2016) 74–82. https://doi.org/10.1016/j.watres.2016.04.046.

[11] C. Joseph, M. Stockmann, K. Schmeide, S. Sachs, V. Brendler, G. Bernhard, Sorption of U(VI) onto Opalinus Clay: Effects of pH and humic acid, Applied Geochemistry. 36 (2013) 104–117. https://doi.org/10.1016/j.apgeochem.2013.06.016.

[12] C. Tournassat, R.M. Tinnacher, S. Grangeon, J.A. Davis, Modeling uranium(VI) adsorption onto montmorillonite under varying carbonate concentrations: A surface complexation model accounting for the spillover effect on surface potential, Geochimica et Cosmochimica Acta. 220 (2018) 291–308. https://doi.org/10.1016/j.gca.2017.09.049.

[13] M.H. Bradbury, B. Baeyens, Sorption modelling on illite. Part II: Actinide sorption and linear free energy relationships, Geochimica et Cosmochimica Acta. 73 (2009) 1004–1013. https://doi.org/10.1016/j.gca.2008.11.016.

[14] M.J. Comarmond, R. Steudtner, M. Stockmann, K. Heim, K. Müller, V. Brendler, T.E. Payne, H. Foerstendorf, The Sorption Processes of U(VI) onto $SiO_2$ in the Presence of Phosphate: from Binary Surface Species to Precipitation, Environ. Sci. Technol. 50 (2016) 11610–11618. https://doi.org/10.1021/acs.est.6b02075.

[15] C. Galindo, M.D. Nero, R. Barillon, E. Halter, B. Made, Mechanisms of uranyl and phosphate (co)sorption: Complexation and precipitation at α-Al2O3 surfaces, Journal of Colloid and Interface Science. 347 (2010) 282–289. https://doi.org/10.1016/j.jcis.2010.03.045.

[16] Z. Guo, C. Yan, J. Xu, W. Wu, Sorption of U(VI) and phosphate on γ-alumina: Binary and ternary sorption systems, Colloids and Surfaces A: Physicochemical and Engineering Aspects. 336 (2009) 123–129. https://doi.org/10.1016/j.colsurfa.2008.11.032.

[17] T.E. Payne, G.R. Lumpkin, T.D. Waite, Uranium (VI) Adsorption on Model Minerals: Controlling factors and surface complexation modelling, (1998).

[18] A. Singh, K.-U. Ulrich, D.E. Giammar, Impact of phosphate on U(VI) immobilization in the presence of goethite, Geochimica et Cosmochimica Acta. 74 (2010) 6324–6343. https://doi.org/10.1016/j.gca.2010.08.031.

[19] E.R. Sylwester, E.A. Hudson, P.G. Allen, The structure of uranium (VI) sorption complexes on silica, alumina, and montmorillonite, Geochimica et Cosmochimica Acta. 64 (2000) 2431–2438. https://doi.org/10.1016/S0016-7037(00)00376-8.

[20] C.J. Chisholm-Brause, J.M. Berg, R.A. Matzner, D.E. Morris, Uranium(VI) Sorption Complexes on Montmorillonite as a Function of Solution Chemistry, Journal of Colloid and Interface Science. 233 (2001) 38–49. https://doi.org/10.1006/jcis.2000.7227.

[21] C. Hennig, T. Reich, R. Dähn, A.M. Scheidegger, Structure of uranium sorption complexes at montmorillonite edge sites, Radiochimica Acta. 90 (2002) 653–657. https://doi.org/10.1524/ract.2002.90.9-11_2002.653.

[22] J.G. Catalano, G.E. Brown, Uranyl adsorption onto montmorillonite: Evaluation of binding sites and carbonate complexation, Geochimica et Cosmochimica Acta. 69 (2005) 2995–3005. https://doi.org/10.1016/j.gca.2005.01.025.

[23] M. Stockmann, K. Fritsch, F. Bok, M.M. Fernandes, B. Baeyens, R. Steudtner, K. Müller, C. Nebelung, V. Brendler, T. Stumpf, K. Schmeide, New insights into U(VI) sorption onto montmorillonite from batch sorption and spectroscopic studies at increased ionic strength, Science of The Total Environment. 806 (2022) 150653. https://doi.org/10.1016/j.scitotenv.2021.150653.

[24] A. Gładysz-Płaska, E. Grabias, M. Majdan, Simultaneous adsorption of uranium(VI) and phosphate on red clay, Progress in Nuclear Energy. 104 (2018) 150–159. https://doi.org/10.1016/j.pnucene.2017.09.010.

[25] L.D. Troyer, F. Maillot, Z. Wang, Z. Wang, V.S. Mehta, D.E. Giammar, J.G. Catalano, Effect of phosphate on U(VI) sorption to montmorillonite: Ternary complexation and precipitation barriers, Geochimica et Cosmochimica Acta. 175 (2016) 86–99. https://doi.org/10.1016/j.gca.2015.11.029.

[26] L. Borgnino, C.E. Giacomelli, M.J. Avena, C.P. De Pauli, Phosphate adsorbed on Fe(III) modified montmorillonite: Surface complexation studied by ATR-FTIR spectroscopy, Colloids and Surfaces A: Physicochemical and Engineering Aspects. 353 (2010) 238–244. https://doi.org/10.1016/j.colsurfa.2009.11.022.

[27] J.K. Edzwald, D.C. Toensing, M.C.-Yew. Leung, Phosphate adsorption reactions with clay minerals, Environ. Sci. Technol. 10 (1976) 485–490. https://doi.org/10.1021/es60116a001.

[28] F. Gérard, Clay minerals, iron/aluminum oxides, and their contribution to phosphate sorption in soils — A myth revisited, Geoderma. 262 (2016) 213–226. https://doi.org/10.1016/j.geoderma.2015.08.036.

[29] M. Dolui, S. Rakshit, M.E. Essington, G. Lefèvre, Probing Oxytetracycline Sorption Mechanism on Kaolinite in a Single Ion and Binary Mixtures with Phosphate using In Situ ATR-FTIR Spectroscopy, Soil Science Society of America Journal. 82 (2018) 826–838. https://doi.org/10.2136/sssaj2018.01.0020.

[30] T.J. Van Emmerik, D.E. Sandström, O.N. Antzutkin, M.J. Angove, B.B. Johnson, $^{31}$ P Solid-State Nuclear Magnetic Resonance Study of the Sorption of Phosphate onto Gibbsite and Kaolinite, Langmuir. 23 (2007) 3205–3213. https://doi.org/10.1021/la062765b.

[31] K.O. Adebowale, I.E. Unuabonah, B.I. Olu-Owolabi, Adsorption of some heavy metal ions on sulfate- and phosphate-modified kaolin, Applied Clay Science. 29 (2005) 145–148. https://doi.org/10.1016/j.clay.2004.10.003.

[32] M.A. Glaus, M. Aertsens, N. Maes, L. Van Laer, L.R. Van Loon, Treatment of boundary conditions in through-diffusion: A case study of 85Sr2+ diffusion in compacted illite, Journal of Contaminant Hydrology. 177–178 (2015) 239–248. https://doi.org/10.1016/j.jconhyd.2015.03.010.

[33] V. Bout-Roumazeilles, E. Cortijo, L. Labeyrie, P. Debrabant, Clay mineral evidence of nepheloid layer contributions to the Heinrich layers in the northwest Atlantic, Palaeogeography, Palaeoclimatology, Palaeoecology. 146 (1999) 211–228.

[34] G.W. Brindley, G. Brown, Crystal Structures of Clay Minerals and Their X-ray Identification., Mineralogical Society, 1980.

[35] M.H. Bradbury, B. Baeyens, Sorption modelling on illite Part I: Titration measurements and the sorption of Ni, Co, Eu and Sn, Geochimica et Cosmochimica Acta. 73 (2009) 990–1003. https://doi.org/10.1016/j.gca.2008.11.017.

[36] M. Del Nero, C. Galindo, R. Barillon, E. Halter, B. Madé, Surface reactivity of α-Al2O3 and mechanisms of phosphate sorption: In situ ATR-FTIR spectroscopy and ζ potential studies, Journal of Colloid and Interface Science. 342 (2010) 437–444. https://doi.org/10.1016/j.jcis.2009.10.057.

[37] Y. Arai, D.L. Sparks, ATR–FTIR Spectroscopic Investigation on Phosphate Adsorption Mechanisms at the Ferrihydrite–Water Interface, Journal of Colloid and Interface Science. 241 (2001) 317–326. https://doi.org/10.1006/jcis.2001.7773.

[38] E.J. Elzinga, D.L. Sparks, Phosphate adsorption onto hematite: An in situ ATR-FTIR investigation of the effects of pH and loading level on the mode of phosphate surface complexation, Journal of Colloid and Interface Science. 308 (2007) 53–70. https://doi.org/10.1016/j.jcis.2006.12.061.

[39] W. Li, A.-M. Pierre-Louis, K.D. Kwon, J.D. Kubicki, D.R. Strongin, B.L. Phillips, Molecular level investigations of phosphate sorption on corundum (α-Al2O3) by 31P solid state NMR, ATR-FTIR and quantum chemical calculation, Geochimica et Cosmochimica Acta. 107 (2013) 252–266. https://doi.org/10.1016/j.gca.2013.01.007.

[40] P. Persson, N. Nilsson, S. Sjöberg, Structure and Bonding of Orthophosphate Ions at the Iron Oxide–Aqueous Interface, Journal of Colloid and Interface Science. 177 (1996) 263–275. https://doi.org/10.1006/jcis.1996.0030.

[41] M.I. Tejedor-Tejedor, M.A. Anderson, The protonation of phosphate on the surface of goethite as studied by CIR-FTIR and electrophoretic mobility, Langmuir. 6 (1990) 602–611. https://doi.org/10.1021/la00093a015.

[42] J.R. Bargar, R. Reitmeyer, J.A. Davis, Spectroscopic Confirmation of Uranium(VI)−Carbonato Adsorption Complexes on Hematite, Environ. Sci. Technol. 33 (1999) 2481–2484. https://doi.org/10.1021/es990048g.

[43] C. Nguyen Trung, G.M. Begun, D.A. Palmer, Aqueous uranium complexes. 2. Raman spectroscopic study of the complex formation of the dioxouranium(VI) ion with a variety of inorganic and organic ligands, Inorg. Chem. 31 (1992) 5280–5287. https://doi.org/10.1021/ic00051a021.

[44] F. Quilès, A. Burneau, Infrared and Raman spectroscopic study of uranyl complexes: hydroxide and acetate derivatives in aqueous solution, Vibrational Spectroscopy. 18 (1998) 61–75. https://doi.org/10.1016/S0924-2031(98)00040-X.

[45] F. Quilès, C. Nguyen-Trung, C. Carteret, B. Humbert, Hydrolysis of Uranyl(VI) in Acidic and Basic Aqueous Solutions Using a Noncomplexing Organic Base: A Multivariate Spectroscopic and Statistical Study, Inorg. Chem. 50 (2011) 2811–2823. https://doi.org/10.1021/ic101953q.

[46] C. Poinssot, B. Baeyens, M.H. Bradbury, Experimental and modelling studies of caesium sorption on illite, Geochimica et Cosmochimica Acta. 63 (1999) 3217–3227. https://doi.org/10.1016/S0016-7037(99)00246-X.

[47] J.A. Davis, D.B. Kent, CHAPTER 5. SURFACE COMPLEXATION MODELING IN AQUEOUS GEOCHEMISTRY, in: M.F. Hochella, A.F. White (Eds.), Mineral-Water Interface Geochemistry, De Gruyter, 1990: pp. 177–260. https://doi.org/10.1515/9781501509131-009.

[48] I. Jeon, K. Nam, Change in the site density and surface acidity of clay minerals by acid or alkali spills and its effect on pH buffering capacity, Sci Rep. 9 (2019) 9878. https://doi.org/10.1038/s41598-019-46175-y.

[49] Y. Arai, D.L. Sparks, Phosphate Reaction Dynamics in Soils and Soil Components: A Multiscale Approach, in: Advances in Agronomy, Elsevier, 2007: pp. 135–179. https://doi.org/10.1016/S0065-2113(06)94003-6.

[50] G.M. Beene, R. Bryant, D.J.A. Williams, Electrochemical properties of illites, Journal of Colloid and Interface Science. 147 (1991) 358–369. https://doi.org/10.1016/0021-9797(91)90168-8.

[51] Q. Du, Z. Sun, W. Forsling, H. Tang, Acid-Base Properties of Aqueous Illite Surfaces, (n.d.) 11.

[52] T. Roy, D. Wisser, M. Rivallan, M.C. Valero, T. Corre, O. Delpoux, G.D. Pirngruber, G. Lefèvre, Phosphate Adsorption on γ-Alumina: A Surface Complex Model Based on Surface Characterization and Zeta Potential Measurements, J. Phys. Chem. C. (2021) acs.jpcc.0c11553. https://doi.org/10.1021/acs.jpcc.0c11553.

[53] R.J. Hunter, A.E. Alexander, Surface properties and flow behavior of kaolinite. Part I: Electrophoretic mobility and stability of kaolinite sols, Journal of Colloid Science. 18 (1963) 820–832. https://doi.org/10.1016/0095-8522(63)90076-X.

[54] W.F. Bleam, P.E. Pfeffer, S. Goldberg, R.W. Taylor, R. Dudley, A phosphorus-31 solid-state nuclear magnetic resonance study of phosphate adsorption at the boehmite/aqueous solution interface, Langmuir. 7 (1991) 1702–1712. https://doi.org/10.1021/la00056a023.

[55] D. Vantelon, M. Pelletier, L.J. Michot, O. Barres, F. Thomas, Fe, Mg and Al distribution in the octahedral sheet of montmorillonites. An infrared study in the OH- bending region, Clay Miner. 36 (2001) 369–379. https://doi.org/10.1180/000985501750539463.

[56] J. Madejová, Baseline Studies of the Clay Minerals Society Source Clays: Infrared Methods, Clays and Clay Minerals. 49 (2001) 410–432. https://doi.org/10.1346/CCMN.2001.0490508.

[57] C.T. Johnston, G.S. Premachandra, Polarized ATR-FTIR Study of Smectite in Aqueous Suspension, Langmuir. 17 (2001) 3712–3718. https://doi.org/10.1021/la010184a.

[58] R. Ellerbrock, M. Stein, J. Schaller, Comparing amorphous silica, short-range-ordered silicates and silicic acid species by FTIR, In Review, 2022. https://doi.org/10.21203/rs.3.rs-1623376/v1.

[59] M. Ritz, L. Vaculíková, E. Plevová, APPLICATION OF INFRARED SPECTROSCOPY AND CHEMOMETRIC METHODS TO IDENTIFICATION OF SELECTED MINERALS, Acta Geodynamica et Geromaterialia. 8 (2011) 47–58.

[60] Y. Jo, J.-Y. Lee, J.-I. Yun, Adsorption of uranyl tricarbonate and calcium uranyl carbonate onto γ-alumina, Applied Geochemistry. 94 (2018) 28–34. https://doi.org/10.1016/j.apgeochem.2018.05.004.

[61] C. Galindo, M.D. Nero, R. Barillon, E. Halter, B. Made, Mechanisms of uranyl and phosphate (co)sorption: Complexation and precipitation at α-Al2O3 surfaces, Journal of Colloid and Interface Science. 347 (2010) 282–289. https://doi.org/10.1016/j.jcis.2010.03.045.

[62] A. Singh, J.G. Catalano, K.-U. Ulrich, D.E. Giammar, Molecular-Scale Structure of Uranium(VI) Immobilized with Goethite and Phosphate, Environ. Sci. Technol. 46 (2012) 6594–6603. https://doi.org/10.1021/es300494x.

[63] R.L. Frost, An infrared and Raman spectroscopic study of the uranyl micas, Spectrochimica Acta Part A: Molecular and Biomolecular Spectroscopy. 60 (2004) 1469–1480. https://doi.org/10.1016/j.saa.2003.08.013.

# Appendix A. Complementary data

*Table A1: Mineralogical composition (semi-quantitative estimation in %) of IdP and NaIdP samples and their clay fractions (< 2 µm).*

| | | Clay | | Carbonate | | Feldspar | | | Iron Oxide | |
|---|---|---|---|---|---|---|---|---|---|---|
| | | *Illite* | *Kaolinite* | *Calcite* | *Siderite* | *Microcline* | *Orthoclase* | *Albite* | *Hematite* | *Quartz* |
| **IdP** | | 18.5 | 5.4 | 32.8 | 3.3 | 18.2 | 11.6 | 6.3 | 0.4 | 3.5 |
| **NaIdP** | | 30.2 | 7.2 | *<5%* | | 20.6 | 20.5 | 16.6 | *<5%* | 4.9 |
| **IdP** | | 79 | 21 | *<5%* | | *Traces* | | | *<5%* | |
| **NaIdP** | <2µm | 76 | 24 | *<5%* | | *Traces* | | | *<5%* | |

*Table A2: Major element composition of IdP and NaIdP samples (in wt/wt percent oxide)*.

| | $SiO_2$ | $Al_2O_3$ | $Fe_2O_3$ | $K_2O$ | CaO | MgO | $TiO_2$ | $P_2O_5$ | $Na_2O$ | MnO | Loss of ignition |
|---|---|---|---|---|---|---|---|---|---|---|---|
| **IdP** | 44.64 | 19.68 | 6.64 | 5.82 | 5.42 | 3.16 | 0.65 | 0.26 | 0.15 | 0.057 | 12.94 |
| **NaIdP** | 51.20 | 22.30 | 7.52 | 6.58 | 0.09 | 3.34 | 0.75 | <0.1% | 0.6 | 0.050 | 8.90 |

*Table A3: Trace element composition (µg·g$^{-1}$) of IdP and NaIdP samples. The analytical uncertainties, which depend on the concentration of element, are in the range of 5-20%.*

| | As | Ba | Be | Bi | Cd | Co | Cr | Cs | Cu | Ga | Ge |
|---|---|---|---|---|---|---|---|---|---|---|---|
| IdP | 31.6 | 316 | 6.72 | 1.05 | 0.17 | 12.9 | 80.5 | 99.4 | 32.3 | 33.8 | 2.12 |
| NaIdP | 22.3 | 207 | 7.35 | 1.09 | 0.07 | 13.7 | 90.7 | 74.2 | 32.4 | 36.7 | 2.06 |

| | Hf | In | Mo | Nb | Ni | Pb | Rb | Sb | Sc | Sn | Sr |
|---|---|---|---|---|---|---|---|---|---|---|---|
| IdP | 1.38 | 0.11 | < D.L. | 14.8 | 34.3 | 33.5 | 551 | 1.16 | 14.28 | 8.77 | 180 |
| NaIdP | 1.42 | 0.11 | < D.L. | 15.9 | 39.3 | 30.8 | 473 | 0.97 | 16.00 | 9.00 | 72.2 |

| | Ta | Th | U | V | W | Y | Zn | Zr | La | Ce | Pr |
|---|---|---|---|---|---|---|---|---|---|---|---|
| IdP | 1.77 | 8.87 | 3.38 | 89.4 | 3.54 | 14.6 | 150 | 45.7 | 22.0 | 43.8 | 5.17 |
| NaIdP | 1.83 | 9.39 | 2.84 | 96.1 | 3.46 | 4.85 | 163 | 42.5 | 15.4 | 26.7 | 3.12 |

| | Nd | Sm | Eu | Gd | Tb | Dy | Ho | Er | Tm | Yb | Lu |
|---|---|---|---|---|---|---|---|---|---|---|---|
| IdP | 19.5 | 4.05 | 0.91 | 3.26 | 0.52 | 2.98 | 0.57 | 1.43 | 0.20 | 1.23 | 0.17 |
| NaIdP | 10.9 | 1.94 | 0.34 | 1.30 | 0.19 | 1.04 | 0.20 | 0.53 | 0.08 | 0.59 | 0.09 |

*Table A4: Final concentrations of cations (µM) in experimental 0.005M NaCl solutions brought in contact with IdP and NaIdP at various values of clay-to-solution ratios – $R_{S/L}$ (1-6g·L$^{-1}$and 0.5-3 g·L$^{-1}$, respectively). Experimental conditions for IdP (initial pH 2.3, reaction time $t_R$ of 5 days), for NaIdP (initial pH 2.6-7.4, $t_R$: 3- or 7-days). The chemical analysis of solution was carried out after phase separation by centrifugation at 9000rpm for 3h (cutoff 16 nm).*

| *IdP - electrolyte solution system - 5 days* | | | | | | |
|---|---|---|---|---|---|---|
| *$R_{S/L}$* | *1.0* | *2.0* | *3.0* | *3.9* | *5.0* | *6.0* |
| *pH $_{Final}$* | *2.6* | *3.2* | *6.0* | *6.6* | *7.0* | *7.2* |
| [Al] | 90.6 ± 0.8 | 111 ± 1 | 10.17 ± 0.30 | 9.21 ± 0.24 | 7.36 ± 0.16 | 9.80 ± 0.03 |
| [Mg] | 54.1 ± 0.5 | 86.6 ± 0.8 | 84.3 ± 0.8 | 97.3 ± 0.90 | 111 ± 1 | 126 ± 1 |
| [K] | 236 ± 2 | 273 ± 2 | 276 ± 3 | 267 ± 3 | 242 ± 2 | 305 ± 1 |
| [Si] | 138 ± 2 | 196 ± 2 | 182 ± 1 | 200 ± 4 | 219 ± 1 | 242 ± 4 |
| [Fe] | 2.59 ± 0.05 | 1.90 ± 0.02 | 3.14 ± 0.51 | 2.73 ± 0.08 | 2.30 ± 0.04 | 2.98 ± 0.02 |
| [Mn] | 2.44 ± 0.06 | 4.05 ± 0.07 | 2.40 ± 0.03 | 2.12 ± 0.05 | 1.79 ± 0.01 | 1.51± 0.03 |
| [Ti] | 0.033 ± 0.020 | 0.018 ± 0.004 | 0.110 ± 0.004 | 0.100 ± 0.004 | 0.090 ± 0.010 | 0.130± 0.004 |
| [Li] | 1.48 ± 0.06 | 2.90 ± 0.03 | 2.64 ± 0.21 | 3.13 ± 0.15 | 3.68 ± 0.12 | 4.22 ± 0.04 |
| [Ca] | 0.87 ± 0.01 | 1.49 ± 0.02 | 1.96 ± 0.01 | 2.26 ± 0.02 | 2.43 ± 0.02 | 2.51 ± 0.03 |

| *NaIdP - electrolyte solution system - 3 days* | | | | | | | | | |
|---|---|---|---|---|---|---|---|---|---|
| *$R_{S/L}$* | *0.5* | *1.5* | *3.0* | *3.0* | *3.0* | *3.0* | *3.0* | *3.0* | *3.0* |
| *pH$_{Final}$* | *3.4* | *3.0* | *2.9* | *3.5* | *4.2* | *5.2* | *7.0* | *7.1* | *7.6* |
| [Al] | 25.6 ± 0.7 | 45.3 ± 0.3 | 92.7 ± 2.1 | 52.9 ± 0.4 | 28.2 ± 0.4 | 5.00 ± 0.32 | 3.99 ± 0.21 | 25.92 ± 0.39 | 37.0 ± 0.31 |
| [Mg] | 13.1 ± 0.2 | 30.7 ± 0.1 | 62.1 ± 1.1 | 14.6 ± 0.1 | 46.3 ± 0.3 | 21.1 ± 0.2 | 5.26 ± 0.03 | 8.15 ± 0.03 | 10.8 ± 0.1 |
| [K] | 50.3 ± 1.0 | 267 ± 1 | 105 ± 2 | 108 ± 1 | 153 ± 1 | 171 ± 2 | 111 ± 1 | 62.0 ± 0.2 | 93.2 ± 0.5 |
| [Si] | 73.5 ± 1.86 | 121 ± 1 | 245 ± 4 | 214 ± 6 | 201 ± 6 | 144 ± 1 | 114 ± 1 | 146 ± 2 | 172 ± 1 |
| [Fe] | 4.15 ± 0.1 | 2.63 ± 0.03 | 3.61 ± 0.07 | 14.2 ± 0.3 | 2.99 ± 0.12 | 0.68 ± 0.02 | 0.71 ± 0.04 | 7.19 ± 0.11 | 10.1 ± 0.1 |
| [Fe] *(3nm)* | <D.L. | 0.89 ± 0.01 | 1.32 ± 0.01 | - | - | - | - | - | - |
| [Mn] | <D.L. | <D.L. | <D.L. | <D.L. | 0.67 ± 0.01 | 0.18 ± 0.01 | <D.L. | <D.L. | <D.L. |
| [Ti] | <D.L. | <D.L. | <D.L. | 0.100 ± 0.003 | 0.060 ± 0.007 | <D.L. | <D.L. | 0.040 ± 0.003 | 0.050 ± 0.001 |
| [Li] | <D.L. | <D.L. | <D.L. | 2.10 ± 0.01 | 2.67 ± 0.02 | 2.14 ± 0.02 | 1.79 ± 0.01 | 1.74 ± 0.01 | 1.86 ± 0.01 |
| [Ca] | 2.90 ± 0.16 | 9.26 ± 0.18 | 14.8 ± 0.4 | 15.0 ± 0.1 | 79.4 ± 0.1 | 45.3 ± 0.1 | 14.6 ± 0.1 | 11.8 ± 0.1 | 8.27 ± 0.02 |

| *NaIdP - electrolyte solution system - 7 days* | | | |
|---|---|---|---|
| *$R_{S/L}$* | *0.5* | *0.5* | *0.5* |
| *pH $_{Final}$* | *6.8* | *6.8* | *4.8* |
| [Al] | 3.41 ± 0.14 | 3.11 ± 0.34 | <D.L. |
| [Mg] | 2.76 ± 0.03 | 2.67 ± 0.09 | 5.51 ± 0.07 |
| [K] | 145 ± 1 | 127 ± 1 | 32.9 ± 0.6 |
| [Si] | 35.8 ± 0.5 | 36.2 ± 1.2 | 35.8 ± 0.7 |
| [Fe] | 1.030 ± 0.025 | 0.960 ± 0.106 | 0.010 ± 0.011 |
| [Mn] | <D.L. | <D.L. | <D.L. |
| [Ti] | <D.L. | <D.L. | <D.L. |
| [Li] | <D.L. | <D.L. | <D.L. |
| [Ca] | 1.79 ± 0.12 | 2.79 ± 0.07 | 0.86 ± 0.18 |

*Table A5: Final concentrations of anions in experimental 0.005M NaCl solutions brought in contact with IdP and NaIdP at various values of clay-to-solution ratios -$R_{S/L}$ (1-6 g·L$^{-1}$and 0.5-3 g·L$^{-1}$, respectively). Experimental conditions for IdP (initial pH2.3, reaction time $t_R$ of 5 days), for NaIdP (initial pH 2.6-7.4, $t_R$:3- or 7-days). Solid-liquid separation was carried out by centrifugation at 9000rpm for 3h (cutoff: 16 nm).*

| | $R_{S/L}$ (g·L$^{-1}$) | pH $_{Final}$ | [$PO_4^{3-}$] (µM) | [$F^-$] (µM) | [$NO_3^-$] (µM) | [$SO_4^{2-}$] (µM) | $t_R$ (days) |
|---|---|---|---|---|---|---|---|
| IdP | 1.0 | 2.6 | 22.2±1.3 | 16.4±0.8 | 7.2±0.4 | 2.0±0.1 | 5 |
| | 2.0 | 3.2 | 40.1±1.3 | 31.1±1.6 | 6.9±0.3 | 3.9±0.2 | |
| | 3.0 | 6.0 | 43.9±1.3 | 24.5±1.2 | 6.0±0.3 | 5.4±0.3 | |
| | 3.9 | 6.6 | 45.2±1.3 | 32.4±1.6 | 6.1±0.3 | 6.3±0.3 | |
| | 5.0 | 7.0 | 48.4±1.3 | 38±1.9 | 7.0±0.3 | 6.7±0.3 | |
| | 6.0 | 7.2 | 45.3±1.3 | 38.8±1.9 | 6.7±0.3 | 7.3±0.4 | |
| NaIdP | 0.5 | 3.4 | 1.14±0.06 | 5.46±0.27 | 1.22±0.06 | < D.L. | 3 |
| | 1.0 | 3.5 | 1.38±0.07 | 6.93±0.35 | 2.02±0.1 | < D.L. | |
| | 1.5 | 3.0 | 1.54±0.08 | 8.4±0.42 | 2.8±0.14 | < D.L. | |
| | 2.0 | 2.9 | 1.87±0.09 | 10.5±0.5 | 2.46±0.12 | < D.L. | |
| | 2.5 | 2.9 | 1.81±0.09 | 8.8±0.44 | 3.1±0.15 | < D.L. | |
| | 3.0 | 2.9 | 1.94±0.1 | 12.8±0.6 | 2.41±0.12 | < D.L. | |
| | 0.5 | 6.8 | < D.L. | 5.08±0.25 | 1.43±0.07 | < D.L. | 7 |
| | 0.5 | 6.8 | < D.L. | 5.7±0.28 | 2.05±0.1 | < D.L. | |
| | 0.5 | 4.8 | < D.L. | < D.L. | 0.97±0.05 | < D.L. | |
| | 0.5 | 4.7 | < D.L. | < D.L. | 10.8±0.5 | < D.L. | |
| | 3.0 | 4.3 | < D.L. | 6.44±0.32 | 2.83±0.14 | < D.L. | |
| | 3.0 | 3.0 | < D.L. | 10.3±0.5 | 2.32±0.12 | < D.L. | |
| | 3.0 | 5.6 | < D.L. | 5.34±0.27 | 0.68±0.03 | < D.L. | |
| | 3.0 | 6.8 | < D.L. | 8.36±0.42 | < D.L. | < D.L. | |

*Table A6: Calculated aqueous species in experimental solutions contacted with IdP at various $R_{S/L}$: 3-6 g·L$^{-1}$, during a reaction time of 5 days. The input data can be found in Tables A4.*

| | Calculated concentration (mol·L$^{-1}$) | | | |
|---|---|---|---|---|
| *$R_{S/L}$* | *3* | *4* | *5* | *6* |
| *$pH_{final}$* | *6.0* | *6.6* | *7.0* | *7.2* |
| $Al(OH)_2^+$ | 1.0E-06 | 7.5E-07 | 4.7E-07 | 7.5E-07 |
| $Al(OH)_3$ (aq) | 1.9E-06 | 1.6E-06 | 1.2E-06 | 1.6E-06 |
| $Al(OH)_4^-$ | 5.4E-06 | 5.1E-06 | 4.5E-06 | 5.0E-06 |
| $AlF_2^+$ | 1.1E-06 | 1.2E-06 | 7.7E-07 | 1.6E-06 |
| $Ca^{2+}$ | 1.9E-03 | 2.2E-03 | 2.4E-03 | 2.5E-03 |
| $CaCl^+$ | 3.1E-05 | 3.6E-05 | 3.8E-05 | 3.9E-05 |
| $CaHPO_4$ (aq) | 4.3E-06 | 5.3E-06 | 6.6E-06 | 5.7E-06 |
| $CaSO_4$ (aq) | 8.1E-07 | 1.0E-06 | 1.2E-06 | 1.3E-06 |
| $Cl^-$ | 1.0E-02 | 1.0E-02 | 1.0E-02 | 1.0E-02 |
| $F^-$ | 2.1E-05 | 2.8E-05 | 3.5E-05 | 3.3E-05 |
| $Fe(OH)_2^+$ | 3.1E-06 | 2.7E-06 | 2.3E-06 | 3.0E-06 |
| $H_2CO_3^*$ (aq) | 1.3E-05 | 1.3E-05 | 1.3E-05 | 1.3E-05 |
| $H_2PO_4^-$ | 2.6E-05 | 2.5E-05 | 2.4E-05 | 2.5E-05 |
| $H_4SiO_4$ | 1.8E-04 | 2.0E-04 | 2.2E-04 | 2.4E-04 |
| $HCO_3^-$ | 3.3E-05 | 3.8E-05 | 4.5E-05 | 3.8E-05 |
| $HPO_4^{2-}$ | 1.2E-05 | 1.3E-05 | 1.5E-05 | 1.3E-05 |
| $K^+$ | 2.7E-04 | 2.7E-04 | 2.4E-04 | 3.0E-04 |
| KCl (aq) | 1.1E-06 | 1.1E-06 | 9.6E-07 | 1.2E-06 |
| $Li^+$ | 2.6E-06 | 3.1E-06 | 3.7E-06 | 4.2E-06 |
| $Mg^{2+}$ | 8.2E-05 | 9.4E-05 | 1.1E-04 | 1.2E-04 |
| $MgCl^+$ | 2.1E-06 | 2.4E-06 | 2.7E-06 | 3.1E-06 |
| $Mn^{2+}$ | 2.4E-06 | 2.2E-06 | 1.7E-06 | 1.5E-06 |
| $Na^+$ | 5.0E-03 | 5.0E-03 | 5.0E-03 | 5.0E-03 |
| NaCl (aq) | 2.0E-05 | 2.0E-05 | 2.0E-05 | 2.0E-05 |
| $NO_3^-$ | 6.0E-06 | 6.1E-06 | 6.9E-06 | 6.6E-06 |
| $SO_4^{2-}$ | 4.5E-06 | 5.1E-06 | 5.4E-06 | 5.8E-06 |

*Table A7: Calculated saturation index of minerals for the experimental 0.005M NaCl solutions contacted with IdP at various $R_{S/L}$: 3-6g·L$^{-1}$, during a reaction time of 5 days. The input data can be found in Tables A4.*

| | Calculated saturation index | | | |
|---|---|---|---|---|
| *$R_{S/L}$* | *3* | *4* | *5* | *6* |
| *pH $_{Final}$* | *6.0* | *6.6* | *7.0* | *7.2* |
| $Al(OH)_3$ (amorphous) | 0.2 | 0.1 | -0.04 | 0.1 |
| $Al(OH)_3$ | 2.7 | 2.6 | 2.5 | 2.6 |
| $Al_2O_3$ | 2.3 | 2.1 | 1.9 | 2.1 |
| $Al_4(OH)_{10}SO_4$ | 2.2 | 1.8 | 1.2 | 1.9 |
| $AlPO_4$ 1.5$H_2O$ | 0.5 | 0.4 | 0.1 | 0.3 |
| Boehmite | 2.4 | 2.3 | 2.2 | 2.3 |
| Diaspore | 4.1 | 4.0 | 3.9 | 4.0 |
| $FCO_3$-Apatite | 12.6 | 14.0 | 15.4 | 14.5 |
| $Fe(OH)_{2.7}Cl_{0.3}$ | 7.3 | 7.3 | 7.3 | 7.3 |
| Ferrihydrite | 6.9 | 3.7 | 3.7 | 3.7 |
| Ferrihydrite (aged) | 4.2 | 4.2 | 4.2 | 4.2 |
| Gibbsite | 3.2 | 3.1 | 3.0 | 3.1 |
| Goethite | 6.4 | 6.4 | 6.4 | 6.4 |
| Halloysite | 4.9 | 4.8 | 4.6 | 5.0 |
| Hematite | 15.2 | 15.2 | 15.2 | 15.3 |
| Hydroxyapatite | 4.2 | 4.8 | 5.4 | 4.9 |
| Imogolite | 5.2 | 5.1 | 4.9 | 5.2 |
| Kaolinite | 7.0 | 6.9 | 6.8 | 7.1 |
| Lepidocrocite | 5.5 | 5.5 | 5.5 | 5.6 |
| Maghemite | 7.4 | 7.4 | 7.4 | 7.5 |
| Magnesioferrite | 6.1 | 6.3 | 6.5 | 6.4 |
| $MnHPO_4$ | 2.1 | 2.1 | 2.1 | 1.9 |
| Quartz | 0.3 | 0.3 | 0.3 | 0.4 |
| Rutile | 0.7 | -1.4 | -1.4 | 0.7 |
| Strengite | 2.4 | 2.3 | 2.2 | 2.3 |
| Variscite | 2.1 | 2.0 | 1.7 | 2.0 |

*Table A8: Calculated saturation index (SI) of a solution at total concentrations of U(VI) and phosphate ions of 10 µM and 100 µM, respectively, at pH 4. Solubility constants of uranium-phosphate minerals used in calculations are reported too (Database: Visual MINTEQ (Ver:3.1) code).*

| Solid phases | Equilibrium Reactions | Log K | SI *(pH4)* |
|---|---|---|---|
| Schoepite | $UO_3 \cdot 2H_2O_{(s)} + 2H^+ \leftrightharpoons UO_2^{2+} + 3H_2O$ | 4.869 | -2.759 |
| $UO_2(OH)_{2\ (beta)}$ | $UO_2(OH)_{2\ (beta)} + 2H^+ \leftrightharpoons UO_2^{2+} + 2H_2O$ | 4.869 | -2.98 |
| $UO_{3\ (s)}$ | $UO_{3\ (s)} + 2H^+ \leftrightharpoons UO_2^{2+} + H_2O$ | 4.869 | -5.068 |
| $(UO_2)_3(PO_4)_{2\ (s)}$ | $(UO_2)_3(PO_4)_{2\ (s)} \leftrightharpoons 3UO_2^{2+} + 2PO_4^{3-}$ | -49.974 | 1.975 |
| H-Autunite | $(UO_2)_2(H_2PO_4)_{2\ (s)} \leftrightharpoons 2UO_2^{2+} + 2PO_4^{3-} + 2H^+$ | -52.843 | -2.126 |
| Na-Autunite | $(UO_2)_2(H_2PO_4)_{2\ (s)} \leftrightharpoons 2UO_2^{2+} + 2PO_4^{3-} + 2Na^+$ | -42.928 | 0.773 |
| Rutherfordine | $UO_2CO_{3(S)} \leftrightharpoons UO_2^{2+} + CO_3^{2-}$ | -16.700 | -4.178 |

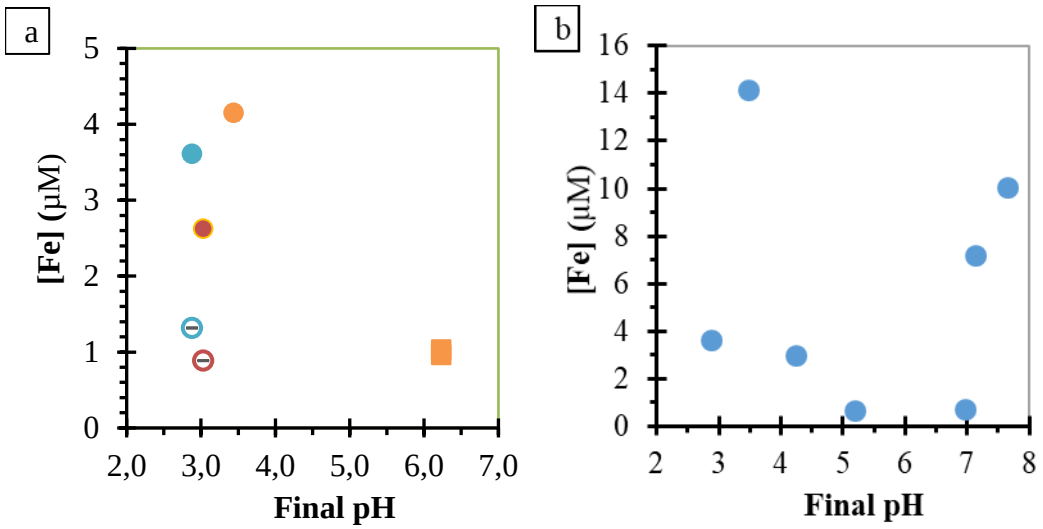


*Figure A1: Concentrations of Fe ions vs. pH of final experimental 0.005M NaCl solutions brought in contact with NaIdP at various clay-to–solution ratios -$R_{S/L}$ (1-3g·L$^{-1}$) (data in Table A4). Experimental conditions: initial pH2.65-7.4: (a) $R_{S/L}$:1-3 g·L$^{-1}$, $t_R$=3-7 days, plain-circle: 16nm cutoff, open-circle: 3ka cutoff (<3nm); (b) $R_{S/L}$:3g·L$^{-1}$, $t_R$=3 days, cutoff: 16nm. $R_{S/L}$ =●○: 0.5g·L$^{-1}$, ●■: 1·5g.L$^{-1}$, ●○: 3.0g·L$^{-1}$.*

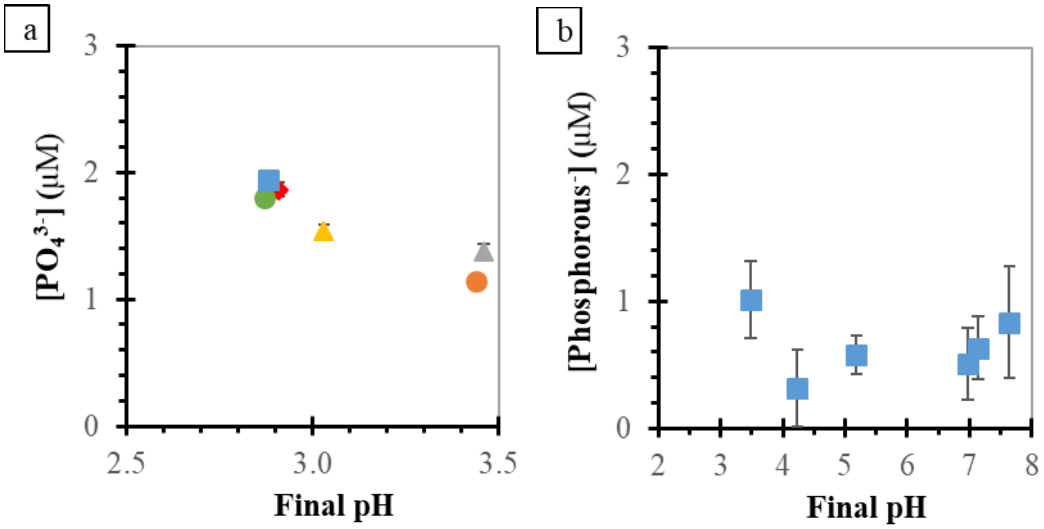


*Figure A2: Concentrations of (a) phosphate ions (Data in Table A5) and (b) phosphate ions vs. pH of final experimental 0.005M NaCl solutions brought in contact with NaIdP at various clay-to-solution ratios -$R_{S/L}$ (0.5-3g.L$^{-1}$). Experimental conditions: initial pH: 2.65-7.4, $t_R$: 3 days. $R_{S/L}$ =●: 0.5g·L$^{-1}$, ▲: 1.0g·L$^{-1}$, ▲: 1.5g·L$^{-1}$, ♦: 2.0g·L$^{-1}$, ●: 2.5g·L$^{-1}$, ■: 3.0g·L$^{-1}$.*

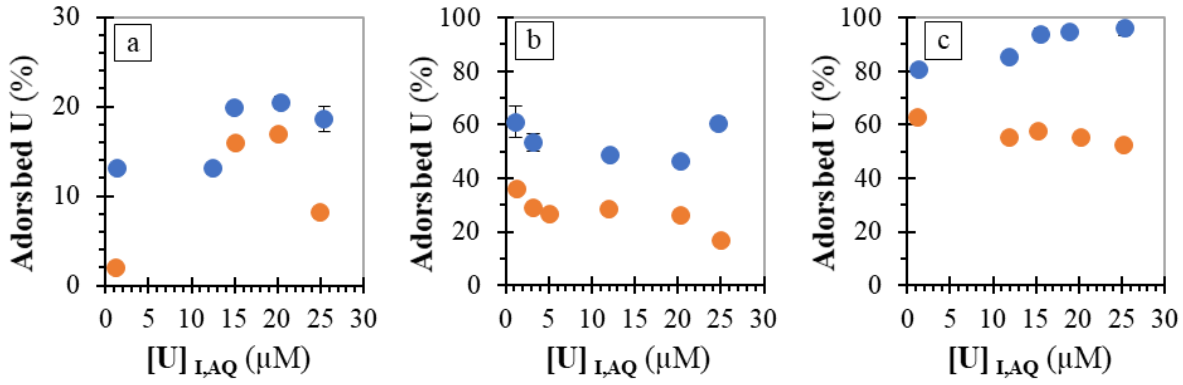


*Figure A3: Sorption isotherms of uranyl ions (% of total U sorbed) onto NaIdP, in the absence and in the presence of phosphate ligands (●: 0µM, ●: 100µM), for experiments conducted at pH: (a) 3.0, (b) 3.5 and (c) 4.1. Experimental conditions: reaction time, $t_R$, of 4 days; clay-to-solution ratio, $R_{S/L}$, of 3g/L, electrolyte solution: 0.005M NaCl electrolyte. Suspensions were pre-equilibrated with electrolyte for a duration ($t_{pre-equil}$) of 3 days prior to addition of the sorbates.*

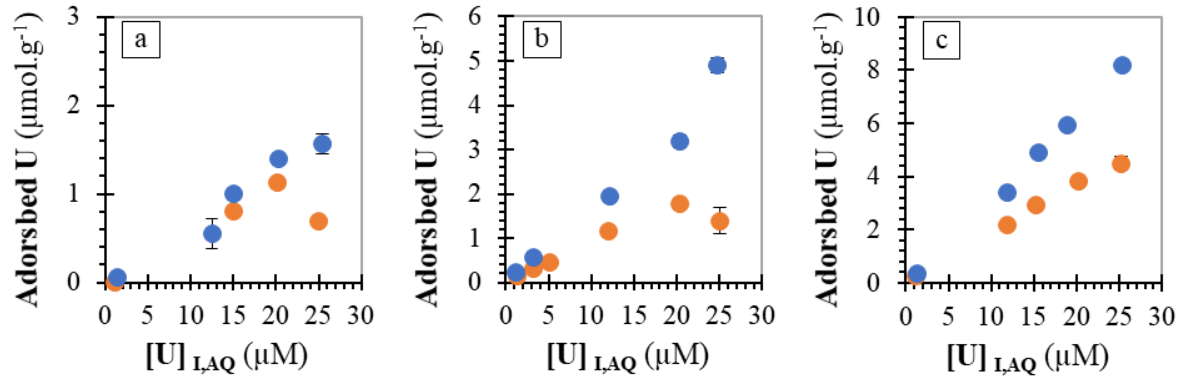


*Figure A4: Sorption isotherms of uranyl ions (in µmol.g$^{-1}$) on NaIdP, in the absence and in the presence of phosphate ligands (●: 0µM, ●: 100µM), for experiments conducted at pH: (a) 3.0, (b) 3.5 and (c) 4.1. Experimental conditions given in caption of Figure A3.*

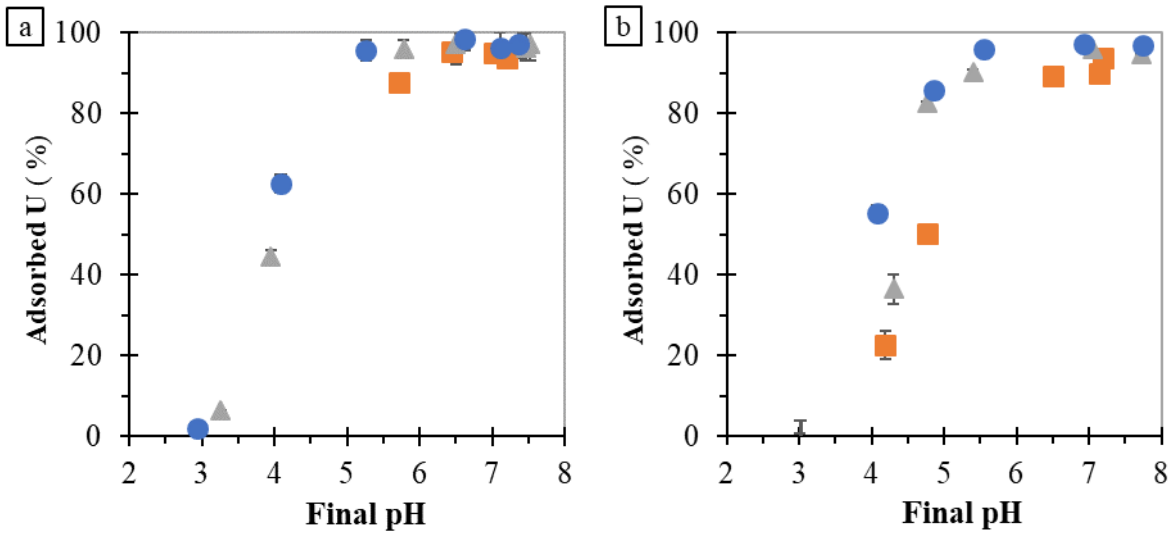


*Figure A5: Percentage of sorption of uranyl ions onto NaIdP as a function of pH (sorption edge) obtained from batch experiments conducted at different clay-to-solution ratios, $R_{S/L}$ (■: 1 g·L$^{1}$, ▲: 2 g·L$^{-1}$ et ●: 3g·L$^{-1}$) and at total U(VI) concentrations of: (a) 1 µM and (b) 12µM. Experimental conditions: reaction time, $t_R$, of 4 days; electrolyte solution: 0.005M NaCl electrolyte. Suspensions were pre-equilibrated with the electrolyte solution for a duration ($t_{preequil}$) of 3 days prior to addition of U.*

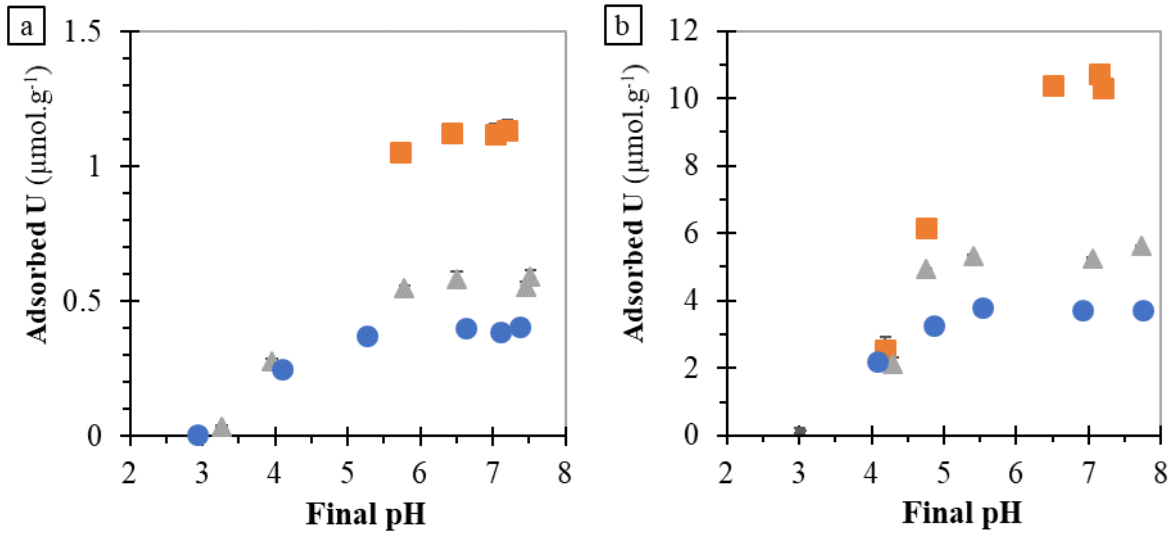


*Figure A6: Surface coverage of NaIdP by uranyl ions (in µmol.g-1) as a function of pH for batch experiments conducted at different clay-to-solution ratios RS/L (■: 1 g.L1, ▲: 2 g.L-1 et ●: 3g.L-1) and at total U(VI) concentrations of: (a) 1 µM and (b) 12µM. Experimental conditions are given in caption of Figure A3.*

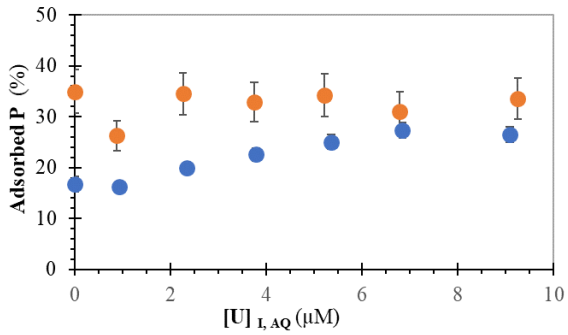


*Figure A7: Percentage of sorption of phosphate ions onto NaIdP as a function of total concentration of uranyl ions ($[U]_{I,aq}$) for U-P co-sorption experiments conducted at two total concentrations of P ($[P]_{I,aq}$ = 20µM (●) and 100µM (●)). Experimental conditions: $R_{S/L}$ = 3g·L$^{1}$, pH 3.5-4.0, reaction time, $t_R$ = 4 days; electrolyte solution: 0.005M NaCl; $t_{pre\text{-}equil}$ = 3 days).*

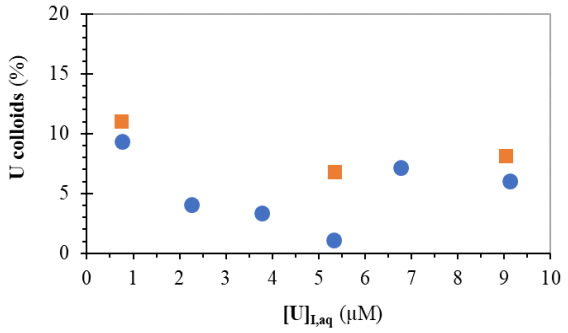


*Figure A8: Results of blank experiments (without NaIdP) on the formation of colloidal phases in solutions aged during 4 days at various total concentrations of U ($[U]_{I,aq}$), in the presence of 20 µM (■) and 100µM (●) of phosphate ions, at acidic pH (3.3-4.1). Electrolyte solution: 0.005M NaCl.*

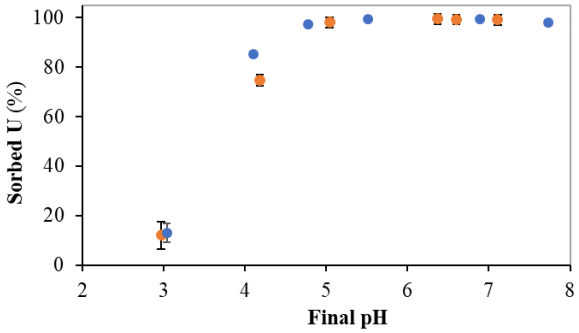


*Figure A9: Results on the macroscopic (co)sorption of (a) $UO_2^{2+}$ ions added simultaneously to $Fe^{3+}$ ions and phosphate ligands to a NaIdP – solution suspension, as a function of final pH ($pH_F$). Conditions (●): $[U]_{I,aq}$=12µM, $[Fe]_{I,aq}$=10µM and $[P]_{I,aq}$=100µM, 0.005M NaCl electrolyte solution at a $R_{S/L}$ equal to 3g·L$^{-1}$, $t_R$=4 days and $t_{pre\text{-}eq}$=3 days. Data of U sorption in the absence of Fe(III) (●)in the absence of U (○) are reported, too.*

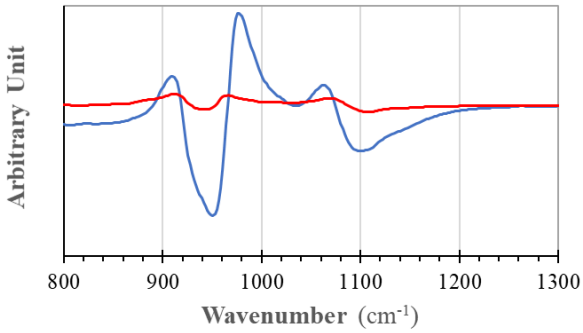


*Figure A10: Results of in situ ATR-FTIR experiments of the sorption of uranyl ions at NaIdP interface (conditions: pH 7.4, under $N_2$ atmosphere (red) and after 165h under 2.5% $CO_2$ (blue), $R_{S/L}$ =3g·L$^{-1}$, 0.005M NaCl electrolyte).*

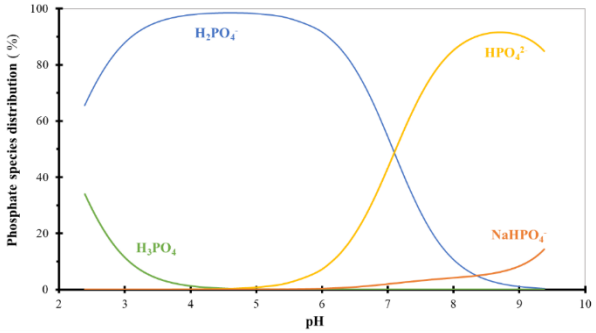


*Figure A11: Calculated distribution of aqueous phosphate species (in %) as a function of pH at $[P]_{l,aq}$: 100µM. Solution electrolyte: 0.005 M NaCl. Visual MINTEQ (Ver 3.1) code and the database are used for the calculation.*

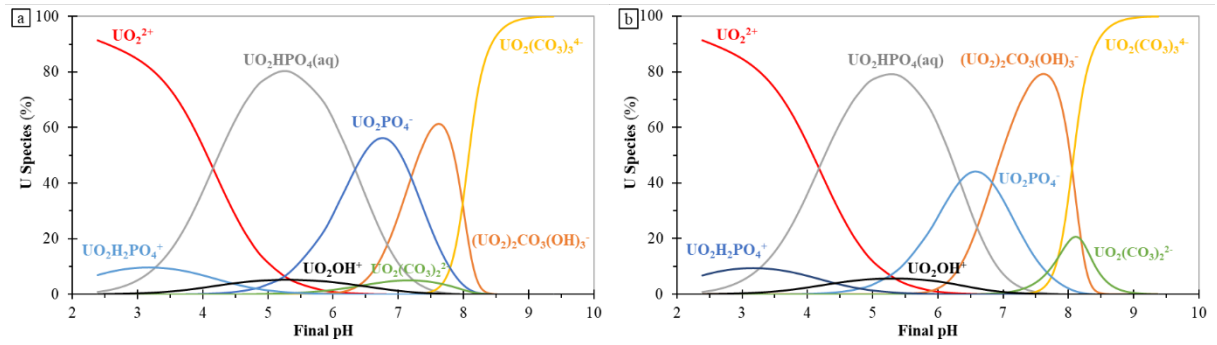


*Figure A12: Aqueous speciation of U(VI) (in %) as a function of pH, as calculated by using the Visual MINTEQ (Ver: 3.1) code and data base, for a total concentration of U(VI) of: (a) 2µM and (b) 10µM, in the presence of 100µM of phosphate ions. Electrolyte solution: 0.005M NaCl.*

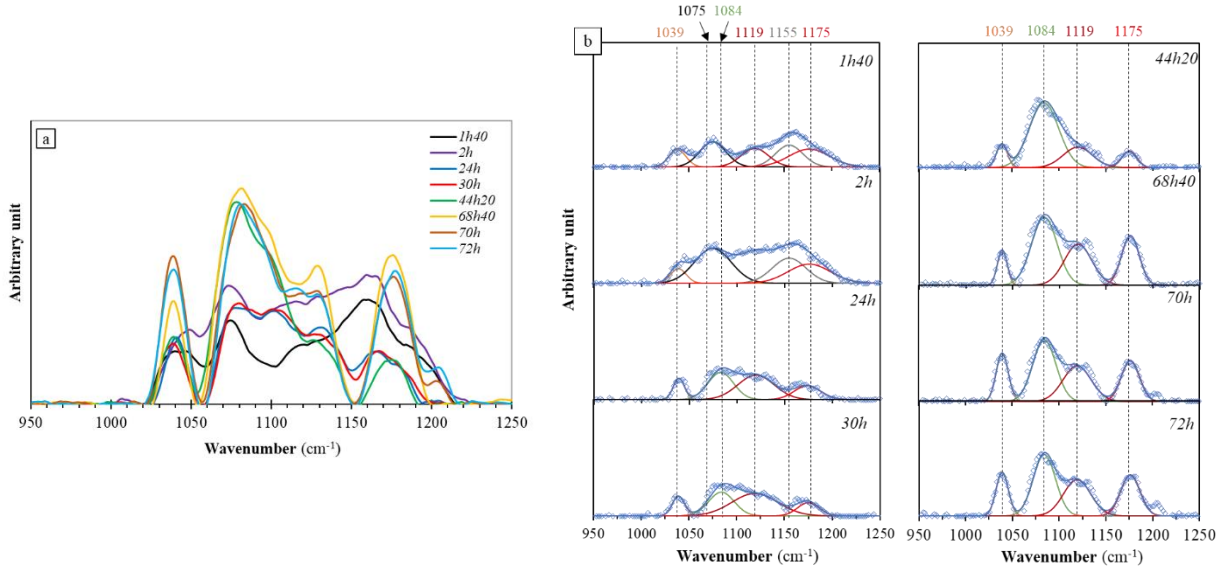


*Figure A13: (a) In-situ ATR-FTIR spectra of simultaneous presence of uranyl, iron, and phosphate ligands at the NaIdP – solution interface and (b) the result of spectral decomposition. The experiment was carried out at pH 4, a $t_R$ of 3 days and $[U]_{l,aq}$=10µm, $[Fe]_{l,aq}$=10µm and $[P]_{l,aq}$=100µm with an IS of 0.005M NaCl.*

# Appendix B. IR analysis in solution

## 1. IR spectra of phosphate solutions

IR spectra of phosphate species sorbed at the NaIdP–solution interface are compared to references such as IR spectra of phosphate species in aqueous solution (at pH 4-7, in an 0.005 M NaCl electrolyte solution) in order to: (i) detect a possible contribution of solution P species to IR signals of Illite–phosphate-solution interface, and (ii) to distinguish outer-sphere surface complexes of phosphate (OSSC) from ISSC of phosphate formed at the interface. *Figure B*a-d show the IR spectra collected for solutions at pH 4, 4.9, 6.2 and 7.0, respectively, in which the phosphate concentration was increased. Diprotonated phosphate ion ($H_2PO_4^-$, $C_{2v}$) is the predominant aqueous phosphate species at pH between 4 and 6.2 (*Figure A11 - Appendix A*) and presents fours bands (at 1160, 1075, 940 $cm^{-1}$ and 870 $cm^{-1}$) ascribed to $\upsilon_3$(P-O), $\upsilon_3$(P-O), $\upsilon_3$(P-OH) and $\upsilon_1$(P-OH) vibrations, with the first three bands corresponding to $u_3$ assignment and the last one to $u_1$ assignment [1,2]. These four bands could be observed in IR spectra recorded at high aqueous phosphate concentration ($[P]_{l,aq}$>1mM). In the range of $[P]_{l,aq}$ values investigated in this study, only the $u_3$(P-O) bands at 1160 and 1075 $cm^{-1}$ were observable, and the relative IR absorption band intensities increased with increasing $[P]_{l,aq}$. There was observed that peak's shape and absorption maxima of these two $u_3$ bands became better defined when increasing phosphate concentration. The detection limit for this aqueous species is thus estimated to be approximately of 45 µM in the pH range 4-6.2, a concentration at which IR band intensities are very close to background noise level. *Figure B*d shows the IR spectra collected as function of $[P]_{l,aq}$ at pH 7, a value close to the constant of deprotonation of $H_2PO_4^-$ (to $HPO_4^{2-}$). At this pH value, a mixture of di- and mono- protonated phosphate ions is expected to be present in the solution. Due to the low phosphate concentration used in this study, only the $\upsilon_3$(P-O) bands of $HPO_4^{2-}$ at 1077 is observable. It seems that the overlapping of $\upsilon_3$(P-O) bands of $H_2PO_4^-$ and $HPO_4^{2-}$ at 1077 $cm^{-1}$ decreases the detection limit to ca. 20 µM.

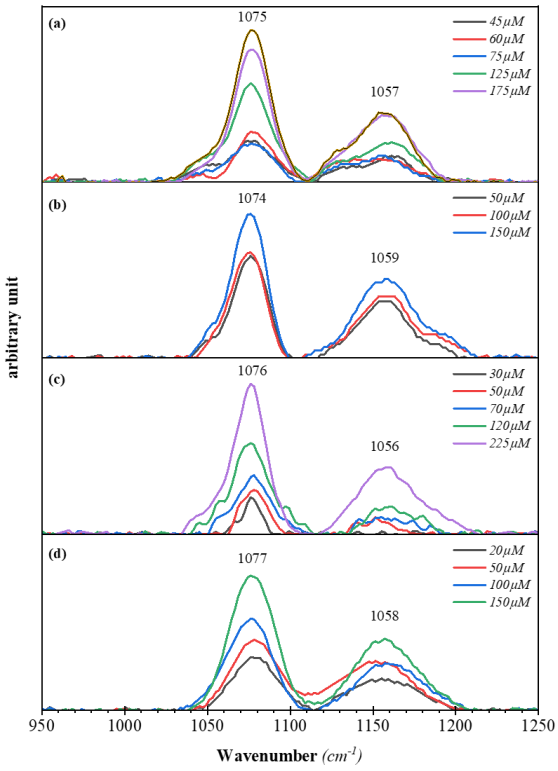


*Figure B14: ATR FTIR spectra of phosphate solutions at increasing $[P]_{l,aq}$ values and at pH of: (a) 4.0, (b) 4.9, (c) pH 6.22, and, (d) pH 7. Background electrolyte: 0.005 M NaCl.*

## 2. Reference IR spectra of uranyl phosphato solution species

Aqueous speciation of U(VI) in the presence of phosphate ligands ($[U]_{I,aq}$ = 2 µM and 10 µM; $[P]_{I,aq}$ = 100 µM), calculated by using the Visual MINTEQ code and data bases, are reported in appendix A (*Figs. A11-A12 and Table A6*). In the pH range 4-8, the major aqueous species are: $UO_2^{2+}$ (pH<4), $UO_2HPO_{4(aq)}$ (4<pH <6), $UO_2PO_4^-$ (6<pH<7) and $(UO_2)_2CO_3(OH)_3^-$ (7<pH<8). *Figure* 5a reports ATR FTIR spectra (in wavenumber region 900-1200$cm^{-1}$) collected during 3 hours for uranyl phosphate solutions at pH 4 ($[U]_{I,aq}$ = 8 µM, $[P]_{I,aq}$ = 100 µM). The spectra show the appearance of IR absorption bands whose intensities were increasing during the first two hours. Three bands were observable, with the most intense one being positioned at 996 $cm^{-1}$ and the others at 1122 and 924 $cm^{-1}$. It is to note that the absorbance of these bands is at least two orders of magnitude higher than that of vibrational bands recorded for the aqueous phosphate species $H_2PO_4^-$ (pH 4, $[P]_{I,aq}$: 100 µM, no U added, 0.005 M NaCl electrolyte solution). FTIR spectra of aqueous uranyl phosphate complexes and/or precipitate(s) forming at pH 4 and at a higher concentration of U ($[U]_{I,aq}$ = 8 µM) are shown in the *Figure* 5b. There was observed an increase in intensity of IR absorption bands during the first 2 hours. In addition to the three above-mentioned IR bands (at 996, 1122 and 924 $cm^{-1}$), two other weak vibrational bands were observable. Weak intensities of these bands made it difficult to determine precisely the position of their maxima (at ca. 1055 and 1170 $cm^{-1}$, respectively). These bands could possibly be ascribed to an aqueous U-P species whose $\upsilon_3$(P-O) bands are shifted compared to those reported (at 1160 and 1075 $cm^{-1}$) for the diprotonated phosphate ion ($H_2PO_4^-$, $C_{2v}$), which is the dominant aqueous phosphate species at pH 4. Maxima positions and relative intensities of the main bands (at 996 $cm^{-1}$, 1122 and 924 $cm^{-1}$) are consistent with previously published IR data by Čejka et al. [3] and Comarmond et al. [4] for uranyl phosphate complexes and/or of U(VI) phosphate minerals, which display almost similar IR features (cf. *Figure B14*). Formation of a U(VI)-phosphate phase is in agreement with calculations indicating that solution used in experiment (at $[U]_{I,aq}$ = 8 µM and $[P]_{I,aq}$ = 100 µM) was highly over-saturated with regard to a U(VI) phosphate mineral, namely $(UO_2)_3(PO_4)_{2(s)}$, and slightly oversaturated with respect to Na-autunite (*Table A8 – Appendix A*). Moreover, batch experiments conducted in the absence of clay indicated the formation of uranyl phosphate colloids (*Figure A8 – Appendix A*) at pH 4, which would represent ca. 5% of total U. Concerning IR spectra of aqueous uranyl ions in the absence of phosphate, no absorption bands were observable for $[U]_{I,aq}$ < 10 µM (data not shown).

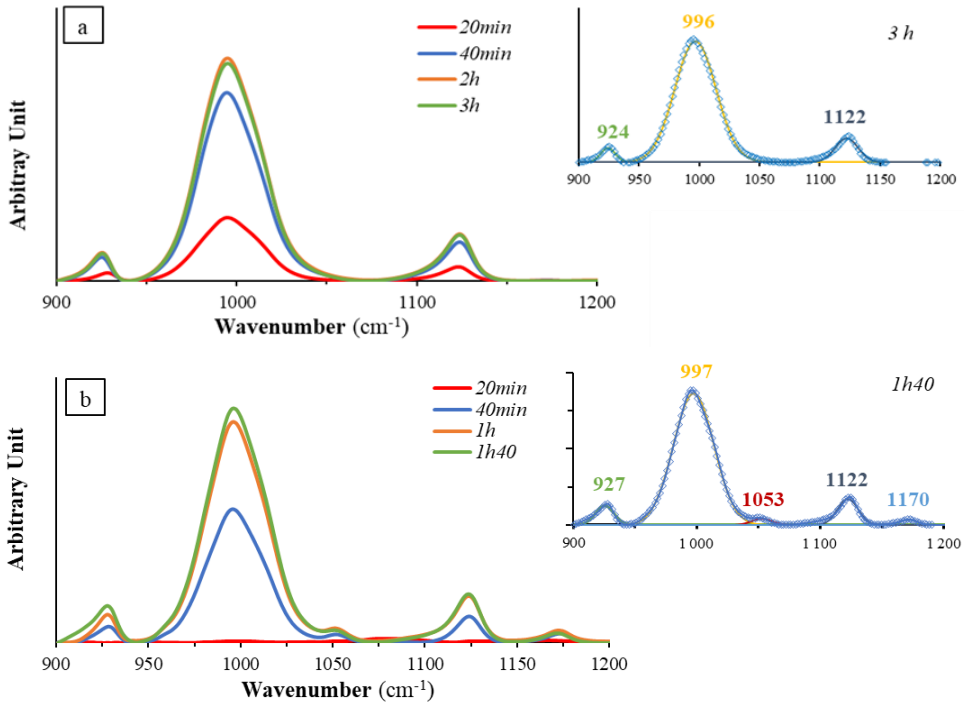


*Figure B15: ATR FTIR spectra of uranyl—phosphate solution species at different reaction time (tR) in a 0.005 M NaCl electrolyte solution at pH 4, at [P]I,aq = 100 µM and (a) [U]I,aq = 2 µM or (b) [U]I,aq = 8 µM (inserted : decomposition of IR spectra).*

### 3. IR spectra of aqueous solutions containing $PO_4^{3-}$ and $Fe^{3+}$ ions

Although the concentration of $Fe^{3+}$ ions released in aqueous solution was found to be low (<4µM) in our experiments of (Na)IdP-solution interactions, ATR FTIR analyses were conducted to determine the IR band positions of aqueous iron(III)–phosphate species. The analysis was expected to be helpful to detect the potential contribution of OSSC and ISSC of iron–phosphate (surface) species to IR signals of the NaIdP-phosphate-solution interface. *Figure B12*6 shows that four IR absorption bands at 1041, 1085, 1124 and 1149 $cm^{-1}$ were resolved upon decomposition of IR spectra of an aqueous solution containing $Fe^{3+}$ and $PO_4^{3-}$ ions. Based on the FTIR data given by Tejedor-Tejedor and Anderson [5], the bands at 1041, 1089 and 1149 $cm^{-1}$ could be attributed to $FeHPO_4^{+}$ aqueous complex, the main species dominating the speciation of Fe under the conditions investigated (and to additional contribution of $FeH_2PO_4^{2+}$, a minor species). The bands at 1043 and 1125 $cm^{-1}$ could relate to the $Fe_2PO_4^{3+}$ species [5]. $Fe_2(OH)PO_3^{2+}$ aqueous species is reported to display a set of bands at 1041,1085 and 1124 $cm^{-1}$ but it is not significantly formed at pH 4, according to speciation calculations.

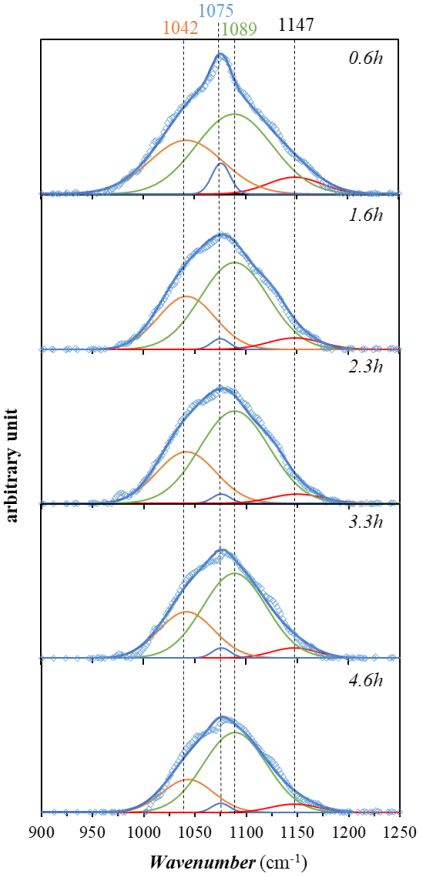


*Figure B126: ATR FTIR spectra of a solution at $[P]_{I,aq}$ of 100 µM and $[Fe]_{I,aq}$ of 10 µM and pH 4. Background electrolyte: 0.005 M NaCl, $t_R$: up to 4.6 hours. Circles: experimental curve; lines: results of spectrum decomposition.*

### 4. IR spectra of aqueous solutions containing $CO_3^{2-}$ and uranyl-carbonato species

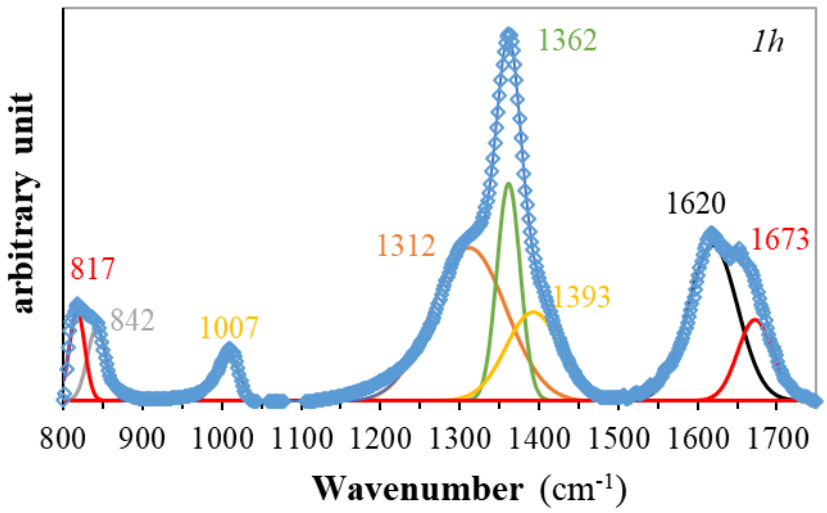


*Figure B17: Decomposition spectra of in situ ATR-FTIR experiments of the (co)sorption of carbonate and uranyl ions at 1h reaction time under $CO_2$ atmosphere (conditions: pH 8, [U]=10µM, [$CO_3^{2-}$]=100mM, , 0.005M NaCl electrolyte).*

**References**

[1] Y. Arai, D.L. Sparks, ATR–FTIR Spectroscopic Investigation on Phosphate Adsorption Mechanisms at the Ferrihydrite–Water Interface, Journal of Colloid and Interface Science. 241 (2001) 317–326. https://doi.org/10.1006/jcis.2001.7773.

[2] K. Nakamoto, Infrared and Raman Spectra of Inorganic and Coordination Compounds, Handbook of Vibrational Spectroscopy. (2006) 21.

[3] J. Čejka, A. Muck, To the infrared spectroscopy of natural uranyl phosphates, Phys Chem Minerals. 11 (1984) 172–177. https://doi.org/10.1007/BF00387848.

[4] M.J. Comarmond, R. Steudtner, M. Stockmann, K. Heim, K. Müller, V. Brendler, T.E. Payne, H. Foerstendorf, The Sorption Processes of U(VI) onto $SiO_2$ in the Presence of Phosphate: from Binary Surface Species to Precipitation, Environ. Sci. Technol. 50 (2016) 11610–11618. https://doi.org/10.1021/acs.est.6b02075.

[5] M.I. Tejedor-Tejedor, M.A. Anderson, The protonation of phosphate on the surface of goethite as studied by CIR-FTIR and electrophoretic mobility, Langmuir. 6 (1990) 602–611. https://doi.org/10.1021/la00093a015.

# 2. Europium Retention on intact Callovo-Oxfordian Clay Rock

Y. Hassan Loni, K. David, S. Ribet, C. Lerouge, C. Bailly, B. Grambow and G. Montavon*
*SUBATECH, Nantes, France*

P. Lach
*BRGM, Orléans, France*

B. Madé
*ANDRA, Châtenay-Malabry Cedex, France*

## Abstract

While $R_d$ values obtained from batch-type experiments with dispersed material are essential for the development of retention models, it is also important to generate retention data under more realistic conditions, in particular with intact samples. Specifically, the literature data on strongly retained radionuclides proves to be very scarce. The present study focuses on the retention of europium at trace concentrations on clay samples extracted from the Callovo-Oxfordian (COx) formation in France. $R_d$ values obtained with intact COx samples are assessed by a methodology coupling percolation experiments (in pressurized microcells), performed using submillimeter-sized samples in thickness, and Laser Ablation Inductively Coupled Plasma Mass Spectrometry measurements. The $R_d$ found at trace concentrations under non-transient conditions are high ($R_d > 10^4$ mL $g^{-1}$) and in agreement with those recorded under classical batch-type conditions or those deduced from the distribution of naturally-occurring Eu between the pore water and the clay rock. They can be described by modelling with existing sorption databases, considering an adsorption process only on the clay fraction. This was validated by solid state LA-ICP-MS analyses of one of the Eu-spiked COx samples; the added europium was found exclusively in the COx clay fraction.

## Introduction

"Safety analyses" generally consider adsorption processes leading to retardation of mass transfer. Scientifically, for clayey rocks, these $R_d$ values can be understood by cation exchange and surface complexation reaction describing the concentration of labile species in rapid equilibrium between a surface and a solution. Experiments are carried out in batch-type mode in a state where the solid is dispersed in large quantities of synthetic pore water for reasons of either duration or ease of experimental implementation. However, it is essential to ensure that the adsorption parameters obtained on dispersed materials are capable of describing adsorption processes on the intact rock/pore water systems.

A review (Miller and Wang, 2012) on the subject highlights various aspects that can lead to differences depending on the state of compactness of the sample (surface-water reactivity, accessibility of sorption sites, electrostatic considerations, double-layer overlapping, etc.).

In the ideal case, it would be possible to carry out batch-type retention experiments intact system, i.e. waiting until a non-transient state is reached when the radionuclide concentration in aqueous solution (in contact with the water-saturated porous system) and the radionuclide concentration in pore water are equal. Under these conditions, the concentrations of radionuclides both in pore water and retained on the solid surface can be measured, which serves to calculate the distribution coefficient describing the retention (Rd) value. However, achieving a non-transient state can take a long time due to the low permeability of the studied compact clay materials. This approach appears to be feasible for highly compact states with poorly or moderately retained radionuclides. A few number of studies can be found in the literature for: $I^-$ (Montavon et al., 2014), $Cs^+$ (André et al., 2009; Chen et al., 2014b; Oscarson, 1994; Van Loon et al., 2009), $Ni^{2+}$ (Montavon et al., 2020), and $Sr^{2+}$ (Van Loon et al., 2005). Overall, no clear evidence suggests that increasing clay compaction will lead to a fundamentally different uptake of radionuclides.

For strongly sorbed ions/radionuclides, like trivalent metal ions, retention data are often deduced from in-diffusion experiments, where information is derived from a transient state (Descostes et al., 2017; Glaus et al., 2020; Kasar et al., 2016; Wang et al., 2004). The information on metal retention is reliable provided species mobility has been adequately described since compaction potentially affects both diffusive mass transfer and retention. Therefore, it is fundamental to develop for strongly sorbed elements, in parallel with transport/diffusion experiments, a set of methodologies yielding retention data in a non-transient state, in order to assess the compaction effect on retention processes.

The objective of this work is to propose a non-transient method adapted to the retention study of strongly sorbed elements on intact clay rock samples. It combines the use of pressurized PEEK (Polyetheretherketone) micro cells, thereby limiting adsorption phenomena (Aertsens et al., 2003) and accommodating submillimeter-thick samples, with a percolation mode to accelerate transport so as to overcome the disadvantages of a long experimental duration by using diffusion cells (Montavon et al., 2020 ; Chen et al., 2014b). After the experiment, the strongly sorbed element is analysed quantitatively on the (inlet) surface and in depth of the compact sample by means of Laser Ablation Inductively Coupled Plasma Mass Spectrometry (LA-ICP-MS). This technique turns out to be essential in the present context (due to its high sensitivity and spatial resolution) to determining metal ion concentration in metal-spiked compact samples as well as to assessing its distribution among the various mineral phases present in the clay rock. The methodology adopted in this study is applied to the Eu/COx system. Europium retention values published in the literature are high and range from $5\times10^4$ to $10^5$ L $kg^{-1}$ for trace concentrations, thus reflecting a strong interaction with COx clay rock (ANDRA, 2005a; Descostes et al., 2017; Schott et al., 2012). Retention data obtained in the compact state are compared herein with data measured in the dispersed state and then discussed in light of both modeling results and a study of naturally-occurring Eu in COx clay rock.

## Materials and methods

Two types of experiments were performed as part of this study, namely: batch-type sorption experiments on crushed COx samples in a dispersed state, and percolation experiments with compact clay rock. All experiments were conducted at T = 22 ± 2°C in the presence of a synthetic pore water (SPW) whose simplified composition was based on geochemical modelling exercises on *in situ* samples (Vinsot et al., 2008; Gaucher et al., 2009): $[Na^+] = 4.6\times10^{-2}$ M, $[K^+] = 10^{-3}$ M, $[Ca^{2+}] = 7.4\times10^{-3}$ M, $[Mg^{2+}] = 6.7\times10^{-3}$ M, $[Sr^{2+}] = 2\times10^{-4}$ M, $[Cl^-] = 4.1\times10^{-2}$ M, $[SO_4^{2-}] = 1.6\times10^{-2}$ M, inorganic carbon = $4.5\times10^{-3}$ M (in equilibrium with calcite), and pH = 7.3. Inorganic carbon was controlled by use a $N_2/CO_2$ (1%) gas mixture ($P_{CO2} = 10^{-2}$ atm) either in a glove box (batch-type experiments) or by bubbling inlet solution (percolation experiments).

### COx samples

The COx samples used were obtained from the Meuse/Haute-Marne Underground Laboratory (depth: ≈ 500 m). They originated from boreholes drilled by Andra (French Radioactive Waste Management Agency). The mineralogical composition and proportions of the major phases have been extensively described in Gaucher et al. (2004), ANDRA (2005b) and Lerouge et al. (2011). This composition mainly consists of phyllosilicates (40-60 wt%, mainly illite and mixed layer illite/smectite, kaolinite and chlorite), carbonates (15-45 wt%, mainly calcite and dolomite), tectosilicates (10-40 wt%, mainly quartz and feldspars) and minority phases such as sulfides (0-3 wt%, mainly pyrite) and natural organic matter (0.5-1 wt%). For the measurement of natural Eu concentrations in the pore water of COx, seepage water from the Callovo-Oxfordian clay-rich rock was collected from borehole GIS1002 in Andra's Meuse/Haute-Marne underground research laboratory. This 16-m long horizontal borehole was drilled at a depth of 490 m in the clay-rich layer. The water sample analyzed was collected 10 years after the borehole began to produce water (Grangeon et al., 2015).

### Methodologies

Europium retention on COx was investigated by means of batch-type experiments as a function of Eu concentration at a fixed solid/liquid (S/L) ratio (0.5 g $L^{-1}$). The methodology applied for percolation

experiments involves injecting the element of interest (at a given concentration) under pressure through the intact clay rock saturated with synthetic pore water (in equilibrium with the phases present). Eu being a strongly retained element, the condition to obtain a non-transient state is difficult to achieve. For illustration purpose, Fig. 1 shows initial simulations that were carried out with literature data, i.e. a value of $R_d$ around $10^5$ L kg$^{-1}$ (ANDRA, 2005a; Descostes et al., 2017; Schott et al., 2012). It can be seen that the non-transient state is reached after about 6 years of experiments, even though the work is being carried out in advective mode with submillimeter-sized samples in thickness (Fig. 1).

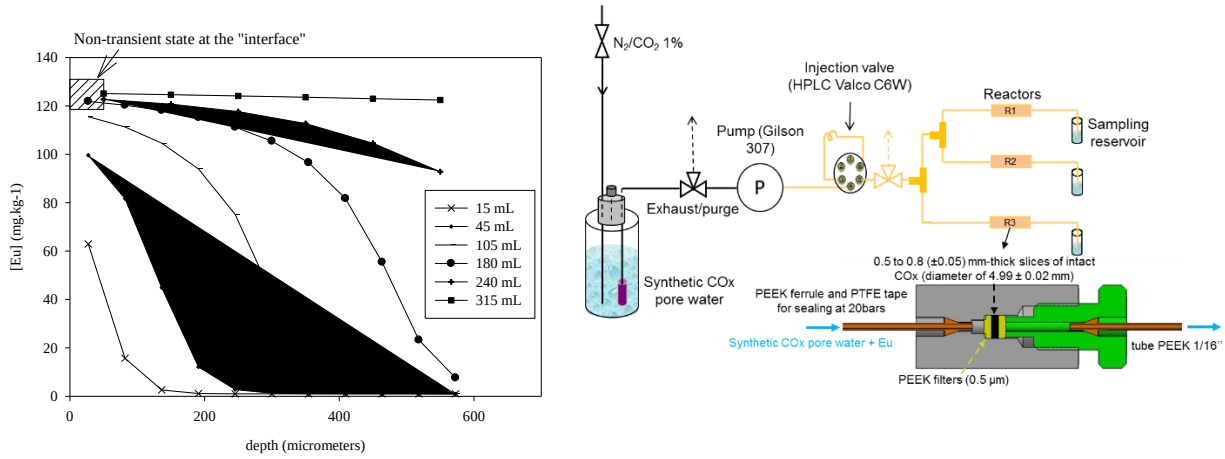


*Figure 1: left: Simulations of Eu profile evolution in a compact COx sample vs. depth for different percolation volumes (for roughly 6 years of experiment). Flow rate: 0.15 mL day$^{-1}$; sample thickness: 0.6 mm; $[Eu]_{injected}$=8.2×10$^{-8}$ M; Rd=7.8×10$^4$ L kg$^{-1}$. Right: The percolation experiment set-up.*

In order to limit the experimental time (i.e. a few months), the strategy adopted in our study sought a non-transient state at the inlet surface, or at least within the first few micrometers. By measuring Eu concentration at the surface by LA-ICP-MS ($[\mathrm{Eu}]_{\mathrm{clay,COx}}$, in mol per mass of COx) with a known Eu concentration in the injection loop ($[\mathrm{Eu}]_{\mathrm{injected}}$, in mol per volume of SPW) it is then be possible to calculate a Rd value:

$$\mathrm{Rd} = \frac{[\mathrm{Eu}]_{\mathrm{clay,COx}}}{[\mathrm{Eu}]_{\mathrm{injected}}} \quad (1)$$

The amount of spiked Eu in the COx was systematically corrected from the amount of Eu naturally present. The retention parameter obtained can subsequently be used as a fixed value in an attempt to reproduce the Eu “percolation depth profiles” using a reactive transport model.

Natural highly compacted intact samples of COx (diameter of 4.99 ± 0.02 mm, thickness: 0.5 - 0.8 ± 0.05 mm) were used. The sample preparation methodology was adapted from Montavon et al. (2020, 2014). The dry bulk densities of the pellets output ranged from 2.18 to 2.28 g cm$^{-3}$.

The percolation experiment set-up is presented in Figure 1. The reactors have been designed to ensure total system tightness and allow for total sample recovery once the experiment has been completed. The material used to make the reactors and the capillary tubes are made of PEEK in order to avoid or limit Eu adsorption phenomena (Molera and Eriksen, 2002). An assembly of three reactors R1, R2 and R3 connected in parallel was installed for the purpose of performing several experiments with just a single pump.

Once the samples had been inserted into the cells (between two PEEK filters), they were first hydrated and equilibrated with SPW. Sample hydration proceeded in stages, initially at low pressure (1 bar) for 3 days before pressure was gradually increased to 20 bar so as to determine the permeability and verify the

applicability of Darcy's Law. Average flows were 158 ± 10, 132 ± 7 and 101 ± 9 mg $d^{-1}$ for R1, R2 and R3, respectively. In order to maintain the pH and carbonate concentration of the SPW constant throughout the duration of the experiment, a bubbling with a $N_2/CO_2$ (1%) gas mixture was carried out for at least 15 min twice a week. SPW with Eu at (8.8 ± 0.9)×$10^{-8}$ mol $L^{-1}$ was injected into the percolation cell at a constant pressure of 20 bar. In order to avoid Eu adsorption on the pump head, the solution was injected via a 7.85 mL injection loop (made of PEEK).

Europium solution percolation through samples R1, R2 and R3 was stopped after 174, 365 and 694 days, respectively. The collected solution volumes were of 25, 49 and 58 mL for R1, R2 and R3, respectively. Compact COx samples extracted from R1 and R2 reactors were recovered and cut in half using a sterilized scalpel. The Eu "percolation depth profiles" were obtained by analysing the side of the pellet in depth (from the surface in contact with the input solution to the end of the pellet from which the solution was recovered). Each half-sample piece was fastened onto a thin petrographic plate with a double-sided adhesive disc for the Eu microanalysis of sample surface and depth profile by means of Laser Ablation Inductively Coupled Plasma Mass Spectrometry. For R1 and R2 samples, Eu concentrations were measured in relation to the mass of COx ablated. For R3, the analysis was concentrated on the clay fraction of the COx.

Further details can be found in (Loni et al., 2021).

### Reactive transport and sorption models

All calculations were carried out using the PhreeqC code (Version 3.3) (Parkhurst and Appelo, 2013) using the Davies Equation (Davies, 1964) to account for the ionic strength correction of solutes. Reactions occurring in the aqueous phase as well as saturation states with respect to solid phases were calculated using the thermodynamic database ThermoChimie v9b (Giffaut et al., 2014) (Grivé et al., 2015; https://www.thermochimie-tdb.com/) (Table A2).

The column hydrodynamic characteristics required for modelling (porosity, samples dimension,….), as well as the data used for describing Eu adsorption, can be found in (Loni et al., 2021). Peclet numbers were estimated in the range of 2 - 4 for compact COx samples, thus indicating the predominance of the advection mode over the diffusion mode for the percolation experiments.

## Results

### Batch-type experiments in the COx dispersed state

Figure 2 presents the sorption isotherm of Eu on COx as well as those published for the Eu/COx system by Descostes et al. (2017) under similar conditions. Europium sorption is constant at the lowest concentration, with $R_d$ values around (3.5 ± 0.5)×$10^4$ L $kg^{-1}$. These values are of the same order of magnitude as those given for similar experimental conditions by both García-Gutiérrez et al. (2009) (> 3.8×$10^4$ L $kg^{-1}$) and ANDRA (2005b) (≈ 5×$10^4$ L $kg^{-1}$) yet lower than that obtained by Descostes et al. (2017) (≈ 1×$10^5$ L $kg^{-1}$).

$R_d$ values then decrease to approx. $10^4$ L $kg^{-1}$ at the highest concentration studied (≈ 2×$10^{-7}$ mol $L^{-1}$ for aqueous Eu concentration). Under these conditions, our data are consistent with those of Descostes et al. (2017).

The simulation results are represented by the solid lines for the lower and upper clay fraction limits. Under the experimental conditions of this study, Eu speciation in solution is dominated by carbonate complexes. Carbonate ions also appear to be important in describing the adsorption of Eu. In this range, the model overestimates our retention data by about one order of magnitude. For the highest concentrations studied, i.e. the zone where the percolation experiments were carried out, the simulation and experimental results are consistent. Under these conditions, the contribution of weak sites to retention becomes significant (≈15%).

Given this study's objective, no further work has been carried out in search of an explanation for this discrepancies observed at the lowest Eu concentrations.

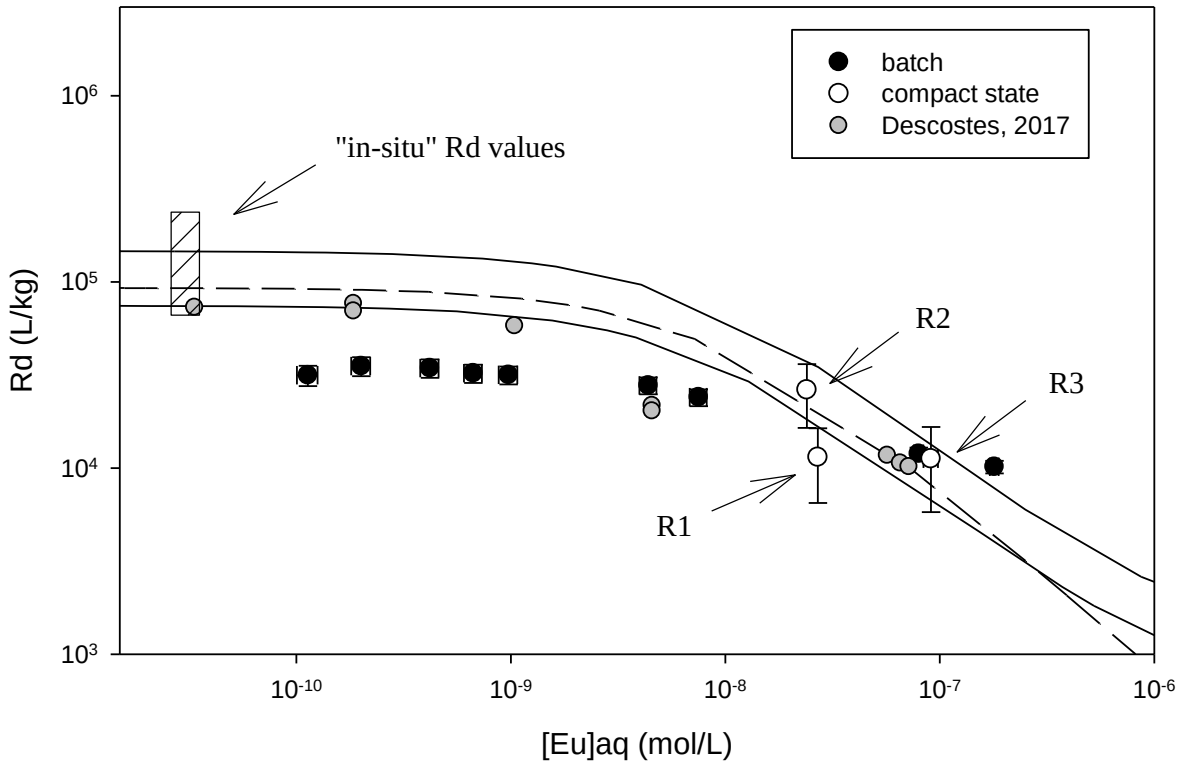


*Figure 2: Eu adsorption onto a COx sample in the presence of SPW and modelling results. (●) Batch-type experiments; (O) Percolation experiments in the compact state (R1, R2 and R3). (▲) Data from Descostes et al. (2017). Solid lines depict simulations performed for the lower and upper clay fraction limits. The dashed line represents the contribution of the two carbonate surface complexes (sOEu($CO_3$) and sOEuOH$CO_3^-$) to the overall retention for the mean COx clay fraction. Simulation details are given in (Loni et al., 2021).*

## Naturally-occurring Eu

Eu is present at trace levels in the clay formation, ~0.9 ± 0.2 µg $g^{-1}$. Europium is mainly present in the clay fraction (1.2 ± 0.5 µg per g of clay fraction) and contributes to about 70% of the inventory (0.9 µg per g of COx) if the average clay content found in the COx (≈ 50 wt%) is taken into account. For calcite (≈ 25 wt%), the average Eu concentration obtained (0.33 ± 0.15 µg per g of calcite) is less than that determined in the clay phase. The contribution of calcite to average Eu concentration in the COx has been estimated at roughly 10%. No Eu was detected in the pyrite phase (i.e. < DL = 0.001 µg·$g^{-1}$). These results indicate that the clay fraction is the main "reservoir" for Eu in the COx.

In assuming that the clay fraction controls adsorption (i.e. the starting hypothesis of the adsorption model), it is then possible to revert to $R_d$ values as long as the concentration of Eu in the pore water remains known. A value of (3.0 ± 0.4)×$10^{-11}$ mol $L^{-1}$ was experimentally measured by means of HR-ICP-MS for the GIS1002 borehole. With these concentrations in water and clay fraction, a range of $R_d$ values can be estimated from around $6.10^4$ to $2.10^5$ L $kg^{-1}$.

## Percolation experiments

For all samples, the linear relationship obtained between flow rate and pressure gradient validates the applicability of Darcy's Law under our experimental conditions. The measured permeability values varied between 3.3×$10^{-13}$ and 4.2×$10^{-13}$ m $s^{-1}$; these values are in good agreement with data for compact rock found in the literature (ANDRA, 2005b; Vinsot et al., 2008). The COx/SPW equilibrium was checked throughout the experiment; more specifically, the alkalinity and pH measured on aliquots at the reactor outlet showed values equivalent to those obtained for SPW, i.e. between 2.1 and 2.4 meq $L^{-1}$ and 7.2-7.4,

respectively. The Eu concentration at the outlet of all reactors remained very low and stable over time, with average values below $7\times10^{-11}$ mol·L$^{-1}$.

### Europium quantification at the surface of spiked samples (R1 and R2)

The analyses of Eu concentrations carried out on the surface at the inlet side of samples were performed for R1 and R2. The ablation depth by the laser beam was estimated at about 10 µm. The average Eu concentration at the surface of spiked samples equals 47 ± 19 and 95 ± 32 µg g$^{-1}$ for R1 and R2, respectively (n = 9).

During dismantling, a few drops of the aqueous solution in the immediate vicinity of the inlet surface were collected, under pressure, in order to measure the Eu concentration as close as possible to the sample surface. This analysis showed a decrease by a factor of about 3 with respect to the concentration of injected solution ($8.8\times10^{-8}$ mol L$^{-1}$ initially), i.e. between $2.4\times10^{-8}$ and $2.7\times10^{-8}$ mol L$^{-1}$. This decrease in concentration is not easily explained. Regardless of the reason (e.g. possible slight adsorption of Eu on the PEEK material of the capillary loop), the measured concentrations injected into the COx sample constitute the data required to revert to the $R_d$ values. Considering that a non-transient state was reached at the surface where pore water concentration corresponds to injected concentration, $R_d$ values of 11,500 ± 5,000 L kg$^{-1}$ and 26,300 ± 9,500 L kg$^{-1}$ were obtained for R1 and R2, respectively. Although a factor of close to two lies between the values, they do agree, within the limits of uncertainty, with the predicted range of Rd values, within which the adsorption data recorded in the dispersed state all lie (open symbols in Fig. 2).

### Eu localization at the surface of the spiked sample R3

Since no significant compaction effect was observed and given that the sorption model satisfactorily predicts the experimental retention data, Eu was expected to be adsorbed by the clay fraction. This outcome was assessed directly on the R3 sample. Note that for this reactor, unlike reactors 1 and 2, the Eu concentration measured at the reactor inlet (9.1±0.7 $10^{-8}$ mol L$^{-1}$) corresponded to the Eu concentration injected into the loop.

The areas rich in clay were previously identified by optical microscopy and several laser ablation lines were carried out. Note that the analysis of the major elements indeed confirms that the clay fraction has been appropriately targeted. As expected, the Eu concentration measured in the clay matrix of the Eu-spiked COx sample ($[Eu]_{clay,R3}$) is clearly higher than that for the natural COx ($[Eu]_{clay,COx}$), i.e. 311 ± 62 µg g$^{-1}$ vs. 1.2 ± 0.5 µg g$^{-1}$. In taking into account the percentage of clay in the COx ($P_{clay,COx}$), as well as the concentration of Eu injected into the compact system ($[Eu]_{injected}$), the molecular weight of Eu ($MM_{Eu}$) and the fact that a non-transient state has been reached at the "interface", an $R_d$ value can be calculated according to the following:

$$\mathrm{Rd} = 10^{-3}\,\frac{([\mathrm{Eu}]_{\mathrm{clay,R3}} - [\mathrm{Eu}]_{\mathrm{clay,COx}})\mathrm{P}_{\mathrm{clay,COx}}}{\mathrm{MM}_{\mathrm{Eu}}[\mathrm{Eu}]_{\mathrm{injected}}} \qquad (2)$$

The $R_d$ value obtained (11,200 ± 5,700 L kg$^{-1}$) also appears to be consistent with the retention data previously determined for reactors R1 and R2 and with the values measured in the dispersed state. These results are entirely consistent with the hypothesis that clay fraction governs Eu adsorption.

### Europium concentration along the spiked COx samples

In a final step, the Eu concentration was assessed along the samples as a function of depth for both the R1 and R2 reactors. The "percolation depth profiles" obtained are shown in Figure 3; let's note that although the profiles resemble one another, the data are rather scattered. As expected, Eu reaches its highest concentrations within the first few micrometers (< 50 µm) of the sample, even though migration was detected up to a depth of approx. 200 µm. From a depth of 200 µm and beyond, the geochemical background of Eu in COx is in fact being analysed, i.e. approx. 0.9 µg·g$^{-1}$.

The percolation profiles were then simulated by coupling the chemistry model applicable for the Eu concentrations investigated (solid lines in Figure 3) with an advective transport model. No adjustment was attempted, as this multi-parametric model lacking constraints does not output precise parameters. The simulation results (solid lines in the figure 3) are in good agreement with experience, provided the trends are well reproduced.

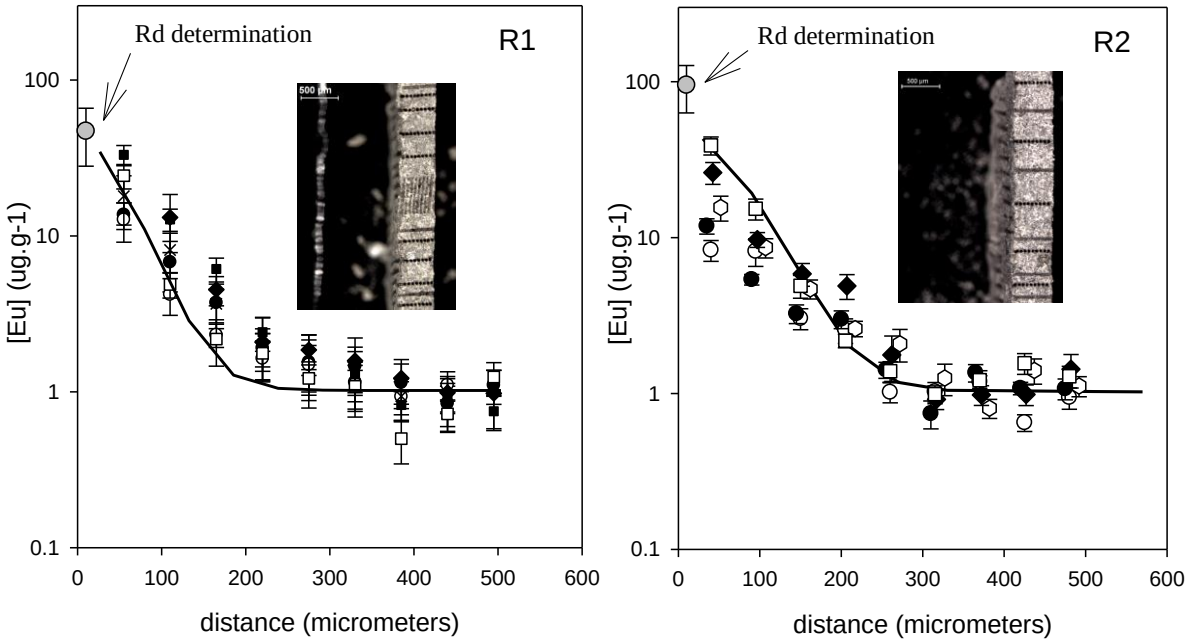


*Figure 3: Europium concentration along the COx sample for R1 (25 mL of percolated Eu-spiked SPW) and R2 (49 mL of percolated Eu-spiked SPW). The various series represent different laser ablation spot lines. The lines reflect simulations made with reactive transport model. The gray symbols correspond to the surface analysis (≈ 10 µm).*

## Discussion

With regard to the key question raised in this work, thanks to the proposed methodology, $R_d$ values could be derived to describe Eu adsorption on intact COx samples. The objective of this work has been to determine these values in a non-transient state, where the thermodynamic model can be directly applied without considering the transport part. This condition is anticipated at the sample surface after a certain contact time, when the pore water concentration corresponds to that of the injected solution (dashed zone in Figure 1).

The contact time required to reach this non-transient state at the COx pellet entry surface has not been evaluated experimentally, as this step would have required excessive experimental work given the difficulty of setting up these experiments. In this context, the simulation results prove to be quite important. As revealed by the simulations of traced concentration profiles through the sample (Figure 3), the agreement between experimental measurements and calculations is satisfactory, especially when considering that no parameters have been adjusted in the model. A more detailed examination indicates that the extrapolation of simulation curves up to the surface explored by laser ablation coincides with the measured Eu concentration values. Recall that these measured values are the origin of the experimental $R_d$ values, which themselves are accurately reproduced by the chemical model (Figure 1). It can thus be concluded that simulations confirm that the experimental time was sufficient to achieve the desired non-transient state at the interface for R1 and R2, as proposed in our strategy. Since the percolated volume is even greater for R3, the conditions are therefore logically applicable to this reactor as well.

Europium adsorption onto COx was shown to be strong ($Rd$ > $10^4$ L $kg^{-1}$) at trace concentrations. Furthermore, the three $R_d$ values obtained for the compact spiked COx samples are consistent, within the experimental uncertainties, with those deduced from conventional batch experiments carried out in dispersed state (black symbols in Figure 1). Similar results had already been obtained for intact COx with iodine (I) (Montavon et al., 2014), cesium (Cs) (Chen et al., 2014b) and nickel (Ni) (Montavon et al., 2020), thus suggesting that this trend seems *a priori* applicable to the retention of metal ions by COx clay rock. The result also appears to be consistent with the recent results of Glaus et al. (2020), derived from diffusion experiments vs. pH for an Eu/compacted illite system. They demonstrated that adsorption models are valid for describing the equilibrium distribution of Eu between aqueous solution and clay phase in the compacted state, provided an electrical double layer is considered to describe the behaviour of mobile species in the diffuse layer.

A combination of the various methods also leads to conclude that the clay fraction effectively governs Eu adsorption. This finding has been indirectly confirmed by modelling the data; in using a bottom-up approach along with the assumption that the clay fraction is responsible for element adsorption on COx, it was possible to explain experimental adsorption data in the conditions chosen for the percolation experiments, during which both strong and weak sites contribute to Eu adsorption. This finding was also validated by direct analysis on the compact Eu-spiked sample (R3); the additional Eu is derived quantitatively, within uncertainties, in the clay fraction. This result is in agreement with qualitative data already published by Menut et al. (2006) on Eu-spiked COx samples obtained from a diffusion experiment and Laser-Induced Breakdown Spectroscopy (LIBS) measurements.

The importance of the clay fraction in Eu retention also corroborates the results of the study conducted with naturally-occurring Eu. The clay fraction represents the main reservoir, with some 70% of the inventory of naturally-occurring Eu found at trace concentrations in the COx (≈ 0.9 mg $kg^{-1}$). Using this value and the natural pore water concentration of Eu, $R_d$ values ranging from $6.10^4$ to $2.10^5$ L $kg^{-1}$ are determined. The domain in $R_d$ values is consistent with predictive simulations yet lies beyond the values potentially extrapolated from adsorption data recorded at the trace scale (in dispersed state); the $R_d$ values over such a range are assumed to be constant (≈ $3.5\times10^4$ L $kg^{-1}$). However, adsorption is not the only process leading to metal retention and one shall recall that the total content of Eu in the clay rock is larger than the fraction bound to the clay phases. On the other hand, only a fraction of the retained Eu is labile and has to be taken into account for the evaluation of the $R_d$ to be compared with the laboratory retention experiments. Other processes leading to non-labile species, such as incorporation of metals into matrices, are likely to occur, in particular for the long times characteristic of sedimentary rocks (e.g. COx) (McKinley and Alexander, 1993). This outcome was recently shown for the Ni/COx system (Montavon et al., 2020), whereby only ≈ 13% of the Ni found in the rock appeared to be labile/adsorbed (and only 24% of Ni found in the clay fraction). The proposed *in situ* range of $R_d$ values (≈ $6.10^4$ to $2.10^5$ L $kg^{-1}$) therefore represents an upper limit, which cannot be simply compared to $R_d$ values measured in the laboratory over short time periods. On the other hand, the deviation between prediction and experiment for equilibrium Eu concentrations below ≈ $10^{-8}$ mol $L^{-1}$ still needs to be elucidated.

## Acknowledgments

The authors would like to thank Andra (GL CTEC), contributors to the "Chaire stockage" unit (EDF, ORANO and Andra).

## References

Aertsens, M., De Cannière, P., Moors, H., 2003. Modelling of silica diffusion experiments with 32 Si in Boom Clay, in: Journal of Contaminant Hydrology. Elsevier, pp. 117–129.

ANDRA, 2005a. Évolution Phénoménologique Du Stockage Géologique. https://www.andra.fr/cigeo/les-documents-de-reference#section-967.

ANDRA, 2005b. Dossier 2005 Argile: Tome Architecture et gestion du stockage géologique.

André, M., Malmström, M.E., Neretnieks, I., 2009. Determination of sorption properties of intact rock samples: New methods based on electromigration. J. Contam. Hydrol. 103, 71–81.

Chen, Z., Montavon, G., Guo, Z., Wang, X., Razafindratsima, S., Robinet, J.C., Landesman, C., 2014a. Approaches to surface complexation modeling of Ni(II) on Callovo-Oxfordian clayrock. Appl. Clay Sci. 101, 369–380.

Chen, Z., Montavon, G., Ribet, S., Guo, Z., Robinet, J.C., David, K., Tournassat, C., Grambow, B., Landesman, C., 2014b. Key factors to understand in-situ behavior of Cs in Callovo-Oxfordian clay-rock (France). Chem. Geol. 387, 47–58.

Davies, C.W., 1964. Ion association. J. Electrochem. Soc. 111, 85C.

Descostes, M., Pointeau, I., Radwan, J., Poonoosamy, J., Lacour, J.L., Menut, D., Vercouter, T., Dagnelie, R.V.H., 2017. Adsorption and retarded diffusion of EuIII-EDTA− through hard clay rock. J. Hydrol. 544, 125–132.

García-Gutiérrez, M., Alonso, U., Missana, T., Cormenzana, J.., Mingarro, M., Morejón, J., Gil, P., 2009. Diffusion Experiments with Opalinus and Callovo-Oxfordian Clays: Laboratory, Large-Scale Experiments and Microscale Analysis by RBS. MADRID, ESPAÑA.

Gaucher, E., Robelin, C., Matray, J.M., Négrel, G., Gros, Y., Heitz, J.F., Vinsot, A., Rebours, H., Cassagnabère, A., Bouchet, A., 2004. ANDRA underground research laboratory: Interpretation of the mineralogical and geochemical data acquired in the Callovian-Oxfordian formation by investigative drilling. Phys. Chem. Earth 29, 55–77.

Gaucher, E.C., Tournassat, C., Pearson, F.J., Blanc, P., Crouzet, C., Lerouge, C., Altmann, S., 2009. A robust model for pore-water chemistry of clayrock. Geochim. Cosmochim. Acta 73, 6470–6487.

Giffaut, E., Grivé, M., Blanc, P., Vieillard, P., Colàs, E., Gailhanou, H., Gaboreau, S., Marty, N., Madé, B., Duro, L., 2014. Andra thermodynamic database for performance assessment: ThermoChimie. Appl. Geochemistry 49, 225–236.

Glaus, M.A., Frick, S., Van Loon, L.R., 2020. A coherent approach for cation surface diffusion in clay minerals and cation sorption models: Diffusion of Cs+ and Eu3+ in compacted illite as case examples. Geochim. Cosmochim. Acta 274, 79–96.

Grangeon, S., Vinsot, A., Tournassat, C., Lerouge, C., Giffaut, E., Heck, S., Groschopf, N., Denecke, M.A., Wechner, S., Schäfer, T., 2015. The influence of natural trace element distribution on the mobility of radionuclides. The exemple of nickel in a clay-rock. Appl. Geochemistry 52, 155–173.

Grivé, M., Duro, L., Colàs, E., Giffaut, E., 2015. Thermodynamic data selection applied to radionuclides and chemotoxic elements: An overview of the ThermoChimie-TDB. Appl. Geochemistry 55, 85–94.

Lerouge, C., Grangeon, S., Gaucher, E.C., Tournassat, C., Agrinier, P., Guerrot, C., Widory, D., Fléhoc, C., Wille, G., Ramboz, C., Vinsot, A., Buschaert, S., 2011. Mineralogical and isotopic record of biotic and abiotic diagenesis of the Callovian-Oxfordian clayey formation of Bure (France). Geochim. Cosmochim. Acta 75, 2633–2663.

Loni, Y.H., David, K., Ribet, S., Lach, P., Lerouge, C., Made, B., Bailly, C., Grambow, B. and Montavon, G. (2021) Investigation of europium retention on Callovo-Oxfordian clay rock (France) by laser ablation inductively coupled plasma mass spectrometry (LA-ICP-MS) and percolation experiments in microcells. Applied Clay Science 214.

McKinley, I.G., Alexander, W.R., 1993. Assessment of radionuclide retardation: realistic application of natural analogue studies. J. Contam. Hydrol. 13, 249–259.

Menut, D., Descostes, M., Meier, P., Radwan, J., Patrick, M., Poinssot, C., 2006. Europium migration in Argilaceous Rocks : on the use of Micro Laser-Induced Breakdown Spectroscopy (micro LIBS) as a Microanalysis Tool. Mater. Res. Soc. 932, 3–9.

Miller, A.W., Wang, Y., 2012. Radionuclide interaction with clays in dilute and heavily compacted systems: A critical review. Environ. Sci. Technol. 46, 1981–1984.

Molera, M., Eriksen, T., 2002. Diffusion of 22Na+, 85Sr2+, 134Cs+ and 57Co2+ in bentonite clay compacted to different densities: Experiments and modeling. Radiochim. Acta 90, 753–760.

Montavon, G., Lerouge, C., David, K., Ribet, S., Hassan-Loni, Y., Leferrec, M., Bailly, C., Robinet, J.-C., Grambow, B., 2020. Nickel Retention on Callovo-Oxfordian Clay: Applicability of Existing Adsorption Models for Dilute Systems to Real Compact Rock. Environ. Sci. Technol.

Montavon, G., Sabatié-Gogova, A., Ribet, S., Bailly, C., Bessaguet, N., Durce, D., Giffaut, E., Landesman, C., Grambow, B., 2014. Retention of iodide by the Callovo-Oxfordian formation: An experimental study. Appl. Clay Sci. 87, 142–149.

Oscarson, D.W., 1994. Surface diffusion: Is it an important transport mechanism in compacted clays? Clays Clay Miner. 42, 534–543.

Parkhurst, D.L., Appelo, C.A.J., 2013. Description of input and examples for PHREEQC version 3: a computer program for speciation, batch-reaction, one-dimensional transport, and inverse geochemical calculations, Techniques and Methods. Reston, VA.

Schott, J., Acker, M., Barkleit, A., Brendler, V., Taut, S., Bernhard, G., 2012. The influence of temperature and small organic ligands on the sorption of Eu(III) on Opalinus Clay. Radiochim. Acta 100, 315–324.

Van Loon, L.R., Baeyens, B., Bradbury, M.H., 2009. The sorption behaviour of caesium on Opalinus Clay: A comparison between intact and crushed material. Appl. Geochemistry 24, 999–1004.

Van Loon, L.R., Baeyens, B., Bradbury, M.H., 2005. Diffusion and retention of sodium and strontium in Opalinus clay: Comparison of sorption data from diffusion and batch sorption measurements, and geochemical calculations. Appl. Geochemistry 20, 2351–2363.

Van Loon, L.R., Glaus, M.A., 2008. Mechanical compaction of smectite clays increases ion exchange selectivity for cesium. Environ. Sci. Technol. 42, 1600–1604.

Vinsot, A., Mettler, S., Wechner, S., 2008. In situ characterization of the Callovo-Oxfordian pore water composition. Phys. Chem. Earth 33.

Wang, X., Chen, Y., Wu, Y., 2004. Diffusion of Eu(III) in compacted bentonite - Effect of pH, solution concentration and humic acid. Appl. Radiat. Isot. 60, 963–969.

# 3. Uranium retention in a Callovo-Oxfordian clay rock formation: From laboratory-based models to *in natura* conditions

G. Montavon, S. Ribet, Y. Hassan Loni, F. Maia, C. Bailly, K. David and B. Grambow
*SUBATECH, Nantes, France*

C. Lerouge
*BRGM, Orléans, France*

B. Madé, J.C. Robinet
*ANDRA,Châtenay-Malabry, France*

## Abstract

For the performance assessment of radioactive waste disposal, it is critical to predict the mobility of radionuclides in the geological barrier hosting the repository. A key challenge is to assess the transferability of current knowledge on the retention properties deduced from model systems to *in natura* situations. The case of the redox-sensitive element uranium in the Callovo-Oxfordian clay formation (COx) is presented herein. The "bottom-up" approach implemented, with illite and montmorillonite as reactive phases, quantitatively explains the adsorption results of U(VI) and U(IV) on COx. While retention is high for U(IV) ($R_d$~$10^4$ L·kg$^{-1}$), it is very low for U(VI) ($R_d$~4 L·kg$^{-1}$) due to the formation of soluble ternary Ca(Mg)-U(VI)-carbonate complexes. The applicability of the sorption model was then assessed by comparing predictive analyses with data characterizing the behaviour of naturally-occurring U (<3 mg·kg$^{-1}$). The clay minerals represent the largest reservoir of naturally-occurring U in COx (~65%) but only a small fraction appears to be adsorbed (~1 %). In this study we have conclude that under representative site specific in situ conditions (especially with respect to redox state of in the natural COx), that ternary U(VI) complexes control U speciation in solution while U(IV) surface species dominate U adsorption, with $R_d$ values > 70 L·kg$^{-1}$.

## Introduction

Several countries are investigating claystone formations (e.g. Opalinus claystone (OPA) in Switzerland, Boda claystone (BODA) in Hungary, Boom clay (BC) in Belgium and Callovo-Oxfordian claystone (COx) in France). The COx formation is located in the eastern part of the Paris Basin (depth: ~400-600 m, thickness: ~120-150 m) and is characterized by low permeability, mineralogical homogeneity and a low variation in other physicochemical properties over a large expanse (ANDRA, 2005).

Uranium and its decay series nuclides are a significant component of radioactive waste. Up to date, just a single study has been devoted to U(VI) retention on COx (Hartmann et al., 2008). These authors showed the importance of ternary complexes in describing the data, but their model was unable to satisfactorily reproduce the experimental results. Furthermore, all studies on claystones (COx, BODA or OPA) focus on the retention of U(VI) (Amayri et al., 2016; Bradbury and Baeyens, 2011; Hartmann et al., 2008; Joseph et al., 2011; Kautenburger et al., 2019; Marques Fernandes et al., 2015), although to the best of our knowledge no experimental data on U(IV) actually exist. Along the same lines, only the U(VI) retention model has been taken into account to simulate the diffusion of U in the OPA formation (Hennig et al., 2020). Given the highly reducing environment of deep formation, a major role played by the tetravalent state of U on uranium retention cannot be excluded.

Given the limited number of published articles, lack of data (notably with respect to U(IV)) and importance of the topic, the objective of this work is to promote a better understanding of uranium retention in the Callovo-Oxfordian formation. The term retention, as used herein, means the adsorption of U on the clay fraction governed by kinetically fast and reversible adsorption processes (ion-exchange, surface complexation) (OECD Nuclear Energy Agency, 2002). Throughout this paper, the term “labile fraction” will

be used in order to characterize the adsorbed U fraction in “equilibrium” with the water-soluble part over a short time scale, whereby the formation can be described by local equilibrium approaches.

We recently published an adsorption model allowing to explain the adsorption of U(VI) and U(VI) on COx (Montavon et al., 2022). The available 2-Site Protolysis, Non-Electrostatic Surface Complexation and Cation Exchange model (2 SPNE SC/CE), proposed by Bradbury and Baeyens (1997) and developed for OPA, was used as a basis. This model makes it possible to predict the adsorption properties of uranium under *in natura* COx conditions by pursuing the "bottom-up" approach with very good knowledge of the COx environment (Gaucher et al., 2009; Lerouge et al., 2011).

Inspired by previous work focusing on uranium-contaminated areas (Curtis et al., 2004; Kohler et al., 2004; Payne et al., 2001), these predictions are compared in this wok with results describing the behaviour of uranium naturally present in the formation at trace concentrations. In addition to the analysis of U distribution in the various COx reservoirs, emphasis has been placed on the labile part of this element, i.e. a fraction which is difficult to characterize at trace concentrations, when spectroscopic tools are not applicable (McKinley and Alexander, 1993). This fraction is needed in order to compare the data with results obtained in the laboratory; it has been estimated by means of sequential extraction (Claret et al., 2010), isotope exchange (Ahmed, 2014) and by following a desorption method successfully tested on the Ni/COx system (Montavon et al., 2020).

In sum, the challenge of this work lies in linking the model system to the natural system and drawing a conclusion on the degree to which uranium remains mobile in the COx formation; the steps involved must identify which physicochemical parameters control uranium mobility from a mechanistic point of view.

## Experimental details

### COx samples

All COx samples used in the present study are core samples from boreholes within the studied area (Meuse/Haute-Marne, France). The claystone consists (in percentage by weight) of a major clay fraction (40-60%), associated with both quartz (25-37%) and carbonate (12-32%) fractions. The clay minerals are mainly illite (ILL) (14-29%) and ordered illite-smectite mixed layers (IS) (18-33%), with minor kaolinite and chlorite contents (Lerouge et al., 2011).

The sample labelled EST25687(ox) corresponds to a portion of the previously preserved EST25687 sample analysed in 2006 and not preserved since then. Analyses conducted on both oxidized and non-oxidized samples allow assessing the potential presence of reduced forms of uranium.

Water samples from three drillings, cored with inert gases ($N_2$ or Ar), were analysed in order to define the representative U concentration values in the pore water of the Callovo-Oxfordian (PAC1002, POX1201, EPT1201) (Vinsot et al., 2013). Data were also collected from GIS1002 (Grangeon et al., 2015); although initially drilled under unpreserved conditions, a state of return to *in natura* equilibrium can now be observed. The effect of an oxidative disturbance on the U pore water concentration has been evaluated from borehole KEY1001 (Grangeon et al., 2015).

Synthetic pore water (SPW) representative of the COx formation, and in equilibrium with calcite, was prepared under controlled anoxic Ar/$CO_2$ conditions ($P_{CO2} = 10^{-2}$ atm or 1%) for evaluating the labile part of naturally-occurring U.

### Batch-type experiments

Desorption (Montavon et al., 2020), isotopic exchange (Ahmed, 2014) and sequential extraction (Claret et al., 2010) experiments were performed at room temperature (T = 22° ± 3°C) in polypropylene copolymer (PPCO) tubes either inside or outside the glove box, depending on the desired atmosphere.

For the desorption experiments, if U in the aqueous phase is controlled by an adsorption equilibrium and given the assumption that the Rd model is applicable, the following relation is obtained for correlating the U concentration in the aqueous solution (in $\mu g \cdot L^{-1}$) with the solid-to-liquid ratio m/V (in $g \cdot L^{-1}$):

$$[U]_{aq} = \frac{n.\frac{m}{V}+[U]_i}{\left(1+Rd.\frac{m}{V}\right)} \quad (1)$$

where $[U]_i$ represents the potential contamination of U initially present in SPW (in $\mu g \cdot L^{-1}$), and *n* the quantity of mobilizable element ($\mu g \cdot g^{-1}$), i.e. the labile quantity associated with COx plus the quantity initially present in pore water and present on the raw solid (in $\mu g \cdot g^{-1}$). The Rd unit of measurement used in this expression is $L \cdot g^{-1}$.

The sequential extraction steps lead to Fraction 1 (F1 - water soluble fraction), Fraction 2 (F2 – part of the adsorbed fraction), Fraction 3 (F3 – part of the adsorbed fraction and U present in carbonate phases), Fraction 4 (F4 - organic matter fraction) and Fraction 5 (F5 - residual fraction):

Further details can be found in (Montavon et al., 2022).

## Results

Based on literature data (Chen et al., 2014; Grangeon et al., 2015; Montavon et al., 2020; Tournassat et al., 2009), it has been assumed that the COx clay fraction controls uranium adsorption. The adsorption mechanism, including both surface complexation and cation exchange, leads to the formation of so-called "labile" chemical forms, i.e. in rapid equilibrium with the fraction in solution. Other retention mechanisms such as incorporation or co-precipitation, which generally lead to so-called "inert" forms, were therefore neglected in our approach. The experimental and simulation approaches were oriented along these lines. The relevance of these assumptions, in particular when linking the model system to the natural system, will be addressed in “Discussion” sections.

### Distribution of naturally-occurring U in COx

In the COx formation, uranium contents are low, i.e. between 0.5 and 2.4 $mg \cdot kg^{-1}$ (Figure 1a). Among the various samples whose U amount has been analysed, a distinct correlation exists with the organic matter: the higher the organic matter (OM) concentration, the greater the amount of U (Figure 1a). For the samples used in laboratory studies, the upper concentration limit is reached, i.e. between 2 and 3 $mg \cdot kg^{-1}$.

Among the various phases, uranium is expected to be incorporated in minor phases, e.g. phosphates (Regenspurg et al., 2010). Calcite might be another possible reservoir due to its high reactivity and ability to trap metals (Zhao and Zheng, 2014). These minerals were therefore singled out in the present study, which also considered organic matter (in relation to the correlation presented above) as well as the clay fraction, given its predominant role in the metal adsorption process.

The analyses of individual mineral phases carried out on sample EST51769 yielded U concentration values of 2.7 ± 0.8, 1.0 ± 0.3 and 0.013 ± 0.004 $mg \cdot kg^{-1}$ for clay, calcite and pyrite fractions, respectively. Four calcium phosphate analyses (EST26536) were performed in line mode and the average uranium content measured to be 32 ± 4 $mg \cdot kg^{-1}$. Lastly, the uranium concentration measured in organic matter led to a U content of 69.2 $\mu g \cdot kg^{-1}$.

Considering the average composition of COx in the clay-rich zone and the U concentration measured for EST51769 (whose main values were obtained), the distribution diagram shown in Figure 1c is derived (due to the low levels measured, U concentrations in pyrite and organic matter are not reported).

The U concentration of the bulk rock (called total (ind.) in Figure 1c), as recalculated from the U concentrations measured in the various phases and their proportion in the COx, corresponds (within the range of uncertainties) to the U concentration measured directly in the bulk rock (called total in Figure 1c). This finding indicates that the major carrier phases have been identified. While the highest U concentrations were found in phosphate minerals, as expected, the clay fraction actually corresponds to the greatest reservoir with ~65% of the uranium present. On the other hand, Figure 1a serves as an "optical illusion" since the organic matter, due to its low quantity in the COx and low U concentration measured in this phase, is clearly not a U-bearing phase. The origin of this visual correlation remains unclear and has not been further investigated herein, given the objectives of this work.

The uranium distribution was then indirectly evaluated by means of sequential extraction; results are shown in Figure 1b. Distributions are similar for all clay-rich samples (~3 mg·kg$^{-1}$ in U). The U in fractions F1 (water soluble fraction), F2 (part of the adsorbed fraction) and F4 (organic matter fraction) accounts for less than 5% of total U. This result is consistent with previous data; U in the organic fraction (F4) can be neglected. Therefore, U is mainly distributed between fractions F3 (part of the adsorbed fraction and U present in carbonate phases) and F5 (residual fraction), with a relatively constant distribution of ~12%:86% F3:F5. Moreover, no significant effect was observed relative to the state of conservation of the COx.

At this stage, it is interesting to compare these sequential extraction results with analyses conducted directly on solids. The uranium fractions present in carbonate phases and on clays (assuming that U is adsorbed) should mostly be found in F3 (the adsorbed part of U found in F2 being considered negligible). If we consider that the uranium in phosphates is trapped in the matrix, a proportion between fractions F3 and F5 on the order of 90%:10% is thus obtained from the direct solid analyses presented in Fig. 4c. While this analysis is consistent with sequential extraction results from a qualitative point of view, such is not the case from a quantitative point of view; in fact, the inverse trend is observed, i.e. ~12%:86% F3:F5. Since the carbonate phases are completely dissolved after step 3, a sizable fraction of the U directly detected in the clay phase is present in a “non-labile” form, i.e. not desorbed with the pH decrease and thus recovered in F5. The U content measured in the F3 fraction therefore stems mainly from the dissolution of carbonate phases.

This result is consistent with the fact that the F3 fraction increases with the amount of carbonate phases, that is ~35% and ~12 % for EST21400 (~81% of carbonate phases) and EST26536, EST25687 and EST26480 (~25% of carbonate phases), respectively. From a quantitative point of view, assuming that the uranium in the clay fraction is completely found in F5, in knowing the carbonates phases content of the COx samples, a U content of ~1.3 mg·kg$^{-1}$ and ~0.9 mg·kg$^{-1}$ in the carbonate phases can be recalculated from the sequential extraction results (F3) for samples rich in clay and carbonate phases, respectively. The order of magnitude is consistent with that found from direct analysis of calcite (the majority phase of carbonate phases), i.e. ~0.4-1 mg·kg$^{-1}$.

In conclusion, if uranium is mainly present in the COx clay fraction, it is not retained (for a large part) in a form expected by our model, namely retained by a surface complexation mechanism.

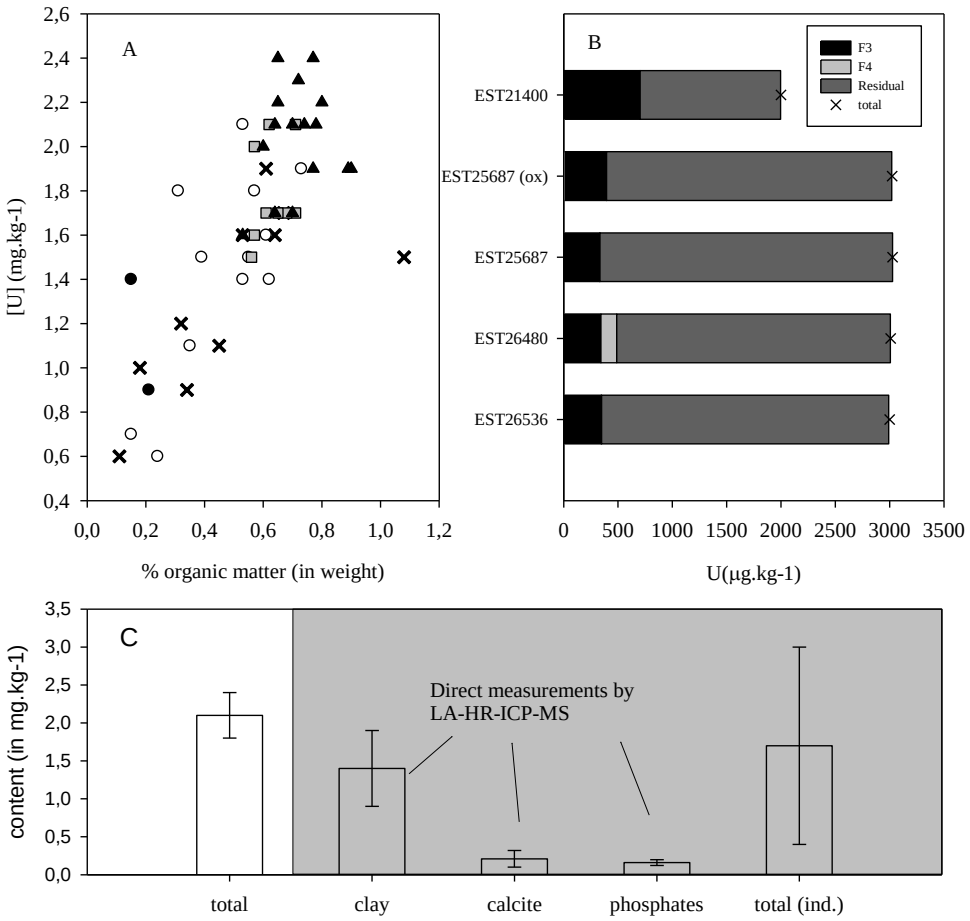


*Figure 1: Naturally-occurring U in the COx: (A) U content vs. organic matter content. (B) Sequential extraction results; the U concentrations in Fractions 1 and 2 are not shown here due to their weak contribution. (C) Distribution of U between the various selected phases.*

## Retention coefficient and labile fraction of naturally-occurring U under both oxidizing and reducing conditions

Results of the isotope exchange method are given in Figure 2a. A fraction of the naturally-occurring U was rapidly resupplied from the clay rock samples in solution, with steady state achieved after less than 1 day of contact. Regarding the samples doped with $^{233}U$, about 3 days were required to reach steady state. We consider that this contact time is insufficient to allow for the exchange of U-233 with U-238 incorporated into the mineral matrix; since this process is controlled by solid diffusion, the kinetics are expected to be very slow. An analysis of the data yields an $R_d$ value of 7.6 ± 2.3 $L \cdot kg^{-1}$ and an amount of labile U present in the COx of 26 ± 7 $\mu g \cdot kg^{-1}$.

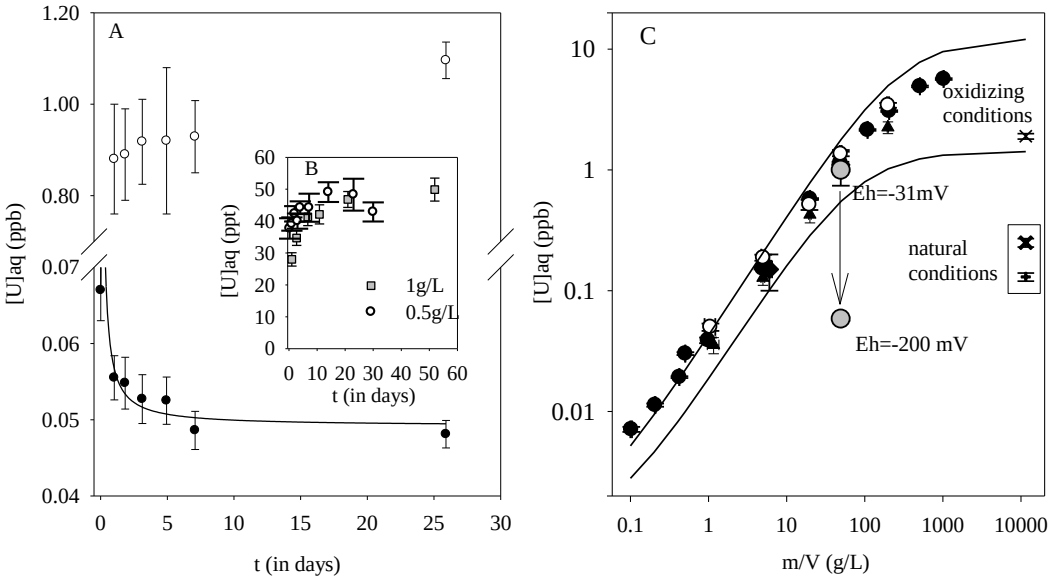


*Figure 2: Results of equilibrium-based methods. (A) Isotopic exchange method with S/L = 49.5 g/L; U-238 (O) and U-233 (●) concentrations measured over time. The line shows a trend curve. (B) U-238 concentration measured over time. (C) Desorption method; the dark symbols correspond to three data series (EST51779, etc.); the white symbol represents the series with EST25687(ox); and the gray symbol denotes the experiment performed over a long contact time. The lines depict the fitting/calculation results (Eq. 1) (see text). The symbols on the right reflect concentrations measured directly in the pore water under preserved and unpreserved conditions.*

For the desorption method, like for the isotope exchange method, contact time is a critical parameter to be assigned. While the time to reach steady state is quick at m/V=50 g·L$^{-1}$, it still might vary with respect to the solid-to-liquid ratio. Two other kinetic experiments were therefore performed for lower solid-to-liquid ratios (i.e. 0.5 and 1 g·L$^{-1}$). The equilibration time was longer (i.e. 4 days instead of 1 day) (Figure 2b), and a contact time of 7 days was thus set for all experiments.

The desorption results obtained as a function of the solid-to-liquid ratio are provided in Figure 2c. Like with the sequential extraction results, no difference has been found between the preserved (black symbols) and unpreserved (white symbols) COx samples. The experimental data can be well explained in considering our simple model (Eq. 1) with $R_d$ and $n$ values at 8.0 ± 4.6 L·kg$^{-1}$ and 30 ± 12 µg·kg$^{-1}$, respectively (solid lines in Figure 2c). Note that the uranium content present in SPW as well as the amount of U in COx originating from pore water are both negligible quantities. The good agreement of results between the two equilibrium-based methods give us confidence in the results. It should also be noted that although the isotope exchange method does make it possible to return to a value for the distribution of uranium (VI) between solid and liquid phases (as translated by an $R_d$ value), the desorption method, owing to the curve shape, exposes this as an adsorption phenomenon. If in fact it was controlled by a solubility mechanism, then the U concentration would not evolve with the mass-to-volume ratio (under saturated conditions).

A final experiment was carried out in the laboratory to assess the relevance of redox potential. A suspension at 50 g·L$^{-1}$ of COx (leading to a measured U concentration of 0.99 µg·L$^{-1}$ for Eh~0 mV / NHE) remained in the glove box (Ar/$CO_2$) for nearly 3 years. The measured potential dropped back to the characteristic value of the site (i.e. Eh~-200 mV) and the U concentration decreased by a factor of nearly 10 (gray symbols in Figure 2c). By considering the labile fraction of U as a fixed parameter, this implies that U speciation at the surface has changed, which results in an increase in the $R_d$ value from 8.0 ± 4.6 to 500 ± 200 L·kg$^{-1}$.

## Discussion

Thanks to the operational model (Montavon et al., 2022), it is possible to analyse the results of equilibrium-based methodologies describing the behaviour of the naturally-occurring U labile fraction for a COx/SPW system representative of the natural environment. In terms of "oxidizing" conditions, this labile fraction is characterized by an $R_d$ value of ~8 L·kg$^{-1}$. According to the model, this finding reflects the presence of U(VI) adsorbed onto the clay surface. Such a result validates the hypothesis of the clay fraction controlling the U adsorption process. The labile fraction however remains low compared to that measured directly by LA-HR-ICP-MS in the clay phases (~1% of total U content). This result confirms our previous hypothesis that a significant fraction of uranium found in the COx clay fraction is in fact incorporated into the matrix in an "inert" form, as found in the residual fraction of the sequential extraction experiments.

In conclusion, we can consider a labile fraction of naturally-occurring U in the formation on the order of 30 ± 12 µg.kg$^{-1}$, to be associated with the clay fraction in an adsorbed form.

At this stage, the purpose of this work is to correlate the results obtained with the information available at the geological formation level, i.e. the concentrations of U in the pore water.

Since no uranium phase has been observed and the labile fraction of naturally-occurring U was found to be adsorbed onto the clay fraction (in the form of U(VI)), we can forward the assumption that *in natura* pore water concentration is also controlled by an adsorption phenomenon. Based on this assumption, the range of *in natura* concentrations in pore water can be predicted from Eq. (1), in knowing: the labile fraction of U, the $R_d$ value (as characterized by the presence of U(VI)), and the high solid-to-liquid ratio characterizing the site (~8% wt. of water, i.e. ~11,500 g.L$^{-1}$). A range of aqueous U concentrations between 1.4 and 12 µg.L$^{-1}$ can thus be calculated (solid lines, Figure 2c).

It is now important to compare this concentration range, deduced from the laboratory experiments, with that measured directly in the pore water collected at the various boreholes. A value of 0.13 µg·L$^{-1}$ has been selected by ANDRA; this value lies close to that measured in this study for the GIS1002 borehole, i.e. 0.25 ± 0.02 µg·L$^{-1}$. It also lies close to the value measured under the undisturbed conditions of the DIR experiment (0.24 µg·L$^{-1}$) (Fralova, 2020). The results are therefore very consistent, and a concentration range of 0.13-0.25 µg·L$^{-1}$ can be given as representative values of the COx formation.

This range appears to be more than 10 times lower than the values deduced from Eq. (1); this information immediately suggests that laboratory experiments are not representative of the natural system.

The uncontrolled parameters in the laboratory are the COx state and redox potential. Three articles focus on the effect of compaction for metal retention parameters on COx clay rocks (Chen et al., 2014; Loni et al., 2021; Montavon et al., 2020); overall, no significant effect was observed. Redox potential is certainly the key parameter; it proves to be even more consistent since uranium is sensitive to redox and the adsorption properties of U(IV) and U(VI) are quite distinct (Montavon et al., 2022). The potential measured in the solutions prepared in the glove box (and in contact with the clay phases) are oxidizing while that expected under *in-natura* conditions is of the order of -190 mV. This result also aligns with the fact that *in natura* aqueous U concentrations measured in KEY1001 under disturbed oxidizing conditions are higher, i.e. around 2 µg·L$^{-1}$, than those representative of the "natural" conditions (0.13-0.25 µg L$^{-1}$). These concentrations are more closely resembling those predicted by our simple model based on laboratory results (1.4 - 12 µg·L$^{-1}$, Fig. 2c).

The following scenario can now be proposed, namely that a more retained form of uranium is present under *in natura* conditions, i.e. the U(IV) form. When the sample is removed from its environment, the U(IV) adsorbed on the surface rapidly oxidizes to U(VI), despite the controlled conditions (with no differences in results between preserved and unpreserved COx samples). In the laboratory, this situation will have the effect of increasing the concentration of aqueous U in suspension since U(VI) is less retained than U(IV). It also explains the decrease in U concentration in equilibrium with the COx as the solution potential decreases over time; this is the opposite case where the equilibria shift towards the sorption of U(IV) retained to a greater extent by the COx clay fraction than U(VI), even in the presence of the soluble ternary complexes of U(VI) (grey symbols in Figure 2b).

According to this reasoning, it becomes possible at this stage to return to $R_d$ values more representative of *in natura*/reducing conditions. Using the labile fraction determined from laboratory experiments and the concentration of U found *in natura* (0.25 - 0.13 µg·L$^{-1}$), a range of *in natura* $R_d$ between 72 and 323 L·kg$^{-1}$ can be calculated. This $R_d$ value range is in agreement with the value deduced from the desorption experiments performed at -200 mV/NHE and Eq. (1), i.e. 500 ± 200 L kg$^{-1}$.

This reasoning must now be compared with the predictive calculations derived from the operational model (Montavon et al., 2022) under *in natura* conditions. Results are presented in Figure 3 as a function of $P_{CO2}$ and redox potential, the two key parameters controlling U speciation in the formation. In these calculations, pH is determined such that calcite is considered in equilibrium in a SPW type solution.

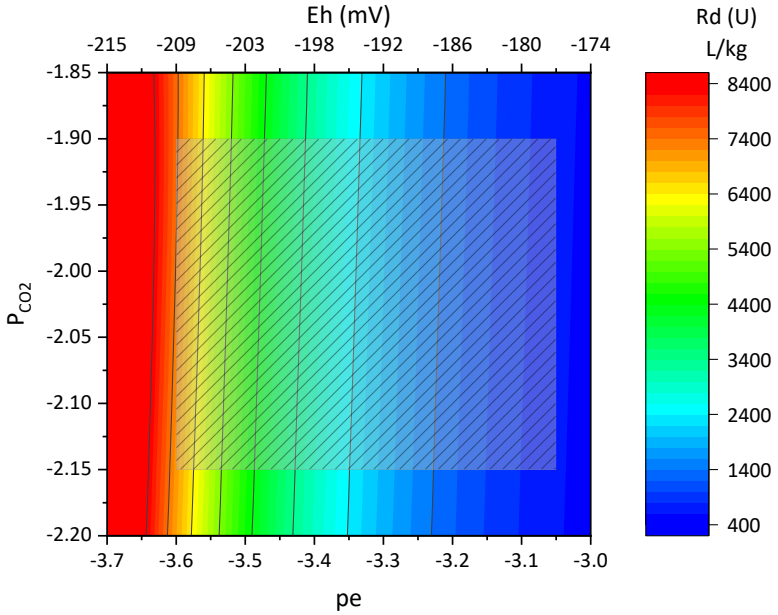


*Figure 3: Variation in the distribution coefficient under in natura conditions vs. pe and $P_{CO2}$ (pH determined for calcite equilibrium, with [Ca]=8.4 mmol/L). The hatched area corresponds to expected in natura conditions.*

Under conditions expected in the formation (hatched area in the figure), $R_d$ values vary greatly, from 640 to 7,400 L·kg$^{-1}$. From a more mechanistic point of view, the speciation in solution is mainly controlled by U(VI) complexed species, whereas at the surface U(IV) surface complexes govern U speciation.

On the one hand, the predicted retention range overestimates the one previously discussed based on experimental data (~70-700 L kg$^{-1}$). Yet on the other, the same conclusion could still be drawn: ternary U(VI) complexes control U speciation in solution while U(IV) surface species dominate U adsorption. It is also important to recall that predictive approaches give trends, since in addition to working with a complex and heterogeneous natural system (other parameters like clay content affect retention values), uncertainties in the model parameters are not taken into account. Let's also recall that the parameters for the U(IV)/COx system are extrapolated using the LFER (Montavon et al., 2022). Therefore, the overlap area between the predicted Rd domain and the Rd domain deduced from experiments allows us to build confidence in our reasoning.

## Conclusion

The aim of this work has been to describe and understand the behavior of U COx under in situ conditions. An operational model based on both a bottom-up approach and the 2SPNE SC/CE model has made it possible to describe the reactivity of U(VI) and U(IV) with respect to COx under laboratory conditions from batch-type experiments (Montavon et al., 2022). Ultimately, it has been well confirmed that the adsorption

of uranium onto COx claystone is controlled by the clay phase (and more specifically, illite). Moreover, the COx clay phase is the largest reservoir of naturally-occurring U. In contrast, only a small fraction appears to have been adsorbed (~1 %, namely ~30 µg·kg$^{-1}$), i.e. the fraction in rapid exchange equilibrium with the fraction in solution. Depending on the experimental conditions imposed in the laboratory, particularly on the redox potential of the solution, $R_d$ values between ~3 and 700 L·kg$^{-1}$ were obtained in order to characterize the behaviour of this labile naturally-occurring U fraction. This variability can mainly be explained by a change in U speciation at the surface, from U(VI) for the lowest $R_d$ values to U(IV) for the highest. Under *in natura* conditions, the results of this work indicate a $R_d$ value > 70 L·kg$^{-1}$, thus reflecting a control of U(IV) at the clay COx surface. This result now needs to be validated by diffusion experiments with intact COx samples.

## References

Ahmed, H.M.M. (2014) Lability and solubility of uranium and thorium in soil. University of Nottingham, p. 290.

Amayri, S., Fröhlich, D.R., Kaplan, U., Trautmann, N. and Reich, T. (2016) Distribution coefficients for the sorption of Th, U, Np, Pu and Am on Opalinus Clay. Radiochimica Acta 104, 33-40.

ANDRA (2005) Dossier 2005. Andra research on the geological disposal of high-level long-lived radioactive waste. Results and perspectives. ANDRA, Châtenay-Malabry (France).

Bradbury, M.H. and Baeyens, B. (1997) A mechanistic description of Ni and Zn sorption on Na-montmorillonite Part II: modelling. Journal of Contaminant Hydrology 27, 223-248.

Bradbury, M.H. and Baeyens, B. (2011) Predictive sorption modelling of Ni(II), Co(II), Eu(III), Th(IV) and U(VI) on MX-80 bentonite and Opalinus Clay: A "bottom-up" approach. Applied Clay Science 52, 27-33.

Chen, Z., Montavon, G., Guo, Z., Wang, X., Razafindratsima, S., Robinet, J.C. and Landesman, C. (2014) Approaches to surface complexation modeling of Ni(II) on Callovo-Oxfordian clayrock. Applied Clay Science 101, 369-380.

Claret, F., Lerouge, C., Laurioux, T., Bizi, M., Conte, T., Ghestem, J.P., Wille, G., Sato, T., Gaucher, E.C., Giffaut, E. and Tournassat, C. (2010) Natural iodine in a clay formation: Implications for iodine fate in geological disposals. Geochimica et Cosmochimica Acta 74, 16-29.

Curtis, G.P., Fox, P., Kohler, M. and Davis, J.A. (2004) Comparison of in situ uranium $K_D$ values with a laboratory determined surface complexation model. Applied Geochemistry 19, 1643-1653.

Fralova, L. (2020) Transport diffusif de l'uranium dans la roche argileuse du Callovo-Oxfordien, mécanismes et sensibilité aux perturbations chimiques. Université Paris sciences et lettres.

Gaucher, E.C., Tournassat, C., Pearson, F.J., Blanc, P., Crouzet, C., Lerouge, C. and Altmann, S. (2009) A robust model for pore-water chemistry of clayrock. Geochimica et Cosmochimica Acta 73, 6470-6487.

Grangeon, S., Vinsot, A., Tournassat, C., Lerouge, C., Giffaut, E., Heck, S., Groschopf, N., Denecke, M.A., Wechner, S. and Schäfer, T. (2015) The influence of natural trace element distribution on the mobility of radionuclides. The exemple of nickel in a clay-rock. Applied Geochemistry 52, 155-173.

Hartmann, E., Geckeis, H., Rabung, T., Lutzenkirchen, J. and Fanghanel, T. (2008) Sorption of radionuclides onto natural clay rocks. Radiochimica Acta 96, 699-707.

Hennig, T., Stockmann, M. and Kühn, M. (2020) Simulation of diffusive uranium transport and sorption processes in the Opalinus Clay. Applied Geochemistry 123, 104777.

Joseph, C., Schmeide, K., Sachs, S., Brendler, V., Geipel, G. and Bernhard, G. (2011) Sorption of uranium(VI) onto Opalinus Clay in the absence and presence of humic acid in Opalinus Clay pore water. Chemical Geology 284, 240-250.

Kautenburger, R., Brix, K. and Hein, C. (2019) Insights into the retention behaviour of europium(III) and uranium(VI) onto Opalinus Clay influenced by pore water composition, temperature, pH and organic compounds. Applied Geochemistry 109, 104404.

Kohler, M., Curtis, G.P., Meece, D.E. and Davis, J.A. (2004) Methods for estimating adsorbed uranium(VI) and distribution coefficients of contaminated sediments. Environmental Science and Technology 38, 240-247.

Lerouge, C., Grangeon, S., Gaucher, E.C., Tournassat, C., Agrinier, P., Guerrot, C., Widory, D., Fléhoc, C., Wille, G., Ramboz, C., Vinsot, A. and Buschaert, S. (2011) Mineralogical and isotopic record of biotic and abiotic diagenesis of the Callovian-Oxfordian clayey formation of Bure (France). Geochimica et Cosmochimica Acta 75, 2633-2663.

Loni, Y.H., David, K., Ribet, S., Lach, P., Lerouge, C., Made, B., Bailly, C., Grambow, B. and Montavon, G. (2021) Investigation of europium retention on Callovo-Oxfordian clay rock (France) by laser ablation inductively coupled plasma mass spectrometry (LA-ICP-MS) and percolation experiments in microcells. Applied Clay Science 214.

Marques Fernandes, M., Vér, N. and Baeyens, B. (2015) Predicting the uptake of Cs, Co, Ni, Eu, Th and U on argillaceous rocks using sorption models for illite. Applied Geochemistry 59, 189-199.

McKinley, I.G. and Alexander, W.R. (1993) Assessment of radionuclide retardation: uses and abuses of natural analogue studies. Journal of Contaminant Hydrology 13, 249-259.

Montavon, G., Lerouge, C., David, K., Ribet, S., Hassan-Loni, Y., Leferrec, M., Bailly, C., Robinet, J.-C. and Grambow, B. (2020) Nickel retention on Callovo-Oxfordian clay: Applicability of existing adsorption models for dilute systems to real compact rock. Environmental Science and Technology 54, 12226-12234.

Montavon, G., Ribet, S., Loni, Y.H., Maia, F., Bailly, C., David, K., Lerouge, C., Made, B., Robinet, J.C. and Grambow, B. (2022) Uranium retention in a Callovo-Oxfordian clay rock formation: From laboratory-based models to in natura conditions. Chemosphere 299.

OECD Nuclear Energy Agency (2002) Radionuclide retention in geologic media, NEA Report. OECD, p. 269.

Payne, T.E., Edis, R., Fenton, B.R. and Waite, T.D. (2001) Comparison of laboratory uranium sorption data with 'in situ distribution coefficients' at the Koongarra uranium deposit, Northern Australia. Journal of Environmental Radioactivity 57, 35-55.

Regenspurg, S., Margot-Roquier, C., Harfouche, M., Froidevaux, P., Steinmann, P., Junier, P. and Bernier-Latmani, R. (2010) Speciation of naturally-accumulated uranium in an organic-rich soil of an alpine region (Switzerland). Geochimica et Cosmochimica Acta 74, 2082–2098.

Tournassat, C., Gailhanou, H., Crouzet, C., Braibant, G., Gautier, A. and Gaucher, E.C. (2009) Cation Exchange Selectivity Coefficient Values on Smectite and Mixed-Layer Illite/Smectite Minerals. Soil Science Society of America Journal 73, 928-942.

Vinsot, A., Linard, Y., Lundy, M., Necib, S. and Wechner, S. (2013) Insights on desaturation processes based on the chemistry of seepage water from boreholes in the Callovo-Oxfordian argillaceous rock Procedia Earth and Planetary Science 7, 871 – 874

Zhao, M.-Y. and Zheng, Y.-F. (2014) Marine carbonate records of terrigenous input into Paleotethyan seawater: Geochemical constraints from Carboniferous limestones. Geochimica et Cosmochimica Acta 141, 508-531.

# 4. Investigation of Pu diffusion in Opalinus Clay rock studied by time-of-flight secondary ion mass spectrometry

M. Breckheimer, F. Berg, S. Amayri, J. Lohmann, C. Sirleaf, T. Reich
*Johannes Gutenberg University Mainz, Mainz, Germany*

## Abstract

In this work the analysis of geochemical interactions of Pu(IV) with Opalinus Clay rock (OPA) via time-of-flight secondary ion mass spectrometry (TOF-SIMS) was investigated. A new preparation procedure for diffusion samples of OPA tailored to this analytical method has been developed and tested for the first time. By applying 3D printing techniques, a more time and cost effective, as well as more scalable approach to study the migration of radionuclides in various materials has been established. First observations in this ongoing study demonstrate the feasibility and potential of using TOF-SIMS for studies related to the safety case of a long-term nuclear waste repository.

## Introduction

A fundamental understanding of mobility of the radionuclide inventory in a deep geological repository is essential for a reliable safety case. In a multi-barrier repository concept the host rock represents the ultimate barrier retaining the radionuclides from the biosphere. Mobility in this natural material is in general determined by retention and migration processes of radionuclide species in the host rock (Maes et al., 2021). Transport in clay rock, considered as potential host rock in this study, is limited by diffusion due to its nano- and micro-scaled structural features as a porous, heterogeneous medium.

Diffusion is experimentally studied by through- and in-diffusion experiments, characterizing the diffusion-accessible porosity of compact clay rock with non-sorbing species (HTO) and subsequently performing in-diffusion experiments with, e.g., strongly-sorbing and redox-sensitive radionuclides like Np and Pu in relevant speciations and feasible time periods. Access to the diffusion profile of the analyte in the material, relevant for the derivation of diffusion parameters for transport modelling, can be achieved with the established method of abrasive peeling (Van Loon et al., 2003; Van Loon and Eikenberg, 2005). The diffusion sample is ablated on abrasive paper, following the diffusion path and gaining a diffusion profile. Applications of this technique for studying the diffusion of actinides in OPA were described in the literature (Wu et al., 2009; Joseph et al., 2013).

A later approach described by Van Loon and Müller (2014) addresses the adverse effect of filters used to confine the clay rock sample in the diffusion cell. They presented a filter-free sample and diffusion setup with an in-diffusion surface exposed to the diffusion solution. Diffusion profiles are also accessible via abrasive peeling (Van Loon and Müller, 2014; Zeisel, 2018; Glückman et al., 2022; Stern, 2022).

One drawback of abrasive peeling is the loss of lateral information in this process, preventing an access to a spatial distribution of the diffused radionuclide and the heterogeneous microstructure of the clay rock, resulting in the loss of information with regard to the geochemical reactivity of the analyte with mineralogical components of the clay matrix.

In this study we describe an approach, based on the experimental setup of Van Loon and Müller (2014), giving access to the diffusion profile through cleaving the sample, exposing an inner surface and imaging the distributions of the diffused analyte and clay matrix elements via TOF-SIMS. This method yields lateral mass distributions of sputtered secondary ions and post-ionized secondary neutrals (resonant Laser-secondary neutrals mass spectrometry, rL-SNMS) of surfaces in a micrometer spatial resolution. This enhanced resolution, compared to the abrasive peeling with achievable resolutions down to 15 µm (Van Loon and Eikenberg, 2005), is especially beneficial in studying the in-diffusion of strongly sorbing reduced actinide species with expected short in-diffusion depths. This analytical approach was demonstrated by

Schönenbach (2020) in imaging a diffusion profile of Pu in OPA, contacted with a solution of Pu(V,VI) in OPA pore water.

## Materials & methods

### Sample preparation for in-diffusion

The original approach by Van Loon and Müller (2014) describes a preparation of OPA samples for a filter-free diffusion experiment by embedding cylindrical OPA samples with a resin coating, stabilizing the sample and containing the swelling pressure of the clay rock after resaturation with a pore water through an exposed in-diffusion surface.

For this study Opalinus Clay rock samples (BHE-D25) from the Mont Terri underground rock laboratory (St-Ursanne, Switzerland) (Thury and Bossart, 1999; Bossart, 2017) were prepared as small cylinders (Ø 5.0 mm x 14.5 mm, $\rho$ = 2.33±0.05 g $cm^{-3}$) by CNC circular milling. For this, a larger fragment, trimmed to appropriate dimensions (ca. 40 x 40 x 15 $mm^3$), was embedded in epoxy resin (EpoxiCure2, Buehler-ITW, Esslingen, Germany) in a cylindrical PMMA segment (Ø 62 mm x 15 mm) serving as a casting mould. This preparation allowed not only a firm but also a more uniform distribution of the mounting forces, minimizing the effect of the machining on the clay rock. The bedding of the clay, also following the approach by Van Loon and Müller (2014), was oriented in parallel to the main rotational axis of the milled cylinders, synonymous with the main diffusion direction along the bedding.

In an extension of the original approach, dedicated sample holders (OD 8.0 mm, ID 6.0 mm, L 24.0 mm) were introduced by Zeisel (2018), constituting not only an embedding mould, incorporating the OPA cylinder (Ø 5.0 mm, L (max.) 13 mm) and embedding resin, but also strengthening this compound sample against the swelling pressure of the clay as well as allowing a flexible mounting in a diffusion setup (cf. *Figure 1* for a schematic overview of the sample and its preparation).

OPA cylinders were mounted inside the sample holders by embedding with the aforementioned epoxy resin, meeting different criteria for a suitable embedding material: An initial low viscosity allowing a superficial pore penetration and surface adhesion with minimal shrinkage of the resin during curing, ideally not inducing any significant transport paths in competition to diffusion in the form of edge gaps, as well as a limited curing temperature (<40 °C), not inducing any structural changes in the clay rock (Reed, 2005).

Essential for a suitable sample is also the precise centering of the OPA cylinder in the sample holder, guaranteeing a uniform resin layer around the sample. Centering can optionally be supported by placing a small polymer sleeve (e.g., PTFE) around part of the OPA cylinder and positioned inside the sample holder far from the in-diffusion surface, as shown exemplarily in *Figure 1*.

Following the curing phase, the in-diffusion surface was smoothed with abrasive paper (SiC, P800). The clay rock in the sample was resaturated and conditioned in an aerobic OPA pore water following the composition described in Van Loon et al. (2003) with an initial pH of 7.3±0.1. If required, surface smoothing, now with the clay rock in a saturated state, was repeated after an initial surface alteration due to the resaturation and associated swelling of the clay. At this stage the outer diameters of the prepared compound samples were measured again with a micrometer (IP65, Mitutoyo Europe GmbH, Neuss, Germany), parallel and perpendicular to the bedding. Relative expansions of (0.82±0.16)% (perpendicular) and (0.20±0.05)% (parallel) were measured, indicating the significance of the (anisotropic) swelling pressure, even in this embedded compound sample.

The duration of resaturation and conditioning amounted to 18 days. No further alterations of the in-diffusion surface were observed.


*Figure 1*: *Schematic illustration of the preparation of in-diffusion samples in a filter-free approach. Left (from top): sample holder (PMMA, OD 8.0 mm, ID 6.0 mm, L 24.0 mm); optional centering sleeve, covering the upper part of the OPA cylinder (Ø 5.0 mm, L (max.) 13.0 mm); structure below visualizing the interspace between OPA and sample holder, filled with epoxy resin. Upper right: compound sample with embedded OPA cylinder and optional centering sleeve. Lower right: rotated compound sample with exposed OPA in-diffusion surface. Visualization generated with Blender (2023).*

## In-diffusion setup

The in-diffusion setup in this study, motivated and based on the respective setups described in Van Loon and Müller (2014) and Zeisel (2018), was designed following several criteria: a further miniaturization of the setup with reducing the required solution volume, the possibility of a flexible sample placement and extraction for time-dependent studies, and with an access for regularly probing the solution regarding the progression of concentration and pH.

An approach was chosen utilizing standard laboratory equipment with good availability and replaceability in combination with a custom designed and 3D printed component, allowing an easy and fast adaptability and scalability of the experiments with regard to the number of samples, chosen radionuclides and solution media, e.g., pore waters of clay rocks or cementitious materials. The vessel containing the solution consisted of a standard 100 mL laboratory bottle (DURAN borosilicate glass, pouring ring, GL45 thread, cap with PTFE faced silicone cap liner). The samples were suspended into the solution with attached screws and nuts (both PA) from a 3D printed adapter (PLA) inserted into the (wide) bottle neck. The setup in this configuration allows the independent placement and extraction of up to six samples. All samples are likewise independently adjustable in height, also during the experiment, allowing the compensation of a possible reduction of solution volume due to a non-returnable sampling. Probing and sampling of the solution is realized through a central opening in the insert.

The application of 3D printing in developing and manufacturing this insert allowed a flexible and fast adaptation during the development process, but also offers the possibility of potentially required modifications, e.g., by integrating possible mounts for sensors etc.


*Figure 2*: *In-diffusion setup (left) during the resaturation/conditioning phase and (right) during the in-diffusion experiment. Standard borosilicate glass laboratory bottle (100 mL), 3D printed insert and mounted samples, immersed in OPA pore water respectively a diffusion solution of $^{239}$Pu(IV) in OPA pore water. Minor condensation at the inner glass wall of the bottle could be observed due to the thermal discharge of the magnetic stirrer. The bottle is placed on a grid allowing a better ventilation of the experiment.*

## In-diffusion experiment

The resaturated and conditioned samples were subjected to an in-diffusion experiment by immersing the exposed OPA in-diffusion surface several millimeters in a solution of $^{239}$Pu(IV) in OPA pore water under aerobic conditions.

The $^{239}$Pu(IV) stock solution was prepared in a sequence of oxidation to Pu(VI) by fuming and dissolving with 1 M $HClO_4$, following potentiostatic electrolysis, first, to Pu(III) and, finally, to Pu(IV). A general description, including the purification of dissolved Pu, can be found in Kaplan et al. (2017). Each speciation step was confirmed via UV-Vis spectroscopy (TIDAS 100, J&M Analytik AG, Essingen, Germany). The final concentration of the Pu(IV) stock solution was determined to 5.5 x $10^{-4}$ M via alpha-spectrometry (CR-SNA-450-100, Ortec, Germany) and liquid scintillation counting (Hidex 300 SL, Hidex Oy, Turku, Finland with Ultima Gold XR scintillation cocktail, PerkinElmer, Waltham, MA, USA).

The initial and total Pu concentration in this diffusion experiment was chosen to be 5 x $10^{-6}$ M, exceeding the solubility limit of Pu(IV) under the experimental conditions (Neck et al., 2007; Altmaier et al., 2013). In this approach, and also under consideration of a potential redox transformation to Pu(V) in OPA pore water (Willberger et al., 2019) and the probable formation of Pu(IV) colloids, the solution should be saturated with a constant equilibrium concentration with regard to Pu over the duration of the diffusion experiment. The diffusion solution was adjusted to an initial pH 7.3±0.1, constantly stirred and preequilibrated with the glass vessel for 4 days. The stability of the Pu concentration, determined via LSC, was confirmed before the beginning of the experiment.

The beginning of the in-diffusion experiment took place by transferring the saturated and conditioned samples, mounted in the diffusion insert, from the resaturation and conditioning to the diffusion solution, guaranteeing a constant saturation of the in-diffusion surface. pH and concentration were monitored regularly, in the beginning of the in-diffusion on a daily basis.

A first sample was drawn 8 days after the beginning of the in-diffusion experiment. During this first time period, the diffusion solution showed a near constant pH 7.4±0.1, but varying Pu concentrations in a range of $2 \times 10^{-7}$ - $4 \times 10^{-6}$ M. This variation could probably be attributed to the sampling with an observed precipitated phase in solution. The identity of this solid phase is still unknown at the time of reporting but will be probed after concluding the experiment.

### TOF-SIMS, Laser-SNMS

TOF-SIMS, utilized in this study as analytical imaging technique, allows for spatially resolved compositional analysis of a samples' surface. Cf. *Figure 3* for a schematic overview. By scanning a pulsed primary ion (PI) beam over the sample, the surface is eroded, secondary ions (SIs) are sputtered and analysed via a time-of-flight-mass spectrometer (TOF-MS) which retrieves a full mass spectrum for every sputtered position. By comparing the relative intensity for a certain mass between sputtered positions, a mapping for this mass is generated and its distribution on the samples' surface can be analysed. Sputtered SIs include elements, but also whole molecules or their fragments. The composition and type of SIs depends on the PI beam but also the samples' chemical matrix. Although modern TOF-MS can reach very high mass resolution, TOF-SIMS can be hampered by isobaric interferences. A solution for this challenge is resonance ionization mass spectrometry (RIMS). Hereby atoms are photoionized via laser light tuned to a multi-step photoionization scheme (Grüning et al., 2004). Due to the unique electronic structure of every element, this process is element selective and isobaric interferences can be efficiently suppressed. The combination of TOF-SIMS and RIMS is called resonant Laser-secondary neutrals mass spectrometry (rL-SNMS). Here, the secondary neutrals (SNs) necessary for RIMS are generated next to SIs during the sputter process via the PI beam and then post-ionized via laser light introduced into the cloud of sputtered species. By delaying the extraction and applying a voltage to the tip of the extraction electrode of the mass analyser between the generation of SIs and the photoionization via the laser light, the SIs are suppressed and only photoionized ions are detected by the mass analyser. In this way, even traces of an element can be detected on the surface that would otherwise be hidden by isobaric interferences.

The setup for TOF-SIMS and rL-SNMS of the Nuclear Chemistry at the JGU Mainz consists of a TOF-SIMS 3 (IONTOF GmbH, Münster, Germany) equipped with a liquid metal ion gun (LMIG) with $^{69}Ga^+$ as PI beam and a control system upgraded to TOF-SIMS 5 level. The custom laser system for rL-SNMS consists of three tunable Ti:Sa lasers jointly pumped 15 W each by a frequency doubled Nd:YAG pump laser (Nexlase GmbH, Gröbenzell, Germany) at 532 nm and 10 kHz. The setup, its development and characterization are described in more detail by Schönenbach et al. (2021).

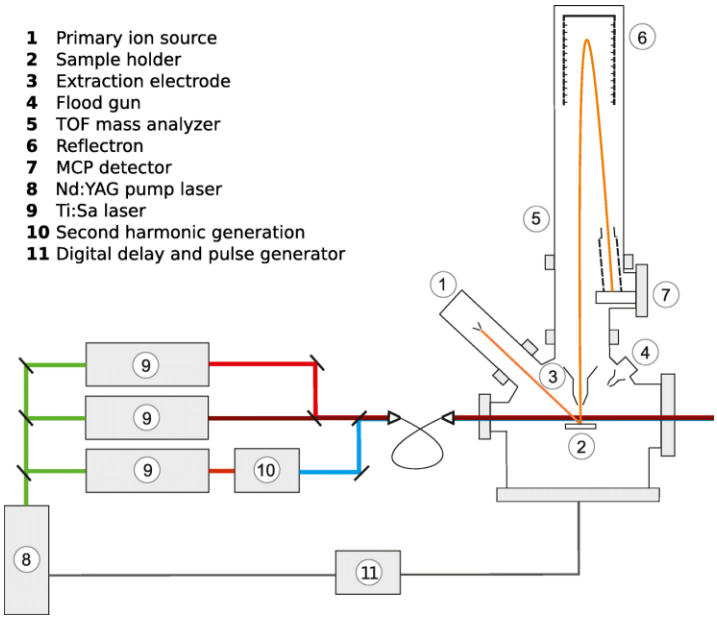


*Figure 3*: *Schematic illustration of the laser secondary neutral mass spectrometry (Laser-SNMS) setup: laser system and time-of-flight secondary ion mass spectrometer (TOF-SIMS) III. Figure and caption reproduced from Schönenbach et al. (2021) under the Creative Commons license (http://creativecommons.org/licenses/by/4.0/).*

## Sample preparation after in-diffusion

Due to the utilized imaging technique and its measurement of surfaces, the in-diffusion samples have to be invasively prepared and adapted to the analytical technique. In this approach the sample is cleaved parallel to the bedding of the clay rock and therefore along the diffusion direction, exposing an inner surface of the OPA clay rock, giving access to a least affected diffusion profile and distribution of OPA matrix components.

After drawing a sample out of the diffusion solution, a sequence of steps is following immediately, preserving the saturated state of the clay rock as much as possible, since cleaving of the clay rock is more simplified and controllable than in a desaturated, dried state. The compound sample is therefore immediately decontaminated at its outer surfaces, except the in-diffusion surface, and unmounted from its attached screw and nut. The upper mounting part (PMMA) of the compound sample is detached by cautiously sawing perpendicular to the OPA cylinder axis at the inner interface of OPA and PMMA with a fine-toothed saw blade (PUK saw blade 312), cf. *Figure 4* (left). Potentially contaminated sawdust has to be considered and contained. All steps of this invasive process are done in a fume hood.

The compound sample, reduced to the length of its inner OPA cylinder, is mounted in a 3D printed prism-like tool (PLA), allowing simultaneously clamping and sawing of the compound sample, cf. *Figure 4* (right) for an earlier trial without activity. The cleaving is achieved by cautiously sawing through the outer PMMA and resin layers on both sides, parallel to the bedding of the clay. With applying a small rotational force with a tool inside the formed saw tracks, the sample cleaves, ideally, along the bedding, resulting in a least processed inner surface of the clay.

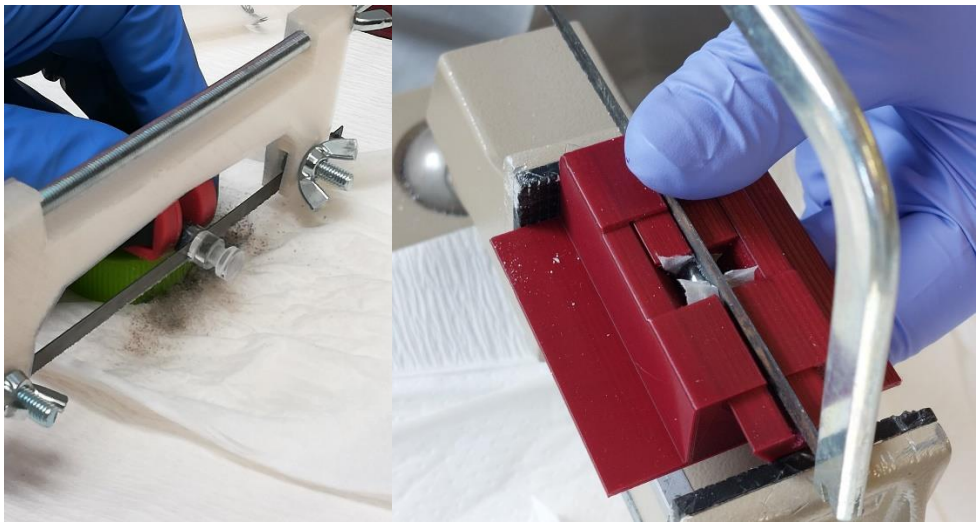

*Figure 4*: *Preparation of an in-diffusion sample for TOF-SIMS measurements. After an initial decontamination of the outer sample holder, the sample is immediately processed, preferably preserving the saturated state of the embedded OPA clay rock. Left: Detaching the upper mounting part (PMMA) of the sample. Right: Isolated subsample mounted in a 3D printed cleaving tool. Sawing of the outer PMMA and resin layer parallel to the bedding. The picture is showing an earlier test without deployed activity. Subsequent processing of in-diffusion samples with $^{239}$Pu was done in the controlled environment of a fume hood, considering the generation of sawdust.*

The sample is left to dry and mounted on a dedicated sample holder for the instrument, fixed with conducting double-sided adhesive carbon-tape (CMC Klebetechnik GmbH, Frankenthal, Germany).

For the TOF-SIMS measurement: After establishing the necessary vacuum (<$10^{-7}$ mbar), the surface of the chosen measurement area is cleaned by sputtering with an increased ion flux to remove any superficial contaminants like, e.g., ubiquitous adventitious carbon. Each sample system requires an adapted set of measuring parameters, considering, among others, the conductivity of the material which can also differ on the same sample. Selected measurement areas of ca. 500x500 µm² are scanned with the PI in a raster of 512x512 pixel, accumulating 100 scans for each imaged region in this study. After calibration, mass-specific (m/Z) images can be reconstructed.

## Results & discussion

### Methodological development

Imaging via TOF-SIMS and its extension rL-SNMS is a technique predestined for analysing plane sample surfaces. A deviating surface topography or sample geometry poses an analytical challenge for this surface-sensitive technique. Cleaving a diffusion sample may most probable not result in a plane surface, limiting the area accessible with this technique. Therefore, a precise determination and tracking of the clay rock bedding during the experiment and the following cleaving is key to a surface least affected by topography, enabling a larger area of accessible surface. Here, the prototype of a 3D printed cleaving tool represents a significant step forward gaining more control of a precise cleaving.

Besides the associated topography of the cleaved sample surface, the general sample geometry has a critical effect on the possible measurement of surface regions, especially in this sample system with the objective of imaging a diffusion profile with an associated edge. In first trials no ion signal could be registered in this edge region. Placing an identical piece of OPA material with precisely adapted dimensions next to this edge (cf. *Figure 7*), provided an access to imaging this sample geometry. With virtually extending the sample surface the ion extraction process is less affected.

## Imaging of the in-diffusion surface

Since the analytical method utilized in this study is in general assessed as a non-destructive technique, two features of the cleaved samples can be studied: the inner surface, ideally obtaining a diffusion profile, and the in-diffusion surface, additionally allowing the investigation of sorption phenomena at this interface between the clay rock and the actinide solution.

First, the in-diffusion surface of the cleaved sample was imaged via TOF-SIMS at a centred position of the accessible surface, least affected by adverse edge effects. A selected region is shown in *Figure 6* with a photographic representation of the sample and an overview of reconstructed mass images.

Elemental distributions are interpreted with corresponding and selected mass numbers as annotated in the mass images. The distribution of Pu, however, is generated by combining the signals of $^{239}Pu^+$ and $^{239}PuO^+$, summing up the respective low intensity signals. *Figure 5* shows a spectral segment of the sum mass spectrum recorded during imaging of the in-diffusion surface, showing the respective signals at m/Z = 239 and 255 and therefore giving evidence of a true Pu distribution. A benefit of the previously described post-ionization of secondary neutrals via rL-SNMS is the significant suppression of background in the mass spectrum and reconstructed images and therefore further improving the detection of Pu (Schönenbach et al., 2021). Unfortunately, no rL-SNMS could yet be applied at the time of reporting but is planned at a later stage of the ongoing study.

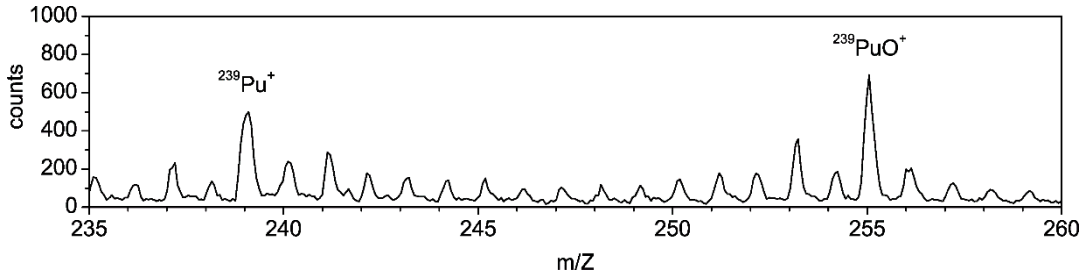


*Figure 5*: *Spectral segment of the sum mass spectrum, accumulating the signal of imaging a region of the in-diffusion surface (cf. Figure 6 for the corresponding reconstructed mass images). Signals at m/Z = 239 and 255 are attributable to $^{239}Pu^+$ and $^{239}PuO^+$.*

*Figure 6* shows a compilation of matrix element distributions of the clay rock as well as the interpreted Pu distribution. The images contain information of the sample topography through the imaging process. For some elements, especially Ca and Fe, a heterogeneous distribution can be observed, hinting at the microstructure of the OPA clay rock (Houben et al., 2014). Comparing the Pu and matrix element distributions a partial correlation between Pu and Fe can be deduced, hinting on the redox activity of ferrous iron mineral phases contained in OPA (Fröhlich et al., 2012). Also possible is an enhanced retention activity of potential ferric iron corrosion phases, exhibiting large specific surfaces. Of course, a reliable interpretation requires a critical number of studied regions and surfaces, unfortunately not yet achieved at this stage of the study.

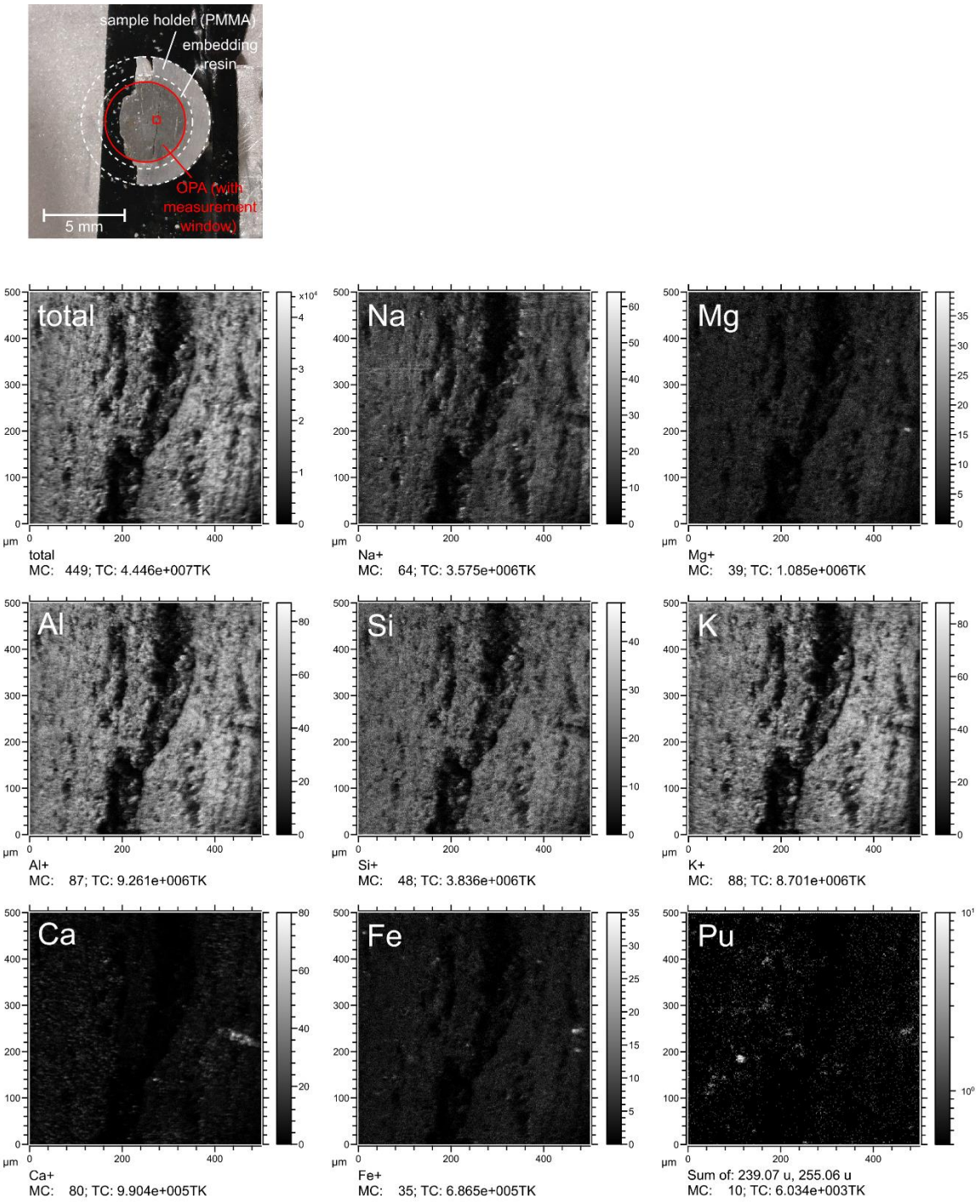


*Figure 6*: *Imaging of a segment of the in-diffusion surface via TOF-SIMS. Top left: Photographic view on the in-diffusion surface. The sample was cleaved unevenly and positioned on adhesive carbon-tape for the measurement. Dashed lines indicate the original contour of the sample. Central, the OPA cylinder with in-diffusion surface and measurement area of ca. 500x500 µm². Below: Overview of mass images with annotated interpreted assignments of elements. 100 scans of 500x500 µm² at 512x512 px. The Pu mass image is created through the sum of $^{239}Pu^{+}$ and $^{239}PuO^{+}$ signals, binned by a factor of 4, reducing the resolution to 256x256 px, and scaled logarithmically for a better representation of the distribution.*

### Imaging of the cleaved surface

*Figure 7* shows the mounted sample as well as an overview of reconstructed mass images. As described earlier, the sample geometry and topography have a significant effect on the imaging. The former could be minimized by virtually extending the OPA surface with an adapted piece of OPA placed next to the in-diffusion edge, allowing the imaging of the edge. The sample topography is recognizable through its effect on the imaging process in TOF-SIMS. Again, some selected matrix elements (Mg, Ca, Fe) show a heterogeneous distribution hinting at the microstructure.

The cleaving process necessary to gain access to the inner surface has to be considered in the interpretation of elemental distributions. Control of the cleaving and therefore on the access to the inner microstructure is limited by the preparation and potential fracture zones of the bedding leading to the cleaved surfaces. This is probably not resulting in a representative image of the microstructure, but overrepresenting structures in the bedding leading to a fracture. Otherwise, these surfaces are least affected by the sample preparation, as it is, e.g., most probably the case for an access to the microstructure via mechanical polishing. A critical number of measurements and samples should compensate for this limitation by averaging of the obtained information with regard to the derived diffusion profiles and possible distributional correlations.

In this sample with an in-diffusion time of 8 days in contact with a 5 x $10^{-6}$ M $^{239}$Pu(IV) solution, no diffusion profile of Pu could be obtained. The mass image consists mainly of unsuppressed background and cannot be interpreted as a true Pu distribution. At the in-diffusion edge a correlation to a Fe heterogeneity can be observed but should be interpreted with caution due to the single occurrence and imaging perspective on this edge of the in-diffusion surface. At the time of reporting, the experiment is being continued and samples will be correspondingly studied.

The imaging method still offers some potential optimizations like an enhanced spatial resolution by further reducing occurring instrument vibrations, a further adaptation of measuring parameters on the specific samples and the application of post-ionization via rL-SNMS to derive a true Pu distribution and eventually diffusion profiles with high sensitivity.

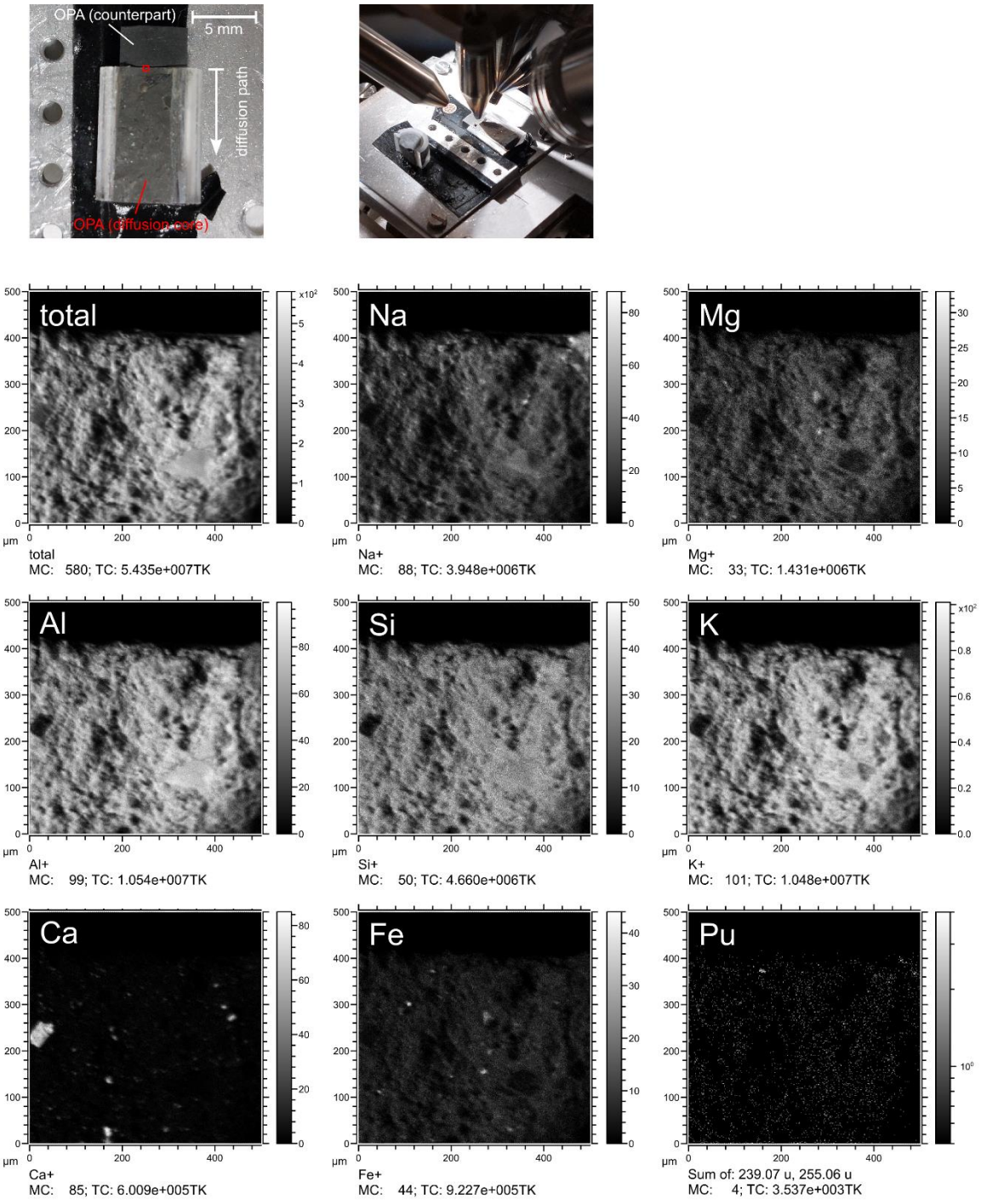


*Figure 7*: *Imaging of a segment of the in-diffusion edge via TOF-SIMS. Top left: photographic view of the cleaved sample with indication of the diffusion direction. Next to the in-diffusion edge a piece of OPA, adapted to the dimensions of the edge and enabling the imaging with this sample geometry. Top centre: Photographic representation of the sample during measurement in the TOF-SIMS instrument. Below: Overview of mass images with annotated interpreted assignments of elements. 100 scans of 500x500 µm² at 512x512 px. The Pu mass image is created through the sum of $^{239}Pu^+$ and $^{239}PuO^+$ signals, binned by a factor of 4, reducing the resolution to 256x256 px, and scaled logarithmically for a better representation of the distribution.*

## Conclusions

In this study a significant progress in assessing the diffusion of strongly sorbing actinides could be made thanks to the methodological developments regarding the sample preparation, experimental setup and analytical technique which were applied for in a diffusion experiment of Pu in Opalinus Clay rock. A sample preparation could be established, and a dedicated diffusion setup was further developed, allowing a further miniaturization of the experiment, leading to a more efficient use of the actinide inventory. Also beneficial is the associated scalability of the experiment using standard laboratory glassware, combined with adaptable 3D printed components, allowing a fast, flexible and scalable experimental approach, e.g., with varying the sample material and geometry, employed actinide species and electrolytes.

By optimizing the sample preparation and measuring parameters, the in-diffusion surface of a sample could be imaged via TOF-SIMS, and distributions of matrix elements and Pu be deduced, gaining first hints on possible geochemical reactivity in the system. Despite employing a concentration of Pu(IV) well above the solubility limit and also expecting the formation of Pu colloids, the concentration was reduced by a factor of 10 compared to previous experiments with an option of further reducing the concentration due to the high sensitivity of TOF-SIMS and rL-SNMS as analytical techniques.

Unfortunately, no diffusion profile could be observed yet, most probably due to the short in-diffusion time and strongly-sorbing characteristic of the employed Pu(IV) species. Experiments are ongoing and should contribute to an experimental approach in studying the diffusion of reduced actinide species, relevant for the environmental conditions in a clay rock as a host rock material.

## Acknowledgments

M.B. acknowledges funding from the European Union's Horizon 2020 project EURAD (WP FUTuRE), EC grant agreement no. 847593. F.B. and C.S. acknowledge funding from the German Federal Ministry of Education and Research under contract number 02NUK075B. The authors acknowledge Daniel Grolimund (microXAS beamline project, Swiss Light Source, Paul Scherrer Institute, 5232 Villigen, Switzerland) for the provision of OPA samples from the Mont Terri underground rock laboratory (St-Ursanne, Switzerland), as well as the mechanical workshops of the research reactor TRIGA Mainz and the Department of Chemistry (Johannes Gutenberg University Mainz, Germany) for the production of components utilized in this study.

## References

Altmaier, M., Gaona, X., Fanghänel, T., 2013. Recent Advances in Aqueous Actinide Chemistry and Thermodynamics. Chemical Reviews 2013, 113, 901-943. https://doi.org/10.1021/cr300379w.

Blender, 2023. Blender, a free and open-source 3D creation suite. Version 3.5.1. Licensed under GNU General Public License (GPL). http://www.gnu.org/copyleft/gpl.html.

Bossart, P., 2017. Twenty years of research at the Mont Terri rock laboratory: what we have learnt. Swiss Journal of Geosciences 110, 405-411. https://doi.org/10.1007/s00015-017-0267-2.

Fröhlich, D.R., Amayri, S., Drebert, J., Grolimund, D., Huth, J., Kaplan, U., Krause, J., Reich, T., 2012. Speciation of Np(V) uptake by Opalinus Clay using synchrotron microbeam techniques. Analytical and Bioanalytical Chemistry 404, 2151-2162. https://doi.org/10.1007/s00216-012-6290-2.

Glückman, D., Geckeis, H., Joseph, C., Kraft, S., Metz, V., Plaschke, M., Quinto, F., 2022. Chapter 5.4 Diffusion. In: Annual Report 2020/2021, Institute for Nuclear Waste Disposal, Karlsruhe Institute of Technology, Karlsruhe, Germany. Editors: Geckeis, H., Altmaier, M., Fanghänel, S. https://doi.org/10.5445/IR/1000143439.

Grüning, C., Huber, G., Klopp, P., Kratz, J.V., Kunz, P., Passler, G., Trautmann, N., Waldek, A., Wendt, K., 2004. Resonance ionization mass spectrometry for ultratrace analysis of plutonium with a new solid state laser system. International Journal of Mass Spectrometry 235, 171-178. https://doi.org/10.1016/j.ijms.2004.04.013.

Houben, M.E., Desbois, G., Urai, J.L., 2014. A comparative study of representative 2D microstructures in Shaly and Sandy facies of Opalinus Clay (Mont Terri, Switzerland) inferred form BIB-SEM and MIP methods. Marine and Petroleum Geology 49, 143-161. http://doi.org/10.1016/j.marpetgeo.2013.10.009.

Joseph, C., Van Loon, L.R., Jakob, A., Steudtner, R., Schmeide, K., Sachs, S., Bernhard, G., 2013. Diffusion of U(VI) in Opalinus Clay: Influence of temperature and humic acid. Geochimica et Cosmochimica Acta 109, 74-89. https://doi.org/10.1016/j.gca.2013.01.027.

Kaplan, U., Amayri, S., Drebert, J., Rossberg, A., Grolimund, D., Reich, T., 2017. Geochemical Interactions of Plutonium with Opalinus Clay Studied by Spatially Resolved Synchrotron Radiation Techniques. Environmental Science and Technology 2017, 51, 7892-7902. http://doi.org/10.1021/acs.est.6b06528.

Maes, N., Glaus, M., Baeyens, B., Marques Fernandes, M., Churakov, S., Dähn, R., Grangeon, S., Tournassat, C., Geckeis, H., Charlet, L., Brandt, F., Poonoosamy, J., Hoving, A., Havlova, V., Fischer, C., Scheinost, A., Noseck, U., Britz, S., Siitari-Kauppi, M., Missana, T., 2021. State-of-the-Art report on the understanding of radionuclide retention and transport in clay and crystalline rocks. Final version as of 30.04.2021 of deliverable D5.1 of the HORIZON 2020 project EURAD. EC Grant agreement no: 847593. https://www.ejp-eurad.eu/sites/default/files/2021-06/eurad_d5_1_sota_future.pdf.

Neck, V., Altmaier, M., Fanghänel, T., 2007. Solubility of plutonium hydroxides/hydrous oxides under reducing conditions and in the presence of oxygen. Comptes Rendus Chimie 10 (10-11), 959-977. https://doi.org/10.1016/j.crci.2007.02.011.

Reed, S.J.B., 2005. Electron Microprobe Analysis and Scanning Electron Microscopy in Geology. Cambridge University Press.

Schönenbach, D., 2020. Ortsaufgelöste Ultraspurenanalyse mittels Sekundärionen-Massenspektrometrie und Laser- Sekundärneutralteilchen-Massenspektrometrie. PhD thesis. Johannes Gutenberg-Universität Mainz, Germany. http://doi.org/10.25358/openscience-5176.

Schönenbach, D., Berg, F., Breckheimer, M., Hagenlocher, D., Schönberg, P., Haas, R., Amayri, S., Reich, T., 2021. Development, characterization, and first application of a resonant laser secondary neutral mass spectrometry setup for the research of plutonium in the context of long-term nuclear waste storage. Analytical and Bioanalytical Chemistry 413, 3987-3997. https://doi.org/10.1007/s00216-021-03350-3.

Stern, T., 2022. Einfluss der Redoxbedingungen auf die Speziation von Actiniden bei der Sorption an Tonmineralien. PhD thesis. Johannes Gutenberg-Universität Mainz, Germany. http://doi.org/10.25358/openscience-7050.

Thury, M., Bossart, P., 1999. The Mont Terri rock laboratory, a new international research project in a Mesozoic shale formation, in Switzerland. Engineering Geology 52, 347–359. https://doi.org/10.1016/S0013-7952(99)00015-0.

Van Loon, L.R., Soler, J.M., Bradbury, M.H., 2003. Diffusion of HTO, $^{36}Cl^-$ and $^{125}I^-$ in Opalinus Clay samples from Mont Terri: Effect of confining pressure. Journal of Contaminant Hydrology 61, 73-83. https://doi.org/10.1016/S0169-7722(02)00114-6.

Van Loon, L.R., Eikenberg, J., 2005. A high-resolution abrasive method for determining diffusion profiles of sorbing radionuclides in dense argillaceous rocks. Applied Radiation and Isotopes 63, 11-21. https://doi.org/10.1016/j.apradiso.2005.02.001.

Van Loon, L.R., Müller, W., 2014. A modified version of the combined in-diffusion/abrasive peeling technique for measuring diffusion of strongly sorbing radionuclides in argillaceous rocks: A test study on the diffusion of caesium in Opalinus Clay. Applied Radiation and Isotopes 90, 197-202. http://doi.org/10.1016/j.apradiso.2014.04.009.

Willberger, C., Amayri, S., Häußler, V., Scholze, R., Reich, T., 2019. Investigation of the Electrophoretic Mobility of the Actinides Th, U, Np, Pu, and Am in Different Oxidation States. Analytical Chemistry 2019, 91, 11537-11543. http://doi.org/10.1021/acs.analchem.9b00997.

Wu, T., Amayri, S., Drebert, J., Van Loon, L.R., Reich, T., 2009. Neptunium(V) Sorption and Diffusion in Opalinus Clay. Environmental Science and Technology 2009, 43, 6567-6571. https://doi.org/10.1021/es9008568.

Zeisel, S., 2018. Diffusion von Neptunium und Cäsium in Tongestein. Diploma thesis. Johannes Gutenberg-Universität Mainz, Germany.

# 5. Diffusion study of $UO_2^{2+}$ on Boda Claystone Formation

O. Czömpöly, M. Fábián, J. Osán, I. Tolnai
*EK, Budapest, Hungary*

## Abstract

Experiments of EK were focused on a natural argillaceous rock system, Boda Claystone Formation (BCF), which is a candidate host rock for high-level radioactive waste in Hungary. Through-diffusion experiments were performed on BCF core samples with $UO_2^{2+}$ containing solutions prepared from natural uranium. Unexpected breakthrough was observed in one of the rock discs in a short time, resulting in a relatively high effective diffusion coefficient and low rock capacity factor. Uranium rock profile obtained using LA-ICP-MS from a 5-year-long diffusion experiment without breakthrough was modelled. Variable rock capacity factor was necessary to fit the profile close to the surface, resulting in reasonable effective diffusion coefficient and rock capacity factor in line with batch sorption results.

## Introduction

In Hungary Boda Claystone Formation (BCF) is considered as a potential host rock for high-level radioactive waste repository (Fedor et al., 2019). BCF is oldest in Europe (265 Ma) and has total clay mineral content similar to other widely studied clay formations (COx, OPA). BCF has a number of unique features, since it is an over-consolidated, highly indurated character with low physical porosity (≈0.02). As the early diagenesis of BCF occurred in oxidative environment, most of the studies regarding the migration of RNs in BCF were investigated under atmospheric conditions previously (Gergely et al., 2016; Marques Fernandes et al., 2015; Mell et al., 2006).

The aim of this study was to investigate the diffusion of $UO_2^{2+}$ in argillaceous rocks of BCF, via through-diffusion experiments at an initial concentration of $2.24 \times 10^{-4}$ M. Synchrotron-radiation microspectrometry was applied for studying the distribution of uranium in the rock after diffusion experiment. Uranium profile inside a BCF rock disc obtained by laser-ablation ICP-MS from a former 5-year-long diffusion experiment (Lázár et al., 2012) was modelled in order to derive the apparent diffusion coefficient and rock capacity factor of $UO_2^{2+}$ and to compare to batch sorption results.

## Materials and methods

### BCF core samples

Representative core sections of the BAF-2 drilling carried out in the Boda Block (April-August 2014) (Sámson, 2015) were provided by the Public Limited Company for Radioactive Waste Management (PURAM, Hungary) and accompanied with characterization results. Core sections from 340–760 m depths representing the major albitic claystone formed under oxidative conditions were selected for the present study. The background concentrations of U in the selected core sections are 3.2–6.8 mg/kg (Sámson, 2015).

### Synthetic porewater

The composition of the formation water was determined and reported in the BAF-2 drilling report (Sámson, 2015), however it is not representative for the porewater itself. For this reason a modelled porewater composition is used for the experiments (Breitner et al., 2015; Marques Fernandes et al., 2015). The major porewater composition is very close to that extracted directly from a BCF core by a modified cryodesiccation (LN2 freezing) method (Fedor et al., 2019).

## Through-diffusion experiments

For the through-diffusion experiment three diffusion cells were applied. Cell 1 and Cell 2 are identical and made of polycarbonate (Mell et al., 2006). A ca. 5-mm thick claystone section divides the cell into upstream and downstream reservoirs with a volume of 165 mL each and a clay surface of 19.64 $cm^2$ (Figure 1). The claystone slices were glued in the cells then the two sides were screwed together. No filter was applied due to the very limited swelling of Boda claystone. After installing the diffusion cells both reservoirs were filled by synthetic porewater to saturate the BCF core discs. During the 6-week conditioning the solutions were changed every 2 days. The through-diffusion experiments were conducted with natural uranium solution prepared from $UO_2(NO_3)_2$ at an initial concentration of $2.24 \times 10^{-4}$ M (at the solubility limit of $UO_2(NO_3)_2$ at pH=8 in synthetic Boda porewater). The effective diameter available for diffusion was 50 mm. Uranium concentrations in the upstream and downstream reservoirs were monitored using ICP-OES. After finishing the experiment (126 days) on the first cell (Cell 1) was disassembled, a piece of 5×10×4.8 $mm^3$ was cut from the centre of the claystone disc and embedded into epoxy resin. Once the resin cured, its surface was grinded and polished for X-ray microspectroscopy investigations. At the end, a 2 mm thick slice was cut for easier handling during spectroscopy measurements.

Cell 3 used the same diffusion cell concept but slightly different dimensions of the reservoir and the sample(Lázár et al., 2011). The volume of the reservoirs was 100 ml each separated with a ca. 10 mm thick Boda claystone disc (from 47 mm borecore). From each reservoir 5 ml of sample were taken out, the activities were measured with a scintillation counter and then the solutions were filled back to the corresponding reservoir. The initial uranyl concentration in the upstream reservoir was $2\times10^{-2}$ M at low pH. The experiment was conducted for ca. 1911 days and then the distribution of uranium was measured along the diffusion direction with laser ablation ICP-MS (Lázár et al., 2012).

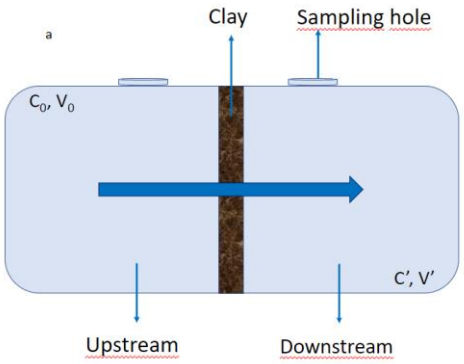


*Figure 1: Schematics of the applied through-diffusion cell.*

## Microscopic X-ray spectrometry

Due to the low concentration of uranium in the claystone samples undergone diffusion, microscopic X-ray spectrometry investigations were performed using synchrotron radiation. Microscopic X-ray fluorescence (μ-XRF) and X-ray absorption near-edge structure (μ-XANES) measurements were carried out at Bessy-II (Berlin, Germany) mySpot beamline (Zizak, 2016). The beam was focused with polycapillary optics to 20 μm spot size. A silicon drift detector (SDD) of 100 $mm^2$ active area was used in 45°/45° geometry. 2D elemental maps were recorded using a 20 μm step-size, and 5 s dwell time per pixel on a selected representative area of a few $mm^2$ on the thin sample prepared from the claystone from Cell 1. Due to the high Fe content of the BCF sample (≈ 5%), a 0.1 mm Al foil was placed in front of the SDD in order to suppress Fe-K X-ray lines and the related background. U-$L_3$ μ-XANES spectra were recorded at positions selected from areas enriched in uranium.

## Diffusion modelling

Diffusion is described by the diffusion equation

$$\frac{\partial C}{\partial t} = D_a \frac{\partial^2 C}{\partial x^2} \tag{3}$$

where $C$ (x,t) is the concentration (mol/m$^3$ or counts/ m$^3$), $x$ is the position (m), $t$ is time (s) and $D_a$ stands for the apparent diffusion coefficient (m$^2$/s). In porous media, diffusion is characterized by two parameters: the apparent diffusion coefficient $D_a$ and the rock capacity $\alpha$ (-).

For linear sorption, the rock capacity $\alpha$ is related to the distribution coefficient $K_d$ (m$^3$/kg) by

$$\alpha = \varepsilon_{tot} + \rho K_d \tag{4}$$

where $\varepsilon_{tot}$ is the total porosity (-) and $\rho$ (kg/m$^3$) the dry bulk density. In that case, the retardation coefficient $R$ is the ratio $R = \alpha/\varepsilon_{tot}$ with $R > 1$. The effective diffusion coefficient $D_e$ (m$^2$/s) is the product $\alpha D_a$ ($D_e = \alpha D_a$).

For non-sorbing (conservative) species,

$$\alpha = \varepsilon \tag{5}$$

with $\varepsilon$ (-) the accessible porosity ($\varepsilon \leq \varepsilon_{tot}$).

For modelling, the diffusion equation is solved numerically. The fitting was carried out in OriginLab, the parameters of the fitting were $D_a$ and $\alpha$. The total porosity and bulk dry density were considered as $\varepsilon_{tot}$ = 0.02 and $\rho$ = 2.7 kg/L.

As in the through-diffusion experiment of Cell 1 neither the upstream nor the downstream reservoir are replaced, basically the VC-VC (Variable Concentration upstream and downstream) case (Takeda et al., 2008) is solved. In case the upstream and downstream compartments are sufficiently large, the VC-VC case is approximated well by the CC-CC (Constant Concentration upstream and downstream with the upstream concentration $C_0$ much higher than the downstream concentration) case (Takeda et al., 2008). Here, after a sufficiently large time a quasi-stationary state is reached, and the concentration $C_{down}(t)$ in the downstream volume is given by (e.g. Aertsens, 2011)

$$\frac{C_{down}(t)}{C_0} = \frac{LA}{V_{down}} \alpha \left( \frac{D_e t}{L^2 \alpha} - \frac{1}{6} \right) \tag{6}$$

where $L$ *is* the clay core length (m) ($L$ = 4.8 mm for Cell 1). This expression is valid only for not too large times (to remain consistent with the basic assumption $C_{down} << C_0$) and the breakthrough time $\tau$ (defined by $C_{down}(\tau) = 0$) is determined by the apparent diffusion coefficient:

$$\tau = \frac{L^2 \alpha}{6\, D_e} \tag{7}$$

In Cell 3 the downstream concentration did not start to increase (viz. only in-diffusion occurred). The diffusion coefficient could be determined based only on the rock profile. The calculations were performed using the analytical expression given by (Shackelford, 1991):

$$\frac{C(x,t)}{C_o} = e^{\frac{\alpha x}{H_f} + \frac{\alpha D_e t}{H_f^2}} \cdot erfc\left( \frac{x}{2\sqrt{D_e t/\alpha}} + \frac{\sqrt{D_e t \alpha}}{H_f} \right) \tag{8}$$

where $H_f$ is the length of the reservoir (m) perpendicular to the rock surface, *erfc*($Z$) is the complementary error function of an argument $Z$.

# Results

## Cell 1

The concentration in the upstream reservoir can be approximated with a constant during the experiment. The concentration in the downstream reservoir started to increase in the early stages of the diffusion experiment, the breakthrough time is calculated to be $\tau$ = 13 days. The concentration change in the downstream reservoir is linear over time, expression (9) describes the concentration profile.

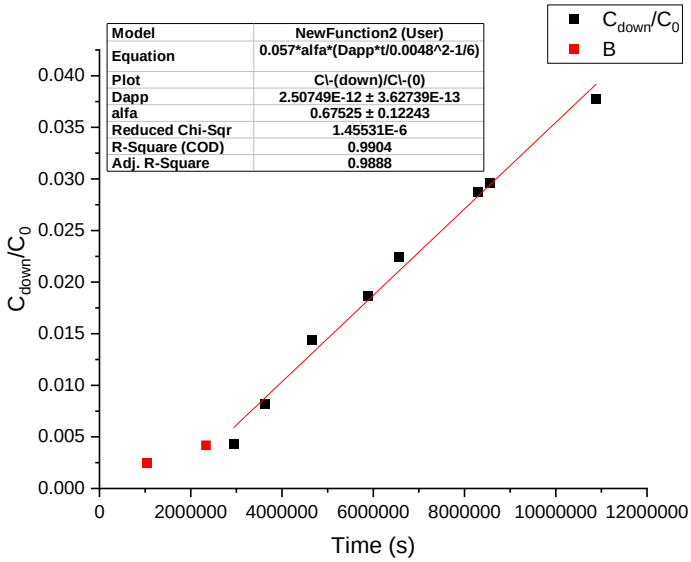


*Figure 2*: *Experimental data and fitting of parameters on the quasi steady-state part of the obtained concentration profile in the downstream reservoir (red dots are not considered in the model).*

Uranium profile in the rock was recorded by synchrotron-radiation µ-XRF. In the first 100 µm of the prepared sample uranium was enriched, however it could not be detected in deeper region along the diffusion axis in the sample (*Figure 3*). At selected positions of the region enriched in uranium, µ-XANES measurements were performed, however beam-induced reduction to U(+IV) was observed.

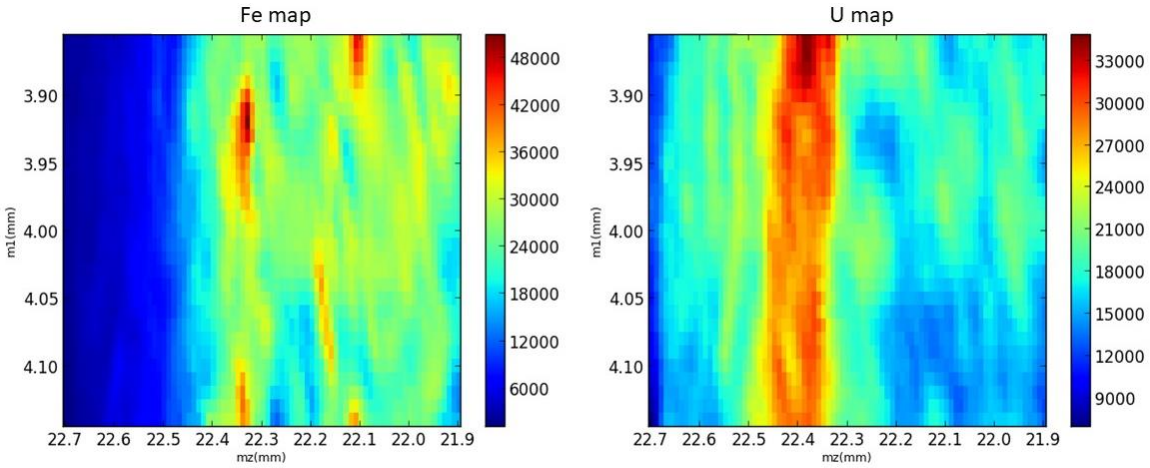


*Figure 3*: *Fe and U elemental maps obtained from the clay section collected from the through-diffusion experiment (Diffusion is from left to right). The elemental distributions were recorded with synchrotron-radiation µ-XRF mapping.*

### Cell 2

In the contrary to Cell 1, no breakthrough was observed even after 190 days. The concentration in the upstream reservoir remained constant during the experiment.

### Cell 3

As breakthrough was not observed after more than 1900 days, the effective diffusion coefficient could be determined based on the uranium profile inside the rock measured with LA-ICP-MS (Lázár et al., 2012). Since the initial concentration of uranyl was high ($2.2 \times 10^{-2}$ mol/L) the experimental data cannot be modelled assuming a constant $\alpha$ value. For the first 1.5 mm increasing $K_d$ (viz. increasing $\alpha$) was assumed up to $K_d$ = 3.26 ($\alpha$=8.8). The increment could be described with a third order polynomial function. After 1.5 mm constant $\alpha$=8.8 fitted the experimental data sufficiently well.

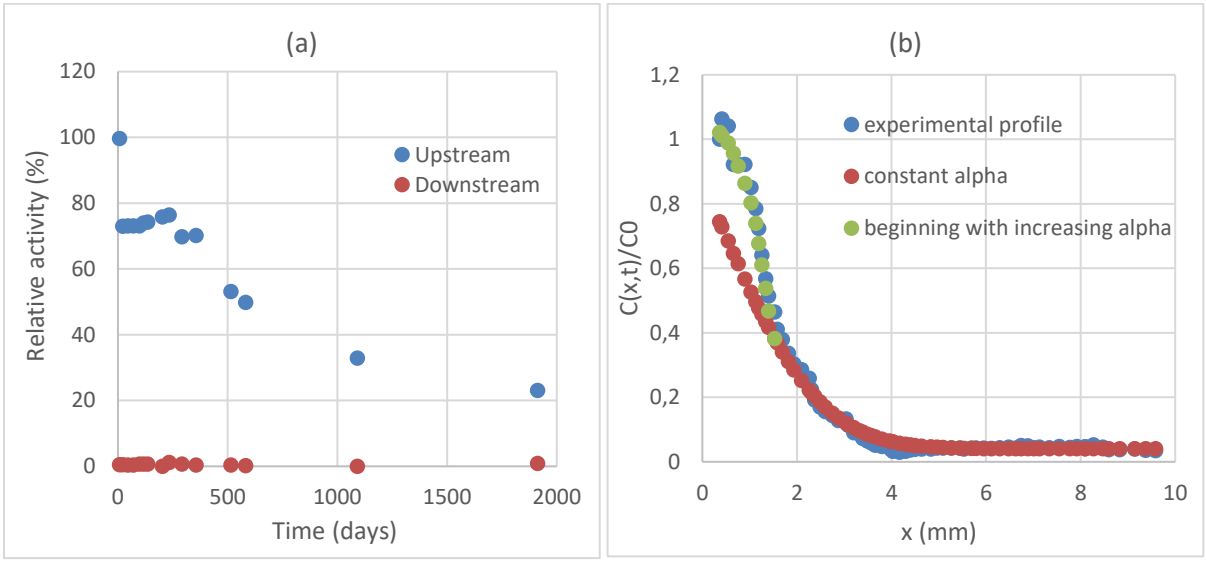


*Figure 4*: *Relative activity change over time in the two reservoirs of Cell 3 (a) and the experimental and modelled diffusion profile in the rock (b). Experimental data are taken from* (Lázár et al., 2012).

The diffusion parameters calculated for Cells 1 and 3 are presented in *Table 1*.

*Table 1*: *Diffusion parameters obtained for Boda Claystone from through diffusion experiments. Available data for Opalinus Clay* (Joseph et al., 2013) *and compacted bentonite in non-saline water under aerobic conditions* (Muurinen et al., 1993) *are also presented for comparison.*

| | **Cell 1 (Boda Claystone)** | **Cell 3 (Boda Claystone)** | **Opalinus Clay** | **Compacted bentonite** |
|---|---|---|---|---|
| $D_e$ **(m²/s)** | $3.7 \times 10^{-12}$ | $8.5 \times 10^{-14}$ | $1.9 \times 10^{-12}$ | $1.9 \times 10^{-12}$ |
| $D_a$ **(m²/s)** | $2.5 \times 10^{-12}$ | $9.7 \times 10^{-15}$ (after 1.5 mm) | $3.1 \times 10^{-14}$ | $6.3 \times 10^{-13}$ |
| $\alpha$ **(-)** | 0.68 | 8.8 (after 1.5 mm) | 61 | |
| $K_d$ **(L/kg)** | 0.24 | 3.3 (after 1.5 mm) | 25 | 3 |
| $\varepsilon_{tot}$ **(-)** | 0.02 | 0.02 | 0.16 | |
| $\rho_{bulk}$**(kg/m³)** | 2700 | 2700 | 2424 | 700 |
| $C_{initial}$ **(mol/L)** | $4 \times 10^{-4}$ | $2.2 \times 10^{-2}$ | $1 \times 10^{-6}$ | $1 \times 10^{-4}$ |

## Discussion

The $\alpha$ value ($\alpha$=0.676) calculated for Cell 1 is rather small even though $K_d$ obtained with batch sorption experiments is below $10^1$ L/kg for BCF rocks at pH=8 around $10^{-4}$ M equilibrium concentration (Marques Fernandes et al., 2015). This $\alpha$ value results in a $K_d$ ($K_d$=0.243, $\varepsilon_{tot}$=0.02) one order of magnitude lower than that of batch sorption experiments. The obtained $D_a = 2.51 \times 10^{-12}$ m$^2$/s value is considered rather high for $UO_2^{2+}$ since the diffusion coefficient of HTO in BCF was measured as $D_e^{HTO} = (1.17 \pm 0.02) \times 10^{-11}$ m$^2$/s (van Loon & Mibus, 2015). The results of Cell 1 are surprising and need to be used carefully since no breakthrough was supposed prior the launch of experiment.

The $D_e = 8.5 \times 10^{-14}$ m$^2$/s obtained from Cell 3 is more than one order of magnitude lower than the one found for Opalinus clay, however the initial concentration in the experiment of Joseph et al. (2013) lays in the concentration range in which $K_d$ reaches its maximum value and can be considered as constant. There is also one order of magnitude difference between the porosity of Boda Claystone and Opalinus Clay. Although the rock capacity factors for Opalinus Clay are nearly seven times higher, the comparison of $D_{app}$ values reveals a difference of only about three times.

## Conclusion

Microanalytical methods such as synchrotron-radiation µ-XRF and LA-ICP-MS revealed high-resolution profiles of U content inside the rocks. The results of the through-diffusion experiment in Cell 1 did not give reasonable diffusion coefficient which could be due to microcracks in the used clay slice (macro cracks were not observed). As the swelling clay content of the studied section of the BAF-2 core of BCF is negligible, the cracks cannot seal themselves. Precipitation was not observed during the experiment, but uranium could be measured only on the part of the clay section which was in contact with the upstream reservoir using synchrotron-radiation µ-XRF. The results from Cell 3 are more reliable and comparable to the one obtained for Opalinus Clay. Even though the high initial concentration a relatively good agreement of model with to the experimental data could be obtained applying varying the rock capacity factor.

## References

Aertsens, M. (2011). *Migration in clay: experiments and models SCK CEN Report SCKCEN-ER-165 (SCK CEN, Mol, Belgium).*

Breitner, D., Osán, J., Fábián, M., Zagyvai, P., Szabó, C., Dähn, R., Marques Fernandes, M., Sajó, I. E., Máthé, Z., & Török, S. (2015). Characteristics of uranium uptake of Boda Claystone Formation as the candidate host rock of high level radioactive waste repository in Hungary. *Environmental Earth Sciences*, *73*(1), 209–219. https://doi.org/10.1007/S12665-014-3413-4

Fedor, F., Máthé, Z., Ács, P., & Koroncz, P. (2019). New results of Boda Claystone research: Genesis, mineralogy, geochemistry, petrophysics. *Geological Society, London, Special Publications*, *482*(1), 75–92.

Gergely, F., Osán, J., Szabó, B. K., & Török, S. (2016). Analytical performance of a versatile laboratory microscopic X-ray fluorescence system for metal uptake studies on argillaceous rocks. *Spectrochimica Acta Part B: Atomic Spectroscopy*, *116*, 75–84.

Joseph, C., Van Loon, L. R., Jakob, A., Steudtner, R., Schmeide, K., Sachs, S., & Bernhard, G. (2013). Diffusion of U(VI) in Opalinus Clay: Influence of temperature and humic acid. *Geochimica et Cosmochimica Acta*, *109*, 74–89. https://doi.org/10.1016/J.GCA.2013.01.027

Lázár, K., Máthé, Z., Megyeri, J., Széles, É., Mácsik, Z., & Suksi, J. (2012). Redox properties of clay minerals and sorption of uranyl species on Boda Claystone. In M. Altmaier, B. Kienzler, L. Duro, M. Grivé, & V. Montoya (Eds.), *KIT Scientific Reports* (Vol. 7626, pp. 231–239).

Lázár, K., Megyeri, J., Mácsik, Z., Széles, É., & Máthé, Z. (2011). Migration of uranyl ions in Boda Claystone samples. In M. Altmaier, B. Kienzler, L. Duro, M. Grivé, & V. Montoya (Eds.), *KIT Scientific Reports* (Vol. 7603, pp. 91–97).

Marques Fernandes, M., Vér, N., & Baeyens, B. (2015). Predicting the uptake of Cs, Co, Ni, Eu, Th and U on argillaceous rocks using sorption models for illite. *Applied Geochemistry*, *59*, 189–199. https://doi.org/10.1016/J.APGEOCHEM.2015.05.006

Mell, P., Megyeri, J., Riess, L., Máthé, Z., Hámos, G., & Lázár, K. (2006). Diffusion of Sr, Cs, Co and I in argillaceous rock as studied by radiotracers. *Journal of Radioanalytical and Nuclear Chemistry*, *268*(2), 411–417. https://doi.org/10.1007/S10967-006-0178-6

Muurinen, A., Ollila, K., & Lehikoinen, J. (1993). Diffusion of uranium in compacted sodium bentonite. *Materials Research Society Symposium Proceedings*, *294*(1), 409–416. https://doi.org/10.1557/PROC-294-409/METRICS

Sámson, M. (ed). (2015). *Final report of borehole BAF-2. (In Hungarian) Manuscript, PURAM, Paks, RHK-N-011/14*.

Shackelford, C. D. (1991). Laboratory diffusion testing for waste disposal — A review. *Journal of Contaminant Hydrology*, *7*(3), 177–217. https://doi.org/10.1016/0169-7722(91)90028-Y

Takeda, M., Nakajima, H., Zhang, M., & Hiratsuka, T. (2008). Laboratory longitudinal diffusion tests: 1. Dimensionless formulations and validity of simplified solutions. *Journal of Contaminant Hydrology*, *97*(3–4), 117–134. https://doi.org/10.1016/J.JCONHYD.2008.01.004

van Loon, L. R., & Mibus, J. (2015). A modified version of Archie's law to estimate effective diffusion coefficients of radionuclides in argillaceous rocks and its application in safety analysis studies. *Applied Geochemistry*, *59*, 85–94. https://doi.org/10.1016/J.APGEOCHEM.2015.04.002

Zizak, I. (2016). The mySpot beamline at BESSY II. *Journal of Large-Scale Research Facilities JLSRF*, *2*, A102–A102. https://doi.org/10.17815/JLSRF-2-113

# 6. Investigation of the diffusion of U(VI) and Am(III) through Opalinus Clay down to ultra trace levels

D. Glückman
*KIT, Karlsruhe, Germany*

*Disclamer: This PhD work was performed in the frame of the iCross project, with partial funding from the German Federal Ministry for Education and Research through the iCross collaborative project under grant agreement 02NUK 053 C, and from the Hemholtz association under grant agreement SO-093. It is provided as an in-kind contribution to the EURAD WP5.*

The abstract of the PhD thesis is provided in this report, for the full text we refer to the PhD thesis:

*"Glückman, D. Investigation of the diffusion of U(VI) and Am(III) through Opalinus Clay down to ultra-trace levels, PhD thesis. Karlsruhe Institute of Technology, Karlsruhe, Germany (2023)".*

## Abstract

Clay rocks are considered as potential host rocks and geoengineered barriers for the disposal of high-level nuclear waste (HLW) in deep geological formations. Although the host rock, geoengineered barriers (e.g., bentonite), and engineered barriers (e.g., waste container) delay groundwater intrusion into the disposal rooms, long-term safety assessments for an HLW repository have to consider water ingress and the consecutive corrosion of containers and waste, resulting in the release of radionuclides. Potentially released actinides, such as uranium (U) and americium (Am), could be transported through the clay matrix of the geoengineered barrier and host rock mainly by diffusion. Actinides are known to exhibit low solubility and to sorb strongly onto clay surfaces under the reducing conditions of a repository. Diffusion experiments at the expected very low actinide concentrations are, thus, difficult to perform due to analytical constraints. Diffusion of U in clay rocks has not been investigated below concentrations of $10^{-4}$ mol/m³ clay. In the case of Am, up to now, no diffusion experiments have been performed in a clay rock, considered suitable as host rock, such as Opalinus Clay (OPA).

This Ph.D. aims at the investigation of the diffusion behaviour of U(VI) and Am(III) down to ultra-trace concentrations (<< $10^{-4}$ mol/m³) in OPA. In particular, potential differences in the diffusion properties of the two investigated actinide elements at ultra-trace concentrations compared to higher concentrations shall be explored.

As part of the investigations, four laboratory-scale diffusion experiments were conducted with samples of OPA, obtained from the Mont Terri underground laboratory (Switzerland) for 20 d, 36 d, 126 d, and 240 d, respectively. Within these experiments, cylindrical OPA samples (length: 10 mm, diameter: 6 mm) were contacted with synthetic pore water (ionic strength: 0.22 mol/L, pH: 7.2) (Gimmi et al., 2014) which was spiked with $1.8\times10^{-11}$ to $3.2\times10^{-9}$ mol/L of $^{233}$U and $9.6\times10^{-13}$ to $3.0\times10^{-9}$ mol/L of $^{243}$Am. After termination of the experiments, the OPA cylinders were segmented via abrasive peeling into thin layers of 20–400 µm. The obtained clay segments were analysed for their $^{233}$U and $^{243}$Am content with accelerator mass spectrometry (AMS), one of the most sensitive analytical techniques for the determination of rare long-lived actinides in environmental samples.

The use of ultra-trace analysis demanded special attention toward actinide tracer background and cross-contamination. Such demands were met by the development of an optimized diffusion setup and sample processing procedure, comprising various preventive measures, in particular the removal of the external surface of the OPA specimens´ sample holder prior to abrasive peeling.

Diffusion profiles of U(VI) and Am(III) were determined down to ≈ $10^{-9}$ mol/m³, which represents an improvement in detection sensitivity for U(VI) by five orders of magnitude compared to a previous study on the U(VI)–OPA system (Joseph et al., 2013). In the case of Am(III), it was the first time that diffusion profiles were determined in OPA. U(VI) showed typical diffusion profiles which were interpreted by applying Fick´s laws. The obtained effective diffusion coefficients were up to ten times higher than previously published

(Joseph et al., 2013). One of the reasons was the present anisotropy of OPA, since diffusion was studied parallel to the clay bedding in the present study in contrast to perpendicular to the bedding in the previous study. No changes in the diffusion behaviour of U(VI) through OPA over a concentration range of $10^{-3}$ mol/m³ to $10^{-9}$ mol/m³ were observed.

The Am profiles were more complex, with a strongly sorbing section (i.e., short diffusion distance) and a "fast runner" section (i.e., long diffusion distance). Such two-part profiles were also observed in diffusion experiments with Eu(III) through OPA in a previous study (PSI, 2019). Eu(III) is considered to behave analogously to Am(III). µCT (X-ray microtomography) investigations of the OPA diffusion samples revealed the presence of micro-fractures 40–80 µm wide, potentially being responsible for the observation of an Am fraction with a higher diffusion length. Modelling of the two parts of the Am profile with a 1D pore diffusion model was possible hypothesizing the presence of two migrating Am species dominating the mobile phase. One was assumed to be the aqueous species $[Am(CO_3)]^+$. This cationic species undergoes strong retardation by negatively charged clay mineral surfaces, resulting in slow migration and causing the observed Am short diffusion profile. The other species is believed to be colloidal, present at approximately 10 times lower concentration compared to the aqueous species, featured by poor retention and faster migration through the micro-fractures in the OPA cylinder.

## REFERENCES

Gimmi, T., Leupin, O. X., Eikenberg, J., Glaus, M. A., Loon, L. R. Van, Waber, H. N., Wersin, P., Wang, H. A. O., Grolimund, D., Borca, C. N., Dewonck, S. & Wittebroodt, C. Anisotropic diffusion at the field scale in a 4-year multi-tracer diffusion and retention experiment - I: Insights from the experimental data. Geochim. Cosmochim. Acta 125, 373–393 (2014).

Joseph, C., Van Loon, L. R., Jakob, A., Steudtner, R., Schmeide, K., Sachs, S. & Bernhard, G. Diffusion of U(VI) in Opalinus Clay: Influence of temperature and humic acid. Geochim. Cosmochim. Acta 109, 74–89 (2013).

Paul-Scherrer-Institut. PSI Progress Report 2019. https://www.psi.ch/de/luc/annual-reports (2019)

# 7. Achievements with respect to project objectives - Conclusions

*New/missing data available for sorption models (e.g. surface complexation constants)*

Sorption data obtained for the strongly sorbing tracers were merely targeted to provide quantitative data on the level of sorption under specific conditions rather than to serve as input for sorption model development.

A combination of macroscopic experiments and in situ ATR FTIR was used to study the (co-)sorption mechanisms of phosphate ions and trace levels of uranyl ions at illite–solution interface. All the macroscopic data reported here pointed at several sorption mechanisms / surface sites contributing to the uptake of uranyl ions by NaIdP and depending on key parameters such as pH, U concentration, clay-to-solution ratio and carbonate or phosphate ligand concentration. In particular, data indicated that a low amount of high affinity sorption sites (<0.02 sites.nm$^{-2}$) existing at NaIdP edge platelets can strongly interact with U and become progressively saturated, while low affinity surface sites are increasingly involved in U sorption, when increasing U concentration (1-10 µM) or decreasing clay-to-solution ratio (1-3 g.L$^{-1}$) in experiment. It was also shown that presence of carbonate ligands at high pH has no significant effect on macroscopic sorption of U, while formation of uranyl carbonate surface complexes is suggested by ATR-FTIR studies. In contrast, phosphate ligands enhance the sorption of U(VI) at acidic pH onto NaIdP and, conversely, the uptake of phosphate ions by the clay surface is promoted by an increase of the U concentration in sorption experiment. Macroscopic and EM data highlighted formation of several types of uranyl phosphate species imparting negative charges to the clay surface and / or several types of sorption sites, with the mechanisms of U-P co-sorption remaining highly reversible. ATR FTIR spectroscopy provided evidence that uranyl ions and phosphate ions were (co)sorbed at acidic pH mainly via the formation of three types of inner-sphere uranyl phosphate surface complexes: a surface complex forming rapidly at high affinity surface sites, an additional complex forming at low affinity sites in increasing amounts with U concentration, -with these two complexes competing successfully against formation of inner sphere phosphate surface complexes-, and, finally, an “autunite-like” uranyl phosphate surface complex (e.g., such as a polynuclear complex) and appearing at a long reaction time (>1 day) and at high U concentration (10 µM).

*Transferability of batch sorption data to compact system*

Europium adsorption onto COx was shown to be strong ($R_d$ > 10$^4$ L kg$^{-1}$) at trace concentrations. Furthermore, the three $R_d$ values obtained for the compact spiked COx samples are consistent, within the experimental uncertainties, with those deduced from conventional batch experiments carried out in dispersed state. Similar results had already been obtained for intact COx with iodine (I) cesium (Cs) and nickel (Ni), thus suggesting that this trend seems *a priori* applicable to the retention of metal ions by COx clay rock. It is furthermore concluded that the clay fraction effectively governs Eu adsorption. This finding has been indirectly confirmed by modelling the data; in using a bottom-up approach along with the assumption that the clay fraction is responsible for element adsorption on COx, it was possible to explain experimental adsorption data in the conditions chosen for the percolation experiments, during which both strong and weak sites contribute to Eu adsorption.

Through diffusion experiments of $UO_2^{2+}$ in BCF provided reasonable effective diffusion coefficients and rock capacity factors in line with batch sorption results.

*Transferability of data from model systems to complex systems*

Eu retention experiments on compacted COx were successfully modelled using the bottom-up approach by considering that sorption was related to the clay fraction only.

Also, the sorption of U(IV/VI) on COx was successfully modelled using a bottom up approach and the 2SPNE SC/CE model approach with illite and montmorillonite as reactive phases. The model was applied to explain the behaviour of naturally occurring uranium.

*Adequate description of sorption competition*

A combination of macroscopic experiments and in situ ATR FTIR was used to study the (co)sorption mechanisms of phosphate ions and trace levels of uranyl ions at illite–solution interface. All the macroscopic data reported here pointed at several sorption mechanisms / surface sites contributing to the uptake of uranyl ions by NaIdP and depending on key parameters such as pH, U concentration, clay-to-solution ratio and carbonate or phosphate ligand concentration.

In peculiar, data indicated that a low amount of high affinity sorption sites (<0.02 sites.nm$^{-2}$) existing at NaIdP edge platelets can strongly interact with U and become progressively saturated, while low affinity surface sites are increasingly involved in U sorption, when increasing U concentration (1-10 µM) or decreasing clay-to-solution ratio (1-3 g.L$^{-1}$) in experiment. It was also shown that presence of carbonate ligands at high pH has no significant effect on macroscopic sorption of U, while formation of uranyl carbonate surface complexes is suggested by ATR-FTIR studies.

In contrast, phosphate ligands enhance the sorption of U(VI) at acidic pH onto NaIdP and, conversely, the uptake of phosphate ions by the clay surface is promoted by an increase of the U concentration in sorption experiment. Macroscopic and EM data highlighted formation of several types of uranyl phosphate species imparting negative charges to the clay surface and / or several types of sorption sites, with the mechanisms of U-P co-sorption remaining highly reversible. ATR FTIR spectroscopy provided evidence that uranyl ions and phosphate ions were (co)sorbed at acidic pH mainly via the formation of three types of inner-sphere uranyl phosphate surface complexes: a surface complex forming rapidly at high affinity surface sites, an additional complex forming at low affinity sites in increasing amounts with U concentration, -with these two complexes competing successfully against formation of inner sphere phosphate surface complexes-, and, finally, an “autunite-like” uranyl phosphate surface complex (e.g., such as a polynuclear complex) and appearing at a long reaction time (>1 day) and at high U concentration (10 µM).

*State-of-the-art spectroscopic, diffractometric and microscopic techniques towards system understanding of irreversible uptake processes*

A combination of macroscopic experiments and in situ ATR FTIR was used to study the (co)sorption mechanisms of phosphate ions and trace levels of uranyl ions at illite–solution interface. All the macroscopic data reported here pointed at several sorption mechanisms / surface sites contributing to the uptake of uranyl ions by NaIdP and depending on key parameters such as pH, U concentration, clay-to-solution ratio and carbonate or phosphate ligand concentration. The information on phosphate surface speciation provided by this study is useful for better understanding the surface reactivity of clays in natural systems. The data also help providing basic knowledge for further studies of complex ternary systems of radionuclide-phosphate-clay-solution.

*Description of transport experiments based on mechanistic understanding (anion exclusion, surface diffusion, saturation degree, pore characteristics,…)*

Transport experiments conducted with the strongly sorbing tracers did not provide adequate data to be used in such a way that we can mechanistically understand their transport behaviour.

*Advanced spectroscopy methods for better understanding of the transport behaviour*

The feasibility of a methodology to determine Pu(IV) diffusion profiles in OPA based on TOF-SIMS was performed. Unfortunately, no diffusion profile could be observed yet, most probably due to the short in-diffusion time and strongly-sorbing characteristic of the employed Pu(IV) species.

Microanalytical methods such as synchrotron-radiation µ-XRF and LA-ICP-MS revealed high-resolution profiles of U content inside BCF rocks allowing an appropriate modelling of diffusion parameters.

Accelerated Mass Spectroscopy (AMS) was successfully used to detect ultra traces of Am and U allowing to study their diffusion behaviour in Opalinus Clay. Diffusion profiles of U(VI) and Am(III) were determined down to ≈ $10^{-9}$ mol/m³, which represents an improvement in detection sensitivity for U(VI) by five orders of magnitude compared to a previous study on the U(VI)–OPA system. The effective diffusion coefficients measured in the present study are in rather good agreement with those earlier measured at higher U(VI) concentrations. A large part of the seeming discrepancy can be explained by anisotropy effects related to the direction of the diffusion in the experiments respective to the bedding orientation of the clay samples. In the case of Am(III), it was the first time that diffusion profiles were determined in OPA.

# Chapter 5: Influence of geometry and saturation degree on radionuclide mobility in clay

To study the influence of the geometry and saturation degree on the mobility of radionuclides in clay systems, 2 teams CEA Saclay (Paris, France) and IC2MP (Poitiers, France) joined forces.

## 1. Influence of geometry and saturation degree on radionuclide mobility in clay

S. Savoye, S. Lefevre
*Université Paris-Saclay, CEA, Paris, France*

E. Ferrage, F. Hubert, E. Tertre
*IC2MP, Poitiers, France*

## Abstract

Due to their high sorption properties and very low permeability, clay-rich porous media are envisaged as barriers against contaminants spreading in radioactive waste disposal facilities. In this situation, the transfer of radionuclides is thus limited to the very slow process of diffusion that is strongly dependent on the types of clay media. In the French Cigéo project of deep geological disposal in the Callovian-Oxfordian argillaceous formation, recent calculations indicate that the generation of hydrogen due to the corrosion of canisters may partially dehydrate clayey host rocks and engineered barriers (including clay-based materials) for more than 100 000 years, and thus may change the confinement properties of these materials.

This work aims to experimentally investigate the effect of water saturation on the diffusion of water and solutes through porous media made with different clay minerals considering an increasing complexity, i.e., kaolinite, a non-swelling and non-charged clay mineral, illite, a non-swelling clay mineral with charged surfaces, and vermiculite, a swelling clay mineral with charged surfaces and a double porosity: (i) an interparticle porosity and (ii) an interlayer porosity where water and solutes mobility is mainly controlled by surface effect. For that purpose, through-diffusion experiments were performed with water tracers (HTO and HDO), anionic tracers ($^{36}Cl^-$ and $^{125}I^-$), and cationic tracer ($^{22}Na^+$) into compacted clay materials to have similar interparticle porosity of 25-29%. The osmosis method was used to impose suction at 1.9 MPa and 9 MPa and to create partially water-saturated conditions throughout the duration of the diffusion tests.

For water-saturated conditions, results confirm the influence of surface charge on ion diffusivity (i.e., effective diffusion coefficient over diffusion coefficient in bulk, $D_e/D_0$). In porous media made with no-charged kaolinite, water and ions behave in the same manner, while with media made with the two charged clay materials an enhanced diffusion for $^{22}Na^+$ and a reduction of diffusive rates for anionic species compared to those of water tracers have been measured. When the clayey materials are partially water-saturated, each type of tracer shows distinct evolution of their diffusivity. We observe a relatively low decrease in the extent of the diffusivity values for water tracers compared to solutes, suggesting that the contribution of water diffusing in the gaseous phase has to be considered in addition to that in the liquid phase. For cationic tracer, i.e., $^{22}Na^+$, diffusivity values show a significant decrease in porous media made with charged clayey materials when dehydrating, associated with a drop of the distribution ratio, $K_D$, suggesting a more limited access to charged surfaces. Lastly, partial dehydration would magnify the effect of anionic exclusion with a strong drop in iodide diffusivity.

## Introduction

Owing to their high retention capacity and their very low permeability, clay-rich media are widely used as barriers against contaminant spreading in many fields. Disposal facilities for high- and mid-level long-lived radioactive waste, in many proposed designs, rely on swelling clay materials as engineered barriers, (Bucher and Müller-Vonmoos, 1989; Landais, 2006) and some disposal facilities should also be directly sited in deep argillaceous formations (Andra, 2005, 2016; Hendry et al., 2015; Rao et al., 2021). Liners

used in subsurface waste landfills are usually made of clay materials (Foose et al., 2002; Katsumi et al., 2001). In the geological storage of $CO_2$ in saline aquifers or depleted oil/gas reservoirs, clay layers serve also as caprocks to prevent any $CO_2$ leakage (Berthe et al., 2011).

In all of these cases, diffusion is the main process responsible for the transport of water and solutes over geological timescales (Descostes et al., 2008; Motellier et al., 2007; Van Loon et al., 2004). In existing studies dealing with the determination of diffusive parameters within these clay-rich media, water tracers, especially tritiated or deuterated water (HTO/HDO), are generally considered as reference tracer for diffusion (Melkior et al., 2009; Tertre et al., 2018). Once the effective diffusion coefficient ($D_e$) of HTO/HDO is acquired, the diffusion rate of anion and cation species can be inferred by taking into account the electrostatic effects induced by the presence of charges at the clay surface. Electrostatic effects are responsible for the phenomenon of surface diffusion for cation species (Lehikoinen et al., 1995; Savoye et al., 2015) and the phenomenon of anion exclusion for anion species (Gvirtzman and Gorelick, 1991; Tournassat and Steefel, 2019; Van Loon et al., 2007).

Most of the diffusion data found in literature are relative to full water saturation conditions (see Appelo and Wersin (2007), Bourg and Tournassat (2015) and Charlet et al. (2017), among others). However, there are many situations wherein these clay-rich porous media can be partially water-saturated. The generation of hydrogen due to the corrosion of canisters may dehydrate host rocks and engineered barriers made of swelling clay materials for more than 100,000 years in deep geological waste disposal facilities (Marschall et al., 2005; Andra, 2016). Additionally, clay liners placed above the groundwater table are generally water-unsaturated, especially for landfills located in arid environments (Katsumi et al., 2001). Due to the $CO_2$ intrusion into caprocks in carbon geosequestration, caprocks can also be partially water-saturated (Minardi et al., 2021; Xiao et al., 2020). In these cases, understanding and parameterizing the diffusion processes under partially saturated media is required to evaluate the performance of the clay system and support engineering purposes. This is a challenging task, as illustrated by the fact that only a few studies have been reported in the literature. For instance, Nunn et al. (2018) presented a new method using X-ray radiography and iodide tracers for quantifying the degree of partial water saturation of shale samples and measuring $D_e$. They showed that the iodide $D_e$ value decreased by around 22% when saturation decreased from 100% to 93%.

Savoye et al. developed an original approach to perform diffusion experiments under partially saturated conditions in illite-sand mixtures (Savoye et al., 2014) and in Callovo-Oxfordien claystones, envisaged to host a French disposal facility for high- and mid-level long-lived radioactive waste (Savoye et al., 2017, 2012, 2010). In these studies, the osmotic method was used to control the partial saturated conditions of the clayey samples over the duration of diffusion experiments. They observed for Callovo-Oxfordien claystones a sharp drop in the $D_e$ values for HTO, $^{125}I^-$ and $^{22}Na^+$ by factors of 6, 50 and 17, respectively, under conditions of 81% water saturation compared to full saturation conditions. The strong decrease in $D_e$ for iodide was explained by the anion exclusion phenomenon that restricted iodide to the largest pores where dehydration was more pronounced. Nevertheless, the distinct behaviour of $D_e$ evolution for HTO and sodium remained to be understood. Two different processes for which their relative contribution requires further investigation were proposed. On the one hand, the extent of surface diffusion may be attenuated when dehydration occurs in claystones, reducing the enhanced diffusion phenomenon for cation species (Savoye et al., 2012). On the other hand, in addition to HTO diffusing in the liquid phase, HTO diffusing in vapor form may contribute to the relatively high (compared to sodium) HTO diffusive rate, even at 81% water saturation (Savoye et al., 2017). This latter process was also proposed by Smiles et al. (1995), and more recently by Maples et al. (2013) to explain the anomalously widespread distribution of HTO in layers adjacent to low-level radioactive waste burial facilities. Then, even though surface effect can be enhanced when water-saturation decreases (Churakov, 2013; Le Crom et al., 2022), the evolution of enhanced diffusion phenomenon for cation species when dehydrating is still an open question.

Therefore, the present work aims to experimentally investigate the effect of water saturation on the diffusion of water and solutes through porous media made with different clay minerals considering an increasing complexity, i.e., kaolinite, illite, and vermiculite. Kaolinite clay mineral is a non-swelling and non-charged clay mineral and diffusion performed in a porous medium made with these type of particles only takes place

in the interparticle porosity. Illite is a non-swelling clay mineral with charged surfaces, which influence aqueous species mobility in the interparticle porosity. Finally, swelling clay mineral like vermiculite has surface charges and porous medium made with these particles present a double porosity: (i) an interparticle porosity and (ii) an interlayer porosity where water and solutes mobility is mainly controlled by surface effect. For that purpose, through-diffusion experiments were performed with water tracers (HTO and HDO), anionic tracers ($^{36}Cl^-$ and $^{125}I^-$), and cationic tracer ($^{22}Na^+$) into compacted clay materials to have similar interparticle porosity of 25-29%. The osmosis method was used to impose suction at 1.9 MPa and 9 MPa to create partially water-saturated conditions throughout the duration of the through-diffusion experiments.

## Materials and Methods

### Materials and sample preparation.

The kaolinite sample used in this study is the KGa-2 kaolinite, which was originally sourced by the University of Western Australia from the Source Clay Repository of the Clay Mineral Society. KGa-2 kaolinite has an average particle size of approximately 0.5 µm (Hassan et al., 2006), a specific area of 10.05±0.02 $m^2/g$ (BET $N_2$ method) and a corresponding CEC of 2.0 meq/100 g (Au et al., 2015). Its structural formula is $[(Al_{3.80}Ti_{0.13}Fe^{3+}_{0.07})(Si_{3.84}Al_{0.16})O_5(OH_4)]$(Mermut, 2001). The mineralogy of KGa-2 consists of approximately 96 wt% kaolinite, 3 wt% anatase, and 1 wt% crandallite with trace amounts of mica and/or illite (Chipera, 2001). The KGa-2 used in our study is Na-saturated, and the preparation procedure is detailed in Dabat et al. (2020). Illite and vermiculite samples correspond to the 0.1-0.2 µm size fractions of illite du Puy (Asaad et al., 2022) and Santa Olalla vermiculite (Reinholdt et al., 2013), respectively. All samples were Na-saturated (Reinholdt et al., 2013). Note that previous studies have shown a similar aspect ratio (i.e., ratio between mean height and diameter of particles) around 0.1 for these three types of clay minerals (Asaad et al., 2022; Reinholdt et al., 2013; Hassan et al., 2006).

The diffusion experiments under partially water-saturated conditions were performed with a through-diffusion set-up adapted from that used by Tertre et al. (2018). Three 10-mm-thick samples were directly prepared in the diffusion cells by compacting clay powder in a body cell with a 9.49 mm inner diameter. The total porosity of the sample ($\varepsilon_{tot.}$) was evaluated according to the following equation:

$$\varepsilon_{tot.} = 1 - \frac{\rho_d}{\rho_s} \quad (1.)$$

where $\rho_s$ denotes the measured grain density of the sample: 2 600 $kg.m^{-3}$ (Hassan et al., 2006 for kaolinite, 2 700 $kg.m^{-3}$ (Asaad et al., 2021) for vermiculite and 2 800 $kg.m^{-3}$ for illite (Asaad et al., 2022); $\rho_d$ is the dried bulk density. In our study, kaolinite and illite samples were compacted at $\rho_d$ allowing to have samples displaying a total porosity $\varepsilon_{tot.}$ of 25 (± 2) % while vermiculite was compacted at a bulk dried density allowing to have a $\varepsilon_{tot.}$ of 50 (± 2) %. Note that for Na-kaolinite and Na-illite, only the interparticle porosity ($\varepsilon_{interp.}$) is accessible by the water tracer, resulting in $\varepsilon_{tot.} = \varepsilon_{interp.}$, whereas Na-vermiculite exhibits both $\varepsilon_{interp.}$ and interlayer porosity ($\varepsilon_{interl.}$). By considering the difference in the c* parameter value between dehydrated layers at 10 Å (Gieseking, 1975) and fully water saturated layers at 14.86 Å (Faurel, 2012), the interlayer volume corresponds approximately to 1/3 of the particle thickness in water-saturated conditions. Consequently, the proportion of the $\varepsilon_{interp.}$ vs. $\varepsilon_{interl.}$ porosities for Na-vermiculite can be calculated for such conditions by using the following relation:

$$\varepsilon_{tot.} = \varepsilon_{interp.} + \varepsilon_{interl.} = \varepsilon_{interp.} + (1- \varepsilon_{interp.})/3 \quad (2)$$

For Na-vermiculite investigated here $\varepsilon_{interp.}$ and $\varepsilon_{interl.}$ were equivalent and equal to 0.25.

Moreover, the volumetric moisture content, $\theta$, was evaluated by using the following expression :

$$\theta = \frac{\omega \times \rho_s}{(1-\omega) \times \rho_w + \omega \times \rho_s} \quad (3)$$

where $\omega$ is the water content of the sample, and $\rho_w$ is the density of the pore water (assumed to be 1000 kg $m^{-3}$). The saturation degree ($S_w$) was further calculated as the ratio of volumetric water content to the total porosity:

$$S_w = \frac{\theta}{\varepsilon_{tot.}} \quad (4)$$

### Procedure for setting saturation and petrophysical measurements.

Different degrees of water saturation for kaolinite, illite and vermiculite samples were achieved via the osmosis method. In this method, a solution concentrated in large-size molecules of polyethylene glycol (PEG) and a type of semipermeable membrane (Spectra por 3500 Da, Spectrum laboratories), which is permeable to all solutes except PEG, were applied. The membranes were installed on both sides of the clayey sample to separate the clay sample from the infiltrating solutions, some of which were PEG-rich. The semipermeable membranes prevent the PEG molecules from entering the sample cell, thus inducing a controlled difference in PEG concentration between the clay pore solution and that in the reservoir chambers. The difference in PEG concentration triggers a suction process that prevents the solution from fully infiltrating the dry clay sample and hence, keeps it in a partially saturated state throughout the duration of the diffusion experiments (more details of the method can be found in Savoye et al. (2010)). Note that the final value of the degree of water saturation for samples depends on the PEG concentration in the infiltrating solution, as shown by Delage and Cui (2008). In our study, suction values of 0 MPa, 1.9 MPa and 9 MPa were achieved by using solutions with PEG concentrations of 0, 0.42 and 0.95 g PEG/g water, respectively.

The hydric procedure lasted approximately 30 days, which is the same duration as that mentioned by Savoye et al. (2014, 2010) for illite/sand and Callovo-Oxfordian claystone samples. For the preparation of solutions, PEG 6000 (Merck, Germany) was added to NaCl 100 mM solutions beforehand, prepared with ultrapure deionized water (18 MΩ $cm^{-1}$) and commercial NaCl salts (American Chemical Society (ACS)) to obtain the targeted PEG concentrations. A 24-hour stirring was necessary for the total dissolution of PEG pills and their homogenization with NaCl solutions.

To determine the values of the degree of water saturation for the samples as a function of imposed suctions, samples were weighed before and after oven-heating at 105 °C. The mass loss during this heating process over the total dry mass gives the water content of the sample. This weight measurement work was performed after the completion of through-diffusion tests and dismantlement of the diffusion cells.

### Through-diffusion experiment.

After the one-month hydric procedure, diffusion cells were connected to upstream and downstream reservoirs. The upstream reservoir was filled with 25 g of 100 mM NaCl (without considering PEG mass) solution spiked with specific tracers, i.e., HDO, HTO (labeled CERCA ELSB45 n◦760,112/4), $^{22}Na^+$ (labeled ELSB45 80693/1), $^{125}I^-$ (labeled ELSB50 82731/1) or $^{36}Cl^-$ (labeled E&Z 1760–100-1) used to determine diffusion parameters for water, cation and anion tracers. The initial activities injected in upstream solution for HTO, $^{36}Cl^-$, $^{125}I^-$ and $^{22}Na^+$ were resp. 0.7 kBq/g, 0.5 kBq/g, 0.8 kBq/g and 0.2 kBq/g (without considering PEG mass). In the case of $^{125}I^-$ diffusion, the stable iodide was added to reach a concentration of $10^{-3}$ M in the upstream reservoir to avoid any strong uptake of iodine, as previously observed by Bazer-Bachi et al. (2006) for lower concentrations (<$10^{-4}$ M). Moreover, thiosulfate at a concentration of $5\times10^{-4}$ M was also added to both reservoirs to ensure that iodide remained in the same redox state (Descostes et al., 2008).

The solution in the downstream reservoir was systematically replaced to maintain the tracer concentration as low as reasonably possible, i.e., less than 3% of the value measured in the upstream reservoir. The activity or concentration of tracers in downstream samples was measured via different techniques depending on the type of tracer. The concentration of HDO in solution was measured by a liquid water isotope analyser (LWIA DLT-100 from Los Gatos Research) based on infrared spectroscopy. Activity for HTO and $^{36}Cl^-$ was measured by a Packard Tri-Carb 2500 liquid scintillation recorder, while activity for $^{125}I^-$ and $^{22}Na^+$ was measured using a gamma counter (Packard 1480 WIZARD).

For the diffusion cell at full water saturation, HTO and $^{36}Cl^-$ were first injected at the same time. Afterward, solutions in both reservoirs were replaced with fresh synthetic water without tracer for the starting out-diffusion stage lasting up to 3 weeks. A through-diffusion test with $^{125}I^-$ was launched as soon as the HTO out-diffusion flux was negligible, i.e., for a residual HTO activity close to the detection limit (0.5 Bq). Then, $^{22}Na^+$ was immediately injected after the end of $^{125}I^-$ through-diffusion since their spectral peaks do not overlap in the measurement of the gamma counter. Note that for the two anion tracers, $^{125}I^-$ was preferred to $^{36}Cl^-$ because of the lack of waste management channels for organic solutions containing long-lived radionuclides, such as $^{36}Cl^-$. For the two cells under partial-water saturation conditions, HDO was first injected, followed by $^{125}I^-$. Then, a $^{125}I^-$ out-diffusion step was carried out to allow the injection of HTO and $^{22}Na^+$ for the last stage, and the HTO measurement was sensitive to the presence of $^{125}I^-$.

### Treatment of experimental results.

The analysis of through-diffusion experiments is based on Fick's second law for one-dimensional transport. Planar through-diffusion was assumed for all tracers, and their diffusion was considered independent; that is, no chemical interactions existed between them. The following form is hence applicable:

$$\frac{\partial C}{\partial t} = \frac{D_e}{\alpha}\frac{\partial^2 C}{\partial x^2} = \frac{D_e}{\theta_{diff}^t + \rho_d R_d}\frac{\partial^2 C}{\partial x^2} = \frac{D_e}{R\theta_{diff}^t}\frac{\partial^2 C}{\partial x^2} \tag{5}$$

where $C$ is the concentration or activity per volume unit in the solute phase (mol $m^{-3}$ of synthetic pore water without PEG or Bq $m^{-3}$); t is the time (s); $D_e$ denotes the effective coefficient diffusion ($m^2\ s^{-1}$), and $\alpha$ is the rock capacity factor:

$$\alpha = \theta_{diff}^t + \rho_d R_d \tag{6}$$

where $\theta_{diff}^t$ is the volumetric water content accessible to the diffusing tracer (-); $\rho_d$ is the dry bulk density (kg $m^{-3}$), and $R_d$ is the distribution ratio ($m^3\ kg^{-3}$). The capacity factor can be written as $R\theta_{diff}^t$ with $R$ being the retardation factor:

$$R = 1 + \frac{\rho_d R_d}{\theta_{diff}^t} \tag{7}$$

According to van Brakel and Heertjes (1974) and Grathwohl (1998), $D_e$ can be expressed as a function of $\theta_{diff}^t$ as follows:

$$D_e = D_p\theta_{diff}^t = \frac{\delta}{\tau^2}D_0\theta_{diff}^t = \frac{1}{G}D_0\theta_{diff}^t \tag{8}$$

where $D_p$ denotes the pore diffusion coefficient ($m^2\ s^{-1}$); $D_0$ denotes the self-diffusion coefficient in water ($m^2\ s^{-1}$); $\delta$ represents the constrictivity factor (-), and $\tau$ is the tortuosity factor (-). Tortuosity and constrictivity are purely geometric factors that, compared with a specific cross-section in free water, lengthen the effective diffusion pathway and reduce the overall diffusion cross-section, respectively (van Brakel and Heertjes, 1974). $G$ denotes the geometric factor (-).

The initial and boundary conditions are:

$C(x,t) = 0, \qquad x > 0, t = 0$

$C(x,t) = C_0, \qquad x = 0, t > 0$

$C(x,t) = 0, \qquad x = L, t > 0$

where $L$ is the sample thickness (m).

Fully analytical solutions of Equation 5 are given by Cranck (1975). The cumulative activity $A_{diff}^t$ can be written as:

$$A_{diff}^t = S \cdot L \cdot A_0 \cdot \left[\frac{D_e t}{L^2} - \frac{\theta_{diff}^t}{6} - \frac{2\theta_{diff}^t}{\pi^2}\sum_{n=1}^{\infty}\frac{(-1)^2}{n^2}exp\left\{-\frac{D_e n^2\pi^2 t}{L^2\theta_{diff}^t}\right\}\right] \tag{9}$$

and the incoming instantaneous flux of tracer $F_i$ in the downstream reservoir is:

$$F_i = \frac{D_e A_0}{L}\left[1 + 2\sum_{n=1}^{\infty}(-1)^2 exp\left\{-\frac{D_e n^2 \pi^2 t}{L^2 \theta_{diff}^t}\right\}\right] \quad (10)$$

where *S* is the surface of the sample perpendicular to the diffusion flux ($m^2$).

The analysis of the results was performed by least squares fitting of the model to the results of the incoming instantaneous flux in the downstream reservoir using Equation 10 (Savoye et al., 2015)

## Results : HTO, Na and I diffusive rates at different water saturation degrees

The normalized diffusive flux (in $m \cdot s^{-1}$) for water tracers (HDO or/and HTO), anion tracers (for $^{125}I^-$ and $^{36}Cl^-$) and cation tracers (for $^{22}Na^+$) under the three levels of suction are reported for kaolinite in Figure 1, for illite in Figure 2, and for vermiculite in Figure 3. Normalized flux was calculated for each tracer using the ratio of instantaneous flux in $Bq \cdot m^{-2}s^{-1}$ (or $mol \cdot m^{-2}s^{-1}$ for HDO) over the concentration in the upstream reservoir in $Bq \cdot m^{-3}$ or $mol \cdot m^{-3}$. The corresponding values of effective diffusion coefficient, $D_e$, estimated from Fick's law are reported in Table 1, as well as values of the rock capacity factor, $\alpha$ and those of the distribution ratio, $R_d$.

### In weakly-charged clay: kaolinite

At full-water-saturation, $D_e$ values of the three tracers are very similar, owing to the very weak charge of the material that cannot induce any significant electrical exclusion for anion or enhanced diffusion for cation. As expected, a clear decrease of the diffusive rates was observed for all the tracers when suction increases in compacted kaolinite. For example, diffusive flux rates decrease for suction values from 0 to 9 MPa by factors of 6.5, 18 and 35 for HTO, $^{125}I^-$ and $^{22}Na^+$, respectively.

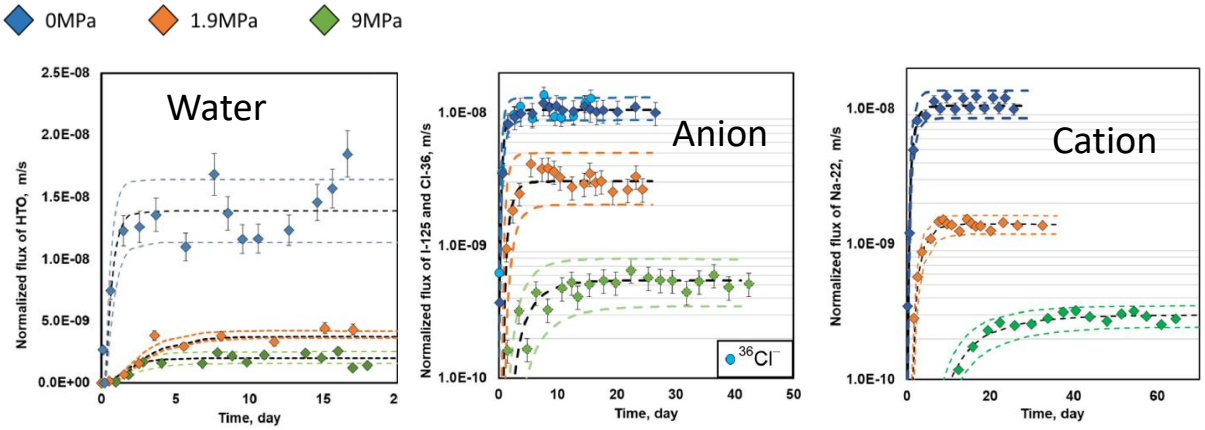


*Figure 1: Normalized diffusive fluxes for HDO, $^{125}I^-$/$^{36}Cl^-$ and $^{22}Na^+$ through compacted kaolinite sample, at three suction levels of resp. 0, 1.9 and 9 MPa. Note that $^{36}Cl^-$ was only used at 0 MPa (at full-saturation).*

### In a charged clay: illite

At full-water-saturation, contrary to the case of kaolinite, each species have distinct diffusive flux in illite due to the effect of surface charge with $D_e$ values for anion 5 times lower than for water tracer and a $D_e$ value for $^{22}Na^+$ 3 times higher than that of water tracer. Moreover, Figure 2 shows a clear effect of water saturation even at only 94% of $S_w$ on diffusive fluxes for the three tracers. Diffusive rates decrease for suction values from 0 to 9 MPa by factors of 8, 11 and 35 for HTO, $^{125}I^-$/$^{36}Cl^-$ and $^{22}Na^+$, respectively. Moreover, a distinct diffusive behaviour of $^{22}Na^+$ is observed compared to that of water and anion associated to a drop of the $R_D$ values (@100%, $R_D$ ~ 2.2 mL/g vs @94 & 88%, $R_D$ ~1,5 mL/g).

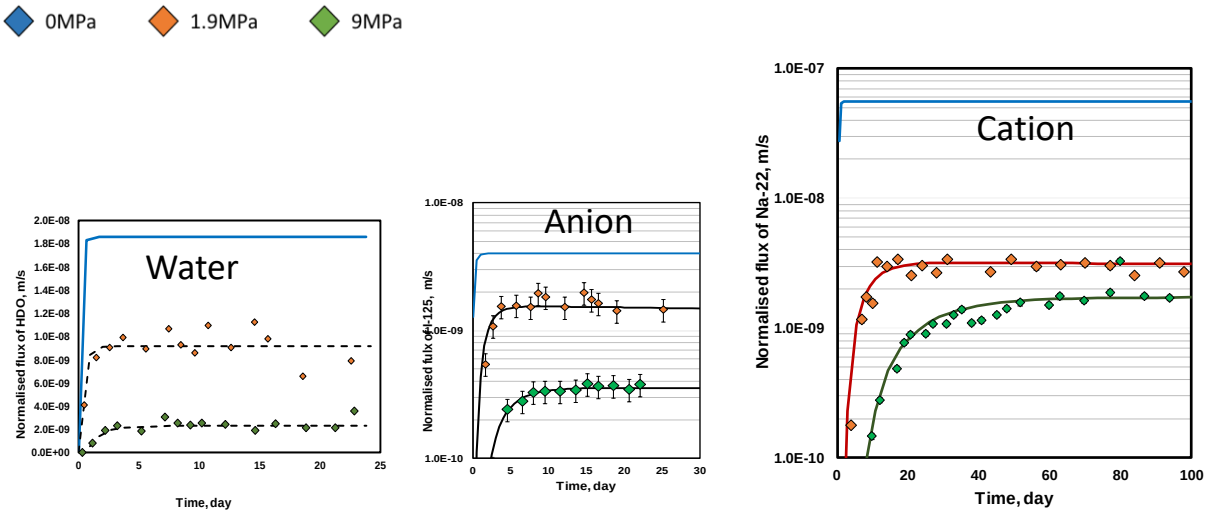


*Figure 2: Normalized diffusive fluxes for HTO, $^{125}I^-$ and $^{22}Na^+$ through compacted illite sample at three suction levels of resp. 0, 1.9 and 9 MPa. Note that data at full-saturation were obtained by Glaus et al. (2010) for HTO, $^{36}Cl^-$ and $^{22}Na^+$ in illite compacted at a similar dry density and at the same ionic strength.*

## In charged clay with a double porosity: vermiculite

At full water-saturation, the occurrence of an interlayer porosity in vermiculite allows $^{22}Na^+$ to diffuse at a very high rate, i.e. almost 20 times higher than water tracer does. The effect of water saturation is also very strong for Na-22 with a decrease of $D_e$ values by a factor of 235 from 0 to 9 MPa of suction, while water tracer shows a smaller reduction by a factor of 8, like for illite. Interestingly, $R_d$ values also display a sharp decrease from 13 and 12.5 mL/g at 0 and 1.9 MPa down to 1.3 mL/g at 9 MPa.

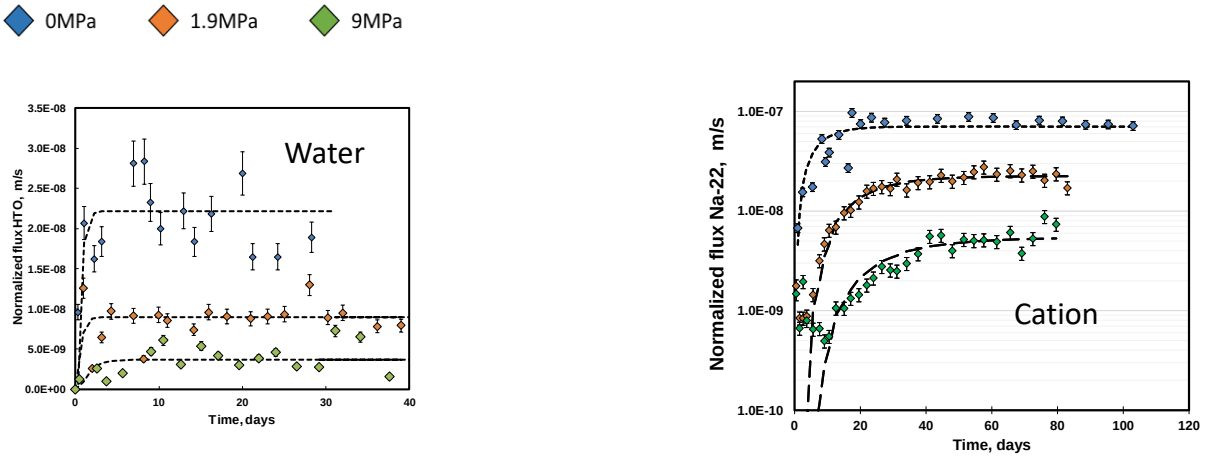


*Figure 3: Normalized diffusive fluxes for HTO and $^{22}Na^+$ through compacted vermiculite sample, at three suction levels of resp. 0, 1.9 and 9 MPa.*

## Discussion

To go further in discussion, the $D_e$ over $D_0$ ratio, i.e. the diffusivity was calculated for each species and reported as a function of the degree of water saturation of the clay-rich materials in Figure 4.

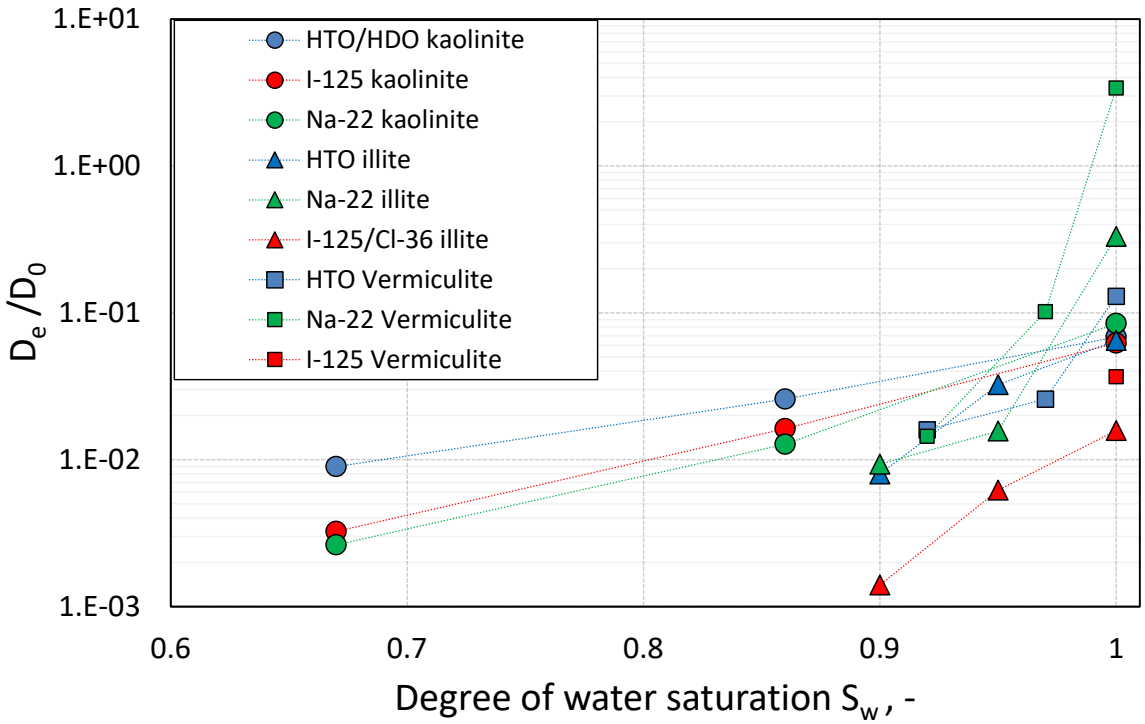


*Figure 4: Evolution of the diffusivity values for water, anion and cation tracers with degree of water saturation of compacted kaolinite, illite, and vermiculite.*

### Role of particle organization on water diffusivities

In the scope of this project, the interpretation of water diffusivities in water-saturated conditions was shown to be strongly dependent on the degree of preferential orientation of clay particles, also denoted $\langle P_2 \rangle$ order parameter. This parameter is very convenient as it can take a value between 0 for an isotropic particle organization and 1 for perfectly anisotropic organization with all particles having the same orientation. Based on X-ray scattering measurements (Dabat et al., 2019), the degree of particles orientation was shown to be a key parameter governing water diffusion in Na-illite and Na-vermiculite (Dabat et al., 2020; Asaad et al., 2021), similar to porosity value. According to these results and the $\langle P_2 \rangle$ values of ~0.05, 0.10, and 0.30 for Na-vermiculite, Na-illite, and Na-kaolinite, respectively, extreme care should be given concerning particle organisation when interpreting the role played by the nature of clay minerals on water and ion diffusions in partially water-saturated conditions. Moreover, a specific attention should be paid to this particle organization parameter in future modelling of transfer process of tracers in these media, especially for water-unsaturated conditions.

### Water tracer in kaolinite for partially water-saturated conditions: diffusion in vapor and liquid phases

Figure 4 shows for kaolinite that while the diffusivity of cation and anions similarly evolves when saturation degree decreases, water diffusivity decreases with a smaller extent. To interpret such a behaviour, a model accounting for the diffusion of water in both gas and liquid phases was developed. To do so, diffusion data obtained for anion, considered as inert species were used. This model was capable of correctly predicting water diffusive flux, especially at a low degree of saturation (67% saturation), for which the assumption

made for the occurrence of air phase continuity throughout the sample appears to be more relevant than at 86% saturation.

### Water tracer in vermiculite: role played by interparticle and interlayer porosities.

As shown in Figure 4, the water diffusivity for vermiculite decreases by the same factor, i.e. 8, as for illite from 0 to 9 MPa of suction. This suggests that the contribution of the interlayer volume in vermiculite on the traversing flux was small compared to the flux related to interparticle volume, given that Na-illite and Na-vermiculite have the same interparticle porosity.

### Behaviour of anion under partially water-saturated conditions

Figure 4 clearly reveals that the drop of the anion diffusivity is more pronounced for illite than for kaolinite, even though the value of the water saturation degree at 9 MPa is smaller in illite than in kaolinite. This is consistent with the role played by surface charges in illite, capable of inducing anionic exclusion, contrary to kaolinite. Thus, in partially-saturated conditions, the largest pores where anion species are mainly restricted are emptied, leading to strong drop of diffusivity.

### Diffusive behaviour of $^{22}Na^{+}$

Figure 4 shows at full-saturation a strong increase of the $^{22}Na^{+}$ diffusivity from the weakly charge clay, kaolinite ($D_e/D_0$ ($^{22}Na^{+}$) = 0,09), illite ($D_e/D_0$ ($^{22}Na^{+}$) = 0,3) and thus to vermiculite with a diffusivity value higher than unit ($D_e/D_0$ ($^{22}Na^{+}$) = 3.4). The enhanced diffusion process is operative in illite with a $K_D$ value of 2.2 mL/g and especially in vermiculite where interlayer porosity would played a major role (with a $K_D$ value equal to 13 mL/g). Interestingly, under partially–water saturated conditions, the drop of the $^{22}Na+$ diffusivity is only effective at 9 MPa in vermiculite, associated to a drop of $K_D$ value down to 1.3 mL/g, $K_D$ value very close to the illite one (1.5 mL/g). Such a convergence of diffusivity and $K_D$ values for illite and vermiculite at 9 MPa suggests a strong reduction of role played by interlayer porosity for controlling $^{22}Na^{+}$ diffusive rate, probably related to a more limited access to this porosity family at 9 MPa of suction.

## Conclusion

For water-saturated conditions, results confirm the influence of surface charge on ion diffusivity (i.e., effective diffusion coefficient over diffusion coefficient in bulk, $D_e/D_0$). In porous media made with no-charged kaolinite, water and ions behave in the same manner, while with media made with the two charged clay materials an enhanced diffusion for $^{22}Na^{+}$ and a reduction of diffusive rates for anionic species compared to those of water tracers have been measured. When the clayey materials are partially water-saturated, each type of tracer shows distinct evolution of their diffusivity. We observe a relatively low decrease in the extent of the diffusivity values for water tracers compared to solutes, suggesting that the contribution of water diffusing in the gaseous phase has to be considered in addition to that in the liquid phase. For cationic tracer, i.e., $^{22}Na^{+}$, diffusivity values show a significant decrease in porous media made with charged clayey materials when dehydrating, associated with a drop of the distribution ratio, $K_D$, suggesting a more limited access to charged surfaces. Lastly, partial dehydration would magnify the effect of anionic exclusion with a strong drop in iodide diffusivity.

## References

Appelo, C.A.J., Wersin, P., 2007.. Environ. Sci. Technol. 41, 5002–5007. https://doi.org/10.1021/es0629256

Andra, 2005. Argile: Évolution phénoménologique du stockage géologique, 2005.

Andra, 2016. Dossier d'options de sûreté, partie après fermeture (DOS-AF) {https://www.andra.fr/sites/default/files/2018-04/dossier-options-surete-apres-fermeture_0.pdf

Asaad, A., Hubert, F., Ferrage, E., Dabat, T., Paineau, E., Porion, P., Savoye, S., Gregoire, B., Dazas, B., Delville, A., Tertre, E., 2021.. Appl. Clay Sci. 207, 106089. https://doi.org/10.1016/j.clay.2021.106089

Asaad A., Hubert F., Dazas B., Razafitianamaharavo A., Brunet J., Glaus M. A., Savoye S., Ferrage E. & Tertre E., 2022. Appl. Clay Sci., 224, 106517. https://doi.org/10.1016/j.clay.2022.106517

Au, P.-I., Clode, P., Smart, R.St.C., Leong, Y.-K., 2015. Colloids Surf. Physicochem. Eng. Asp. 484, 354–364. https://doi.org/10.1016/j.colsurfa.2015.08.013

Bazer-Bachi, F., Tevissen, E., Descostes, M., Grenut, B., Meier, P., Simonnot, M.-O., Sardin, M., 2006. Phys. Chem. Earth Parts ABC 31, 517–522. https://doi.org/10.1016/j.pce.2006.04.015

Berthe, G., Savoye, S., Wittebroodt, C., Michelot, J.-L., 2011. Energy Procedia 4, 5314–5319. https://doi.org/10.1016/j.egypro.2011.02.512

Bourg, I.C., Tournassat, C., 2015. Chapter 6 - Self-Diffusion of Water and Ions in Clay Barriers, in: Tournassat, C., Steefel, C.I., Bourg, I.C., Bergaya, F. (Eds.), Developments in Clay Science. Elsevier, pp. 189–226. https://doi.org/10.1016/B978-0-08-100027-4.00006-1

Bucher, F., Müller-Vonmoos, M., 1989. Appl. Clay Sci. 4, 157–177. https://doi.org/10.1016/0169-1317(89)90006-9

Charlet, L., Alt-Epping, P., Wersin, P., Gilbert, B., 2017. Advances in Water Resources, 106, 39–59. https://doi.org/10.1016/j.advwatres.2017.03.019

Chipera, S.J., 2001. Baseline Studies of the Clay Minerals Society Source Clays: Powder X-ray Diffraction Analyses. Clays Clay Miner. 49, 398–409. https://doi.org/10.1346/CCMN.2001.0490507

Churakov, S.V., 2013. Environ. Sci. Technol. 47, 9816–9823. https://doi.org/10.1021/es401530n

Crank, J., 1975. The mathematics of diffusion, 2d ed. ed. Clarendon Press, Oxford Science Publication : New York.

Dabat, T., Porion, P., Hubert, F., Paineau, E., Dazas, B., Grégoire, B., Tertre, E., Delville, A., Ferrage, E., 2020. Appl. Clay Sci. 184, 105354. https://doi.org/10.1016/j.clay.2019.105354

Dabat, T., Hubert, F., Paineau, E., Launois, P., Laforest, C., Grégoire, B., Dazas, B., Tertre, E., Delville, A., Ferrage, E., 2019. Nat Commun 10, 5456. https://doi.org/10.1038/s41467-019-13401-0

Delage, P., Cui, Y.J., 2008. Geomech. Geoengin. 3, 1–11. https://doi.org/10.1080/17486020701868379

Descostes, M., Blin, V., Bazer-Bachi, F., Meier, P., Grenut, B., Radwan, J., Schlegel, M.L., Buschaert, S., Coelho, D., Tevissen, E., 2008. Appl. Geochem. 23, 655–677. https://doi.org/10.1016/j.apgeochem.2007.11.003

Faurel, M., 2012. Conception et mise en place d'expériences de diffusion de l'eau et de solutés dans des milieux poreux modèles d'argiles gonflantes. Université de Poitiers, Poitiers, France.

Foose, G.J., Benson, C.H., Edil, T.B., 2002. J. Geotech. Geoenvironmental Eng. 128, 391–403. https://doi.org/10.1061/(ASCE)1090-0241(2002)128:5(391)

Gieseking, J.E. (Ed.), 1975. Soil Components Vol. 2: Inorganic Components, 1st ed. Springer Verlag Berlin Heidelberg.

Glaus, M.A., Frick, S., Rossé, R., Loon, L.R.V., 2010. Geochim. Cosmochim. Acta 74, 1999–2010. https://doi.org/10.1016/j.gca.2010.01.010

Grathwohl, P., 1998. Modelling of Diffusion Processes, in: Diffusion in Natural Porous Media. Springer, pp. 43–81.

Gvirtzman, H., Gorelick, S.M., 1991. Nature 352, 793–795. https://doi.org/10.1038/352793a0

Hassan, M.S., Villieras, F., Gaboriaud, F., Razafitianamaharavo, A., 2006. J. Colloid Interface Sci. 296, 614–623. https://doi.org/10.1016/j.jcis.2005.09.028

Hendry, M.J., Solomon, D.K., Person, M., Wassenaar, L.I., Gardner, W.P., Clark, I.D., Mayer, K.U., Kunimaru, T., Nakata, K., Hasegawa, T., 2015. Geofluids 15, 381–386. https://doi.org/10.1111/gfl.12132

Katsumi, T., Benson, C.H., Foose, G.J., Kamon, M., 2001. Eng. Geol., Geoenvironmental Engineering 60, 139–148. https://doi.org/10.1016/S0013-7952(00)00096-X

Landais, P., 2006. J. Geochem. Explor. 88, 32–36. https://doi.org/10.1016/j.gexplo.2005.08.011

Le Crom, S., Tournassat, C., Robinet, J.Ch, Marry, V., 2022. J. Phys. Chem. C 2022, 126, 1, 647–654.

Lehikoinen, J., Carlsson, T., Muurinen, A., Olin, M., Salonen, P., 1995. MRS Proc. 412, 675. https://doi.org/10.1557/PROC-412-675

Maples, S.R., Andraski, B.J., Stonestrom, D.A., Cooper, C.A., Pohll, G., Michel, R.L., 2013. Vadose Zone J. 12, vzj2013.05.0080. https://doi.org/10.2136/vzj2013.05.0080

Marschall, P., Horseman, S., Gimmi, T., 2005. Oil Gas Sci. Technol. 60, 121–139. https://doi.org/10.2516/ogst:2005008

Melkior, T., Gaucher, E.C., Brouard, C., Yahiaoui, S., Thoby, D., Clinard, Ch., Ferrage, E., Guyonnet, D., Tournassat, C., Coelho, D., 2009. J. Hydrol. 370, 9–20. https://doi.org/10.1016/j.jhydrol.2009.02.035

Mermut, A.R., 2001. Clays Clay Miner. 49, 381–386. https://doi.org/10.1346/CCMN.2001.0490504

Minardi, A., Giger, S.B., Ewy, R.T., Stankovic, R., Stenebråten, J., Soldal, M., Rosone, M., Ferrari, A., Laloui, L., 2021. Geomech. Energy Environ. 25, 100210. https://doi.org/10.1016/j.gete.2020.100210

Motellier, S., Devol-Brown, I., Savoye, S., Thoby, D., Alberto, J.-C., 2007. J. Contam. Hydrol. 94, 99–108. https://doi.org/10.1016/j.jconhyd.2007.05.012

Nunn, J.A., Xiang, Y., Al, T.A., 2018. Appl. Geochem. 97, 93–101. https://doi.org/10.1016/j.apgeochem.2018.08.004

Rao, Z., Li, G., Liu, X., Liu, P., Li, H., Liu, S., Zhu, M., Guo, C., Ni, F., Gong, Z., Asghar, F., 2021. Minerals 11, 941. https://doi.org/10.3390/min11090941

Reinholdt, M.X., Hubert, F., Faurel, M., Tertre, E., Razafitianamaharavo, A., Francius, G., Prêt, D., Petit,S., Béré, E., Pelletier, M., Ferrage, 2013. Appl. Clay Sci 77-78, 18-32.

Savoye, S., Beaucaire, C., Grenut, B., Fayette, A., 2015. Appl. Geochem. 61, 41–52. https://doi.org/10.1016/j.apgeochem.2015.05.011

Savoye, S., Frasca, B., Grenut, B., Fayette, A., 2012. J. Contam. Hydrol. 142–143, 82–92. https://doi.org/10.1016/j.jconhyd.2012.10.003

Savoye, S., Imbert, C., Fayette, A., Coelho, D., 2014. Geol. Soc. Lond. Spec. Publ. 400, 579–588. https://doi.org/10.1144/SP400.9

Savoye, S., Lefevre, S., Fayette, A., Robinet, J.-C., 2017. Geofluids 2017, 1–17. https://doi.org/10.1155/2017/1683979

Savoye, S., Page, J., Puente, C., Imbert, C., Coelho, D., 2010. Environ. Sci. Technol. 44, 3698–3704. https://doi.org/10.1021/es903738t

Smiles, D.E., Gardner, W.R., Schulz, R.K., 1995. Water Resour. Res. 31, 1483–1488. https://doi.org/10.1029/94WR02013

Tertre, E., Savoye, S., Hubert, F., Prêt, D., Dabat, T., Ferrage, E., 2018. Environ. Sci. Technol. 52, 1899–1907. https://doi.org/10.1021/acs.est.7b05343

Tournassat, C., Steefel, C.I., 2019. Comput. Geosci. https://doi.org/10.1007/s10596-019-09845-4

van Brakel, J., Heertjes, P.M., 1974. Int. J. Heat Mass Transf. 17, 1093–1103. https://doi.org/10.1016/0017-9310(74)90190-2

Van Loon, L.R., Glaus, M.A., Müller, W., 2007. Appl. Geochem. 22, 2536–2552. https://doi.org/10.1016/j.apgeochem.2007.07.008

Van Loon, L.R., Soler, J.M., Müller, W., Bradbury, M.H., 2004. Environ. Sci. Technol. 38, 5721–5728. https://doi.org/10.1021/es049937g

Xiao, T., Xu, H., Moodie, N., Esser, R., Jia, W., Zheng, L., Rutqvist, J., McPherson, B., 2020. Water Resour. Res. 56, e2020WR027193. https://doi.org/10.1029/2020WR027193

# 2. Achievements with respect to project objectives - Conclusions

*Description of transport experiments based on mechanistic understanding (anion exclusion, surface diffusion, saturation degree, pore characteristics,…)*

The degree of particles orientation was shown to be a key parameter governing water diffusion in Na-illite and Na-vermiculite (Dabat et al., 2020; Asaad et al., 2021), similar to porosity value. According to these results and the $\langle P_2 \rangle$ values of ~0.05, 0.10, and 0.30 for Na-vermiculite, Na-illite, and Na-kaolinite, respectively, extreme care should be given concerning particle organisation when interpreting the role played by the nature of clay minerals on water and ion diffusions in partially water-saturated conditions. Moreover, a specific attention should be paid to this particle organization parameter in future modelling of transfer process of tracers in these media, especially for water-unsaturated conditions.

For water-saturated conditions, results confirm the influence of surface charge on ion diffusivity (i.e., effective diffusion coefficient over diffusion coefficient in bulk, $D_e/D_0$). In porous media made with no-charged kaolinite, water and ions behave in the same manner, while with media made with the two charged clay materials an enhanced diffusion for $^{22}Na^+$ and a reduction of diffusive rates for anionic species compared to those of water tracers have been measured.

When the clayey materials are partially water-saturated, each type of tracer shows distinct evolution of their diffusivity. A relatively low decrease is observed in the extent of the diffusivity values for water tracers compared to solutes, suggesting that the contribution of water diffusing in the gaseous phase has to be considered in addition to that in the liquid phase. For cationic tracer, i.e., $^{22}Na^+$, diffusivity values show a significant decrease in porous media made with charged clayey materials when dehydrating, associated with a drop of the distribution ratio, $K_D$, suggesting a more limited access to charged surfaces. Lastly, partial dehydration would magnify the effect of anionic exclusion with a strong drop in iodide diffusivity.

# Chapter 6: General Conclusions

Within the EURAD WP5 FUTURE project, tasks 2.1 and 2.3 deal with the mobility of radionuclides in compacted clay and the reversibility of sorption, respectively.

The objectives of these tasks are to enhance the quantitative and mechanistic understanding of the impact on radionuclide mobility wrt. effects of solution composition and speciation, surface charge and microstructural properties of argillaceous porous media.

A “bottom-up” approach was followed using three pathways: i) *From dispersed to compacted solids* (Are sorption data measured in dispersed systems applicable for compacted systems?), ii) *From single minerals to clay rocks* (Can we describe the sorption and transport behaviour of radionuclides in mineral assemblages/clay host rocks by adding up effects described by model developed for the main mineral components?) and iii) *From single radionuclide to multi-component chemical systems* (How does the presence of competing elements influence the mobility of the radionuclide under study?).

These schemes were applied to three main groups of elements/radionuclides: weakly sorbing (anionic Se-species), moderately sorbing (Ra, Ba), and strongly sorbing (transition metals and lanthanides/actinides) and on a selection of clay phases (pure minerals: illite, smectites, kaolinite and their mixtures: clay rocks: Opalinus Clay (OPA), Callovo Oxfordian Clay (COx), Boda Claystone Formation (BCF).

For various elements and species (Selenite, Ra, Ba, Cd, Zn, Uranyl, phosphate), new sorption data were established on single clay phases (illite, different smectites, kaolinite). The widely applied 2SPNE-SC/CE model had to be extended in single cases in terms of types of sites in order to match new experimental data on Na-illite&montmorilloinite, such as for $Ba^{2+}$ and $Ra^{2+}$. Selectivity coefficients for cation exchange at the planar surfaces were also measured in single cases (illite, FBEX bentonite and nontronite). Although these sites may have a subordinate role for the sorption of transition elements and representatives from the lanthanide and actinide series, these data are important in view of the assessment of mobile surface species, which may lead to enhanced diffusion of cationic radioelements.

A rather new field has been opened by the investigation of the sorption of phosphate on illite and its influence on the sorption of uranyl. Co-sorption of uranyl with phosphate was observed leading to enhanced $K_d$ values under acidic pH. While these data have been corroborated in detail with attenuated toral reflection (ATR) infrared spectroscopy measurement, quantitative thermodynamic models are not yet available.

For various types of radioelements, such as Se, Ba, Ra (and Sr), Zn and Eu, a rather consistent sorption behaviour between experiments using dispersed clay suspensions and compacted clay samples (single phases and natural clayrock samples) has been observed. Slight discrepancies were present in certain cases with natural rock samples. These may, however, be explained by differences in pore water composition or by the dynamics of sorption kinetics versus diffusion rates in experiments with compacted clay minerals. While the equilibrium solution can be adjusted in a targeted manner in experiments with disperse clay suspensions, the in-situ pore water composition in diffusion experiments using intact clay rock samples may even differ from synthetic pore waters in contact with diffusion samples. The experiments conducted as part of this project have made it clear how important it is to be able to compare the chemical conditions in the different types of experiments.

New methods were developed e.g. to derive in-situ sorption coefficients for intact clay rock samples. The results obtained from this project also highlighted the importance of the knowledge on sorption competition phenomena. For an appropriate assessment of in-situ sorption distribution coefficients, the competition of radioelements with the solutes of the intrinsic pore water plays a pivotal role. Sorption competition between representatives of various types of elements (e.g. between transition elements of same or different charge, or between lanthanides/actinides versus alkaline earth cations) has to be properly known. Results obtained from a single type of competitive interaction cannot be undeliberately transferred to different situations. A rather broad knowledge of competitive interactions and on various issues of transferability can be noted during the past years and in the course of this project.

The scarce pre-existing database for accessible porosity of differently charged anions in compacted clay minerals was improved by measuring anion exclusion of Se species which proves an increase in anion exclusion for bivalent ($SeO_4^{2-}$) vs monovalent anions ($I^-$). Surface diffusion of divalent transition metals in compacted illite has been demonstrated not only to be governed by solution characteristics, such as ionic strength, but also by the type of cations associated with the planar surfaces of illite.

A broad study of diffusion of variously charged radiotracers in compacted kaolinite, illite and vermiculite has shown that surface diffusion of cationic species and exclusion of anionic species is influenced in very different and special ways in cases of partial saturated conditions. A relatively low decrease is observed in the extent of the diffusivity values for water tracers compared to solutes, suggesting that the contribution of water diffusing in the gaseous phase has to be considered in addition to that in the liquid phase. For cationic tracer, i.e., $^{22}Na^+$, diffusivity values show a significant decrease in porous media made with charged clayey materials when dehydrating, associated with a drop of the distribution ratio, $K_D$, suggesting a more limited access to charged surfaces. Lastly, partial dehydration would magnify the effect of anionic exclusion with a strong drop in iodide diffusivity.

Spectroscopic and microscopic methods were applied in various cases for a corroboration of current concepts of uptake through characterisation of the solids (sorption sites) and identification of the aqueous and surface speciation of radionuclides (TEM, EDS, EXAFS, STEM-HAADF, ATR-FTIR, RAMAN), and transport processes (XANES, µ-XRF, LA-ICP-MS, TOF-SIMS/rL-SNMS, AMS). New methods were e.g. developed to measure diffusion profiles of various radiotracers in clay minerals or clay rocks at ultra-trace concentrations (TOF-SIMS/rL-SNMS, AMS). This is an important pre-requisite for an appropriate assessment of the diffusion behaviour of strongly sorbing radioelements from the lanthanide and actinide series.

Results obtained in the project provide convincing arguments that bottom-up schemes are applicable for the description of sorption processes albeit not always straightforward, as relevant underlying mechanisms and sorption competition aspects must be taken into account properly. The transferability of data and models has been established from dispersed to compacted systems and from single mineral to complex mineral assembly. New/missing data became available and were successfully fed into sorption models.

It is further demonstrated that mechanistic sorption models obtained from sorption studies can be applied in the interpretation of transport experiments if the pore water chemistry are properly taken into account.

Mechanistic understanding of anion exclusion and surface diffusion processes in saturated and partial saturated conditions matures and more and more high-resolution techniques become available which enable the measurement of diffusion patterns for highly sorbing radionuclides.